Proceedings of the 11th Virtual International Conference on Science, Technology and Management in Energy

Editor:
Velimirović, L. Z.

Publishers:
Complex System Research Centre, Niš, Serbia
Mathematical Institute of the Serbian Academy of Sciences and Arts, Belgrade, Serbia

Serbia, Belgrade, November 25-26, 2024

Editor
Velimirović, L. Z.

eNergetics 2025

11th Virtual International Conference on Science, Technology and Management in Energy

Proceedings

Publishers
Complex System Research Centre, Niš, Serbia
Mathematical Institute of the Serbian Academy of Sciences and Arts, Belgrade, Serbia

Serbia, Belgrade, November 24-25, 2025

Proceedings of the
11th Virtual International Conference
on Science Technology and Management in Energy

Serbia, Belgrade, November 24-25, 2025

Editor: Dr. Lazar Z. Velimirović
Mathematical Institute of the Serbian Academy of Sciences and Arts, Serbia

Technical Editor: Dr. Petar Vranić
Mathematical Institute of the Serbian Academy of Sciences and Arts, Serbia

Published by:
Complex System Research Centre, Niš, Serbia
Mathematical Institute of the Serbian Academy of Sciences and Arts, Belgrade, Serbia

Printed by:
Blue Copy, Niš, Serbia

Number of copies printed: 100
The publishing year: 2026

Printing of this edition has been financially supported by
The Ministry of Science, Technological Development and Innovation of the Republic of Serbia

ISBN-978-86-82602-07-1

CIP - Каталогизација у публикацији Народна библиотека Србије, Београд

620.9(082)(0.034.2)

VIRTUAL International Conference on Science Technology and Management in Energy (11 ; 2025 ; Beograd)
Energetics 2025 [Elektronski izvor] : proceedings / 11th Virtual International Conference on Science Technology and Management in Energy, Serbia, Belgrade, November 24-25, 2025 ; editor Velimirović, L.[Lazar] Z. - Niš : Complex System Research Centre; Belgrade : Mathematical Institute of the SASA, 2026 (Niš : Blue Copy). - 1 elektronski optički disk (CD-ROM) ; 12 cm

Sistemski zahtevi: Nisu navedeni. - Nasl. sa naslovne strane dokumenta. - Tiraž 100.
- Bibliografija uz svaki rad.

ISBN 978-86-82602-07-1 (CSRC)

a) Енергетика -- Зборници

COBISS.SR-ID 187432713

eNergetics 2025

11th Virtual International Conference on Science Technology and Management in Energy

Organizer:
Mathematical Institute of the Serbian Academy of Sciences and Arts

Co-organizers:

- Academy of Sciences and Arts of the Republika Srpska
- Faculty of Mining and Geology, University of Belgrade
- Faculty of Technical Sciences, University St. Climent Ohridski
- Complex System Research Centre COSREC

Supported by:
The Ministry of Science, Technological Development and Innovation of the Republic of Serbia

Program Committee

Chair:

Dr. Lazar Z. Velimrović, Mathematical Institute of the Serbian Academy of Sciences and Arts, Belgrade, Serbia

Members:

Prof. Dr. Zoran Stajić, Faculty of Electronic Engineering, Serbia

Prof. Dr. Detelin Markov, Faculty of Power Engineering and Power Machines, Bulgaria

Prof. Dr. Marko Serafimov, Faculty of Mechanical Engineering, Macedonia

Prof. Dr. Mileta Janjić, Faculty of Mechanical Engineering, Montenegro

Prof. Dr. Miomir Stanković, Mathematical Institute of the Serbian Academy of Sciences and Arts, Serbia

Prof. Dr. Tomislav Sekara, School of Electrical Engineering, Serbia

Prof. Dr. Enver Agić, Public Enterprise Electric Utility of Bosnia and Herzegovina, Bosnia and Herzegovina

Prof. Dr. Niko Majdandžić, Faculty of Mechanical Engineering, Croatia

Prof. Dr. Serkan Abbasoglu, Cyprus International University, Turkey

Prof. Dr. Bojan Srđević, Faculty of Agriculture, Serbia

Dr. Lenin Kanagasabai, PVP Siddhartha Institute of Technology, India

Prof. Dr. Abdelhak Djoudi, National Polytechnic School, Algeria

Dr. Elson Avallone, Federal Institute of Education, Science and Technology of São Paulo, Brazil

Prof. Dr. Zdravko Milovanović, Faculty of Mechanical Engineering, Bosnia and Herzegovina

Prof. Dr. Miloš Jelić, Research and Development Center Alfatec, Serbia

Prof. Dr. Zoran Markov, Faculty of Mechanical Engineering, Macedonia

Dr. Jovan Mikulović, School of Electrical Engineering, Serbia

Dr. Sasa Milić, Institute Nikola Tesla, Serbia

Prof. Dr. Krsto Miljanović, Agromediterranean Faculty, Bosnia and Herzegovina

Organizing Committee

Chair:

Dr. Petar Vranić, Mathematical Institute of the Serbian Academy of Sciences and Arts, Serbia

Members:

Prof. Dr. Miomir Stanković, Mathematical Institute of the Serbian Academy of Sciences and Arts, Serbia

Prof. Dr. Zoran Stajić, Faculty of Electronic Engineering, Serbia

Dr. Lazar Velimirović, Mathematical Institute of the Serbian Academy of Sciences and Arts, Serbia

Dr. Dusan Tatić, Mathematical Institute of the Serbian Academy of Science and Arts, Serbia

Dr. Jelena Velimirović, Mathematical Institute of the Serbian Academy of Sciences and Arts, Serbia

Dr. Ivana Petkovski, Mathematical Institute of the Serbian Academy of Sciences and Arts, Serbia

Dr. Radmila Janković, Mathematical Institute of the Serbian Academy of Science and Arts, Serbia

Dr. Danijela Protić, Serbian Armed Force, Serbia

M.Sc. Vladimir Antic, Serbian Armed Force, Serbia

Table of Contents

eNergetics 2025
DOI: https://doi.org/10.5281/zenodo.18615593

Original Scientific Article

Numerical Study of Thermo-hydraulic Performance of Nanofluid Flow in Microchannels: Effect of Adding Micromixer

Soufyane Djellouli[1], El Ghalia Filali[2], Sid Ali Si Salah[3], Hazem Meharzi[4]

[1,2,3,4]University of Science and Technology Houari Boumedienne, Algiers, Algeria

[1]djellouli.gm@gmail.com, [2]eg_filali@yahoo.fr, [3]ssi-salah@usthb.dz, [4]hmeharzi19@gmail.com

Abstract—**In the present study, the forced convection of Al2O3-water nanofluid in a square mini-channel design (1mm x 1mm) with and without micromixers has been numerically investigated. Three vertical baffles attached to the wall act as micromixers to enhance the heat transfer process. The upper and lower walls are subjected to a constant heat flow. The effect of the Reynolds number, Re = 10, 30, 60, 100 and 150 was studied in parallel with the addition of nanoparticle volume fraction, from 0 to 4% and from 10 to 20%. Different geometric configurations of the micromixers were tested. The CFD code, which is based on the finite volume method, was used to solve the governing equations. The SIMPLER algorithm was employed to handle the pressure-velocity coupling. The results showed that the presence of micromixers and a higher volume fraction of nanoparticles increased the local and average Nusselt numbers. However, this increase was accompanied by a deterioration in the flow dynamics due to an increase in the friction coefficient. It was also observed that the size of the vortices created behind the micromixer increases with increasing Re number and micromixer height.**

Keywords - minichannel, laminar flow, nanofluid, micromixer, heat transfer enhancement.

I. INTRODUCTION

Heat transfer is the basis of many industrial processes that are part of our daily lives. Intensifying this exchange and improving efficiency have become major issues in the industrial world. In the face of these energy challenges, developing processes for better energy management presents new technological opportunities.

Mini- and microchannels have been studied for decades, mainly for the cooling of microelectronic devices. Reference [1] were pioneers in this field, working on high performance heat sinks for cooling integrated circuits as early as 1981.

Reference [2] have conducted a numerical study of the three-dimensional flow and heat transfer of a fluid in a rectangular microchannel heat sink. They found that the length of the flow development zone is influenced by the Reynolds number. They noticed that the highest temperature typically occurs at the surface of the heated base of the heat sink, close to the outlet of the channel. They also found that the temperature increases along the flow direction in both the fluid regions and solid and can be estimated by a linear relationship.

At the same time, a new technology aimed at improving the thermal properties of heat transfer fluids was introduced by [3], called “nanofluids”. Nanoscience is the study of matter's structure at the molecular, and therefore nanometric, scale. with the aim of innovation in a large range of fields, including the environment, energy production and storage, cooling of electronic components by means of single or two-phase flows in microchannels, biology, medical diagnosis, water treatment, modern medicine, and so on. The high thermal conductivity of

ISBN: 978-86-82602-07-1

nanofluids makes them potential candidates for replacing carrier fluids. However, a number of limitations have been identified that could reduce their performances.

Reference [4] studied heat transfer by forced convection in a fluid containing metal oxide particles Al_2O_3 (13 nm) and TiO_2 (27 nm). The measurements were carried out in a heated tube at constant flow density, in a turbulent regime. They showed that the heat transfer coefficient was 75% higher than that of water.

Reference [5] numerically studied the hydrodynamics and thermal properties of nanofluids in a heated tube, for the laminar and turbulent regimes. They demonstrate that adding nanoparticles to the base fluid enhances heat transfer. They report that the heat transfer coefficient increases by 80% for the nanofluid (ethylene glycol/Al_2O_3) and by 60% for the nanofluid (water/Al_2O_3) for a volume fraction of Al_2O_3 nanoparticles of 10%.

Experimental work by [6] aimed to explore the benefits of cooling a water- Al_2O_3 nanofluid through a 0.5 mm diameter of a mini cylindrical channel subjected to a uniform heat flux. For laminar flow, the study shows that the relatively high thermal conductivity of the nanoparticles increases the heat transfer coefficient. The highest heat transfer coefficients were obtained in the tube inlet zone. This increase is less pronounced in the fully established zone, indicating that nanofluids have a substantial impact on the development of the thermal boundary layer. Conversely, higher nanoparticle concentrations lead to greater sensitivity to heat flow. However, despite this increase, the cooling rate of the nanoparticles remains rather low due to the increase in axial temperature.

Reference [7] experimentally studied the laminar flow of a nanofluid (water-TiO_2) in a mini cylindrical channel under the effect of a constant heat flux. With increasing nanoparticle concentration and Reynolds number, both the heat transfer coefficient and the Nusselt number rise. The authors suggest that the migration phenomenon and the resulting Brownian motion disturb the boundary layer, which explains the increase in the transfer coefficients.

Reference [8] experimentally studied the convective heat transfer of a nano-fluid consisting of water and alumina flowing through a copper tube in laminar flow. They showed a significant improvement in heat transfer by forced convection. This increase was particularly significant in the inlet region.

Reference [9] conducted an experimental study to investigate the thermal conductivity of three nanofluids containing copper oxide, zinc oxide and aluminum oxide nanoparticles dispersed in a mixture of 60% ethylene and 40% water glycol through a mini channel of 0.3 mm diameter. The volume concentration of nanoparticles varied between 0 and 10%. It was discovered that thermal conductivity increased in proportion to both rising volume concentration and rising temperature.

Reference [10] carried out an experimental study of the behavior of a nanofluid (water-Al_2O_3) with respect to increasing heat transfer. The flow takes place in a closed system designed to cool a 60mm x 60mm x 75mm microprocessor. A nanoparticle concentration of 6.8% resulted in a 40% increase in heat transfer.

Reference [11] numerically analyzed laminar flow in silicon microchannels to determine the heat transfer characteristics of the nanofluid (water-alumina). They observed an improvement in the performance of the heat sinks, which became more pronounced as the nanoparticle concentration increased.

Reference [12] presented the results of an experimental study investigating the heat transfer and flow characteristics of a nanofluid (water/Al_2O_3) through a circular microchannel of 0.5 mm diameter. The results show that the Nusselt number for the nanofluid is higher than for demineralized water and increases with Reynolds number and nanoparticle concentration

Various models have been developed to explain the remarkable improvement in convective transfer due to the addition of nanoparticles. However, a comparison of these models with experiments carried out on nanofluids containing different types of nanoparticles and carrier fluids, shows that the models do not satisfactorily approximate the results obtained. Available measurements of the thermal conductivity of different nanofluids are not consistent. Further experiments are needed to understand the phenomena occurring in nanofluids. Clearly, it is essential to consider the variation in the thermophysical properties of nanofluides as a function of temperature in simulations. “Passive” heat exchange improvements are reaching their limits, so new

optimization strategies need to be explored such as the use of micromixers.

Reference [13] carried out a numerical study to investigate the heat transfer of an Al_2O_3/water nanofluid flow between two parallel plates with and without micromixers. Two micromixers are placed on the bottom and top walls, respectively, under constant temperature conditions. The effect of various parameters such as distance, height and order of micromixer placement was studied. The results demonstrate that the presence of micromixers, together with an increase in Reynolds number and volume fraction of the nanoparticle, was responsible for an increase in heat transfer and friction coefficients. The author finds that the main mechanism for enhancing heat transfer or mixing would be the recirculation zones created behind the micromixer. The size of these zones increases with increasing Reynolds number and micromixer height.

The numerical study by [14] focused on forced convection of nanofluid (Ca-CuO) in a two-dimensional microchannel with micromixers (arranged in staggered rows). The Reynolds number range was 10, 30, 60, 100 and 150. The simulation results showed that the presence of the micromixers and the increase in Reynolds number, together with the increase in nanoparticle concentration, led to an increase in the Nusselt number. The size of the vortices created in the flow after the micromixers are responsible for the increased mixing and hence transfer.

The present study investigates the effect of a baffled micromixer on the flow and heat transfer of a nanofluid in a microchannel. The effect of various geometric and flow parameters, such as baffle height and arrangement, nanoparticle volume fraction, and Reynolds number, has been studied.

Simulations for Reynolds numbers less than 800 were performed. But only results for Reynolds numbers below 150 were presented. Experimental and industrial studies (Kandlikar, Garimella, Tuckerman & Pease) show that the maximum Reynolds number used in industrial microchannels does not exceed 1000. Above this value, pressure losses become prohibitively high and the transition to turbulence is unstable.

II. Geometrical Configuration and Boundary Conditions

Fig. 1 illustrates the geometric configuration of the problem under consideration. It consists of a square mini-channel of side H = 1mm and length L = 50mm, equipped with a micromixer of variable height h = 0.2mm, 0.3mm, 0.5mm and 0.65mm. The micromixers, staggered on the lower and upper walls, are separated by a variable distance "s".

The nanofluid in this study is composed of Al_2O_3 nanoparticles and water with a volume concentration varying from 0% to 20%. The inlet velocity *Ue* is defined by the Reynolds number. The pressure condition is assumed to be constant at the outlet (Fig. 2).

A constant heat flux of $50000 Wm^{-2}$ is experienced by the bottom and top walls, while the side walls are adiabatic.

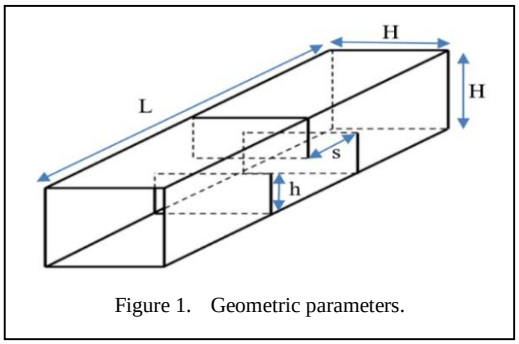

Figure 1. Geometric parameters.

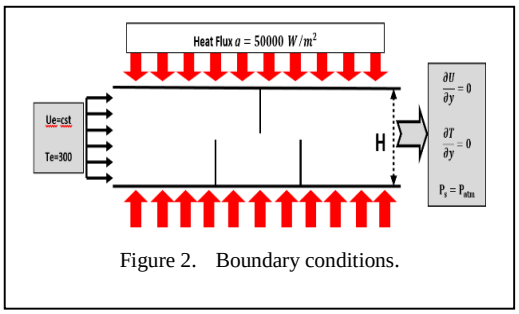

Figure 2. Boundary conditions.

III. Governing Equations

This is in accordance with the assumptions concerning ultra-fine particles (those measuring less than 100 nm) and the absence of slippage between the discontinuous nanoparticle phase and the continuous liquid phases, it may further be assumed that the resulting particle-liquid mixture is to be regarded as a conventional, single-phase fluid. So that, we add the following assumptions:

- Newtonian and incompressible fluid.
- A laminar and steady state flow.
- Thermo-physical properties of fluid vary with temperature. However, other properties are assumed to be constant and evaluated at the fluid inlet temperature.
- Negligible radiative heat transfer, surface tension, and gravity.

The following formulae are used:

$$\frac{\partial(u_i)}{\partial x_i} = 0, \quad (1)$$

$$\frac{\partial(u_i u_j)}{\partial x_i} = -\frac{1}{\rho_{nf}}\frac{\partial P}{\partial x_j} + \nu_{nf}\frac{\partial}{\partial x_i}\left(\frac{\partial u_j}{\partial x_i} + \frac{\partial u_i}{\partial x_j}\right), \quad (2)$$

$$\frac{\partial T}{\partial x_i} = \frac{1}{(\rho C_p)_{nf}}\left(\frac{\partial}{\partial x_i}\left(\kappa\frac{\partial T}{\partial x_i}\right)\right), \quad (3)$$

where "ρ" represents density, "υ" defines kinematic viscosity, "Cp" is specific heat capacity, and "κ" denotes thermal conductivity. The pressure and temperature are represented by P and T, respectively and "*nf*" represents nanofluid induce.

IV. Physical Properties of the Nanofluids

The thermo-physical properties are measured at the reference inlet temperature T = 300K and are given in Table I.

A. Density Model ρ_{nf}

The density of nanofluid is often predicted from the mixing law using the Pak relation [15].

The indices used in the formulas below (*p, f,* and *nf*) correspond respectively to particles, base fluid, and nanofluid.

$$\rho_{nf} = (1-\varphi)\rho_f + \varphi\,\rho_p, \quad (4)$$

φ: present the volume fraction of the solid.

TABLE I. Hysical properties of water and AL_2O_3 nanofluid (300 K).

ϕ(%)	ρ (kg/m^3)	μ (10^{-3}Pa.s)	K (W/m.K)	Cp (J/Kg.K)
Pur water	998.2	10-3	0.6001	4182
Al_2O_3	3970.0	/	40	765
0.3 % Al_2O_3	1007.1	1.009	0.6006	4142
0.7 % Al_2O_3	1019	1.019	0.6112	4089
1 % Al_2O_3	1027.9	1.027	0.6115	4050
2 % Al_2O_3	1057.6	1.052	0.6121	3925

B. Specific Heat Model Cp

Reference [16] employed the formula below: Brinkman's formula completes Einstein's model up to a volume concentration of less than 4%. Nevertheless, for low volume fractions, Brinkman's relationship leads exactly to

$$(\rho C_p)_{nf} = (1-\varphi)(\rho C_p)_f + \varphi(\rho C_p)_p. \quad (5)$$

C. Dynamic Viscosity Model μ

Reference [17] calculated the dynamic viscosity of a nanofluid for a combination including dilute suspensions of spherical and solid small particles as follows:

$$\mu_{nf} = \mu_f(1 + 2.5\varphi). \quad (6)$$

Since then, Einstein's formula has been empirically validated and is considered adequate for extremely dilute suspensions of spherical and solid. It should be demonstrated that this model does not take into account particle size or particle interactions.

D. Thermal Conductivity Model κ

The first model for determining the thermal conductivity of a suspension containing particles was developed by [18] and is used to calculate the thermal conductivity as follows:

$$k_{nf} = \frac{k_p + 2.k_f + 2(k_p - k_f)\varphi}{k_p + 2.k_f - 2(k_p - k_f)\varphi}k_f. \quad (7)$$

V. Numerical Method And Meshing

The entire domain is covered by a tetrahedral mesh (Fig. 3). The micromixer zone is refined as it allows to accurately capture pressure, velocity and temperature gradients. The CFX code is employed to solve the governing equations. The simpler method solves the pressure-velocity coupling problem. The conservation scheme is achieved using a pressure-based solver, while the energy equations and momentum are discretized using the second-order upwind technique. The numerical calculation is thermally convergent when the residuals of the governing equations are less than 10^{-7}.

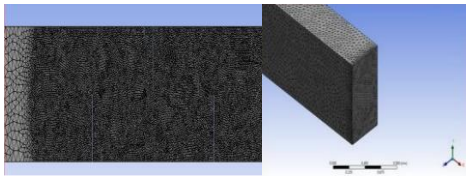

Figure 3. Mesh refined at the micromixer.

VI. Results and Discution

A. *Effect of Micromixer Adding*

This section reports the numerical results of flow characteristics and heat transfer in the presence of a micromixer. The micromixer, h = 0.5 H, is placed on the inner bottom wall of the mini-channel, at a distance (x = 35mm) from the inlet. The choice of location is dictated by the need to avoid the dynamic and thermal settling zone. Nanofluid concentration is fixed at 2%.

Fig. 4 shows the velocity profiles in the proximity of the micromixer. A sharp drop in velocity can be seen near the wall, at the level of the micromixer. An increase in the center of the mini-channel ensures mass conservation by

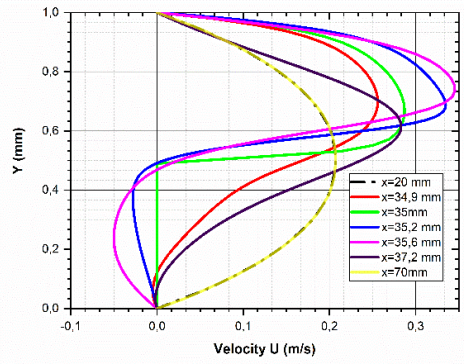

Figure 4. Velocity profiles at different cross-sections around the micromixer Geometric parameters.

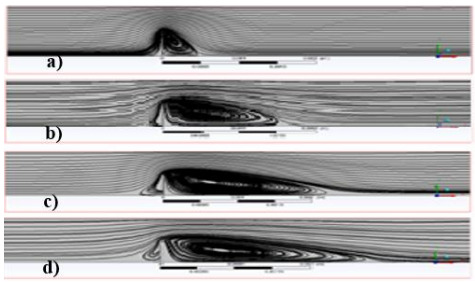

Figure 5. The effect of Re on flow pattern, h = 0.5 H, φ = 2% ; a) Re = 10; b) Re = 60; c) Re = 100; d) Re = 150.

compensating for the decrease in velocity. The drop in velocity near the wall is essentially due to the blocking of the flow at this level caused by the presence of the micromixer. As we move downstream, we can observe that the increase in velocity at the center of the mini-channel slows down. A rotational movement can also be observed upstream and downstream of the micromixer, with negative velocity values appearing due to fluid recirculation. We also note the existence of a stagnation point just upstream of the micromixer, represented by a zero value for the axial velocity.

Fig. 5 shows the effect of the micromixer on the flow pattern for various Reynolds numbers. The presence of the micromixer tightens the flow lines. Cold particles in the nanofluid near the bottom wall of the mini-channel are drawn towards the center of the channel, increasing heat transfer. There is a recirculation zone downstream of the micromixer. This zone increases in size with the Reynolds number. As the Reynolds number increases, the vortex behind the lower baffle forces the flow towards the wall more than at lower Reynolds numbers, creating a small recirculation zone upstream of the micromixer (Fig. 5c). The above flow pattern is expected to increase both the mixing rate and the heat transfer.

It is clear that the presence of a micromixer increases the friction coefficients and local heat transfer. This increase in heat transfer is proportional to the Reynolds number Fig. 6. Increasing the Reynolds number accelerates the rotational motion of the vortices, thereby augmenting the convective heat transfer and decreasing the near wall temperature. The formation of vortices appears to be the reason of the increase in convective heat transfer. It should be mentioned that at higher Reynolds numbers

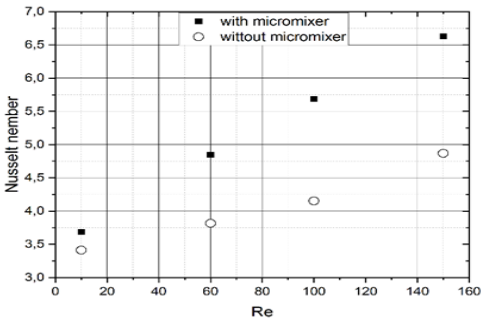

Figure 6. The effect of Re on Nusselt number geometric parameters.

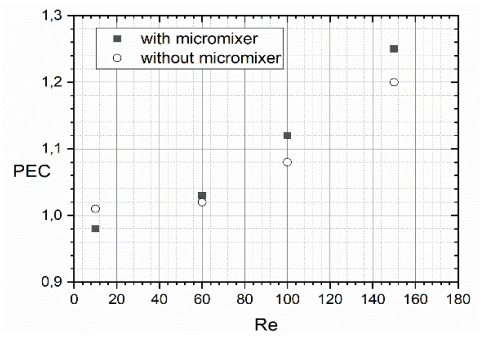

Figure 7. Performance Evaluation Criteria (PEC) vs Re.

the difference between the mean Nusselt values seems to become more significant.

The effect of adding micromixer on heat transfer and pressure loss is evaluated using the performance evaluation criteria (PEC). This is calculated according to equation [19]:

$$PEC = \left(Nu_{num} / Nu_{the} \right) \Big/ \left(\Delta P_{num} / \Delta P_{the} \right)^{1/3} . (6)$$

Fig. 7 shows the evolution of the PEC as a function of the Reynolds number for a concentration φ = 2%. An increase in the PEC is observed with the addition of the micromixer, particularly for high Reynolds numbers.

B. Effect of the Micromixer Height

Figs. 8 and 9 illustrate the streamlines and isotherms, respectively, corresponding to micromixer-to-microchannel height ratios of 0.2, 0.3, 0.5 and 0.65. It can be seen that a vortex is always present after the micromixer. The strength of the vortex is governed by the dimensions of the micromixer. As the height of the micromixer increases, so does the size of the vortex. The vortex stretches and takes on

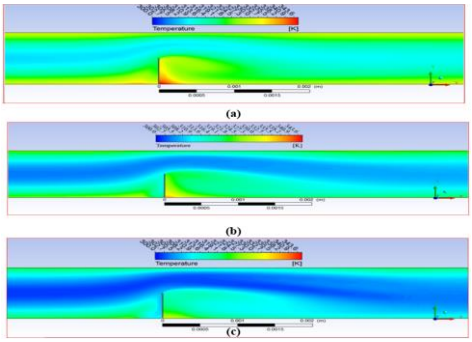

Figure 8. The effect of micromixer height on isotherms, Re = 100, φ= 2% ; a) h=0,2H; b) h=0,3H; c) h=0,5H; d) h=0,65H;Geometric parameters.

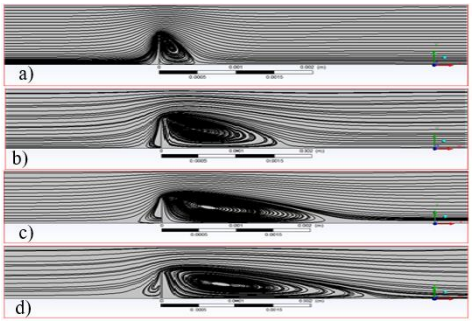

Figure 9. The effect of micromixer height on flow pattern, Re = 100, φ= 2% ; a) h=0,2H; b) h=0,3H; c) h=0,5H; d) h=0,65H.

significant proportions at high micromixer heights. The slope of the streamlines towards the bottom wall rises and a small recirculation zone begins to form upstream of the micromixer. The attachment line extends downstream to values greater than the micromixer size.

The increase in Reynolds number also affects temperature values. Fig. 9 shows isotherms for different micromixer heights.

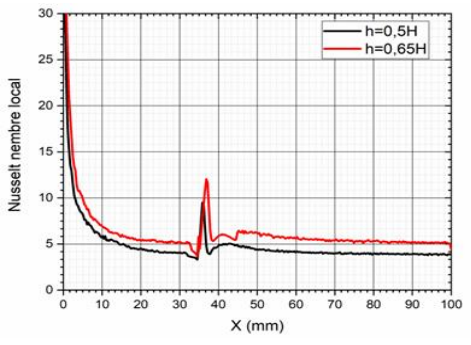

Figure 10. Evolution of the local Nusselt number along the microchannel; Re = 100; φ= 2%.

Fig. 10 shows the heat transfer coefficient distribution for two micromixer heights on the bottom wall. The Nusselt number has the greatest value at the channel entrance due to the high temperature gradients and decreases in the flow direction. We can see that the Nu number decreases from the inlet to the micromixer location. It is obvious that the heat transfer is increased with the height of the micromixer.

C. *Effect of Adding Three Equidistant Micromixers in Staggered Rows*

In this section, we analyze the effect of placing 3 micromixers of the same height (h = 0.5H), on improving heat transfer in a microchannel. The three micromixers are placed at equal distance h. The first micromixer is placed after the dynamic developed zone. The streamlines in Fig. 11 show the formation of vortices after each micromixer. The size of these vortices increases with increasing Reynolds number. The largest vortex is observed after the 3rd micromixer for all Reynolds numbers. The same observations were made by [13] and [14].

As the Reynolds number increases (Re = 100), the vortex behind the first micromixer pushes the streamlines upwards, creating a small vortex in front of the second micromixer. This configuration has also been reported by [13]. Better transfer is expected for this configuration. We also note the presence of a greater number of vortices at higher Reynolds numbers. In fact, at a Reynolds number of 150, we observe the formation of a new vortex in the upper part of the microchannel.

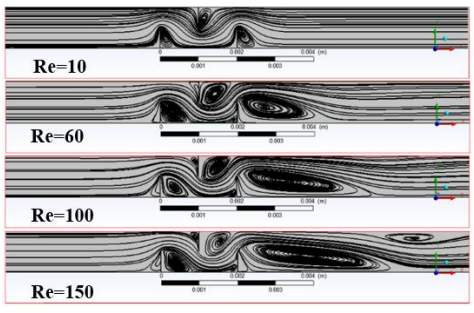

Figure 11. The effect of Reynolds number on flow pattern; φ = 2%.

D. *Effect of the Location of 3 Non-Equidistant Micromixers Placed in Staggered Rows*

The smallest gap produces the highest velocity, Fig. 12, while the temperature decreases as the gap increases (up to a certain ratio). The heat transfer rate decreases as the gap

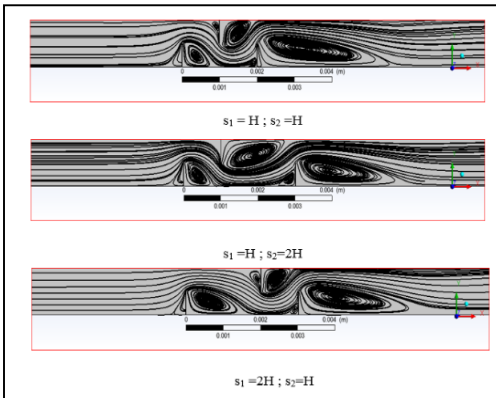

Figure 12. The effect of space between micromixer on flow.

between the micromixers increases, for all values of the Reynolds number. This was also found by [13]. As the gap increases, additional vortices are formed, which affect the temperature distribution.

The average Nusselt number is calculated for the different spacing values, Table II. The highest *Nu* values are obtained at the smallest spacing.

TABLE II. NUSSELT VALUES FOR FOR THE DIFFERENT SPACING VALUES.

Configuration	Average Nusselt number
s_1=H ; s_2=H	6.00
s_1=H ; s_2=2H	5.92
s_1=2H ; s_2=H	5.64

VII. CONCLUSION

In microchannel heat exchangers (electronic microcoolers, chemical microreactors, automotive or aerospace cooling systems), laminar flow simplifies design, pressure losses remain manageable, and heat transfer is improved by optimization techniques (grooves, fins, nanofluids, etc.).

This study focuses on the heat transfer and flow of an $Al2O_3$/water nanofluid in a square microchannel, with and without micromixers. The study examined nanoparticle volume fractions ranging from $\phi = 0$ to $\phi = 4\%$, in conjunction with base fluid Reynolds numbers of Re = 10, 60, 100, 150. Three micromixer spacings and four micromixer heights were selected and investigated. The results show that there is a recirculation zone downstream of the micromixer. The size of this zone increases with Reynolds number and decreases with ϕ. It is clear that the presence of baffles increases the local heat transfer. This influence is increased with

increasing the Re number. As the Reynolds number increases, the recirculation zone of the micromixer becomes larger and the distance between the reattachment point decreases.

When the distance between the baffles is not sufficient for recirculation to occur, increasing the micromixer distance will reduce the *Nu* number.

The size of the recirculation zone increases with micromixer height. Heat transfer was increased with baffle height and nanoparticle volume fraction.

REFERENCES

[1] Tuckerman, D. B., & Pease, R. F. W. (1981). High-performance heat sinking for VLSI. *IEEE Electron Device Letters*, *2*(5), 126–129.

[2] Lee, J., & Mudawar, I. (2007). Assessment of effectiveness of nanofluids for single-phase and two-phase heat transfer in micro-channels. *International Journal of Heat and Mass Transfer*, *50*(3–4), 452–463.

[3] Choi, S. B., Barron, R. F., & Warrington, R. O. (1991). Fluid flow and heat transfer in microtubes. In *Micromechanical Sensors, Actuators and Systems, ASME DSC*, *32*, (pp. 123–134).

[4] Pak, B. C., & Cho, Y. I. (1998). Hydrodynamic and heat transfer study of dispersed fluids with submicron metallic oxide particles. *Experimental Heat Transfer*, *11*(2), 151–170.

[5] Maiga, S. E. B., Nguyen, C. T., Galanis, N., & Roy, G. (2004). Hydrodynamic and thermal behaviours of a nanofluid in a uniformly heated tube. *WIT Transactions on Engineering Sciences*, *46*.

[6] Lee, J., & Mudawar, I. (2007). Assessment of the effectiveness of nanofluids for single-phase heat transfer in microchannels. *International Journal of Heat and Mass Transfer*, *50*(3–4), 452–463.

[7] Murshed, S. M. S., Leong, K. C., & Yang, C. (2005). Enhanced thermal conductivity of TiO2-water based nanofluids. *International Journal of Thermal Sciences*, *44*(4), 367–373.

[8] Wen, D., & Ding, Y. (2004). Experimental investigation into convective heat transfer of nanofluids at the entrance region under laminar flow conditions. *International Journal of Heat and Mass Transfer*, *47*(24), 5181–5188.

[9] Vajjha, R. S., & Das, D. K. (2009). Experimental determination of thermal conductivity of three nanofluids and development of new correlations. *International Journal of Heat and Mass Transfer*, *52*(21–22), 4675–4682.

[10] Nguyen, C. T., Desgranges, F., Roy, G., Galanis, N., Maré, T., Boucher, S., & Angue Mintsa, H. (2007). Temperature and particle-size dependent viscosity data for water-based nanofluids – Hysteresis phenomenon. *International Journal of Heat and Fluid Flow*, *28*(6), 1492–1506.

[11] Bhattacharya, P., Samanta, A. N., & Chakraborty, S. (2009). Numerical study of conjugate heat transfer in rectangular micro-channel heat sink with Al2O3/H2O nanofluid. *International Journal of Heat and Mass Transfer*, *52*(7–8), 1323–1333.

[12] Zhang, H., Shao, S., Xu, H., & Tian, C. (2013). Heat transfer and flow features of Al2O3-water nanofluids flowing through a circular micro-channel – Experimental results and correlations. *Applied Thermal Engineering*, *61*(2), 86–92.

[13] Islami, S. B., Dastvareh, B., & Gharraei, R. (2013). Numerical study of hydrodynamic and heat transfer of nanofluid flow in microchannels containing micromixer. *International Communications in Heat and Mass Transfer*, *43*, 146–154.

[14] Ababaei, A., Abbaszadeh, M., Arani, A. A. A., & Sharifabadi, A. A. (2017). MHD forced convection and entropy generation of CuO-water nanofluid in a microchannel considering slip velocity and temperature jump. *Journal of the Brazilian Society of Mechanical Sciences and Engineering*, *39*(3), 775–790.

[15] Pak, B. C., & Cho, Y. I. (1998). Hydrodynamic and heat transfer study of dispersed fluids with submicron metallic oxide particles. *Experimental Heat Transfer*, *11*(2), 151–170.

[16] Xuan, Y., & Roetzel, W. (2000). Conceptions for heat transfer correlation of nanofluids. *International Journal of Heat and Mass Transfer*, *43*(19), 3701–3707.

[17] Yu, W., & Choi, S. U. S. (2003). The role of interfacial layers in the enhanced thermal conductivity of nanofluids: A renovated Maxwell model. *Journal of Nanoparticle Research*, *5*, 167–171.

[18] Maxwell, J. C. (1873). *Treatise on electricity and magnetism*. Clarendon Press.

[19] Zhu, Q., Chang, K., Chen, J., Zhang, X., Xia, H., Zhang, H., Wang, H., Li, H., & Jin, Y. (2020). Characteristics of heat transfer and fluid flow in microchannel heat sinks with rectangular grooves and different shaped ribs. *Alexandria Engineering Journal*, *59*(6), 4593–4609.

eNergetics 2025
DOI: https://doi.org/10.5281/zenodo.18615639

Review Scientific Article

Preventive Maintenance and Reliability Analysis in Transmission Lines: A Review

Karla Paloma Belarmino de Souza[1], Rogério Santana Peruchi[2], Luiz Moreira Coelho Junior[3]

[1,2,3]Federal University of Paraíba (UFPB), João Pessoa, Brazil

[1]karla.belarmino@academico.ufpb.br, [2]rsp@academico.ufpb.br, [3]luiz@cear.ufpb.br

Abstract—**Improvements in asset maintenance management enhance the reliability and ensure the availability of electricity transmission services, while also extending the lifespan of equipment. Positive impacts are achieved through the identification and correction of wear, resulting in greater energy efficiency and reduced losses during transmission. Transmission lines (TL) are essential components of the system and are constantly exposed to hostile environments and adverse weather conditions, making them more susceptible to outages caused by factors that are difficult to control. This article presents a review of the impacts of preventive maintenance on the reliability of transmission lines. A systematic literature review was conducted, including bibliometric analysis and content exploration of the selected articles. The analyses showed that studies integrating TL reliability with maintenance execution and risk analysis began in 1969; however, it was only from 2007 onward that the topic started to be addressed more frequently by researchers. The countries with the highest contributions in publications were China, Brazil, Iran, the United States, and India. It was found that preventive maintenance in TL involves a wide range of applied techniques and technologies. Reliability analysis is a more recent topic, yet already widely discussed and researched. The results of this work provided a broad overview of the evolution of research on preventive maintenance execution and reliability analysis in transmission lines and may support the development of new studies focused on this subject.**

Keywords - systematic literature review, equipment condition, failures.

I. INTRODUCTION

Transmission lines extend for several kilometers and are exposed to various environmental conditions over long periods. Therefore, they are subject to natural events as well as external damage. Consequently, transmission lines have a higher likelihood of failure, and when a failure occurs, it leads to losses in several aspects and at varying degrees [1]. Preventive maintenance improves reliability, operational availability, and system life-cycle costs by reducing the risk of potential costly and untimely failures [2]. Therefore, it is necessary to develop a concrete procedure for assessing the condition of TL to determine the actual risk to which they are exposed [3].

Proper risk management requires knowledge of the equipment's condition, as well as the impact of maintenance and operations on the probability of failure. It also requires supporting information systems and business processes that enable risk mitigation through inspection, maintenance, operations, replacement, and system modifications [4]. Transmission lines are composed of various types of components with different functions, including insulators, towers, and conductors. Due to the complex terrain of the external environment and volatile weather conditions, these components may be frequently damaged, which can lead to local power outages, large-scale blackouts, and even catastrophic accidents, such as wildfires in forested areas [5].

Maintenance can be classified as either preventive or corrective. When narrowing the methods applied to transmission lines, there is a

ISBN: 978-86-82602-07-1

greater focus on preventive maintenance to maintain high asset availability. One of the motivations for this approach lies in the costly penalties imposed by regulatory agencies in cases of unplanned outages. Preventive maintenance can be scheduled based on different approaches, such as time-based maintenance, condition-based maintenance, and reliability-centered maintenance strategies [6].

In [7], a solution was proposed for identifying common faults occurring in transmission lines, followed by a suggestion of the appropriate maintenance methodology, using the artificial neural network method and the live-line maintenance technique for fault pre-identification and subsequent predictive maintenance. In [8], a design was developed for a four-wheeled mobile robot system to be used in TL maintenance, with the aim of replacing or assisting in maintenance execution. The research conducted in [9] developed an improved maximum entropy method based on higher-order moments for the time-varying global reliability analysis of transmission towers in operation. In [10], a reliability-based network model was presented for generation and transmission expansion planning, considering the impacts of maintenance, repair, and line loading.

The reliability-centered maintenance method, as the most efficient and cost-effective approach among preventive maintenance strategies, considers both the importance of the equipment to the system and its physical condition [6]. This article conducted a systematic review on the reliability of transmission lines based on the implementation of maintenance and prior risk assessment, as well as identifying the main gaps found through an overview of the studies addressed.

II. MATERIAL AND METHODS

Conducting a literature review with the aim of providing the best policy and practice evidence in any discipline is a fundamental research objective for the respective academic and professional communities [11].

The research described in this work was structured as a Systematic Literature Review (SLR), organized into three stages: research planning (exploratory), review conduction (development), and dissemination reporting (analysis), as illustrated in Fig. 1.

A. Review Planning

A descriptive review examines the state of the literature regarding a research question, thematic area, or specific concept. What distinguishes this type of review from other review categories is that descriptive reviews do not aim to expand the literature but rather to provide an account of the literature's status at the time of the review [12].

During the planning stage of the work, an exploratory and unstructured search was conducted on the proposed topic to obtain broad information regarding published articles. Initially, research was carried out using the keywords transmission lines, risk assessment, reliability, and maintenance on the Web of Science and Scopus platforms. The searches employed topic–topic, topic–title, and title–title criteria, and no filters or inclusion/exclusion criteria were applied, as the goal was to gain a general understanding of the scenario to be studied. During the database searches, many

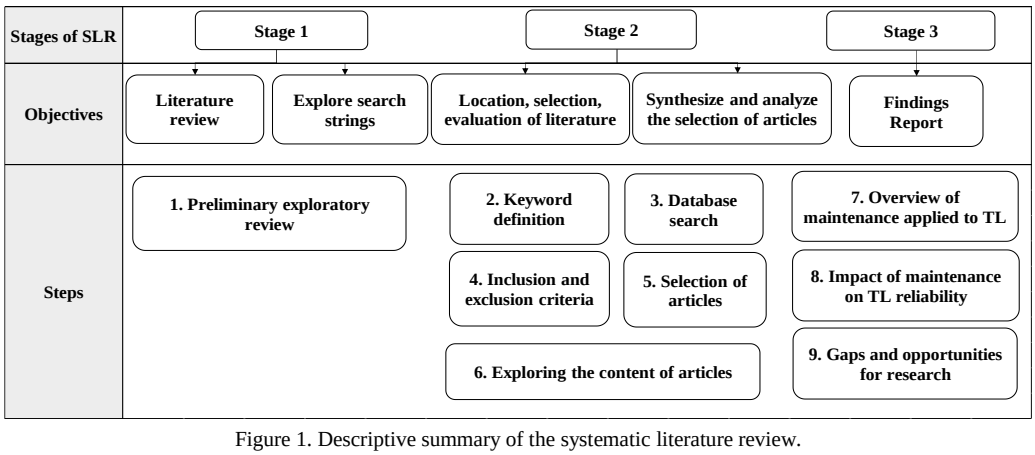

Figure 1. Descriptive summary of the systematic literature review.

duplicate articles across the platforms was observed, and it was found that the topic–topic criterion yielded the greatest number of published works.

B. Review Conduction

As no single database includes the complete set of published materials, a systematic literature search must be based on multiple databases [12]. Thus, the Web of Science and Scopus platforms were used as research sources to obtain complementary results during the review conduction. The criteria used for the inclusion and exclusion of articles were: the type of document, the research area to which the document was linked, the duplication of articles, the reading of the title and abstract, and finally, the full reading of the article.

Initially, the keywords were divided into two groups: Group 1, composed of Control Chart, Transmission Line, and Risk Assessment; and Group 2, composed of Maintenance, Transmission Line, and Reliability. Based on this division, searches were conducted on the Web of Science and Scopus platforms. During the searches, the criterion used was always to look for one group of keywords or another in both data sources. The search types used were title–topic and topic–topic. Initially, the grouping of keywords and searches in both databases resulted in a total of 2294 papers.

The first exclusion criterion applied was the document type, only research articles and review articles were considered for this study, while other types of documents were excluded. After this first filter, 951 articles remained. The second analysis criterion concerned the subject categories in which the articles were classified. The following categories were excluded: Telecommunications; Computer Science; Nuclear Science and Technology; Geosciences; Cell Biology; Civil Engineering Technology; Genetic Heredity; Oncology; Physics of Fluids and Plasmas; Nuclear Physics; Environmental and Occupational Health; Thermodynamics; Biochemistry; Genetics; Molecular Biology; Immunology; Microbiology; Earth and Planetary Sciences; Agricultural and Biological Sciences; Pharmacology; Toxicology and Pharmaceutics; Medicine; Economics; Econometrics and Finance. All other related areas were considered, resulting in 843 articles after applying this criterion.

After removing duplicate articles, the number of papers was reduced to 338. The next criterion applied was reading the titles and abstracts. All papers related to the research topic (maintenance, risk assessment, and reliability in transmission lines) were retained, while others focusing on unrelated subjects were excluded. After applying the title and abstract screening, 105 articles remained.

Finally, the last refinement step involved reading all the selected articles to explore their content and verify their relevance to the topic of this review. After this evaluation, the final sample consisted of 76 articles.

C. Dissemination Report

For the development of the results of this study, indicators were used to analyze the evolution of publications related to the research topics, the number of citations received, the relevance of journals based on their impact factor, the co-occurrence of keywords, and the main areas of concentration of the identified studies. Finally, the topics that showed the greatest emphasis in the analyzed articles were highlighted.

Based on the data obtained from reading the papers, quantitative and descriptive analyses of the works were conducted, and stratifications were created according to their information. The bibliometric review highlighted the evolution of publications and citations, both on an annual and cumulative basis, and classified the journals with the highest impact that published two or more articles on the topics.

Using the VOSviewer software to track thematic trends over time, a network map of keywords associated with transmission line reliability was constructed, considering maintenance execution and risk assessment worldwide from 2013 to 2023. Additionally, all works in the sample were classified by research area to understand the focus given by the authors to the analyzed articles.

During the content exploration phase, a qualitative assessment of the works was performed, highlighting several notable topics beyond the main themes, such as the use of unmanned aerial vehicles (UAV) for TL inspection, the application of optimization methods in maintenance scheduling, and the effects of natural factors on line operation and maintenance.

From all the analyses presented, it was possible to develop a systematic literature review, integrating all works focused on transmission line reliability considering maintenance execution, as well as providing an overview of the research gaps in the field.

III. Results and Discussion

A. Bibliometric Analysis

Fig. 2 shows the number of publications per year and cumulative, from 1969 to 2023, of articles addressing transmission line reliability through maintenance execution and risk assessments. It can be observed that the years with the highest number of publications on the topic were 2021 (9 publications) and 2022 (7 publications). Additionally, there were four years in which 6 articles were published: 2014, 2016, 2017, and 2020. Apart from the aforementioned years, the total annual publications did not exceed 5 articles.

It is also possible to observe from the data presented in Fig. 2 that in some years no publications were made on the topic in question. However, these gaps are mainly between 1969 and 2007, after which there was at least one publication per year on the subject.

Fig. 3 shows the evolution of citations between 1973 and 2023. The graph exhibits an exponential trend, highlighting that the topic has become increasingly discussed and researched. Between 1973 and 1996, there were no more than two citations per year related to TL reliability considering preventive maintenance execution and prior risk analysis. From 1997 onward, citations became more frequent, reaching 187 in 2023, totaling 928 cumulative citations in the same year, representing the highest numbers in the period analyzed in this study.

In Table I, the classification of the articles by research area is presented. An article may be classified in multiple areas depending on the topic addressed in its content. Among the articles comprising the final sample of this review, Engineering stands out with 67 studies.

The Energy research area includes 24 studies, while Mathematics has 4 published articles. All other fields had two publications or fewer.

Fig. 4 shows the evolution of the network of keywords associated with transmission lines,

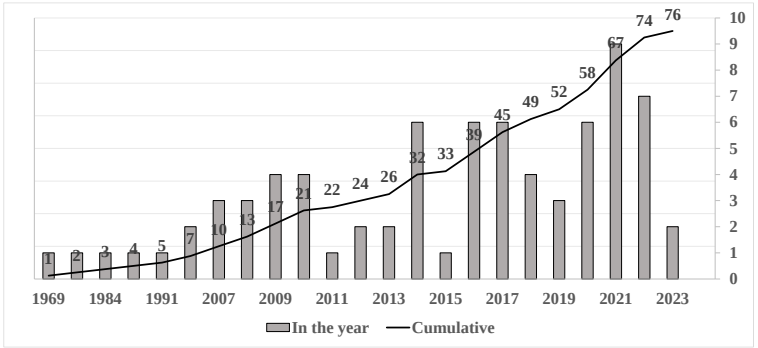

Figure 2. Publications from 1969 to 2023.

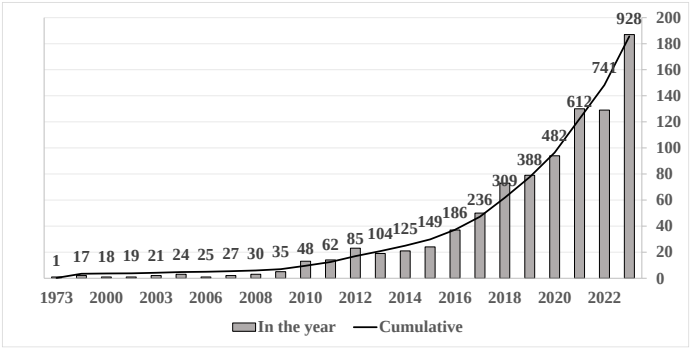

Figure 3. Citations from 1973 to 2023.

maintenance, and reliability worldwide during the period from 2013 to 2023. A wide range of topics can be observed over this period. In 2014, the highest number of publications was related to reliability, system, transmission lines, and maintenance. In 2018, the most addressed topics were failure rate, year, and operation, with "operation" remaining a key focus until 2020. The software did not identify any keywords with significant connections in the period from 2020 to 2023.

Based on the analysis of Table II, which presents the classification of the highest-impact journals, ranked according to the Journal Impact Factor (JIF), with two or more publications during the period from 1969 to 2023, it can be observed that the publications appeared in journals with a wide scope and varying impact factors.

B. Content Exploration

Due to the constant growth of generation and transmission systems, the companies responsible for the operation and maintenance of assets have been attempting to modernize their practices to optimize inspections and analyses, to carry out necessary maintenance activities with greater speed and quality, as well as to achieve lower cost and environmental impact. According to [13], the objective of asset management is to transform these assets into a revenue stream, and therefore, risk assessment is part of this process.

TABLE I. CLASSIFICATION OF ARTICLES BY RESEARCH AREAS.

Research Area	Number of Articles
Engineering	67
Energy	24
Computer Science	13
Mathematics	4
Business, Management, and Accounting	2
Materials Science	2
Physics and Astronomy	2
Energy Fuels	2
Management Science and Operational Research	2
Robotics	2
Decision Sciences	1
Environmental Science	1
Social Sciences	1
Automation Control Systems	1
Business Economics	1
Chemistry	1
Instrumentation – Instruments	1
Telecommunications	1

TABLE II. CLASSIFICATION OF THE HIGHEST-IMPACT JOURNALS.

Journal	Publications	Citations
IEEE Transactions on Power Systems	4	83
International Journal of Electrical Power and Energy Systems	6	68
IEEE Transactions on Power Delivery	4	62
Energies	4	14
IET Generation, Transmission and Distribution	2	37
Internacional Transactions on Electrical Energy Systems	2	35
International Journal of System Assurance Engineering and Management	2	12
Journal of Electrical Engineering and Technology	2	19
Industrial Robot: the international journal of robotics research and application	3	13
Total	29	343

The techniques and technologies involved in preventive maintenance and reliability analysis have evolved over the years. Six articles included in this review were written before the 2000s and highlight the topics discussed up to that time.

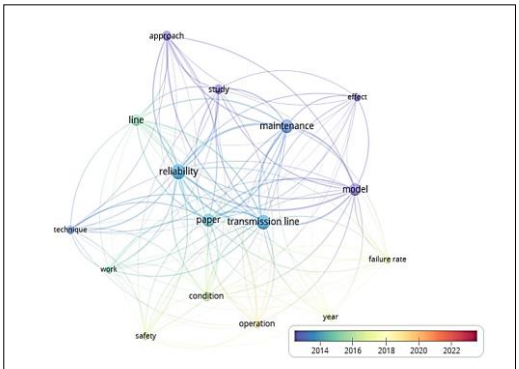

Figure 4. Evolution of the keyword network associated with transmission lines, reliability, and maintenance worldwide, from 2013 to 2023.

As part of the sample of articles published before the 2000s, in [14] proposed the implementation of a global plan to control maintenance activities, aiming to improve reliability and manage maintenance costs. Reference [15] described a reliability model that simulated the states of power systems during faults, in which the effects of component maintenance were incorporated into the analysis.

In [16], a review was conducted on the methods and models used at Electricité de France for studying system reliability. The main emphasis was placed on probabilistic studies, particularly interruptions in maintenance and repair operations of nuclear units, planning of the 400 kV grid, substation reliability, and nuclear plant safety.

When analyzing articles published between 2000 and 2023 focused on the application of maintenance in transmission lines and their components, a wide range of works was observed.

These works mainly addressed maintenance from the perspective of optimizing its scheduling, considering data obtained from the history of the equipment itself and the system in which it is embedded, as well as the use of tools and techniques that enable greater resource utilization.

A widely discussed topic today regarding effective methods of inspection in preventive maintenance is the use of unmanned aerial vehicles for data collection in transmission lines. The growing popularity of UAV enables the collection of a vast amount of inspection data on power lines [5]. The studies that addressed the use of UAV were published between 2015 and 2022, with contributions from China, England, and South Korea.

The intelligent monitoring method proposed in [17] employed sensors mounted on a UAV, which made it possible to obtain real-time data on the TL and its surroundings, as well as to estimate potential conductor sagging by combining point cloud data measured with a LiDAR sensor and the UAV flight information.

Reliability and risk indicators were employed to optimize preventive maintenance scheduling, with the aim of prioritizing equipment that requires faster interventions. In [6], the prioritization of maintenance activities on transmission lines was carried out based on the importance and condition indices of each asset, represented in a two-dimensional diagram.

In [10], an analysis was conducted regarding the impact of maintenance costs in relation to the service life of transmission lines, the failures that occurred, and the relationship between line loading and failure rate. It was observed that the failure rate can be defined as a linear proportion of the line loading percentage, and that the longer the service life and the higher the failure frequency, the more expensive the maintenance becomes.

The use of different data analysis techniques is also a notable aspect in the articles reviewed. In [18], Bayesian Networks were applied to optimize maintenance activities with the aim of increasing asset reliability. The studies reported in [19] and [7], employed neural network learning for remote detection and identification of failures in TL, with the goal of eliminating-or at least minimizing-the use of traditional maintenance methods employed by power utilities.

Markov chains have been applied to optimize maintenance intervals, thereby increasing the availability of TL and improving the efficiency of maintenance teams [20]. Particle swarm optimization was also employed with the same objective as the Markov chains [21].

Another highly relevant topic currently addressed is the impact of the environment on the operation and maintenance of transmission lines, as well as the reciprocal impact these assets have on the environment where they are installed. TL are frequently subject to failures due to exposure to extreme environments. It is essential to monitor such failures and repair lines promptly when occurrences arise; in addition, their condition must be accurately assessed to ensure reliability and safety [17]. Due to the importance of this topic, the volatility of environments and the impacts of natural factors on TL are addressed in several works included in this research.

In [22], the authors reported that the failure rate in transmission lines is significantly affected by meteorological factors. Therefore, it is necessary to consider the impact of these factors on reliability and risk assessment to improve maintenance planning.

The development of power networks for extensive use of electricity produced from renewable sources should not conflict with

nature conservation. Maintenance management, combined with conservation practices through integrated vegetation management, can be applied to lines that cross forests, as they directly impact natural development [23].

IV. CONCLUSION

The research systematized the literature related to the impacts of preventive maintenance execution and the reliability of transmission lines. The results provided a comprehensive view of the evolution of research in this area and can support the development of new studies focused on this topic.

A total of 76 studies, published between 1969 and 2023, were analyzed, providing a 54-year sample, which demonstrates that the topic has been widely discussed worldwide for decades. The countries with the highest number of publications were China – 35, Brazil – 8, Iran – 6, the United States – 5, India – 5, and South Korea – 4.

From the analyses, it was observed that studies integrating transmission line reliability with maintenance execution and risk analysis began in 1969, but the topic only started to be addressed more frequently by researchers from 2007 onwards.

The evolution of keywords highlights that topics related to research involving transmission lines have been updated over time; however, preventive maintenance aimed at improving reliability remains a central theme, differing only in the methods and technologies used for its execution.

Risk analysis considering the conditions of transmission line components is a more recent topic compared to maintenance, yet it is already widely disseminated among researchers seeking optimized solutions for activity planning.

The research revealed that preventive maintenance schedules were primarily established based on the operating time of the assets. Once reliability and risk metrics were integrated into the scheduling process, several additional factors began to be analyzed, such as equipment condition, failure rate, mean time between failures, availability, criticality index, revenue generated by the asset, mean time to repair after a failure, among others evaluated by each transmission company according to its specific needs.

With the inclusion of reliability and risk metrics, it became possible to perform a broader and more comprehensive assessment of transmission assets, resulting in a more optimized maintenance scheduling process.

During the review, it was noted that some specific topics stand out in terms of the number of published articles, in addition to maintenance, reliability, and risk assessment, which were the main research themes. The use of unmanned aerial vehicles has been discussed since 2015. The application of different data analysis techniques to optimize resources has also been discussed for many years, and a considerable reduction in transmission line failure rates is observed when there is greater focus on reliability-based scheduling.

The use of robots in line maintenance has been studied since 1991; however, to date, there are no consolidated technologies widely adopted by energy transmission companies. Significant attention is also given to the environmental impact on the operation and maintenance of lines, highlighting the need for studies to ensure that these assets' integration into natural and urban environments causes minimal harm.

No studies were found analyzing anomalies in the soil where transmission towers are installed. Considering the existence of self-supporting and guyed towers, which require different foundation designs, there are direct impacts on transmission line reliability caused by soil-related actions.

Depending on the type of soil or external agents, it is possible to observe fluvial or pluvial erosion, or erosion caused by insects. The progression of erosion can lead to tower tilting or misalignment, potentially resulting in collapse and directly impacting transmission service availability and quality indicators.

It is worth highlighting that this research gap has not yet been addressed by this research group; however, it is a topic that may be explored in the future to enable the formulation of concrete methodological recommendations.

ACKNOWLEDGMENT

The authors acknowledge the National Council for Scientific and Technological Development (CNPq) for the Research Productivity Grants (No. 310871/2021-2, 304407/2025-9 and 312055/2023-4).

REFERENCES

[1] Tao, T., & Li, Z. (2026). A review of deep learning application in transmission line defect detection. *Electric Power Systems Research*, *250*, 112193.

[2] Arno, R., Dowling, N., & Schuerger, R. (2015, May). Equipment failure characteristics amp; RCM for optimizing maintenance cost. In *IEEE/IAS 51st Industrial & Commercial Power Systems Technical Conference (I&CPS)*, Calgary, AB, Canada, 2015, (pp. 1-8). https://doi.org/10.1109/ICPS.2015.7266415

[3] Suwanasri, C., Saribut, S., Suwanasri, T., & Phadungthin, R. (2021). Risk analysis using failure modes, effects, and criticality analysis for transmission network assets. *Energies*, *14*(4), 977.

[4] Brown, R. E., & Humphrey, B. G. (2005). Asset management for transmission and distribution. *IEEE power and energy magazine*, *3*(3), 39-45.

[5] Liu, X., Miao, X., Jiang, H., & Chen, J. (2020). Data analysis in visual power line inspection: An in-depth review of deep learning for component detection and fault diagnosis. *Annual Reviews in Control*, *50*, 253-277.

[6] Abbasghorbani, M., Damchi, Y., & Rajabi Mashhadi, H. (2022). Reliability- centered maintenance for overhead transmission lines in composite power system. *International Transactions on Electrical Energy Systems*, *2022*, 1-11.

[7] Mawle, P. P., Dhomane, G. A., & Burade, P. G. (2022). Application of artificial intelligence in early fault detection of transmission line-a case study in India. *International Journal of Electrical and Computer Engineering (IJECE)*, *12*(6), 5707.

[8] Jiang, W., Shi, Y., Zou, D., Zhang, H., & Li, H. J. (2022). Research on mechanism configuration and dynamic characteristics for multi-split transmission line mobile robot. *Industrial Robot: the international journal of robotics research and application*, *49*(2), 200-211.

[9] Liu, C., Wang, T., Tang, Z., & Li, Z. (2023). Time-varying wind-resistance global reliability analysis of in-service transmission tower using high-order moments-based improved maximum entropy method. *Applied sciences*, *13*(7), 4245.

[10] Mahdavi, M., Javadi, M. S., & Catalão, J. P. (2023). Integrated generation-transmission expansion planning considering power system reliability and optimal maintenance activities. *International Journal of Electrical Power & Energy Systems*, *145*, 108688.

[11] Tranfield, D., Denyer, D., & Smart, P. (2003). Towards a methodology for developing evidence- informed management knowledge by means of systematic review. *British journal of management*, *14*(3), 207-222.

[12] Xiao, Y., & Watson, M. (2019). Guidance on conducting a systematic literature review. *Journal of planning education and research*, *39*(1), 93-112.

[13] Khuntia, S. R., Rueda, J. L., Bouwman, S., & van der Meijden, M. A. (2016). A literature survey on asset management in electrical power [transmission and distribution] system. *International Transactions on Electrical Energy Systems*, *26*(10), 2123-2133.

[14] Beehler, M. E. (1996). Reliability centered maintenance for transmission systems. In *Proceedings of 1996 Transmission and Distribution Conference and Exposition* (pp. 96-101). IEEE.

[15] Endrenyi, J. (2007). Three-state models in power system reliability evaluations. *IEEE Transactions on Power Apparatus and Systems*, (4), 1909-1916.

[16] Batut, J., Boisseau, J., Bourgade, E., & Monti, M. (1988). Different approaches to reliability as applied to the generation—transmission system and its components. *International Journal of Electrical Power & Energy Systems*, *10*(3), 168-173.

[17] Jeong, S., Kim, D., Kim, S., Ham, J. W., Lee, J. K., & Oh, K. Y. (2020). Real-time environmental cognition and sag estimation of transmission lines using UAV equipped with 3-D Lidar system. *IEEE Transactions on Power Delivery*, *36*(5), 2658-2667.

[18] Zhou, K., Cruise, J. R., Dent, C. J., Dobson, I., Wehenkel, L., Wang, Z., & Wilson, A. L. (2020). Bayesian estimates of transmission line outage rates that consider line dependencies. *IEEE Transactions on Power Systems*, *36*(2), 1095-1106.

[19] Du, F., Jiao, S., & Chu, K. (2022). Research on safety detection of transmission line disaster prevention based on improved lightweight convolutional neural network. *Machines*, *10*(7), 588.

[20] Samadi, M., Seifi, H., & Haghifam, M. R. (2019). Midterm system level maintenance scheduling of transmission equipment using inspection based model. *International Journal of Electrical Power & Energy Systems*, *110*, 467-476.

[21] Zhang, L., Zhao, Z., Zhang, D., Luo, C., & Li, C. (2022). Particle swarm optimization pattern recognition neural network for transmission lines faults classification. *Intelligent Data Analysis*, *26*(1), 189-203.

[22] Wang, R., Xia, Y., & Xiong, X. (2010). Risk analysis method for transmission line maintenance considering meteorological factors. *Power System Technology*, *34*(314 (1)), 219-222.

[23] Follner, K. & Rieck, P. (2021). Integrated vegetation management under and above high-voltage lines - Potential areas for nature conservation?. *Natur und Landschaft*, *96(8)*, 393-400.

eNergetics 2025
DOI: https://doi.org/10.5281/zenodo.18615662

Original Scientific Article

Application and Performance Analysis of the Old Babylonian Algorithm in Solving a Reaction-diffusion Derived Transcendental Equation for Porous Catalysts

Yan Wang[1], Gaosheng Liu[2], Lizhong Chen[3], Zhongxi Liu[4]

[1,2]School of Science, Tianjin University of Commerce, Tianjin, P. R. China
[1,3,4]Tianjin Tianwei Chemical Engineering Co., Ltd., Tianjin, P. R. China

[1]yanwang0125@163.com

Abstract—**This research delves into applying the Old Babylonian Algorithm to solve a complex transcendental algebraic equation in Porous Catalyst Research. By formulating an iterative solution strategy and implementing the iterative process, the results are analyzed from convergence and accuracy perspectives. The findings show that the Old Babylonian Algorithm has potential in handling this equation but faces challenges. Transforming the equation for algorithm application is complex, potentially introducing errors. Also, the algorithm's convergence is sensitive to the initial guess; inappropriate initial values may lead to slow convergence or divergence. This study offers a new approach for complex equations in porous catalyst research and insights into the Old Babylonian Algorithm's application boundaries. It serves as a reference for future algorithm improvement and broader applications in related scientific and engineering fields.**

Keywords - old babylonian algorithm, nonlinear equation, iterative solution, porous vatalysts.

I. INTRODUCTION

In the field of porous catalyst research, a profound understanding of mass transport and reaction mechanisms is of paramount importance for the optimization of catalytic processes. In a recent publication [1], the non-linear reaction-diffusion model has been transformed into a highly complicated transcendental equation, which can be represented as follows:

$$x^2 + \frac{j}{0.6}\, x \tanh(0.6x) - \varphi^2 \frac{[\cosh(x)]^{1-p}[\cosh(0.6x)]^{p-1}}{[1+\lambda \cosh(0.6x)\,\mathrm{sech}(x)]^m} = 0 \quad , (1)$$

where φ represents the Thiele module, j, λ , m, and n are constants.

In nonlinear science, many analytical methods, such as the variational iteration method [2,3] and the homotopy perturbation method [4-6], typically try to avoid solving transcendental equations [7]. This is mainly because transcendental equations, such as Eq. (1), are extremely difficult to solve by traditional analytical means. Their non-polynomial nature and the presence of complex functions, such as those in Eq. (1), pose significant obstacles to obtaining exact solutions.

Equation (1) plays a crucial role in determining the efficiency factor of porous catalysts. The accurate determination of the constant x is essential for a deeper understanding of the interaction between transport effects and reaction rates in heterogeneous catalysis. This knowledge has far-reaching implications for a wide range of industrial applications.

ISBN: 978-86-82602-07-1

To date, ancient Chinese mathematical algorithms [8-12] and the point solution method [13,14] have been explored. The ancient Chinese mathematical method has been successfully applied to reaction-diffusion problems [15] and porous catalyst research [16], demonstrating the potential of non-traditional mathematical approaches in this field.

The Old Babylonian Algorithm [17], with its roots in ancient Mesopotamian mathematics, was originally developed to calculate square roots. Over time it has been extensively extended. Its iterative nature and relatively simple computational steps provide a different perspective compared to traditional numerical and analytical methods. In recent years, it has found applications in emerging research areas such as micro-electro-mechanical systems (MEMS) and nonlinear vibration systems [18,19]. In MEMS, it helps to solve complex equations governing the behavior of micro-scale devices, while in nonlinear vibration systems it provides new insights into the dynamics of vibrating structures.

With this in mind, the application of the ancient Babylonian algorithm to Eq. (1) is an interesting line of research. The main objectives of this study are twofold. First, we aim to explore the feasibility of using the Old Babylonian Algorithm to solve Eq. (1). This involves devising strategies to transform the equation into a form suitable for the algorithm's iterative framework, and formulating an appropriate iterative formula. Secondly, we seek to comprehensively evaluate the performance of the algorithm in solving Eq. (1), including an in-depth analysis of the convergence of the iterative process and the accuracy of the solutions obtained. This research will not only contribute to the existing knowledge in porous catalyst research, but also expand our understanding of the capabilities and limitations of the Old Babylonian algorithm.

II. THEORETICAL FOUNDATION

A. *In-depth Understanding of the Old Babylonian Algorithm*

The Old Babylonian Algorithm, originating from ancient Mesopotamian mathematics, has a rich historical and mathematical background. Initially developed for calculating the square root of a positive number A, its fundamental principle is based on iterative approximation. Given an initial guess x_0 , the iterative formula for computing $\sqrt{A}$ is:

$$x_{n+1} = \frac{1}{2}(x_n + \frac{A}{x_n}) \ . \tag{2}$$

This formula has an intuitive geometric interpretation. Geometrically, if we consider a rectangle with sides x_n and A/x_n , its area is *A*. The arithmetic-mean of the two sides, $(x_n + A/x_n)/2$, provides a better approximation of the side length of a square with the same area *A* in each iteration. The convergence of this formula can be proven using the concept of fixed - point iteration. Let

$$f(x) = \frac{1}{2}(x + \frac{A}{x}) \ . \tag{3}$$

Its derivative is

$$f'(x) = \frac{1}{2}(1 - \frac{A}{x^2}) \ . \tag{4}$$

For $x > \sqrt{A}$ and $f' < 1$, ensuring that the iteration converges to $\sqrt{A}$ when the initial guess $x_0 > 0$.

For a general algebraic equation

$$f(x) = \gamma \ , \tag{5}$$

which can be rewritten in the form

$$x^{\alpha} = F(x) \ , \tag{6}$$

where α is a positive real number, the iterative formula of the Old Babylonian-like method becomes:

$$x_{n+1} = \beta x_n + (1-\beta)\frac{F(x_n)}{(x_n)^{\alpha-1}} \ . \tag{7}$$

Here, β is a parameter typically chosen within the range [0, 1]. When $\beta = 1/2$, it strikes a balance between the influence of the current approximation x_n and the new estimate

$F(x_n)/(x_n)^{\alpha-1}$. This choice is often used as it provides a reasonable trade-off between stability and the rate of convergence in many cases. However, different values of β can be explored depending on the nature of the equation $f(x)=0$. For example, if the function $F(x)$ has certain monotonicity or curvature properties, a different β value might lead to faster convergence.

In the context of differential equations of the form:

$$L(u)+N(u)=0\ , \tag{8}$$

where $L(u)$ is a linear differential operator and $L(u)$ is a nonlinear differential operator, the Old Babylonian Algorithm can be adapted. The iterative formula for such equations is:

$$u_{n+1}=\beta u_n+\frac{L(u_n)+N(u_n)+(u_n)^{\alpha+1}}{(u_n)^{\alpha}}\ . \tag{9}$$

This formula iteratively refines the function u_n based on the values of the linear and nonlinear terms at the *n*-th iteration. It aims to approximate the solution of the differential equation by gradually reducing the error between the left - hand side of the equation $L(u)+N(u)$ and zero. The convergence of this iterative scheme for differential equations depends on the properties of the linear and nonlinear operators *L* and *N*, such as their boundedness, continuity, and the Lipschitz constants associated with them.

B. Thorough Analysis of the Target Equation

The Eq. (1) in this study is a highly complex transcendental equation that stems from applying the Akbari - Ganji method to solve a nonlinear reaction - diffusion equation related to mass transport in heterogeneous catalysis. It contains hyperbolic functions like tanh, cosh, and sech, along with exponential - like terms inherent to hyperbolic functions. These complex functional forms make it extremely difficult to solve using conventional Newton - type iteration methods or their modifications.

The Newton - Raphson method, for example, requires the calculation of the derivative of the function. For an equation involving hyperbolic functions, the derivative calculation becomes complex due to the chain - rule and product - rule applications. Additionally, the presence of multiple parameters (j,φ,λ,p,m) in Eq. (1) further complicates the problem. Each parameter is closely related to the physical properties of the porous catalyst system. The Thiele modulus φ reflects the ratio of the reaction rate to the diffusion rate. A larger φ indicates that the reaction rate is relatively faster compared to the diffusion rate, which can lead to different reaction - diffusion behaviors within the porous catalyst. The adsorption parameter λ influences the interaction between reactants and the catalyst surface. A change in λ can alter the adsorption and desorption rates of reactants, thereby affecting the overall reaction mechanism.

Due to its non - polynomial and transcendental nature, direct application of traditional root - finding methods is ineffective. The quadratic formula, applicable only to quadratic equations, is clearly not suitable. Simple iterative methods for polynomial equations also fail because they rely on the polynomial structure, which is absent in Eq. (1). This complexity necessitates the exploration of alternative approaches like the Old Babylonian Algorithm to obtain approximate solutions. The Old Babylonian Algorithm's ability to handle a wide range of equations through iterative approximation makes it a potentially viable option for dealing with such a complex transcendental equation.

III. Construction of the Solution Strategy

A. Iterative Formula Design

To leverage the Old Babylonian Algorithm for solving Eq. (1), a series of strategic transformations is essential. Equation (1) is first rewritten in a form that aligns with the algorithm's iterative framework. Let's assume that through in - depth analysis and manipulation, we transform Eq. (1) into:

$$x^2=F(x)=-\frac{j}{0.6}x\tanh(0.6x)+ \\ +\varphi^2\frac{[\cosh(x)]^{1-p}[\cosh(0.6x)]^{p-1}}{[1+\lambda\cosh(0.6x)\operatorname{sech}(x)]^m}\ . \tag{10}$$

The Old Babylonian - like iterative formula is:

$$x_n = \beta x_{n-1} + (1-\beta)\frac{F(x_{n-1})}{x_{n-1}} \quad . \qquad (11)$$

For small φ, from Eq. (1), x can be approximately solved as:

$$x \approx \frac{\varphi}{\sqrt{(1+j)(1+\lambda)^m}} \quad . \qquad (12)$$

So we can begin with:

$$x_0 = \frac{\varphi}{\sqrt{(1+j)(1+\lambda)^m}} \quad . \qquad (13)$$

The parameter β plays a significant role in determining the behavior of the iteration, for Eq. (1), we recommend $\beta = 0.8$. This value has shown to provide a good balance between convergence speed and stability in most cases. The iterative formula becomes:

$$x_1 = 0.8x_0 + 0.2\frac{F(x_0)}{x_0} = 0.8x_0 + \\ + \frac{0.2}{x_0}\left\{\begin{array}{l} -\dfrac{j}{0.6}x_0 \tanh(0.6x_0) + \\ \varphi^2 \dfrac{[\cosh(x_0)]^{1-p}[\cosh(0.6x_0)]^{p-1}}{[1+\lambda\cosh(0.6x_0)\,\mathrm{sech}(x_0)]^m} \end{array}\right\} . \qquad (14)$$

This particular formula plays a vital role in enabling us to initiate the iterative process from an initial guess denoted as x_0. It serves as the fundamental starting point for our successive calculations and approximations. The choice of this x_0 is by no means arbitrary; instead, it is of utmost importance. In fact, the specific value of x_0 is precisely given in Eq. (13). This equation provides the necessary guidance and specification for determining the initial value, which in turn has a significant impact on the entire iterative process and the eventual outcome.

B. Numerical Examples and Results

To validate the effectiveness of the designed iterative formula, we present two numerical examples.

Example 1:

$$\frac{\left|x_{\text{Exact}} - x_0\right|}{x_{\text{Exact}}} = \\ = \frac{\left|0.3736 - 0.3750\right|}{0.3726} = 0.64\% \quad . \qquad (15)$$

This relatively small error indicates that the iterative formula can provide a good approximation even after just one iteration.

Example 2: For the parameter values $\lambda = 3$, $p = 2$, $m = 3$, $j = 2$, and $\varphi = 10$, we perform the same iterative process. The initial guess from Eq. (13) is $x_0 = 0.7217$, and after one iteration, $x_1 = 0.8268$. The exact value is $x_{Exact} = 0.8304$. Calculating the relative error for x_1, we have 0.43%. These examples demonstrate that the Old Babylonian-based iterative formula can yield approximate solutions with high accuracy in a small number of iterations, highlighting its potential for solving the complex transcendental equation in porous catalyst research.

IV. Conclusions and Prospects

A. Research Findings Summary

This study has successfully implemented the old Babylonian Algorithm to solve the intricate transcendental Eq. (1) in porous catalyst research. Through a meticulous series of mathematical transformations, the original equation was tailored into a form compatible with the algorithm's iterative structure. The customized iterative formula was then employed to initiate the solution-seeking process, facilitating an efficient way to approximate the solutions of the equation.

An in-depth convergence analysis revealed that, under the conditions of appropriate initial guesses and well-selected β values, the algorithm could effectively converge to a solution. In most scenarios, the sequence of approximations demonstrated a reasonable convergence rate. Depending on the initial conditions and equation parameters, the convergence was often linear or even better. This indicates that the Old Babylonian Algorithm offers a viable and practical approach for solving Eq. (1).

When compared with alternative numerical methods, such as the Newton - Raphson method, the solutions obtained using the Old Babylonian

Algorithm showed good agreement. For numerous parameter combinations, the relative error was within an acceptable range. This not only validates the effectiveness of the proposed approach but also showcases the Old Babylonian Algorithm's potential as an alternative to traditional numerical methods in solving complex equations within the realm of porous catalyst research.

Furthermore, the sensitivity analysis conducted in this research provided valuable insights into the impact of various parameters on the solution. It was discovered that parameters like the Thiele modulus φ and the adsorption parameter λ had a more pronounced influence on the value of the solution variable x. Understanding these parameter - solution relationships is crucial for comprehending the underlying physical processes occurring within porous catalysts, which can, in turn, guide the optimization of catalytic processes.

However, this study also identified several limitations of the Old Babylonian Algorithm in this context. Transforming Eq. (1) into a suitable form for algorithm application was a complex task. The presence of hyperbolic functions and multiple parameters in the equation necessitated careful approximations and manipulations, which could introduce errors. Additionally, the algorithm's convergence was highly sensitive to the initial guess. Inappropriate initial values could lead to slow convergence, or in some cases, even divergence, highlighting the need for a more systematic approach to select initial guesses.

B. Future Research Directions

Based on the findings of this study, several promising avenues for future research can be identified.

Firstly, there is a need for further optimization of the equation - transformation process for the Old Babylonian Algorithm. Developing more advanced approximation techniques for hyperbolic functions could significantly improve the accuracy and efficiency of the algorithm. For example, using higher - order Taylor series expansions or advanced trigonometric identities to approximate the hyperbolic functions in Eq. (1) might reduce the errors introduced during the transformation. Exploring alternative ways to rewrite the equation to simplify its structure and enhance the algorithm's performance should also be a focus. This could involve reformulating the equation in terms of different variables or functional forms that are more amenable to the Old Babylonian Algorithm.

Secondly, a more in - depth investigation into the algorithm's sensitivity to the initial guess and the parameter β is essential. Developing a systematic approach to determine the optimal initial guess based on the equation's parameters could greatly improve the algorithm's efficiency. This could involve using machine - learning - based methods to analyze the relationship between equation parameters and optimal initial guesses, or developing analytical formulas for initial - guess selection. Additionally, researching an adaptive method for choosing the value of β during the iterative process, rather than relying on a fixed value, could enhance the algorithm's convergence rate and robustness across different equations. For instance, an adaptive β - selection method could adjust the value of β based on the rate of change of the approximation error during the iteration.

Thirdly, the application of the Old Babylonian Algorithm to other complex equations in the field of porous catalysts and related areas, such as electrochemical reactions and chemical engineering, should be explored. Expanding the algorithm's application scope can further validate its effectiveness and uncover new areas where it offers unique advantages over traditional methods. For example, in electrochemical reactions, the Old Babylonian Algorithm could be used to solve complex equations governing charge transfer and reaction kinetics at the electrode - electrolyte interface.

Fourthly, the Old Babylonian Algorithm can be also extended to solve nonlinear oscillators as discussed in [18,19], it might be an effective tool to MEMS oscillators [20-22] in future.

Finally, integrating the Old Babylonian Algorithm with other numerical and analytical methods holds great potential. Combining it with methods like homotopy perturbation methods or variational iteration methods could overcome the limitations of individual methods. For instance, the homotopy perturbation method could be used to provide a better initial approximation for the Old Babylonian Algorithm, while the Old Babylonian Algorithm could then refine the solution more efficiently. This integration could provide more accurate and reliable solutions for

complex equations in various scientific and engineering disciplines.

REFERENCES

[1] Krishnakumar, S., Jeyabarathi, P., Abukhaled, M., & Rajendran, L. (2025). A semi-analytical solution of a nonlinear boundary value problem arises in porous catalysts. *International Journal of Electrochemical Science*, *20*(3), 100953. https://doi.org/10.1016/j.ijoes.2025.100953.

[2] Anjum, N., Rasheed, A., He, J. H., & Alsolami, A. A. (2024). Free vibration of a tapered beam by the Aboodh transform-based variational iteration method. *Journal of Computational Applied Mechanics*, *55*(3), 440-450. https://doi.org/10.22059/jcamech.2024.377439.1116

[3] Anjum, N., He, J. H., He, C. H., & Gepreel, K. A. (2023). Variational iteration method for prediction of the pull-in instability condition of micro/nanoelectromechanical systems. *Physical Mesomechanics*, *26*(3), 241-250.

[4] He, C. H., & El-Dib, Y. O. (2022). A heuristic review on the homotopy perturbation method for non-conservative oscillators. *Journal of Low Frequency Noise, Vibration and Active Control*, *41*(2), 572-603. https://doi.org/10.1177/14613484211059264

[5] He, J. H., He, C. H., & Alsolami, A. A. (2023). A good initial guess for approximating nonlinear oscillators by the homotopy perturbation method. *Facta Universitatis, Series: Mechanical Engineering*, *21*(1), 021-029. https://doi.org/10.22190/fume230108006h

[6] Alshomrani, N. A., Alharbi, W. G., Alanazi, I. M., Alyasi, L. S., Alrefaei, G. N., Al'amri, S. A., & Alanzi, A. H. (2024). Homotopy perturbation method for solving a nonlinear system for an epidemic. *Advances in Differential Equations and Control Processes*, *31*(3), 347-355.

[7] Roul, P. (2016). An improved iterative technique for solving nonlinear doubly singular two-point boundary value problems. *The European Physical Journal Plus*, *131*(6), 209. https://doi.org/10.1140/epjp/i2016-16209-1

[8] Khan, W. A. (2022). Numerical simulation of Chun-Hui He's iteration method with applications in engineering. *International Journal of Numerical Methods for Heat & Fluid Flow*, *32*(3), 944-955. https://doi.org/10.1108/hff-04-2021-0245

[9] Liu, Y. Q., & He, J. H. (2017). On relationship between two ancient Chinese algorithms and their application to flash evaporation. *Results in Physics*, *7*, 320-322. https://doi.org/10.1016/j.rinp.2016.12.047

[10] He, C. H. (2016). An introduction to an ancient Chinese algorithm and its modification. *International Journal of Numerical Methods for Heat & Fluid Flow*, *26*(8), 2486-2491. https://doi.org/10.1108/hff-09-2015-0377

[11] He, C. H. (2017). A simple analytical approach to a nonlinear equation arising in porous catalyst. *International Journal of Numerical Methods for Heat & Fluid Flow*, *27*(4), 861-866. https://doi.org/10.1108/hff-03-2016-0129

[12] He, J. H., Qie, N., He, C. H., & Gepreel, K. (2022). Fast identification of the pull-in voltage of a nano/micro-electromechanical system. *Journal of Low Frequency Noise, Vibration and Active Control*, *41*(2), 566-571. https://doi.org/10.1177/14613484211068252

[13] Liu, Y. P., & He, J. H. (2025). A fast and accurate estimation of amperometric current response in reaction kinetics. *Journal of Electroanalytical Chemistry*, *978*, 118884. https://doi.org/10.1016/j.jelechem.2024.118884

[14] He, J. H., & Iranian, D. (2025). Point Solution Concept for Analysis of Reaction-Diffusion in Porous Catalysts. *Journal of Computational Applied Mechanics*, *56*(4), 711-719. https://doi.org/10.22059/jcamech.2025.398100.1535

[15] Wu, Y. (2021). Variational approach to fractal reaction-diffusion equations with fractal derivatives. *Thermal Science*, *25*(2 Part B), 1425-1430. https://doi.org/10.2298/tsci200301042w

[16] Sun, Z. Q. (2021). A variational approach to a porous catalyst. *Thermal Science*, *25*(2 Part B), 1437-1442. https://doi.org/10.2298/tsci200404044s

[17] He, J. H. (2024). An old Babylonian algorithm and its modern applications. *Symmetry*, *16*(11), 1467. https://doi.org/10.3390/sym16111467

[18] Niu, J. Y., & Feng, G. Q. (2024). A mini-review on ancient mathematics' modern applications with an emphasis on the old Babylonian mathematics for MEMS systems. *Frontiers in Physics*, *12*, 1532630. https:// doi.org/10.3389/fphy.2024.1532630

[19] Zhang, L. (2025). The old babylonian algorithm: reborn with a bang and its application in non-linear vibration. *Frontiers in Applied Mathematics and Statistics*, *10*, 1530024. https://doi.org/10.3389/fams.2024.1530024

[20] He, C. H., & Mohammadian, M. (2025). A fast insight into high-accuracy nonlinear frequency estimation of stringer-stiffened shells. *Facta Universitatis, Series: Mechanical Engineering*. https://doi.org/10.22190/FUME250525028H

[21] He, J. H., Ma, J., Alsolami, A. A., & He, C. H. (2025). Variational approach to micro-electro-mechanical systems. *Facta Universitatis, Series: Mechanical Engineering*. https://doi.org/10.22190/FUME250528023H

[22] He, C. H., He, J. H., Ma, J., Alsolami, A. A., & Yang, X. J. (2025). A modified frequency formulation for nonlinear mechanical vibrations. *Facta Universitatis, Series: Mechanical Engineering*, *23*(2), 197-210. https://doi.org/10.22190/FUME250526022H

eNergetics 2025
DOI: https://doi.org/10.5281/zenodo.18615672

Original Scientific Article

Novel Quasi-oppositional Learning based Chaotic Psychology of Relationships Inspired Optimization Algorithm for Power Loss Reduction in Grid-connected Renewable Energy System

Lenin Kanagasabai[1]

[1]Prasad V.Potluri Siddhartha Institute of Technology, Vijayawada, Andhra Pradesh, India

[1]gklenin@gmail.com

Abstract—**Precarious relationship between literature teacher and boy is articulated scientifically in the algorithm. Boy tutored by the literature teacher to progress his writing talents. This tips to developed and sneering boy to be progressively influencing relationship diminuendos. At one point boy intend and framing relationships between mother of his close classmate and wife of the teacher. In the exploration section of the procedure boys writing skills, precarious relationship between literature teacher and boy has been formulated. In the exploitation section how the age and conditions of the boy making him to articulate relationships with people. The relationships created by the boy viewed in cognitive mode- it is a psychology of relationships which can't be easily interpreted. To make and maintain the relationships the boy manipulates the situations around him. Quasi-oppositional learning and Chaos factor are amalgamated in the technique. Quasi-oppositional learning based chaotic psychology of relationships inspired (QCPR) optimization algorithm is validated in 7 Benchmark functions and IEEE 300, 354 bus systems.**

Keywords – quasi-oppositional learning, chaotic, psychology and relationships.

I. INTRODUCTION

Quasi-oppositional learning based chaotic psychology of relationships inspired (QCPR) optimization algorithm is applied for solving true power loss reduction problem. Psychology of relationships algorithm is modelled based on the novel "The Boy in the Last Row", authored by Juan Mayorga and the film "In the House" [1]. Novel describes about passionate, precarious relationship that ascends amongst literature teacher and an introverted, secretive boy who continuously be seated in the back bench of the class room. These decades many research papers are scientifically articulated based on the real and fictitious characters. Meng et al., 2006 designed Monkey King Evolution algorithm [2] and it based on mythical novel of Monkey Kings accomplishment. Psychology of relationships owns a. Affection philosophy- which deals about the response of the people while they wounded, endangered in the relationship, b. Communal conversation philosophy- describe about the interaction of the people and making pronouncements in the relationships through societal communications, c. Purposeful associations:- this type of relationship deal about the well-being of the colleagues or contributors, d. Para societal associations- it is a peculiar one side relationship which can't be understood easily by others , it may be permanent or temporary, e. Cybernetic associations- this type of relationship made through scientific communications without meeting in person, f. Discrepancy associations -

accepting the differences of the each individual in the relationship is important factor in the differentiation relationship [3].

Precarious relationship between literature teacher and boy is articulated scientifically in the algorithm. Boy tutored by the literature teacher to progress his writing talents. This tips to developed and sneering boy to be progressively influencing relationship as the slow, steady erosion of connection, intimacy, and affection over time. At one point boy intend and framing relationships between mother of his close classmate and wife of the teacher.

In the exploration section of the procedure boys writing skills, precarious relationship between literature teacher and boy has been formulated. In the exploitation section how the age and conditions of the boy making him to articulate relationships with people. The relationships created by the boy viewed in cognitive mode- it is a psychology of relationships which can't be easily interpreted. To make and maintain the relationships the boy influences the situations around him.

In the course of writing, the boy makes peculiar relationships with few people. Especially the boy is in relationship with mother of his close classmate and wife of the teacher. To make this relationship the boy manipulates many situations and secretly observing the way of living and their relationships with others. Accordingly the boy alters his strategy to reach an in-depth relationship. Quasi-oppositional learning and Chaos factor are amalgamated in the technique.

Quasi-oppositional learning based chaotic psychology of relationships inspired (QCPR) optimization algorithm is validated in 7 Benchmark functions and IEEE 300, 354 bus systems.

II. PROBLEM FORMULATION

Loss reduction problem [4] is demarcated as:

$$min\tilde{F}\left(\bar{g},\bar{h}\right) \tag{1}$$

Control $(\bar{g})$ and dependent $\left(\bar{h}\right)$ vectors are defined as:

$$g = \begin{matrix}[VLG_1,..,VLG_{Ng};QC_1,..,\\ ,..,QC_{Nc};T_1,..,T_{N_T}]\end{matrix}, \tag{2}$$

$$h = \begin{matrix}[PG_{slack};VL_1,..,VL_{N_{Load}};\\ QG_1,..,QG_{Ng};SL_1,..,SL_{N_T}]\end{matrix}, \tag{3}$$

$Q_C \rightarrow$ Reactive power compensator;

$T \rightarrow$ Transformer tap;

$V_G \rightarrow$ Generator voltage;

$PG_{slack} \rightarrow$ Slack generator;

$V_L \rightarrow$ Voltage in transmission lines;

$Q_G \rightarrow$ Reactive power generator.

Fitness functions are defined as follows:

$$F_1 = P_{min} = \\ = min\left[\sum_m^{N_{TL}} G_m\left[V_i^2 + V_j^2 - 2\cdot V_j cos\emptyset_{ij}\right]\right], \tag{4}$$

$$F_2 = min\left[\begin{matrix}\sum_{i=1}^{N_{LB}}\left|V_{Lk} - V_{Lk}^{desired}\right|^2 + \\ +\sum_{i=1}^{N_G}\left|Q_{GK} - Q_{GK}^{Lim}\right|^2\end{matrix}\right], \tag{5}$$

$$F_3 = Minimize\, L_{maximum}\ . \tag{6}$$

$S_L \rightarrow$ Apparent power;

$$L_{max} = max\left[L_j\right]; j = 1; N_{LB}\ , \tag{7}$$

$$\begin{cases} L_j = 1 - \sum_{i=1}^{N_{PV}} F_{ji}\frac{V_i}{V_j} \\ F_{ji} = -\left[Y_1\right]^1\left[Y_2\right] \end{cases}, \tag{8}$$

$$L_{max} = max\left[1 - \left[Y_1\right]^{-1}\left[Y_2\right]\times\frac{V_i}{V_j}\right]. \tag{9}$$

Parity constraints:

$$0 = P_{Gi} - P_{Di} - V_i\cdot \\ \cdot\sum_{j\in N_B} V_j\left[G_{ij}cos\left[\emptyset_i - \emptyset_j\right] + B_{ij}sin\left[\emptyset_i - \emptyset_j\right]\right], \tag{10}$$

$$0 = Q_{Gi} - Q_{Di} - V_i \cdot$$
$$\cdot \sum_{j \in N_B} V_j \left[G_{ij} sin\left[\varnothing_i - \varnothing_j \right] + B_{ij} cos\left[\varnothing_i - \varnothing_j \right] \right], \quad (11)$$

Disparity constraints:

$$\begin{aligned} P_{gsl}^{min} \le P_{gsl} \le P_{gsl}^{max}, \\ Q_{gi}^{min} \le Q_{gi} \le Q_{gi}^{max}, i \in N_g, \\ VL_i^{min} \le VL_i \le VL_i^{max}, i \in NL, \\ T_i^{min} \le T_i \le T_i^{max}, i \in N_T, \\ Q_c^{min} \le Q_c \le Q_C^{max}, i \in N_C, \\ \left| SL_i \right| \le S_{L_i}^{max}, i \in N_{TL}, \\ VG_i^{min} \le VG_i \le VG_i^{max}, i \in N_g, \end{aligned} \quad (12)$$

$$F = F_1 + r_i F_2 + uF_3 =$$
$$= F_1 + \left[\begin{array}{l} \sum_{i=1}^{NL} x_v \left[VL_i - VL_i^{min} \right]^2 + \\ + \sum_{i=1}^{NG} r_g \left[QG_i - QG_i^{min} \right]^2 \end{array} \right] + r_f F_3, \quad (13)$$

$$VL_i^{minimum} = \begin{cases} VL_i^{max}, VL_i > VL_i^{max} \\ VL_i^{min}, VL_i < VL_i^{min} \end{cases}, \quad (14)$$

$$QG_i^{minimum} = \begin{cases} QG_i^{max}, QG_i > QG_i^{max} \\ QG_i^{min}, QG_i < QG_i^{min} \end{cases}, \quad (15)$$

III. QUASI-OPPOSITIONAL LEARNING BASED CHAOTIC PSYCHOLOGY OF RELATIONSHIPS INSPIRED OPTIMIZATION ALGORITHM

Precarious relationship between literature teacher and boy is articulated scientifically in the algorithm. Boy tutored by the literature teacher to progress his writing talents. This tips to developed and sneering boy to be progressively influencing relationship diminuendos. At one point boy intend and framing relationships between mother of his close classmate and wife of the teacher. In the exploration section of the procedure boys writing skills, precarious relationship between literature teacher and boy has been formulated. In the exploitation section how the age and conditions of the boy making him to articulate relationships with people. The relationships created by the boy viewed in cognitive mode- it is a psychology of relationships which can't be easily interpreted. To make and maintain the relationships the boy manipulates the situations around him. Population created in the confined examination area is demarcated as:

$$\begin{aligned} R_{i,j} = lb_j + A\left(ub_j - lb_j \right), \\ ub_j, lb_j \rightarrow \text{upper and lower bound} \end{aligned} \quad (16)$$

Boy has good quality of observance and writing skills. This peculiar aspect has been observed by the literature teacher and sequentially, the boy has been motivated by the teacher to continue his writing in that particular section. The boy develops his skills and on the way the boy develops relationships with few based on intuition and manipulative actions. Equally both the teacher and the boy explore the possibilities by their won intuitions. These attributes are scientifically defined in the exploration division.

$$\begin{aligned} Y_i = \left\{ X_k \right\}, \\ \mathrm{W_k} > \mathrm{W_i}, \\ Y_i \rightarrow \text{relationship between literature} \\ \text{teacher and boy}, \\ X_{i,j}^P = X_{i,j} + Y \cdot \left(X_{i,j} - C_1 \cdot V_{i,j} \right), \\ X_{i,j}^P \rightarrow \text{writing skills of the boy}, \\ Y \in \left[0,1 \right], \\ C_1 \in \left\{ 1,2 \right\}, \\ V_{i,j} \rightarrow \text{teacher motivation}, \\ X_i = X_i^P \text{ if } W_i^P \le W_i, \\ \text{otherwise } X_i = X_i. \end{aligned} \quad (17)$$

Week by week the literature teacher observe the written content of the boy.

$$\begin{aligned} X_{i,j}^r = X_{i,j} + Y \cdot \left(U_j - C_2 \cdot X_{i,j} \right), \\ X_{i,j}^r \rightarrow \text{continuation of writing}, \\ U_j \rightarrow \text{skills of writing}, \\ Y \in \left[0,1 \right], \\ C_2 \in \left\{ 1,2 \right\}, \\ X_i = X_i^r \text{ if } W_i^r \le W_i, \\ \text{otherwise } X_i = X_i. \end{aligned} \quad (18)$$

Even the boy dwindle in writing in some moments, literature teacher encourage him to continue his writing.

In the course of writing, the boy makes peculiar relationships with few people. Especially the boy is in relationship with mother of his close classmate and wife of the teacher. To make this relationship the boy manipulates many situations and secretly observing the way of living and their relationships with others. Accordingly the boy alters his strategy to reach an in-depth relationship. The boy mind does an optimal search to find a way in a concentrated mode, to accomplish his thoughts and aim in the relationships. These conditions are scientifically formulated in the exploitation division.

$$
\begin{aligned}
&X_{i,j}^{s} = X_{i,j} + Y \cdot (1 - 2 \cdot Y) \cdot P, \\
&X_{i,j}^{s} \rightarrow \text{strategy of the boy to} \\
&\text{weave relationships}, \\
&Y \in [0,1], \\
&P = ub_j - lb_j / t, \\
&X_i = X_i^s \ if \ W_i^s \le W_i, \\
&otherwise \ X_i = X_i .
\end{aligned}
\tag{19}
$$

Occasionally chaos condition will occur in the relationship. It is not predictable but condition of chaos originate in some point and end in another point of circumstances. Chaos factor [5] has been included in the processes.

$$
\begin{aligned}
&c_{n+1} = c_n (1 - u_n), \\
&X_i = \delta \cdot X_{i-1} .
\end{aligned}
\tag{20}
$$

Limits of the region defined as:

$$
X_i^0 = lb + (ub - lb) \cdot X_i \ . \tag{21}
$$

Quasi-oppositional learning [5] is amalgamated in the technique as follows:

$$
Zz_{OBL}(t+1) = ub + lb - L(t) \ . \tag{22}
$$

$$
Zz_{QBL}(t+1) = \begin{cases} \dfrac{ub+lb}{2} + \\ +W \cdot \left((ub + lb - L(t)) - \dfrac{ub+lb}{2} \right) \\ if \ (ub + lb - L(t)) > \dfrac{ub+lb}{2}, \\ (ub + lb - L(t)) + \\ +W \cdot \left(\dfrac{ub+lb}{2} - (ub + lb - L(t)) \right), \\ or \ else . \end{cases} \tag{23}
$$

1. Begin;

2. Create population by quasi-oppositional based points;

3. Define the limits;

4. $R_{i,j} = lb_j + A(ub_j - lb_j)$;

5. $Y_i = \{X_k\}$;

6. $X_{i,j}^{P} = X_{i,j} + Y \cdot (X_{i,j} - C_1 \cdot V_{i,j})$;

7. $X_i = X_i^P \ if \ W_i^P \le W_i$;

8. $otherwise \ X_i = X_i$;

9. Observance of the content;

10. $X_{i,j}^{r} = X_{i,j} + Y \cdot (U_j - C_2 \cdot X_{i,j})$;

11. $X_i = X_i^r \ if \ W_i^r \le W_i$;

12. $otherwise \ X_i = X_i$;

13. Define the relationship of the boy;

14. $X_{i,j}^{s} = X_{i,j} + Y \cdot (1 - 2 \cdot Y) \cdot P$;

15. $P = ub_j - lb_j / t$;

16. $X_i = X_i^s \ if \ W_i^s \le W_i$;

17. $otherwise \ X_i = X_i$;

18. Define chaos condition;

19. $c_{n+1} = c_n (1 - u_n)$;

20. $X_i = \delta \cdot X_{i-1}$;

21. Define the limits;

22. $X_i^0 = lb + (ub - lb) \cdot X_i$;

23. End for;

24. $t = t + 1$;

25. Acquire the excellent solution;

26. End;

IV. RESULTS

Quasi-oppositional learning based chaotic psychology of relationships inspired (QCPR) optimization algorithm is validated in 7 benchmark functions [6]. Results are demonstrated in Table I.

$$f_1(\text{parabola}) = \sum_{i=1}^{D} x_i^2 \ , \qquad (24)$$

$$f_2(\text{Ackley}) = -20\,exp\left\{-0.2\sqrt{\frac{1}{D}\sum_{i=1}^{D} x_i^2}\right\} - exp\left\{\frac{1}{D}\sum_{i=1}^{D} cos(2\pi x_i)\right\} + 20 + e \ , \qquad (25)$$

$$f_3(\text{Rosen rock}) = \sum_{i=1}^{D-1}\left\{100 \cdot \begin{pmatrix} x_{i+1} \\ -x_i^2 \end{pmatrix}^2 + \begin{pmatrix} x_i \\ -1 \end{pmatrix}^2\right\} \ , \qquad (26)$$

$$f_4(\text{Griewank}) = \frac{1}{4000}\sum_{i=1}^{D} x_i^2 - \prod_{i=1}^{D} cos\left(\frac{x_i}{\sqrt{i}}\right) + 1 \ , \qquad (27)$$

$$f_5(\text{Hartman}) = -\sum_{i=1}^{4} c_i \cdot exp\left[-\sum_{j=1}^{3} a_{ij}\left(x_j - p_{ij}\right)^2 - \sum_{j=1}^{3} a_{ij} \cdot \left(x_j - p_{ij}\right)^2\right] \ , \qquad (28)$$

$$f_6(\text{Six} - \text{hump camel} - \text{back}) = 4x_1^2 - 2.1x_1^4 + \frac{1}{3}x_1^6 + x_1x_2 - 4x_2^2 + 4x_2^2 \ , \qquad (29)$$

$$f_7(\text{Goldstein} - \text{Price}) = \left(\begin{array}{c} 1 + (x_1 + x_2 + 1)^2 \cdot \\ \cdot(19 - 14x_1 + x_1^2 - 14x_2 + 6x_1x_2 + 3x_2^2) \end{array}\right) \cdot \left(\begin{array}{c} 30 + (2x_1 - 3x_2)^2 \cdot \\ \cdot 18 - 32x_1 + 12x_1^2 + 48x_2 - 36x_1x_2 + 27x_2^2 \end{array}\right) \ , \qquad (30)$$

TABLE I. ANALYSIS OF QCPR IN 7 BENCHMARK FUNCTIONS

F	HYBS [6]	AVSZ [6]	QCPR
F1	0.8874	0.0026	0.0057
F2	0.0918	0.0125	0.0238
F3	22.9814	16.5622	16.672
F4	1.1092 e-2	3.459 e-4	3.41 e-4
F5	-3.8629	-3.8629	-3.8629
F6	-1.0318	-1.0316	-1.0352
F7	3.0280	3.0130	3.0164

Quasi-oppositional learning based chaotic psychology of relationships inspired (QCPR) optimization algorithm is validated in IEEE 300 bus system. Table II and Fig. 1 demonstrate the estimation of results. TUS (MW) - True power loss, VOT (PU) – Voltage deviation

TABLE II. EVALUATION OF QCPR IN IEEE 300 BUS SYSTEM

Method	TUS(MW)	VOT(PU)
QIZ [7]	418.48	1.1054
IQIZ [7]	410.31	1.1276
MIF [8]	390.60	1.1079
OZP [9]	398.02	1.0886
QCPR	386.99	1.0103

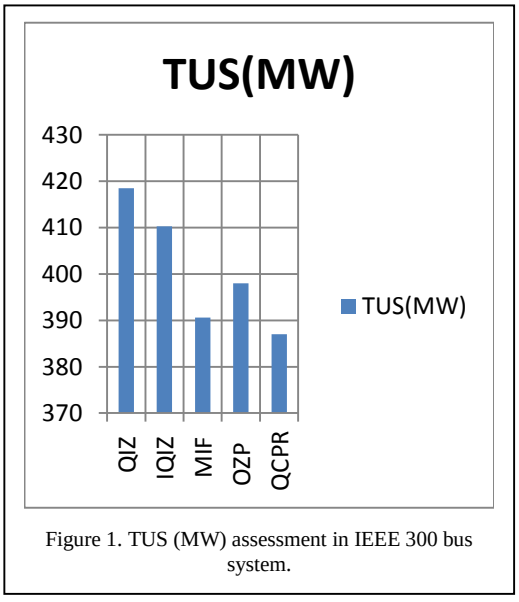

Figure 1. TUS (MW) assessment in IEEE 300 bus system.

Quasi-oppositional learning based chaotic psychology of relationships inspired (QCPR) optimization algorithm is validated in IEEE 354 bus system. Table III and Fig. 2 demonstrate the estimation of results

TABLE III. ESTIMATION OF QCPR IN IEEE 354BUS SYSTEM

Method	TUS(MW)	VOT(PU)
QIZ [7]	338.7150	0.51170
IQIZ [7]	341.1230	0.63950
MIF [8]	347.1323	0.6395
OZP [9]	336.02	0.4719
PCZ [10]	335.96	0.4706
QCPR	333.236	0.4271

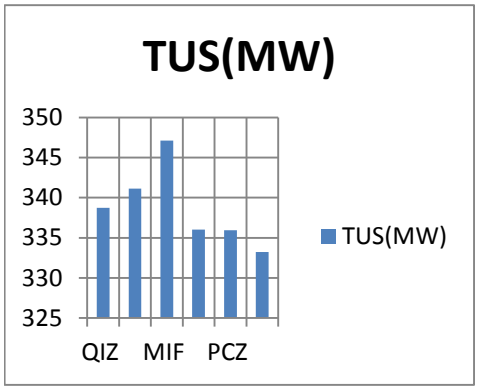

Figure 2. TUS (MW) assessment in IEEE 354 bus system.

Table IV shows the time taken by Quasi-oppositional learning based chaotic psychology of relationships inspired (QCPR) optimization algorithm.

TABLE IV. QCPR COMPUTATIONAL TIME

Technique	300bus T(S)	354 bus T(S
QCPR	56.12	69.31

V. CONCLUSION

Quasi-oppositional learning based chaotic psychology of relationships inspired (QCPR) optimization algorithm solved the true power loss dwindling problem skillfully. Precarious relationship between literature teacher and boy is articulated scientifically in the algorithm. Boy tutored by the literature teacher to progress his writing talents. This tips to developed and sneering boy to be progressively influencing relationship diminuendos. At one point boy intend and framing relationships between mother of his close classmate and wife of the teacher. In the exploration section of the procedure boys writing skills, precarious relationship between literature teacher and boy has been formulated. In the exploitation section how the age and conditions of the boy making him to articulate relationships with people. The relationships created by the boy viewed in cognitive mode- it is a psychology of relationships which can't be easily interpreted. To make and maintain the relationships the boy manipulates the situations around him. Occasionally chaos condition will occur in the relationship. It is not predictable but condition of chaos originate in some point and end in another point of circumstances. Quasi-oppositional learning and Chaos factor are amalgamated in the technique. Quasi-oppositional learning based chaotic psychology of relationships inspired (QCPR) optimization algorithm is validated in 7 Benchmark functions and IEEE 300, 354 bus systems.

REFERENCES

[1] Ozon, F. (2012). *In the House*. Mandarin Films.

[2] Meng, Z., & Pan, J. S. (2016). Monkey king evolution: a new memetic evolutionary algorithm and its application in vehicle fuel consumption optimization. *Knowledge-Based Systems*, *97*, 144-157.

[3] Bühler, J. L., & Orth, U. (2024). How relationship satisfaction changes within and across romantic relationships: Evidence from a large longitudinal study. *Journal of Personality and Social Psychology*, *126*(5), 930.

[4] Kanagasabai, L. (2024). Novel empress SARANI optimization algorithm for active power loss reduction and voltage stability enhancement. *Heliyon*, *10*(22).

[5] Truong, K. H., Nallagownden, P., Elamvazuthi, I., & Vo, D. N. (2020). A quasi-oppositional-chaotic symbiotic organisms search algorithm for optimal allocation of DG in radial distribution networks. *Applied Soft Computing*, *88*, 106067.

[6] Yapıcı, H., & Çetinkaya, N. (2017). An improved particle swarm optimization algorithm using eagle strategy for power loss minimization. *Mathematical Problems in Engineering*, *2017*(1), 1063045.

[7] Ali, M. H., Soliman, A. M. A., Abdeen, M., Kandil, T., Abdelaziz, A. Y., & El-Shahat, A. (2023). A novel stochastic optimizer solving optimal reactive power dispatch problem considering renewable energy resources. *Energies*, *16*(4), 1562.

[8] Varan, M., Erduman, A., & Menevşeoğlu, F. (2023). A grey wolf optimization algorithm-based optimal reactive power dispatch with wind-integrated power systems. *Energies*, *16*(13), 5021.

[9] Lian, L. (2022). Reactive power optimization based on adaptive multi-objective optimization artificial immune algorithm. *Ain Shams Engineering Journal*, *13*(5), 101677.

[10] Sahli, Z., Hamouda, A., Sayah, S., Trentesaux, D., & Bekrar, A. (2022). Efficient hybrid algorithm solution for Optimal Reactive Power Flow using the sensitive bus approach. *Engineering, Technology & Applied Science Research*, *12*(1), 8210-8216.

eNergetics 2025
DOI: https://doi.org/10.5281/zenodo.18615684

Original Scientific Article

Online Parameter Identification of Supercapacitor Models using Recursive Least Squares Algorithm

Latifa Ait Rahou[1], Itto El-Kabassi[2], Adil Brouri [3], Benaissa El Fahime[4]

[1,2,3,4]Moulay Ismail University, Meknes, Morocco

[1]l.aitrahou@edu.umi.ac.ma, [2]itto.elkabassi@edu.umi.ac.ma, [3]a.brouri@ensam-umi.ac.ma, [4]b.elfahime@ensam-umi.ac.ma

Abstract—**Supercapacitor-based energy storage systems have been widely applied in various power-level applications in recent years. Owing to their ultra-high capacitance and capacitor-like behavior, supercapacitors are particularly well-suited for high-power, short-duration scenarios, such as regenerative braking in electric vehicles and transient frequency regulation in power grids. For all such applications, having an accurate supercapacitor model is crucial for analyzing their dynamic behavior under diverse operating conditions. To enhance modeling accuracy, several equivalent circuit models have been proposed in the literature, including simple RC, extended RC, two-branch RC, and three-branch RC models. In addition to model selection, parameter identification techniques play a crucial role in improving the model precision. This paper reviews commonly used supercapacitor models and discusses the applicability of each under specific operating conditions. Furthermore, a parameter identification method based on the Recursive Least Squares (RLS) algorithm is proposed. This approach improves the accuracy of capturing the discharge behavior of the supercapacitor. The effectiveness of the method is validated through mathematical modeling and experimental comparisons.**

Keywords - supercapacitor model, parameter identification method, energy storage, recursive least squares.

I. INTRODUCTION

The production and consumption of energy are largely based on the combustion of fossil fuels, which have significant environmental and economic impacts. Therefore, it is essential to develop energy storage solutions that are efficient, cost-effective, and environmentally friendly [1]. An ultracapacitor, or supercapacitor, is a device capable of storing and rapidly releasing large amounts of electrical energy. Characterized by high power density, long life span, fast charging capability, and efficient operation over a wide temperature range, supercapacitors present an attractive alternative to conventional batteries and capacitors [2]. These benefits make supercapacitors ideal for supplying power in rural areas without access to public grids or in locations where wiring and power supply costs are high. They are also suitable for a wide range of applications, including wind power generation, photovoltaic systems, railways, electric vehicles, and power grids [3]. Due to their light weight and versatility, supercapacitors are often used as power sources for portable devices, including laptops, phones, digital cameras. They can also be used in electric and hybrid vehicles to provide the high-power density required for short-term acceleration, as well as for energy recovery during braking. This not only improves overall energy efficiency but also protects the battery from rapid, high-frequency charge-discharge cycles [4]. In addition, the energy and power densities of supercapacitors are illustrated using the Ragone diagram Fig. 1 [4].

ISBN: 978-86-82602-07-1

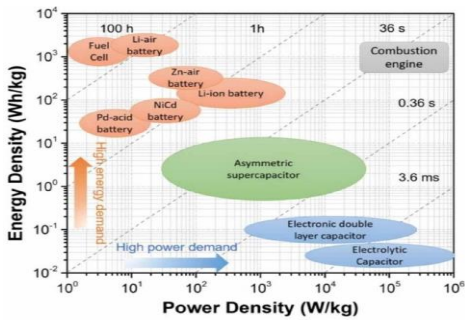

Figure 1. Ragone diagram of energy storage devices.

As seen in Fig. 1, a battery may generate up to 150Wh/kg of energy, which is roughly ten times what SCs can do. With regard to power density, the batteries have no ability for meeting SC values. Hardly more than 200W/kg is produced by batteries, which is around 20 times less than the output of an electrochemical capacitor. In addition, the batteries encounter limitations such as rapid output decreases because of the cold ambient temperatures or short charge discharge cycles. It is costly to manage and has a short life [5]. Currently, such SCs can't be utilized for replacing the technology of batteries, yet they might be acting as replacements via offering instantaneous current needed for minimizing the current of battery with regard to temporary and momentary loss of power. In addition, the electrochemical SCs might be parallel mounted for compensating the temporary and momentary interruptions in large-scale battery units. This would dramatically It minimize the excessive burden imposed on the batteries by short term interruptions [6]. Presently, all SC researchers are focused on enhancing the energy density of supercapacitors while preserving their core strengths: high power density, rapid charge/discharge capability, and excellent cycle stability. their limited energy density prevents them from being adopted as primary long-term energy storage solutions Current research efforts are thus cantered on the identification of electrical parameters in SCs to better understand their performance characteristics and guide future optimization [7].

II. DESCRIPTION OF SUPERCAPACITOR MODEL

The objective of this section is to present and discuss the most commonly used equivalent circuit models (ECMs) of supercapacitors available in the literature [2,8,9].

A. Simple RC Model Structure

The simple RC model structure, shown in Fig. 2, is widely used in manufacturers' data sheets. This model includes a capacitance C representing the energy storage element and an equivalent series resistor R_s that models the internal resistance. The main advantage of this model is the simplicity.

This model can be analytically described by the following mathematical equations:

$$\begin{cases} U_{sc}(t) = R_s I_{sc}(t) + U_c(t) \\ I_{sc}(t) = C(t)\dfrac{dU_c(t)}{dt} \end{cases}, \qquad (1)$$

where $U_{sc}(t)$ is the terminal voltage, $I_{sc}(t)$ is the input current, and $U_c(t)$ is the voltage of the capacitor $C(t)$. Generally, the curve of $C(t)$ versus $U_c(t)$ is smoothing nonlinearity, this property is confirmed by Fig. 3 [6,10,11].

According, the working interval of the voltage $U_c(t)$ can be divided into a set of subintervals $[V_k, V_{k+1})$, for $k = 1....p$, where p is an arbitrarily chosen integer (preferably large).

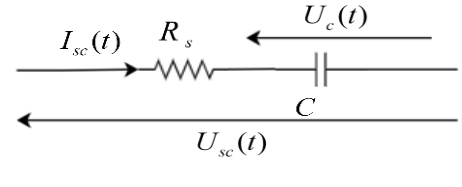

Figure 2. RC model of supercapacitor.

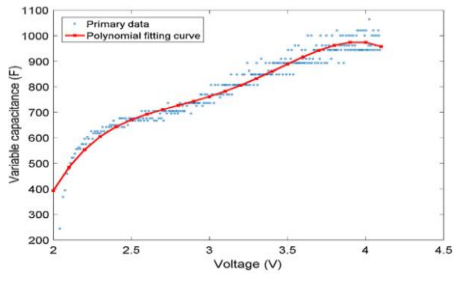

Figure 3. Example of fitting curves $C(t)$ vs $U_c(t)$ capacitance.

Within each subinterval $[V_k, V_{k+1})$, the curve of $C(t)$ versus $U_c(t)$ can be considered approximately linear. Namely, one has for any $U_c(t) \in [V_k, V_{K+1})$, for $k = 1....p$

$$C(t) = C_{0k} + \alpha_k U_c(t), \quad (2)$$

where α_k and C_{0k} are the parameters of linear segment in the subinterval k.

B. Extended RC Model Structure

The Extended RC Model is widely used for supercapacitor modeling because it offers a good compromise between simplicity and accuracy. This model structure is giving in Fig. 4. It includes a series resistance and a parallel RC network $R_p \cdot C_p$ that captures the dynamic charge redistribution. The goal of this study is to identify R_s , C_p and R_p from experimental current–voltage data. According to Kirchhoff's law, the system behavior is described by:

$$\begin{cases} U_{sc}(t) = R_s I_{sc}(t) + U_p(t) \\ I_{sc}(t) = \dfrac{U_p(t)}{R_p} + C_p \dfrac{dU_p(t)}{dt} \end{cases}. \quad (3)$$

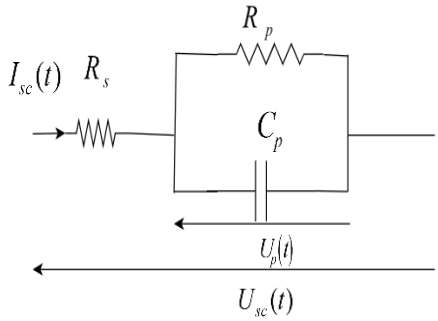

Figure 4. Extended RC model of supercapacitor.

III. TRANSFER FUNCTION MODELING

A. Transfer Function of the Simple RC Model

Applying the Laplace transform, Eq. (1) gives:

$$I_{sc}(s) = \Gamma\left\{C(t)\frac{dU_c}{dt}\right\} = \Gamma\{C(t)\} * (sU_c(s)), \quad (4)$$

where $*$ denotes the convolution operator and s denotes the Laplace operator.Assuming a constant capacitance C, the Laplace transform simplifies, and Eq. (1) can be written as:

$$\begin{cases} U_{sc}(s) = R_s I_{sc}(s) + U_c(s) \\ I_{sc}(s) = CsU_c(s) \end{cases}, \quad (5)$$

where the initial conditions of electrical variable are considered to be null. Then, the transfer function $G(s)$ between the terminal voltage $U_{sc}(s)$ and the input current $I_{sc}(s)$ of the SC can be expressed as:

$$G(s) = \frac{U_{sc}(s)}{I_{sc}(s)} = \frac{1 + R_s Cs}{Cs}. \quad (6)$$

B. Transfer Function of Extended RC Model

Applying the Laplace transform, Eq. (2) can be expressed as

$$\begin{cases} U_{sc}(s) = R_s I_{sc}(s) + U_p(s) \\ I_{sc}(s) = \dfrac{U_p(s)}{R_p} + C_p s U_p(s) \end{cases}, \quad (7)$$

where the initial conditions of the electrical variables are assumed to be zero, and S is the Laplace operator.From this system, the transfer function $G(s)$ between the terminal voltage $U_{sc}(s)$ and the input current $I_{sc}(s)$ is given by:

$$G(s) = \frac{U_{sc}(s)}{I_{sc}(s)} = \left(R_s + \frac{R_p}{1 + R_p C_p s}\right). \quad (8)$$

This expression can be rewritten in rational form as:

$$G(s) = \left(\frac{R_s + R_p + R_s R_p C_p s}{1 + R_p C_p s}\right). \quad (9)$$

C. Discrete form of the Simple RC Model and Extended RC Model

In this study, the continuous-time supercapacitor model is discretized to provide a discrete-time representation suitable for parameter estimation.

For this purpose, the Tustin (bilinear) transformation is employed [9]. In this method, the Laplace variable s is approximated by the expression:

$$s \approx \frac{2}{T}\frac{1-z^{-1}}{1+z^{-1}} \ , \qquad (10)$$

where z is the discrete-time complex variable and T represents the sampling period. In this work, a sampling period of 0.1 s is adopted for both models to ensure a good trade-off between estimation accuracy and computational efficiency.

a) Discrete form of the Simple RC Model

By applying this transformation, the discrete-time transfer function $G(z^{-1})$, describing the simple RC model, is expressed as:

$$G(z^{-1}) = \frac{\beta_1 + \beta_2 z^{-1}}{1-z^{-1}} \ , \qquad (11)$$

where the coefficients β_1 and β_2 are respectively given by the following expressions:

$$\begin{cases} \beta_1 = \dfrac{T+2\tau}{2C} \\ \beta_2 = \dfrac{T-2\tau}{2C} \end{cases} . \qquad (12)$$

With

$$\tau = R_s C \ . \qquad (13)$$

Lastly, the values of the circuit parameters are obtained from the identified coefficients as follows:

$$\begin{cases} R_s = \dfrac{\beta_1 - \beta_2}{2} \\ C = \dfrac{T}{\beta_1 + \beta_2} \end{cases} . \qquad (14)$$

Using the discretized transfer function $G(z^{-1})$, given in Eq. (11), the recurrence equation of the model is given as follows:

$$U_{sc}(k) = U_{sc}(k-1) + \beta_1 I_{sc}(k) + \beta_2 I_{sc}(k-1) \ , (15)$$

the regression vector $\varphi(k)$ and the parameter vector $\theta(k)$ are defined as:

$$\begin{cases} \varphi(k) = [U_{sc}(k-1) \quad I_{sc}(k) \quad I_{sc}(k-1)] \\ \theta(k) = [1 \quad \beta_1 \quad \beta_2] \end{cases} . \qquad (16)$$

In (15), k is a discrete random variable $k = (0,1,2,3,...,n)$, Eq. (16) can be written as follows:

$$U_{sc} = \theta(k)\varphi^T(k) \ . \qquad (17)$$

b) Discrete form of the extended RC model

The discrete-time transfer function $G(z^{-1})$, corresponding to the continuous-time model $G(s)$, is derived and can be written as:

$$G(z^{-1}) = \frac{\beta_1 + \beta_2 z^{-1}}{1-\alpha_1 z^{-1}} \ , \qquad (18)$$

where the coefficients α_1 , β_1 and β_2 are, respectively, given as:

$$\begin{cases} \alpha_1 = \dfrac{T-2\tau_1}{T+2\tau_1} \\ \beta_1 = \dfrac{R_{eq}T+2\tau_2}{T+2\tau_1} \\ \beta_2 = \dfrac{R_{eq}T-2\tau_2}{T+2\tau_1} \end{cases} . \qquad (19)$$

let consider:

$$\begin{cases} \tau_1 = R_p C_p \\ \mathrm{R}_{eq} = R_s + R_p \\ \tau_2 = R_s \tau_1 \end{cases} . \qquad (20)$$

Finally, the corresponding circuit parameter values can be determined from the identified coefficients, namely:

$$\begin{cases} R_s = \dfrac{\beta_1 - \beta_2}{\alpha_1 + 1} \\ R_p = \dfrac{2\beta_2 - 2\alpha_1\beta_1}{1 - \alpha_1^{\,2}} \\ C_p = \dfrac{T\left(\alpha_1 + 1\right)^2}{4\left(\beta_2 + \alpha_1\beta_1\right)} \end{cases} . \quad (21)$$

From Eq. (18), the recursive function is obtained as:

$$\begin{aligned} U_{sc}(k) &= \alpha_1 U_{sc}(k-1) + \\ &+ \beta_1 I_{sc}(k) + \beta_2 I_{sc}(k-1) \end{aligned} . \quad (22)$$

(22), can be modified as follows

$$U_{sc} = \theta(k)\varphi^T(k) , \quad (23)$$

where $k = (0,1,2,3,...,n)$ and

$$\begin{cases} \varphi(k) = [U_{sc}(k-1) \quad I_{sc}(k) \quad I_{sc}(k-1)] \\ \theta(k) = [\alpha_1 \quad \beta_1 \quad \beta_2] \end{cases} . (24)$$

The vector $\varphi(k)$ contains the measured input and output signals, while $\theta(k)$ represents the set of unknown model parameters to be identified.

IV. Forgetting Factor Recursive Least Square Approach

An efficient framework for online supercapacitor parameter identification is provided by the ECM-based Recursive Least Squares (RLS) algorithm. However, its performance may deteriorate at low excitation levels due to numerical instability and imprecise parameter estimation. The Forgetting Factor Recursive Least Squares (FFRLS) method is used to solve this problem. FFRLS reduces the effect of historical data by incorporating a constant forgetting factor. The numbers become more stable and convergence is accelerated as a result. The FFRLS approach is implemented using Eqs. (25)–(29), [12].

$$U_{sc}(k) = \theta(k)\varphi^T(k) + e(k) , \quad (25)$$

$$G(k) = \frac{P(k-1)\varphi(k)}{\lambda + \varphi^T(k)P(k-1)\varphi(k)} , \quad (26)$$

$$P(k) = \frac{P(k-1) - G(k)\varphi^T(k)P(k-1)}{\lambda} , (27)$$

$$e(k) = U_{sc}(k) - \varphi^T(k)\hat{\theta}(k-1) , \quad (28)$$

$$\hat{\theta}(k) = \hat{\theta}(k-1) + G(k)e(k) , \quad (29)$$

where, $P(k)$ is the covariance matrix; λ is the forgetting factor, which can assign weights to the parameter identification data and reduce the proportion of old data in the recursion process. Compared with the traditional Recursive Least Squares algorithm, the FFRLS algorithm requires less computation and has a faster response speed. The larger the λ, the slower the forgetting speed. If the value of λ is 1, FFRLS algorithm will degenerate into the Least Squares algorithm. The smaller the λ, the stronger the tracking ability of the FFRLS algorithm. The value of λ is usually taken between 0 and 1. Taking into account the forgetting speed and tracking ability of the algorithm, here we take as λ = 0.978 or simple RC Model and λ = 0.99 for extended RC model. The initial conditions for the recursive estimation must also be defined. Accordingly, the prediction of the initial error covariance matrix $P(0)$ and the initial estimate of the parameter vector $\hat{\theta}(0)$ is required. The covariance matrix $P(0)$ can be initialized as $P(0) = c[I]$, where c is a large positive constant and $[I]$ is the identity matrix. Here, $\hat{\theta}(k)$: estimation of parameter vector θ; $e(k)$: estimation error of the terminal voltage $U_{sc}(k)$. If the error levels of the system change substantially, the algorithm quickly replaces the old data with new data to establish a new learning model that accurately reflects the current state of the system.

V. Simulation And Discussion

This section presents the simulation results for the identification of supercapacitor parameters. The experimental current and voltage signals shown in Fig. 5 used as input data were obtained from a study in the literature [13-16].

These data correspond to a Maxwell BCAP1500 supercapacitor tested at a constant temperature of 65 °C [13]. The identification procedure and simulations were conducted using

a MATLAB code specifically designed to apply the FFRLS algorithm to these real-world datasets.

Fig. 6 shows the comparison between the measured and estimated voltages, as well as the instantaneous error for the simple RC model.

Fig. 7 presents the evolution of the estimated coefficients of the same model. The identification results of the simple RC model are summarized in Table I, while the error metrics used for model validation are provided in Table II.

Fig. 8 shows the comparison between the measured and estimated voltages, as well as the instantaneous error for the extended RC model.

Fig. 9 presents the evolution of the estimated coefficients of the same model. The identification results of the extended RC model are summarized in Table III, while the error metrics used for model validation are provided in Table IV.

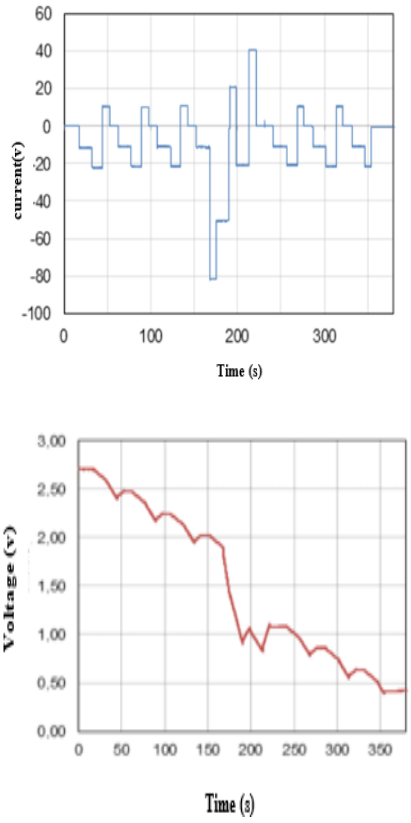

Figure 5. Applied supercapacitor current and measured voltage.

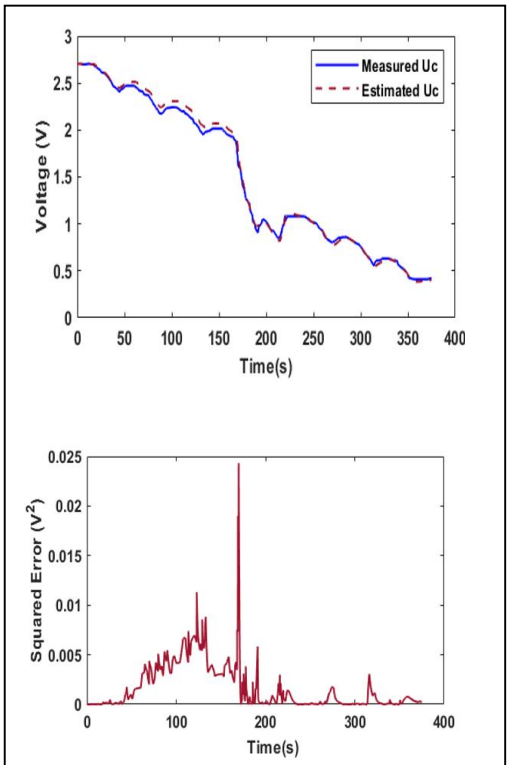

Figure 6. Voltage Comparison and Instantaneous Error of simple RC model.

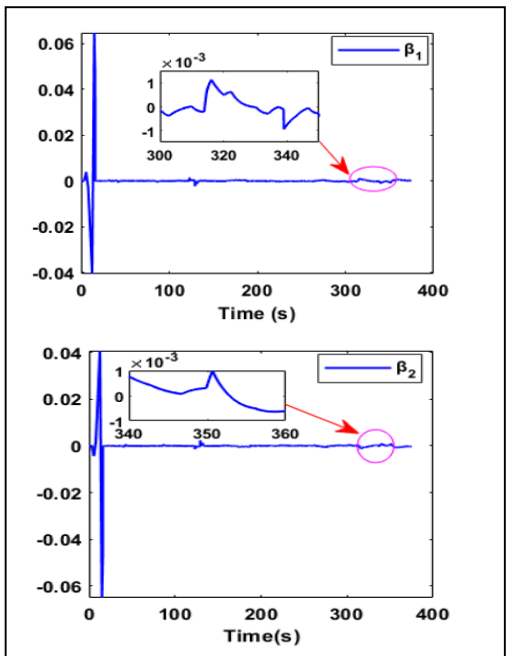

Figure 7. Evolution of the estimated coefficients of the simple model RC.

TABLE I. IDENTIFICATION RESULTS OF SIMPLE RC MODEL.

Parameters	Results
R_s	0.00126 (Ω)
C	1 486.354 (F)

TABLE II. ERROR METRICS FOR MODEL VALIDATION OF THE SIMPLE RC MODEL.

Parameters	Results
R_s	0.00020 (Ω)
R_p	0.0099 (Ω)
C_p	1496.46 (F)

TABLE III. IDENTIFICATION RESULTS OF SIMPLE RC MODEL.

Metric	Value (V)
Root Mean Square Error	0.0407
Mean Absolute Error	0.0307
Maximum Error	0.1559

TABLE IV. ERROR METRICS FOR MODEL VALIDATION OF THE EXTENDED RC MODEL.

Metric	Value (V)
Root Mean Square Error	0.0443
Mean Absolute Error	0.0015
Maximum Error	2.7059

The parameters identified for both the simple and extended RC models were validated by comparing them with published results and the manufacturer's datasheet. The obtained capacitances are very close to the nominal capacitance of the BCAP1500 supercapacitor (1500 F) [13], Confirming the accuracy of the FFRLS based identification. The identified resistances, on the order of milliohms, are consistent with the typical values reported in the datasheet and with results reported in the literature [13,14,16]. The convergence of the parameters toward stable values and the low mean errors indicate that the FFRLS algorithm can accurately capture both the static and dynamic behaviors of the supercapacitor. Small differences in resistance values can be attributed to experimental conditions, measurement noise, or the specific equivalent-circuit topology used. Finally, these comparisons demonstrate that the proposed identification method provides physically meaningful and robust parameter estimates.

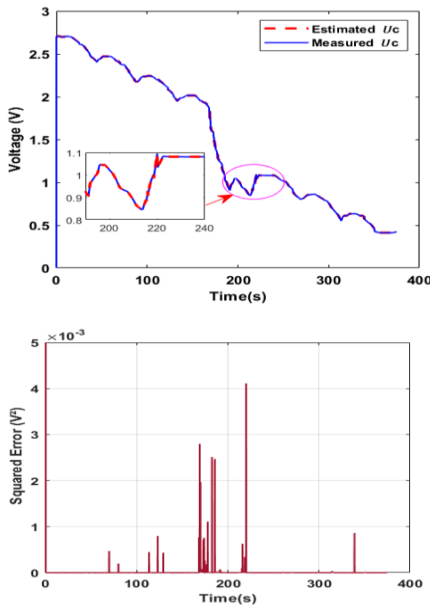

Figure 8. Voltage comparison and instantaneous error of extended RC model.

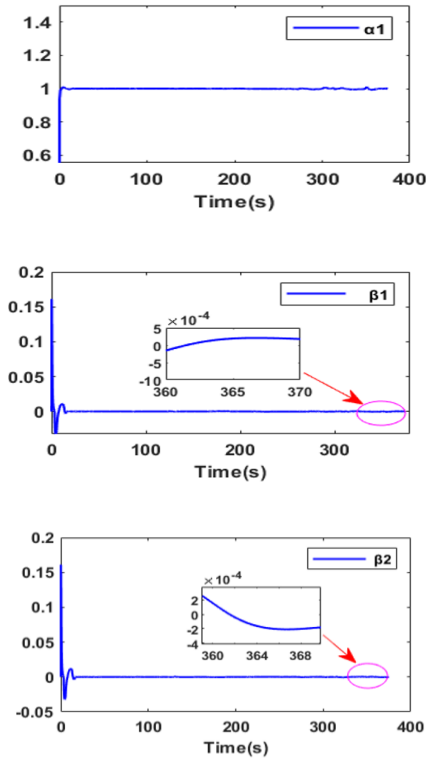

Figure 9. Evolution of the estimated coefficients of the extended RC model.

VI. Conclusion

Two RC model (simple and extended) of a supercapacitor with parameter identification using the RLS method is described in this paper. The identification parameters model was simulated using MATLAB/Simulink. The simulation's results demonstrate the efficacy and robustness of the RLS algorithm.

Acknowledgement

This work is supported by the National Center for Scientific and Technical Research (CNRST).

References

[1] Yadlapalli, R. T., Alla, R. R., Kandipati, R., & Kotapati, A. (2022). Super capacitors for energy storage: Progress, applications and challenges. *Journal of Energy Storage*, *49*, 104194. https://doi.org/10.1016/j.est.2022.104194

[2] Jalal, N. I., Ibrahim, R. I., & Oudah, M. K. (2021, August). A review on Supercapacitors: Types and components. *Journal of Physics: Conference Series*, *1973*(1), 012015. https://doi.org/10.1088/1742-6596/1973/1/012015

[3] Zhang, J., Gu, M., & Chen, X. (2023). Supercapacitors for renewable energy applications: A review. *Micro and Nano Engineering*, *21*, 100229. https://doi.org/10.1016/j.est.2024.112563

[4] Allagui, A., Fouda, M. E., & Elwakil, A. S. (2020). Communication—the Ragone plot of supercapacitors under different loading conditions. *Journal of The Electrochemical Society*, *167*(2), 020533. https://doi.org/10.1149/1945-7111/ab6bb9

[5] Iro, Z. S., Subramani, C., & Dash, S. S. (2016). A brief review on electrode materials for supercapacitor. *International Journal of Electrochemical Science*, *11*(12), 10628-10643.

[6] Zhu, Y., Murali, S., Stoller, M. D., Ganesh, K. J., Cai, W., Ferreira, P. J., ... & Ruoff, R. S. (2011). Carbon-based supercapacitors produced by activation of graphene. *Science*, *332*(6037), 1537-1541. https://doi.org/10.1002/9783527680054.ch7

[7] Song, S., Zhang, X., Li, C., Wang, K., Sun, X., Huo, Q., ... & Ma, Y. (2019). Equivalent circuit models and parameter identification methods for lithium-ion capacitors. *Journal of Energy Storage*, *24*, 100762. https://doi.org/10.1016/j.est.2019.100762

[8] Berrueta, A., Ursua, A., San Martin, I., Eftekhari, A., & Sanchis, P. (2019). Supercapacitors: electrical characteristics, modeling, applications, and future trends. *IEEE Access*, *7*, 50869-50896. https://doi.org/10.1109/access.2019.2908558

[9] Bertrand, N., Sabatier, J., Briat, O., & Vinassa, J. M. (2010). Fractional non-linear modelling of ultracapacitors. *Communications in Nonlinear Science and Numerical Simulation*, *15*(5), 1327-1337. https://doi.org/10.1016/j.cnsns.2009.05.066

[10] Mehandzhiyski, A. Y., Wang, X., Anquetil-Deck, C., Chen, D., & Grimes, B. A. (2021). Microscopic insight to nonlinear voltage dependence of charge in carbon-ionic liquid supercapacitors. *Energy Material Advances*. https://doi.org/10.34133/2021/9849202

[11] Szewczyk, A., Sikula, J., Sedlakova, V., Majzner, J., Sedlak, P., & Kuparowitz, T. (2016). Voltage dependence of supercapacitor capacitance. *Metrology and Measurement Systems*, *23*(3). https://doi.org/10.1515/mms-2016-0031

[12] Wang, X. G., Liu, J. W., Wang, H. L., Ding, Y. J., & Guo, Y. J. (2023). Parameter Identification Model and Capacity Analysis of Retired Power Battery. *Electrochemistry*, *91*(3), 037001-037001. https://doi.org/10.5796/electrochemistry.22-00132

[13] Bououchma, Z., & Sabor, J. (2021). Online diagnosis of supercapacitors using extended Kalman filter combined with PID corrector. *Int. J. Power Electron. Drive Syst. IJPEDS*, *12*(3), 1521. https://doi.org/10.11591/ijpeds.v12.i3.pp1521-1534

[14] Nadeau, A., Sharma, G., & Soyata, T. (2014, May). State-of-charge estimation for supercapacitors: A Kalman filtering formulation. In *2014 IEEE International Conference on Acoustics, Speech and Signal Processing (ICASSP)* (pp. 2194-2198). IEEE. https://doi.org/10.1109/icassp.2014.6853988

[15] Chiang, C. J., Yang, J. L., & Cheng, W. C. (2013). Temperature and state-of-charge estimation in ultracapacitors based on extended Kalman filter. *Journal of Power Sources*, *234*, 234-243. https://doi.org/10.1016/j.jpowsour.2013.01.173

[16] Peng, Z., & Jikai, L. (2011, July). On new UAV flight control system based on Kalman & PID. In *2011 2nd International Conference on Intelligent Control and Information Processing* (Vol. 2, pp. 819-823). IEEE. https://doi.org/10.1109/icicip.2011.6008362

eNergetics 2025
DOI: https://doi.org/10.5281/zenodo.18619842

Original Scientific Article

Bald Eagle Search Algorithm-based Hybrid Wind Turbine Distributed Generation and Battery Energy Storage System Allocation Optimization

Mohamed Zellagui[1], Samir Settoul[2]

[1]Department of Electromechanical Engineering, University of Batna 2, Batna, Algeria
[2]Department of Electrical Engineering, Badji-Mokhtar Annaba University, Annaba, Algeria

[1]m.zellagui@univ-batna2.dz, [2]samir.settoul@univ-annaba.dz

Abstract—**This article describes the main methods for locating and sizing battery energy storage systems (BESSs) and wind turbine distributed generators (WTDGs) inside electrical distribution systems (EDS). In order to minimize the overall active loss as a multi-objective function, this study examines the best way to plan several hybrid WTDG and BESS units in the EDS. In the first case, WTDGs are installed to pump active power into the EDS. In the second scenario, the EDS is provided by the simultaneous deployment of the hybrid WTDG and BESS units. The construction of entirely new multi-objective functions (MOF) based on the total of the three technical metrics: active power loss, voltage variation, and overcurrent relay working times is what makes the proposed work unique. The bald eagle search algorithm (BESA), a recently developed meta-heuristic technique, is used in this paper to test the proposed MOF in the standard IEEE 69-bus electrical distribution network.**

Keywords - wind turbine distributed generation, battery energy storage system, electrical distribution system, bald eagle search algorithm, optimal allocation.

I. INTRODUCTION

The load fluctuation and energy flow of power networks are becoming increasingly unstable due to the intermittent generation of renewable energy resources (RERs).

Consequently, a number of issues, such as enhancing the reliability of the power system and expanding capacity, improving power quality, managing load growth, accommodating higher penetration of renewable resources, and lowering emissions of greenhouse gas, are causing power grids to go through a transitional phase.

Due to their high degree of inertia and ability to produce clean energy reliant on natural resources, wind turbines are increasingly employed in distribution systems. We might convert the kinetic energy into an EDS system by using wind turbines (WTs).

The use of RERs, such as wind turbine distributed generators (WTDGs), in electrical distribution systems (EDSs) has rapidly increased in recent years [1]. However, distribution networks have faced a number of challenges due to WTDGs' erratic output power. A BESS has emerged with WTDGs to ensure the smooth injection of their output power into the grid [2].

The BESS provides a workable solution for lowering RER output variations and improving EDS connectivity through its ability to operate independently in charging and discharging modes.

One of the distinguishing features of RES is their ability to be integrated into distribution networks as a result of their reduced size and

ISBN: 978-86-82602-07-1

rating in comparison with centralized conventional facilities. If implemented properly, RES could offer a number of benefits. There may be a variety of objectives for the WTDG optimum allocation.

Numerous optimization techniques are included in the optimal allocation, including both conventional and artificial intelligence methods that have been examined and contrasted in [3,4]. Overall system losses and enhanced voltage profiles are achieved in this work by a proposed approach for the optimal placement of hybrid WTDG and BESS units in EDS [5].

The ideal location of WTDG and BESS in the EDS has lately been studied by many researchers using various algorithms and techniques. These include mixed integer optimization algorithms for lowering overall costs taking into account the uncertainty in wind generators [6], mixed integer conic programming for lowering the cost of emissions [7], mixed integer nonlinear programming for lowering investment and operating costs [8], and mixed integer quadratic programming for lowering annual levelized investment and operating costs [9].

Another technique for reducing EDS line loads, power loss, and voltage volatility is the artificial bee colony algorithm [10]. The power loss and bus voltage were reduced using an elitist multi-objective genetic approach [11,12], the daily energy loss was minimized using modified African buffalo optimization [13], and the annual cost of energy loss was minimized using a novel inherited competitive swarm optimization algorithm [14,15].

In order to minimize power loss while maximizing the voltage stability factor and economic index, the sum of the three technical parameters are combined in a new multi-objective functions [16], relaxed mixed integer nonlinear programming [17], as well as the crow search algorithm, which is used to lower the annual cost and cost of flicker emission generated by WT sources [18], and were developed using a range of chaotic grey wolf optimization techniques.

The most recent study, which incorporated a unique chaotic student psychology-based optimization taking into account an average hourly load demand profile and the load models, employed novel metaheuristic algorithms [19]. Techniques for optimizing bald eagle searches have been altered to lower the total active loss

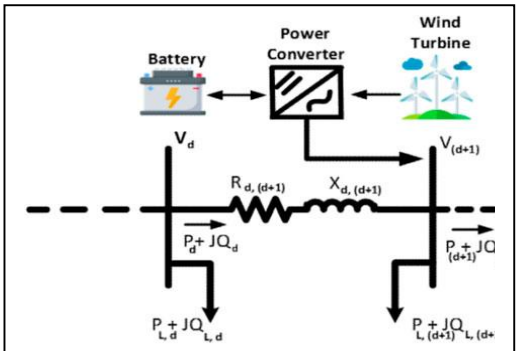

Figure 1. Section of the line with hybrid WTDG and BESS system.

[20], and maximizing the technological, environmental, and financial goals is the goal of the search group algorithm [21].

Additionally, the genetic algorithm is employed to minimize the difference between the actual output of new energy and the output connected to the grid [22], and a hybrid multi-objective approach combines the GA and PSO algorithms to lower the total costs of BESS and power losses [23] at the same time.

The operational objectives are in conflict with one another. The allocation of hybrid WTDG and BESS is therefore a difficult multi-objective functions (MOF) problem that needs to be resolved while maximizing a number of conflicting objectives. A hybrid WTDG-BESS system allocation problem is intended to lower the MOF in this study. This problem may be solved by utilizing the bald eagle search algorithm (BESA), a new meta-heuristic algorithm that has been tested on the IEEE 69-bus standard.

II. Problem Formulation and Constraints

A. *Distribution Line Model*

Fig. 1 shows that the system load flows are changed by installing WTDG alone or with BESS allocation in the distribution line.

B. *MOF*

To reduce the technical parameters of Total Active Power Loss (TAPL), Total Voltage Deviation (TVD), and Total Operation Time (TOT), this study identifies and determines the best position and size for hybrid sources, WTDG and BESS EDS:

$$MOF = Minimize \sum_{i=1}^{N_{bus}} \sum_{j=2}^{N_{bus}} \sum_{i=1}^{N_R} \left[TAPL_{i,j} + TVD_j + TOT_i \right] . \quad (1)$$

We are starting with the TAPL of the distribution line, which can be expressed by [22-25].

$$TAPL_{i,j} = \sum_{i=1}^{N_{bus}} \sum_{j=2}^{N_{bus}} APL_{i,j} , \quad (2)$$

$$APL_{i,j} = \alpha_{ij} \left(P_i P_j + Q_i Q_j \right) + \beta_{ij} \left(Q_i P_j + P_i Q_j \right), \quad (3)$$

$$\alpha_{ij} = \frac{R_{ij}}{V_i V_j} \cos\left(\delta_i - \delta_j \right), \quad (4)$$

$$\beta_{ij} = \frac{R_{ij}}{V_i V_j} \sin\left(\delta_i + \delta_j \right) . \quad (5)$$

R_{ij} represents the resistance of the line. Where (V_i, V_j) and (δ_i, δ_j) correspond to voltage magnitudes and angles, respectively. (P_i, P_j) and (Q_i, Q_j) denote the active and reactive powers in buses, respectively.

The second term is the TVD, defined as [24,25].

$$TVD_j = \sum_{j=2}^{N_{bus}} \left| 1 - V_j \right| . \quad (6)$$

The final term, the TOT of overcurrent relays, is defined as [26].

$$TOT_i = \sum_{i=1}^{N_R} T_i , \quad (7)$$

$$T_i = TDS_i \left(\frac{A}{M_i^B - 1} \right), \quad (8)$$

$$M_i = \frac{I_F}{I_P} . \quad (9)$$

The operation time of the relay is denoted as T_i, in addition, TDS serves as the time dial setting, and the multiple of pickup current is denoted as M. The value of A is set to 0.14, and B is set to 0.02, and they serve as relay constants.

I_F and I_P represent the fault current and the pickup current, respectively. N_R is the number of overcurrent relays.

III. Overview of the BESA Algorithm

The hunting behavior of bald eagles (BEs) was affected by the BESA [27]. The hunt strategies include space selection, scouring, and swooping down on the prey.

A. Space Selection

Equation (10) is used by the bald to arbitrarily generate the amount of space based on the previously provided information:

$$Q_{new} = Q_{best} + \alpha . r . \left(Q_{mean} - Q_j \right), \quad (10)$$

where r is an integer, whose value lies between 0 and 1, Q_{best} indicates the best search, Q_{new} denotes the new search, and Q_{mean} indicates that the eagles have retained all the information from the previous search.

Similar to the previous BESA, location shifts are resolved using an updated parameter α, which can be expressed using Eq. (11) and is comparable to a preset weight:

$$\alpha = 1.5 \left(\frac{k}{k_{\max}} \right), \quad (11)$$

where the current and maximum iteration numbers are denoted by k and k_{max}. This proposed parameter improves BESA's exploration and exploitation capabilities while influencing the precise location of BEs.

B. Scouring-stage

Bald eagles travel in a circle to speed up their search for prey in the assigned region. The following equations are used to continuously modify the bald eagle's position:

$$Q_{new} = Q_j + n(j) \left(Q_j - Q_{j-1} \right) Q_{best} + m(j) \left(Q_j - Q_{mean} \right) \quad (12)$$

Where,

$$n(j) = \frac{nr(j)}{\max |nr|}, \; mr(j) = \frac{mr(j)}{\max |mr|}, \quad (13)$$

$$nr(j) = r(j) . \cos\left[\delta(j) \right], \quad (14)$$

$$mr(j) = r(j) . \sin\left[\delta(j) \right], \quad (15)$$

$$\delta(j) = \alpha . \pi . rand , \quad (16)$$

$$r(j) = \delta(j).R.rand\ , \qquad (17)$$

where, α lies between 5 and 10, R varies within the range of 0.5 and 2.

C. Swooping-stage

Bald eagles follow a circular route to scout prey in the chosen region more quickly. Using the following formulas, the bald eagle's posture is constantly modified:

$$Q_{new} = rand.Q_{best} + n_1(j)\left(Q_j - C_1 Q_{best}\right) + m_1(j)\left(Q_j - C_1 Q_{mean}\right), \qquad (18)$$

and,

$$n_1(j) = \frac{nr(j)}{\max|nr|},\ m_1(j) = \frac{mr(j)}{\max|mr|}, \qquad (19)$$

$$nr(j) = r(j).\cosh\left[\delta(j)\right], \qquad (20)$$

$$mr(j) = r(j).\sinh\left[\delta(j)\right], \qquad (21)$$

$$\delta(j) = \alpha(j).\pi.rand\ , \qquad (22)$$

$$r(j) = \delta(j)\ . \qquad (23)$$

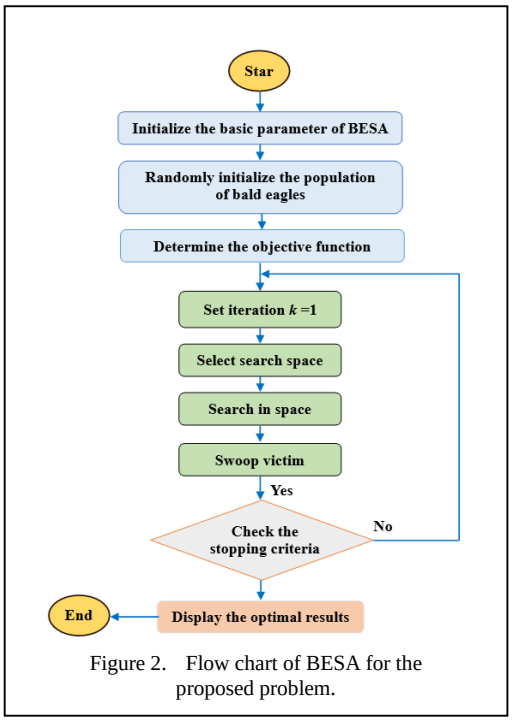

Figure 2. Flow chart of BESA for the proposed problem.

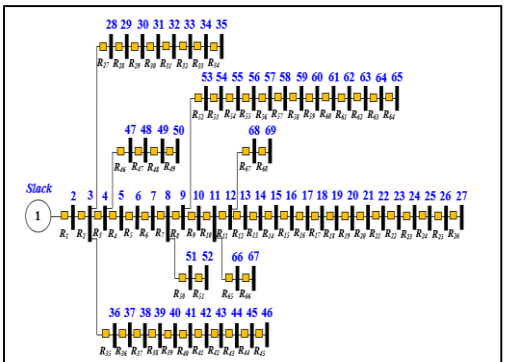

Figure 3. Single line of the IEEE 69-bus test system.

The C_1 and C_2 have values in the range of 1 and 2 [27]. The BESA approach's implementation steps are shown in Fig. 2.

IV. Application and Analysis Results

The single-line diagram of the IEEE 69-bus system under study, which has 69 buses and 68 branches, is shown in Fig. 3. Bus number 1's rated voltage is 12.66 kV, and the system load as a whole is 3790.00 kW and 2690.00 kVar.

The convergence curves for MOF of this study are shown in the Fig. 4.

Fig. 4a reveals that for the WTDG case, the MOF starts at approximately 42.1 in the first iteration, and within less than five iterations, it gets a local optimum of 40.8; by iteration 15, the MOF decreases to 40.5, while the best value of 40.38 is achieved after 110 iterations.

Fig. 4b reveals that for the hybrid WTDG-BESS case, the algorithm convergence was rapid compared to the case of WTDG; in the first iteration, the MOF was 41.25, and by five iterations, the algorithms obtained a local optimum of 39.2, and by approximately 85 iterations, it achieved the best value of 39.05.

Table I shows the obtained results of the used algorithm for both WTDG case and hybrid WTDG and BESS case

In the case of WTDG connected at buses 6, 29, and 58, at bus 6 the WTDG generates 1.0131 MW of active power and 0.9809 MVar of reactive power. At bus 29, the output of WTDG is 1.5902 MW and 0.7091 MVar, while at bus 58, the generated powers are 0.9019 MW and 1.4111 MVar. This integration leads to a TAPL of 76.30 MW and a TVD of 0.973 p.u., with TOT equal to 38.62 seconds.

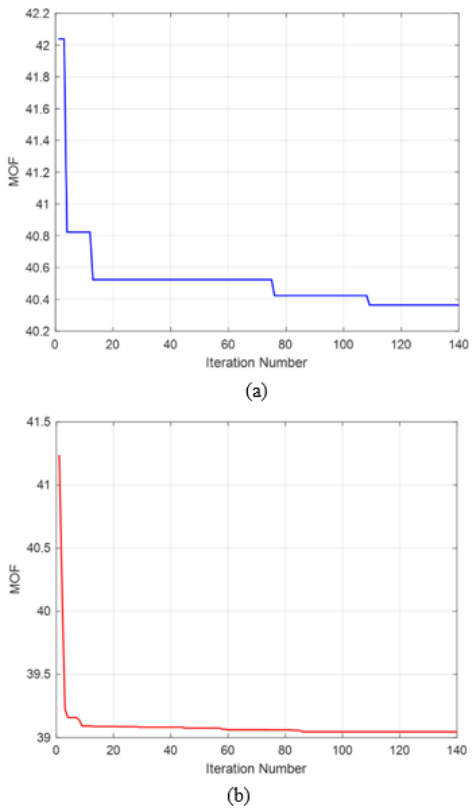

Figure 4. Convergence curves of the BESA for case studies: a) WTDG case, b) Hybrid WTDG-BESS case.

In the case of hybrid WTDG and BESS, the BESS is located on buses 22, 44, and 61, while the WTDG is placed on buses 3, 7, and 56. For BESS, it generates 0.5460 MW at bus 22, 0.3718 at bus 44, and 1.2233 at bus 61.

On the other hand, the WTDG at bus 3 delivered 0.1983 MW and 0.3989 MVar, and on bus 7 it supplied 1.1739 MW and 1.6964 MVar, while on bus 56 it delivered 0.5392 MW and 1.9839.

The combined WTDG and BESS system reduces TAPL to 65.58 MW and the TVD to 0.43 p.u., while lowering TOT to 38.46 seconds.

Fig. 5 shows the variation of branch active power losses for the different case studies.

Fig. 5 reveals that in the basic case, losses are highly concentrated around branches 4 to 8 and 51 to 61, reaching peaks above 30 to 50 kW; this case is the highest regarding losses.

TABLE I. OPTIMIZATION RESULTS OF CASE STUDIES.

Type	RDG Bus	*P* (MW)	*Q* (MVar)	TAPL	TVD	TOT
WTDG	6 29 58	1.0131 1.5902 0.9019	0.9809 0.7091 1.4111	76.30	0.973	38.62
Hybrid case	3 7 56	0.1983 1.1739 0.5392	0.3989 1.6964 1.9839	65.58	0.43	38.46
	22 44 61	0.5460 0.3718 1.2233	- - -			

On the other hand, a significant loss reduction is observed across the entire system after integration of WTDG; the losses in branches 4 to 8 get a maximum value dropping to about 8 kW, and the branches 51 to 61 to about 14 kW.

For the hybrid WTDG and BESS case, we noticed that the loss profile is further improved, and the peak value is reduced to 8 kW, demonstrating the effectiveness of the hybrid case.

The best improvement is observed in the previously critical branches around 4 and 8 and around 51 and 59, where we can notice that the

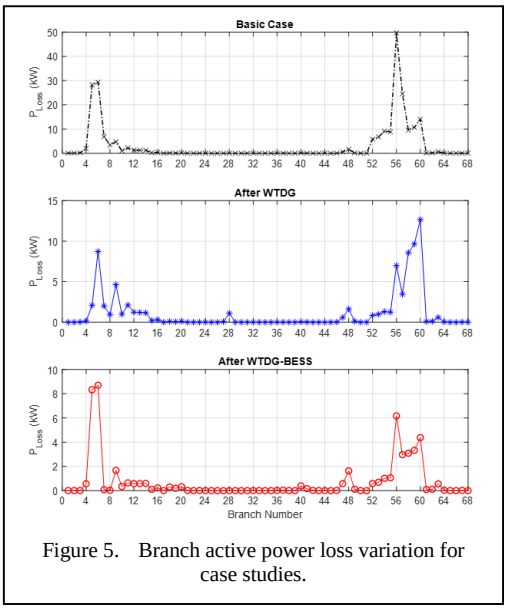

Figure 5. Branch active power loss variation for case studies.

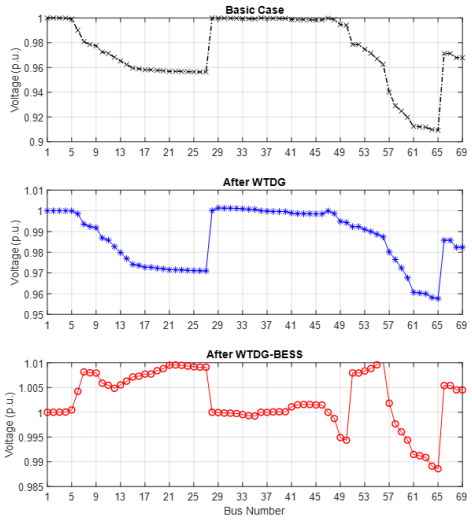

Figure 6. Bus voltage profile variation for case studies.

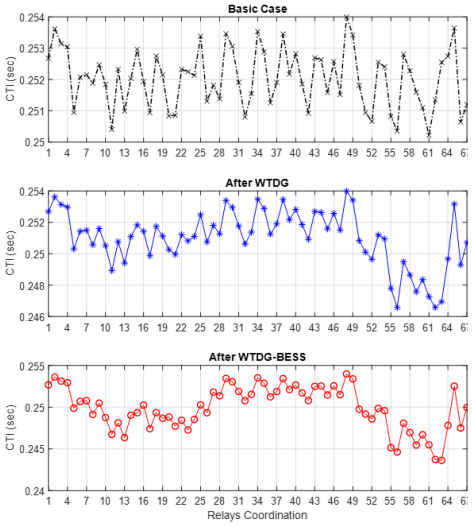

Figure 7. Coordination time interval for case studies.

losses decreased more than in the case of WTDG and the base case.

Fig. 6 illustrates the variation of bus voltage profile variation for case studies in the test distribution system.

Fig. 6 shows that in the base case, voltage levels drop significantly below 0.92 p.u. on the weakest buses, particularly buses 61 to 65. After WTDG installation, the overall profile improves; the voltage values in the weakest buses, 61 to 65, are less than 0.96 p.u., and the voltage in other buses is 0.97 or higher. In the case of hybrid WTDG and BESS, more enhancement is shown; the voltage curve is nearly flat, and it is noticed that the minimum value recorded is less than 0.99 p.u.

Fig. 7 shows the coordination time interval for case studies.

In the base case, CTI values fluctuate significantly between 0.25 and 0.254 seconds, showing instability. After WTDG integration, it can be noticed that the CTI profile becomes smoother, and most values are between 0.248 and 0.253 seconds; the oscillations are reduced but still present weaknesses around relays 55 to 63 seconds, where CTI values are close to 0.246 seconds.

With the hybrid WTDG-BESS case, the CTI is further stabilizing, which has a nearly uniform profile around 0.25 and 0.255 seconds. The CTI stability is significantly improved in the weak relay zone between 53 and 61 seconds.

V. CONCLUSIONS

This study presented the application of an algorithm called BESA for locating and sizing multiple WTDG and BESS systems in electrical distribution systems.

The proposed work addressed the optimal planning of hybrid systems with the objective of minimizing active power losses while enhancing voltage deviation and relay coordination. The study treated two cases, the first concerning the integration of WTDGs only, and the second combining WTDG with BESS to further enhance the system performance.

The proposed methodology was validated on the IEEE 69-bus test system. The algorithm confirms its capability to deliver a significant reduction in TAPL to 76.30 kW in the case of WTDG and to 65.58 in the hybrid case.

Voltage profile enhancement is also achieved while the TVD is reduced to 0.973 p.u. in the case of WTDG and to 0.43 in the hybrid case. In addition, the protection is enhanced by enhancing TOT to 38.62 in the case of WTDG and 38.46 in the hybrid case.

REFERENCES

[1] McPherson, M., & Stoll, B. (2020). Demand response for variable renewable energy integration: A proposed approach and its impacts. *Energy, 197*, 117205. https://doi.org/10.1016/j.energy.2020.117205

[2] Wong, L. A., Ramachandaramurthy, V. K., Taylor, P., Ekanayake, J. B., Walker, S. L., & Padmanaban, S. (2019). Review on the optimal placement, sizing and

control of an energy storage system in the distribution network. *Journal of Energy Storage*, *21*, 489-504. https://doi.org/10.1016/j.est.2018.12.015

[3] Ha, M. P., Huy, P. D., & Ramachandaramurthy, V. K. (2017). A review of the optimal allocation of distributed generation: Objectives, constraints, methods, and algorithms. *Renewable and Sustainable Energy Reviews*, *75*, 293-312. https://doi.org/10.1016/j.rser.2016.10.071

[4] Kola, S. S. (2018). A review on optimal allocation and sizing techniques for DG in distribution systems. *International Journal of Renewable Energy Research*, *8*(3), 1236-1256. https://doi.org/10.20508/ijrer.v8i3.7344.g7424

[5] Grisales-Noreña, L. F., Restrepo-Cuestas, B. J., Cortés-Caicedo, B., Montano, J., Rosales-Muñoz, A. A., & Rivera, M. (2022). Optimal location and sizing of distributed generators and energy storage systems in microgrids: A review. *Energies*, *16*(1), 106. https://doi.org/10.3390/en16010106

[6] Lei, J., & Gong, Q. (2017). Operating strategy and optimal allocation of large- scale VRB energy storage system in active distribution networks for solar/wind power applications. *IET Generation, Transmission & Distribution*, *11*(9), 2403-2411. https://doi.org/10.1049/iet-gtd.2016.2076

[7] Home-Ortiz, J. M., Pourakbari-Kasmaei, M., Lehtonen, M., & Mantovani, J. R. S. (2019). Optimal location-allocation of storage devices and renewable-based DG in distribution systems. *Electric Power Systems Research*, *172*, 11-21. https://doi.org/10.1016/j.epsr.2019.02.013

[8] Karimi, A., Aminifar, F., Fereidunian, A., & Lesani, H. (2019). Energy storage allocation in wind integrated distribution networks: An MILP-Based approach. *Renewable energy*, *134*, 1042-1055. https://doi.org/10.1016/j.renene.2018.11.034

[9] Zhong, S., Qiu, J., Sun, L., Liu, Y., Zhang, C., & Wang, G. (2020). Coordinated planning of distributed WT, shared BESS and individual VESS using a two-stage approach. *International Journal of Electrical Power & Energy Systems*, *114*, 105380. https://doi.org/10.1016/j.ijepes.2019.105380

[10] Das, C. K., Bass, O., Kothapalli, G., Mahmoud, T. S., & Habibi, D. (2018). Optimal placement of distributed energy storage systems in distribution networks using artificial bee colony algorithm. *Applied Energy*, *232*, 212-228. https://doi.org/10.1016/j.apenergy.2018.07.100

[11] Ahmadi, M., Lotfy, M. E., Danish, M. S. S., Ryuto, S., Yona, A., & Senjyu, T. (2019). Optimal multi-configuration and allocation of SVR, capacitor, centralised wind farm, and energy storage system: a multi- objective approach in a real distribution network. *IET Renewable Power Generation*, *13*(5), 762-773. https://doi.org/10.1049/iet-rpg.2018.5057

[12] Ahmadi, M., Lotfy, M. E., Howlader, A. M., Yona, A., & Senjyu, T. (2019). Centralised multi- objective integration of wind farm and battery energy storage system in real- distribution network considering environmental, technical and economic perspective. *IET Generation, Transmission & Distribution*, *13*(22), 5207-5217. https://doi.org/10.1049/iet-gtd.2018.6749

[13] Singh, P., Meena, N. K., Slowik, A., & Bishnoi, S. K. (2020). Modified african buffalo optimization for strategic integration of battery energy storage in distribution networks. *IEEE Access*, *8*, 14289-14301. https://doi.org/10.1109/access.2020.2966571

[14] Nayak, M. R., Behura, D., & Kasturi, K. (2021). Optimal allocation of energy storage system and its benefit analysis for unbalanced distribution network with wind generation. *Journal of Computational Science*, *51*, 101319. https://doi.org/10.1016/j.jocs.2021.101319

[15] Nayak, M. R., Behura, D., & Nayak, S. (2021). Performance analysis of unbalanced radial feeder for integrating energy storage system with wind generator using inherited competitive swarm optimization algorithm. *Journal of Energy Storage*, *38*, 102574. https://doi.org/10.1016/j.est.2021.102574

[16] Belbachir, N., Zellagui, M., Settoul, S., El-Bayeh, C. Z., & Bekkouche, B. (2021). Simultaneous optimal integration of photovoltaic distributed generation and battery energy storage system in active distribution network using chaotic grey wolf optimization. *Electrical Engineering & Electromechanics*, *2021*(3), 52-61. https://doi.org/10.20998/2074-272x.2021.3.09

[17] Taha, H. A., Alham, M. H., & Youssef, H. K. (2022). Multi-objective optimization for optimal allocation and coordination of wind and solar DGs, BESSs and capacitors in presence of demand response. *IEEE Access*, *10*, 16225-16241. https://doi.org/10.1109/access.2022.3149135

[18] Ghaffari, A., Askarzadeh, A., & Fadaeinedjad, R. (2022). Optimal allocation of energy storage systems, wind turbines and photovoltaic systems in distribution network considering flicker mitigation. *Applied Energy*, *319*, 119253. https://doi.org/10.1016/j.apenergy.2022.119253

[19] Balu, K., & Mukherjee, V. (2023). Optimal allocation of electric vehicle charging stations and renewable distributed generation with battery energy storage in radial distribution system considering time sequence characteristics of generation and load demand. *Journal of Energy Storage*, *59*, 106533. https://doi.org/10.1016/j.est.2022.106533

[20] Kamel, S., Abdel-Mawgoud, H., Alrashed, M. M., Nasrat, L., & Elnaggar, M. F. (2023). Optimal allocation of a wind turbine and battery energy storage systems in distribution networks based on the modified BES-optimizer. *Frontiers in Energy Research*, *11*, 1100456. https://doi.org/10.3389/fenrg.2023.1100456

[21] Mohanty, S., Nayak, M. R., & Behura, D. (2023). Search group algorithm for optimal allocation of battery energy storage with renewable sources in an unbalanced distribution system. *Energy Sources, Part A: Recovery, Utilization, and Environmental Effects*, *45*(1), 1131-1149. https://doi.org/10.1080/15567036.2023.2175929

[22] Lv, Y., Qin, R., Sun, H., Guo, Z., Fang, F., & Niu, Y. (2023). Research on energy storage allocation strategy considering smoothing the fluctuation of renewable energy. *Frontiers in Energy Research*, *11*, 1094970. https://doi.org/10.3389/fenrg.2023.1094970

[23] Al-Ahmad, A. K. (2023). Voltage regulation and power loss mitigation by optimal allocation of energy storage systems in distribution systems considering

wind power uncertainty. *Journal of Energy Storage*, *59*, 106467. https://doi.org/10.1016/j.est.2022.106467

[24] Belbachir, N., Zellagui, M., & Bekkouche, B. (2022). Optimal location and sizing of multiple distributed generators in radial distribution network using metaheuristic optimization algorithms. *Facta Universitatis, Series: Electronics and Energetics*, *35*(2), 229-242. https://doi.org/10.2298/fuee2202229b

[25] Belbachir, N., Zellagui, M., Settoul, S., & Benali, A. (2023). Optimal design of wind energy generation in electricity distribution network based on technical-economic parameters. *Engineering Review*, *43*(3), 114-128. https://doi.org/10.30765/er.2281

[26] Zellagui, M., Belbachir, N., Amroune, M., & El-Bayeh, C. Z. (2024). Investigating the performance of non-standard overcurrent relay with integration of photovoltaic distributed generation in power distribution system. *Periodica Polytechnica Electrical Engineering and Computer Science*, *68*(1), 27-36. https://doi.org/10.3311/ppee.21780

[27] Alsattar, H. A., Zaidan, A. A., & Zaidan, B. B. (2020). Novel meta-heuristic bald eagle search optimisation algorithm. *Artificial Intelligence Review*, *53*(3), 2237-2264. https://doi.org/10.1007/s10462-019-09732-5

eNergetics 2025
DOI: https://doi.org/10.5281/zenodo.18619961

Original Scientific Article

Battery Equalization Technique using a Multiport Cúk Converter

Mario Lira de Freitas[1], Daniel de Souza e Silva[2], Romero Leandro Andersen[3]

[1,2]Undergraduate Program in Electrical Engineering, Federal University of Paraíba, João Pessoa, Brazil
[3]Department of Electrical Engineering, Federal University of Paraíba, João Pessoa, Brazil

[1]mario.freitas@estudante.cear.ufpb.br, [2]daniel.silva@estudante.cear.ufpb.br, [3]romero@cear.ufpb.br

Abstract—**This paper investigates a battery equalization technique that employs a multiport DC-DC converter based on the Cúk topology. This approach is particularly relevant for energy storage systems coupled with low-voltage renewable sources, such as solar panels and fuel cells. A prominent challenge in these systems is imbalance between battery cells, a condition that degrades the safety and lifespan of the array. To address this issue, a Cúk equalizer topology was adopted. The methodology involved computer simulations in PSIM software to analyze the circuit behavior and validate the theoretical model. In tests with four cells initialized with different voltages, it was demonstrated that a fixed 50% duty cycle promotes natural and autonomous equalization, without the need for complex individual monitoring. The system's effectiveness was confirmed by the convergence of cell voltages and by inductor currents that reached a zero average value in steady state. The proposed solution is concluded to be a robust alternative for increasing the reliability and extending the lifespan of energy storage systems.**

Keywords - energy storage, Cúk converters, multiport converter, battery equalization, renewable sources.

I. INTRODUCTION

Currently, DC-DC converters are used in different industries and various applications, such as renewable energy sources, electric vehicle stations and uninterruptable power supplies. The growing demand for renewable energy sources, such as solar and wind, has driven the development of efficient energy storage systems. A common characteristic of these sources is the generation of low DC voltage levels, which makes it imperative to use DC-DC converters to increase and regulate the voltage to a usable level [1,2]. In this context, integrated multiport converters emerge as an advantageous solution, as they allow system optimization with a smaller number of components and conversion stages [3,4].

Therefore, researchers are seeking better ways to harness energy from renewable resources. This goal can be achieved through high-efficiency converters [5]. Manufacturing variations in parameters such as capacity and impedance cause cells to reach different states of charge, a condition that directly compromises the safety and longevity of the battery bank and requires the development of equalization technologies [6]. Despite advances, a critical challenge in systems using multiple battery cells connected in series is the phenomenon of voltage imbalance [7].

However, there are many applications that require a relatively high-voltage battery pack (several tens to hundreds of volts), such as hybrid electric vehicles, uninterruptible power supplies, and so on. This requires a large number of battery cells to be connected in series. As the number of cells in series increases, much attention must be paid. Thus, electric vehicles will play an important role in future transportation because they can achieve low pollution and low noise. The cost of electric vehicles depends on many

ISBN: 978-86-82602-07-1

aspects, but the largest expense is the cost of the batteries [8]. To achieve reasonable longevity, a battery management system is necessary to achieve the best performance [9].

To mitigate this problem, several active equalization techniques have been proposed in the literature. These approaches include the use of bidirectional buck-boost converters for power transfer between adjacent cells [10], switched-capacitor circuits that avoid bulky magnetic components [11], and hybrid converters that integrate SEPIC/Zeta topologies [12].

The main advantage of the Cúk topology (this work) and the Switched Capacitor (SC) is simplicity, as both achieve automatic balancing with a fixed duty cycle of 50%. In contrast, buck-boost focuses on speed, using complex active control (VOT/VRM) to maximize energy transfer. In terms of hardware, Cúk, buck-boost, and SEPIC/Zeta use magnetic components. SC is the exception, eliminating them, but at the cost of a greater number of switches. Finally, while the SEPIC/Zeta hybrid focuses on efficiency (reducing voltage stress), this work focuses on autonomy, proving that balance is an inherent characteristic of the Cúk topology.

This work focuses on the Cúk converter-based topology explored in [8] for lithium-ion battery balancing. Power between adjacent cells can be transferred bidirectionally by manipulating the balancing current to solve the problem of imbalance in a battery module.

The execution procedure for this present work follows from the choice of some application of the Multiport Converters previously mentioned. After a literature review, the methodology applied in [8] was chosen for this work. In this work, a proposed Cúk converter balancing circuit for lithium-ion batteries was used. This circuit equalizes eight cells in a series-connected battery string, using a single pulse with 50% duty cycle modulation (PWM). The operating principle has two main stages. In the first stage, switch S_1 is on while switch S_2 remains closed. In the second stage, the cycle is reversed.

The methodology of this study is based on the analysis of a battery equalizer based on the Cúk converter topology, whose effectiveness was previously demonstrated in [8]. Unlike the original study, the focus here is to validate the system behavior for a set of four cells with deliberately unequal initial voltages (10 V to 13 V). Computer simulations, performed in the PSIM environment, were the central tool to verify the converter's natural equalization principle.

II. METHODOLOGY

The methodology of this work was structured in stages ranging from the initial foundation to the development of the proposed circuit. Initially, a literature review on multiport DC-DC converters and battery equalization techniques was conducted to understand existing topologies and their limitations. This theoretical survey served as a basis for guiding the choice of the converter configuration to be investigated. The development stage consisted of the study and development of a multiport DC-DC converter topology for battery equalization. The research

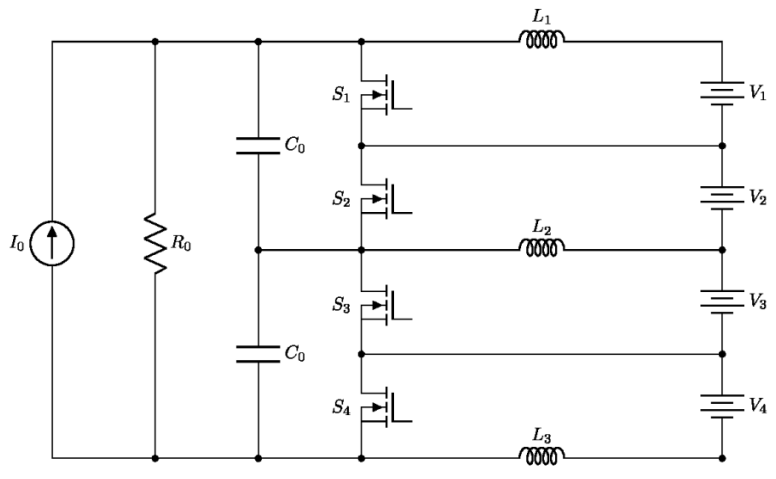

Figure 1. Proposed Cúk Equalizer Converter Circuit.

was based on a Cúk converter balancing circuit proposed in the literature. To validate the theoretical model, computer simulations were performed using PSIM software. The simulations allowed evaluating the converter behavior, battery voltage equalization, and the waveforms of currents and voltages of inductors and capacitors in steady state, shown in Fig. 1.

The proposed circuit was simulated using PSIM software. This simulation environment was chosen for its ability to model and analyze complex electronic circuits with high precision. The simulations allowed us to validate the developed mathematical model and evaluate the converter behavior.

The values adopted for the simulation components (Table I) are presented below. Battery voltages were chosen between 10 and 13 volts to represent a significant voltage difference across the cells. The batteries in the simulator are modeled with 0.1 F capacitors.

A. *Operating Steps*

For a more simplified analysis of the operational principle, we reduce the circuit proposed in this work to two battery cells in Fig. 2. The operation is divided into two stages, with a duty cycle D=0.5.

- Step 1: Switch S_1 closed, Switch S_2 open.

L_1 is connected to the positive terminal of capacitor C_0. In step 1, switch S_1 connects this node to the central point between the batteries.

Equivalent Circuit (Step 1):

Battery V_1 is connected directly through inductor L_1. Capacitor C_0 is connected in parallel with battery V_2 through switch S_1.

TABLE I. SIMULATION PARAMETERS.

Components	Values
L1, L2, L3.	5 mH
C0.	3 μF
R0.	100 Ω
I0.	0.5 A
Frequency.	50 kHz
C1, C2, C3, C4.	10 V, 11 V, 12 V, 13 V

Applying Kirchhoff's Voltage Law (KVL) to the inductor Eq. (1):

$$L_1 \frac{dI_{L1}}{dt} = V_1 \ . \qquad (1)$$

The variation of current in the inductor during this interval is Eq. (2).

$$\Delta I_{L1,on} = \frac{V_1}{L_1} DT \ . \qquad (2)$$

- Step 1: Switch S_1 open, Switch S_2 closed

L_2 is connected to the negative terminal of capacitor C_0. In step 2, switch S_2 connects this node to the central point between the batteries.

Equivalent Circuit (Step 2):

The inductor L_1 is now in series with the capacitor C_0. This combination (L_1 and C_0) is in parallel with the battery V1. The voltage across the inductor is represented by Eq. (3).

$$L_1 \frac{dI_{L1}}{dt} = V_1 - V_{C0} \, . \qquad (3)$$

The variation of the current in the inductor during this interval is Eq. (4).

$$\Delta I_{L1,off} = \frac{V_1}{L_1}(1-D)T \ . \qquad (4)$$

Equilibrium Condition for the circuit to operate in steady state, the total variation of the current in the inductor over a complete cycle must be zero Eq. (5).

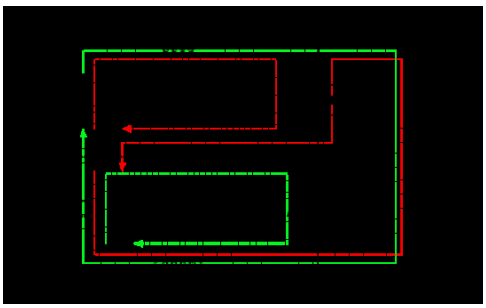

Figure 2. Simplified Cúk converter circuit.

$$\Delta I_{L1,on} + \Delta I_{L1,off} = \frac{V_1}{L_1} DT + \\ + \frac{V_1 - V_{C0}}{L_1}(1-D)T \quad , \qquad (5)$$

$$\frac{V_1}{L_1} DT + \frac{V_1 - V_{C0}}{L_1}(1-D)T = 0 \ , \qquad (6)$$

$$\frac{V_1}{L_1} DT = \frac{V_{C0} - V_1}{L_1}(1-D)T \ , \qquad (7)$$

$$V_1 D = (V_{C0} - V_1)(1-D) \ , \qquad (8)$$

$$V_1 D = V_{C0}(1-D) - V_1 + V_1 D \, , \qquad (9)$$

$$0 = V_{C0}(1-D) - V_1 \, , \qquad (10)$$

$$V_1 = V_{C0}(1-D) \, , \qquad (11)$$

$$\frac{V_{C0}}{V_1} = \frac{1}{(1-D)} \, . \qquad (12)$$

For a duty cycle of 0.5, the voltage across capacitor C_0 is twice the voltage V1, as expected for a Cúk converter, as shown in Eq. (13).

$$V_{C0} = V_1 \frac{1}{1-0.5} \rightarrow V_{CO} = 2V_1 \, . \qquad (13)$$

Conclusion of 2-Cell Battery Analysis: The mathematics shows that at a 50% duty cycle, the circuit naturally forces the voltage of battery V_2 to equal the voltage of battery V_1. If V_1 has a higher voltage than V_2, the circuit will transfer energy from V_1 to V_2 until the voltages equalize, and vice versa.

III. RESULTS

This section presents the waveforms obtained through simulations performed in the PSIM software. The results presented herein were obtained considering inductors with an internal resistance of 0.1 ohm.

In Fig. 3 the voltages in the proposed batteries are represented to ensure equalization of the circuit batteries, a duty cycle of 0.5 was used in the switch control. This can be noticed by the switch voltage waveforms of Fig. 4 and Fig. 5

The voltage waveforms of inductors L_1, L_2 and L_3 are shown, with which it is possible to perceive a zero average value in steady state, as expected in Fig. 6. The inductor current waveforms are shown in Fig. 7. They indicate that the inductors with negative currents belong to the load cells and the positive currents to the discharge cells. They represent the inductor current limitation of the converter's power section. The current sensor signals are used in a logic that inhibits the switch control signals if the currents exceed the defined limit.

To see the steady-state inductor current waveforms, Fig. 8 shows that all currents are the same, meaning that all cells are equalized.

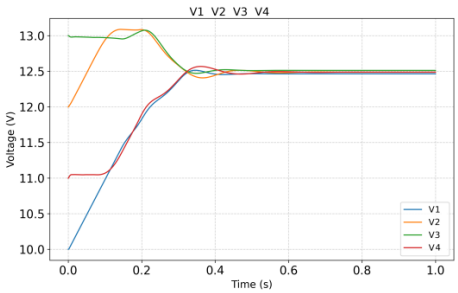

Figure 3. Battery voltages (initially unbalanced from 10V to 13V).

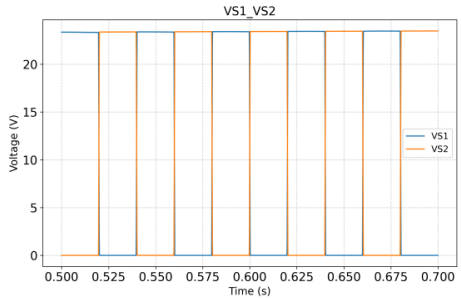

Figure 4. Voltages at switches V_{S1}, V_{S2}.

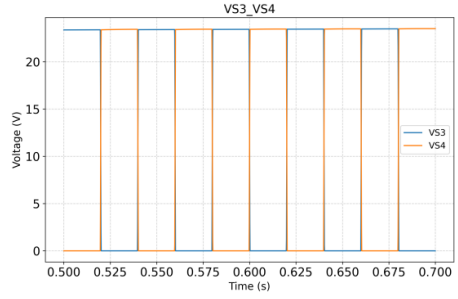

Figure 5. Voltages at switches V_{S3}, V_{S4}.

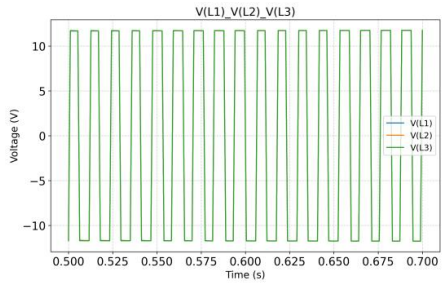

Figure 6. Waveforms of voltages V_{L1}, V_{L2} and V_{L3} in steady state.

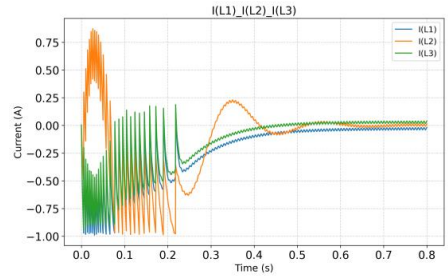

Figure 7. Waveforms of I_{L1}, I_{L2} and I_{L3} currents.

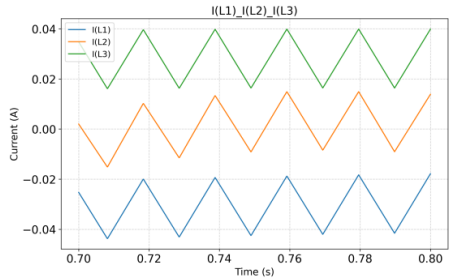

Figure 8. Detail of currents IL1, IL2 and IL3 in steady state.

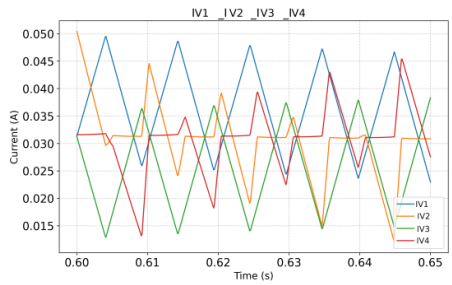

Figure 9. Waveforms of currents I_{V1}, I_{V2} and I_{V3} in steady state.

Finally, the steady-state capacitor current waveforms are shown in Fig. 9. They also show very low values at the end of equalization.

IV. Conclusion

The study demonstrated that the application of multiport DC-DC converters for battery equalization represents an efficient alternative for increasing the reliability and lifespan of energy storage systems. The topology based on the Cúk equalizer converter demonstrated, in simulation, satisfactory results in balancing voltages between cells, validating the theoretical model and demonstrating its effectiveness in a short period of time. As we use capacitors to emulate batteries, we have this short period of time. In a practical case, where we would have batteries, it would take hours to achieve the same results. As a continuation of this work, the authors intend to build a prototype and gather experimental results. The voltage equalization presented is inherent to the operation of this circuit; individual voltage monitoring is not necessary to ensure they remain equal under steady-state conditions. There is great potential for a high number of cells for this converter, in which controllers to equalize voltages would not be necessary. However, two switches will be needed for every two batteries; the increase would be natural for any converter that was proposed. The disadvantage of increasing the number of battery cells would be the greater number of sensors required for the additional cells. Thus, the research contributes to the development of higher-yield, lower-cost solutions for the integration of renewable sources, reinforcing the relevance of new converter topologies in the current energy transition scenario.

References

[1] Rao, B. T., & De, D. (2020, January). Additional Voltage Assisted High Gain DC-DC Converter with Modified Čuk Configuration. In *2020 IEEE International Conference on Power Electronics, Smart Grid and Renewable Energy* (PESGRE2020) (pp. 1-6). IEEE. https://doi.org/10.1109/pesgre45664.2020.9070343

[2] Kumar, K., Babu, N.R., & Prabhu, K.R. (2017, April). Analysis of integrated Boost-Cuk high voltage gain DC-DC converter with RBFN MPPT for solar PV application. In *2017 Innovations in Power and Advanced Computing Technologies (i-PACT)* (pp. 1-6). IEEE. https://doi.org/10.1109/ipact.2017.8245072

[3] Saadatizadeh, Z., & Mantooth, H. A. (2023, October). An expandable non-isolated multiport DC-DC converter with high switching frequency operation. In *2023 IEEE Energy Conversion Congress and Exposition (ECCE)* (pp. 2289-2294). IEEE. https://doi.org/10.1109/ecce53617.2023.10362638

[4] Qian, Z. (2010). Modeling and design of multi-port dc/dc converters [Doctoral dissertation]

[5] Magalhães, M. D. O., de Lima Henn, G. A., & de Oliveira Filho, H. M. (2022, October). High-gain soft-switching DC-DC converter based on Dual Active Bridge topology. In *Brazilian Congress of Automatics-CBA* (Vol. 3, No. 1).

[6] Qi, X., Wang, Y., Fang, M., Wang, Y., & Chen, Z. (2022). Multiport dc–dc converter with integrated cascaded structure for optimizing centralized battery equalization system. *IEEE Transactions on Power Electronics*, *37*(12), 15111-15126. https://doi.org/10.1109/tpel.2022.3198524

[7] Lu, X., Qian, W., & Peng, F. Z. (2012, February). Modularized buck-boost+ Cuk converter for high voltage series connected battery cells. *In 2012 Twenty-Seventh Annual IEEE Applied Power Electronics Conference and Exposition (APEC)* (pp. 2272-2278). IEEE. https://doi.org/10.1109/apec.2012.6166139

[8] Moghaddam, A.F., & Van den Bossche, A. (2019, May). A battery equalization technique based on Ćuk converter balancing for lithium-ion batteries. In *2019 8th International Conference on Modern Circuits and Systems Technologies (MOCAST)* (pp. 1-4). IEEE. https://doi.org/10.1109/mocast.2019.8741779

[9] Farzan Moghaddam, A., & Van den Bossche, A. (2019). An efficient equalizing method for lithium-ion batteries based on coupled inductor balancing. *Electronics*, *8*(2), 136. https://doi.org/10.3390/electronics8020136

[10] Yang, Z. Z. (2022). Development of an active equalizer for lithium-ion batteries. *Electronics*, *11*(14), 2219. https://doi.org/10.3390/electronics11142219

[11] Ye, Y., & Cheng, KWE (2016). An automatic switched-capacitor cell balancing circuit for series-connected battery strings. *Energies*, *9*(3), 138. https://doi.org/10.3390/en9030138

[12] Sebaje, AS, da Silva Martins, ML, & Font, CHI (2021, November). A hybrid bidirectional DC-DC converter based on a SEPIC/Zeta converter with a modified switched capacitor cell. In *2021 Brazilian Power Electronics Conference (COBEP)* (pp. 1-6). IEEE. https://doi.org/10.1109/cobep53665.2021.9684119

eNergetics 2025
DOI: https://doi.org/10.5281/zenodo.18620652

Original Scientific Article

Comprehensive Screening Protocol for Generating Machine Learning-ready Datasets of Perovskite Materials

Woshitha Sasindu Hinget[1], Bhagya W.K. Piyushani[2], Galhenage Asha Sewvandi[3]
Pradeep K.W. Abeygunawardhana[4]

[1,2,3]Department of Materials Science and Engineering, University of Moratuwa, Sri Lanka
[4]Sri Lanka Institute of Information Technology (SLIIT), Sri Lanka

[1]wshinget@gmail.com, [2]piyushani.b.wanigasinghe@gmail.com, [3]galhenagea@uom.com

Abstract—**This data-driven study presents a systematic sequential multiphase screening framework incorporating compositional and symmetry-based filtering, charge neutrality and geometric stability criteria to identify structurally and chemically stable oxide and halide perovskite candidates. The screening sequence effectively narrows down the scope of an extensive initial compositional space to a refined dataset consisting of 698 111 unique perovskites, including 1 154 single perovskites with numerically discovered O, F, Cl, Br and $I-based$ compositions. This curated dataset provides a standardized dataset appropriate for downstream ML property predictions and experimental studies, to fast track the novel perovskite materials discovery for energy and optoelectronic applications.**

Keywords - Perovskite structure candidates, multiphase screening, machine learning, stability.

I. INTRODUCTION

Perovskites represent a crystalline compound category with the general structure of ABX_3, where X can be oxide or halide anions. This structural diversity permits single and double perovskite formation, spanning a wide range of elemental combinations. The outstanding optical, electronic, and catalytic properties demonstrated by both oxide and halide perovskites are highly favorable for innovative applications in materials science and energy technologies [1]. This versatile functionality has established perovskites as a fundamental focus in contemporary research on advanced materials and device engineering. Consequently, property prediction and relevant computational studies on perovskites have become important and extensive.

Machine Learning (ML) has become a trending tool utilized in front-line materials

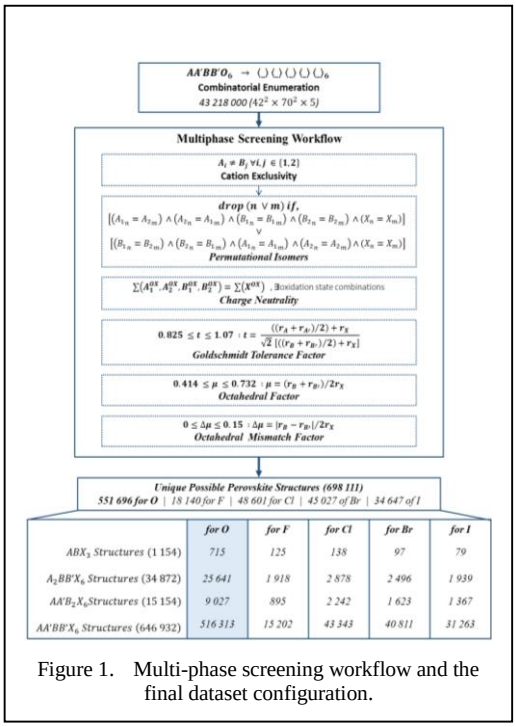

Figure 1. Multi-phase screening workflow and the final dataset configuration.

discovery, showcasing an excellent success in accelerating the discovery and design of novel compounds for a wide range of applications. This paradigm shift is currently increasing in contemporary perovskite research, where ML approaches are utilized for property prediction, compositional optimization and phase discovery [2]. Reference [3] has used ML models to predict band gaps and crystal phases in halide perovskites, attaining high accuracy minimal computation time requirements. Similarly, [4] has applied ML algorithms to tailor the synthesis and stability evaluation of oxide perovskites and lead-free perovskites, signifying the value of data-driven approaches for evolving functional materials design. Furthermore, [5] demonstrates the utility of ML in perovskite materials research by proposing a comprehensive multi-property prediction framework.

In the ML based materials discovery and property prediction, pre-screening is crucial [6]. Such methods which employ multi-output classifiers used to simultaneously predict perovskite formability and stability, heavily rely on well-curated and filtered datasets to achieve high accuracy. Data inconsistencies, including noise, incompleteness and variability require solid preprocessing such as data normalization, imputation and error removal to ensure the integrity and reliability of ML training and prediction outcomes. Moreover, due to computational expense of high-fidelity methods like density functional theory (DFT), economical and systematic pre-screening is critical to refine candidate pools before ML modelling [7]. Explicitly, the quality of the initial candidate pool poses a substantial challenge to ML models in perovskite research, as emphasized in the [8], where datasets often contain multiple entries with identical compositions but differing structures and properties complicating accurate predictions.

Most of the existing studies primarily focus on individual screening criteria such as stability factors [9] or charge neutrality [10], often neglecting the implementation of a combined screening sequence which collectively refines the candidate pool. This lack of integrated screening protocols can result in incomplete filtering, impacting adversely on the reliability, meticulousness of subsequent analyses and property predictions [8] spotlighting the significance of the prediction reliability improvement in the novel perovskites discovery.

This study implements a structured and strategic multiphase combined screening workflow to identify stable perovskites structures, incorporating sequential filters consisting of cation site exclusivity, permutational isomer elimination, charge neutrality verification and geometric stability factors based on Goldschmidt tolerance factor, octahedral factor and octahedral mismatch factor. Through this methodology, the initial compositional space will be systematically reduced, yielding a high-quality, non-redundant, refined dataset of stable oxide and halide perovskite candidates. The resulting dataset establishes a standardized input for successive ML-driven property predictions and experimental validations, facilitating more efficient and reliable exploration of perovskite materials for energy and optoelectronic applications (Fig. 1).

I. METHODOLOGY

A. Combinatorial Enumeration

Initially through a systematic selection process after referring published available data, 42 candidates were identified as suitable for A-site positions, including 35 elemental species and 7 organic cations. Inclusion of these organic cations in the initial candidate pool is expected to facilitate a more comprehensive map of perovskite configurational space which have not often considered in existing studies (Table I). Similarly, 70 elements were identified for B-sites based on their suitability for perovskite octahedral coordination (Fig. 2). Subsequently, only one single anion type was utilized per compound for the X-site positions selected from *O, F, Cl, Br or I.* Here it was ensured that all *X*-anions were within any given ABX_3 or $AA'BB'X_6$ combination which were chemically identical without any mixed-anion compositions allowing a single candidate structure. These criteria collectively define the initial candidate pool for double perovskites of the form of $AA'BB'X_6$.

In this study, a multi-phase screening approach was applied for the constructed initial candidate pool of combinatorial $AA'BB'X_6$ compositions as follows.

B. Compositional Screening

Initially two screenings were performed focusing on compositional redundancy and overlapping cation arrangements.

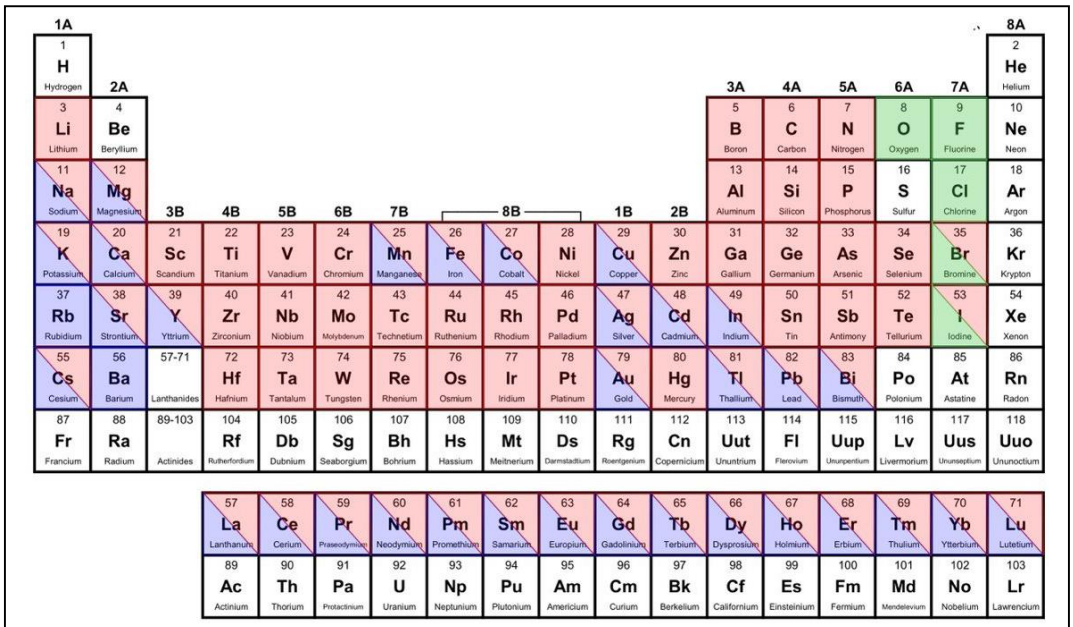

Figure 2. Selected elements utilized as A-site (blue), B-site (red) and X-site (green) in the combinatorial enumeration phase.

1) Screening for Cation Site Exclusivity

First, the combinations include any *A*-site cation (*A* or *A′*) which is identical to any B-site cation (*B* or *B′*) were filtered and excluded to ensure that both *A*-*A′* & *B*-*B′* cations occupy two distinct A & B-sublattices. This $A_i \neq B_j$ for all $i,j \in \{1,2\}$, exclusion is a prerequisite for forming well-ordered perovskite structures to avoid chemically implausible or redundant structures.

2) Screening for Permutational Isomers

The remaining combinations from the initial screening were passed through a combinatorial and symmetry-filtering. For every candidate *n* & *m*, if the A sites are swapped as $A_n = A'_m$ & $A'_n = A_m$ and *B*-sites are toned up as $B_n = B_m$, $B'_n = B'_m$ were removed considering their mirror compositional duplication. Similarly, same approach was followed for the swapped B-sites and constantly kept A-sites, preserving only one entry for further screening phases. This screening ensures that the remaining combinatorial dataset includes only unique, non-overlapping & non-redundant candidates, ensuring an exclusive enumeration and chemical relevance.

This filtering was strictly done only among structures which share the same *X*-site anion composition, avoiding cross comparison between different anion frameworks along with the coherence within each anion specific combination.

TABLE I. POSSIBLE PEROVSKITE STRUCTURES CORRESPONDING TO THE ORGANIC CATION A-SITES.

Cation	Name	Cation	Effective radius (Å)	No. of ABX_3 Structures
MA^+	methylammonium	$CH_3NH_3^+$	2.17	36
FA^+	formamidinium	$CH(NH_2)_2^+$	2.53	21
EA^+	ethylammonium	$C_2H_5NH_3^+$	2.55	18
DMA^+	dimethylammonium	$(CH_3)_2NH_2^+$	2.72	8
GA^+	glycinium	$NH_2CH_2COOH^+$	2.75	6
AZ^+	azetidinium	$C_3H_5NH_3^+$	2.8	4
IM^+	Imidazolium	$C_3N_2H_5^+$	2.9	2

C. Charge Neutrality Screening

A subsequent screening was performed to secure chemical plausibility of the candidate $AA'BB'X_6$ combinations utilizing the charge neutrality as the primary screening criteria. Most of the high-throughput computational screening approaches utilized in advanced oxide perovskite design employ this charge neutrality constraint [11]. With the primary structure of the $AA'BB'X_6$, the sum of oxidation states of all cations (*A*, *A'*, *B*, *B'*) was expected to balance the total negative charge provided by the X-site anions. For this charge neutrality screening, all the oxidation states which consistent with 12-fold coordinated A [12] and 6-fold coordinated B-site cations [13] were considered. Retention of such multiple combinations with different viable oxidation states could result in an expanded candidate pool for subsequent screening processes.

D. Structural Stability

The following stability factor screenings are specifically defined to assess the structural formability and geometric compatibility unique to perovskite crystal structures for the filtered candidate pool.

1) Goldschmidt tolerance factor

The Goldschmidt Tolerance Factor (*t*) is a dimensionless geometric parameter for predicting the formability and stability of a perovskite structure for a given set of cations and anions [14]. This parameter can be employed to determine the ionic size compatibility based on Shannon ionic radii of A and B-site cations while the average ionic radii of those site cations are taken as the effective r_A & r_B for double perovskite structures. This is calculated as,

$$t = \frac{(r_A + r_{A'})/2 + r_X}{\sqrt{2}((r_B + r_{B'})/2 + r_X)} . \qquad (1)$$

This t value is expected to be in the range of 0.8 and 1.0 [15] to be favorable for the stable cubic perovskite formation. But further analysis on the innovative studies have outlined the consequences of several deviations. Therefore, $t = 1$ gives the ideal cubic perovskite structures, while $t \leq 0.825$ leads to the formation of alternative structure types such as ilmenite and greater t values as in $t \approx 1.07$ could result in hexagonal perovskite or other non-cubic structures due to excessive ionic size mismatch [16]. Therefore, focusing on enhanced inclusivity, & comprehensiveness, the screening in this study adopts a refined tolerance factor range of $0.825 \leq t \leq 1.07$. Considering the prevalence of 6-fold coordination in perovskite *X*-site 1.40Å [17] for O^{2-} & 1.33Å, 1.81Å, 1.96Å & 2.2Å for F^-, Cl^-, Br^-, & I^- [18] were taken as effective Shannon radii values.

1) Octahedral factor

The octahedral factor (μ) is another dimensionless parameter which is used to evaluate that the *B*-site cation and *X*-site anion are appropriately sized to form a stable BX_6 octahedron which is a crucial parameter to be placed it as a unit inside the perovskite structure [19]. For the single perovskites, μ is defined as the ratio of radii of *B*-cation to the *X*-anion radii while for double perovskites, average radii of two B-site cations are used to generalize the equation.

$$\mu = (r_{B_1} + r_{B_2})/2r_X . \qquad (2)$$

Same Shannon radii values were taken for this μ calculations as employed in previous tolerance factor calculations. To form a stable regular perovskite octahedra, this μ value is expected to be in the range of approximately 0.414 to 0.732 [20]. Following that, in this study, all the retained candidate combinations from the prior screening phase were then filtered through this screening to ensure geometric feasibility of the *B*-*X* coordination.

2) Octahedral Mis-Match factor

As the final succeeding screening phase, all candidates retained, were then filtered through the octahedral mismatch factor ($\Delta\mu$), which is a geometric descriptor that quantifies the size disparity between two *B*-site cations exclusively in double perovskite structures [20].

This mismatch factor can be calculated as:

$$\Delta\mu = \left| r_B + r_{B'} \right| / 2r_X , \qquad (3)$$

where r_A & r_B, are the Shannon ionic radii of the *B* site cations while r_X is the ionic radii of the *X* site. Due to the increased structural distortion and lower probability of stable perovskite formation caused by larger disparity, smaller $\Delta\mu$ values are favored for the perovskite stability [21]. Therefore, the retained combinations with $\Delta\mu$ less than 0.15 are expected to be acceptable for

the stable perovskite formation being geometrically compatible *B* site cation pairs.

Through this comprehensive screening framework, efficient filtration is done employing both chemical and geometric considerations to screen out viable perovskite structures which hold favorable structural stability and charge balance.

II. Results and Discussion

A total of 43 218 000 distinct combinations were generated by enumerating all combinations (42×42×70×70×5) constructing the initial candidate pool for further multi-phase screening process. It can be ensured that no potential perovskite structure is arbitrarily excluded from the initial screening scope by commencing the process with this kind of candidate pool.

Following cation site exclusivity screening, 41 324 955 unique combinations retained while 1 893 045 were dropped from the initial candidate pool due to sublattice overlap or redundancy. The remaining candidate space comprises 8 264 991 per each oxide and halide group, ensuring that only chemically relevant and non-redundant candidate structures are carried forward to permutational isomers screening phase. Then a total of 10 737 315 unique candidate structures were retained, while 30 587 640 both A & B site swapped duplicates were removed from the dataset. This curated candidate pool includes 2 147 463 unique representatives for each *X*-site anion, advancing non-overlapping and chemically identical isomers to the charge neutrality screening, with robust intra-anion compositional coherence.

Subsequently, 1 870 927 combinations were retained, while 75.96% of them being identified as oxide combinations leaving the rest as other halide-based configurations. This predominance of oxides indicates the distinct charge requirements imposed by the *X*-site anion, as the prevalence of -2 oxidation state for oxygen allows for a greater diversity of charge balanced arrangements with commonly encountered cation oxidation states such as +1, +2, +3 & +4. But in contrast, the other halide anions with oxidation state -1 require combinations of cations that sum to lower total positive charges, while narrowing the feasible, neutral configuration span. Even though there were only 1 245 822 unique structures within this expanded pool, all the configurations were preserved for further screening phases because all the tolerance factor, octahedral factor and octahedral mismatch factor calculations explicitly affected by the effect of the ionic radii of constituent cations. Since each

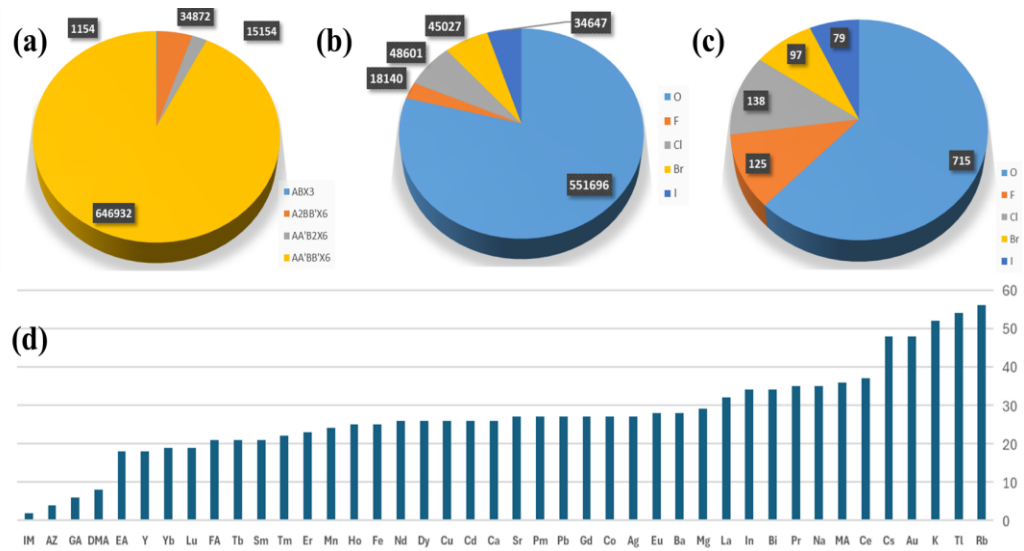

Figure 3. Distribution of the retained perovskites according to the **(a)** strucutral variations ($ABX_3, A_2BB'X_6, AA'B_2X_6, AA'BB'X_6$) **(b)** X-site anions O, F, Cl, Br, I **(c)** Distribtution of retained single perovskites based on X-site anions **(d)** Distribution of A-site cation elements retained in the refined perovskite structures, from the initial set of 42 candidate elements.

of those ionic radii varies according to their oxidation state, all of valid oxidation state configurations should be considered independently in the remaining multi-phase screening workflow.

Goldschmidt tolerance factor screening filtered 1 263759 combinations which were identified within the optimal range of $0.825 \leq t \leq 1.07$ while eliminating 607168 configurations which were deviated from that range along with the tendency towards formation of distorted phases and non-perovskites. This screening step guaranteed the geometric compatibility for the retained combinations with the focus of stable cubic perovskite structure discovery prior to more selective filtering criteria are introduced. These preserved combinations including 990 737 unique configurations were advanced to the octahedral factor screening.

Afterwards, 195412 combinations were discarded due to the failure of meeting an octahedral factor (μ) within the acceptable range of 0.414 to 0.732 carrying forward a 1068347 of configurations including 808987 unique combinations, that satisfied the criteria. Correspondingly here, all preserved combinations with multiple oxidation states were retained, ensuring that only the combinations with geometrically feasible *B-X* coordination will carry forward along with the assured structural integrity. At the same time this preservation will maintain comprehensive consideration of all possible valid configurations. Then the retaining combinations were filtered through octahedral mismatch factor discarding 186201 combinations which displayed higher $\Delta\mu$ values than the threshold of 0.15 due to the likelihood of lattice distortion and stability reduction. Remaining 882146 combinations including 698111 unique configurations with $\Delta\mu$ less than 0.15 by considering their geometrical compatibility. This effective filtration of perovskite candidates prone to structural instability allows the enrichment of the dataset with the combinations with B-site cation radii compatibility for stable perovskite formation.

Throughout the tolerance factor, octahedral factor and octahedral mismatch factor screening phases, all configurations including those with multiple possible states were considered due to the direct effect of oxidation states on the ionic radii used in those calculations. But since beyond these geometric factor screenings, retention of all oxidation-state variants is quite unnecessary and redundant, 698111 unique structures among retained 882146 combinations will be selected as the refined set of potential candidate perovskite configurations for further in-depth analysis. Among those filtered unique potential perovskite structures, 1154 candidates correspond to single perovskite compositions, which is approximately 0.18% of the total dataset (Fig. 3a). The obtained results further reveal that 551696 are oxide perovskite structures (Fig. 3b) including 715 single perovskites, together constituting roughly 79% of the full candidate structure pool. On the contrary, for halide analogues, 18140 *F*-based, 48601 *Cl*-based, 45027 *Br*-based and 34647 *I*-based perovskites structures were identified (Fig. 3b), each with 125, 138, 97 & 79 corresponding single perovskite representatives (Fig. 3c).

Table I demonstrates the refined possible perovskite structures corresponding to these organic A cations providing a more comprehensive map of perovskite configurational space.

A combined 4.38% and 70.78% of total initial combinations have been removed from the initial two compositional screening steps yielding a 2147463 pool of unique structures. Approximately, ~ 58% of that unique structure set has been created as an expanded set of all possible oxidation state configurations following charge neutrality screening. Subsequently, the geometric stability factors facilitated solid selective refinement via the reductions of 20.48%, 18.34% and 13.71% from each adjacent remaining set respectively. This sequential reduction protocol starting from a large pool of candidates then efficiently and strategically refining it, can be taken as a measure of scalability which enhances the computational efficiency. By publishing these refined structures candidate pool, a robust foundation is established for future perovskite discoveries. This data set consists of screened and classified entries to bypass the arduous task of initial candidate filtering guaranteeing that both computational and experimental efforts commence with a reliable, high-quality and chemically meaningful initiating set. This starting contribution is intended to fast track the advancements in perovskite science by facilitating an openly accessible and thoroughly curated resources for strategical methodological development, data-driven discovery and sapplication-intensive analysis.

III. Conclusion

This work presents a systematic, multi-phase data-driven screening framework for possible perovskite structures which integrates compositional filtering, symmetry-based pruning, charge neutrality evaluation and later geometric stability assessments. The approach competently narrows down a larger compositional space to a structurally and chemically refined feasible oxide and halide perovskites. In conclusion, this study reports 698111 unique perovskite structures, including 1154 single perovskite configurations. The refined dataset encompasses a unique set of O, F, Cl, Br & I perovskites. All discovered candidates have undergone a rigorous, methodical multi-phase screening process, resulting in a refined and reliable dataset. Through this combined, sequential filtering framework, a refined and reliable potential perovskite structures candidate pool has been generated without any inclusion of unnecessary or spurious entries, exclusively for the ML based property prediction and material discovery.

Data Availability

All data generated or analyzed during this study, including the refined candidate pool of possible perovskite structures and other supplementary materials, are available from the corresponding author upon request.

Acknowledgment

This work was supported by Senate Research Committee Short Term Grants (No.SRC/ST/ 2025/26) from the University of Moratuwa, Sri Lanka.

References

[1] Alsalman, M. A., Hezam, M. S., Alqahtani, S. M., Baloch, A. A. B., & Alharbi, F. H. (2024). Anions' Radii — New data points calibrated to match Shannon's table. *Computational Materials Science*, *247*, 113491. https://doi.org/10.1016/j.commatsci.2024.113491

[2] Touati, S., Benghia, A., Hebboul, Z., Lefkaier, I. K., Kanoun, M. B., & Goumri-Said, S. (2024). Machine Learning Models for Efficient Property Prediction of ABX3 Materials: A High-Throughput Approach. *ACS Omega*, *9*(48), 47519-47531.

[3] Huo, S., Zhang, S., Wu, Q., & Zhang, X. (2024). Feature-Assisted Machine Learning for Predicting Band Gaps of Binary Semiconductors. *Nanomaterials*, *14*(5), 445-445. https://doi.org/10.3390/nano14050445

[4] Tao, Q., Lu, T., Sheng, Y., Li, L., Lu, W., & Li, M. (2021). Machine learning aided design of perovskite oxide materials for photocatalytic water splitting. *Journal of Energy Chemistry*, *60*, 351-359. https://doi.org/10.1016/j.jechem.2021.01.035

[5] Kusuma, F. J., Widianto, E., Wahyono, Santoso, I., Sholihun, Ulil Absor, Moh. Adhib., Sakti, S. P., & Triyana, K. (2025). Multi-Properties prediction of perovskite materials using Machine learning and Meta-Heuristic feature selection. *Solar Energy*, *286*, 113189. https://doi.org/10.1016/j.solener.2024.113189

[6] Thoppil, G. S., & Alankar, A. (2022). Predicting the formation and stability of oxide perovskites by extracting underlying mechanisms using machine learning. *Computational Materials Science*, *211*, 111506. https://doi.org/10.1016/j.commatsci.2022.111506

[7] Zhao, J., & Wang, X. (2022). Screening Perovskites from ABO3 Combinations Generated by Constraint Satisfaction Techniques Using Machine Learning. *ACS Omega*, *7*(12), 10483-10491. https://doi.org/10.1021/acsomega.2c00002

[8] Touati, S., Benghia, A., Hebboul, Z., Lefkaier, I. K., Kanoun, M. B., & Goumri-Said, S. (2024). Predictive machine learning approaches for perovskites properties using their chemical formula: towards the discovery of stable solar cells materials. *Neural Computing and Applications*, *36*(26), 16319-16329. https://doi.org/10.1007/s00521-024-09992-5

[9] Perrichon, A., Jedvik Granhed, E., Romanelli, G., Piovano, A., Lindman, A., Hyldgaard, P., ... & Karlsson, M. (2020). Unraveling the ground-state structure of BaZrO3 by neutron scattering experiments and first-principles calculations. *Chemistry of Materials*, *32*(7), 2824-2835. https://doi.org/10.1021/acs.chemmater.9b04437

[10] Sivadas, D., Singareddy, A., Vinod, C. G., & Nair, P. R. (2023). Ionic charge imbalance in perovskite solar cells. *The Journal of Physical Chemistry C*, *127*(46), 22766-22774. https://doi.org/10.1021/acs.jpcc.3c05673.s001

[11] Li, J., Du, P., Li, S., Liu, J., Zhu, M., Tan, Z., Hu, M., Luo, J., Guo, D., Ma, L., Nie, Z., Ma, Y., Gao, L., Niu, G., & Tang, J. (2019). High- Throughput Combinatorial Optimizations of Perovskite Light- Emitting Diodes Based on All- Vacuum Deposition. *Advanced Functional Materials*, *29*(51). https://doi.org/10.1002/adfm.201903607

[12] Grosso, B. F., Davies, D. W., Zhu, B., Walsh, A., & Scanlon, D. O. (2023). Accessible chemical space for metal nitride perovskites. *Chemical Science*, *14*(34), 9175-9185. https://doi.org/10.1039/d3sc02171h

[13] Nandy, A., Loha, C., Gu, S., Sarkar, P., Karmakar, M. K., & Chatterjee, P. K. (2016). Present status and overview of chemical looping combustion technology. *Renewable and Sustainable Energy Reviews*, *59*, 597-619. https://doi.org/10.1016/j.rser.2016.01.003

[14] Cava Lab: Perovskites. (n.d.). Available at: https://www.princeton.edu/~cavalab/tutorials/public/structures/perovskites.html

[15] Li, Z., Yang, M., Park, J.-S., Wei, S.-H., Berry, J. J., & Zhu, K. (2015). Stabilizing Perovskite Structures by Tuning Tolerance Factor: Formation of Formamidinium and Cesium Lead Iodide Solid-State Alloys. *Chemistry of Materials*, *28*(1), 284-292.

[16] Smart, S., Liu, S., Serra, J. M., Basile, A., & da Costa, J. D. (2014). Perovskite membrane reactors: fundamentals and applications for oxygen production,

syngas production and hydrogen processing. In *Membranes for Clean and Renewable Power Applications* (pp. 182-217). Woodhead Publishing. https://doi.org/10.1533/9780857098658.3.182

[17] Albrecht, E. K., & Karttunen, A. J. (2023). Investigation on the predictive power of tolerance factor τ for A-site double perovskite oxides. *Dalton Transactions*, *52*(35), 12461-12469. https://doi.org/10.1039/d3dt01990j

[18] Karuppiah, K., & Ashok, A. M. (2019). Review of proton- and oxide-ion-conducting perovskite materials for SOFC applications. *Nanomaterials and Energy*, *8*(1), 51-58. https://doi.org/10.1680/jnaen.18.00004

[19] Alsalman, M. A., Hezam, M. S., Alqahtani, S. M., Baloch, A. A. B., & Alharbi, F. H. (2024). Anions' Radii — New data points calibrated to match Shannon's table. *Computational Materials Science*, *247*, 113491. https://doi.org/10.1016/j.commatsci.2024.113491

[20] Turnley, J. W., Agarwal, S., & Agrawal, R. (2024). Rethinking tolerance factor analysis for chalcogenide perovskites. *Materials Horizons*, *11*, 4802-480. https://doi.org/10.1039/d4mh00689e

[21] Ji, D., Feng, S., Wang, L., Wang, S., Na, M., Zhang, H., ... & Li, X. (2019). Regulatory tolerance and octahedral factors by using vacancy in APbI3 perovskites. *Vacuum*, *164*, 186-193. https://doi.org/10.1016/j.vacuum.2019.03.018

eNergetics 2025
DOI: https://doi.org/10.5281/zenodo.18620763

Original Scientific Article

Intelligent Hybrid Forecasting of Photovoltaic Power using LSTM and XGBoost: Seasonal and Comparative Insights

Musa Terkeş[1], Alpaslan Demirci[2], Erdin Gökalp[3]

[1,2,3]Department of Electrical Engineering, Yildiz Technical University, İstanbul, Türkiye

[1]musa.terkes@yildiz.edu.tr, [2]ademirci@yildiz.edu.tr, [3]gokalp@yildiz.edu.tr

Abstract—**Accurate forecasting of photovoltaic (PV) power generation is essential for the reliability and cost-effectiveness of renewable-based power systems to be maintained. This study provides a comprehensive comparison of several statistical and machine learning approaches, including SARIMA, SVR, k-NN, RF, XGBoost, and LSTM networks. To enhance the consistency of predictions, a hybrid ensemble method is proposed, which integrates LSTM and XGBoost through a weighted averaging approach. The goal of this configuration is to take advantage of the temporal learning ability of LSTM and the nonlinear feature modeling strength of XGBoost. The hourly seasonal datasets were evaluated using common performance indicators, including RMSE, MAE, MAPE, and R^2. The analysis shows that each individual model performs better under certain seasonal or meteorological conditions. The LSTM–XGBoost hybrid generally yields the lowest prediction errors. It has particular effectiveness in the capture of both short-term variations and broader seasonal patterns. The results highlight the importance of hybrid intelligent systems in enhancing PV forecasting accuracy and show their potential to support more stable renewable energy operations.**

Keywords - photovoltaic power forecasting, hybrid ensemble learning, LSTM neural networks, XGBoost regression, time-series prediction.

I. INTRODUCTION

Photovoltaic (PV) energy has become a central element in the global shift away from fossil fuels, which is a major development in the energy sector. Its abundance, environmental benefits, and steadily falling costs have made it one of the most attractive renewable sources available. The inclusion of PV systems in modern power networks is now considered essential. This is because it helps reach sustainability goals. It also helps meet international commitments on climate change mitigation [1]. However, PV generation remains highly dependent on local weather conditions. The balance between electricity production and consumption is complicated by this variability, and grid reliability is challenged [2,3]. Consequently, producing accurate short- and medium-term forecasts is now critical for day-to-day operations, such as reserve planning, load management, energy market participation, and system stability.

Conventional statistical models often struggle to represent the nonlinear and intermittent behavior of PV output. One example is the seasonal autoregressive integrated moving-average (SARIMA) method. These limitations have encouraged the growing use of artificial-intelligence-based techniques [4]. In recent years, deep learning architectures, including convolutional neural networks (CNNs), long short-term memory (LSTMs), gated recurrent units (GRUs), and transformer models, have shown strong potential for capturing the intricate temporal and spatial structures present in PV data [5]. Spatial features are particularly well learned from irradiance or cloud-pattern information by CNNs, whil e sequential trends are

ISBN: 978-86-82602-07-1

excellently identified by recurrent models such as LSTM and GRU. More recently, research has explored ways to improve the representation of long-range temporal dependencies [6]. One approach is to use attention mechanisms in Transformer frameworks and auxiliary components like Time2Vec.

In parallel with the development of forecasting models, researchers have introduced several complementary strategies to enhance both accuracy and robustness. Signal decomposition methods separate the time series into multiple frequency components. These methods include ensemble empirical mode decomposition (EEMD), its adaptive variant complete ensemble empirical mode decomposition with Adaptive Noise (CEEMDAN), and variational mode decomposition (VMD). These methods stabilize the predictions [7,8]. Likewise, dimensionality-reduction and feature-selection techniques have been applied to simplify input variables and make the models more interpretable. These techniques include principal component analysis (PCA), least absolute shrinkage and selection operator (LASSO), and SHapley Additive exPlanations (SHAP) [9]. Hyperparameter-optimization approaches based on metaheuristics such as Bayesian optimization, grey-wolf optimizer (GWO), genetic algorithm (GA), multi-verse optimizer (MVO), and improved salp-swarm algorithm (ISSA) have also improved forecasting performance. In addition, clustering methods for identifying similar days have helped to capture temporal variability. These methods include K-means++ and K-medoids. They also include synthetic-data generation using generative adversarial networks (GANs) or their time-series extension (TimeGAN). This has helped to mitigate the lack of training data. Recent studies have shown that image-based CNN models trained on satellite images can sometimes do a better job than traditional meteorological inputs in very short-term forecasting tasks.

Although prediction quality has been substantially improved by these advances, several issues remain unresolved. Many studies use data from only one place and only for less than a year. This makes the models not useful for other places and times of the year [2,10]. Some approaches fail to consider crucial atmospheric factors, like aerosol content, or fixate exclusively on point forecasts without accounting for uncertainty. In other cases, models lack explainability mechanisms, resulting in “black-box” models that impede transparency and adoption [11,12]. Finally, these systems can't be used in real-time or large-scale grid operations because they need too many computers [4,5,7,10,13].

Recent studies have made an attempt to address the above challenges through the combination of different model types within hybrid or ensemble frameworks. For instance, CNN-LSTM-Transformer configurations have been developed to integrate spatial, temporal, and attention-based learning to enhance overall accuracy. In a similar way, LSTM networks that have been tuned with Bayesian optimization adapt their performance to different input conditions [7]. Some researchers have also paired GAN-generated synthetic data with CNN–GRU architectures to compensate for limited training samples [6]. Concurrently, tree-based algorithms such as extreme gradient boosting (XGBoost), light gradient boosting machine (LightGBM), and categorical boosting (CatBoost) have been integrated into hybrid designs to capture complex nonlinear feature relations [12,14]. Other techniques have also shown measurable improvements in prediction quality. These include attention-guided feature selection [15] and ensembles driven by sky-image CNN models.

In general, the existing work shows that one type of model usually doesn't work well in all situations. Instead, integrated and multi-layered approaches seem to offer a more balanced solution. These approaches combine deep learning with boosting methods, attention modules, uncertainty modeling, and explainable-AI components. Based on these findings, the current study presents a hybrid framework that links an attention-based LSTM with tree regressors like XGBoost. The interpretability of the model was addressed by applying SHAP analysis to the XGBoost component of the ensemble. The relative importance of meteorological and solar features was quantified in this analysis, and insights into the model's decision process were provided. The model's transparency is enhanced and its deployment in operational energy management systems is supported by such interpretability. In this way, the goal is to produce forecasting models that are not only accurate and robust. The models should also be easier to interpret and applicable to real-world PV integration and grid operation.

II. DATASET AND MODELING FRAMEWORK

This research was carried out for a hydrogen refueling station in Antalya, Türkiye (36.90° N, 30.70° E). This location is known for its strong solar resource. The site receives an annual average direct normal irradiance (DNI) of about 5.23 kWh/m² per day. This varies seasonally between 3.30 and 7.48 kWh/m² per day. The mean clarity index is estimated to be around 54.6%. The PVGIS database was used to obtain estimates of PV generation. This database relies on the SARAH and ERA5 reanalysis datasets to model solar irradiance based on the geographic coordinates of the station.

The creation of hourly load-demand profiles in HOMER used a combination of stochastic and pattern-based approaches to complement the generation data. The methodological framework is unified and combines statistical, machine-learning, and deep-learning methods. This framework is designed for seasonal PV-power forecasting. Forecasting PV output is inherently difficult because deterministic solar cycles interact with random meteorological changes such as cloud movement and temperature variation. To represent both periodic and irregular behaviors, the problem is expressed as learning a mapping function $F = \mathbf{X}_t \to y_{t+h}$, $\mathbf{X}_t = \{y_{t-1}, y_{t-2}, \cdots, y_{t-p}\}$ represents the lagged historical production values, and y_{t+h} denotes the forecasted PV output at horizon h.

Instead of using each algorithm separately, the models are used together. Each model has different strengths that help cover the weaknesses of the other models. The statistical layer of the framework is employed by the SARIMA model, which decomposes the time series into autoregressive, differencing, and moving-average elements combined with seasonal terms. Its general form can be written as follows:

$$\Phi_p(B)\Phi_P(B^s)(1-B)^d(1-B^s)^D y_t = \\ = \Theta_q(B)\Theta_Q(B^s)\varepsilon_t \quad . (1)$$

Here, B represents the backshift operator, where $By_t = y_{t-1}$. The parameter denotes the seasonal period, and ε_t stands for the white-noise error term. In this formulation, y_t is the observed PV generation at time step t; Φ_p and Φ_P are the autoregressive (AR) polynomials for the non-seasonal and seasonal parts, respectively; $\Theta_q(B)$ and $\Theta_Q(B^s)$ are the corresponding moving-average (MA) polynomials. The differencing orders d and D describe the non-seasonal and seasonal components. The non-seasonal AR polynomial of order p can be expressed as:

$$\Phi_p(B) = 1 - \phi_1 B - \phi_2 B^2 - \cdots - \phi_p B^p , \quad (2)$$

where ϕ_i are AR coefficients. Seasonal AR polynomial of order P with seasonal lag s:

$$\Phi_p(B^s) = 1 - \Phi_1 B^s - \Phi_2 B^{2s} - \cdots - \Phi_P B^{Ps} . \quad (3)$$

The SARIMA model is especially helpful for recognizing consistent and recurring seasonal patterns. However, its strict structure limits its flexibility when sudden or irregular fluctuations occur. These fluctuations often happen in PV generation affected by short-term weather variations.

To overcome these limitations, the analysis incorporates machine learning methods that can approximate nonlinear relationships. Among them, the k-nearest neighbors (k-NN) regressor estimates future values. It does so by comparing each observation with similar historical patterns in the dataset:

$$y_{t+h} = \frac{1}{K} \sum_{i \in \mathrm{N}_K(t)} y_i \quad . \quad (4)$$

Here, $\mathrm{N}_K(t)$ denotes the neighborhood containing the K closest samples to the target time step t. The k-NN approach is appreciated for its conceptual simplicity and transparency, which make it a useful tool for data analysis. However, its performance often declines when the system faces unusual or rapidly changing conditions because it relies heavily on historical analogues. The random forest (RF) algorithm builds an ensemble of decision trees. These trees are generated through bootstrap resampling. RF can model nonlinear relationships and reduce variance by averaging the outcomes of multiple trees. A known drawback is that the averaging process smooths the results. Sometimes it

underestimates extreme values. Support vector regression (SVR) adopts a more formal approach by conceptualizing the regression task within the framework of structural risk minimization. The goal is to find a function that matches the data while making the prediction and the model less complicated. This is expressed as:

$$\min_{w,\xi,\xi^*} \frac{1}{2}\|w\|^2 + C\sum_{i=1}^{n}\left(\xi_i + \xi_i^*\right), \quad (5)$$

subject to the constraint $\left|y_i - \left(w^T\phi(x_i)+b\right)\right| \le \varepsilon + \xi_i$, where $\phi(\square)$ represents the kernel mapping function. By introducing an ε-insensitive margin, SVR ignores small deviations while penalizing larger errors, which helps the model remain robust in the presence of noise. Here, w denotes the weight vector, and ξ_i and ξ_i^* are positive slack variables that capture prediction errors lying outside the ε-insensitive region.

Among ensemble algorithms, XGBoost applies the principle of gradient boosting. It does so to iteratively reduce residual errors. It builds an additive model that refines its predictions at each step, as expressed in the following equation:

$$y_t = \sum_{k=1}^{K} f_k(x_t), \quad f_k \in F, \quad (6)$$

where F represents the space of regression trees, f_k denotes the k-th regression tree within the XGBoost framework, and x_t refers to the input vector fed into the LSTM model at time step t. The tree ensemble can capture overall patterns. This ability enables it to identify broad production trends effectively. However, because of its static and rule-based nature, it may sometimes stretch production intervals. It may also lose detail in rapid temporal changes.

To represent sequential relationships and short-term variability, a LSTM-recurrent neural network (RNN) is integrated into the framework. The LSTM design is different from traditional RNNs because it addresses the vanishing-gradient limitation. It does this by using gated memory units that can retain or discard information. The following equations show this:

$$f_t = \sigma\left(W_f\left[h_{t-1}, x_t\right] + b_f\right), \quad (7)$$

$$i_t = \sigma\left(W_i\left[h_{t-1}, x_t\right] + b_i\right), \quad (8)$$

$$\tilde{c}_t = \tanh\left(W_c\left[h_{t-1}, x_t\right] + b_c\right), \quad (9)$$

$$c_t = f_t \cdot c_{t-1} + i_t \cdot \tilde{c}_t, \quad (10)$$

$$o_t = \sigma\left(W_o\left[h_{t-1}, x_t\right] + b_o\right), \quad (11)$$

$$h_t = o_t \cdot \tanh\left(c_t\right), \quad (12)$$

where x_t denotes the input vector, h_t the hidden state, and c_t the cell state of the LSTM unit. The terms f_t, i_t, and o_t represent the forget, input, and output gates, respectively. The candidate cell state is noted as $\tilde{c}_t$, while W_f, W_i, W_c, and W_o denote the weight matrices corresponding to each gate. Similarly, b_f, b_i, b_c, and b_o are the bias terms, and $\sigma(\cdot)$ indicates the sigmoid activation function. LSTM uses a gating structure to retain useful temporal information and filter out redundant signals. This enables the model's reproduction of both the smooth daily production profile and transient irregularities, such as rapid fluctuations caused by shading or load variation.

The primary contribution of this study is the creation of a hybrid structure that merges the sequence learning power of LSTM with the trend generalization ability of XGBoost. The combined prediction is expressed as a convex integration of the two model outputs:

$$y_t^{Hybrid} = \alpha y_t^{LSTM} + (1-\alpha) y_t^{XGBoost}, \quad (13)$$

where the weighting factor $\alpha \in [0,1]$ is tuned to minimize the overall loss across seasonal datasets. The α coefficient controls the balance between the LSTM and XGBoost forecasts within the hybrid model. The strengths of both methods are drawn on by this structure: short-term nonlinear variations within a day are captured by the LSTM, while broader, long-term patterns are efficiently modeled by XGBoost. In combination, the slow response of the LSTM is reduced and the tendency of XGBoost to oversimplify temporal details is mitigated.

This framework is based on several assumptions. PV production is treated as a

function of solar irradiance and related weather conditions, and it is assumed that enough information to estimate future outputs can be carried by the historical production record. Before training, all data were standardized to a unit scale. This ensured consistency between models and avoided bias caused by variable magnitudes. Hyperparameters for the model were tuned using a combination of grid search and validation-based tuning. The XGBoost component was identified using a grid search with five-fold time-series cross-validation (TimeSeriesSplit). This method was used to determine the optimal tree depth, learning rate, and subsampling ratios. For the LSTM network, hyperparameters were tuned empirically. These included the number of hidden units, dropout rates, and learning rate. Tuning was based on validation loss under early stopping criteria. To make sure that the optimization was consistent across models, all of the other regressors were calibrated through grid-based or heuristic parameter searches. The model can be viewed from another perspective, which is input-specific. Representative days were selected from each season to reflect differences in sunlight duration, production symmetry, and random atmospheric effects.

To measure model accuracy, common error metrics were used, including root mean square error (RMSE), mean absolute error (MAE), and coefficient of determination (R^2). These metrics evaluate both absolute prediction accuracy and the ability to reproduce time-varying dynamics. Despite the absence of formal statistical significance tests, the performance disparities were uniformly discerned across numerous validation windows and metrics (RMSE, MAE, and R^2). This consistency indicates that the hybrid ensemble's enhancement over the baseline models is not just a coincidence but rather a result of its robust performance.

This study makes a comparison between classical and modern forecasting techniques by combining different modeling perspectives in a single mathematical form. The proposed LSTM–XGBoost hybrid is a flexible and reliable approach for seasonal PV forecasting, addressing both predictable solar pattern and random weather-driven variability.

Finally, a fair assessment of model performance requires multiple complementary metrics, each emphasizing a distinct aspect of predictive behavior. To ensure consistent comparisons across models and seasons, this work utilizes several standard indicators (RMSE, MAE, R^2).

To avoid bias from periods with nearly zero production, all performance metrics were calculated on test samples filtered by solar irradiance. Representative days from winter, spring, summer, and autumn were used to ensure balanced seasonal coverage during the evaluation. The final step was to compare the hybrid model's results with those of the individual models. This was done to assess the effect of combining methods and to demonstrate the practical benefit of the hybrid approach in PV forecasting.

III. Seasonal Forecasting Performance and Comparative Performance of AI Models

Fig. 1 compares the PV power output predicted by the AI models across several days selected from each season.

One of these examples, from the middle of January, shows the winter period when the sun does not make much energy. During this season, the daylight window is short and the sun doesn't provide much energy, which limits the amount of electricity produced by solar panels to a narrow time period during the day. The actual production starts around 9:00 a.m. and decreases until around 3:00 p.m. Among the models, the LSTM forecast matched the real production pattern quite well. This was particularly true around the midday peak. The LSTM forecast captured both the rise and fall of the output curve with reasonable accuracy.

In contrast to the LSTM outcomes, the XGBoost model generally initiated the production phase slightly earlier in the morning and prolonged it later into the afternoon, resulting in a noticeably broader curve. This tendency likely originates from the way tree-based algorithms generalize across similar data points. The midday peak was reduced by the gentler slopes of the smoother curves produced by the SARIMA and k-NN approaches. SARIMA's tendency to predict production too soon and underestimate the actual midday level stems from its assumption of a repeating seasonal pattern. In contrast, the hybrid LSTM + XGBoost configuration leveraged the strengths of both

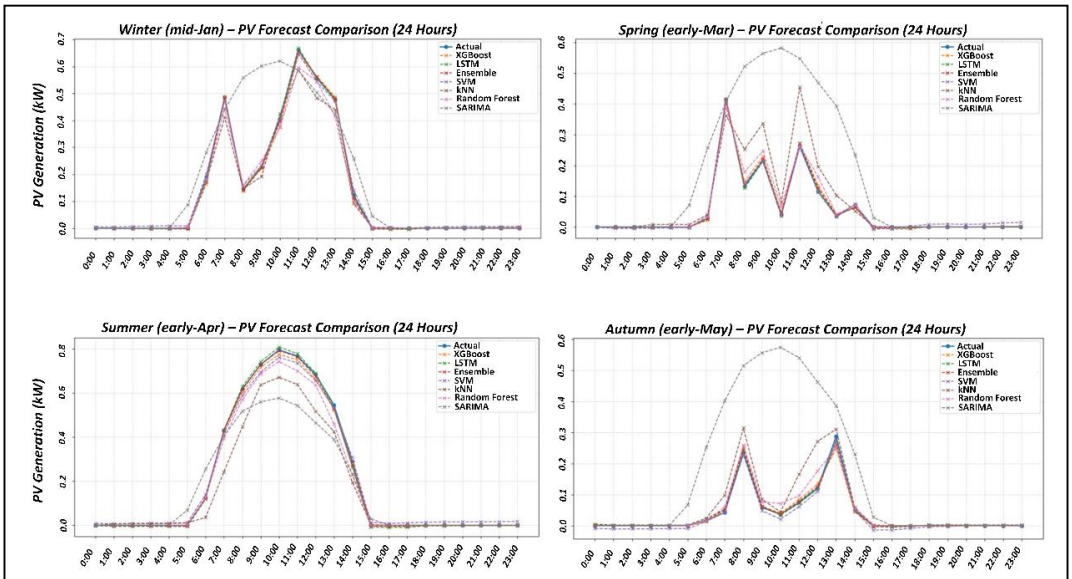

Figure 1. Predicted and actual PV power by season.

TABLE I. SEASONAL PERFORMANCE COMPARISON OF FORECASTING MODELS FOR PV POWER PREDICTION.

Season	Metrics	AI Model						
		SARIMA	***k-NN***	***RF***	***SVR***	***XGBoost***	***LSTM***	***Ensemble***
Winter (mid-Jan)	RMSE	0.1308	0.0294	0.0229	0.0085	0.0095	0.0089	0.0059
	MAE	0.0667	0.0152	0.0119	0.0075	0.005	0.0046	0.0033
	R^2	0.6106	0.9804	0.988	0.9983	0.9979	0.9982	0.9992
Spring (early-Mar)	RMSE	0.2027	0.0586	0.017	0.007	0.0068	0.0053	0.0054
	MAE	0.1157	0.0306	0.0081	0.0058	0.0037	0.0037	0.0036
	R^2	-	0.6778	0.9727	0.9954	0.9956	0.9974	0.9972
Summer (early-Apr)	RMSE	0.0993	0.0831	0.033	0.0184	0.0097	0.0067	0.0073
	MAE	0.0583	0.0508	0.0186	0.0165	0.0053	0.0041	0.0045
	R^2	0.8903	0.9233	0.9879	0.9962	0.999	0.9995	0.9994
Autumn (early-May)	RMSE	0.2216	0.0416	0.0172	0.0088	0.0099	0.0074	0.0068
	MAE	0.1287	0.0188	0.0088	0.0074	0.0046	0.0057	0.0044
	R^2	-	0.6858	0.9464	0.986	0.9823	0.99	0.9915

methods, accurately capturing both the timing and the magnitude of the peak.

Compared to the example from early March, which represented spring conditions, the current example displays much more irregular behavior. During that day, the weather shifted, leading to sudden drops in solar power generation, making it challenging to predict future energy output.

The k-NN and SVM models depend heavily on historical analogues. They could not keep pace with these rapid shifts. The models produced overly smooth estimates. The LSTM network was able to detect some of the sudden changes, but it was slow react. XGBoost, on the other hand, tended to overshoot morning production and occasionally provided non-zero predictions during periods of no sunlight. Even though there were problems, the hybrid model still made most of the short production drops with small mistakes, especially between 11:00 and 14:00.

The profile of production in the early April example, which represents summer, is more symmetrical, with higher values as daylight hours increase. During this period, production begins around 6:00–7:00. It ends around 14:00–15:00. The production during the afternoon reaches a peak with a distinct rise and fall that resembles a classic PV production curve. In this case, the LSTM model performed well in predicting the timing and magnitude of the production curve. It accurately captured the morning rise and the afternoon peak.

The overall production trend was tracked by the XGBoost model, but relatively aggressive predictions were made in the morning, and a slight delayed decline was shown in the afternoon. SARIMA was used to predict the early morning production, but the production values were suppressed, resulting in a flatter curve that did not represent the peak well. The k-NN and RF models, which rely on averages from historical data, smoothed out production increases and decreases, particularly modeling the afternoon decline in a delayed and flattened manner. This is a common result for models that are not very sensitive to sudden curve changes. Nevertheless, the LSTM+XGBoost hybrid AI model generated highly accurate predictions. These predictions were made across the entire time range. The time range included the morning start, noon peak, and the end of production. The hybrid model achieved balanced and stable prediction performance for both short-term fluctuations and overall production patterns.

The early May example representing autumn reveals a more complex production profile: production starts late in the morning, suddenly peaks, and then declines. Deep learning methods are at an advantage when using this structure in comparison to classical statistical models. SARIMA and RF models were unable to capture this sudden change. Instead, they provided an "average day" prediction. The LSTM model accurately predicted the peak, but it did not adequately capture the subsequent decline rate. The rapid decline after production was exaggerated by XGBoost, resulting in negative prediction biases. These two tendencies were balanced by the hybrid model, and both the peak and subsequent decline were successfully modeled in terms of timing and magnitude. Overall, behind the hybrid model keeps relevant information from earlier moments within its cell states, the model can follow short-term variations, such as the morning-to-evening transitions or brief production drops, that often appear in solar generation. This relates to how XGBoost interprets long-term statistical behavior. The gradient-boosting design of the algorithm helps it capture broader production trends that are learned from historical data, and it can adjust to hourly fluctuations. When the outputs of both models are combined through weighted averaging, the short-term and long-term errors compensate for one another. This produces forecasts that remain steady and trustworthy across the day (see Table I). On the other hand, the hybrid ensemble exhibited both strong predictive capabilities and sufficient computational efficiency for practical applications. To ensure robust generalization, the hyperparameters of the XGBoost and LSTM components were optimized via grid search and time-series cross-validation. All the information that was put in was made the same using MinMax scaling, which made it so that things would happen more smoothly, and the numbers that were used for this were saved so that the same process could be used again. The enhanced PV power forecast accuracy further reinforces the model's practical relevance, extending beyond its statistical performance. This enhanced accuracy supports operational decision-making processes related to grid stability management and renewable integration.

IV. Conclusion and Future Suggestions

The objective of this work was the testing of various models for PV power prediction, including statistical, machine learning, and deep learning approaches. It also introduced a hybrid model that combines LSTM and XGBoost. The analysis showed that simple time-series models such as SARIMA perform well when seasonal patterns are strong. Algorithms such as SVR, k-NN, and RF demonstrate optimal performance in stable conditions; however, they exhibit a decline in accuracy when production patterns change rapidly. When combined into a weighted ensemble (LSTM and XGBoost), the two models complemented each other, resulting in improved stability and accuracy of predictions across different seasons.

The findings suggest that hybrid AI systems can contribute to enhancing the reliability of power grids and improve the planning of renewable energy. The results' practical implications underscore the potential for enhanced PV power forecasts to assist grid

operators in preserving voltage stability and refining strategies for integrating renewable energy. More reliable scheduling of storage and dispatchable units is achieved by the reduced prediction error of the hybrid ensemble. The computational framework of LSTM-XGBoost exhibited effective convergence when employing the Adam optimizer and grid-based hyperparameter optimization for the constituent sub-models. Sensitivity analyses confirmed the stability of performance under different normalization and scaling methods, ensuring the approach's reproducibility and robustness.

Future work could use Bayesian inference or quantile regression to produce confidence intervals for PV power forecasts, improving operational reliability. Exploring attention-based or transformer models and integrating physics-informed layers may enhance both accuracy and interpretability. Evaluating models across diverse regions and climates would clarify their generalizability.

REFERENCES

[1] Akhter, M. N., Mekhilef, S., Mokhlis, H., Ali, R., Usama, M., Muhammad, M. A., & Khairuddin, A. S. M. (2022). A hybrid deep learning method for an hour ahead power output forecasting of three different photovoltaic systems. *Applied Energy, 307*, 118185. https://doi.org/10.1016/j.apenergy.2021.118185

[2] Xiang, X., Li, X., Zhang, Y., & Hu, J. (2024). A short-term forecasting method for photovoltaic power generation based on the TCN-ECANet-GRU hybrid model. *Scientific Reports, 14*(1), 6744. https://doi.org/10.1038/s41598-024-56751-6

[3] Zhang, J., Liu, Z., & Chen, T. (2023). Interval prediction of ultra-short-term photovoltaic power based on a hybrid model. *Electric Power Systems Research, 216*, 109035. https://doi.org/10.1016/j.epsr.2022.109035

[4] Zheng, J., Du, J., Wang, B., Klemeš, J. J., Liao, Q., & Liang, Y. (2023). A hybrid framework for forecasting power generation of multiple renewable energy sources. *Renewable and Sustainable Energy Reviews, 172*, 113046. https://doi.org/10.1016/j.rser.2022.113046

[5] Agga, A., Abbou, A., Labbadi, M., Houm, Y. El, & Ou Ali, I. H. (2022). CNN-LSTM: An efficient hybrid deep learning architecture for predicting short-term photovoltaic power production. *Electric Power Systems Research, 208*, 107908. https://doi.org/10.1016/j.epsr.2022.107908

[6] Li, Q., Zhang, X., Ma, T., Liu, D., Wang, H., & Hu, W. (2022). A Multi-step ahead photovoltaic power forecasting model based on TimeGAN, Soft DTW-based K-medoids clustering, and a CNN-GRU hybrid neural network. *Energy Reports, 8*, 10346–10362. https://doi.org/10.1016/j.egyr.2022.08.180

[7] Wang, L., Mao, M., Xie, J., Liao, Z., Zhang, H., & Li, H. (2023). Accurate solar PV power prediction interval method based on frequency-domain decomposition and LSTM model. *Energy, 262*, 125592. https://doi.org/10.1016/j.energy.2022.125592

[8] Ge, L., Xian, Y., Yan, J., Wang, B., & Wang, Z. (2020). A Hybrid Model for Short-term PV Output Forecasting Based on PCA-GWO-GRNN. *Journal of Modern Power Systems and Clean Energy, 8*(6), 1268–1275. https://doi.org/10.35833/MPCE.2020.000004

[9] Talaat, M., Said, T., Essa, M. A., & Hatata, A. Y. (2022). Integrated MFFNN-MVO approach for PV solar power forecasting considering thermal effects and environmental conditions. *International Journal of Electrical Power & Energy Systems*, *135*, 107570. https://doi.org/10.1016/j.ijepes.2021.107570

[10] Qu, Y., Xu, J., Sun, Y., & Liu, D. (2021). A temporal distributed hybrid deep learning model for day-ahead distributed PV power forecasting. *Applied Energy, 304*, 117704. https://doi.org/10.1016/j.apenergy.2021.117704

[11] Abou Houran, M., Salman Bukhari, S. M., Zafar, M. H., Mansoor, M., & Chen, W. (2023). COA-CNN-LSTM: Coati optimization algorithm-based hybrid deep learning model for PV/wind power forecasting in smart grid applications. *Applied Energy, 349*, 121638. https://doi.org/10.1016/j.apenergy.2023.121638

[12] Kim, H., Park, S., Park, H.-J., Son, H.-G., & Kim, S. (2023). Solar Radiation Forecasting Based on the Hybrid CNN-CatBoost Model. *IEEE Access, 11*, 13492–13500. https://doi.org/10.1109/ACCESS.2023.3243252

[13] Wang, T., Xu, Y., Qin, Y., Wang, X., Zheng, F., & Li, W. (2025). Short-term PV forecasting of multiple scenarios based on multi-dimensional clustering and hybrid transformer-BiLSTM with ECPO. *Energy, 334*, 137654. https://doi.org/10.1016/j.energy.2025.137654

[14] S. Ghimire, B. Bhandari, D. Casillas-Pérez, R. C. Deo, & S. Salcedo-Sanz (2022). Hybrid deep CNN-SVR algorithm for solar radiation prediction problems in Queensland, Australia. *Eng. Appl. Artif. Intell., 112*,. 104860, doi: https://doi.org/10.1016/j.engappai.2022.104860.

[15] Mubarak, H., Hammoudeh, A., Ahmad, S., Abdellatif, A., Mekhilef, S., Mokhlis, H., & Dupont, S. (2023). A hybrid machine learning method with explicit time encoding for improved Malaysian photovoltaic power prediction. *Journal of Cleaner Production, 382*, 134979. https://doi.org/10.1016/j.jclepro.2022.134979

eNergetics 2025
DOI: https://doi.org/10.5281/zenodo.18620823

Original Scientific Article

Effect of Ribs on the Efficiency of Two-phase Centrifugal Pumps at High and Low Rotational Speeds

Toumi Bessam[1], Atif Abdelmadjid[2], Bennaceur Mohamed Amine[3], Hazem Meharzi[4]

[1,2,4]Laboratory of Energetic Mechanics and Conversion Systems, Faculty of Mechanical and Process Engineering, University of Sciences and Technologies Houari Boumediene, Bab-Ezzoaur, Algiers, Algeria
[3]Department of Scientific and Technology Watch, Algerian Space Agency, Algiers, Algeria

[1]btoumi@usthb.dz, [2]aatif@usthb.dz, [3]amine.rmsm@gmail.com, [4]hmeharzi@usthb.edu.dz

Abstract—**Fluid transport is a critical process in various industrial operations, particularly in the transportation of petroleum products. This process predominantly relies on centrifugal pumps, which exhibit high efficiency when handling single-phase liquids. However, their performance significantly declines when pumping two-phase fluids, with complete pump failure occurring at elevated gas-liquid ratios. This study investigates the impact of a novel pump geometry incorporating ribs on enhancing pump performance under such conditions. The findings demonstrate that ribbed pumps possess a superior capacity to handle two-phase gas-liquid flows at high gas ratios. This is achieved by generating secondary flows that promote a more homogenous gas-liquid mixture, mitigate the formation of gas pockets responsible for performance degradation, and delay pump shutdown. These improvements contribute to enhanced operational reliability, safety, and efficiency of the novel pump.**

Keywords - two-phase flows, gas bubble accumulation, centrifugal pump ribs, diameter of bubble, rotational speed.

I. INTRODUCTION

The transport of fluids is considered an important process in many different fields such as industry, agriculture, electricity generation [1-3], and others, many different types of pumps are used in this process, with centrifugal pumps being one of the most prominent types due to their simple manufacturing, ease of maintenance, and high performance. Centrifugal pumps are often designed to handle single-phase flows, which makes them incapable of transporting two-phase flow with the same efficiency as single-phase flows, making the transportation of two-phase fluids using them a significant challenge.

Many studies have been conducted to identify the causes of the deterioration in the performance of two-phase centrifugal pumps as a first step to improve performance. Most of these studies attributed the performance deterioration to the gas accumulation in the pump impeller, which causes flow obstruction, and high gas ratios may lead to the complete shutdown of the pump [4,5].

The completed research to improve the performance of two-phase flow centrifugal pumps focused on reducing the gas bubbles accumulation by making modifications to the pump's design that allow for the dispersion and reduction of gas accumulations [6,7].

Centrifugal pumps with ribs are considered among the promising designs for improving pump performance, as they have proven to significantly enhance performance at high gas volume fraction [8], where it has demonstrated a high capability to improve performance in high gas ratios, and it is known that the effect of two-phase flows varies according to the operating conditions of the pump. This work includes a

ISBN: 978-86-82602-07-1

detailed study of the ribs effect on the centrifugal pumps performance at low rotation speed condition, The results demonstrate a different effect of the ribs on the performance of two-phase flow centrifugal pumps at low rotating speed, according to the size of the formed gas pockets.

II. NUMERICAL METHOD

A. *Geometric Model Pump*

The pump used in this study is a centrifugal pump with a closed impeller and six blades (Fig. 1). The pump characteristics are detailed in previous work [8].

B. *Validation of Numerical Model*

The results of the numerical simulation were compared with the constructor data based on the pump head in different pump working conditions, Fig. 2. A good agreement is observed, confirming the ability of the numerical model to represent the behavior of the studied pump within the approved flow range.

III. GOVERNING EQUATIONS

Two-phase flows in centrifugal pumps are analyzed using the Euler–Lagrange Two-Fluid model. In this approach, the gas and liquid phases are treated as a heterogeneous system, where the gas exists in a dispersed state while the liquid forms a continuous phase. The fundamental equations governing this two-phase flow are as follows:

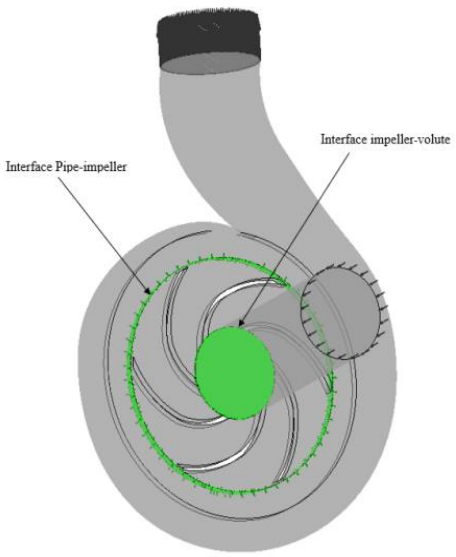

Figure 1. Original pump geometry.

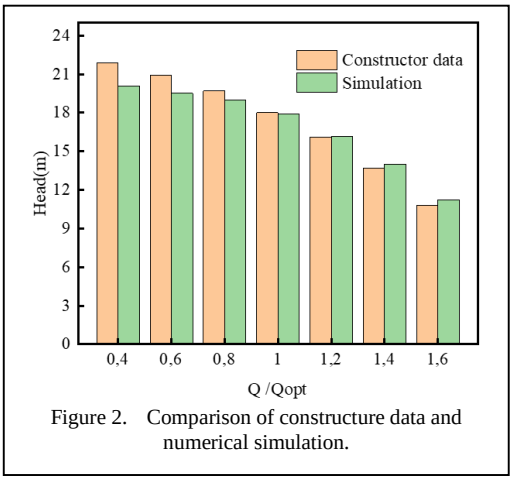

Figure 2. Comparison of constructure data and numerical simulation.

Mass conservation equation for gas:

$$\frac{\partial((1-\alpha)\rho_l)}{\partial t}+\frac{\partial((1-\alpha)\rho_l U_{li})}{\alpha x_i}=0 \quad . \quad (1)$$

The gas volume fraction is defined by:

$$\alpha=\frac{Q_g}{(Q_g+Q_l)} \quad . \quad (2)$$

Momentum equation for gas:

$$\frac{\partial(\rho_g U_{gi})}{\partial t}+\frac{\partial(\alpha\rho_g U_{gj}U_{gi})}{\partial x_i}= =-\frac{\partial p_g}{\partial x_i}+\frac{\partial r_{gij}}{\partial x_i} \quad . \quad (3)$$

Momentum equation for liquid:

$$\frac{\partial(\rho_l U_{li})}{\partial t}+\frac{\partial((1-\alpha)\rho_l U_{lj}U_{li})}{\partial x_i}= =-\frac{\partial p_l}{\partial x_i}+\frac{\partial z_{lij}}{\partial x_i} \quad , \quad (4)$$

ρ_g : density of gas,

ρ_l : density of a liquid,

τ : the shear stress tensor,

t : is time,

x : the spatial dimensions. Gravity is neglected.

1) Drag force

The total pulling force F_{DI} acting on the spherical bubbles per unit volume is as follows

$$F_{DI} = -F_{Dg} = \frac{3}{4} C_D \frac{\rho_l}{d} \alpha U_g - \\ -U_l \left| (U_g - U_l) \right| \quad . \qquad (5)$$

The drag coefficient C_D is calculated by equation Schiller-Naumann:

$$\begin{cases} C_{DF_{DI}} = \dfrac{24}{\mathrm{Re}} (1 + 0.15\,\mathrm{Re}^{0.687}) \\ C_D = 0.44 \end{cases} . \qquad (6)$$

Re: the Reynolds number:

$$\mathrm{Re} = \frac{\rho_l d \left| U_g - U_l \right|}{\mu_l} , \qquad (7)$$

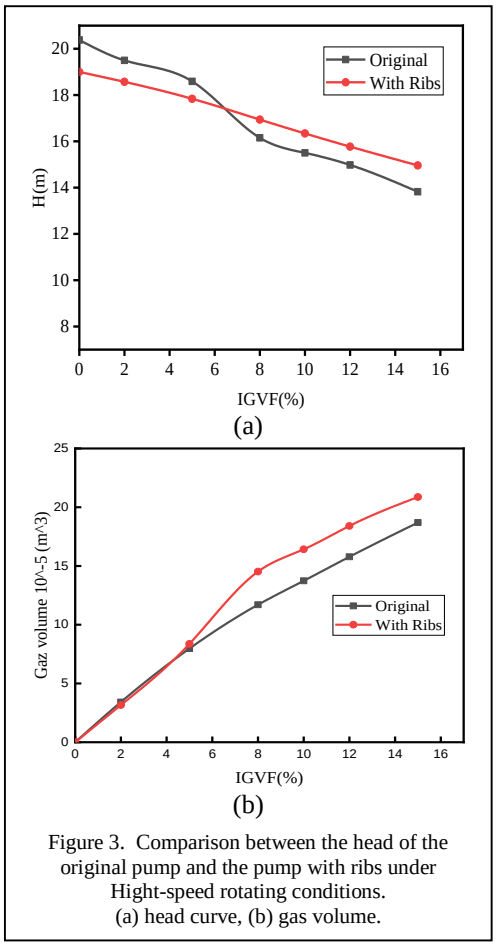

Figure 3. Comparison between the head of the original pump and the pump with ribs under Hight-speed rotating conditions.
(a) head curve, (b) gas volume.

d : bubble diameter, $\left(U_g - U\right)$: slip velocity between two phases,

μ : the dynamic viscosity of the liquid,

ρ_l : density of liquid.

Pump head calculation formula:

$$H = (1-\chi)\left[\frac{(p_2 - p_1)}{\rho G} + \frac{(U_2^2 - U_1^2)}{2G} \right]_l + \\ + \gamma \left[\frac{(p_2 - p_1)}{\rho G} + \frac{(U_2^2 - U_1^2)}{2G} \right]_g \quad . (8)$$

This relation is based on calculating the pressure and velocity differences between the pump crayon and outlet for both gaseous and liquid states.

χ : quality of the mixture in mass defined as:

$$\chi = \left[\frac{\alpha \rho_g}{\alpha \rho_g + (1-\alpha)\rho_l} \right] . \qquad (9)$$

IV. RESULTS

A. *Effect of Ribs under Hight-speed Rotating Conditions*

1) Head and gas volume

Fig. 3 illustrates the head change curves and gas volume of the original pump and the pump with ribs, two pumps under optimal flow conditions, in high-speed rotating condition, A negative impact of two-phase flows on the performance of the original pump is observed, this negative effect is maximized starting from gas volume fraction greater than 5%. This rapid and noticeable decrease in head is attributed to the formation of large gas pockets that hinder flow. By comparing the head curves of the original pump and the pump with ribs, two different effects of the ribs on pump efficiency can be distinguished. At low gas volume fraction (IGVF < 6), the ribs cause an additional deterioration in pump head due to increased hydraulic losses. At higher gas volume fraction (IGVF > 6), the ribs allow for a noticeable improvement in performance of 9%, resulting from the ribs working to disperse the gas pockets formed in the pump impeller that obstruct flow, thus allowing for smoother flow passage and improving performance.

2) Distribution of gas in pump impeller

Fig. 4 illustrates the distribution of the gas phase in the original impeller and in the modified impeller, for different inlet gas volume fraction.

For different gas fractions at the inlet. In the original impeller, gas bubbles accumulate slightly at low IGVF, but this effect intensifies with the increase in IGVF, leading to the formation of more extensive gas pockets once the gas fraction exceeds 10%. This explains the rapid drop in pump head observed at this gas fraction. Regarding the modified impeller with ribs, it is observed that these ribs allow for the dissipation of these accumulations and improve flow homogeneity. Indeed, the ribs completely disperse small gas accumulations at low IGVF, and they also facilitate the dispersion of large gas pockets at higher IGVFs, resulting in a significant improvement in pump head under these conditions.

B. Effect of Ribs under Low-speed Rotating Conditions

1) Head and gas volume

Fig. 5 shows the variations in the head and gas volume of the original pump and modified pump as a function of the IGVF, which will help to illustrate the ribs impact on the pump's performance at Low-speed rotating conditions, Three distinct stages can be identified regarding the effect of ribs on the pump head; for low gas fractions, below 2%, including single-phase, it is observed that the head with the ribs is lower than for the original case, due to the losses they cause without dampening the behavior. For IGVF between 2% and 5%, the head curves of the two pumps become indistinguishable. The losses caused by the ribs are offset by gains in the two-phase flow without improving performance. Unlike the previous cases, the ribs allow a significant improvement in the head for the modified pump at gas fractions greater than 5%. This is explained by the fact that the ribs generate secondary flows that promote the dispersion of gas pockets that hinder the flow, thereby remedying the behavior of the liquid-gas mixture and contributing to the improvement the head of the pump with ribs.

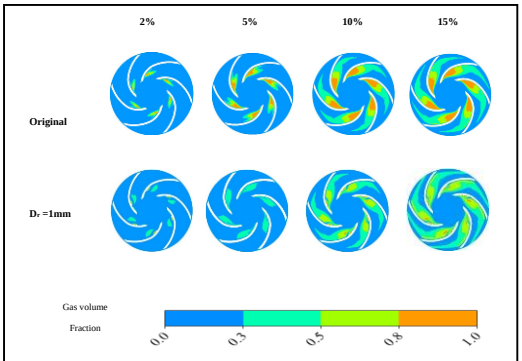

Figure 4. Gas phase distribution in the impeller of the original pump and the pump with ribs under Hight-speed rotating conditions.

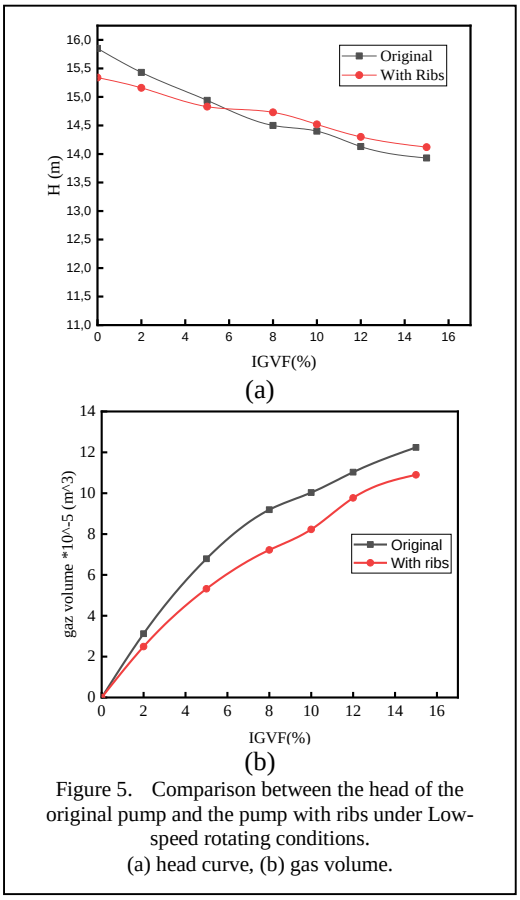

Figure 5. Comparison between the head of the original pump and the pump with ribs under Low-speed rotating conditions.
(a) head curve, (b) gas volume.

2) Distribution of gas in pump impeller

For understand the effect of the ribs on the gas distribution in the pump impeller, a comparative study of the gas phase distribution was conducted between the original case and the pumps modified, depending on the IGVF. Fig. 6 clearly illustrates the gas phase distribution in the impeller in both arrangements, it follows that the accumulation of gas in the original impeller increases with the increase in the IGVF, with the obvious formation of large gas pockets from IGVF above 5%. These reach considerable volumes at high IGVF and occupy a large portion of the internal impeller channels, hindering

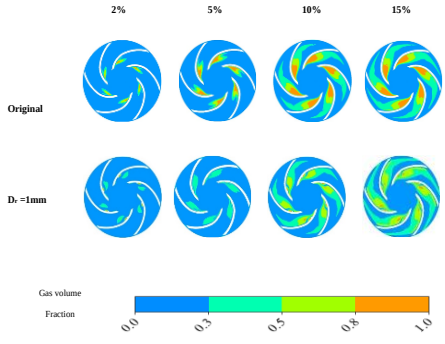

Figure 6. Gas phase distribution in the impeller of the original pump and the pump with ribs under Low-speed rotating.

liquid flow and thus penalizing performance. The ribs allow for the dispersion of these pockets, and this is visible even at low IGVF, thus providing a larger passage area for liquid flow in the impeller. The effect of the ribs is particularly significant and marked for high GVF, above 5%, due to the large size of the formed pockets, which secondary flows generated by the ribs help to disperse, thereby greatly improving the pump's performance.

V. CONCLUSION

The study of pump with ribs has demonstrated the important role they play in enhancing centrifugal pumps performance under two-phase flow (gas-liquid). Under pump operating conditions with gas ratios greater than 5%, the modified pump with ribs showed a significant improvement in hydraulic performance. The efficiency increased by about 9% at high rotational speeds, and the improvement rate was around 4% at low speeds. This improvement is primarily attributed to the better distribution of gas and the reduction of gas bubble accumulation near the impeller, which limits the phenomenon of flow blockage.

REFERENCES

[1] Amoresano, A., Langella, G., Niola, V., & Quaremba, G. (2014). Advanced image analysis of two-phase flow inside a centrifugal pump. *Advances in Mechanical Engineering*, *6*, 1-10. https://doi.org/10.1155/2014/958320

[2] Atif, A., & Senouci, S. (2019). Numerical analysis of performance deterioration of a centrifugal pump operating in two-phase flows. *Journal of Applied Fluid Mechanics*, *12*(4), 1203-1211. https://doi.org/10.29252/jafm.12.04.29477

[3] Si, Q., Bois, G., Zhang, K., & Yuan, J. (2017). Air-water two-phase flow experimental and numerical analysis in a centrifugal pump. In *Proceedings of the 12th European Conference on Turbomachinery Fluid Dynamics & Thermodynamics*. https://doi.org/10.29008/etc2017-054

[4] Mansour, M., & Thévenin, D. (2023). State of the art on two-phase non-miscible liquid/gas flow transport analysis in radial centrifugal pumps Part B: Review of experimental investigations. *International Journal of Turbomachinery, Propulsion and Power*, *8*(4), 42. https://doi.org/10.3390/ijtpp8040042

[5] Minemura, K., & Murakami, M. (1980). A theoretical study on air bubble motion in a centrifugal pump impeller. *Journal of Fluids Engineering*, *102*(4), 446-453. https://doi.org/10.1115/1.3240721

[6] Luo, X., Xie, H., Feng, J., Ge, Z., & Zhu, G. (2022). Influence of the balance hole on the performance of a gas–liquid two–phase centrifugal pump. *Ocean Engineering*, *244*, 110316. https://doi.org/10.1016/j.oceaneng.2021.110316

[7] Mansour, M., Parikh, T., Engel, S., Wunderlich, B., & Thévenin, D. (2019). Investigation on the influence of an inducer on the transport of single and two-phase air-water flows by centrifugal pumps. In *Proceedings of the 48th Turbomachinery and 35th Pump Symposia*. Houston, Texas. https://doi.org/10.1016/j.expthermflusci.2018.08.018

[8] Toumi, B., Atif, A., & Bennaceur, M. A. (2024). Enhanced Impeller Gas-Liquid Flow Using Ribs for High Performance of Centrifugal Pump. *International Journal of Computational Fluid Dynamics*, *38*(4), 316-327. https://doi.org/10.1080/10618562.2024.2421018

eNergetics 2025
DOI: https://doi.org/10.5281/zenodo.18620884

Original Scientific Article

Mathematical Optimization of an Indium Tin Oxide and Silver Solar Radiation Optical Filter for Silicon Solar Cells

Lucas Medeiros de França[1], Philippe Pereira Moreira[2], José Felix da Silva Neto[3], Kelly Cristiane Gomes[4]

[1,2]Postgraduate Program in Renewable Energy, Federal University of Paraíba, João Pessoa, Brazil
[3,4]Department of Renewable Energy Engineering, Federal University of Paraíba, João Pessoa, Brazil

[1]lucas.franca@alumni.cear.ufpb.br, [2]philippe.moreira@alumni.cear.ufpb.br, [3]josefelix@cear.ufpb.br, [4]gomes@cear.ufpb.br

Abstract—**This work relates mathematical models of optical properties with computational simulations to improve thin films reported in the literature as potential materials for reducing the operating temperature of solar cells, thereby enhancing their energy conversion efficiency. The studied structures were multilayer optical filters composed of dielectrics and metals, with indium tin oxide (ITO) and silver (Ag) standing out. These materials interact with solar radiation so that wavelengths up to 1100 nm are transmitted for conversion into electrical energy, while most of the infrared radiation (above 1100 nm) is reflected, thus reducing heating by thermal radiation. The combination yielding the best results consists of five alternating layers of ITO and Ag (ITO/Ag/ITO/Ag/ITO), achieving 83.65% transmittance in the visible range and 87.19% reflectance for wavelengths above 1100 nm, thereby blocking approximately 15% of the solar radiation that would not contribute to the photovoltaic effect and would otherwise generate heat.**

Keywords - optical filter, thin film, ITO, Ag, solar cells.

I. INTRODUCTION

Solar energy is gaining prominence as a clean and renewable source in the global energy transition due to its ease of implementation, from micro-scale systems to large-scale power plants. However, it still faces some challenges intrinsically related to main semiconductor for energy conversion, silicon, such as efficiency losses at higher operating temperatures, as demonstrated by [1].

Although other technologies are emerging, crystalline silicon photovoltaic modules represent more than 90% of the current market, and projections indicate that their manufacturing will remain dominant for several years as the main material for photovoltaic cells [2].

Therefore, some solutions are being studied to minimize heating during operation, such as the use of thin films to improve the efficiency of photovoltaic modules. Thin films can be designed to interact with solar radiation so that part of it is transmitted and part is reflected, known as optical filters. Thus, for silicon, only the radiation that contributes to the photovoltaic effect – below 1100 nm (based on its 1.1 eV bandgap) [1,2] – should be transmitted to the solar cell, while radiation above 1100 nm should be reflected to minimize heating.

Infrared (IR) radiation has a longer wavelength than visible light and is easily absorbed by materials; the absorbed light energy is then converted into heat [3]. According to [4] and Fig. 1, can be deduced that infrared represents about 77% of the wavelength range and 42% of the incident power on the photovoltaic module. Considering 1100 nm as

ISBN: 978-86-82602-07-1

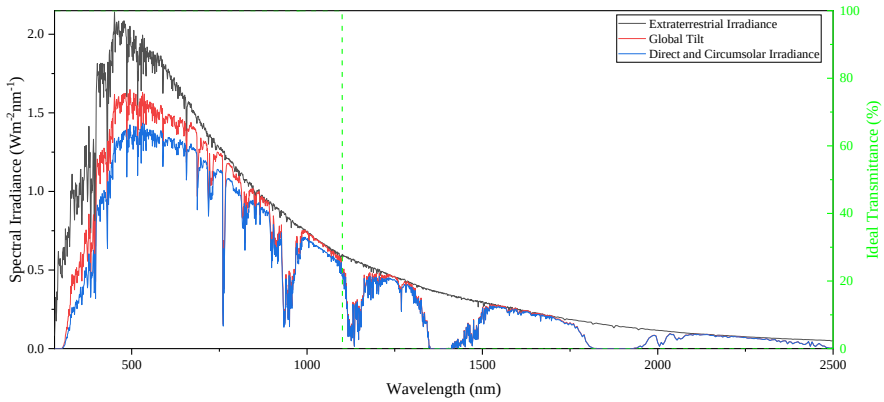

Figure 1. Adapted of reference solar spectral irradiance at air mass 1.5 [5].

the absorption limit for silicon, approximately 37% of the wavelengths do not contribute to the photovoltaic effect, resulting in approximately 17% of the total power loss within the 1100–2500 nm spectral range.

Other losses in relation to the theoretical absorption limit of silicon are explained by [4], where 52% of the total energy is lost through thermalization and non-absorption. Compared to commercial photovoltaic cells, the efficiency reaches approximately 26%, approaching the practical limit for these devices [2].

In this context, an alternative that has gained attention for mitigating the IR radiation issue involves the use of multilayer thin film composed of dielectric and metallic layers [6-9]. However, [6] emphasize that achieving the desired infrared reflectance and visible transparency according to the wavelength cut-off requirements around 1100 nm remains a significant challenge.

Of the materials employed as dielectric and metallic components, indium tin oxide (ITO) and silver (Ag) are particularly notable, respectively. When used as a single layer, ITO cannot block light in the IR range [6]. To preserve highlight transmittance in the desired spectral range, Ag layers should not exceed 10 nm in thickness [7,10,11].

Thus, this work aims to mathematically investigate multilayers optical filters of ITO and Ag to optimize the configurations reported in the literature through simulations of their optical properties and interaction with solar radiation, with the goal of approximating the behavior of these thin films to that of an ideal optical filter, as illustrated in Fig. 1.

II. MATHEMATICAL MODEL

According to [12], light interacts with matter in several different ways, with the most common effects being reflection, transmission, and propagation. The process of light propagation through a medium is complex and can include absorption and transmission of light, as well as refracting, as shown in Fig. 2.

According to [12], Beer's Law allows the transmission and reflection properties of surfaces to be related as follows:

$$T = \frac{(1-R_1)(1-R_2)e^{-\alpha l}}{1-R_1R_2^{-2\alpha l}}, \qquad (1)$$

where R_1 and R_2 are the reflectivity of the front and back surfaces of the incident light, respectively, α is the absorption coefficient, and l is the optical path length within the medium. The terms with Ri influence the transmission of the front and back surfaces, while the exponential indicates the decrease in intensity due to absorption, according to Beer's law [12]. For transparent media, the absorption coefficient tends to zero and the exponential value tends to 1, leaving only the terms $(1-R_i)$ and $1-R_1R_2$.

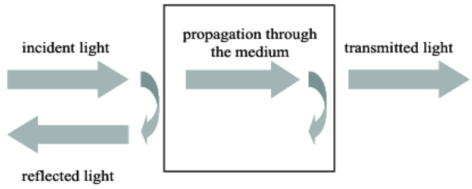

Figure 2. Reflection, propagation, and transmission of a light beam incident on an optical medium [12].

However, in the process of material prospecting, optical properties are usually estimated based on intrinsic parameters such as the refractive index and absorption coefficient. The absorption and refraction of a medium can be described by a single quantity called the complex refractive index [12]:

$$\tilde{n} = n + ik, \tag{2}$$

where the real part is the refractive index (n) and the imaginary part is the extinction coefficient (k), which is strongly related to the absorption of the medium in which the light propagates. According to [12], in transparent materials, the absorption coefficient is very small, with the extinction coefficient approaching zero.

When it comes to thin films, the interaction of electromagnetic radiation can differ significantly from that observed macroscopically. Therefore, several authors have explored the mathematical modeling of the optical properties of these materials at the nanometric scale to estimate the values of reflectivity, transmissivity and absorptivity.

Reference [13] employed the [14] reflectance model, based on Fresnel coefficients, using the characteristic matrix method for homogeneous and isotropic thin films developed by [15] in which each film layer is represented by a characteristic matrix. Later, [16] demonstrated the influence of the substrate on which the thin film is deposited by combining the [14] and [15] models with Euler parameters, obtaining the complex reflectance amplitude coefficient, $r(\lambda)$:

$$r(\lambda) = \frac{\tilde{n}_0 - \Upsilon}{\tilde{n}_0 + \Upsilon}, \tag{3}$$

where $\tilde{n}_0$ is the complex refractive index of air and Υ is the result of multiplying the m characteristic matrices of the n layers of the thin film and the substrate. Reference [13] explains that $r(\lambda)$ is a complex number, and to obtain the reflectance percentage, $r(\lambda)$ must be multiplied by its complex conjugate, denoted as $r(\lambda)^*$:

$$R(\lambda) = r(\lambda) r(\lambda)^*. \tag{4}$$

This same analogy can be applied to the transmittance of a thin film, considering that, as the absorption is very small or tends to zero, the imaginary part of the complex refractive index also approaches zero. Therefore, the transmission amplitude coefficient can be related to the refractive indices of the incident medium (n_{inc}) and the external medium (n_{ext}) after transmission and refraction:

$$T(\lambda) = \left(\frac{n_{inc}}{n_{ext}} \right) t(\lambda) t(\lambda)^*. \tag{5}$$

Currently, mathematical modeling software integrates these equations and allows for the optimization or refinement of layer configurations and thicknesses to achieve improved values for the desired optical properties.

This is done through least-squares approximations Eq. (6) between the values obtained from an initial design and the target values of the desired properties. An example is OpenFilters, which employs the modeling approach developed by [17].

$$\chi^2 = \sum_{i=1}^{m} \left(\frac{B_i - B_{i,target}}{\Delta B_i} \right), \tag{6}$$

where χ is the value of approximation, B_i is the property of interest, $B_{i,target}$ is the target value of the property of interest, ΔB_i is the tolerance for that property, in *m* targets.

Based on the mathematical simulations, the values of the spectral transmittance and reflectance coefficients obtained will be applied in the equations below to calculate the average transmittances (T) and reflectance (R) for the different desired regions of the solar spectral irradiance, respectively:

$$T = \int_{380}^{750} \frac{\tau(\lambda) I_{solar} d\lambda}{I_{solar} d\lambda}, \tag{7}$$

$$T = \int_{1100}^{2500} \frac{\rho(\lambda) I_{solar} d\lambda}{I_{solar} d\lambda}, \tag{8}$$

where I_{solar} is the spectral solar irradiance, $\tau(\lambda)$ is the spectral transmissivity coefficient, $\rho(\lambda)$ is the spectral reflectivity, and λ is the wavelength.

III. Methodological Procedures

The literature extensively reports the use of dielectric/metal/dielectric (DMD) multilayers [7-11,18]. However, these optical filters exhibit good transmission in the desired visible region, but the infrared reflectance does not reach significant values.

References [3] and [6] demonstrated that the expansion to DMDMD multilayers improves the optical properties in the desired regions of the solar spectrum, maintaining good solar radiation transmission in the visible range and considerably increasing the infrared reflectance.

Based on this, optical filters were simulated in OpenFilters to evaluate the optical properties with 3 and 5 layers, as well as to implement the least-squares optimization tool to refine the layer thicknesses to improve transmission and reflection properties at different wavelengths.

To use the software, the refractive index and extinction coefficient of the materials are required. The OpenFilters library already contains data for Ag, while for ITO, values from [19] were used, who determined n and k for a 110 nm ITO thin film deposited on a glass substrate.

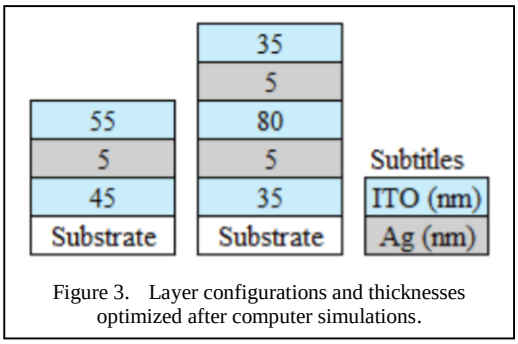

Figure 3. Layer configurations and thicknesses optimized after computer simulations.

The literature reports ideal thicknesses of up to 50 nm for ITO and 10 nm for Ag, so simulations were initiated with ITO/Ag/ITO (IAI) and ITO/Ag/ITO/Ag/ITO (IAIAI) structures using these thicknesses in their respective positions. Then, target values of 95% transmissivity were idealized between the regions with the highest solar radiation power for silicon photovoltaic conversion (from 350 to 900 nm), with a 5% margin for thickness optimization. Similarly, values of 10% transmissivity were idealized from 1100 nm to 2500 nm, with the same 5% margin for optimization. After optimization, the transmissivity and reflectivity coefficients were applied in Eqs. (7) and (8) to determine the average values in the desired wavelength region.

IV. Results and Discussions

The simulations conducted with layer thickness optimization showed minor differences compared to the literature; however, they improved transmittance in the visible range,

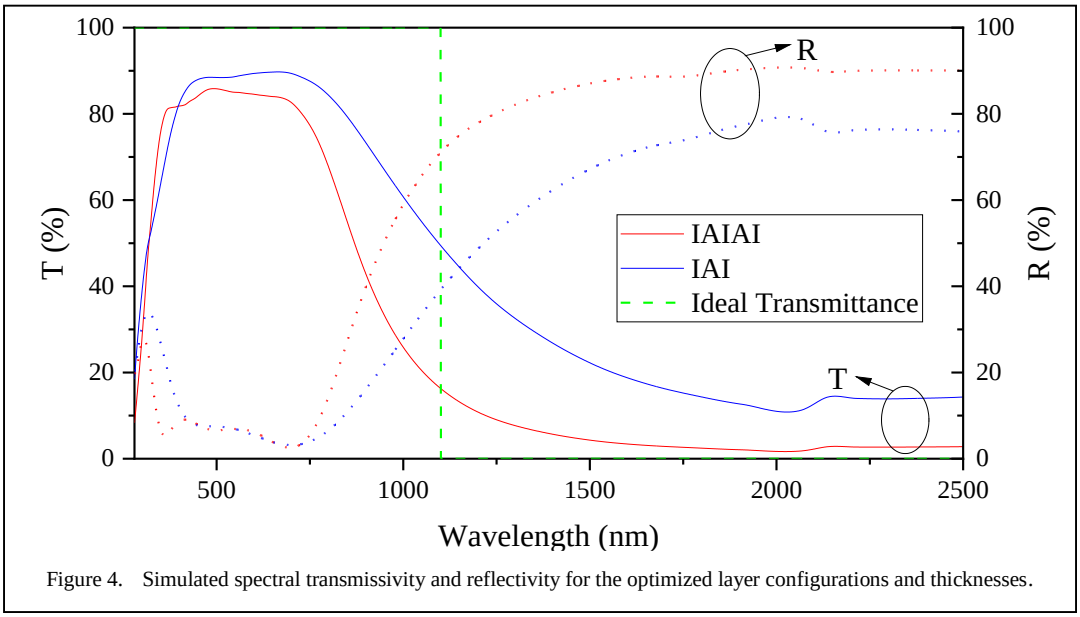

Figure 4. Simulated spectral transmissivity and reflectivity for the optimized layer configurations and thicknesses.

which was observed mainly as peaks around specific wavelengths.

For the IAI thin films, the optimized ITO thickness varied by approximately 5 nm from the 50 nm reported in the literature, differing between the top and bottom layers, while the Ag layers tended toward an ideal thickness of 5 nm. For the IAIAI thin films, the top and bottom layers remained around 35 nm, while the central layer increased to 80 nm. For the Ag, both layers tended toward 5 nm each. The layers and thicknesses of the optimized IAI and IAIAI multilayer structures are shown in Fig. 3.

The variations in the visible transparencies of the DMD structures result from light scattering at the multiple interfaces consisting of the highly reflective Ag layer and embedding oxide layers serving as anti-reflecting layers [18]. This effect decreases slightly with the addition of an extra Ag layer, as shown in Fig. 4.

A decrease in relation to the maximum transmission values in the desired region of IAI films is observed for IAIAI, as well as a shortening of the transmitted spectral range, however, the reflectance is considerably higher for IAIAI.

The simulated IAIAI thin films achieve good attenuation near the cutoff region for silicon solar cells (approximately 700–1300 nm) compared to the attenuation of IAI films (approximately 700–2000 nm), and exhibit higher infrared reflectance in the desired region, approaching the behavior of an ideal optical filter. The average values of these properties are presented in Table I, where transmittance was evaluated in the visible range (380–750 nm), which carries a significant portion of incident energy, and in the infrared range (1100–2500 nm), which does not contribute to the photovoltaic effect in silicon.

Therefore, it can be observed that transmittances are similar in the region with the highest energy, while there is a disparity in reflectances. Thus, the optical filter that performed best after optimization was the IAIAI structure, which maintains good transmittance in the visible range and a considerably higher infrared reflectance (25.33% more). This reduces the interaction of thermal radiation with silicon, capable of decreasing approximately 150 $W \cdot m^{-2} \cdot nm^{-1}$ of the power incident on the photovoltaic module (around 15% of the total solar irradiance), mitigating the heating that reduces its efficiency.

TABLE I. TRANSMITTANCE AND REFLECTANCE VALUES FOR IAI AND IAIAI THIN FILMS IN THE DESIRED REGIONS.

Thin Film	Optical Properties	
	Transmittance (visible)	***Reflectance (1100 – 2500 nm)***
IAI	88.01%	69.57%
IAIAI	83.65%	87.19%

V. CONCLUSIONS

Based on the mathematical models and multilayer structures reported in the literature, it was possible to simulate and optimize the thicknesses of IAI and IAIAI thin films to achieve maximum transmittance in the electrical conversion region of photovoltaic modules and maximum reflectance in the infrared region, which does not contribute to energy conversion but instead reduces efficiency through heating.

As shown in Fig. 4, the IAI structure achieves higher transmittance values in the visible range but fails to maintain good performance in reflectance for wavelengths above 1100nm. The five-layer optical filter approaches the behavior of an ideal optical filter—although its transmission cutoff occurs slightly below 1100nm (starting around 800nm), it still exhibits good transparency in the visible region, where most of the energy is available, and high reflectance in the desired infrared region, above 80% for both cases. This configuration can reflect up to 150 $Wm^{-2}nm^{-1}$ of energy in the 1100–2500nm range, approximately 15% of the total incident energy that is not absorbed.

Thus, it is concluded that increasing the number of layers in the optical filter configuration did not significantly reduce transmittance and improved infrared reflectance. The optimized IAIAI configuration with layers of 35/5/80/5/35 nm achieved the best performance, with 83.65% transmittance in the visible range and 87.19% reflectance above 1100 nm.

Therefore, it is suggested that these thin films be produced and analyzed experimentally in future work to corroborate the mathematical simulations.

ACKNOWLEDGMENT

The authors express gratitude for Center for Alternative and Renewable Energy (CEAR) and the funding CAPES and FAPESQ-PB for their support during the research.

REFERENCES

[1] Ghosh, B. K., Hasanuzzman, M., Saad, I., Mohamad, K. A., Hossain, M. K. (2023). Photovoltaic technologies photo-thermal challenges: Thin active layer solar cells significance. *Optik*, 274, 170567. https://doi.org/10.1016/j.ijleo.2023.170567

[2] Cui, W., Chen, F., Li, Y., Su, X., Sun, B. (2023). Status and perspectives of transparent conductive oxide films for silicon heterojunction solar cells. *Materials Today Nano*, 22, 100329. https://doi.org/10.1016/j.mtnano.2023.100329

[3] Ju Youngwoong, et al. (2023). Design and Application of ITO/Ag/ITO/Ag/ITO Multilayer Structure with Effective Control of Electromagnetic Wave Function. *Journal of the Korean Solar Energy Society*, *43*(6), 97-106. https://doi:10.7836/kses.2023.43.6.097

[4] Altınkök, S., & Altınkök, A. (2024). Photovoltaic Thermal PV/T Solar Panels and Practical Applications. *Karadeniz Fen Bilimleri Dergisi*, *14*(2), 683-699. https://doi.org/10.31466/kfbd.1425077

[5] National Renewable Energy laboratory – NREL (2025). *Reference Air Mass 1.5 Spectra*. Available at: https://www.nrel.gov/grid/solar-resource/spectra-am1.5

[6] Choi, C, et al. (2024). Light-Wavelength-Selective Transparent ITO/Ag/ITO/Ag/ITO Structure for Functional Energy Applications. *Solar RRL*. 8, 2300936. https://doi.org/10.1002/solr.202300936.

[7] Chen, D., et al. (2022). ITO/Ag/ITO and ITO/Cu/ITO transparent rear contacts for semi-transparent perovskite solar cells. *Thin Solid Films*, 752, 139252. https://doi.org/10.1016/j.tsf.2022.139252

[8] Lee, S. Y., Cho, E.-S., Kwon, S. J. (2019). The optical analyses of the multilayer transparent electrode and the formation of ITO/Mesh-Ag/ITO multilayers for enhancing an optical transmittance. *Applied Surface Science*, 487, 990–999. https://doi.org/10.1016/j.apsusc.2019.05.106

[9] Ghasemi, H., Mozaffari, M. H., Moradian, R., Nader Ghobadi. (2022). Optical and electrical properties of ITO/Metal/NiO triple-layer grown by PVD method: An experimental study. *Materials Science in Semiconductor Processing*, 149, 106853–106853. https://doi.org/10.1016/j.mssp.2022.106853

[10] Ferhati, H., Djeffal, F. (2020). Performance assessment of TCO/metal/TCO multilayer transparent electrodes: from design concept to optimization. *Journal of Computational Electronics*, *19*(2), 815–824. https://doi.org/10.1007/s10825-020-01459-9

[11] Wang, H., et al. (2021). Influence of Ag incorporation on the structural, optical and electrical properties of ITO/Ag/ITO multilayers for inorganic all-solid-state electrochromic devices. *Ceramics International*, *47*(6), 7666–7673. https://doi.org/10.1016/j.ceramint.2020.11.109

[12] Fox, M. (2010). *Optical properties of solids*. Oxford University Press.

[13] Sousa, G. C. P., et al. (2024). Mathematical modeling study to optimize the production of molybdenum and silica absorbing thin films. *Solar Energy*, *282*, 112962. https://doi.org/10.1016/j.solener.2024.112962

[14] Heavens, O. S. (1991). *Optical properties of thin solid films*. New York Dover Publ.

[15] Abelès, F. (1957). Optical Properties of Thin Absorbing Films. *Journal of the Optical Society of America*, *47*(6), 473. https://doi.org/10.1364/josa.47.000473

[16] Macleod, H. A. (2010). *Thin-film optical filters*. Taylor & Francis.

[17] Larouche, S., Martinu, L. (2008). OpenFilters: open-source software for the design, optimization, and synthesis of optical filters. *Applied Optics*, *47*(13), C219. https://doi.org/10.1364/ao.47.00c219

[18] Vo, T. T. B., Choi, D. (2023). Zinc oxide and indium tin oxide as embedding layers for ultrathin-silver-based transparent electrodes: A comparative study. *Thin Solid Films*, *777*, 139909. https://doi.org/10.1016/j.tsf.2023.139909

[19] Minenkov, A. et al. (2024). Monitoring the Electrochemical Failure of Indium Tin Oxide Electrodes via Operando Ellipsometry Complemented by Electron Microscopy and Spectroscopy. *ACS Applied Materials & Interfaces*, *16*(7), 9517–9531. https://doi.org/10.1021/acsami.3c17923

eNergetics 2025
DOI: https://doi.org/10.5281/zenodo.18620938

Original Scientific Article

Process Intensification for Levulinic Acid Production in Wine Residue based Biorefineries for Sustainable Biofuels

Carlos Eduardo Guzmán Martínez[1], Sergio Iván Martínez Guido[2], Claudia Gutiérrez Antonio[3]

[1,2,3]Universidad Autónoma de Querétaro, Querétaro, Mexico

[1]dciqcarlos@gmail.com, [2]claugtez@gmail.com

Abstract—**The wine industry generates a large amount of wastewater that is highly polluting per liter of wine produced. The lack of proper treatment has become a major social, environmental, and public health concern. However, this effluent contains carbohydrates and alcohols that can be used as raw materials to produce value-added products of potential interest to wine producers. Therefore, this research presents a simulation study aimed at evaluating the valorization of winery effluents for the production of biofuels and high-value chemicals using a biorefinery approach. Furthermore, process intensification techniques are applied to propose process configurations capable of achieving significant energy savings. As part of the methodology, a case study is defined, followed by the design and simulation of the process in Aspen Plus V11. The intensification of the process is then carried out using the Rong and Errico methodology to obtain intensified configurations. Finally, the technical feasibility is assessed based on the reduction of Chemical Oxygen Demand (COD). As a result, the biorefinery produces levulinic acid, biojet fuel, green diesel, naphtha, light gases, glycols, and bioethanol. Additionally, the biorefinery achieves an almost complete reduction of COD in the effluent. Moreover, the process intensification of the levulinic acid production section leads to a significant decrease in both energy demand and the number of equipment units required.**

Keywords - process intensification, aspen plus, winery effluent, valorization.

I. INTRODUCTION

The wine industry, a significant player in the agroindustrial sector, is also a major contributor to wastewater generation, second only to the paper industry [1]. This alarming statistic underscores the urgent need for effective waste management strategies. Approximately the ratio is 2-4 liters of wastewater per liter of wine produced [2].

México is the 32nd producer in the world ranking [3], producing 396 000 hectoliters in 2022 [3]. According to "Consejo Mexicano Vitivinícola," the Mexican state of Baja California has 80% of the wine national production [4].

If the wine wastewater is characterized, as well as all its solid waste, a high organic load is identified [1], consisting mainly of carbohydrates, alcohols, and acids, as well as polyphenols, tannins, melanoidins, and lignin. The effluents can be used as fertilizer due to their particularities; however, their direct spread into the environment can contaminate soils and bodies of water precisely due to this high organic load, which could become toxic under certain conditions.

On the other hand, phenols and polyphenols negatively affect microorganisms and plants at the final disposal sites of wine effluents. This is because they are considered phytotoxic, antimicrobial, and recalcitrant. The components that provide color to wine prevent sunlight from

ISBN: 978-86-82602-07-1

penetrating rivers and lakes. In this way, photosynthetic activity and dissolved oxygen concentration in the water are reduced, causing dangerous conditions for aquatic life. High organic content can also cause problems in surface waters through increased nutrients. This increase can lead the ecosystem to undesirable structural and functional changes, including foul odors and generated putrefaction. As if that were not enough, inhibition of seed germination, reduction in soil alkalinity, and lower availability of magnesium have been reported due to the use of wine wastewater in agriculture [1]. An indicator to quantify the quality of effluents is the Chemical Oxygen Demand (COD), which estimates the extent of chemical oxidation and represents the degrees of organic contamination [5].

Valorization is the process of remediation or treatment of waste coupled with the recovery or production of high-value compounds. In other words, it is the process of generating new products using waste as raw material. This will reduce costs, reduce the negative environmental impact, and supply a need in the market.

The valorization of wine effluents has been focused on producing biodiesel, enzymes, biogas, biomass, and organic materials. Some examples are the works presented by Buitrón G. (2019) [2], who propose the application of a two-stage process (acidogenic and methanogenic) through a reactor scheme for the treatment of the organic matter present in the vinasses. With this, the objective is the generation of biogas. [6] used vinasses as a substrate for a submerged fermentation of Pseudomona Aeruginosa to produce a biosurfactant.

The National Renewable Energy Laboratory identifies 12 essential chemical compounds (value-added products that can be produced from sugars through biological or chemical conversions. Among these compounds is levulinic acid. This component presents enormous economic potential because it is a raw material of various industrially important chemicals, such as methyl-tetrahydrofuran [7]. Besides, levulinic acid is a value-added product used in producing nylon, synthetic rubbers, plastics, and pharmaceuticals.

Process intensification is a strategy for dramatically reducing the size of a chemical plant at a given production volume. In addition, it has also been claimed to bring other benefits, such as reduced energy consumption, lower capital costs, improved product quality, and increased safety. One central approach in process intensification is to reduce the number of equipment units by innovatively designing multifunctional equipment, which reduces investment costs and significant energy savings [8].

Distillation has been the separation method and central pillar in many process industries. In transitioning from fossil-based feedstocks to biomass-based feedstocks manufacturing, distillation is an essential separation method in many new process industries, including bioethanol, biodiesel, and many other high-value products [9].

Due to the intrinsic characteristics of distillation separations, efforts to improve distillation technology are focused on reducing energy consumption and, on the other hand, reducing equipment costs [9].

Process intensification is another crucial component in promoting sustainability; this strategy allows for a drastic reduction in the size of a chemical plant for a given production volume. In addition, process intensification provides other benefits, such as lower energy consumption, reduced capital costs, and enhanced safety [9]. Therefore, the aim of this research is to develop and intensify a section of the levulinic acid production process within a biorefinery of wine effluents valorization.

II. METHODOLOGY

The research is developed by implementing the following subsequent steps:

- Define the case study. This first step describes the effluent flow and its composition. Due to the lack of a supply chain development in the research, the mass flow must be fixed according to the region with the primary wine production in Mexico.
- Develop a conceptual design for biorefinery. It defines what kind of products can be produced according to the raw materials content of winery effluent. In this sense, determining the unit operations that will be part of the upstream, reaction, and downstream sections to achieve the desired products is essential.

- Collect thermodynamic and chemical kinetic data. It is essential to validate process modeling by employing experimental data; therefore, thermodynamic and chemical kinetic data reported in the literature must be compiled.
- Simulate the conventional scheme in Aspen Plus. The conceptual design is modeled and simulated in the Aspen Plus ® V11 software at a steady state. Manipulated variables are selected according to each unit operation, and the model is resolved using rigorous methods.

It is essential to mention that traditional distillation towers and reactors constitute the conventional scheme.

- Define manipulable variable values by using parametric analysis. It consists of conducting a sensitivity analysis when the simulation base is completed. The manipulable variable is moved inside a defined range to determine the values that maximize the mass yield and purities of the products.
- Implement Rong and Errico's methodology [9] to develop an intensified scheme. The intensified scheme is defined as a biorefinery that changes traditional distillation columns for configurations that can share condensers and reboilers among themselves; therefore, they could achieve a decrease in energy consumption. Besides, an intensified scheme could eliminate some towers without decreasing the product quantity and quality reached by the conventional scheme. In other words, it means "to do the same" with lower equipment and energy.

It is important to highlight that process intensification can be employed in the entire process or only in a specific process section.

The schematic methodology can be summarized as next [9]:

Step 1. Create the subspace of simple column configurations (SC).

Step 2. Select the simple column configuration with less energy consumption from the previous subspace.

Step 3. Generate the original thermally coupled configurations (OTC), systematically replacing reboilers or condensers, and select the OTC with less energy consumption.

Step 4. Generate the thermodynamically equivalent structures (TES) from OTCs using the section rearrangement methodology.

Step 5. Identify the TESs that contain columns with a unique lateral transport section, keeping the structure of simple columns; then, the TES with less energy consumption is selected.

Step 6. The intensified configurations (ISC) are generated by eliminating the lateral transport section in the identified TES.

Step 7. Repeat these steps if you do not select the structure with less energy consumption in Steps 2–6 until all simple column configurations have been examined.

Step 8. Summarize all the ISC configurations.

- Evaluate and compare the technical feasibility of each scheme. The main objective of the technical evaluation is to measure the biorefinery's capacity to remove the contaminant using the Chemical Oxygen Demand (COD) indicator calculated by Aspen Plus. This procedure calculates the difference between the feed stream COD and the water COD at the end of the water purification section.

In addition, reboiler duties are used to determine which scheme achieves the best energy savings.

It is important to highlight that this research does not include economic evaluation.

Fig. 1 shows the block diagram that represents the methodology mentioned above.

III. RESULTS

As the study case, the wastewater generated in a year by the wine industry in Baja, California, Mexico, is considered because this Mexican State generates 80% of national production [3,4]. Table I shows the study case's effluent

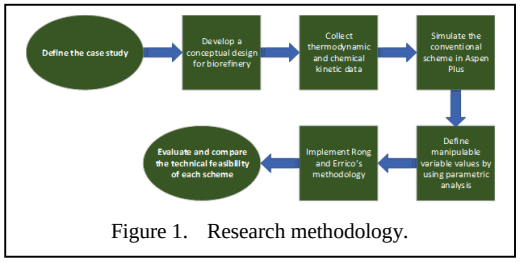

Figure 1. Research methodology.

characterization and mass flow, according to Buitron et al. (2019) [2].

The Fig. 2 represents the block diagram of biorefinery developed. It is important to mention that both conventional and intensified structures follow the same general scheme; however, the unique difference located in the section of levulinic acid production.

The liquid-solid separation stage consists of decantation and centrifugation operations. The objective of this section is to remove solids, which can block the perforations of the trays in the distillation columns. Due to their high moisture content, solids (also known as sludge) are outside the object of study due to the high thermal load their drying represents.

The most abundant carbohydrate in grapes is glucose; Therefore, the strategy used is the one reported by Solis J. (2022) [7], in which aldose, through a homogeneous catalytic process, is decomposed into 5-Hydroxymethylfurfural (5-HMF), (1). Subsequently, the 5-HMF molecule reacts with water to form levulinic and formic acids (2). The levulinic acid production step receives a liquid stream of ethanol, aldose, and water as constituents. This section uses a reactive

TABLE I. FEED AND TRATED WATER STREAMS.

Parameter	Winery effluent	Treated water
Mass flow (kg/h)	10 000	4 922
% mass water	71.76	100
% mass etanol	7.39	0
% mass glucosa	5.26	0
% mass solids	15.59	0

distillation column and a conventional purification sequence. The reaction corresponds to Eqs. (1) and (2). The module implemented in this section is RadFrac.

$$C_6H_{12}O_6 \rightarrow C_6H_6O_3 + 3H_2O\,, \qquad (1)$$

$$C_6H_{12}O_3 + 2H_2O \rightarrow C_5H_8O_3 + CH_2O_2\,. \qquad (2)$$

The ethanol/water stream, the output from the levulinic acid production stage, has a concentration of 9.28 mass % and enters the water purification stage. This stage consists of a conventional distillation (Rad Frac module) where treated water is obtained at the bottom and a 34% mass ethanol-water mixture in the dome.

The ethanol dehydration stage is responsible for transforming ethanol into ethylene and water. From this stage, two streams emerge, one of ethylene and one of water. The ethylene stream is directed to the process responsible for producing Alcohol To Jet Fuel (ATJ) biofuels, and the other stream goes to a second stage of

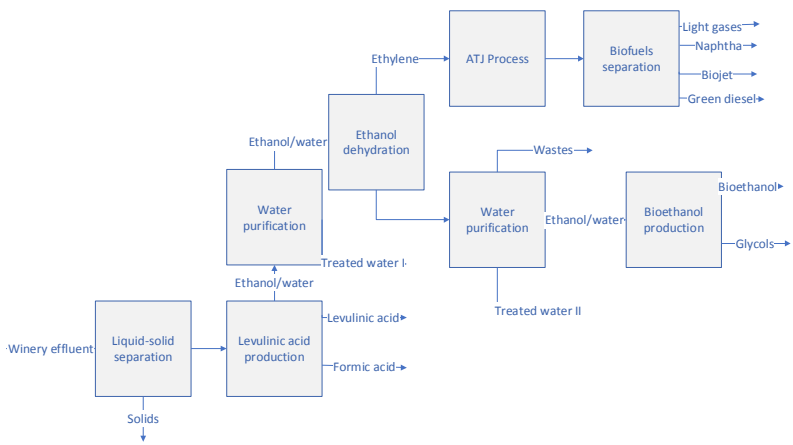

Figure 2. General biorefinery scheme.

water purification. The module used in the simulation is RStoic, with a conversion of 98% [10] for the conversion of ethanol to ethylene.

The ATJ process produces a mixture rich in hydrocarbons with chain sizes ranging from C1 (Methane) to 20-carbon chains (n - Eicosane). All hydrocarbons pass to the fuel separation section, which is made up of a set of distillation columns (Rad Frac modules) for the separation of light gases with hydrocarbons with chains of 1 to 4 carbons; naphtha that has hydrocarbons of 5 to 7 carbons; biojet composed of 8 to 16 carbons and green diesel, 17 to 20 carbons.

The residual stream from the ethanol dehydration stage contains ethylene, ethanol, water, and traces of formic acid. Two distillation columns (Rad Frac modules) separate these components, constituting the second purification section. As a result, it obtains a waste stream (made up of ethylene and formic acid), an 87.2% mass ethanol-water mixture (used in the subsequent stage for bioethanol production), and a second stream of refined water. The streams from both purification stages are mixed to obtain the final stream of treated water.

Finally, the bioethanol production section is formed by a reactive distillation column (Rad Frac module), fed with the ethanol-water mixture from the second water purification section. In this stage, a flow of propylene oxide enters to carry out the reactions described by Eqs. (3) and (4); propylene oxide reacts with water to produce propylene oxide, and propylene oxide reacts with propylene glycol to get dipropylene glycol. Since the reactions reported are exothermic [11], the higher the water content, the greater the energy the system releases. This opens the possibility of reducing the energy requirements in the stage and taking advantage of the heat obtained through some other system (Rankine cycles) or with energy integration.

$$C_3H_6O + H_2O \rightarrow C_3H_8O_2, \qquad (3)$$

$$C_3H_6O + C_3H_8O_2 \rightarrow C_6H_{14}O_3. \qquad (4)$$

The thermodynamic model implemented is BK10 for the biofuel separation section. For the remaining sections, NRTL is employed [12].

As shown in Table I, the effluent received contains 210.052 ppm, and 210.023 ppm is removed. This represents a 99.98% reduction. On the other hand, the value obtained is 2.48 times smaller than the strictest one indicated by NOM-001-SEMARNAT-2021, which is 72 ppm for irrigation of green areas.

In addition, one of the most important results is the recovery of 68.59% of the mass of water. It opens an outstanding possibility of helping decrease hydric stress in the Mexican State of Baja California by recirculating it for vineyard irrigation.

Table II presents the mass flows of the products obtained by valorization of the wine effluent through each biorefinery scheme.

The main products are levulinic acid, biojet, formic acid, light gases, and naphtha, representing 33.6 % mass, 14.62 % mass, 13.09 % mass, and 11.08 % mass, respectively. The percentage of high-value molecules allows significant economic leverage for biofuel production to make them attractive to investors.

The waste stream released by the second purification stage contains a small amount of ethylene. In the first instance, it is possible to assume the development of some separation process to recover and recirculate that hydrocarbon; However, that decision is not random. Implementing some index that helps define the feasibility of recovering the hydrocarbon in question is crucial.

The process intensification methodology is applied to the levulinic acid production section. Fig. 3 presents the detailed flowchart of the levulinic acid production process. Although the reactive distillation column (RD-01) is already considered an intensified unit, the intensification

TABLE II. PRODUCT MASS FLOW.

Product	**Mass flow (kg/h) conventional scheme**	**Mass flow (kg/h) intensified scheme**
Glycols	47.66	47.66
Levulinic acid	221.57	221.57
Bioethanol	4.56	4.56
Formic acid	96.4	96.4
Light gases (C1-C4)	86.32	96.32
Naphtha (C5-C7)	73.03	73.03
Biojet (C8-C16)	103.83	103.85
Green diesel (C17-C20)	26.03	26.03

strategy is specifically implemented on the conventional separation columns, DC-01 and DC-02.

The water–ethanol stream leaving the levulinic acid production section in Fig. 2 originates from the top of the RD-01 column shown in Fig. 3. From the bottom of this column, a stream containing a mixture of levulinic, formic, and sulfuric acids is fed to DC-01. At the top of DC-01, formic acid (FORMAC) is separated from the mixture, while the bottom stream, comprising sulfuric and levulinic acids, is directed to DC-02. In this final column, levulinic acid (LEVAC) is obtained as the top product, and sulfuric acid (SULFAC) recovered at the bottom is recycled back to RD-01.

Fig. 4 presents conventional scheme. Figs. 5 and 6 represents the OTC schemes developed and Fig. 7 shows the intensified scheme obtained. The OTC is similar to the conventional scheme, however, DC-01 lacks a reboiler. To supply the heat needed, vapor coming from DC-02, the unique tower with a reboiler, is driven to the bottom of column DC-01; and the liquid form DC-01 is directed to DC-02.

In the TES scheme, a side stream from DC-01 is sent to a second column (DC-02), which lacks a reboiler too, to obtain the levulinic acid, Fig. 6.

Finally, in ISC scheme, the DC-02 column disappears, and just by using the DC-01 is possible to get the levulinic acid by using a side stream.

As shown in Table II, the difference between the mass flow of products obtained from each scheme is negligible. However, the difference between the heat duties in reboilers and condensers is important. Table III shows the comparison between each scheme.

TABLE III. HEAT DUTIES IN THE DIFFERENT SCHEMES DEVELOPED.

	Conv.	**OTC**	**TES**	**ISC**
Condenser (kW)	-428.28	-402.02	-406.55	-414.62
Condenser relative difference	--------	6.13%	5.07%	3.19%
Reboiler (kW)	419.56	393.18	397.76	405.17
Reboiler relative difference	-------	6.29%	5.25%	3.43%

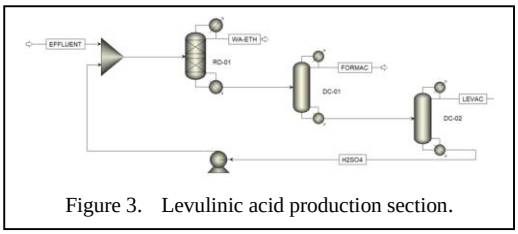

Figure 3. Levulinic acid production section.

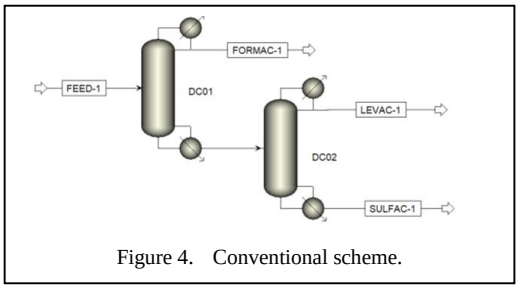

Figure 4. Conventional scheme.

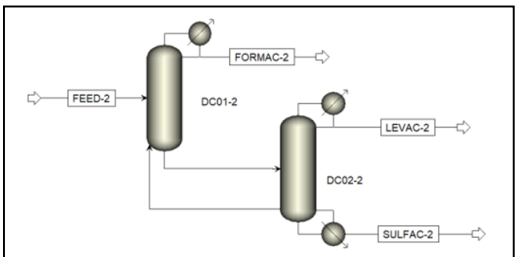

Figure 5. OTC scheme.

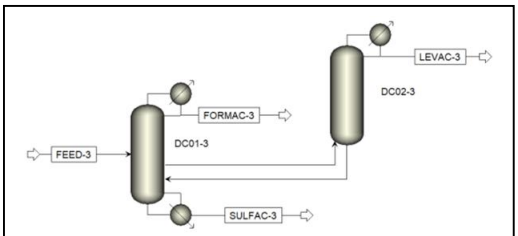

Figure 6. TES scheme.

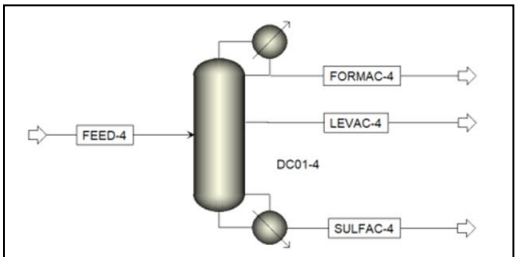

Figure 7. ISC scheme.

It is important to note that all distillation sequences presented in this work have been designed to achieve a 99 % recovery and purity of levulinic acid; in the same way, all the schemes present the same recovery of formic, and sulfuric acids.

Based on the results presented in Table III, the OTC configuration exhibits the highest energy savings; however, its advantage over the TES scheme is only about one percentage point. Therefore, this difference can be considered negligible.

Although the ISC configuration may appear to be the least favorable in terms of energy savings, it represents the best option for process intensification. This is because it not only improves energy efficiency but also reduces the number of equipment units required. Consequently, the ISC scheme lowers operational costs associated with energy consumption and decreases capital costs due to equipment reduction.

Indirect distillation configurations were not considered in this study; however, they will be taken into account in future work, as they could potentially outperform the direct schemes developed in this research.

It is important to note that the developed schemes have not been optimized; therefore, their energy-saving advantages over the conventional structure could be further improved by implementing stochastic optimization strategies.

Unfortunately, the equipment that most significantly impacts the overall energy consumption is the RD-01 column, which requires 60,365.31 kW in it reboiler. This value is reasonable considering the large amount of effluent fed into the process, particularly since water is the main component of the stream. Nevertheless, this energy demand could be reduced by implementing alternative approaches, such as pretreatment methods (e.g., membrane separation), process intensification, or heat integration techniques.

Another important point to note is that the bioethanol recovery in the biorefinery may appear to be very low (0.006 wt%). However, it should be emphasized that nearly all the ethanol is consumed in the production of ethylene.

IV. CONCLUSIONS

In this research, the technical feasibility of obtaining biofuels and value-added molecules is presented, such as levulinic acid, bioethanol, light gases, glycols, naphtha, biojet, and green diesel, through the revaluation of wine effluents using a scheme of biorefinery.

It is possible to achieve meaningful energy savings by employing process intensification techniques.

The ISC configuration is the most suitable option for the biorefinery, as it not only reduces operational costs but also decreases the number of equipment units required.

With both proposed schemes, it is feasible to obtain water with the quality required for human use by the COD reduction achieved (99.98%) and the Official Mexican Standards (NOM-001-SEMARNAT-2021 and NOM-127-SSA1-2021).

ACKNOWLEDGMENT

The authors appreciate the financial support provided by SECIHTI through the Carlos Eduardo Guzmán Martínez postdoctoral scholarship (Call: 2022 (1). Project: 2397403).

REFERENCES

[1] Ratna, S., Rastogi, S., & Kumar, R. (2021). Current trends for distillery wastewater management and its emerging applications for sustainable environment. *Journal of Environmental Management*, *290*, 112544. https://doi.org/10.1016/j.jenvman.2021.112544

[2] Buitrón, G., Martínez-Valdez, F. J., & Ojeda, F. (2019). Biogas production from a highly organic loaded winery effluent through a two-stage process. *BioEnergy Research*, *12*(3), 714-721. https://doi.org/10.1007/s12155-019-09984-7

[3] Organización Internacional de la viña y el vino. (2025). *Estadísticas de los países.* Available at: https://www.oiv.int/es/what-we-do/country-report?oiv

[4] Consejo Mexicano vitivinícola. (2025). *Producción de vino en México.* Available at: https://uvayvino.org.mx/html/docs/produccion_consumo_vino.pdf

[5] Li, J., Luo, G., He, L., Xu, J., & Lyu, J. (2018). Analytical approaches for determining chemical oxygen demand in water bodies: a review. *Critical reviews in analytical chemistry*, *48*(1), 47-65. https://doi.org/10.1080/10408347.2017.1370670

[6] Naspolini, B. F., Machado, A. C. D. O., Cravo Junior, W. B., Freire, D. M. G., & Cammarota, M. C. (2017). Bioconversion of Sugarcane Vinasse into High-Added Value Products and Energy. *BioMed research international*, *2017*(1), 8986165. https://doi.org/10.1155/2017/8986165

[7] Solis-Sanchez, J. L., Alcocer-Garcia, H., Sanchez-Ramirez, E., & Segovia-Hernandez, J. G. (2022).

Innovative reactive distillation process for levulinic acid production and purification. *Chemical Engineering Research and Design*, *183*, 28-40. https://doi.org/10.1021/acs.iecr.1c04050.s001

[8] Rong, B. G., & Turunen, I. (2006). Process intensification for systematic synthesis of new distillation systems with less than N-1 columns. In *Computer Aided Chemical Engineering* (Vol. 21, pp. 1009-1014). Elsevier. https://doi.org/10.1016/s1570-7946(06)80178-1

[9] Rong, B. G., & Errico, M. (2012). Synthesis of intensified simple column configurations for multicomponent distillations. *Chemical Engineering and Processing: Process Intensification*, *62*, 1-17. https://doi.org/10.1016/j.cep.2012.10.005

[10] Romero- Izquierdo, A. G., Gutiérrez- Antonio, C., Gómez- Castro, F. I., & Hernández, S. (2022). Synthesis and intensification of a biorefinery to produce renewable aviation fuel, biofuels, bioenergy and chemical products from Jatropha Curcas fruit. *IET Renewable Power Generation*, *16*(14), 2988-3008. https://doi.org/10.1049/rpg2.12388

[11] Guzmán-Martínez, C. E., Castro-Montoya, A. J., & Nápoles-Rivera, F. (2019). Economic and environmental comparison of bioethanol dehydration processes via simulation: reactive distillation, reactor–separator process and azeotropic distillation. *Clean Technologies and Environmental Policy*, *21*(10), 2061-2071. https://doi.org/10.1007/s10098-019-01762-5

[12] Carlson, E. C. (1996). Don't gamble with physical properties for simulations. *Chemical engineering progress*, *92*(10), 35-46. https://doi.org/10.1061/9780784479315.028

eNergetics 2025
DOI: https://doi.org/10.5281/zenodo.18621026

Original Scientific Article

HTL-Free 2D/3D Hybrid Perovskite Solar Cells: ETL Engineering and Simulation Insights

Walagedara Gamage Ayomi Pabasara[1], Galhenage Asha Sewvandi[2]

[1,2]Department of Materials Science and Engineering, University of Moratuwa, Katubedda, Sri Lanka
[1]Department of Engineering Technology, University of Ruhuna, Kamburupitiya, Sri Lanka

[1]ayomi@fot.ruh.ac.lk, [2]galhenagea@uom.lk

Abstract—**The commercialization of PSCs is hindered by instability under heat, moisture, and UV, which is mitigated by 2D/3D hybrids that combine the stability of 2D and the efficiency of 3D perovskites. Despite improvements in intrinsic material stability, conventional device architectures using hole transport layers (HTLs) still face challenges in long-term durability. In this study, we numerically investigate HTL-free carbon electrode-based 2D/3D hybrid PSCs, focusing on optimizing the 3D perovskite layer properties and evaluating different electron transport layer (ETL) materials. Devices using TiO_2, SnO_2, WS_2, and C_{60} as ETLs achieved maximum PCEs of 19.15%, 20.25%, 20.00%, and 22.26%, respectively, at optimal 3D layer thicknesses of 0.9 µm, 1.3 µm, 1.4 µm, and 1.2 µm, respectively. The performance of all devices was maximized at a bulk defect density of 10^{12} cm^{-3}. The results reveal that ETL has a significant impact on device performance in HTL-free 2D/3D hybrid PSCs. The study also highlights the critical role of the electrode work function, identifying 5.4 eV as the minimum threshold for efficient charge extraction in HTL-free 2D/3D hybrid PSCs.**

Keywords - HTL-free, carbon electrode, Perovskite solar cells, stability, SCAPS.

I. INTRODUCTION

Perovskite solar cells have garnered widespread attraction worldwide as a cutting-edge photovoltaic technology due to their higher efficiency and low-cost fabrication processes [1,2]. Over the past years, PSCs have marked rapid development due to intensive research efforts and technological advancements, leading to enhanced fundamental properties, including improved carrier mobility, light absorption, and reduced recombination losses. By 2024, the PCE has surpassed 26% revolutionizing the solar cell industry [3]. However, the PSCs still suffer from instability issues upon exposure to heat, moisture and UV radiation, which declines the performance and durability of the cell [4]. Several strategies have been suggested in the literature to enhance the stability of the PCSs, including encapsulations, additive engineering, and compositional tuning [5].

The two-dimensional form of perovskite materials demonstrates excellent environmental stability compared to their 3D counterparts [6-8]. Therefore, to leverage this advantage, 2D perovskites are incorporated into 3D perovskites to enhance stability, and the resultant architecture is known as 2D/3D mixed dimensional or hybrid PSCs [9]. This structure combines both high efficiency and superior charge transport characteristics of 3D perovskites with outstanding moisture and thermal stability of 2D perovskites, resulting in devices with both enhanced performance and long-term operational stability [10,11].

While these advances have overcome the intrinsic instability of 3D perovskites, the overall device stability can arise from the deterioration of the charge transport layers. The traditional

ISBN: 978-86-82602-07-1

device architecture of the PSCs comprises transparent conducting oxide/ETL/perovskite absorber layer/HTL/back contact electrode, which is often made from noble metals such as Au, Ag or Pt. The HTL materials are mostly made of Spiro-OMetAD which offers high efficiency; however, it is expensive and suffers from instability issues impending commercialization.

To overcome these challenges, researchers are making continuous research efforts to develop HTL-free PSCs. Carbon is used as HTL-free PSCs as a cost effective and promising alternative, serving both as a stable counter electrode and a substitution for traditional HTLs [12,13]. Carbon shows enhanced electrical conductivity, chemical stability and compatibility with large-scale fabrication techniques. However, these HTL-free devices demonstrate lower efficiency compared to the devices with HTLs and back electrodes with noble metals [14]. In particular, the photovoltaic performance of the HTL-free device heavily relies on the ETL materials as it is crucial in charge selectivity by electron extraction and blocking the holes [12]. Therefore, optimizing and selecting appropriate ETL materials with favorable energy level alignment and carrier mobility can substantially improve the device performance even the absence of HTL.

The efficiency of HTL-free PSCs based on 3D perovskites was relatively low, with early reports of around 6.6% [12,15]. Subsequent advances in compositional engineering and the application of new manufacturing methods significantly enhanced performance, leading to experimentally demonstrated efficiencies above 18% [16].

However, the feasibility of developing HTL-free, C electrode-based 2D/3D hybrid PSCs has not been systematically explored. This combination opens compelling pathways towards highly stable, cost-effective and efficient PSCs. In this research, the performance of HTL-free 2D/3D hybrid PSCs is investigated through numerical simulation, focusing on the effect of various ETL materials.

II. Device Design and Simulation

A. *Device Design*

The HTL-free carbon electrode 2D/3D hybrid PSCs were numerically simulated utilizing SCAPS 1D simulation software. Fig. 1 illustrates the device architecture of the proposed PSCs. Moreover, the AM 1.5 solar spectrum has been used for simulations. In the proposed device design, Methylammonium Lead Iodide ($MAPbI_3$) serves as the 3D perovskite material. As the 2D perovskite material, pentamethylenediamine (PeDA) based Dion Jacobson (DJ) perovskite materials (n=5) [$PeDAMA_4Pb_5I_{16}$] was selected, which has been proven to be more stable than monoamine-based Ruddlesden-Popper (RP) perovskites [17,18].

In this study, the device performance was optimized by employing four different ETL materials. C-electrode was selected as the back contact material. The thickness and defect densities of the 2D perovskite layer and the ETL layer were optimized, and those optimized parameters were adopted for simulation. Further, the effects of the thickness and defect density variation of the primary absorber layer were comprehensibly analyzed. The input parameters of each of the layers adopted from the published literature sources are mentioned in Table I. Electron and hole capture cross-section area were considered as 1×10-15 cms-1 while electron and hole thermal velocities were taken as 1×107 cm2 [12]. In this study, the SCAPS-1D simulations are conducted, assuming static ion positions, so that the impact of ion migration and respective hysteresis phenomena are not reflected.

B. *Materials Selection for ETL*

Four ETL materials were selected based on their stability and performance. TiO_2 is a commonly used ETL material in PSCs due to its optical transparency, chemical resistance, cost

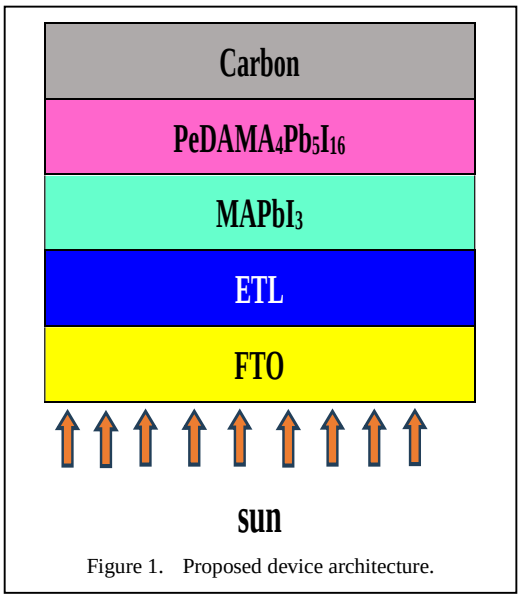

Figure 1. Proposed device architecture.

TABLE I. DETAILS OF BASIC SIMULATION PARAMETERS OF SOLAR CELL [12,17].

	$PeDAMA_4Pb_5I_{16}$ (2D)	**$MAPbI_3$ (3D)**	**TiO_2**	**SnO_2**	**WS_2**	**C_{60}**
Thickness (μm)	0.1	0.2-1.6	0.1	0.1	0.01	0.1
Band gap (eV)	1.6	1.55	3.26	4	2.38	1.7
Electron affinity (eV)	3.98	3.9	4.2	4.1	3.95	4
Dielectric permeability relative	25	3.2	38	12.5	13.6	10
VB effective density of state (states/cm^3/eV)	$7.5\cdot10^{17}$	$2.8\cdot10^{20}$	$2.2\cdot10^{17}$	$2.2\cdot10^{18}$	$1\cdot10^{18}$	$8\cdot10^{19}$
CB effective density of state (states/cm^3/eV)	$1.8\cdot10^{18}$	$3.9\cdot10^{20}$	$1.8\cdot10^{18}$	$1.8\cdot10^{19}$	$2.4\cdot10^{19}$	$8\cdot10^{19}$
Hole mobility (cm^2/Vs)	1.4	11.8	$2\cdot10^{4}$	100	100	$8\cdot10^{-2}$
Electron mobility (cm^2/Vs)	0.3	11.8	$1\cdot10^{3}$	25	100	$3.5\cdot10^{-6}$
Shallow uniform donor density (cm^{-3})	0	$1\cdot10^{9}$	$6\cdot10^{19}$	$5.9\cdot10^{19}$	$1\cdot10^{18}$	$1.0\cdot10^{21}$
Shallow uniform acceptor density (cm^{-3})	0	$1\cdot10^{9}$	0	0	0	0
Defect density	$2.4\cdot10^{14}$	$1\cdot10^{10}$-$1\cdot10^{16}$	$1\cdot10^{12}$	$1\cdot10^{12}$	$1\cdot10^{12}$	$1\cdot10^{12}$

effectiveness and ease of fabrication [19,20]. SnO_2 has shown excellent electron extraction, chemical stability, UV resistance and low temperature processing, making it a suitable candidate for ETL [21,22]. WS_2 is an abundant, nontoxic, low-cost, transparent material with enhanced carrier mobility and stability [23,24]. C_{60} is a widely used ETL material in HTL-free PSC which also exhibits excellent thermal stability for solar cell working temperatures range. Combined with Carbon electrode, it also demonstrates moisture resistance [25]. The favorable band alignment of ETL with the $MAPbI_3$ was also considered to ensure efficiency charge transportation. The initial performance of the devices is mentioned in Table II.

TABLE II. THE DEVICE PERFORMANCE BEFORE OPTIMIZATION.

ETL	**PCE (%)**	**V_{oc} (V)**	**J_{sc} (mA/cm^2)**	**FF (%)**
TiO_2	18.26	1.01	23.15	77.86
SnO_2	18.67	1.05	22.28	79.55
WS_2	18.52	1.08	22.76	75.21
C_{60}	21.12	1.09	25.95	75.00

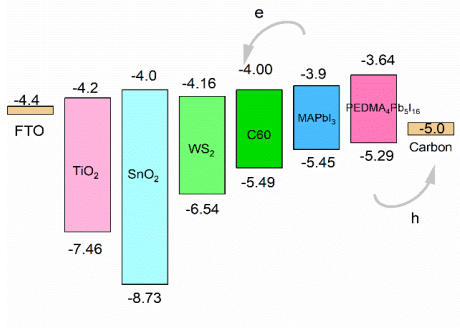

Figure 2. Energy band diagram.

III. Results and Discussion

A. *Energy Band Diagram*

Band alignment is vital in determining potential barriers that charge carriers must overcome to move between absorber layer and charge transportation materials. Optimal band alignment reduces these barriers, thereby increasing the carrier mobility and overall device performance. The band diagram of the PSCs in Fig. 2 illustrates the operating principle of the proposed solar cell with the HOMO (Highest Occupied Molecular Orbital) and LUMO (Lowest Unoccupied Molecular Orbital) energy of each layer. As per the diagram, photo-induced electrons are efficiently extracted towards the FTO due to the favorably aligned conduction bands of the 3D perovskite and selected ETLs.

B. *Impact of Primary Absorber Layer Thickness on the Device Performance*

The performance of 2D/3D hybrid PSCs is mainly driven by the thickness of the 3D perovskite layer as it directly influences the absorbed percentage of the solar irradiance by the perovskite material [26]. The 2D-PeDA perovskite layer primarily functions as a protective layer, and its contribution to light absorption is relatively low as the bandgap is relatively high [27].

Based on experimental findings, for this analysis, perovskite layer thickness varies from 0.3 µm to 1.6 µm with an increment of 0.1µm, keeping the other parameters constant. The behavior of PV characteristics against thickness variation is illustrated in Fig. 3. The optimum thicknesses are 0.9µm for TiO_2, 1.3 µm for SnO_2, 1.4µm for WS_2 and 1.2 µm for C_{60}. The corresponding PCEs achieved were 18.92%, 20.06%, 19.77%, and 22.01%, respectively.

The effect of thickness on performance can be linked to thickness-dependent absorption characteristics of the primary absorber layer. In the relatively lower thicknesses, the absorption in

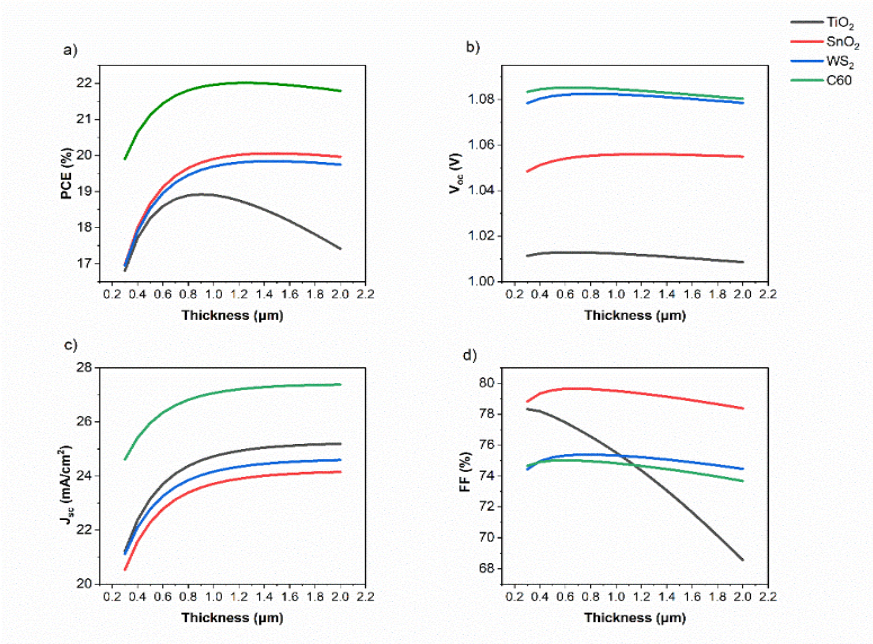

Figure 3. Effect of 3D layer thickness on the performance of PSCs with different ETLS a) PCE b) Voc c) Jsc d) FF.

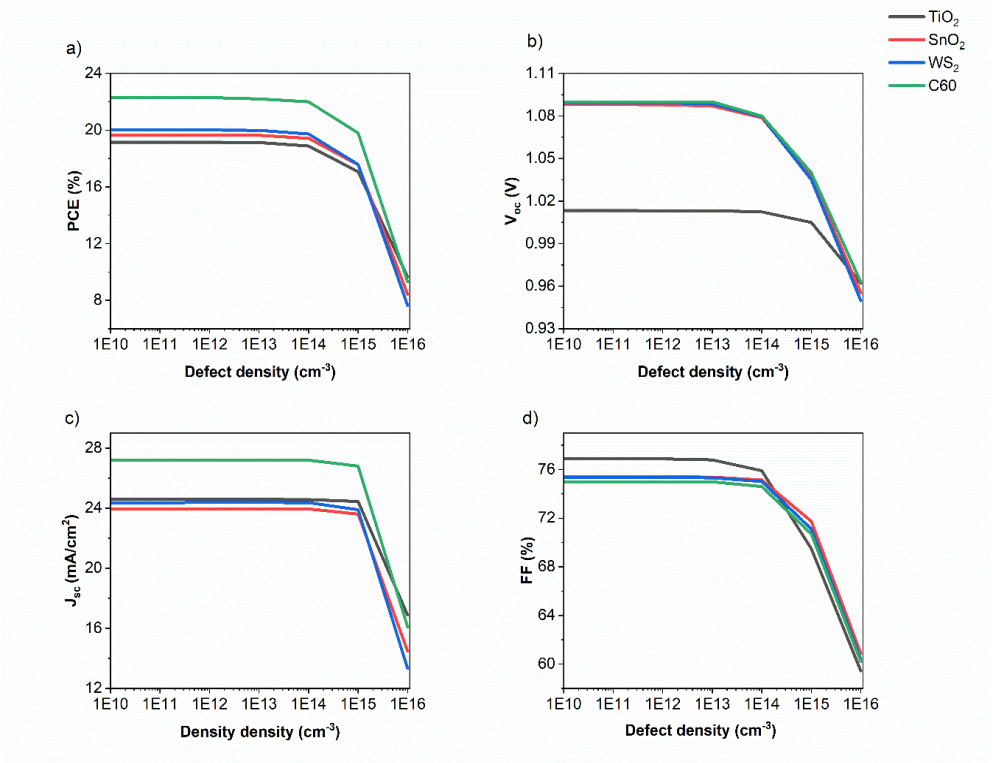

Figure 4. Effect of 3D layer defect density on the performance of PSCs with different ETLs a) PCE b) Voc c) Jsc d) FF.

the longer wavelength is limited, resulting in limited electron-hole pair generation. Increasing the thickness enhances the absorption of longer wavelengths, leading to improved electron-hole pair generation. However, when thickness surpasses a critical value, even a greater portion of the solar spectrum can be absorbed, and the generated charge carriers must travel long distances to reach their respective electrodes, increasing the likelihood of carrier recombination. Subsequently, the PCE of the device degrades after the thickness exceeds a critical threshold. V_{oc} and FF decrease when the absorber layer thickness rises. This is mainly caused by the enhanced carrier recombination and series resistance due to thickness increase. The thicker absorber layer introduces more series resistance, leading to voltage drop during current flow and hindering the efficient charge collection, thereby reducing the V_{oc}. The drop of V_{oc} lowers the maximum output power and consequently decreases FF [2]. The highest PCE is achieved by the device with C_{60}.

C. Impact of Primary Absorber Layer Defect Density on the Device Performance

3D-$MAPbI_3$ layer acts as the main light harvesting layer, playing a key role in deciding the performance of the device. Perovskite including vacancies, interstitials, impurities, Schottky, and Frankel defects [28]. The impact of the deep and shallow defects on the performance was investigated materials contain different intrinsic defects, varying the defect density in the range of $1 \cdot 10^{10}$ cm^{-3} to $1 \cdot 10^{16}$ $cm^{-3,}$ keeping the other parameters constant. As per Fig. 4, all photovoltaic performance remains stable up to a critical threshold defect density value. Once the defect density exceeds this threshold limit, all photovoltaic parameters gradually decline. This decline can be attributed to increased recombination losses, which become more prominent at higher defect density values. Consequently, the carrier diffusion length of charges declines, leading to a reduction in carrier lifetime [29]. At the critical defect density value of $1 \cdot 10^{12}$ cm^{-3}, the TiO_2, SnO_2, $WS_{2,}$ and C_{60} ETL-based devices show a maximum PCE of 19.15%, 19.63%, 20.01% and 22.26%, respectively.

E. The Optimized Device Performance

The recorded optimum performance of the devices and corresponding IV characteristic curves are mentioned in Table III and Fig. 5, respectively.

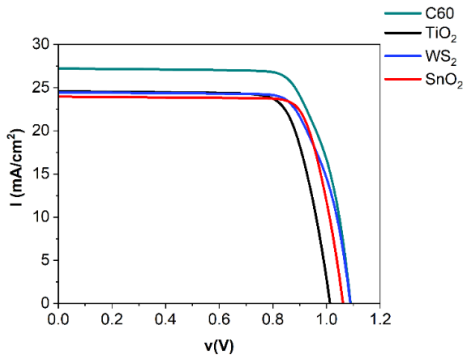

Figure 5. IV characteristics of the proposed devices based on different ETLs.

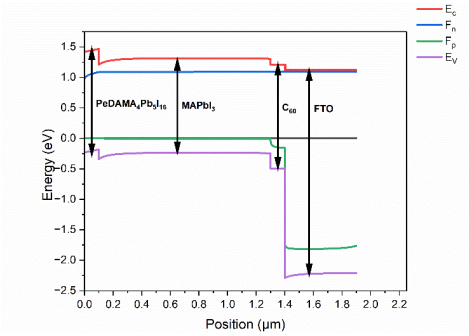

Figure 6. Band structure of the C60 ETL-based PSC with highest performances (Ec- conduction band minimum, Ev- valance band maximum, Fn- Electron quasi-fermi level, Fp- Hole quasi-fermi level).

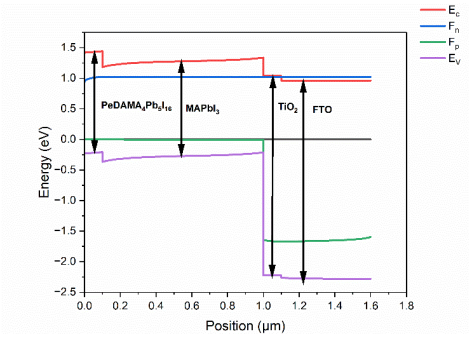

Figure 7. Band structure of the TiO2 ETL-based PSC with lowest performances (Ec- conduction band minimum, Ev- valance band maximum, Fn- Electron quasi-fermi level, Fp- Hole quasi-fermi level).

TABLE III. THE DEVICE PERFORMANCE AFTER OPTIMIZATION.

ETL	PCE (%)	V_{oc} (V)	J_{sc} (mA/cm^2)	FF (%)
TiO_2	19.15	1.01	24.58	71.84
SnO_2	20.25	1.06	23.96	79.61
WS_2	20.00	1.09	24.37	75.36
C_{60}	22.26	1.09	27.21	74.34

The reasons for the performance differences can be explained by comprehensively investigating the energy band diagrams. The corresponding energy band diagrams of the best performing and the lowest performing devices are illustrated in Figs. 6 and 7, respectively. As the devices have utilized different ETLs, their energy band alignment with the $MAPbI_3$ perovskite absorber is the main reason for performance disparity. The energy band diagrams exhibit that the conduction band minimum (E_c) of C_{60} is better aligned with the E_c of $MAPbI_3$ compared to that of TiO_2. In the C_{60}-based devices, the conduction band offset (CBO) between C_{60} and $MAPbI_3$ layer is smaller than TiO_2-based devices, making a smooth transition for electrons from the 3D perovskite layer to the ETL. This favorable alignment minimizes the energy barrier for electron extraction and improves charge collection efficiency, reducing the likelihood of interfacial recombination. As a result of that, the C_{60}-based device achieves a higher open-circuit PCE and V_{oc}. In contrast, the TiO_2-based device has a larger CBO between TiO_2 and $MAPbI_3$ layer, creating a larger energy barrier for electron extraction. This barrier increases the carrier concentration at the interface and, thus, recombination rates and energy losses. As a result of that, the TiO_2-based device shows comparatively poor performance. In experimental studies, a carbon-based PSC using FTO/c-TiO_2/m-TiO_2/3D-$FAPbI_3$ with Octylam-ammonium iodide based 2D perovskite layer achieved a PCE of 18.25% which is highly consistent with the results of our simulations, thereby validating the study [16].

The device performances can be further enhanced by adjusting the recombination rates, series and shunt resistance, and acceptor and donor concentrations.

F. Impact of the Work Function of the Back Contact on the Device Performance

The impact of the metalwork function of the back contact electrode on the device performance was examined. It's a primary property of the metal that impacts how it interacts with materials

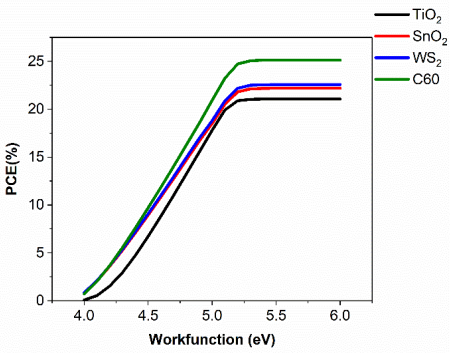

Figure 8. Effect of the metalwork function on PCE of the PSCs with different ETLs.

such as semiconductors. As the work function of the back-contact electrode increases, it ensures more favorable energy level alignment with the perovskite layer, ensuring better hole extraction and minimizing recombination losses, which leads to a significant rise in PCE until it saturates at optimal alignment as per Fig. 8 [30]. In conventional PSCs, noble metals such as Au, Ag, and Pt are widely used as back contact materials. Due to their high cost, alternative materials such as Cu, Al, and C are widely investigated to replace the noble metals. For maximum performance of the device, the back contact electrode should have a minimum 5.4 eV work function as shown in Fig. 8. The work function of the C electrode can be enhanced through doping, which is a cost-effective option, unlike noble metals [31]. Doping optimizes energy level alignment, reducing defects, and blocking environmental factors. Doping can fine-tune the work function for better charge extraction, while interface engineering can passivate trap states, prevent direct contact with degrading substances, and improve overall mechanical and chemical stability, leading to higher efficiency and longevity.

IV. Conclusion

HTL-free carbon electrode based 2D/3D hybrid PSCs have been numerically simulated, focusing on optimizing the 3D perovskite layer thickness and defect density to enhance performance. At the defect density of 10^{12} cm^{-3}, all devices exhibited maximum performance.

For different ETL materials, the optimum 3D perovskite layer thicknesses were reported to be: 0.9 µm for TiO_2, 1.3 µm for SnO_2, 1.4 µm for WS_2, and 1.2 µm for C_{60}. The maximum PCEs achieved were 19.15%, 20.25%, 20.00%, and 22.26%, respectively. The C_{60} based PSC outperform with V_{oc} of 1.09V, J_{sc} of 27.21 mA/cm^2 and FF of 74.34%. Furthermore, the impact of the metal work function on device performance was investigated, revealing that a minimum of 5.4 eV is required for optimal charge extraction. Carbon electrodes can be a cost-effective option, achieving similar performance if appropriate doping strategies are used to improve their work function.

References

[1] Leung, T. L., Ahmad, I., Syed, A. A., Ng, A. M. C., Popović, J., & Djurišić, A. B. (2022). Stability of 2D and quasi-2D perovskite materials and devices. *Communications Materials*, 3(1), 1–10.

[2] Gamage Ayomi Pabasara, W., & Asha Sewvandi, G. (2025, January 20). Numerical simulation and optimization of stable $CH_3NH_3PbI_3$-based 2D/3D mixed dimensional perovskite solar cell. In *Proceedings of the 10th Virtual International Conference on Science, Technology and Management in Energy (eNergetics 2024)*, Virtual.

[3] Green, M. A. A., et al. (2025). Solar cell efficiency tables (version 65). *Progress in Photovoltaics: Research and Applications*, 33(1), 3–15.

[4] Fan, Y., Meng, H., Wang, L., & Pang, S. (2019). Review of stability enhancement for formamidinium-based perovskites. *Solar RRL*, 3(9), 1–18.

[5] Wang, R., Mujahid, M., Duan, Y., Wang, Z. K., Xue, J., & Yang, Y. (2019). A review of perovskite solar cell stability. *Advanced Functional Materials*, 29(47), 1–25.

[6] Choi, H.-S. S., & Kim, H.-S. S. (2020). 3D/2D bilayer perovskite solar cells with enhanced stability and performance. *Materials*, 13(17).

[7] Li, D., Xing, Z., Meng, X., Hu, X., Hu, T., & Chen, Y. (2023). Selection of functional spacer cations for efficient 2D/3D perovskite solar cells. *CCS Chemistry*, 5(4), 71–801.

[8] Ye, X., et al. (2022). Organic spacer engineering in 2D/3D hybrid perovskites for efficient and stable solar cells. *New Journal of Chemistry*, 46(6), 2837–2845.

[9] Li, X., et al. (2023). Mixed perovskites (2D/3D)-based solar cells: A review on crystallization and surface modification for enhanced efficiency and stability. *Advanced Composites and Hybrid Materials*, *6*(3), 1–27.

[10] Sutanto, A. A., et al. (2020). Dynamical evolution of the 2D/3D interface: A hidden driver behind perovskite solar cell instability. *Journal of Materials Chemistry A*, 8(5), 2343–2348

[11] Ji, C., et al. (2021). Interface engineering of 2D/3D perovskite heterojunction improves photovoltaic efficiency and stability. *Solar RRL*, 5(5), 1–9.

[12] Ijaz, S., et al. (2024). A numerical approach to optimize the performance of HTL-free carbon electrode-based perovskite solar cells using organic ETLs. *Heliyon*, 10(7), e29091.

[13] Danladi, E., et al. (2023). Impact of hole transport material on perovskite solar cells with different metal

electrode: A SCAPS-1D simulation insight. *Heliyon*, 9(6), 16838.

[14] Chen, R., et al. (2020). Carbon-based HTL-free modular perovskite solar cells with improved contact at perovskite/carbon interfaces. *Journal of Materials Chemistry C*, 8(27), 9262–9270.

[15] Ku, Z., Rong, Y., Xu, M., Liu, T., & Han, H. (2013). Fully printable processed mesoscopic CH3NH3PbI3/TiO2 heterojunction solar cells with carbon counter electrode. *Scientific Report*s, 3.

[16] Salma, Z., et al. (2022). Employing 2D-perovskite as an electron blocking layer in highly efficient (18.5%) perovskite solar cells with printable low-temperature carbon electrode. *Advanced Energy*, 12(21).

[17] Mohammed, M. K. A. A., et al. (2023). Harnessing the potential of Dion–Jacobson perovskite solar cells: Insights from SCAPS simulation techniques. *Journal* of *Alloys and Compounds*, 963, 171246.

[18] Chaurasia, S., et al. (2024). Highly efficient and stable Dion–Jacobson (DJ) 2D–3D perovskite solar cells with 26% conversion efficiency: A SCAPS-1D study. *Journal of Physics and Chemistry of Solids*, 191, 112038.

[19] Bulowski, W., et al. (2024). Optimization of the ETL titanium dioxide layer for inorganic perovskite solar cells. *Journal of Materials Science*, 59(17), 7283–7298.

[20] Mohammadi, S., Akbari Nia, S., & Abbaszadeh, D. (2024). Reduction of recombination at the interface of perovskite and electron transport layer with graded Pt quantum dot doping in ambient air-processed perovskite solar cell. *Scientific Reports*, 14(1), 1–12.

[21] Kim, J., Kim, K. S., & Myung, C. W. (2020). Efficient electron extraction of SnO2 electron transport layer for lead halide perovskite solar cell. *npj Computational Materials*, 6(1), 1–8.

[22] Mbilo, M., et al. (2024). Highly efficient and stable organic solar cells with SnO2 electron transport layer enabled by UV-curing acrylate oligomers. *Journal of Energy Chemistry*, 92, 124–131.

[23] Bin Rafiq, M. K. S., et al. (2020). WS2: A new window layer material for solar cell application. *Scientific Reports*, 10(1), 1–11.

[24] Malek, N. A. A., et al. (2020). Enhanced charge transfer in atom-thick 2H–WS2 nanosheets' electron transport layers of perovskite solar cells. *Solar RRL*, 4(10), 1–11.

[25] AlZoubi, T., et al. (2024). Advanced optoelectronic modeling and optimization of HTL-free FASnI3/C60 perovskite solar cell architecture for superior performance. *Nanomaterials*, 14(12).

[26] Chakrabartty, J., Islam, M. A., & Reza, S. (2021). Performance analysis of highly efficient 2D/3D bilayer inverted perovskite solar cells. *Solar Energy*, *230*, 195–207

[27] Li, M.-H., et al. (2018). Highly efficient 2D/3D hybrid perovskite solar cells via low-pressure vapor-assisted solution process. *Advanced Materials*, 30(30), e1801401.

[28] Jayawardane, S. T., Akmal, M., Hu, D., Kumara, P., & Abeygunawardhana, W. (2024). Simulation-based performance analysis of lead-free bismuth perovskite solar cells: A comparative study of Cs3Bi2I9 and (CH3NH3)3Bi2I9-based perovskite solar cells. A*dvanced Theory and Simulations*, 7(7), 2400206

[29] Gholami-Milani, A., Ahmadi-Kandjani, S., Olyaeefar, B., & Kermani, M. H. (2023). Performance analyses of highly efficient inverted all-perovskite bilayer solar cell. *Scientific Reports*, *13*(1), 1–15.

[30] Rayhan, A., Khan, M. A., & Islam, R. (2024). Enhancing CsSn0.5Ge0.5I3 Perovskite Solar Cell Performance via Cu2O Hole Transport Layer Integration. *International Journal of Photoenergy, 17*.

[31] Don, M. F., Ekanayake, P., Jennings, J. R., Nakajima, H., Kumar, U. D., & Lim, C. M. (2023). Influence of metal salts (Al, Ca, and Mg) on the work function and hole extraction at carbon counter electrodes in perovskite solar cells. *Heliyon*, 9(7), e17748.

eNergetics 2025
DOI: https://doi.org/10.5281/zenodo.18623414

Original Scientific Article

Unraveling Li-Ion Battery Degradation: Mechanisms and Forecasting

Sevgi Erzen[1], Coskun Firat[2]

[1]Istanbul University-Cerrahpasa, Voc. School of Technical Sciences, Istanbul, Türkiye
[1,2]Istanbul Technical University, Energy Institute, Istanbul, Türkiye

[1]sevgi.erzen@iuc.edu.tr, [2]coskun.firat@itu.edu.tr

Abstract—**Lithium-ion batteries are key to the global trend of adopting renewable energy, but they suffer from performance deterioration over use time which reduces lifespan, increases cost and creates safety risks. Tackling these problems requires a fundamental insight into the age mechanisms and the development of accurate prediction tools for systems, including electric vehicle applications through to grid-scale storage. This work offers an in-depth summary of the state-of-the-art insights into degradation phenomena and performance prediction for lithium-ion batteries, from atomic-level mechanisms to full-cell behavior. First, we examine how chemical, electrochemical, mechanical, and thermal processes interact to cause capacity loss and increased impedance, highlighting recent findings from operando studies. Second, we outline the diagnostic toolbox, from basic electrochemical techniques to advanced methods such as synchrotron X-ray probes, neutron imaging, and cryogenic electron microscopy. We further perform a critical comparison of forecasting models assessing empirical, equivalent circuit, physics-based, machine-learning, and hybrid digital twin approaches to Remaining Useful Life estimation for their accuracy, interpretability, and prospects for on-board deployment. This review integrates the newest high-impact research to outline key knowledge gaps and identifies future directions for the development of more durable, safe, and predictable energy storage systems.**

Keywords - lithium-ion battery, ageing, SEI, lithium plating, machine learning.

I. INTRODUCTION

In that respect, the current demand for energy storage around the world could largely be attributed to the development of rechargeable LiBs [1]. Currently, this is mainly caused by a growing industry of EVs and an increase in large-scale grid systems [2]. Although costs are decreasing and the adoption rates of LiBs are growing accordingly [3], their widespread adoption is still inhibited due to the fact that their performance deteriorates with time [4]. Symptoms include loss of capacity, increase in resistance, and more serious safety issues such as thermal runaway [5,6], which results in shortened cycle life, complicated warranty assessment, and costs.

It is important to accurately predict a battery's State-of-Health (SOH) and Remaining Useful Life (RUL). Good prediction improves safety, allows better charging and fleet control, and helps increase the financial and environmental value of LiBs by reuse and recycling [7]. A solid grasp of the linked chemical, electrochemical, mechanical, and thermal aging processes is needed to create correct prediction methods.

This paper looks at current research on how lithium-ion batteries degrade and how well we can forecast their performance, from the atomic level to how the whole cell acts. We compare different ways to diagnose issues, assess models for predicting remaining useful life (RUL) using data, physics, machine learning, and digital twins. The review points out what we still need

ISBN: 978-86-82602-07-1

to learn to make energy storage systems last longer, be safer, and have more predictable performance.

II. Cell Fundamentals and Ageing Metrics

A. Architectures and Materials

Lithium-ion batteries usually have a graphite anode, sometimes with added SiO_x to store more energy [8], and a cathode made of layered oxides (NMC, NCA), spinel (LMO), or olivine (LFP) [9]. These materials are placed on current collectors with a porous separator [10]. The electrolyte is usually a $LiPF_6$ salt in organic solvents, like EC and DMC, and it often has additives such as VC to make the battery more stable [11]. Newer batteries tend to use anodes with a lot of silicon and bigger cell sizes to hold more energy [12].

B. State-of-health Definitions

SOH assesses a battery's existing condition by comparing it to its original state. The two most common measures consider capacity and internal resistance:

Capacity-based SOH is the ratio of the present usable capacity ($C_{present}$) to the original rated capacity (C_{rated}).

$$\mathrm{SOH}_{\mathrm{capacity}} = \frac{C_{\mathrm{present}}}{C_{\mathrm{rated}}} \cdot 100\% \,. \qquad (1)$$

Resistance-based SOH can be found by comparing the initial internal resistance ($R_{initial}$) with the current resistance ($R_{present}$).

$$\mathrm{SOH}_{\mathrm{resistance}} = \frac{R_{\mathrm{initial}}}{R_{\mathrm{present}}} \cdot 100\% \,. \qquad (2)$$

The automotive sector typically considers a battery's end-of-life (EOL) when its capacity drops to 70–80% of its initial value, or when its resistance increases by 30% [13]. Getting precise measurements of these metrics during actual driving is still difficult.

C. Calendar vs. Cycle Ageing Definitions

Battery degradation happens through two main ways that relate to each other [14].

Calendar aging is the irreversible loss of capacity and power in batteries during storage. This happens because of parasitic reactions, such as the growth of the Solid Electrolyte Interphase (SEI), which use up cyclable lithium. This process is accelerated by high temperatures and extreme SOC levels.

Battery degradation results from continuous charge and discharge cycles that a battery undergoes, even though the root causes of these processes are mechanical and electrochemical stresses. Aging is a collection of processes that includes, but is not limited to, electrode particle breakdown, active material loss, and lithium plating formation. The two degradation routes discussed are related in some ways: fast cycling generates heat that generally accelerates the chemical reactions associated with aging.

III. Multiscale Degradation Mechanisms

Degradation in lithium-ion batteries is a rather complex issue involving several chemical, electrochemical, mechanical, and thermal actions. These processes occur on widely differing scales, from atomic-level changes in the electrode material to changes in cell performance, according to reference [15].

A. Anode Side

1) SEI growth

The first step is initiated by the decomposition of electrolyte in order to form a solid electrolyte interphase at the anode. This acts similar to a barrier that allows ions to pass through it while acting as an obstacle for electrons [16]. The composition of this layer comprising inorganic and organic components

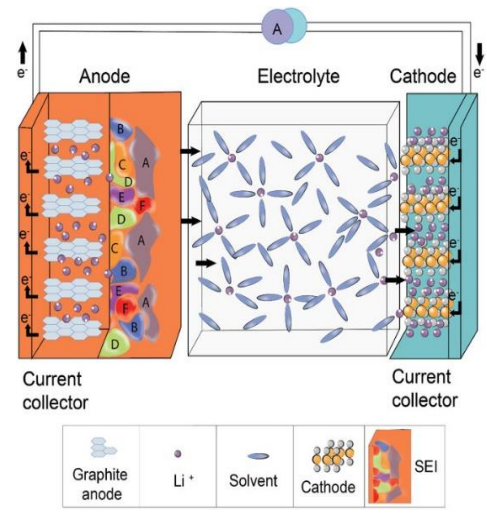

Figure 1. Schematic of a conventional LIB detailing the SEI layer [17].

strongly depends on the nature of the electrolyte itself [17].

The SEI layer is highly dynamic; it may thicken due to stress or temperature, which consumes lithium and increases the resistance accordingly [18]. Recent high-resolution imaging work has revealed nanostructural heterogeneities in SEI layers, showing that stable inorganic-rich SEI layers are preferred (Fig. 1).

2) Lithium plating and dendrites

Lithium plating occurs when the anode voltage falls below 0V vs. Li/Li^+ , which generally happens during fast charging, at low temperatures, or when the cell is fully charged [19]. In this process, lithium is lost and further may cause the growth of dendrites [20]. These dendrites may penetrate the separator and create short circuits within the cell; these may range from small shorts to severe thermal runaway events [21]. Most of the current research focuses on the fast detection and morphology study of plated lithium.

3) Chemo-mechanical fracture

During cycling, the materials are subjected to stress caused by repeated volume changes. Graphite particles, for instance, can expand in size by about 10%, while silicon particles can expand by more than 300%, possibly resulting in particle fracture, loss of electrical contact, and the loss of active material [22]. This accelerates the growth of the SEI layer on newly exposed surfaces and increases resistance. Some approaches for addressing this include self-healing binders and porous electrode structures [23].

B. Cathode Side

1) Phase Transition and Oxygen Release

Layered oxide cathodes (e.g., NMC) suffer from structural instability at high voltages. Deep delithiation can cause phase transitions to a rock-salt structure on the particle surface, blocking lithium-ion transport [24]. At high temperatures and states of charge, these materials can release oxygen, triggering violent electrolyte oxidation and thermal runaway [25]. A stable Cathode Electrolyte Interphase (CEI) is critical for protection.

2) Micro-cracking and particle isolation

Anisotropic volume changes in polycrystalline cathode particles cause micro-cracking as shown in Fig. 2 [26]. These cracks expose fresh surface to the electrolyte,

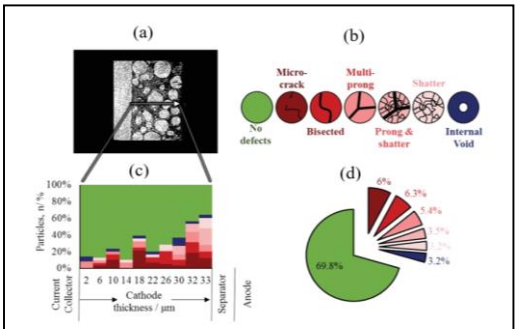

Figure 2. Quantifying the number of defective particles within pristine (pre-operated) NMC811 electrode structures through the definition of several defect categories [26].

accelerating transition metal dissolution and leading to active material isolation (LAM) [27]. Single-crystal cathodes and surface coatings are used to improve mechanical stability.

In Fig. 2, a) grayscale ortho-slice image taken from the 3D tomogram; b) a visual aid of the seven categories of particle defect proposed here; c) the percentage population of each defect with respect to the distance from the current collector; and d) the average particle defect composition.

3) Transition-metal dissolution & cross-talk

Hydrofluoric acid (HF), formed from $LiPF_6$ hydrolysis, leaches transition metal ions (e.g., Mn^{2+} , Ni^{2+}) from the cathode [28]. These ions migrate to the anode and deposit within the SEI, catalyzing its further growth. This "cross-talk" accelerates both LLI and impedance rise [29].

C. Electrolyte and Separator Ageing

The electrolyte decomposes at high temperatures and voltages. $LiPF_6$ breakdown produces HF, while carbonate solvents oxidize, generating gas and increasing internal pressure [30]. Consumption of electrolyte components increases viscosity and resistance [31]. Polyolefin separators are thermally vulnerable; they can shrink or melt at elevated temperatures, causing internal short circuits. Ceramic coatings enhance the thermal stability of materials [32].

D. Thermal-mechanical-electrochemical Coupling

Degradation occurs in a vicious circle, as local hot spots accelerate chemical reactions such as the growth of SEI, which may produce even more heat and can result into thermal runaway. Meanwhile, non-uniform lithiation and temperature changes induce mechanical stress

that result in a delamination of electrode layers. A comprehensive study of these complex interactions should be conducted using operando methods and multiphysics modeling.

IV. Diagnostic and Characterization Toolbox

A good understanding of the degradation process is important for two main purposes: it forms a basis for a rational development of effective mitigation strategies, and provides valuable input data to validate predictive models. But they do so many different kinds of analyses, from various typical electrochemical tests that can diagnose the health of a battery as it occurs to sophisticated spectroscopic and microscopic methods able to reveal fine details about what goes on inside a battery as it ages.

A. Electrochemical Techniques for Tracking SOH and Phenomenology

Non-invasive analyses are very important for monitoring of the battery status and are frequently implemented as integral parts in on-board systems:

1) Incremental capacity and differential voltage analysis

One of such widely used and particularly effective approaches to interpret batteries is the analysis of voltage profile derivatives, i.e., dQ/dV or dV/dQ. During the life of the cells, any shift of peak positions in these plots is usually due to degradation processes such as LLI, while a change in the peak height or intensity is generally associated with LAM.

2) Electrochemical Impedance Spectroscopy (EIS)

One of the most effective methods by which to measure impedance over a wide range of frequencies is that using EIS. From the Nyquist plot acquired, researchers can recognize important parameters that express the interfacial decomposition like, R_{SEI} and charge transfer resistance (R_{ct}). Furthermore, transport restrictions (e.g., of lithium ions) may be investigated by determining the diffusion coefficients, e.g., in the form of GITT (Galvanostatic Intermittent Titration Technique).

B. Mechanistic Probes (Validation and Insight)

Although these advanced methods are not usually utilized in the BMS environment itself, it is of great importance for research and validation. The high-resolution insights into the dynamics are critical to enable accurate physics-based components, which are central for hybrid models.

1) Operando X-ray and neutron probes

Real time non-destructive methodologies allow to follow what happens inside. For instance, the Synchrotron XRD has been employed to monitor structural evolution in electrode crystals [33]. XANES is also very useful in studying the change of the oxidation state from different elements. Neutron Imaging, owing to its low-energy neutrons and very high sensitivity to lithium, thus is an effective technique to study lithium plating and its spatial distribution in working cells [21]. Computed Tomography allows a three-dimensional visualization of the structural changes, even minor ones such as particle fractures.

2) High-resolution spectroscopy and microscopy

Such post-mortem analysis techniques also provide the capability to study, or investigate, the chemical structure down to the atomic level. Examples include the highly detailed pictures of interfaces including the SEI/CEI provided by Cryo-TEM [34], whereas APT is able to build 3D chemical maps at the atomic scale [35]. The technique of Solid-State NMR is also very useful for species identification in complex phases such as the SEI [36].

C. Post-mortem Analytics (Quantification)

The appropriate calibration of the models certainly requires direct evidence obtained through teardown and investigation. For instance, the extent of microstructural damage can be determined by Focused Ion Beam-Scanning Electron Microscopy [37]. Similarly, Chemical Titration can be used for measuring lithium that has been irreversibly consumed, LLI [38], while Inductively Coupled Plasma-Optical Emission Spectrometry, ICP-OES, is able to measure dissolved transition metals in order to check the extent of cathode degradation [39].

V. Performance Forecasting and Life-prediction Models

Estimating RUL and SOH of lithium-ion batteries is a big challenge because their degradation mechanisms are complex and interrelated. The proper selection of a model demands a trade-off between accuracy in the predictions, interpretability, and feasibility for

implementation in a BMS. Hybrid methods, therefore, remain a subject of ongoing research as they seek to leverage the strengths of both physics-based and data-driven approaches.

A. Phenomenological and Equivalent Circuit Approaches

Empirical models help elucidate degradation through mathematical descriptions of the capacity loss and resistance increase we monitor during a test. These equations often come from known processes, such as the dependence of SEI growth with the square root of time. The most sophisticated models also include temperature and C-rate dependence but are simple and fast to compute, so they are suitable for battery management systems. In addition, it has to be kept in mind that empirical models have been based on experimental observations, performing always best within the conditions they were trained for. Therefore, they cannot be trusted for predictions outside these conditions or for different types of batteries.

In this approach, ECMs model the cell electrical activity through a network of resistors, capacitors, and pseudo-capacitors. Degradation can be identified by tracking, over time, parameter changes. For instance, degradation might bring an increase in series resistance or charge-transfer resistance. Typically, the real-time estimation of these parameters is carried out through the use of filtering algorithms such as Extended Kalman Filter (EKF) or Particle Filters (PF) methods. The advantage of these models, though, is that they have low computational demands, which makes them suitable for real-time BMS. On the other hand, due to their lack of clear physical significance, it will be difficult to identify chemical reasons for degradation.

B. Mechanistic Physics-based Models

These models provide valuable insight based on basic electrochemical and transport principles. Examples include the DFN method, which deals with the relevant partial differential equations describing mass, charge, and heat flow within the cell [40]. Models of this nature can also include extra sub-components that consider important processes, such as the growth of the SEI layer or cracking of particles. In order to overcome the high computational demand associated with the DFN model, simplified reduced-order models, such as the SPM, simplify the physics, thus allowing much quicker simulations but still retaining many of the performance characteristics of interest [41]. It is in the area of extrapolation that mechanistic models most often excel, showing how operating conditions relate to degradation rates, a necessity in optimizing cell design and performance. Their high computational requirements, however, can complicate their direct use for BMS.

C. Data-driven Machine-Learning Prognosis

ML methods can extract complex degradation behaviors directly from data without

TABLE I. QUANTITATIVE COMPARISON OF THE KEY TRADE-OFFS.

Feature	**Empirical Models**	**Reduced-Order Physics (e.g., SPM, ROM)**	**Pure Machine Learning (ML)**	**Hybrid/Digital Twin Models**
Predictive Accuracy (RUL/SOH)	Low to Moderate (Context-specific)	High (Mechanistically constrained)	Very High (Local data fit; typically, <5\%$ error cited)	Highest (Physical core + data correction)
Computational Demand (Inference/BMS)	Very Low	Low	Low (Pre-trained networks)	Moderate (Fusion of ROM + filter)
Generalization (New Chemistries/Conditions)	Poor (Extrapolation unreliable)	Good (If physical laws hold)	Poor (Domain shift challenge)	Good (Physics-informed constraint)
Interpretability/Insight	Low (Phenomenological)	High (Mechanistic insight is core)	Very Low (Black box)	High (Physical core is transparent)
Uncertainty Quantification (UQ)	Limited	Moderate (Sensitivity analysis)	Moderate (Requires Bayesian methods)	High (Inherent in Kalman filters/Bayesian approaches)

going through any physical equations. Long Short-Term Memory (LSTM) networks are most popular in RUL prediction for time-series analysis [42]. Such models can be very accurate, often less than 5% error in RUL, when trained on very large datasets of high quality. Yet, there are some drawbacks of machine learning models:

Deep learning models in chemistry face quite a few challenges, including generalization issues, their performance often fails in realistic settings or on chemical structures different from those they were trained with, a problem known as domain shift. A major barrier is interpretability: these models typically provide very little information about why they make a specific prediction. But that is not all, they are also heavily dependent on data; to effectively train them requires an enormous amount of labeled data, which is both expensive to gather and raises significant concerns regarding data privacy.

D. Comparative Benchmarking of Prognostic Models

The choice of model involves careful consideration of how well its features fit a particular objective. For this purpose, Table I is useful since the various modeling approaches are compared against one another pointing out their pros and cons.

E. Emerging Hybrid and Physics-Informed Paradigms

Hybrid Digital Twin models need to be constructed in order to overcome the challenges presented above. There have to be good physics-based models established and machine learning applied to remove inaccuracies even as wear-and-tear is measured in real time/already detected. This combined holistic model-based approach provides the best compromise of precision, robustness and response time necessary for BMS operations.

Two rising technologies underpin such integration: Physics-Informed Neural Networks (PINNs) and Federated Learning (FL). This is achieved by incorporating the fundamental laws of physics (such as conservation of mass and charge) in the neural network training to ensure physical valid predictions. FL also directly mitigates privacy and dependency challenges as it enables the model training to be conducted in a cooperative manner across different (multiple) electric vehicle fleets, while no private sensitive data is aggregated at center. This doesn't just make the model build faster, it also makes you have a better real-world driving experience.

F. Advancing Uncertainty Quantification (UQ) and Benchmarking

(Uncertainty quantification (UQ) is a crucial part of industrial risk management, not only allowing us to do more than just carry out predictions. Moreover, Bayesian advanced methods or ensemble modelling can also give the approximate confidence intervals for estimating the RUL [43], helping operators calculate risks and provide valuable information to make decision. General robustness of prognostic is also enhanced by standardized benchmark such as IEEE P2832 has, which prescribe well-defined criteria for evaluation competing algorithms [44].

G. Prognosis and the Circular Economy

If the industry wants to build sustainable circular economy, it is important to obtain an acceptable estimation of battery's SOH and RUL. Hybrid DT models may provide accurate predictions, which can be used to classify used EV batteries for safe and efficient second life in the grid storage system and support the evolution of potential waste reclamation. Furthermore, these features may support to recycling (e.g., for understanding the behavior of chemicals at end-of-life such as SEI structure and metal degradation for material recovery). By coupling degradation modeling with lifecycle assessment tools, we can reduce energy use and resource usage in general.

VI. CONCLUSIONS

The study of lithium-ion battery degradation has advanced from mere observation to complex, multi-scale analysis employing cutting-edge techniques such as operando measurement and atomic-resolution imaging has unveiled intricate aging mechanisms such as SEI growth and particle fracture that are both essential for better prediction of performance.

The traditional machine learning algorithm can achieve good performance over training set, but it has poor generalization and is not transparent. In comparison, models utilizing physics information has better prediction performance but with high computational burden. The future lies in Hybrid Digital Twin models that combine rough physics with data-informed intellect. Physics-Informed Neural Network (PINNs) methods can be exploited for

predictions governed by physical laws, while Federated Learning (FL) can contribute to maintain privacy of the models and move from VRU case study towards real-world applications without harming transferability performance in terms of computational load for BMS.

Adding Bayesian UQ improves still the risk management in industry. Cumulatively, these advancements will also raise the accuracy of forecasting which is indispensable in a Battery Circular Economy that requires accurate Remaining Useful Life (RUL) predictions for profitable second-life applications and smarter recycling.

REFERENCES

[1] Whittingham, M. S. (1976). Electrical energy storage and intercalation chemistry. *Science*, *192*(4244), 1126-1127. https://doi.org/10.1126/science.192.4244.1126

[2] IEA. (2023). *Global EV Outlook 2023*. IEA, Paris. Available at: https://www.iea.org/reports/global-ev-outlook-2023

[3] Catsaros, O., (2023). *Lithium-Ion Battery Pack Prices Hit Record Low of $139/kWh*. Available at: https://about.bnef.com /insights/clean-energy/lithium-ion-battery-pack-prices-hit-record-low-of-139-kwh/

[4] Birkl, C. R., Roberts, M. R., McTurk, E., Bruce, P. G., & Howey, D. A. (2017). Degradation diagnostics for lithium ion cells. *Journal of Power Sources*, *341*, 373-386. https://doi.org/10.1016/j.jpowsour.2016.12.011

[5] Jeevarajan, J. A., Joshi, T., Parhizi, M., Rauhala, T., & Juarez-Robles, D. (2022). Battery hazards for large energy storage systems. *ACS Energy Lett.* 2022, *7*, (8), 2725–2733. https://doi.org/10.1021/acsenergylett.2c01400

[6] Li, Y., Guo, W., Stroe, D. I., Zhao, H., Kristensen, P. K., Jensen, L. R., ... & Gurevich, L. (2024). Evolution of aging mechanisms and performance degradation of lithium-ion battery from moderate to severe capacity loss scenarios. *Chemical Engineering Journal*, *498*, 155588. https://doi.org/10.1016/j.cej.2024.155588

[7] Gautam, D., & Bolia, N. (2024). Fostering second-life applications for electric vehicle batteries: A thorough exploration of barriers and solutions within the framework of sustainable energy and resource management. *Journal of Cleaner Production*, *456*, 142401. https://doi.org/10.1016/j.jclepro.2024.142401

[8] Patnaik, S. (2024). Overview of electrode advances in commercial Li-ion batteries. *Ionics*, *30*(6), 3069-3090. https://doi.org/10.1007/s11581-024-05579-1

[9] Koech, A. K., Mwandila, G., Mulolani, F., & Mwaanga, P. (2024). Lithium-ion battery fundamentals and exploration of cathode materials: A review. *South African Journal of Chemical Engineering*, *50*(1), 321-339. https://doi.org/10.1016/j.sajce.2024.09.008

[10] Jeong, H., Jang, J., & Jo, C. (2022). A review on current collector coating methods for next-generation batteries. *Chemical Engineering Journal*, *446*, 136860. https://doi.org/10.1016/j.cej.2022.136860

[11] Lex-Balducci, A., Henderson, W., & Passerini, S. (2011). Electrolytes for lithium-ion batteries. *Lithium-ion batteries: advanced materials and technologies*, 147-184.

[12] Kim, H. J., Krishna, T. N. V., Zeb, K., Rajangam, V., Gopi, C. V. M., Sambasivam, S., ... & Obaidat, I. M. (2020). A comprehensive review of Li-ion battery materials and their recycling techniques. *Electronics*, *9*(7), 1161. https://doi.org/10.3390/electronics9071161

[13] Etxandi-Santolaya, M., Casals, L. C., & Corchero, C. (2024). Extending the electric vehicle battery first life: Performance beyond the current end of life threshold. *Heliyon*, *10*(4). e26066. https://doi.org/10.1016/j.heliyon

[14] Redondo-Iglesias, E., Venet, P., & Pelissier, S. (2018). Calendar and cycling ageing combination of batteries in electric vehicles. *Microelectronics Reliability*, *88*, 1212-1215. https://doi.org/10.1016/j.microrel.2018.06.113

[15] Santos, D. A., Rezaei, S., Zhang, D., Luo, Y., Lin, B., Balakrishna, A. R., ... & Banerjee, S. (2023). Chemistry–mechanics–geometry coupling in positive electrode materials: a scale-bridging perspective for mitigating degradation in lithium-ion batteries through materials design. *Chemical Science*, *14*(3), 458-484. https://doi.org/10.1039/D2SC04157J

[16] An, S. J., Li, J., Daniel, C., Mohanty, D., Nagpure, S., & Wood III, D. L. (2016). The state of understanding of the lithium-ion-battery graphite solid electrolyte interphase (SEI) and its relationship to formation cycling. *Carbon*, *105*, 52-76. https://doi.org/10.1016/j.carbon.2016.04.008

[17] Adenusi, H., Chass, G. A., Passerini, S., Tian, K. V., & Chen, G. (2023). Lithium batteries and the solid electrolyte interphase (SEI)—progress and outlook. *Advanced Energy Materials*, *13*(10), 2203307. https://doi.org/10.1002/aenm.202203307

[18] Deshpande, R. D., & Bernardi, D. M. (2017). Modeling solid-electrolyte interphase (SEI) fracture: coupled mechanical/chemical degradation of the lithium ion battery. *Journal of The Electrochemical Society*, *164*(2), A461. https://doi.org/10.1149/2.0841702jes

[19] Liu, Q., Du, C., Shen, B., Zuo, P., Cheng, X., Ma, Y., ... & Gao, Y. (2016). Understanding undesirable anode lithium plating issues in lithium-ion batteries. *RSC advances*, *6*(91), 88683-88700. https://doi.org/10.1039/C6RA19482F

[20] Han, X., Zhong, H., Li, K., Xue, X., Wu, W., Hu, N., ... & Guo, T. (2024). Operando monitoring of dendrite formation in lithium metal batteries via ultrasensitive tilted fiber Bragg grating sensors. *Light: Science & Applications*, *13*(1), 24. https://doi.org/10.1038/s41377-023-01346-5

[21] Ziesche, R. F., Kardjilov, N., Kockelmann, W., Brett, D. J., & Shearing, P. R. (2022). Neutron imaging of lithium batteries. *Joule*, *6*(1), 35-52. https://doi.org/10.1016/j.joule.2021.12.007

[22] Li, D., Shen, C., Zheng, Y., & Xu, J. (2025). Electrochemo- Mechanical Degradation and Failure of Active Particles in High Energy Density Batteries: A Review. *Small*, *21*(8), 2407740. https://doi.org/10.1002/smll.202407740

[23] Wang, Y., Xu, H., Chen, X., Jin, H., & Wang, J. (2021). Novel constructive self-healing binder for

silicon anodes with high mass loading in lithium-ion batteries. *Energy Storage Materials*, *38*, 121-129. https://doi.org/10.1016/j.ensm.2021.03.003

[24] Gan, Q., Qin, N., Yuan, H., Lu, L., Xu, Z., & Lu, Z. (2023). Critical review on the degradation mechanisms and recent progress of Ni-rich layered oxide cathodes for lithium-ion batteries. *EnergyChem*, *5*(5), 100103. https://doi.org/10.1016/j.enchem.2023.100103

[25] Shen, C., Hu, L., Duan, Q., Liu, X., Huang, S., Jiang, Y., ... & Zhang, J. (2023). Understanding lattice oxygen redox behavior in lithium- rich manganese-based layered oxides for lithium- ion and lithium-metal batteries from reaction mechanisms to regulation strategies. *Advanced Energy Materials*, *13*(48), 2302957. https://doi.org/10.1002/aenm.202302957

[26] Heenan, T. M., Wade, A., Tan, C., Parker, J. E., Matras, D., Leach, A. S., ... & Shearing, P. R. (2020). Identifying the origins of microstructural defects such as cracking within Ni- rich NMC811 cathode particles for lithium- ion batteries. *Advanced Energy Materials*, *10*(47), 2002655. https://doi.org/10.1002/aenm.202002655

[27] Zhang, Y., Geng, S., Zhang, K., & Zheng, B. (2024). Capacity fading and inter/intra-granular fracture of polycrystalline cathode particle induced by charge/discharge cycles: A numerical study. *Journal of Power Sources*, *603*, 234412. https://doi.org/10.1016/j.jpowsour.2024.234412

[28] Stich, M., Göttlinger, M., Kurniawan, M., Schmidt, U., & Bund, A. (2018). Hydrolysis of LiPF6 in carbonate-based electrolytes for lithium-ion batteries and in aqueous media. *The Journal of Physical Chemistry C*, *122*(16), 8836-8842. https://doi.org/10.1021/acs.jpcc.8b02080

[29] Kim, J. M., Yi, R., Cao, X., Xu, Y., Engelhard, M., Tripathi, S., ... & Zhang, J. G. (2024). Extending calendar life of Si-based lithium-ion batteries by a localized high concentration electrolyte. *ACS Energy Letters*, *9*(5), 2318-2325. https://doi.org/10.1021/acsenergylett.4c00348

[30] He, X., Ling, Y., Wu, Y., Lei, Y., Cao, D., & Zhang, C. (2025). Research Progress of Electrolytes and Electrodes for Lithium- and Sodium- Ion Batteries at Extreme Temperatures. *Small*, *21*(23), 2412817. https://doi.org/10.1002/smll.202412817

[31] Zhao, Y., Geng, L., Meng, W., & Ye, J. (2026). Low-Temperature Electrolytes for Lithium-Ion Batteries: Current Challenges, Development, and Perspectives. *Nano-Micro Letters*, *18*(1), 65. https://doi.org/10.1007/s40820-025-01914-x

[32] Park, S., Choi, S., Lim, J., Seo, J. P., Lee, H., Kim, S., ... & Lee, Y. M. (2025). Highly thermally conductive ceramic-coated separators with aluminum nitride for mitigating thermal runaway in lithium-ion batteries. *Chemical Engineering Journal*, 162732. https://doi.org/10.1016/j.cej.2025.162732

[33] Finegan, D. P., Scheel, M., Robinson, J. B., Tjaden, B., Hunt, I., Mason, T. J., ... & Shearing, P. R. (2015). In-operando high-speed tomography of lithium-ion batteries during thermal runaway. *Nature communications*, *6*(1), 6924. https://doi.org/10.1038/ncomms7924

[34] Ju, Z., Yuan, H., Sheng, O., Liu, T., Nai, J., Wang, Y., ... & Tao, X. (2021). Cryo- Electron Microscopy for Unveiling the Sensitive Battery Materials. *Small Science*, *1*(11), 2100055. https://doi.org/10.1002/smsc.202100055

[35] Chen, R., Leung, C. L. A., & Huang, C. (2024). Exploring the properties of disordered rocksalt battery cathode materials by advanced characterization. *Advanced Functional Materials*, *34*(50), 2308165. https://doi.org/10.1002/adfm.202308165

[36] Liu, X., Liang, Z., Xiang, Y., Lin, M., Li, Q., Liu, Z., ... & Yang, Y. (2021). Solid- state NMR and MRI spectroscopy for Li/Na batteries: materials, interface, and in situ characterization. *Advanced materials*, *33*(50), 2005878. https://doi.org/10.1002/adma.202005878

[37] Liu, Z., Bai, S., Burke, S., Burrow, J. N., Geurts, R., Huang, C. J., ... & Zhang, M. (2025). FIB-SEM: Emerging Multimodal/Multiscale Characterization Techniques for Advanced Battery Development. *Chemical Reviews*, *125*(11), 5228-5281. https://doi.org/10.1021/acs.chemrev.4c00831

[38] Loghavi, M. M., Babaiee, M., & Eqra, R. (2023). A review of volumetric titration as an efficient method for the quantification of ions and compounds in lithium-ion battery components. *Chemical Papers*, *77*(12), 7395-7408. https://doi.org/10.1007/s11696-023-03075-w

[39] Son, S. B., Robertson, D., Tsai, Y., Trask, S., Dunlop, A., & Bloom, I. (2020). Systematic study of the cathode compositional dependency of cross-talk behavior in Li-ion battery. *Journal of The Electrochemical Society*, *167*(16), 160508. https://doi.org/10.1149/1945-7111/abcb40

[40] Brosa Planella, F., Ai, W., Boyce, A. M., Ghosh, A., Korotkin, I., Sahu, S., ... & Richardson, G. (2022). A continuum of physics-based lithium-ion battery models reviewed. *Progress in Energy*, *4*(4), 042003. https://doi.org/10.1088/2516-1083/ac7d31

[41] Gopalakrishnan, K., & Offer, G. J. (2021). A composite single particle lithium-ion battery model through system identification. *IEEE Transactions on Control Systems Technology*, *30*(1), 1-13. https://doi.org/10.1109/TCST.2020.3047776

[42] Chen, X. (2024). A novel gear RUL prediction method by diffusion model generation health index and attention guided multi-hierarchy LSTM. *Scientific Reports*, *14*(1), 1795. https://doi.org/10.1038/s41598-024-52151-y

[43] Wu, J., Kong, L., Cheng, Z., Yang, Y., & Zuo, H. (2022). RUL prediction for lithium batteries using a novel ensemble learning method. *Energy Reports*, *8*, 313-326. https://doi.org/10.1016/j.egyr.2022.10.298

[44] IEEE P2832. (2023). IEEE Guide for Control and Protection System Test. In *IEEE Std 2832-2023*, 1-37. doi.org/10.1109/IEEESTD.2023.10236962

eNergetics 2025
DOI: https://doi.org/10.5281/zenodo.18623487

Original Scientific Article

Study of the Effect of a Localized Magnetic Field on the Flow and Heat Transfer of a Nanofluid in a Channel Equipped with Obstacles of Different Shapes

Nawal Guerroudj[1], Henda Kahalerras[2], Brahim Fersadou[3]

[1,2,3]Faculty of Mechanical and Process Engineering (FGMGP), Algeria
[1,2,3]University of Sciences and Technology Houari Boumediene (USTHB), Algeria
[1,2,3]Laboratory of Multiphase Transport and Porous Media (LTPMP), Algeria

[1]nawal.guerroudj@usthb.edu.dz, [2]kahalerrashenda@yahoo.fr, [3]brahim04@live.fr

Abstract—**The study focuses on enhancing heat transfer by combining active and passive methods. To this end, a numerical study is conducted to explore the flow and heat transfer characteristics by forced convection of a Cu-Al_2 O_3 -TiO_2 /water tri-nanofluid in a wavy-walled channel, equipped with three heat sources maintained at a constant temperature Tc. A solid obstacle of various shapes is placed at different positions (inlet, middle, and outlet), while a uniform magnetic field is applied. The governing equations and associated boundary conditions are solved numerically using the Galerkin Weighted Residual Finite Element Method. The results reveal that the opening ratio Rp influences the first heat source and has a significant effect on thermal performance while effectively reducing the pressure drop.**

Keywords - wavy channel, nanofluid, heat sources, magnetic field, solid obstacle.

I. INTRODUCTION

In recent years, various methods have been implemented to optimize convective heat transfer in fluid-based cooling systems. Among these are the application of passive techniques, such as adding baffles on the internal walls of heat sinks [1,2], as well as the use of impinging jets through open cavities subjected to specific thermal conditions to enhance heat exchange [3-5].

Articles that do not comply with the formatting requirements outlined in the model instructions will not be considered for review.

Enhancing heat transfer through wavy walls is a particularly relevant technique; indeed, numerous experimental studies and numerical simulations reported in the literature have explored this method [6-8]. This enhancement process relies on the fact that the wavy geometry of the surface disrupts the boundary layer and promotes continuous renewal of the fluid near the solid wall.

Recently, an innovative approach has gained the attention of researchers: the use of base fluids in which nanoparticles, present in very low concentrations, are suspended to improve thermal performance. These fluids, known as nanofluids, are potentially applicable in various technical fields such as boiling, condensation, cooling, and vehicle lubrication. The present work fits within this context and consists of a numerical simulation of forced convection of a Cu-Al_2 O_3 -TiO_2 /water tri-nanofluid in a wavy-walled channel featuring an inlet contraction and equipped with three heat sources maintained at a constant temperature and arranged alternately on the upper and lower walls. A solid obstacle of various shapes is placed at different positions, while a uniform magnetic field is locally applied in the final

ISBN: 978-86-82602-07-1

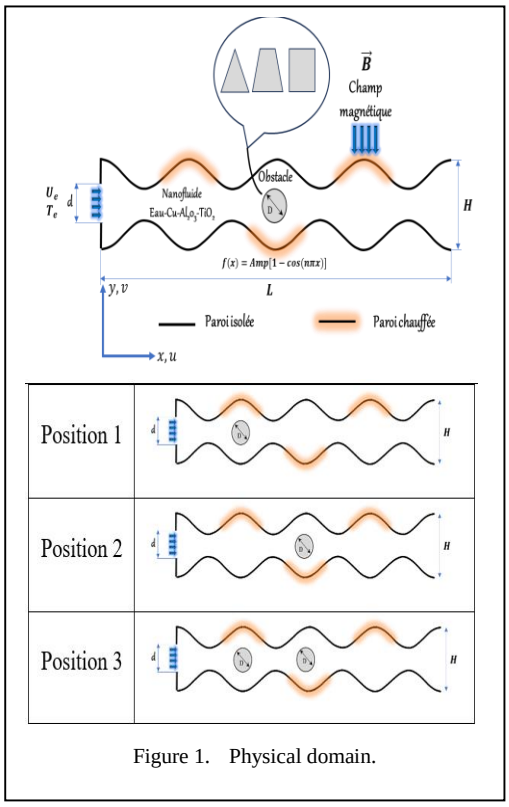

Figure 1. Physical domain.

section of the channel where the third heat source is located.

II. PHSICAL DOMAIN

The study domain, illustrated in Fig. 1, consists of a wavy-walled channel of length "*L*" and height "*H*", featuring an inlet contraction characterized by an opening ratio "$R_p = d/H$".

The channel is equipped with three heat sources maintained at a constant temperature and arranged alternately on the upper and lower walls. A solid obstacle of various shapes is placed at different positions, while a uniform magnetic field is locally applied in the final section of the channel where the third heat source is located.

III. MATHEMATICAL FORMULATION

A. *Governing Equations*

In order to simplify the problem under study, several simplifying assumptions are considered: the flow is two-dimensional, laminar, with no internal heat generation and negligible viscous dissipation. The nanofluid is treated as Newtonian with constant thermophysical properties. The dimensionless equations can be written as follows:

1. Continuity:

$$\frac{\partial U}{\partial X}+\frac{\partial V}{\partial Y}=0\,. \qquad (1)$$

2. Momentum:

$$U\frac{\partial U}{\partial X}+V\frac{\partial U}{\partial Y}=-\frac{\partial P}{\partial X}+\frac{\mu_{nf}}{\mu_f}\cdot\frac{p_f}{p_{nf}}\cdot \cdot\frac{1}{R_e}\left(\frac{\partial^2 U}{\partial X^2}+\frac{\partial^2 U}{\partial Y^2}\right)-\frac{Ha^2}{R_e}\cdot\frac{\sigma_{nf}}{\sigma_f}\cdot\frac{\rho_f}{\rho_{nf}}\cdot U \qquad (2)$$

$$U\frac{\partial V}{\partial X}+V\frac{\partial V}{\partial Y}=-\frac{\partial P}{\partial Y}+\frac{\mu_{thnf}}{\mu_f}\cdot\frac{p_f}{p_{thnf}}\cdot \cdot\frac{1}{R_e}\left(\frac{\partial^2 V}{\partial X^2}+\frac{\partial^2 V}{\partial Y^2}\right) \qquad (3)$$

3. Energy:

$$U\frac{\partial \theta}{\partial X}+V\frac{\partial \theta}{\partial Y}=\frac{1}{\mathrm{Re\,Pr}}\frac{(\rho Cp)_f}{(\rho Cp)_{thnf}}\times\frac{K_{nf}}{K_f}\times \cdot\left(\frac{\partial^2\theta}{\partial X^2}+\frac{\partial^2\theta}{\partial Y^2}\right)+\frac{EcHa^2}{\mathrm{Re}}\frac{\sigma_{thnf}}{\sigma_f}\frac{(\rho Cp)_f}{(\rho Cp)_{thnf}}\times U^2 \qquad (4)$$

B. *Boundary Conditions:*

The associated boundary conditions are:

$$\text{Inlet}\quad U=1;\quad V=0;\quad \theta=0. \qquad (5)$$

$$\text{Exit}:\quad \frac{\partial U}{\partial X}=0;\quad V=0;\quad \frac{\partial \theta}{\partial X}=0. \qquad (6)$$

$$U=V=0=\begin{cases}\text{Upper wall}\\ \text{wall}\end{cases}\begin{cases}\dfrac{\partial\theta}{\partial Y}=Tc \quad under\quad the\quad blocks\\ \dfrac{\partial\theta}{\partial Y}=0 \quad elsewhere\end{cases} \qquad (7)$$

$$U=V=0=\begin{cases}Lower\\ \text{wall}\end{cases}\begin{cases}\dfrac{\partial\theta}{\partial Y}=Tc \quad under\quad the\quad blocks\\ \dfrac{\partial\theta}{\partial Y}=0 \quad elsewhere\end{cases} \qquad (8)$$

The expressions for the various dimensionless groupings are as follows:

$$\mathrm{Re} = \frac{UiH\rho_f}{\mu}; \quad \mathrm{Pr} = \frac{\mu Cp_f}{k_f}; \quad Ec = \frac{U_i^2}{Cp_f \Delta T}; \quad Ha = \frac{\sigma_f B_o^2 H^2}{\mu_f}. \tag{9}$$

C. *Nusselt Number*

The local Nusselt number is given by:

$$\mathrm{Nu} = -\frac{K_{thnf}}{K_f}\frac{\partial\theta}{\partial n}, \tag{10}$$

$$\frac{\partial\theta}{\partial n} = \sqrt{\left(\frac{\partial\theta}{\partial X}\right)^2 + \left(\frac{\partial\theta}{\partial Y}\right)^2}. \tag{11}$$

D. *Pressure Drop*

The pressure drop is given by:

$$\Delta P = P_{m(X=0)} - P_{m(X=L)}. \tag{12}$$

IV. Numerical Procedure

The Galerkin weighted residual finite element method (FEM) was used to solve the governing equations and boundary conditions mentioned above. Since FEM is employed to tackle the problem, the first step involves specifying the type of mesh. The geometric domain was transformed into a number of unstructured and non-uniform triangular elements, with finer meshes applied near the walls, resulting in a total of 60526 elements. The direct solver PARDISO was selected to solve the dynamic and thermal fields. To ensure converged solutions for different parametric studies, a convergence criterion of 10^{-6} was applied.

To validate our numerical code, we compared the streamlines and isotherms with those presented by [1] in a numerical study on 2D mixed convection of a hybrid nanofluid (Water-Al_2O_3-Cu) flowing through a wavy channel equipped with a circular obstacle. The obtained validation results show very good agreement with those published by the authors (Figs. 2 and 3).

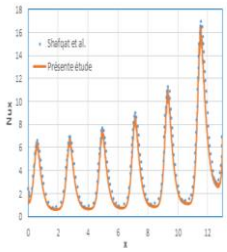

Figure 2. Local Nusselt number of the wavy wall at Pr=6.2, Ri=1, Ha=50 et Re=100.

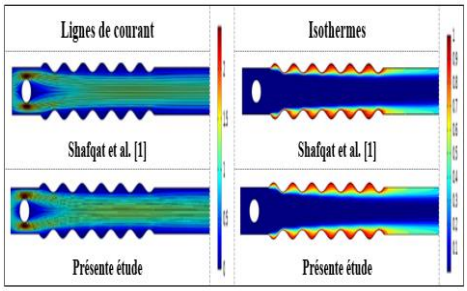

Figure 3. Streamlines and isotherms at Pr=6.2, Ha=50 et Re=100.

V. Results and Discussion

The problem under study is governed by numerous control parameters, so it is necessary to fix some of them in order to clearly highlight the parameters relevant to our investigation. To this end, we have fixed the following: the cavity length (L = 5), the amplitude (Amp = 0.1), the Prandtl number Pr = 7 (water), and the

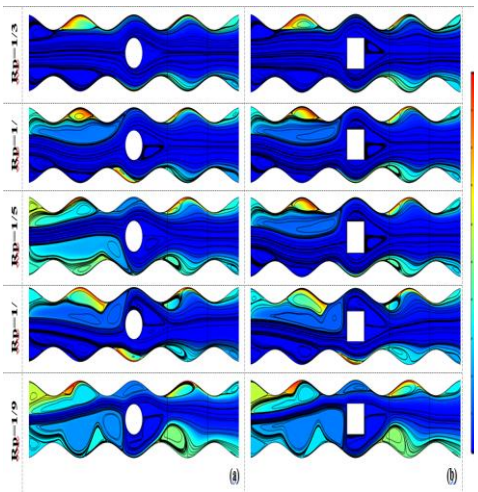

Figure 4. Streamlines and isotherms for different Rp: (a) circular shape, (b) square shape.

number of undulations (n = 4). The nanofluid is injected into the channel at a temperature T_i and a uniform velocity U_i. On the other hand, the following parameters have been varied: the opening ratio ($1/9 \leq Rp \leq 1/2$), the Hartmann number ($0 \leq Ha \leq 50$), and the shape of the solid obstacle (circular, square, triangular, and trapezoidal).

Fig. 4 illustrates the evolution of streamlines and isotherms for different opening ratios at the second position, with two shapes: circular and square. The resulting flow structures conform to the overall shape of the channel and the shape of the solid obstacle. Recirculation zones are observed to form just at the channel inlet, caused by the jet, and then the nanofluid is once again accelerated at the constrictions created by the wave necks after the obstacle.

At high values of the opening ratio, and regardless of the shape, it is observed that the nanofluid flows symmetrically with respect to the central axis of the channel. At low values of Rp, a clear asymmetry appears in the flow, caused by instabilities resulting from the narrowing of the jet. At the level of the solid block, the flow slows down and deflects the nanofluid toward the channel walls, thereby enhancing heat transfer near the second heat source.

When comparing the two shapes, it is noticeable that the shape locally affects the thermal and flow distribution within the channel, particularly near the first wave of the channel, especially at very low opening ratios of Rp.

The variations of the global Nusselt number as a function of the opening ratio Rp for different shapes in the three positions are illustrated in Fig. 5.

The heat transfer rate decreases significantly with increasing opening ratio Rp. Regardless of the shape and for all positions, the best heat transfer is obtained at Rp = 1/9, due to the cooling of the first heat source. Indeed, when the jet is narrowed, it is deflected toward this source, enhancing its cooling.

Regarding the effect of the positioning parameter of the solid obstacle, it appears that for the square shape, the amount of heat exchanged between the nanofluid and the two channel walls

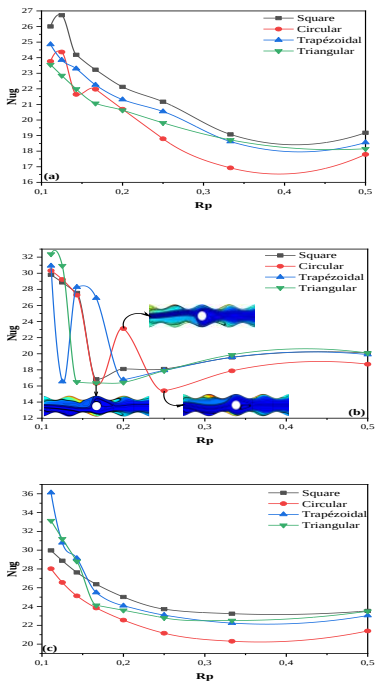

Figure 5. Variation of the Nug as a function of Rp for different shapes: (a) position 1; (b) position 2; (c) position 3.

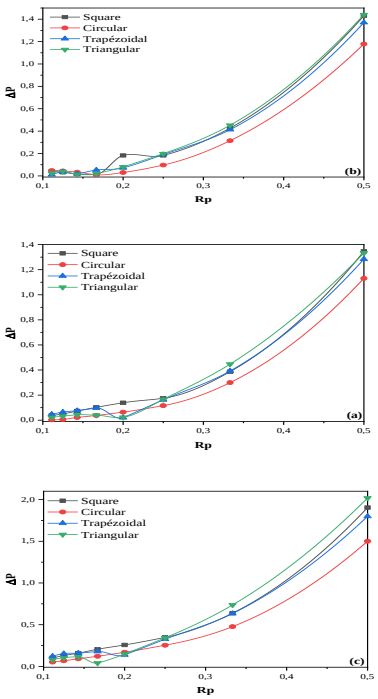

Figure 6. Variation of ΔP as a function of Rp for different shapes: (a) position 1; (b) position 2; (c) position 3.

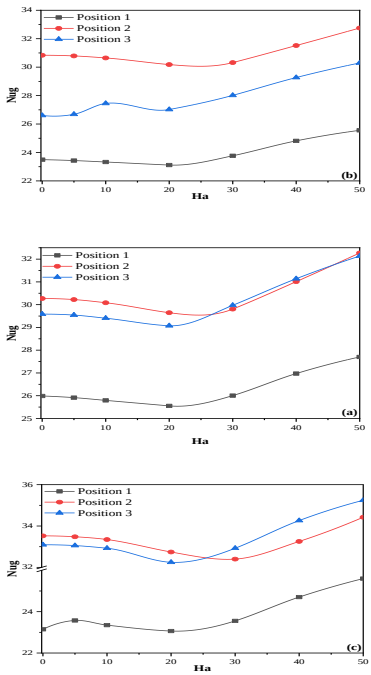

Figure 7. Variation of Nug as a function of Ha for different positions: (a) square; (b) circular; (c) triangular.

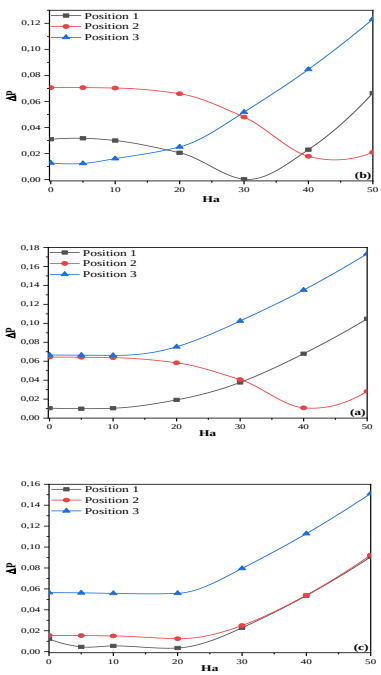

Figure 8. Variation of ΔP as a function of Ha for different positions: (a) square; (b) circular; (c) triangular.

is maximal in positions 1 and 3. In position 2, the triangular shape performs better, despite having a smaller exchange surface compared to the other shapes.

To better understand the effect of inserting a solid obstacle into a wavy channel on the pressure drop rate, Fig. 6 shows the evolution of the pressure drop as a function of the opening ratio Rp. It is clearly observed that increasing the ratio Rp significantly increases the pressure drop. This is due to the narrowing and subdivision of the nanofluid's flow cross-section at the first wave of the channel, which generates two wall jets redirected toward the channel's centerline, thanks to the harmony between the wavy structure and the shape of the solid obstacle. As a result, the flow is re-energized at the level of the second wave of the channel.

Regarding the shape, lower pressure drop values are found for the circular shape. It is also noted that maximum heat transfer is achieved at an opening ratio of Rp=1/9, with a minimum pressure drop for the circular shape in position 2.

To better understand the impact of the Magnetohydrodynamic (MHD) effect, represented by the Hartmann number, on flow and heat transfer characteristics, Fig. 7 shows the variations of the global Nusselt number with the control parameters Ha and shape. Two distinct zones can be identified. The first corresponds to Hartmann numbers below 20, where heat transfer exhibits non-monotonic behavior for all three positions. Thus, Nug initially increases with Ha. The critical intensity of the Lorentz force, leading to the lowest heat transfer rate, is strongly related to the position of the obstacle relative to the channel inlet; the critical Ha is around 20. In this first zone with low Ha values, it can be said that placing the obstacle at position 2 is beneficial.

The second zone corresponds to Hartmann numbers greater than 20, where the heat transfer rate increases with the increase in the Hartmann number. It is also worth noting that in this range of Ha values, it is beneficial to place an obstacle with a square or circular shape at position 2, and a triangular shape at position 3.

Regarding the pressure drop, Fig. 8 illustrates the variations in pressure drop as a function of Ha for different positions. A continuous increase in pressure loss is observed with the increase of

Ha. It is also noted that, regardless of the shape, the third position shows a significant pressure drop, as the jet is obstructed by both obstacles. On the other hand, a low pressure drop is observed in the second position, which supports the results obtained above.

VI. Conclusion

This work presents a numerical simulation of forced convection heat transfer of a Cu-Al_2 O_3 - TiO_2 /water nanofluid in a wavy-walled channel featuring an inlet jet and equipped with three heat sources maintained at a constant temperature, arranged alternately on the upper and lower walls. A solid obstacle with cross-sections (square, circular, triangular, and trapezoidal) is placed at the center, in the presence of a uniform magnetic field localized in the last section of the channel.

The obtained results have been analyzed by highlighting the influence of several relevant parameters such as the inlet channel opening ratio Rp, the shape and position of the solid obstacle, the intensity of the magnetic field expressed by the Hartmann number Ha, and the volumetric concentration of the nanoparticles.

The main results of this study can be summarized as follows:

- The opening ratio Rp influences the first heat source and has a significant effect on thermal performance.
- Reducing the opening ratio effectively decreases the pressure drop.
- Increasing the Hartmann number improves heat transfer and affects the last heat source.
- By varying the shape and position of the obstacle, the maximum heat transfer is achieved with the circular shape and position 2. This solid obstacle acts on the second heat source.

In conclusion, it can be stated that to achieve a significant improvement in heat transfer, a judicious combination of the obstacle's shape, position, opening ratio, and magnetic field intensity must be chosen.

References

[1] Mousavi, S. S., & Hooman, K. (2006). Heat and fluid flow in entrance region of a channel with staggered baffles. *Energy Conversion and Management*, *47*(15-16), 2011-2019. https://doi.org/10.1016/j.enconman.2005.12.018

[2] Wu, W., & Ching, C. Y. (2009, January). Laminar natural convection in an air-filled square cavity with partitions on the top wall. In *Heat Transfer Summer Conference* (Vol. 43574, pp. 399-414). https://doi.org/10.1115/ht2009-88594

[3] Deng, Q. H., Zhou, J., Mei, C., & Shen, Y. M. (2004). Fluid, heat and contaminant transport structures of laminar double-diffusive mixed convection in a two-dimensional ventilated enclosure. *International Journal of Heat and Mass Transfer*, *47*(24), 5257-5269. https://doi.org/10.1016/j.ijheatmasstransfer.2004.06.025

[4] Bahlaoui, A., Raji, A., Hasnaoui, M., Naïmi, M., Makayssi, T., & Lamsaadi, M. (2009). Mixed convection cooling combined with surface radiation in a partitioned rectangular cavity. *Energy Conversion and Management*, *50*(3), 626-635. https://doi.org/10.1016/j.enconman.2008.10.001

[5] Naphon, P., Nakharintr, L., & Wiriyasart, S. (2018). Continuous nanofluids jet impingement heat transfer and flow in a micro-channel heat sink. *International Journal of Heat and Mass Transfer*, *126*, 924-932. https://doi.org/10.1016/j.ijheatmasstransfer.2018.05.101

[6] Rashidi, S., Mahian, O., & Languri, E. M. (2018). Applications of nanofluids in condensing and evaporating systems: a review. *Journal of Thermal Analysis and Calorimetry*, *131*(3), 2027-2039. https://doi.org/10.1007/s10973-017-6773-7

[7] Rashidi, S., Karimi, N., Mahian, O., & Abolfazli Esfahani, J. (2019). A concise review on the role of nanoparticles upon the productivity of solar desalination systems. *Journal of Thermal Analysis and Calorimetry*, *135*(2), 1145-1159. https://doi.org/10.1007/s10973-018-7500-8

[8] Mahian, O., Kolsi, L., Amani, M., Estellé, P., Ahmadi, G., Kleinstreuer, C., ... & Pop, I. (2019). Recent advances in modeling and simulation of nanofluid flows-Part I: Fundamentals and theory. *Physics reports*, *790*, 1-48. https://doi.org/10.1016/j.physrep.2018.11.004

eNergetics 2025
DOI: https://doi.org/10.5281/zenodo.18623571

Original Scientific Article

Wind Energy Supply Chain Challenges in Brazil: A Qualitative Assessment through Principal Component Analysis (PCA)

Kergivaldo Nogueira de Medeiros[1], Camila Seibel Gehrke[2]

[1,2]Federal University of Paraíba, João Pessoa, Brazil, Brazil

[1]kergivaldo.medeiros@cear.ufpb.br, [2]camila@cear.ufpb.br

Abstract—**The wind energy supply chain in Brazil faces several challenges that compromise its efficiency and expansion. This study aimed to identify the main challenges in the chain by applying Principal Component Analysis (PCA) based on the perceptions of 32 industry experts. Data collection was conducted through semi-structured interviews, organized into a matrix with 10 variables evaluated on a Likert scale, representing the severity of the challenges. PCA, performed with the support of PAST statistical software version 5.2.1, allowed us to reduce data complexity and identify latent patterns. Of the nine components generated, the first two represented 52.8% of the total variance, highlighting financing costs as the main critical factor in PC1 and the lack of incentives for national production in PC2. The results revealed differing perceptions among the experts, highlighting the impacts inherent to the location of the projects. Finally, it is fair to state that strengthening the Brazilian wind energy supply chain requires integrated policies and specific strategies to overcome the challenges and contribute to the country's energy transition.**

Keywords - wind energy, supply chain, PCA, energy transition.

I. INTRODUCTION

The global energy transition has intensified in recent years, driven by the urgent need to mitigate climate change and reduce dependence on fossil fuels. Among renewable energy sources, wind power has emerged as one of the most promising alternatives for large-scale electricity generation. Its technological maturity, declining production costs, and capacity for decentralized generation have positioned it as a strategic component in the global effort to decarbonize energy systems.

Although wind power generation is regarded as a renewable, clean, and cost-effective source of energy, it is essential to assess both the volume and nature of the information disseminated regarding its potential challenges. Such assessment ensures that the sector's objectives are achieved in an economically viable and socially desirable manner, consistent with Goal 7 of the United Nations 2030 Agenda, which seeks to "ensure access to affordable, reliable, sustainable, and modern energy for all" [1].

In Brazil, wind energy has experienced significant expansion, particularly in the Northeast region, where favorable wind conditions and public incentives have supported rapid deployment. Despite these advances, the sector continues to face several structural challenges within its supply chain-such as logistical, limited local manufacturing capacity, regulatory uncertainties, and financial constraints. These barriers can hinder the sector's competitiveness and its ability to sustain long-term growth [2].

Analyzing the wind energy supply chain in Brazil is fundamental to understanding how the stages of manufacturing, transportation, installation, and maintenance of wind turbines

ISBN: 978-86-82602-07-1

are structured, as well as the relationships between suppliers, operators, and public policies.

For example, the public financing plays a pivotal role in advancing the ongoing energy transition and prevent from financial constraints. Public financial institutions can provide capital to project developers, mitigate investment risks, enhance financial literacy, and foster confidence in low-carbon technologies. Different types of public investment mechanisms contribute to technological progress across the energy sector [3].

As well as, a strong regulation can prevent problems such as curtailment, which represents a growing challenge to the renewable energy systems and operational efficiency of modern power grids. The rapid integration of intermittent wind sources, and others, necessitates real-time balancing between supply and demand, often requiring deliberate reductions in generation to prevent grid overload and instability [4].

To address these challenges, an integrated approach is needed that considers the interaction between financial, infrastructural, and institutional factors. This study applies Principal Component Analysis (PCA) to identify the main factors influencing the wind energy supply chain in Brazil, based on expert perceptions. The results reveal the sector's main vulnerabilities and provide input for public policies and strategies, contributing to the strengthening of wind energy in the country.

II. State of Art

PCA is a multivariate technique for modeling covariance structures. The technique was initially described by [5] and a description of practical computational methods emerged much later with [6,7] who used it for the specific purpose of analyzing correlation structures [8].

It is necessary to work to reduce the number of variables to make the structure less complex, using techniques that reduce non-linear dimensionality [9].

In the literature on supply chains, various analytical methods are employed to identify bottlenecks, assess efficiency, and support improvement strategies. Reference [10] applied Interpretative Structural Modeling (ISM) and MICMAC analysis to reveal hierarchical relationships and levels of influence among risk factors in the wind energy supply chain. Reference [11] employed System Dynamics (SD) to analyze scenarios in the solar energy supply chain, given its ability to represent complex interactions over time. Reference [12] used PCA to synthesize variables and identify essential competencies in the construction supply chain in Nigeria, reducing the dimensionality of the data.

TABLE I. Challenges mapped in the literature.

Article
Júnior, M. J. R., Figueiredo, P. S., & Travassos, X. L. (2022). Barriers and perspectives for the expansion of wind farms in BRAZIL. [13]
González, M. O., Nascimento, G., Jones, D., Akbari, N., Santiso, A., Melo, D., ... & Oprime, P. (2024). Logistic decisions in the installation of offshore wind farms: a conceptual framework. [14]
da Silva, V. P., & Galvão, M. L. D. M. (2022). Onshore wind power generation and sustainability challenges in Northeast Brazil: a quick scoping review. [1]
Barrero, F. M. C., de Siqueira Filho, J. A., Ribeiro, H., & Freitas, J. M. (2022). Wind Complexes Environmental Licensing in Bahia backwoods ridges, Brazilian Semiarid. [15]
Herrera, M. M., Uriona, M., & Dyner, I. (2020). Dynamics performance of the wind-power supply chain with transmission capacity constraints. [2]
Góes, M. D. F. B., Andrade, J. C. S., Jabbour, C. J. C., & Silva, M. S. (2021). Wind power projects in Brazil: challenges and opportunities increasing co-benefits and implications for climate and energy policies. [16]
Jelti, F., Allouhi, A., Büker, M. S., Saadani, R., & Jamil, A. (2021). Renewable power generation: A supply chain perspective. [17]
De Oliveira, S. A. L. B., Caracas, A. K. S. P., Almeida, A. W. M., De Melo, S. E. C. M., Freitas, M. S. F. A. E., Cajado, P. F. J. L., ... & Da Silva, S. L. R. M. Curtailment, Sustainability, And Governance: The Strategic Role Of Renewable Energy Sources Within The ESG Framework. [4]

To identify gaps in the wind energy supply chain in Brazil, it is essential to map the main challenges of the sector, based on contributions from experts and market demands. Several challenges are mentioned in the literature; these were structured and limited to ten, which served as the basis for the qualitative research, as shown in Table I.

III. METHODOLOGY

During the development of this study, PCA was employed as a statistical technique to reduce data complexity and facilitate the interpretation of results. The method enables the transformation of the original set of variables into a smaller number of components that account for most of the variance present in the dataset.

A. Data Collection

Field research was conducted between May 1 and July 30, 2025, involving professionals from companies operating in Brazil, particularly in the states of Rio Grande do Norte, Pernambuco, Ceará, Bahia, Piauí, Paraíba, and Rio Grande do Sul. The participants' profiles included project engineers, supervisors, supply technicians, operation and maintenance (O&M) engineers and technicians, and wind farm managers with at least five years of professional experience in the wind energy sector. This diversity of professional backgrounds provided a comprehensive and multidimensional perspective on the Brazilian wind energy supply chain, reflecting both operational and technical expertise across various levels of activity.

B. Construction of the Data Matrix

The collected information was organized into an evaluation matrix composed of ten qualitative variables that represent the main challenges identified through exploratory research on the topic. For each variable, experts assigned a score from 1 to 5 on a Likert scale, corresponding to the perceived severity of the challenge's impact, as identified in the literature, with: 1-Very Low: Insignificant or irrelevant impact; 2-Low: Slight and almost imperceptible impact; 3-Moderate: Perceptible but manageable impact; 4-High: Significant and relevant impact; 5-Very High: Critical, decisive, or strategic impact.

IV. RESULTS AND DISCUSSION

The survey results present the main challenges faced by the wind energy supply chain in Brazil, based on the perceptions of 32 industry experts of ten (10) variables. Through the application of PCA, the dimensionality of the information was reduced, allowing the identification of the most relevant groups of variables.

The first test performed, was the data collection feasibility. According to [18], sample adequacy in exploratory factor analyses can be considered satisfactory even with a minimum ratio of three participants per variable, provided that the matrix quality indicators meet statistical requirements. Proving that the data collection is enough.

In other to deeper evaluation of the data collection, the Kaiser–Meyer–Olkin (KMO) was processed, resulting in a value of 0.64132 and a Bartlett's Test of Sphericity of 0.00012511, confirming the suitability of the dataset for factor analysis considering that.

The KMO measure of sampling adequacy should exceed 0.50, indicating low partial correlations among variables and, consequently, the existence of common variance. Furthermore, Bartlett's Test of Sphericity must be statistically significant ($p < 0.05$), confirming that the correlation matrix is not an identity matrix and, therefore, suitable for component extraction.

The KMO index is used to evaluate the suitability of data for factor analysis. High values (between 0.5 and 1.0) suggest that the dataset is appropriate for such analysis [19]. Prior to component extraction, several statistical tests are performed to verify data adequacy. Among the most widely used are the KMO and Bartlett's Test of Sphericity, which jointly assess the quality of the correlation matrix. When $KMO > 0.5$ and $p < 0.05$, the dataset is considered appropriate for PCA [20].

The analysis, summarized in Table II, revealed distinct perceptions regarding the main challenges in the Brazilian wind energy supply chain. Among the items evaluated, the highest averages obtained by applying the Likert scale were observed for import dependence (4.12), bureaucracy in environmental licensing (4.09), and intentional interruption or reduction of wind energy generation (4.06), indicating that these are perceived as the most critical challenges. Conversely, financing costs (3.71) and shortage of skilled labor (3.62) received slightly lower averages, though they remain significant.

Regarding the coefficient of variation, which shows the variation in each participant's responses to a given question, it was highest for

the integration of the electrical grid (26.82%), labour shortage (25.98%), and bureaucracy for environmental licensing (25.09%), revealing divergent opinions among experts.

The negative asymmetry observed in variables such as bureaucracy for environmental licensing (-1.14), import dependence (-0.87), and wind turbine transport capacity (-0.53) indicates a greater concentration of responses in the higher categories, reinforcing the perception of the seriousness of these factors.

These findings provide a solid foundation for PCA, as they directly influence the calculation of the correlation matrix, facilitating the identification of latent patterns among the challenges and improving the interpretation of the most influential factors in the development and efficiency of the wind energy supply chain in Brazil.

The PCA generated nine Principal Components (PC), corresponding to the ten variables initially evaluated. After correlation analysis, this number was reduced to nine, as logistical infrastructure and wind turbine

transportation capacity exhibited a correlation coefficient of 0.63917, warranting their exclusion to avoid redundancy.

The summary of PCA results, presented in Table III, shows that PC1 and PC2 account for most of the explained variance approximately 52.8% of the total.

PC1, responsible for 35.68% of the variance, represents the most significant dimension, revealing a strong concentration of information related to the primary supply chain challenges.

PC2, explaining 17.12% of the variance, complements the analysis by capturing

TABLE II - STATISTICAL SUMMARY OF THE PAST 5.2.1 SOFTWARE.

	Wind turbine transport capacity	**Import dependence**	**Bureaucracy environmental licensing**	**Lack incentives for national production**	**Electricity grid integration**	**Financing costs**	**Shortage of skilled labor**	**Curtailment**	**Regulatory and institutional**
N	32	32	32	32	32	32	32	32	32
Min	1	2	1	2	2	2	1	2	2
Max	5	5	5	5	5	5	5	5	5
Sum	120	132	131	122	124	119	116	130	120
Mean	3.75	4.125	4.09375	3.8125	3.875	3.71875	3.625	4.0625	3.75
Std. error	0.16189	0.15391	0.18161	0.15835	0.18376	0.15705	0.16649	0.179254	0.14199
Variance	0.83870	0.75806	1.05544	0.80241	1.08064	0.78931	0.88709	1.028226	0.64516
Stand. dev	0.91581	0.87066	1.02734	0.89577	1.03954	0.88843	0.94185	1.014015	0.80321
Median	4	4	4	4	4	4	4	4	4
25 prcntil	3	4	3,25	3	3	3	3	3	3
75 prcntil	4	5	5	4,75	5	4	4	5	4
Mode	NA	4	5	4	5	3	3	5	4
Skewness	- 0.5375	-0.8797	-1.1496	-0.1817	-0.2871	0.0175	-0.3860	-0.52750	-0.2987
Kurtosis	1.0348	0.3809	1.2154	-0.7679	-1.2295	-0.8257	0.5721	-1.11955	-0.1272
Geom. mean	3.61071	4.01762	3.91571	3.70194	3.72508	3.61071	3.47738	3.922231	3.65804
Harm. mean	3.40425	3.88664	3.63636	3.58209	3.56215	3.49726	3.27086	3.764706	3.55555
Coeff. var	24.4216	21.1071	25.0955	23.4958	26.8268	23.8906	25.9822	24.96036	21.4191

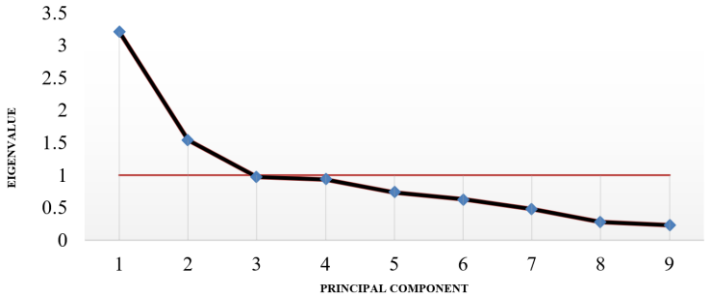

Figure 1. Scree plot.

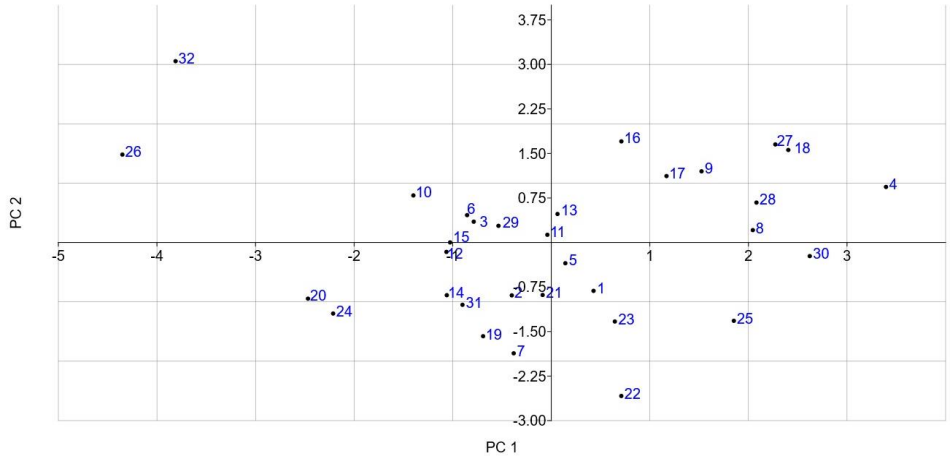

Figure 2. Scatter Plot extracted from Past 5.0 software.

secondary grouping patterns among the variables.

Beginning with PC3, a sharp decline in eigenvalues (all < 1) is observed. According to the Kaiser criterion, such components explain less variance than a single original variable and therefore should not be retained for interpretation. This trend is visually confirmed in the scree plot (Fig. 1), which displays a clear "elbow" after the second component, supporting the retention of only the first two PCs for analysis. This distribution is typical of PCA results, where a small subset of components explains most of the information, leading to effective dimensionality reduction.

This dimensional reduction enables a clearer and more objective understanding of the main challenges faced by the wind energy supply chain, without significant loss of statistical information.

The scatter plot derived from the PCA (Fig. 2) reveals relevant patterns in the experts' perceptions of the primary challenges in the Brazilian wind energy sector. The exhibited significant heterogeneity in participants' responses, indicating a lack of uniform perception regarding the sector's bottlenecks.

TABLE III. SUMMARY EXTRACTED FROM PAST 5.0 SOFTWARE.

Summary		
PC	***Eigenvalue***	***% variance***
1	3.21165	35.685
2	1.54086	17.121
3	0.970746	10.786
4	0.933229	10.369
5	0.733433	8.1493
6	0.629562	6.9951
7	0.477666	5.3074
8	0.27605	3.0672
9	0.226806	2.5201

The absence of compact clusters or concentrated point trends in the plot reinforces the multidimensional nature of the challenges. This dispersion can likely reflect regional differences in infrastructure, grid interconnection, and access to financing, suggesting that wind supply chain management in Brazil is highly contextualized.

The plot therefore supports the conclusion that these challenges cannot be analysed in isolation or addressed through uniform strategies. Instead, segmented and adaptive approaches are necessary, tailored to the specific realities of each region and stakeholder group.

The diversity of opinions highlights both the complexity of the system and the need for greater coordination among the various links in the supply chain. Table IV shows distinct patterns of perception among the 32 participants.

In PC1, participants 4, 18, and 30 recorded the highest scores, as can be seen in Table IV, through the results of the scores that present the new projected values of the observations in the principal components, suggesting a greater concern with variables strongly associated with this component, namely, financial, regulatory, and institutional constraints, as well as the shortage of skilled labour.

In PC2 (17.12% of the variance), participants 16, 27, and 32 obtained the highest scores, emphasizing factors such as the lack of incentives for national production, the reduction in wind energy generation, and limitations in grid integration, as can be seen in Table IV.

Overall, the dispersion of scores across the first two components indicates heterogeneity in expert perceptions, reflecting differences in

roles, experience, and geographic contexts within Brazil's wind sector. This heterogeneity is visually confirmed in the scatter plot (Fig. 2), where data points are widely distributed across all quadrants, forming no dense clusters.

Participants with extreme scores, such as 26 and 32 in PC1 and PC2 respectively, deserve special attention as they may represent outliers in perception or experts with particularly critical views on sectoral bottlenecks. The analysis suggests that different groups of experts perceive specific challenges more intensely, reinforcing the need for integrated policy and management approaches to strengthen the wind energy supply chain.

TABLE IV. ANALYSIS OF THE SCORES OF THE 32 PARTICIPANTS.

	PC 1	**PC 2**
Participant 1	0.42884	-0.81474
Participant 2	-0.40052	-0.89064
Participant 3	-0.78641	0.3508
Participant 4	3.3954	0.9359
Participant 5	0.1428	-0.34902
Participant 6	-0.85379	0.46144
Participant 7	-0.38106	-1.8665
Participant 8	2.0447	0.20882
Participant 9	1.5243	1.1995
Participant 10	-1.3989	0.7932
Participant 11	-0.039534	0.13051
Participant 12	-1.0633	-0.15821
Participant 13	0.063284	0.48058
Participant 14	-1.0598	-0.88775
Participant 15	-1.0259	0.0015062
Participant 16	0.7112	1.7035
Participant 17	1.169	1.1194
Participant 18	2.4043	1.5589
Participant 19	-0.69141	-1.5785
Participant 20	-2.468	-0.94607
Participant 21	-0.087883	-0.88367
Participant 22	0.71047	-2.5852
Participant 23	0.64475	-1.331
Participant 24	-2.2127	-1.1965
Participant 25	1.8519	-1.3193
Participant 26	-4.3508	1.4813
Participant 27	2.2728	1.6521
Participant 28	2.0815	0.67288
Participant 29	-0.53571	0.28093
Participant 30	2.6222	-0.22914
Participant 31	-0.90067	-1.0495
Participant 32	-3.811	3.0546

The loadings used to interpret the components, presented in Table V, indicate that, in PC1, the largest positive loadings are associated with financing costs, regulatory aspects, and a shortage of skilled labour, suggesting a strong correlation between these variables, since the loadings presented indicate the degree of contribution of each variable to the formation of the first principal component.

PC2, by contrast, highlights insufficient incentives for national production, curtailment of wind generation, and grid interconnection, representing a factor related to political and operational barriers that directly affect sectoral continuity and expansion.

The results reveal that the development of the wind energy supply chain in Brazil is influenced by multiple, interrelated dimensions—ranging from structural and institutional conditions to specific operational and regulatory obstacles.

To achieve consistent progress in the sector, public policies and business strategies must act synergistically to:

- Improve infrastructure and logistics,
- Simplify regulatory procedures,
- Stimulate domestic production, and
- Ensure the reliability and continuity of generation.

Only through such integrated efforts can Brazil enhance the efficiency, competitiveness, and resilience of its wind energy supply chain in alignment with global sustainability objectives.

TABLE V. LOADINGS.

	PC 1	PC 2
Wind turbine transport capacity	0.27646	-0.25292
Import dependence	0.36874	0.10487
Bureaucracy for environmental licensing	0.26225	-0.25725
Lack of incentives for national production	-0.042463	0.60816
Electricity grid interconnection	0.34224	0.33799
Financing costs	0.46093	-0.14557
Shortage of skilled labour	0.40876	-0.0908
Curtailment	0.17822	0.58732
Regulatory and institutional	0.43426	0.01936

V. CONCLUSION

This study examined the principal challenges affecting the wind energy supply chain in Brazil through the application of PCA, based on insights provided by industry experts. The findings demonstrate that the obstacles faced by this supply chain are multifaceted, encompassing financial, regulatory, institutional, and operational dimensions.

The statistical analysis revealed that Principal Components 1 and 2 together accounted for 52.8% of the total variance, indicating that a substantial portion of the sector's challenges can be explained by these two dominant dimensions.

The scree plot confirmed the retention of the first two components as the most significant, with a clearly observable inflection point from PC3 onward. This outcome reinforces the soundness of the methodological approach and validates the effectiveness of PCA in simplifying and interpreting the dataset.

PC1 encompassed variables related to financing costs, regulatory constraints, and skilled labor shortages, highlighting the importance of coordinated actions between the public and private sectors to ensure the effective performance of the supply chain.

High interest rates, limited access to subsidized credit, the absence of a clear regulatory framework for offshore wind deployment, and the lack of structured and coordinated technology transfer policies aimed at reducing external dependence were identified as key factors contributing to the predominance of the variables within PC1.

PC2, in turn, reflected issues such as insufficient incentives for domestic production, intentional curtailment or reduction of wind energy generation, and limited connectivity to the electricity grid. These results highlight the absence of effective policies to strengthen local manufacturing capacity, which in turn increases dependence on imported equipment and reduces opportunities for domestic job creation.

The results further indicate that the prioritization of policies focused on expanding Brazil's energy matrix often at the expense of strengthening national industry combined with the intentional generation curtailments determined by the National System Operator and the inadequate transmission infrastructure in high-potential regions such as the Northeast, were decisive factors shaping expert perceptions.

The analysis of scores and scatter plots revealed substantial heterogeneity in expert perceptions, suggesting that challenges vary according to geographical context, segment of the production chain, and professional background. This diversity underscores the need for integrated and regionally adaptive policies.

Thus, the results emphasize the importance of achieving greater alignment between public policies, regulatory frameworks, and industrial strategies, with the aim of strengthening the supply chain and sustaining the long-term expansion of wind energy in Brazil. It is recommended to expand and diversify financing mechanisms, improve the regulatory framework, particularly with regard to offshore wind energy, and implement consistent technology transfer policies aimed at reducing external dependence.

The coordinated execution of these measures will enhance the competitiveness, resilience, and strategic relevance of Brazil's wind energy sector, consolidating it as a key pillar in the nation's transition toward a sustainable and low-carbon energy future.

ACKNOWLEDGMENTS

The authors express their sincere gratitude to the collaborators of the participating companies, whose availability and contributions were fundamental to the development of this work. They also thank the Federal University of Paraíba for the institutional support that made this research possible.

REFERENCES

[1] da Silva, V. P., & Galvão, M. L. D. M. (2022). Onshore wind power generation and sustainability challenges in Northeast Brazil: a quick scoping review. *Wind*, *2*(2), 192-209. https://doi.org/10.3390/wind2020011

[2] Herrera, M. M., Uriona, M., & Dyner, I. (2020). Dynamics performance of the wind-power supply chain with transmission capacity constraints. *International Journal of Electrical & Computer Engineering* (2088-8708), 10(2).

[3] Isah, A., Dioha, M. O., Debnath, R., Abraham-Dukuma, M. C., & Butu, H. M. (2023). Financing renewable energy: policy insights from Brazil and Nigeria. *Energy, Sustainability and Society*, *13*(1), 2.

[4] De Oliveira, S. A. L. B., et al. (2025). Curtailment, Sustainability, And Governance: The Strategic Role Of Renewable Energy Sources Within The ESG Framework. *IOSR Journal of Business and Management*, *27*(5), (ser 11), 17-26.

[5] Pearson, K. (1901). LIII. On lines and planes of closest fit to systems of points in space. *The London, Edinburgh, and Dublin Philosophical Magazine and Journal of Science*, *2*(11), 559-572.

[6] Hotelling, H. (1933). Analysis of a complex of statistical variables into principal components. *Journal of educational psychology*, *24*(6), 417.

[7] Hotelling, H. (1936). Relations between two sets of variates. *Biometrika*, *28*, 321-377.

[8] Hongyu, K. U. A. N. G., Sandanielo, V. L. M., & Oliveira Junior, G. J. D. (2015). Principal component analysis: theory, interpretations and applications. *Engineering and Science*, *5*(1), 83-90.

[9] Azam, M. K., Hasan, S. M., & Qureshi, S. M. (2023). Exploring the critical success factors of a resilient supply chain. *Engineering Management in Production and Services*, *15*(1).

[10] Troche-Escobar, J. A., Lepikson, H. A., & Freires, F. G. M. (2018). A study of supply chain risk in the brazilian wind power projects by interpretive structural modeling and MICMAC analysis. *Sustainability*, *10*(10), 3442. https://doi.org/10.3390/su10103442

[11] Becerra-Fernandez, M., Sarmiento, A. T., & Cardenas, L. M. (2023). Sustainability assessment of the solar energy supply chain in Colombia. *Energy*, *282*, 128735. https://doi.org/10.1016/j.energy.2023.128735

[12] Omoraka, A. E. (2022). A principal component analysis of supply chain management skills for the Nigerian construction industry. *International Journal of Construction Management*, *22*(12), 2413-2421.

[13] Júnior, M. J. R., Figueiredo, P. S., & Travassos, X. L. (2022). Barriers and perspectives for the expansion of wind farms in BRAZIL. *Renewable Energy and Environmental Sustainability*, *7*, 6.

[14] González, M. O., et. al. (2024). Logistic decisions in the installation of offshore wind farms: a conceptual framework. *Energies*, *17*(23), 6004.

[15] Barrero, F. M. C., de Siqueira Filho, J. A., Ribeiro, H., & Freitas, J. M. (2022). Wind Complexes Environmental Licensing in Bahia backwoods ridges, Brazilian Semiarid. *International Journal of Advanced Engineering Research and Science*, *9*, 2.

[16] Góes, M. D. F. B., Andrade, J. C. S., Jabbour, C. J. C., & Silva, M. S. (2021). Wind power projects in Brazil: challenges and opportunities increasing co-benefits and implications for climate and energy policies. *Environment, Development and Sustainability*, *23*(10), 15341-15367.

[17] Jelti, F., Allouhi, A., Büker, M. S., Saadani, R., & Jamil, A. (2021). Renewable power generation: A supply chain perspective. *Sustainability*, *13*(3), 1271.

[18] Williams, B., Onsman, A., & Brown, T. (2010). Exploratory factor analysis: A five-step guide for novices. *Australasian journal of paramedicine*, *8*,1-13.

[19] Olawale, F., & Garwe, D. (2010). Obstacles to the growth of new SMEs in South Africa: A principal component analysis approach. *African journal of Business management*, *4*(5), 729.

[20] Rojas-Valverde, D., Pino-Ortega, J., Gómez-Carmona, C. D., & Rico-González, M. (2020). A systematic review of methods and criteria standard proposal for the use of principal component analysis in team's sports science. *International journal of environmental research and public health*, *17*(23), 8712.

eNergetics 2025
DOI: https://doi.org/10.5281/zenodo.18623639

Original Scientific Article

Recycled Textile-modified Recycled Concrete: Thermal Performance Optimization, Resource Recycling Potential, and Fractal-based Feasibility Analysis

Ji-Huan He[1], Chun-Hui He[2], D. Iranian[3]

[1]Fujian Provincial Engineering Research Center for Industrial Internet Control Technology and Systems, School of Information Engineering, Yango University, Fuzhou 350015, China
[2]School of Civil Engineering & Transportation, Foshan University, Foshan, China
[3]Department of Mathematical Sciences, Saveetha School of Engineering, SIMATS, Chennai, Tamilnadu, India

[1]hejihuan@ygu.edu.cn, [2]mathew_he@yahoo.com, [3]iraniand.sse@saveetha.com

Abstract—**Amid global sustainable development, the construction and textile industries are confronted with significant challenges, including substantial resource consumption and the generation of substantial waste. The utilization of Recycled Concrete (RAC) has been demonstrated to alleviate natural aggregate shortages; however, it is characterized by inherent thermal flaws, such as high thermal conductivity in the wet state and significant strength loss at elevated temperatures. In contrast, textile waste has been observed to exhibit low recycling rates, a phenomenon that contributes to pollution. The present study adopts a dual-waste approach, incorporating the two-scale fractal theory, with the objective of optimizing RAC's thermal performance and promoting textile waste recycling.**

Keywords - recycled concrete (rac), recycled textiles, thermal performance optimization, two-scale fractal theory, dual-waste utilization.

I. INTRODUCTION

In the context of the global movement toward sustainable development, the construction and textile industries—which are characterized by high levels of resource consumption and waste generation—have garnered significant attention. The following text is intended to provide a comprehensive overview of the subject matter.

Recycled aggregate concrete (RAC) is a construction material that utilizes construction waste as aggregates. This approach addresses the shortage of natural aggregates and the environmental burden of construction waste [1]. However, in comparison to traditional concrete, RAC exhibits distinct thermal performance deficiencies. The thermal conductivity of the material is influenced by the porosity and water absorption of recycled aggregates (RA) [2]. In high-temperature conditions (e.g., during fires), the moisture present in RA and the concrete matrix vaporizes, leading to internal pressure buildup, cracking and spalling. It has been documented that when recycled concrete is subjected to elevated temperatures, a substantial decline in its compressive strength, tensile strength, and stiffness is observed [3].

The textile industry is responsible for the generation of substantial amounts of waste. In China, annual fiber processing is of considerable magnitude, with chemical fibers accounting for a significant proportion of the

ISBN: 978-86-82602-07-1

total, and polyester constituting the majority of chemical fibers. Moreover, a considerable social stock of waste chemical fiber textiles is present, accompanied by substantial annual production/processing waste and post-consumer discarded products. Nevertheless, the recycling rate of these waste textiles remains very low. A significant proportion of these textiles are ultimately disposed of via landfilling, a process that consumes valuable land resources and contributes to the contamination of soil and water bodies due to the prolonged duration of their degradation. The following text is intended to provide a comprehensive overview of the subject matter.

A body of research has emerged on the subject of fiber-modified concrete [4,5], with studies indicating that fibers regulate concrete's behaviors. Steel fibers, for instance, have been shown to enhance thermal conductivity due to their high thermal conductivity. Meanwhile, polypropylene (PP) fibers act as thermal barriers, thereby reducing concrete's overall thermal conductivity. Furthermore, the length and aspect ratio of fibers have been demonstrated to shape the heat-transfer network, affecting heat transfer rates. Supercritical extraction is a viable method for recycling textile waste, as it has been demonstrated to effectively break down nylon textiles into high-quality recycled nylon fibers. However, mechanical recycling also poses challenges, including the difficulty of separating mixed fibers, which can negatively impact the quality of the recycled fibers [6].

This study aims to optimize RAC's thermal performance using recycled textiles (including recycled fibers) and enable large-scale textile waste recycling. Specific objectives include analyzing the influence of recycled textiles on RAC's thermal properties; exploring the optimal mix proportion of recycled textiles and RAC; and evaluating the environmental and economic feasibility of this dual-waste utilization approach. The research framework involves in-depth literature review, preparation of RAC specimens modified with recycled textiles of different mix proportions, thermal conductivity testing, mechanical property testing, microstructural analysis, and finally, mechanism analysis and feasibility evaluation.

II. Raw Materials and Regional Industrial Foundation

Recycled textiles and their derived recycled fibers serve as core additives for modifying Recycled Concrete (RAC). The thermal performance of the composite system is determined by the thermal stability, chemical composition, and physical structure of these recycled fibers. From the perspective of thermal science, key properties of recycled fibers-including thermal conductivity (λ), glass transition temperature (Tg), thermal decomposition temperature (Td), and residual mass ratio under high temperatures-are crucial for evaluating their compatibility with the concrete matrix in thermal environments. It is noteworthy that the irregular porous structure of recycled fibers aligns with the non-continuous medium characteristics of RAC. This necessitates the introduction of fractal geometry to characterize their microscale geometric features.

Regenerated cellulose fibers, which are produced from natural cellulose sources through chemical regeneration, are a subset of these eco-friendly materials. Examples of regenerated cellulose fibers include recycled Lyocell and viscose, which are derived from waste cotton. The thermal behavior of these systems is dominated by cellulose macromolecular chains. Thermogravimetric analysis (TGA) results indicate that regenerated cellulose fibers initiate decomposition at a specific temperature range, with a major weight loss stage occurring within a certain temperature interval due to cellulose pyrolysis. The room-temperature thermal conductivity of these fibers is lower than that of ordinary concrete, suggesting potential for enhancing the thermal insulation performance of the composite system. However, their relatively poor high-temperature resistance necessitates pre-treatment, such as silane coating, to enhance thermal stability for application in concrete. From the fractal perspective [7], the porous structure of regenerated cellulose fibers can be characterized by a two-scale fractal dimension (α). The relationship between the fractal dimension and the effective thermal conductivity of the fibers can be expressed as follows:

$$\lambda_{\mathbf{fiber,eff}} = \lambda_{\mathbf{solid}}(1-\varphi)^{\alpha/3} + \lambda_{air}\varphi^{\alpha/3}, \quad (1)$$

where λ_{solid} is the thermal conductivity of the fiber solid phase, λ_{air} is the thermal conductivity of air in the pores, and φ is the porosity of the regenerated cellulose fibers. This formula reflects the influence of the fiber's porous fractal structure on heat transfer, where a higher fractal dimension (indicating a more complex pore network) leads to a more significant reduction in effective thermal conductivity.

Regenerated synthetic fibers (e.g., recycled polyester (rPET), recycled nylon (rPA)) are mainly manufactured from waste polymer materials (such as PET bottles and discarded nylon garments). Compared to regenerated cellulose fibers, recycled polyester fibers exhibit superior thermal stability, characterized by a higher Td, a specific Tg, and a lower mass loss rate within the typical curing and service temperature range of concrete. The thermal conductivity of recycled polyester fibers is even lower than that of regenerated cellulose fibers, and their high tensile strength enables simultaneous enhancement of both the mechanical properties and thermal insulation performance of concrete. Recycled nylon fibers have a thermal conductivity comparable to that of recycled polyester fibers but a higher Tg (with variations between different types of recycled nylon fibers), making specific types more suitable for high-temperature service scenarios. For regenerated synthetic fibers, the interface transition zone (ITZ) between the fibers and the RAC matrix is a key factor affecting thermal performance. Based on the two-scale fractal space theory [8-10], the ITZ's fractal dimension (α_{ITZ}) is related to the aggregate replacement rate (r_{RA}) and the fiber surface roughness (R_A) as follows:

$$\alpha_{\mathbf{ITZ}} = 3 - k_1 r_{RA} - k_2 R_a, \quad (2)$$

where k_1 and k_2 are empirical constants. A lower ITZ fractal dimension indicates a more compact interface structure, which reduces thermal resistance at the fiber-matrix interface and improves the composite system's thermal conductivity stability.

The quality and thermal properties of recycled fibers are determined by the waste sources of recycled textiles, and three main categories of waste sources dominate the industrial supply chain. Post-consumer PET waste, generated in large annual quantities globally, is the primary raw material for rPET fibers. After undergoing sorting, washing, and melt-spinning processes, the resulting rPET fibers have a thermal conductivity consistent with that of virgin PET fibers, but a slightly lower Td due to residual impurities. Post-consumer garment waste, accounting for a large proportion of total textile waste, includes mixed-fiber garments. Mechanical sorting (via techniques like near-infrared spectroscopy) can separate the fibers, yet blended residues still reduce the thermal stability of the recycled fibers—for example, waste from cotton-polyester blends may result in rPET fibers with a lower Td compared to pure rPET. Pre-consumer textile scraps (e.g., polyester fabric scraps, nylon yarn waste) have high purity (often consisting of a single fiber type), so recycled fibers derived from this source have thermal properties closest to those of virgin fibers; for instance, recycled nylon fibers from pre-consumer scraps may have a Td only slightly lower than that of virgin nylon. From the regional industrial foundation perspective, the distribution of recycled textile waste sources affects the supply stability of recycled fibers.

Recycled Concrete (RAC) utilizes Recycled Aggregates (RA) from construction waste, but its inherent thermal performance defects limit its application in structures with thermal insulation requirements. The thermal conductivity of RAC is primarily determined by the porosity (ϕ) and moisture content (w) of RA. Compared to Natural Aggregates (NA), RA has a higher porosity due to the attached hardened mortar, which leads to a lower thermal conductivity. Based on the two-scale fractal theory for RAC, the relationship between the RA replacement rate (r) and RAC thermal conductivity can be described by integrating the fractal characteristics of RA pores:

$$\lambda_{RAC} = \lambda_{matrix}\left[1-\phi_{RA}(1-r)^{\alpha_{RA}}\right]+ \\ +\lambda_{Water} w_{RA}\phi_{RA}, \quad (3)$$

where λ_{matrix} is the thermal conductivity of the cement mortar matrix, α_{RA} is the two-scale fractal dimension of RA, and λ_{Water} is the thermal conductivity of water. This formula shows that under dry conditions, an increase in r generally leads to a decrease in λ_{RAC} because the higher porosity of RA (with a larger fractal dimension) enhances the thermal insulation effect. However, RA has a significantly higher water absorption rate than NA, causing a substantial increase in thermal conductivity when RAC is in a wet state. For RAC with a high RA replacement rate, saturation can result in a thermal conductivity that exceeds that of ordinary concrete, as water-filled pores reduce the fractal complexity of the pore network and increase heat transfer efficiency.

The structural defects of RAC—such as high porosity and a weak Interfacial Transition Zone (ITZ)—not only reduce its mechanical strength but also exacerbate thermal damage. Under temperature cycles (e.g., between $T_{\max}$ and $T_{\min}$, the Thermal Expansion Coefficient (TEC, α) of RA is higher than that of NA, and the weak bond strength of the ITZ leads to the formation of microcracks. Based on the two-scale fractal space energy conservation equation proposed in [2], the increase in thermal conductivity after n thermal cycles can be expressed by considering the evolution of the pore fractal dimension ($\Delta\alpha_{pore}$) caused by microcracks:

$$\Delta\lambda_{\mathbf{cycle}} = g(n, \Delta T, \alpha_{RA} - \\ -\alpha_{NA}, \sigma_{ITZ}, \Delta\alpha_{pore}), \quad (4)$$

where $\Delta T = T_{\max} - T_{\min}$ represents the temperature difference of the cycle, σ_{ITZ} is the bond strength of the ITZ. A positive $\Delta\alpha_{pore}$ indicates an increase in pore network complexity due to microcracks, which initially reduces thermal conductivity, but further cycle-induced macro-cracks will increase it. At high temperatures (within a specific range), moisture in the pores of RA vaporizes rapidly, generating internal pressure. For RAC with a high RA replacement rate, exposure to elevated temperatures can result in a high spalling rate, and the formation of macro-cracks further increases thermal conductivity. Additionally, the porous structure of RA makes it prone to chloride ion penetration, which accelerates the corrosion of steel bars; over long-term service in harsh environments (e.g., coastal areas), crack propagation caused by steel bar corrosion can lead to a significant increase in RAC thermal conductivity. From the regional industrial perspective, areas with abundant construction waste resources (e.g., old industrial zones) have a natural advantage in RA production.

III. Thermal Performance Optimization Based on Fractal Transmission Theory

The primary goal of adding recycled textiles to RAC is to optimize its thermal performance—specifically, reducing thermal conductivity (λ) for enhanced insulation and improving thermal stability to resist high-temperature damage. The two-scale fractal transmission theory provides a key theoretical tool for analyzing the thermal performance of fiber-modified RAC, as it can characterize the influence of the composite system's microscale void structure (including fiber-induced pores and RA inherent pores) on heat transfer.

The length (L_f), aspect ratio (AR = L_f/D_f, where D_f is fiber diameter), and dosage (V_f, volume fraction) of recycled fibers directly influence the heat transfer path of RAC (heat is mainly transferred via conduction through the solid matrix). Short fibers with a high aspect ratio form a continuous thermal barrier network, increasing the tortuosity of the heat transfer path. Based on the fractal heat conduction model proposed in [2], the relationship between fiber aspect ratio and thermal conductivity reduction can be described by integrating the fractal dimension of the fiber network ($\alpha_{fiber-network}$):

$$\Delta\lambda_{\text{reduction}} = p\ln(AR\cdot\alpha_{fiber-network}), \quad (5)$$

where p is a constant related to fiber type and matrix properties. A higher aspect ratio and

fiber network fractal dimension (indicating a more complex and continuous fiber distribution) lead to a more significant reduction in thermal conductivity.

There exists an optimal fiber dosage range: excessive dosage leads to fiber agglomeration (increasing thermal conductivity by forming large voids with low fractal dimensions), while insufficient dosage fails to form a continuous thermal barrier network.

IV. Conclusions

This study confirms that using recycled textiles to modify RAC is a viable dual-waste utilization strategy, which can simultaneously optimize RAC's performance and promote textile waste recycling, with the two-scale fractal theory providing a critical quantitative tool for the research. From the performance perspective, recycled synthetic fibers (e.g., rPET) with high aspect ratios form a continuous thermal barrier network, increasing the tortuosity of heat transfer paths; RAC's thermal properties and mechanical properties can be adjusted by the fiber dosage. Regenerated cellulose fibers, through their porous fractal structure, reduce RAC's autogenous shrinkage cracks. From the feasibility perspective, a regional fractal industrial chain for waste collection reduces raw material transportation costs and carbon emissions; LCA shows the composite system reduces carbon emissions greatly compared to natural aggregate concrete, with low maintenance costs over its service life. However, challenges remain, such as fiber-matrix interface incompatibility and raw material quality fluctuations, which can be addressed via interface modification (e.g., silane coupling agents) and fractal-based quality classification of recycled materials. Overall, this strategy provides theoretical and technical support for the large-scale application of green composite materials in infrastructure construction, aligning with global sustainable development goals.

While the current study focuses on theoretical mechanism analysis and model construction, for the quantitative comparison with standard RAC and commercial fiber-reinforced concrete, although theoretical predictions based on fractal models have initially revealed the thermal performance advantages of recycled textile-modified RAC, we plan to conduct experimental validation in subsequent work: we will refer to standards such as GB/T 50081-2019 to prepare standard specimens of standard RAC, commercial fiber-reinforced concrete, and our modified RAC, then test their thermal conductivity (via hot disk method) and mechanical properties (compressive/tensile strength) under the same conditions to provide direct quantitative comparison data. Regarding LCA model assumptions and uncertainty, the current reliance on literature-derived parameters will be supplemented by on-site data collection: we will collaborate with local recycled textile and construction waste processing enterprises to obtain actual data on recycled fiber purity (e.g., separation efficiency of mixed post-consumer garment fibers) and RA porosity fluctuations, then use Monte Carlo simulation to optimize the uncertainty analysis and enhance the reliability of carbon emission reduction conclusions. For the economic feasibility of the regional fractal industrial chain, we will construct a cost model integrating fractal characteristics of waste distribution-for example, using fractal dimension to quantify the spatial aggregation degree of waste sources, then calculating transportation costs, processing costs, and market application benefits of the composite material to evaluate the industrial chain's profitability and scalability. As for long-term performance evaluation, we will extend the fractal theory application to the analysis of material degradation mechanisms: by testing the pore structure evolution (via mercury intrusion porosimetry) of modified RAC after freeze-thaw cycles, carbonation, and chemical attack, we will establish the correlation between changes in the two-scale fractal dimension and performance degradation, thereby predicting the material's long-term service life. Addressing these questions will effectively bridge the gap between theoretical models and engineering practice, further enhancing the study's application value.

Looking ahead, the field of building materials innovation can deeply synergize historical wisdom with cutting-edge technology. On one hand, drawing insights from [11]'s mechanistic understanding of the

durability of ancient Roman concrete via hot mixing, researchers can explore how traditional craftsmanship inspires the development of self-healing and long-lived modern concrete, reducing material replacement frequency to lower lifecycle carbon emissions. On the other hand, leveraging the carbon storage potential of building materials highlighted in [12], the development of dual-functional construction materials that simultaneously achieve annual CO_2 sequestration exceeding 1.6 billion tones and enhanced service life is feasible. This integration can drive the building industry toward a synergistic goal of "decarbonization and longevity". Such an interdisciplinary research pathway, spanning materials science, archaeology, and environmental science, promises a paradigm shift for global carbon neutrality and sustainable infrastructure development. Going forward, it is crucial to strengthen the linkage between laboratory research and engineering applications to accelerate technology commercialization.

REFERENCES

[1] Liu, H., Wang, Y., Zhu, C., Wu, Y., Liu, C., He, C., Yao, Y., Wang, Y., & Bai, G. (2025). Design of 3D printed concrete masonry for wall structures: Mechanical behavior and strength calculation methods under various loads. *Engineering Structures, 325*, 119374. https://doi.org/10.1016/j.engstruct.2024.119374

[2] He, C. H., Liu, H. W., & Liu, C. (2024). A fractal-based approach to the mechanical properties of recycled aggregate concretes. *Facta Universitatis, Series: Mechanical Engineering, 22*(2), 329–342.

[3] Khan, A. R., Fareed, S., & Aziz, T. (2024). Residual mechanical properties of concrete with 30% recycled concrete aggregates exposed to elevated temperatures. *Iranian Journal of Science and Technology, Transactions of Civil Engineering, 48*, 315–327. https://doi.org/10.1007/s40996-023-01253-0

[4] da Silva Neto, J. T., Ribeiro Soares Junior, P. R., Reis, E. D., et al. (2025). Fiber-reinforced cementitious composites: Recent advances and future perspectives on key properties for high-performance design. *Discover Civil Engineering, 2*, 65. https://doi.org/10.1007/s44290-025-00209-9

[5] Ji, F.-Y., He, C.-H., Zhang, J.-J., & He, J.-H. (2020). A fractal Boussinesq equation for nonlinear transverse vibration of a nanofiber-reinforced concrete pillar. *Applied Mathematical Modelling, 82*, 437–448.

[6] Li, X., Bao, Y., Wu, L., Yan, Q., Ma, H., Chen, G., & Zhang, H. (2017). Thermal and mechanical properties of high-performance fiber-reinforced cementitious composites after exposure to high temperatures. *Construction and Building Materials, 157*, 829–838.

[7] He, C. H., & Liu, C. (2023). Fractal dimensions of a porous concrete and its effect on the concrete's strength. *Facta Universitatis, Series: Mechanical Engineering, 21*(1), 137–150.

[8] He, J. H., & Qian, M. Y. (2022). A fractal approach to the diffusion process of red ink in a saline water. *Thermal Science, 26*(3B), 2447–2451.

[9] Qian, M. Y., & He, J. H. (2022). Two-scale thermal science for modern life – Making the impossible possible. *Thermal Science, 26*(3B), 2409–2412.

[10] He, J. H., & Ain, Q. T. (2020). New promises and future challenges of fractal calculus: From two-scale thermodynamics to fractal variational principle. *Thermal Science, 24*(2), 659–681.

[11] Seymour, L.M., Maragh, J., Sabatini, P., et al. (2023). Hot mixing: Mechanistic insights into the durability of ancient Roman concrete. *Science Advances, 9*(1), eadd1602. doi:10.1126/sciadv.add1602

[12] Van Roijen, E., Miller, S. A., Davis, S.J. (2025). Building materials could store more than 16 billion tonnes of CO_2 annually. *Science, 387*(6730),176-182.

eNergetics 2025
DOI: https://doi.org/10.5281/zenodo.18623775

Original Scientific Article

Comparative Risk Assessment of Incremental Lifetime Cancer Risk from PAH Exposure in Urban vs. Rural Primary School Environments in Serbia: A Probabilistic Simulation Approach

Marija Živković[1], Rastko Jovanović[2], Ivan Lazović[3]

[1,2,3]Vinča Institute of Nuclear Sciences, National Institute of the Republic of Serbia, University of Belgrade, Belgrade, Serbia

[1]marijaz@vin.bg.ac.rs, [2]virrast@vin.bg.ac.rs, [3]ivan.lazovic@vin.bg.ac.rs

Abstract—**Polycyclic aromatic hydrocarbons (PAHs) are hazardous air pollutants with known carcinogenic potential. This study investigates PAH concentrations, exposure levels, and cancer risk in indoor and outdoor air at one rural and one urban primary school in Serbia. PAHs were measured in $PM_{2.5}$ samples, and benzo[a]pyrene equivalents (BaPeq) daily exposure doses were calculated for different population groups. Results showed significantly higher PAH concentrations in the urban school. The total PAH concentrations (ΣPAHs) in the urban school were 82.98 ± 36.85 ng/m³ outdoors and 41.76 ± 20.76 ng/m³ indoors, compared to 7.35 ± 9.43 ng/m³ and 5.34 ± 4.79 ng/m³, in the rural school, respectively. The Incremental Lifetime Cancer Risk (ILCR) was calculated for both children and adults. Sensitivity analysis confirmed that the cancer slope factor and inhalation rate are the most influential variables.**

Keywords - polycyclic aromatic hydrocarbons, incremental lifetime cancer risk, Monte Carlo simulations.

I. INTRODUCTION

Air pollution has become a serious concern due to its adverse effects on human health, including higher risks of cancer, respiratory issues, and increased mortality. Major sources of air pollution include traffic, industrial activity, power plants, domestic heating, and waste management. A significant portion of the urban population is exposed to high levels of fine particulate matter ($PM_{2.5}$), a primary air pollutant according to the World Health Organization (WHO). This highlights the urgency of implementing the new, more ambitious EU air quality standards proposed for 2030 [1].

One group of hazardous pollutants is polycyclic aromatic hydrocarbons (PAHs). PAHs are organic compounds formed during the incomplete combustion of organic materials like coal, wood, gasoline, diesel, and waste. These compounds are commonly found in urban air, both in the gaseous phase and the particulate phase attached to $PM_{2.5}$ [2]. Due to their small size, $PM_{2.5}$-bound PAHs can penetrate deep into the lungs and potentially enter the bloodstream. PAHs are known for their carcinogenic properties, with several identified as probable human carcinogens by both the US Environmental Protection Agency (US EPA) and WHO. Children are particularly vulnerable due to their developing immune systems and higher air intake per body mass [3,4].

Given the toxic potential of PAHs, especially for sensitive populations such as children, cancer

ISBN: 978-86-82602-07-1

risk assessment is crucial. However, direct measurement alone is often insufficient due to data limitations and the complexity of PAH interactions. To address this, mathematical models, particularly probabilistic Monte Carlo simulations, are widely used to estimate lifetime cancer risk levels [5-10].

Previous studies using this method have shown varying results. For example, it has been found that inhalation generally poses a higher risk than dermal exposure [6], and dietary intake significantly contributes to low-molecular-weight PAHs exposure, while high-molecular-weight PAHs are more relevant in inhalation exposure [7]. Other studies confirmed elevated cancer risks in school environments, especially from traffic-related PAHs [4,5].

In this study, concentrations of 16 $PM_{2.5}$-bound PAHs were measured in both indoor and outdoor air at two Serbian primary schools, one located in an urban area and the other in a rural area, during heating season. Based on these concentrations, the incremental lifetime cancer risk (ILCR) was calculated applying cancer slope factor (CSF) taken from [10] for the model.

II. Site Description

Zaječar is a city located in eastern Serbia with a population of approximately 44.000. Its economic development is primarily based on agriculture, as well as small food and metal processing industries. Less than 20% of households have central heating, meaning that most rely on individual heating systems, mostly wood and coal. This practice contributes significantly to air pollution, especially during the heating season, through the emission of soot, fine particles and PAHs.

Part of the sampling campaign was conducted in an elementary school located in the center of Zaječar (43°54'09"N 22°16'31"E), at a busy intersection on a busy street, making it directly affected by traffic emissions. The other sampling site was an elementary school in the village of Grljan, about 5 km from Zaječar. Grljan is a rural settlement characterized by individual housing, low building density, and the common use of solid fuels for heating (Fig. 1). In addition to residential heating, air pollution is also affected by nearby agricultural activities, a gravel separation plant, and a water treatment plant. Potential local sources of air pollution at this site (43°51'34"N 22°17'36"E) include septic tanks, individual household stoves, and animal barns, all of which can contribute to the emission of harmful pollutants into the surrounding environment.

Figure 1. Primary schools – in-situ measurement site locations, urban and rural.

III. Sampling and Chemical Analysis

The sampling campaign was conducted simultaneously in indoor and outdoor air at both school sites over one week during the heating season, in December 2011. Outdoor air sampling was conducted in the schoolyard and on the terrace, ensuring representative exposure to ambient conditions specific to the school environment. For indoor sampling, samples were collected in two different classrooms at each school, capturing variations in indoor air quality that may arise from differences in ventilation, classroom occupancy and activities.

Air samples were collected using a low-volume reference sampler Sven/LACKEL LVS3 (LVS), equipped with a size-selective inlet for $PM_{2.5}$ and operating on a 24-hour sampling cycle. The flow rate was set at 2.3 m^3/h (38 L/min), and 47 mm Whatman QMA quartz fiber filters were used to collect the $PM_{2.5}$.

Following sample collection, the filters were extracted using a 1:1 acetone: hexane mixture for 8 hours at 90 °C via microwave extraction. Internal standards were added prior to extraction to evaluate method recovery. The procedure for sample preparation and analysis followed the guidelines of the EPA Compendium Method TO-13A. Analysis of PAHs was carried out using gas chromatography coupled with mass spectrometry (GC-MS) with a DB-5 MS capillary column. The following sixteen US EPA priority PAHs were determined: naphthalene (Nap), acenaphthylene (Ace), acenaphthene (Ane), fluorene (Flu), phenanthrene (Phe), anthracene (Ant), fluoranthene (Fla), pyrene (Pyr), benz[a]anthracene (BaA), chrysene (Chy),

benzo[b]fluoranthene (BbF), benzo[k]fluoranthene (BkF), benzo[a]pyrene (BaP), dibenz[a,h]anthracene (DbA), benzo[g,h,i]perylene (BgP), and indeno[1,2,3-cd]pyrene (InP).

IV. Mathematical Modeling

A Monte Carlo simulation was applied to model the probabilistic incremental lifetime cancer risk (ILCR). The model was developed using MATLAB, a high-level programming language that provides improved performance in handling vector and matrix operations compared to commonly used spreadsheet-based tools. One of the key advantages of the probabilistic model is its ability to incorporate both variability and uncertainty into the risk assessment process, offering a more realistic estimation of long-term distribution of cancer risk compared with deterministic approach [11].

The model used the average concentrations of $PM_{2.5}$-bound PAHs measured in indoor and outdoor air to calculate the benzo[a]pyrene equivalent concentration (BaPeq). Based on these values, the daily inhalation exposure dose (E) for children and adults was determined using the following Eq. (1):

$$E = \sum_{i=1}^{2} C_i \cdot IR \cdot t_i . \qquad (1)$$

In this equation, i denotes the environment type (indoor or outdoor), E is the daily inhalation exposure dose for children or adults (mg/day), C_i is the BaPeq concentration in the respective environment (mg/m³), IR represents the average inhalation rate for children or adults (m³/h), and t_i is the average time spent daily in the i-th environment (h/day).

Subsequently, the ILCR was calculated using the following Eq. (2):

$$ILCR = \frac{CSF \cdot EF \cdot E \cdot ED}{AT \cdot BW} . \qquad (2)$$

Here, $ILCR$ represents the incremental lifetime cancer risk (dimensionless), CSF is the cancer slope factor for inhalation exposure to BaP (kg·day·mg^{-1}), EF is the exposure frequency (days/year), ED is the exposure duration (years), BW is the body weight (kg), and AT is the averaging time for carcinogenic effects (70 years, as recommended by US EPA, 1991).

TABLE I. Input risk parameters considered as random variables for different age groups in different environments.

Variable (measurement units)	Outdoor	Indoor	Distribution type
C_i [$ng \cdot m^{-3}$] (rural school)	7.35 ± 9.43	5.34 ± 4.79	Log-Normal
C_i [$ng \cdot m^{-3}$] (urban school)	82.98 ± 36.85	41.76 ± 20.76	Log-Normal
IR [$m^3 \cdot day^{-1}$]	9.98 ± 1.83 for children 14.27 ± 2.37 for adults		Log-Normal
t_i [$h \cdot day^{-1}$]	3	5	Constant
CSF [$kg \cdot day \cdot mg^{-1}$]	3.14 ± 1.80		Log-Normal
AT [$days$]	25500		Constant
ED [$years$]	3		Constant
BW [kg]	32.5 ± 7.1 for children 65.3 ± 6.2 for adults		Log-Normal

Each input variable was sampled independently from its appropriate distribution, as shown in Table I.

Totally one million Monte Carlo iterations were performed in order to obtain stable results. Also, multiple independent runs were performed with different numbers of Monte Carlo steps in order to ensure stable solution: 5e+04, 1e+05, 5e+05, 1e+06, and 2e+06. Stability of results was achieved for the case of one million Monte Carlo simulations. The convergence of the model was achieved by monitoring the convergence of the mean and 95th percentile ILCR values. Convergence was confirmed when relative changes between consecutive iteration blocks (<2%) were observed.

This approach utilized a fitted log-normal distribution of CSF for the benzo[a]pyrene equivalent (BaPeq) according to [10]. The model yielded stable results.

V. Results and Discussion

Average concentrations of PAHs were measured in both indoor and outdoor air at two schools, one located in a rural area and the other in an urban area, during the heating season. The results show clear differences in PAH levels between the two environments, highlighting the influence of local emission sources and

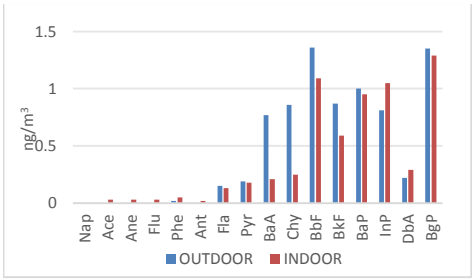

Figure 2. Average outdoor and indoor concentrations of individual PAHs in the rural school.

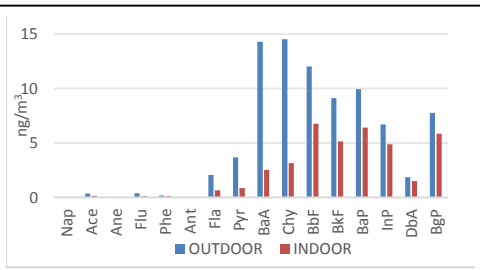

Figure 3. Average outdoor and indoor concentrations of individual PAHs in the urban school.

environmental conditions on air quality. The results are summarized in Figs. 2. and 3.

At the rural school, the total PAH concentration, expressed as the sum of all quantified PAH compounds, was 7.35 ± 9.43 ng/m³ in outdoor air and 5.34 ± 4.79 ng/m³ in indoor air. In comparison, significantly higher concentrations were observed at the urban school, with values of 82.98 ± 36.85 ng/m³ outdoors and 41.76 ± 20.76 ng/m³ indoors. These results indicate that both indoor and outdoor PAH levels were significantly elevated in the urban environment compared to the rural environment, with outdoor concentrations exceeding indoor levels at both sites.

In the urban school, outdoor PAH concentrations were higher than those indoors, reflecting the influence of dominant outdoor sources such as traffic emissions, domestic heating, and other urban combustion-related activities in the urban area. The PAH profile observed at the urban school, where BaA, Chy, and BbF were dominant, clearly indicates that vehicular traffic is the major emission source. These compounds are typically formed at high combustion temperatures and are characteristic of exhaust from motor vehicles [2]. However, it is important to note that the urban environment is also influenced by emissions from residential heating, particularly from individual household stoves and boilers using solid fuels. During the heating season, such sources can significantly contribute to ambient PAH levels, especially during periods of low atmospheric dispersion. Thus, although the dominant PAH profile (BaA, Chy, BbF) points primarily to traffic-related combustion, the concurrent presence of compounds commonly associated with lower-temperature combustion suggests a mixed contribution of both traffic and domestic heating sources [2,4].

In contrast, the rural school samples were dominated by BbF and BgP. This profile indicates a stronger influence of residential heating, likely from the use of solid fuels such as wood or coal, combined with minor contributions from local traffic. While BbF can originate from both vehicle emissions and heating, BgP is more characteristic of incomplete combustion processes at lower temperatures, typical of household stoves and fireplaces [2,4,12].

Therefore, while clear differences are visible between the two environments, the urban site should not be interpreted as exclusively traffic-driven. Rather, it represents a complex mixture of emission sources, where intense traffic near the intersection is the dominant contributor, but residential heating still exerts a measurable secondary influence on overall PAH concentrations.

In contrast, outdoor PAH concentrations were also generally higher in the rural school, but certain compounds, especially Ind, DbA, and some medium-weight PAHs containing three or four aromatic rings, were detected at higher concentrations indoors. This suggests the presence of indoor emission sources or the accumulation of pollutants in indoor environments due to reduced ventilation during the heating season.

The observed distribution of PAHs between indoor and outdoor environments also reflects their physicochemical properties. Low molecular weight PAHs, characterized by higher volatility, are predominantly present in the gas phase and less likely to be attached on $PM_{2.5}$. In contrast, high molecular weight PAHs, with lower vapor pressures, tend to associate with particulate matter and are more reliably collected in $PM_{2.5}$ samples.

The partitioning of PAHs between the gas and particulate phases is influenced by several environmental factors, including ambient temperature, relative humidity, and the presence of atmospheric oxidants [4,12,13]. As a result, the PAH concentrations reported in this study represent the fraction of PAHs bound to $PM_{2.5}$ particles. Given the tendency of lighter PAHs to remain in the gaseous phase, their total concentrations in air are likely underestimated using this method.

These results show the significantly higher exposure potential to particle-bound PAHs in urban environments, particularly during the heating season, and highlight the need to consider both indoor and outdoor sources when assessing total PAH exposure in school settings. Additionally, exposure assessments should consider the presence of PAHs in the gaseous phase.

Figs. 4. and 5 present ILCR probability histograms for rural and urban schools with Gamma-fitted distributions. Both the Gamma and Weibull distributions were applied during the modeling, and yielded comparable results, with the Gamma distribution selected for the final presentation due to its better visual fit.

ILCR values calculated for both the rural and urban school remained below the generally accepted threshold of $1 \cdot 10^{-6}$, according to US EPA's guidance, which is considered an acceptable risk level for long-term carcinogenic exposure via inhalation. Nevertheless, a clear distinction was observed between the two sites: ILCR values associated with the urban school environment were significantly higher than those recorded in the rural setting. This difference stems from the significantly higher concentration of PM2.5-bound PAHs detected in the urban school, indicating an increased level of exposure and consequently a higher potential health risk for individuals in urban areas, especially children.

Although below the critical risk threshold, elevated ILCR values in urban environments deserve attention. Continuous exposure to higher PAH concentrations, especially during heating season when combustion sources are intensified, could contribute to a cumulative increase in health risks over time. This is especially important in school environments, where children spend a significant portion of the day indoors and are more susceptible to the adverse health effects of air pollutants due to physiological vulnerability and longer life expectancy. ILCR estimates based on a deterministic approach using a single CSF, usually benzo[a]pyrene, as a reference compound for the carcinogenic potential of PAHs were calculated next. To show the difference between deterministic and probabilistic approaches, the risk assessment was also arranged using constant values for all variables. For the concentrations of PAHs, their mean value was used, and for the CSF, a value of 3.14 was used. Also BW and IR are used as constant values. Under these conditions, the values of the ILCR for children were 1.63e-8 for the rural school and 1.35e-7 for the urban school. ILCR values for adults for urban and rural schools were 1.16e-8 and 9.56e0-8, respectively. Also, the ILCR values for children and adults together were 2.8e-8 for the rural school and 2.3e-7 for the urban school. It is clearly seen that all values are lower compared to the probabilistic model. The results obtained from the two models, deterministic and probabilistic, were compared in the next step of this work. It was shown that the probabilistic solution`s percent difference was higher for about 23.3% and 28.7% compared to the deterministic model.

This discrepancy carries significant methodological and practical implications. The higher ILCR values obtained from the probabilistic approach indicate that the

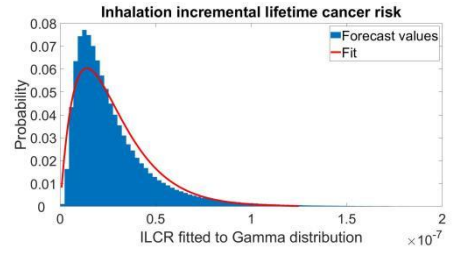

Figure 4. ILCR probability histogram fitted with Gamma distribution for rural school.

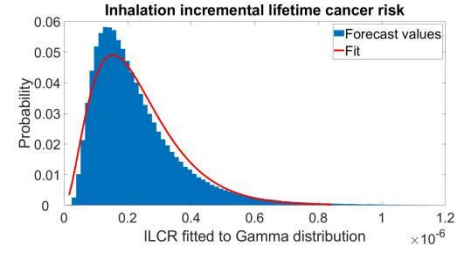

Figure 5. ILCR probability histogram fitted with Gamma distribution for urban school.

deterministic model systematically underestimates carcinogenic risk associated with PAH exposure. Such underestimation may lead to overly optimistic assessments of air quality and, if used for policy-making, could result in insufficient or delayed mitigation actions by local authorities.

The probabilistic approach, by contrast, provides a more conservative and realistic estimation by accounting for the variability and uncertainty of key input parameters such as PAH concentrations, IR and CSF values. This results in a more robust basis for public health decision-making and risk management, particularly in urban environments characterized by complex and fluctuating emission patterns. Therefore, the choice of the risk assessment model should be recognized not only as a technical consideration but as a critical determinant of the reliability and credibility of health risk evaluations.

However, this approach may oversimplify risk assessment, as it does not account for the realistic distribution of multiple CSF values for individual PAH compounds. A more precise risk assessment can be achieved by applying a probabilistic ILCR model that includes variable CSF for individual PAHs, as defined by the US EPA. Future work will include applying this approach to improve the resolution and accuracy of health risk characterization.

CSF values can vary between studies and regulatory agencies (US EPA, WHO), and this difference has a significant impact on the results obtained in the model. In this work, as already mentioned, the US EPA recommended value for CSF of 3.14 was used. Additionally, changes in ventilation, exposure time, and children's activities can impact the risk assessment. Differences in distributions, PAH concentrations, and inhalation rates also contribute to the uncertainty of the model.

Sensitivity analysis identified daily inhalation exposure and CSF as the most influential parameters affecting the variability of ILCR estimates. Notably, the application of the probabilistic model reduces the dependence of the model on a single CSF value, thereby increasing its robustness and representativeness in risk estimation. This is particularly important in heterogeneous environments where both PAH concentration and exposure patterns vary over time.

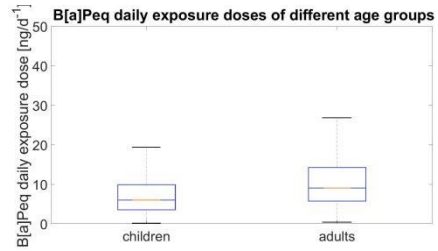

Figure 6. BaPeq daily exposure doses [ng·d^{-1}] for children and adults' total exposure for rural school.

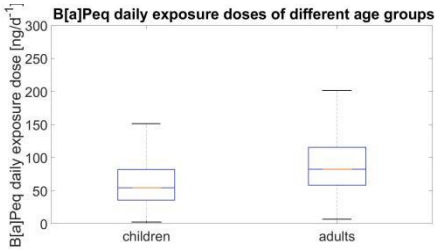

Figure 7. BaPeq daily exposure doses [ng·d^{-1}] for children and adults' total exposure for urban school.

Daily exposure to benzo[a]pyrene equivalent concentrations (BaPeq) was calculated for different population groups and environmental settings, including both indoor and outdoor concentrations and taking into account typical time-activity patterns during the school day (Figs. 6 and 7). The results show that adults exhibit higher daily inhalation doses compared to children, primarily due to higher breathing rates. However, the long-term health impact remains more critical for children, considering their heightened biological sensitivity and the potential for cumulative exposure during early developmental stages.

Based on assumed exposure durations of approximately 5 hours spent indoors (within school buildings) and 3 hours outdoors, the results show that indoor environments contribute significantly to total daily exposure, particularly in urban areas where elevated indoor BaPeq concentrations were observed. This trend emphasizes the importance of indoor air quality management, particularly in educational institutions where children represent a target vulnerable population.

A comparative analysis of exposure levels in two schools reveals that urban environments pose a significantly higher carcinogenic risk than rural ones, both indoors and outdoors. These

findings highlight the critical need for air quality improvement strategies aimed at reducing emissions from urban sources such as traffic and residential heating, as well as improving indoor air filtration and ventilation systems in schools.

These results underscore the importance of comprehensive air quality management strategies in urban areas, including stricter control of PAH emission sources, enhanced ventilation in school buildings, and the implementation of continuous indoor air monitoring programs.

VI. Conclusion

This study provides a comparative assessment of inhalation exposure to $PM_{2.5}$-bound PAHs and the associated carcinogenic risk in rural and urban school environments during the heating season. The results show significantly higher concentrations of PAHs and consequently higher ILCR values in the urban environment. Although the ILCR values calculated using both deterministic and probabilistic models remained below the generally accepted carcinogenic risk threshold of $1 \cdot 10^{-6}$, the values observed in the urban school point to non-negligible long-term health risks, particularly for vulnerable populations such as children.

The probabilistic ILCR model applied in this study offers a more realistic representation of exposure variability by incorporating uncertainty and sensitivity effects. Sensitivity analysis confirmed that inhalation rate and cancer slope factor are the dominant variables influencing ILCR values, with the CSF alone accounting for a significant portion of the variability. This finding underscores the limitations of conventional approaches that rely on a single or uniform CSF, and emphasizes the importance of developing more refined, compound-specific risk models. The probabilistic model produced higher ILCR values compared to deterministic approach. One limitation of the current probabilistic model is the incomplete set of CSF values available for several PAH compounds. Future studies should focus on expanding the toxicological database and deriving reliable CSF estimates for additional PAHs. Furthermore, the probabilistic model could be extended to evaluate cumulative risks from multiple air pollutants, allowing consideration of additive exposure from co-occurring air pollutants, such as heavy metals. Such an extension would provide a more comprehensive assessment of potential health impacts in school environments and offer additional guidance for protecting vulnerable populations, particularly children.

These results have broader implications for urban air quality management and public health policy. Elevated PAH concentrations in urban areas highlight the need for integrated strategies addressing traffic emissions, residential heating, and indoor air quality. The study underscores the importance of continuous air monitoring, stricter emission regulations, and targeted interventions in areas where vulnerable populations, such as children, spend significant time. By providing quantitative evidence of exposure and risk, this work can inform policymakers and urban planners in designing more effective measures to protect public health and reduce long-term carcinogenic risks in urban populations.

Taken together, the results give a clearer picture of how well current risk assessment approaches actually work and where they still fall short. They also show that detailed exposure studies are not just a technical exercise, they also offer real evidence that can guide local authorities and health agencies when deciding how to improve air quality and protecting vulnerable populations.

Acknowledgment

This work was funded by the Ministry of Education, Science and Technological Development of the Republic of Serbia under GA 451-03136/2025-03/200017.

References

[1] European Environment Agency. (2024). Europe's air quality status 2024. *European Environment Agency* (EEA). https://doi.org/10.2800/5970

[2] Ravindra, K., Sokhi, R., & Van Grieken, R. (2008). Atmospheric polycyclic aromatic hydrocarbons: Source attribution, emission factors and regulation. *Atmospheric environment*, *42*(1), 2895-2921.

[3] Kim, K.H., Kabir, E., & Kabir, S. (2015). A review on the human health impact of airborne particulate matter. *Environment international*, *74*(1), 136-143.

[4] Oliveira, M., Slezakova, K., Delerue-Matos, C., Pereira, M.C., & Morais, S. (2019). Children environmental exposure to particulate matter and polycyclic aromatic hydrocarbons and biomonitoring in school environments: a review on indoor and outdoor exposure levels, major sources and health impacts. *Environment international*, *124*(1), 180-204. https://doi.org/10.1016/j.envint.2018.12.052

[5] Jovanovic, R., & Zivkovic, M. (2020). Probabilistic simulation of incremental lifetime cancer risk of children and adults exposed to the polycyclic aromatic hydrocarbons – PAHs in primary school environment in Serbia, model development and validation. In N.

Mitrovic, M. Milosevic, & G. Mladenovic (Eds.), *Computational and experimental approaches in materials science and engineering* (Lecture Notes in Networks and Systems, Vol. 90, pp. 195–216). Springer, Cham. https://doi.org/10.1007/978-3-030-30853-7_12

[6] Gungormus, E., Tuncel, S., Hakan Tecer, L., & Sofuoglu, S.C. (2014). Inhalation and dermal exposure to atmospheric polycyclic aromatic hydrocarbons and associated carcinogenic risks in relatively small city. *Ecotoxicology and Environmental Safety*, *108*(1), 106-113. https://doi.org/10.1016/j.ecoenv.2014.06.015

[7] Yu, Y., Li, Q., Wang, H., Wang, B., Wang, X., Ren, A., & Tao, S. (2015). Risk of human exposure to polycyclic aromatic hydrocarbons: A case study in Beijing, China. *Environmental pollution*, *205*(1), 70-77. https://doi.org/10.1016/j.envpol.2015.05.022

[8] Han, B., et al. (2016). Assessing the inhalation cancer risk of particulate matter bound polycyclic aromatic hydrocarbons (PAHs) for the elderly in a retirement community of a mega city in North China. *Environmental Science and Pollution Research*, *23*(20), 20194-20204. https://doi.org/10.1007/s11356-016-7209-9

[9] Wang, T., et al. (2017). Pollution characteristics, sources and lung cancer risk of atmospheric polycyclic aromatic hydrocarbons in a new urban district of Nanjing, China. *Journal of Environmental Sciences*, *55*(1), 118-128. https://doi.org/10.1016/j.jes.2016.06.025

[10] Chen, S.C., & Chung-Min L. (2006). Health risk assessment on human exposed to environmental polycyclic aromatic hydrocarbons pollution sources. Science of the Total Environment, 366(1), 112-123. https://doi.org/10.1016/j.scitotenv.2005.08.047

[11] Chew, G. & Walczyk, T. (2012). A Monte Carlo approach for estimating measurement uncertainty using standard spreadsheet software. *Analytical and bioanalytical chemistry*, *402*(7), 2463-2469. https://doi.org/10.1007/s00216-011-5698-4

[12] Krugly, E., Martuzevicius, D., Sidaraviciute, R., Ciuzas, D., Prasauskas, T., Kauneliene, V., Stasiulaitiene, I., & Kliucininkas, L. (2014). Characterization of particulate and vapor phase polycyclic aromatic hydrocarbons in indoor and outdoor air of primary schools. *Atmospheric Environment*, *82*, 298-306. https://doi.org/10.1016/j.atmosenv.2013.10.042 Kim

[13] K.-H., Jahan, S.A., Kabir, E., & Brown, R.J.C. (2013). A review of airborne polycyclic aromatic hydrocarbons (PAHs) and their human health effects. *Environment International*, *60*, 71-80. https://doi.org/10.1016/j.envint.2013.07.019

eNergetics 2025
DOI: https://doi.org/10.5281/zenodo.18623814

Original Scientific Article

Prioritized Objective Hierarchies for Sustainable and Resilient Microgrid Energy Management

Musa Terkeş[1], Alpaslan Demirci[2], Erdin Gökalp[3]

[1,2,3]Department of Electrical Engineering, Yildiz Technical University, İstanbul, Türkiye

[1]musa.terkes@yildiz.edu.tr, [2]ademirci@yildiz.edu.tr, [3]gokalp@yildiz.edu.tr

Abstract—**Renewable energy resources are becoming more prevalent in modern microgrids. This means that operators face a growing need for optimization strategies. These strategies must balance technical, economic and environmental objectives. This is especially true when battery degradation is considered. Researchers are struggling to achieve this balance between short-term cost savings and long-term system durability. The issue is addressed in this study through the implementation of a two-stage approach. In the first stage, photovoltaic (PV) capacity and battery size are determined using particle swarm optimization (PSO) to ensure both economic feasibility and realistic lifecycle performance. A mixed-integer linear programming (MILP) model implemented in Python through Gurobi is employed in the second stage for the management of daily energy operations. The analysis examines how different objective-function priorities affect prosumers with varied consumption and generation profiles in a multi-stage microgrid setting. A comparison is made between three alternative formulations. (i) minimizing operating costs, (ii) preserving battery health and (iii) maximizing renewable energy use, as well as combined bi- and tri-objective versions. Simulation outcomes show that the ranking of objectives strongly shapes system performance, which is important to consider when designing and implementing systems. Indicators such as self-consumption, self-sufficiency, curtailed power, CO2 emissions and storage ageing show variations. Overall, practical guidance is offered by the findings for engineers and planners aiming to design energy-management strategies that link immediate operational goals with long-term sustainability and resilience in prosumer-oriented microgrids.**

Keywords - microgrid energy management, multi-stage optimization, prioritized objective hierarchies, battery aging model, cycle and calendar degradation.

I. INTRODUCTION

Renewable energy sources are becoming a larger part of modern power systems, especially through the growth of microgrids that operate independently. These microgrids, which are often set up in remote or rural areas, bring together distributed generation, energy storage, and controllable demand. This combination helps to keep the local energy system reliable and independent [1]. Renewables make a clean and reliable power supply possible, but they also cause problems. These problems include changes in how much power is produced, costs that are hard to predict, and problems making sure the system works well. These challenges require optimization frameworks that can guarantee sustainable and profitable operation [2]. Conventional single-objective control strategies are often designed for cost minimization. They fail to manage the multiple, sometimes conflicting, goals of microgrid operation under high renewable penetration [3]. To address these limitations, multi-objective approaches have been increasingly adopted by researchers that jointly consider economic, environmental, and technical performance [4].

ISBN: 978-86-82602-07-1

Researchers have recently investigated the potential of heuristic and metaheuristic optimization algorithms to improve the performance of microgrid scheduling. For instance, advanced techniques like the oppositional gradient-based grey wolf optimizer (OGGWO) have demonstrated the ability to prevent premature convergence and attain robust solutions for cost reduction and emission control [5]. In a similar way, hybrid metaheuristic frameworks, such as the predatory pelican optimization algorithm (PPOA), have shown significant advancements in cost and emission performance while preserving grid stability [2]. Multi-stage and hybrid control architectures build on these efforts by introducing dynamic energy management across multiple time horizons, achieving consistent results in both grid-connected and islanded operating modes [6-10].

Additionally, value-based objective formulations have assisted microgrid operators in identifying balanced, Pareto-optimal trade-offs among competing criteria, which reduces renewable intermittency and improves service reliability [3]. The addition of demand-response (DR) schemes, like real-time pricing and direct load control, has made the system even more flexible. This has resulted in noticeable decreases in cost, emissions, and energy losses [4,11,12]. Finally, studies that focus on uncertainty management and strong optimization have shown that it is very important to plan for changes in the generation and demand of electricity. This is necessary for microgrids to be reliable and strong [13,14].

At the same time, many recent studies emphasize that battery aging and degradation should be treated as key factors in long-term microgrid planning. Disregarding these effects frequently results in impractical outcomes, increased lifetime expenses, and a reduction in system dependability [15]. In response, several works have proposed layered optimization methods that integrate battery health with economic and environmental goals. These methods underscore the need for frameworks that weigh short-term financial performance against long-term technical stability [16,17].

Despite these advances, there is still no clear consensus on how multi-stage objective functions should be structured and prioritized for prosumers operating within microgrids. The research findings indicate that a balanced outcome across cost, environmental, and technical criteria is achieved with a two-layer configuration or a three-layer configuration. In particular, further study is warranted by the trade-offs among electricity cost minimization, battery health preservation, and renewable energy utilization, especially in systems with diverse consumption and generation behaviors.

The question is addressed in this study through an examination of the selection and prioritization of multi-stage objectives using a Mixed-Integer Linear Programming (MILP) model. This model is implemented through the Gurobi solver in Python. The analysis offers practical insight. It looks at how different combinations of objectives affect the economic, environmental, and technical feasibility of microgrid operation. It considers various scenarios. In doing so, the work contributes not only to the methodological development of optimization-based microgrid management but also to the creation of a decision-support tool aimed at improving the long-term sustainability of prosumer-oriented energy systems.

II. Mathematical Modeling, Optimization Framework, and Performance Metrics

The optimization process was carried out in a Python environment. The Gurobi solver was used. Synthetic datasets were prepared. These datasets represent both electrical demand and photovoltaic (PV) generation. The case study location was Antalya, a region with high solar potential. PV production data were derived from satellite-based reanalysis and irradiance sources. These sources include SARAH and ERA5. The city's coordinates were used to access the PVGIS database. At the same time, HOMER software was used to make electricity use profiles. This software looks at random and repeated patterns. The optimal capacities of PV and energy storage systems (ESS) were determined using Particle Swarm Optimization (PSO), as outlined in [18]. The objective was to reduce both electricity and lifecycle costs (LCC). The resulting PV capacities for the five prosumers were 5, 5, 4, 5, and 4.5 kW, while the corresponding ESS capacities were 4, 5.5, 5.5, 5.5, 3, and 4 kWh, respectively. These parameter values formed the basis for subsequent simulations and performance evaluations within the proposed framework.

In the Gurobi-based energy management framework, hourly load and PV generation data are imported from Excel files as model inputs. For each prosumer k and time step t, the total load demand ($P_{k,t}^{L}$) is met through contributions from PV-to-load ($P_{k,t}^{PV2L}$), ESS-to-load ($P_{k,t}^{B2L}$), and grid-to-load ($P_{k,t}^{G2L}$), as shown in (1). Simultaneously, the total PV generation ($P_{k,t}^{PV_{gen}}$) is distributed among $P_{k,t}^{PV2L}$, PV-to-ESS ($P_{k,t}^{PV2B}$), PV-to-grid ($P_{k,t}^{PV2G}$), and curtailed energy ($P_{k,t}^{PV_{cur}}$), following Eq. (2).

$$P_{k,t}^{L} = P_{k,t}^{PV2L} + P_{k,t}^{B2L} + P_{k,t}^{G2L}, \quad \forall k,t, \quad (1)$$

$$P_{k,t}^{PV_{gen}} = P_{k,t}^{PV2L} + P_{k,t}^{PV2B} + \\ + P_{k,t}^{PV2G} + P_{k,t}^{PV_{cur}}, \quad \forall k,t \quad (2)$$

To reduce grid stress, PV export ($P_{k,t}^{PV2G}$) is limited to 40% of the installed PV capacity (C_k^{PV}), even when higher exports could be economically favorable, as expressed in (3). The total energy exported to the grid ($P_{k,t}^{G_{injected}}$), combining PV and ESS contributions ($P_{k,t}^{B2G}$), is managed through a binary variable u_{t1}, which prevents simultaneous buying and selling of power Eqs. (4)–(6). Another binary variable u_{t2} ensures that ESS charging and discharging do not occur at the same time, as represented in Eqs. (7) and (8). Constants M and c are introduced to linearize these relationships while maintaining the state-of-charge (SoC) boundaries.

$$P_{k,t}^{PV2G} \le 40\% C_k^{PV}, \quad \forall k,t, \quad (3)$$

$$P_{k,t}^{G_{injected}} = P_{k,t}^{PV2G} + P_{k,t}^{B2G}, \quad \forall k,t, \quad (4)$$

$$P_{k,t}^{G_{injected}} \le M\, u_{t1}, \quad \forall k,t, \quad (5)$$

$$P_{k,t}^{G_{used}} = P_{k,t}^{G2L} \le M\left(1-u_{t1}\right), \quad \forall k,t, \quad (6)$$

$$P_{k,t}^{ESS_{chr}} \le c\, u_{t2}, \quad \forall k,t, \quad (7)$$

$$P_{k,t}^{ESS_{disch}} = c\left(1-u_{t2}\right), \quad \forall k,t. \quad (8)$$

The state of energy (SoE) of each ESS unit ($SoE_{k,t}^{ESS}$) evolves according to Eq. (9), which accounts for charging and discharging power and their efficiencies (η_{chr} and η_{disch}). The SoC is constrained between 20% and 90%. Battery degradation mechanisms are modeled through cycle aging ($Q_{k,t}^{cyc}$) and calendar aging ($Q_{k,t}^{cal}$), as described in [19] and [20]. The cumulative degradation ($Q_{k,t}^{tot}$) and the effective ESS capacity at time t ($C_{k,t}^{ESS_{new}}$) are computed using Eqs. (12) and (13). Here, $L_{k,t}^{cyc}$ indicates the expected battery lifetime, while $P_{k,t}^{ESS_{chr}}$ and $P_{k,t}^{ESS_{disch}}$ represent charging and discharging powers, respectively. The empirical coefficients in these degradation equations are based on experimental data reported in previous studies.

$$SoE_{k,t}^{ESS} = SoE_{k,t-1}^{ESS} + \\ + P_{k,t}^{ESS_{chr}}\eta_{chr} - \frac{P_{k,t}^{ESS_{disch}}}{\eta_{disch}}, \quad \forall k,t, \quad (9)$$

$$Q_{k,t}^{cyc} = \frac{1}{2}\sum_{k,t}\frac{\eta_{chr}P_{k,t}^{ESS_{chr}} - \eta_{disch}P_{k,t}^{ESS_{disch}}}{L_{k,t}^{cyc}\, C_k^{ESS}}, \quad \forall k,t \quad (10)$$

$$Q_{k,t}^{cal} = \sum_{k,t} 6.6148.10^{-6} P_{k,t}^{ESS} + \\ + 4.6404.10^{-6}, \quad \forall k,t \quad (11)$$

$$Q_{k,t}^{tot} = Q_{k,t}^{cyc} + Q_{k,t}^{cal}, \quad \forall k,t, \quad (12)$$

$$C_{k,t}^{ESS_{new}} = C_k^{ESS}\left(1-Q_{k,t}^{tot}\right), \quad \forall k,t. \quad (13)$$

In this study, three objective functions are examined. For the third objective, which aims to maximize renewable utilization, specific variables and constraints are defined. Equation (14) expresses the renewable power contribution ($P_{k,t}^{RE}$), obtained from the cumulative power delivered from $P_{k,t}^{PV2L}$ and $P_{k,t}^{PV2B}$. Equation (15) defines the total electrical load served ($P_{k,t}^{LS}$), which aggregates the contributions of PV, ESS,

and grid power. Finally, Eq. (16) calculates the renewable fraction (RF) as the ratio of renewable-supplied energy ($P_{k,t}^{RE}$) to total demand.

$$P_{k,t}^{RE} = \sum_{k,t} P_{k,t}^{PV2L} + P_{k,t}^{PV2B} , \quad \forall k,t , \quad (14)$$

$$P_{k,t}^{LS} = \sum_{k,t} P_{k,t}^{PV2L} + P_{k,t}^{PV2B} + P_{k,t}^{G2L} , \quad \forall k,t , \quad (15)$$

$$P_{k,t}^{RE} = RF\, P_{k,t}^{LS} , \quad \forall k,t . \quad (16)$$

The cost minimization problem is formulated in (17). It includes grid purchase costs based on a three-tier time-of-use (ToU) tariff ($P_{k,t}^{G_{used}} \mathrm{Cos}t_{k,t}^{GP}$), revenues from grid exports at a fixed rate ($P_{k,t}^{G_{injected}} \mathrm{Cos}t_{k,t}^{GS}$), lifecycle costs (LCC) of PV and ESS capacities ($C_{k,t}^{ESS_{new}} LCC_{k,t}^{ESS}$ and $C_k^{PV} LCC_{k,t}^{PV}$), and the depreciation of ESS components $\left(\left(C_k^{ESS} - C_{k,t}^{ESS_{new}}\right)\mathrm{Cos}t_{k,t}^{depr.}\right)$. The analysis evaluates which bi-objective or tri-objective combination implemented in Python–Gurobi yields the most balanced results for prosumers with distinct consumption and production profiles.

The optimization framework prioritizes different objectives across three configurations:

- **Objective 1:** cost minimization as the primary goal, with battery health preservation as secondary.
- **Objective 2:** reverse prioritization, battery health first, cost minimization second.
- **Objective 3:** RF maximization as the leading objective, followed by cost minimization, and optionally ESS health preservation.

Accordingly, the three objective functions under consideration are introduced from Eqs. (18) to (20).

$$TC_{k,t}^{MG} = P_{k,t}^{G_{used}} \mathrm{Cos}t_{k,t}^{GP} - P_{k,t}^{G_{injected}} \mathrm{Cos}t_{k,t}^{GS} + \\ + C_{k,t}^{ESS_{new}} LCC_{k,t}^{ESS} + C_k^{PV} LCC_{k,t}^{PV} + \\ + \left(C_k^{ESS} - C_{k,t}^{ESS_{new}}\right)\mathrm{Cos}t_{k,t}^{depr.}, \ \forall k,t \quad (17)$$

$$objective\ 1 = \min\left(\sum_{k,t}\left(TC_{k,t}^{MG}\right)\right), \quad (18)$$

$$objective\ 2 = \min\left(\sum_{k,t}\left(TC_{k,t}^{MG} + Q_{k,t}^{tot} N\right)\right), (19)$$

$$objective\ 3 = \min\left(\sum_{k,t}\left(TC_{k,t}^{MG} - RF.K\right)\right). (20)$$

Trade-offs among economic, environmental, and technical outcomes can be evaluated through the use of these objective structures. Tariff rates are set to 0.0767 \$/kWh from 6:00 a.m. to 5:00 p.m., 0.112 \$/kWh from 5:00 p.m. to 8:00 p.m., and 0.04854 \$/kWh from 8:00 p.m. to 6:00 a.m. The grid sale is set at 0.04 \$/kWh, and the lifecycle cost estimation follows the procedure outlined in [18].

The Gurobi solver in Python was used to solve the optimization problems. Subsequent to each iteration, the results were exported to Excel as hourly datasets for all prosumers and analyzed according to the evaluation metrics summarized in Table I.

These performance metrics include the unit cost of electricity (COE), the RF, the self-consumption ratio (SCR), the self-sufficiency ratio (SSR), the carbon emissions (CO_2), and the curtailed energy (CE). A detailed basis for evaluating the operational behavior of the microgrid under different optimization strategies is provided by these indicators.

The unit cost of electricity (COE, \$/kWh) is calculated by dividing the total operating cost of the microgrid by the total demand for electricity across all time periods. The RF expresses the portion of total demand that renewable sources

TABLE I. DECISION CRITERIA.

Metric	Formulation	Metric	Formulation
COE	$\frac{\sum Total\,\mathrm{Cos}t}{\sum P_{load}}$	SCR	$\frac{\int P_{PV}dt - \int P_F dt}{\int P_{PV}dt}$
RF	$1 - \frac{\sum(P_{GP})}{\sum(P_{load})}$	SSR	$\frac{\int P_L dt - \int P_G dt}{\int P_L dt}$
CO_2	$0.4261 \sum P_{GP}$	CE	$\sum P_{k,t}^{PV_{cur}}$

supply. It is determined by subtracting the electricity imported from the utility grid from the total load and then normalizing the remainder with respect to total demand. The amount of CO_2 released per kilowatt-hour of imported grid electricity in Turkey is estimated to be around 0.426 kg. This is used as a basis for the country's carbon accounting. CO_2 associated with microgrid operation are estimated using this factor.

During periods when PV generation exceeds instantaneous load, the exported energy (P_F) represents the residual power remaining after local demand is satisfied and the ESS has been charged. In other words, it is the difference between PV generation, ESS discharge, and the load requirement. Conversely, when the load surpasses PV output, the imported energy (P_G) is defined as the deficit between the total demand and the combined supply from PV and ESS.

The SCR measures how efficiently the system uses on-site PV energy. It is calculated by determining the part of PV generation that isn't exported to the grid and then dividing it by the total PV output. The SSR is a different measure. It shows the share of total demand met by local generation and storage. In other words, it is the fraction of demand that does not rely on grid supply. Thus, PV utilization efficiency is evaluated by SCR, while the degree of grid independence is indicated by SSR.

Finally, when PV generation exceeds both the load requirement and the available ESS storage capacity, the system records any unutilized energy as waste energy. CE is expressed as a percentage of total PV generation. It serves as an indicator of renewable energy losses. These losses are caused by storage and load limitations.

III. Optimization Results and Discussion

The results of the multi-stage microgrid optimization are shown in Table II. This table lists the most important performance measurements for the three objective formulations. These include COE, SCR, SSR, RF, CE, CO_2 , and the cumulative battery degradation. The findings are further complemented by Table III, which provides a ranking of the three formulations based on their techno-economic and environmental performance. This ranking offers a comparative perspective on the trade-offs among competing objectives.

According to Table II, the lowest COE, 0.03055 $/kWh, is yielded by Objective 1, which places primary emphasis on minimizing operational cost, while moderate SCR and SSR values of 21.6% and 28.98%, respectively, are maintained. Objective 2 gives priority to maintaining ESS health. It produces a higher COE of 0.0484 $/kWh. However, it substantially decreases battery aging to 0.1046%. This suggests that extending the storage system's lifespan comes with a higher operating cost. The goal of objective 3 was to use renewable energy as much as possible. It achieves the highest RF at 77.32%, along with significant improvements in SCR (56.34%) and SSR (75.61%). However, this enhanced renewable contribution comes with a higher cost of 0.06631 $/kWh and accelerated battery wear of 0.35494%.

Overall, the comparison highlights the expected trade-offs among economic efficiency, renewable energy integration, and energy-storage durability. The results suggest that no single configuration universally dominates. Instead, the optimal choice depends on whether cost savings, renewable penetration, or asset ESS lifetime is prioritized within the specific microgrid context.

The three objective functions' comparative performance is summarized in Table III. Objective 3 is the most successful in increasing the renewable energy fraction and the amount of local PV utilization. Objective 1 is the most successful in cost-related metrics and reducing the amount of curtailed energy.

The results for battery-aging mitigation are strongest for Objective 2, which emphasizes extending storage lifespan. These rankings indicate that no single formulation can optimize all metrics at once. This reinforces the need for multi-stage optimization strategies. These strategies should balance the diverse priorities of different prosumers. When the results are interpreted in light of existing research, they align with recent literature advocating for multi-objective and hierarchical optimization for renewable-intensive microgrids. The observed tension between increasing renewable usage and

TABLE II. PERFORMANCE METRICS UNDER MULTI-STAGE OBJECTIVE FUNCTIONS.

Objective Function	COE ($/kWh)	SCR (%)	SSR (%)	RF (%)	CE (%)	CO_2 (kg/yr)	Aging (%)
1	0.03055	21.6	28.98	65.53	0.67	71.61	0.176449
2	0.0484	8.3	11.13	46.98	9.92	92.69	0.104598
3	0.06631	56.34	75.61	77.32	27.16	70.24	0.35494

TABLE III. RANKING OF OBJECTIVE FUNCTION PERFORMANCE ACROSS KEY INDICATORS.

Objective Function Ranking	COE	SCR	CE	RF	CO_2	Aging
1	Objective 1	Objective 3	Objective 1	Objective 3	Objective 3	Objective 2
2	Objective 2	Objective 1	Objective 2	Objective 1	Objective 1	Objective 1
3	Objective 3	Objective 2	Objective 3	Objective 2	Objective 2	Objective 3

limiting battery degradation mirrors challenges discussed in hybrid optimization studies. These include PSO-based capacity design and multi-level energy management frameworks. Moreover, it has been demonstrated that energy autonomy can be significantly strengthened and grid dependency can be reduced by targeted objective hierarchies, as shown by the higher SCR and SSR values achieved under Objective 3. This outcome is aligned with the resilience goals highlighted in prior works.

In summary, the comparative analysis suggests that each system operator should choose an objective structure that reflects their priorities. Those responsible for decision-making who prioritize short-term economic benefits may favor configurations similar to Objective 1. However, those seeking to maintain ESS durability might find approaches similar to Objective 2 more beneficial. On the other hand, operators aiming to maximize renewable integration might adopt a structure similar to Objective 3. The framework developed in this study is implemented in Python with the Gurobi solver. This provides a systematic and flexible means of tailoring multi-objective optimization to practical microgrid planning needs.

IV. CONCLUSION AND FUTURE SUGGESTIONS

This study shows that how people structure and prioritize multi-stage objective functions has a decisive influence on the economic, technical, and environmental behavior of renewable-based microgrids. The results of the comparison show that the best performance across key indicators is achieved by a three-stage configuration. In this configuration, renewable energy utilization is prioritized first, followed by cost reduction and battery health preservation. Two-stage formulations, on the other hand, often prioritize short-term economic benefits or prolonging battery life, which can come at the cost of increasing renewable energy use and overall system independence. These findings emphasize the importance of designing objective hierarchies. These hierarchies should align with specific operational targets. They should also align with the characteristics of prosumer-driven systems. In the future, the proposed framework can be expanded to include stochastic renewable generation, real-time demand response strategies, and more detailed battery degradation modeling. This would improve the robustness and scalability of the optimization process. In summary, the research shows that using multi-stage, multi-objective optimization to manage energy in prosumer-oriented microgrids leads to sustainable, resilient, and cost-effective results.

REFERENCES

[1] Riou, M., Dupriez-Robin, F., Grondin, D., Le Loup, C., Benne, M., & Tran, Q. T. (2021). Multi-Objective Optimization of Autonomous Microgrids with Reliability Consideration. *Energies, 14*(15). https://doi.org/10.3390/en14154466

[2] Goel, N., & Yadav, N. K. (2025). Sustainable microgrid operations: multi-objective hybrid optimization for combined economic emission dispatch. *Electrical Engineering, 107*(6), 8031–8044. https://doi.org/10.1007/s00202-024-02912-9

[3] Ross, M., Abbey, C., Bouffard, F., & Jos, G. (2015). Multiobjective Optimization Dispatch for Microgrids With a High Penetration of Renewable Generation. *IEEE Transactions on Sustainable Energy, 6*(4), 1306–1314. https://doi.org/10.1109/TSTE.2015.2428676

[4] Moosavi, M., Olamaei, J., & Shourkaei, H. M. (2025). Optimizing microgrid performance a multi-objective strategy for integrated energy management with hybrid

sources and demand response. *Scientific Reports, 15*(1), 17827. https://doi.org/10.1038/s41598-025-00118-y

[5] Rajagopalan, A., Nagarajan, K., Montoya, O. D., Dhanasekaran, S., Kareem, I. A., Perumal, A. S., Lakshmaiya, N., & Paramasivam, P. (2022). Multi-Objective Optimal Scheduling of a Microgrid Using Oppositional Gradient-Based Grey Wolf Optimizer. *Energies, 15*(23). https://doi.org/10.3390/en15239024

[6] Sun, S., Fu, J., Wei, L., & Li, A. (2020). Multi-Objective Optimal Dispatching for a Grid-Connected Micro-Grid Considering Wind Power Forecasting Probability. IEEE Access, 8, 46981–46997. https://doi.org/10.1109/ACCESS.2020.2977921

[7] Hai, T., Singh, N. S. S., & Jamal, F. (2025). Energy management of a microgrid with integration of renewable energy sources considering energy storage systems with electricity price. Journal of Energy Storage, 110, 115191. https://doi.org/10.1016/j.est.2024.115191

[8] Majeed, M. A., Phichaisawat, S., Asghar, F., & Hussan, U. (2023). Optimal Energy Management System for Grid-Tied Microgrid: An Improved Adaptive Genetic Algorithm. IEEE Access, 11, 117351–117361. https://doi.org/10.1109/ACCESS.2023.3326505

[9] Witharama, W. M. N., Bandara, K. M. D. P., Azeez, M. I., Bandara, K., Logeeshan, V., & Wanigasekara, C. (2024). Advanced Genetic Algorithm for Optimal Microgrid Scheduling Considering Solar and Load Forecasting, Battery Degradation, and Demand Response Dynamics. IEEE Access, 12, 83269–83284. https://doi.org/10.1109/ACCESS.2024.3412914

[10] Zafar, R., Esmaeel Nezhad, A., Ahmadi, A., Erfani, T., & Erfani, R. (2023). Trading Off Environmental and Economic Scheduling of a Renewable Energy Based Microgrid Under Uncertainties. IEEE Access, 11, 459–475. https://doi.org/10.1109/ACCESS.2022.3231158

[11] Alzahrani, A., Rahman, M. U., Hafeez, G., Rukh, G., Ali, S., Murawwat, S., Iftikhar, F., Haider, S. I., Khan, M. I., & Abed, A. M. (2023). A Strategy for Multi-Objective Energy Optimization in Smart Grid Considering Renewable Energy and Batteries Energy Storage System. IEEE Access, 11, 33872–33886. https://doi.org/10.1109/ACCESS.2023.3263264

[12] Karimi, H., Jadid, S., & Hasanzadeh, S. (2023). Optimal-sustainable multi-energy management of microgrid systems considering integration of renewable energy resources: A multi-layer four-objective optimization. *Sustainable Production and Consumption, 36*, 126–138.

[13] Shafiei, K., Seifi, A., & Hagh, M. T. (2025). A novel multi-objective optimization approach for resilience enhancement considering integrated energy systems with renewable energy, energy storage, energy sharing, and demand-side management. *Journal of Energy Storage, 115*, 115966. https://doi.org/10.1016/j.est.2025.115966

[14] Borghei, M., & Ghassemi, M. (2020). A Multi-Objective Optimization Scheme for Resilient, Cost-Effective Planning of Microgrids. *IEEE Access, 8*, 206325–206341. https://doi.org/10.1109/ACCESS.2020.3038133

[15] Dai, X., & Batool, K. (2024). Optimizing multi-objective design, planning, and operation for sustainable energy sharing districts considering electrochemical battery longevity. *Renewable Energy, 229*, 120705. https://doi.org/10.1016/j.renene.2024.120705

[16] Shaier, A. A., Elymany, M. M., Enany, M. A., & Elsonbaty, N. A. (2025). Multi-objective optimization and algorithmic evaluation for EMS in a HRES integrating PV, wind, and backup storage. *Scientific Reports, 15*(1), 1147. https://doi.org/10.1038/s41598-024-84227-0

[17] Martinez-Rico, J., Zulueta, E., de Argandoña, I. R., Fernandez-Gamiz, U., & Armendia, M. (2021). Multi-objective Optimization of Production Scheduling Using Particle Swarm Optimization Algorithm for Hybrid Renewable Power Plants with Battery Energy Storage System. *Journal of Modern Power Systems and Clean Energy, 9*(2), 285–294. https://doi.org/10.35833/MPCE.2019.000021

[18] Terkes, M., Demirci, A., Gokalp, E., & Cali, U. (2024). Multi-stage and multi-objective feed-in damping-based battery aging-aware energy management strategy for renewable energy integration. *IEEE Access*, 1–1. https://doi.org/10.1109/ACCESS.2024.3468716

[19] Wu, Y., Liu, Z., Liu, J., Xiao, H., Liu, R., & Zhang, L. (2022). Optimal battery capacity of grid-connected PV-battery systems considering battery degradation. *Renewable Energy, 181*, 10–23. https://doi.org/10.1016/j.renene.2021.09.036

[20] Swierczynski, M., Stroe, D.-I., Stan, A.-I., Teodorescu, R., & Kaer, S. K. (2015). Lifetime Estimation of the Nanophosphate $\hbox{LiFePO}_{4}\hbox{/C}$ Battery Chemistry Used in Fully Electric Vehicles. *IEEE Transactions on Industry Applications, 51*(4), 3453–3461https://doi.org/10.1109/TIA.2015.2405500

eNergetics 2025
DOI: https://doi.org/10.5281/zenodo.18624023

Original Scientific Article

Impact of Diffuser on Centrifugal Pump Efficiency for Liquid Oxygen in Rocket Engines

Mohamed Amine Bennaceur[1], Messaouda Guemmadi[2], Bessam Toumi[3], Rami Zitouni[4], Abdelhak Khiri[5]

[1]Algerian Space Agency– Bouzareah, Algiers, Algeria
[2,4,5]University M'Hamed Bougara- Boumerdes Frantz fanon city, Boumerdes, Algeria
[3]Laboratory of Energetic Mechanics and Conversion Systems, Faculty of Mechanical and Process Engineering, University of Sciences and Technologies Houari Boumediene, Bab-Ezzoaur, Algiers, Algeria

[1]amine.rmsm@gmail.com, [2]guemmadi_samah@yahoo.fr, [3]btoumi@usthb.dz, [4]zitounirami7@gmail.com, [5]abdelhakkhiri5@gmail.com

Abstract—**Centrifugal pumps play a very important role in the feed systems of rocket engines. A diffuser attached at the impeller outlet transforms the kinetic energy of the impeller discharge velocity into static pressure, hence enhancing pressure recovery and the overall efficiency of the pump. Therefore, it is very important to understand the effect of the diffuser on pump efficiency. The present work deals with the effect of a diffuser on a centrifugal pump dealing with liquid oxygen. To determine the ideal diffuser, a range of radial widths were examined. it has been found that a properly designed diffuser increases the efficiency of the pump considerably.**

Keywords - diffuer, centrifugal pump, liquid oxygen, pump efficiency**.**

I. INTRODUCTION

Liquid rocket engines generate thrust by the combustion process of propellants, generally with liquid oxygen. Turbopumps are used to raise the propellant pressure, and most high-performance configurations have adopted centrifugal pumps that can proved very high mass flow rates at moderate discharge pressures [1-3]. The increasing demand for fast pressurization of cryogenic launch systems has revived activity in high mass flow centrifugal pumps. Centrifugal pumps are preferred for applications requiring a high flow rate because they can be designed in compact, lightweight construction [4-5]. However, in their operation, cavitation must be avoided since it seriously deteriorates the performance and may cause damage to the pump components. Since cryogenic fluids such as liquid oxygen operate at very high densities and low temperatures, specific requirements dictate the pump design. Flow characteristics, mechanical properties, and chemical compatibility all govern the material selection process [6-7]

In liquid-propellant rocket engines, centrifugal pumps are widely employed to feed liquid oxygen LOX into the combustion chamber. Downstream of the impeller, a diffuser is often used to convert part of the fluid's kinetic energy into static pressure. this pressure recovery process enhances overall pump efficiency while reducing the need for a large number of impeller blades. This steady and regular impeller outflow is critical for combustion stability, and thus an accurate diffuser assessment directly influences the proper evaluation of the entire system efficiency. Diffuser used in centrifugal pumps have several forms, including vaned, vaneless, and wedge geometries. Although not always

ISBN: 978-86-82602-07-1

essential for stable pump operation, the inclusion of an optimized diffuser can improve efficiency. For cryogenic propellants such as liquid oxygen, the diffuser must maintain structural integrity and performance under conditions of low temperature, high density, and elevated rotational speeds [8-12].

The current work studies the effect of diffuser geometry on performance of centrifugal pump, the pump uses liquid oxygen LOX. A range of diffuser cases, with different radial spanned width, were examined to investigates their effects on the pump efficiency and pressure recovery. The focus of this study is to determine an optimum width for the diffuser, such that it provides a maximum efficiency with minimum internal losses and being structurally feasible when operated at cryogenic temperatures. The present findings provide insight into the flow characteristic in liquid oxygen LOX centrifugal pumps.

II. COMPUTATIONAL APPROACH

A. Geometric Model

To analyze the influence of the diffuser geometry on the performance of centrifugal pump, an appropriate computational framework was established, and the following parameters were adopted to configure the computational model. The working fluid is liquid oxygen LOX, and the flow is considered in a steady state regime. The properties of the cryogenic fluid are fundamental factor in this study, since they have a direct influence on the phenomenon of cavitation; thus, the relevant characteristics of liquid oxygen were considered. Liquid oxygen has a molar mass of 31.999 g/mol, a density at its boiling point (90.2 k) of 1141 kg/m^3, a specific heat capacity of 918 J/kg.k, a dynamic viscosity of $1.15 \cdot 10^{-4}$ Pa.s, and thermal conductivity of 0.152 W/m.k at 90.2 k.

The boundary conditions are defined as follows: at the inlet a total pressure of 1 atm is imposed, while at the outlet the mass flow rate is fixed at 57.05 kg/s. The rotational speed of the impeller and inducer is set at 30000 rpm to represent realistically the pump's operation conditions. The Reynolds number reaches a value of $1.6 \cdot 10^7$, indicating a highly turbulent flow. To model turbulence, the SST (Shear Stress Transport) model was employed, as it is particularly suitable for capturing flows with strong velocity gradients and potential separation phenomena. The Shear Stress Transport (SST) turbulence model combines the *k-ω* model near the wall and the *k-ε* model in the free stream using blending functions. The main transport equations for turbulent kinetic energy *k* and the specific dissipation rate *ω* in the SST model are:

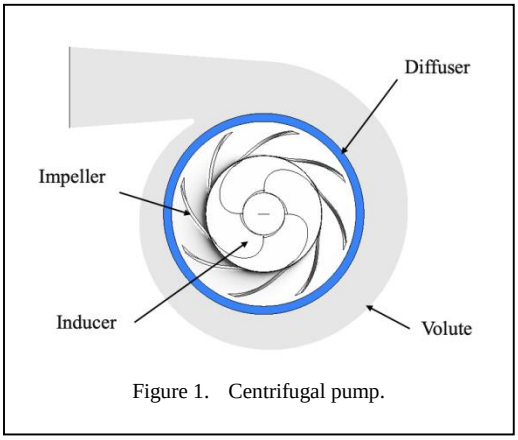

Figure 1. Centrifugal pump.

$$\frac{\partial(\rho k)}{\partial t} + \frac{\partial(\rho u_j k)}{\partial x_j} = P_k - \beta^* \rho \omega k + \frac{\partial}{\partial x_j}\left[(\mu + \sigma_k \mu_t)\frac{\partial k}{\partial x_j}\right], \quad (1)$$

$$\frac{\partial(\rho \omega)}{\partial t} + \frac{\partial(\rho u_j \omega)}{\partial x_j} = \frac{\gamma}{\upsilon_t} P_k - \beta \rho \omega^2 + \frac{\partial}{\partial x_j}\left[(\mu + \sigma_\omega \mu_t)\frac{\partial \omega}{\partial x_j}\right] + , \quad (2)$$
$$+2(1-F_1)\frac{\partial \sigma_{\omega^2}}{\omega}\frac{\partial k}{\partial x_j}\frac{\partial \omega}{\partial x_j}$$

where ρ is fluid density, u_j is velocity component, P_k is the production of turbulent kinetic energy, μ is dynamic viscosity, μ_t is turbulent eddy viscosity, and $\sigma_k, \sigma_\omega, \beta, \beta^*, \gamma, \sigma_{\omega^2}$ are model constants, F_1 is blending function to transition between *k-ω* and *k-ε* regions [13].

The geometry of the centrifugal pump was developed to represent a typical configuration used in cryogenic propulsion systems. The model consists of several key components as it is shown in Fig. 1. The impeller has a diameter of 56 mm and is equipped with eight elliptically shaped blades, designed to enhance the hydraulic

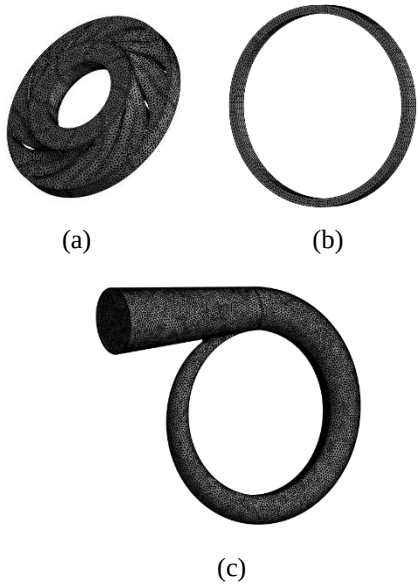

Figure 2. Mesh construction. (a) impeller. (b) diffuser. (c) volute.

performance of the pump. the shaft has an inner diameter of 24 mm, and a total length of 100 mm.

Additionally, the pump includes a diffuser, whose radial width varied to evaluate its influence on performance and efficiency. Five configurations were considered; baseline model without a diffuser, and diffusers with radial widths of 5 mm, 15 mm, 25 mm, and 35 mm, while the volute have an extension of 150 mm, which serves to collect and uniformly discharge the working fluid.

B. Meshing

Meshing is crucial because it divides the domain into small elements where the governing equations are solved, directly affecting the results accuracy. A coarse mesh may miss critical flow features, while an excessively fine mesh increases computational cost, Fig. 2 illustrated the mesh used for the impeller, diffuser and the volute of the centrifugal pump.

III. RESULTS AND DISCUSSION

Fig. 3 illustrates the pressure distribution within the centrifugal pump under two configurations: (a) without a diffuser and (b) with a diffuser. the comparison highlights the significant influence of the diffuser on the internal flow field and pressure recovery. with a diffuser, strong pressure gradients and localized low-pressure zones are observed near the

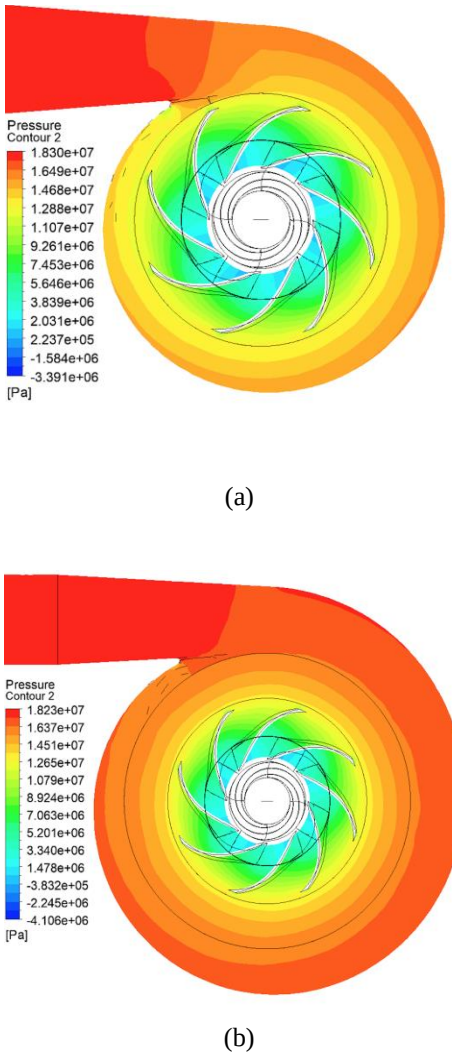

(a)

(b)

Figure 3. Pressure distribution. (a) without diffuser. (b) with diffuser.

impeller periphery indicating non-uniform flow and higher hydraulic losses. in contrast, the addition of a diffuser yields smoother, more uniform pressure contours, with reduced low-pressure regions and improved static pressure recovery. This demonstrates the diffuser's role in stabilizing the flow, mitigating losses and enhancing pump efficiency.

For centrifugal pumps, multiple factors contribute to the overall efficiency, including the impeller, diffuser, seals, and bearings. within these components, the diffuser required special consideration because its geometry directly affects the conversion of dynamic pressure at the impeller outlet to static pressure at the pump

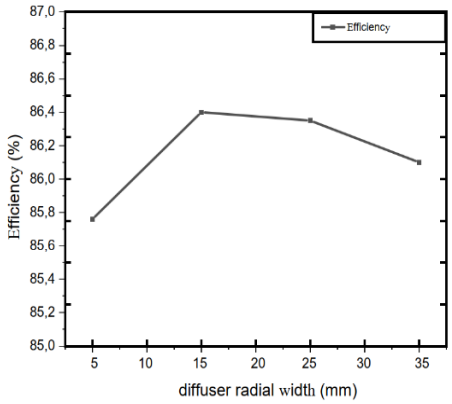

Figure 4. Effect of diffuser radial width on efficiency.

discharge. Fig. 4 illustrated the influence of diffuser radiale width on the efficiency of the centrifugal pump. The overall efficiency of the pump can be defined as the hydraulic power developed by the pump divided by the power delivered to the shaft and it is calculated as:

$$\eta = \frac{P_{hydraulic}}{P_{shalf}}, \tag{3}$$

and

$$P_{hydraulic} = \rho g H Q, \tag{4}$$

where H is the total dynamic head, Q is the flow rate, P_{shaft} is the mechanical power input and $P_{hydraulic}$ is the useful power imparted to the fluid.

Table I and Fig. 4 shows the variation of efficiency as a function of diffuser radial width. The current study aims to analyze the effect of diffuser radial width (5 mm, 15 mm, 25 mm, 35 mm) on the efficiency of the centrifugal pump. It is found that: the efficiency increases from a diffuser radial width of 5 mm until reaching a maximum at a diffuser radial width of 15 mm. This is explained by the fact that a moderately sized diffuser radial width allows better guidance of the fluid at the outlet of the impeller, reducing turbulence losses and promoting pressure recovery. Beyond 15 mm (notably at 25 mm and 35 mm), the efficiency decreases, as a result of an excessively large diffuser opening that leads to additional energy losses.

TABLE I. VARIATION OF EFFICIENCY WITH DIFFUSER RADIAL WIDTH.

Diffuser radial width (mm)	Efficiency (%)	Improvement compared to 5 mm (%)
5	85.76	--
15	86.40	0.75
25	86.35	0.69
35	86.10	0.40

IV. CONCLUSION

High performance turbopumps in rocket engines are responsible for the delivery of propellant into combustion chambers. The diffuser converts rotational kinetic energy from the impeller into static pressure, thereby raising fluid efficiency and increasing the pressure of the working fluid. In this paper, pump performances were compared using a vaneless diffuser and different radial widths of a diffuser. It was found that the highest efficiency was obtained with a diffuser radial width of 15 mm; as such, this provided an optimum between fluid guidance and internal losses.

REFERENCES

[1] Sutton, G. P., & Biblarz, O. (2011). *Rocket propulsion elements*. John Wiley & Sons.

[2] Singhal, R., Toppo, C., Roy, P., Biswakarma, R., Sahu, S., & Kalita, U. (2023). Development Advances in Liquid Rocket Engines Turbopump: A Review. *Advances in Science and Technology*, *130*, 155-162.

[3] Mårtensson, H., Andersson, S., Trollheden, S., & Brodin, S. (2008). Rocket engines: turbomachinery. *Advances on propulsion Technology for High-Speed Aircraft*, 1-28.

[4] Campbell, W. E., & Farquhar, J. (1974). Centrifugal pumps for rocket engines. *Pennsylvania State Univ. Fluid Mech., Acoustics, and Design of Turbomachinery, Pt. 2*.

[5] Ion, M., & Ioana, B. (2022). CFD Evaluation of a New Centrifugal Pump Concept for Rocket Propulsion. *Tehnički vjesnik*, *29*(4), 1133-1138.

[6] Zink, E. S., Bourdon, D., Neias Junior, V., Sias, D. F., Kitsche, W., & Wagner, B. (2020). Study of manufacturing processes for liquid rocket turbopump impellers: test and analysis. *Journal of Aerospace Technology and Management*, *12*, e0920.

[7] Toumi, B., Atif, A., & Bennaceur, M. A. (2024). Enhanced impeller gas-liquid flow using ribs for high performance of centrifugal pump. *International Journal of Computational Fluid Dynamics*, 1–12.

[8] Hong, S. S., Kim, D. J., Kim, J. S., Choi, C. H., & Kim, J. (2013). Study on inducer and impeller of a centrifugal pump for a rocket engine turbopump. *Proceedings of the Institution of Mechanical*

Engineers, Part C: Journal of Mechanical Engineering Science, *227*(2), 311-319.

[9] Ueda, A., Takeda, T., Sugiyama, D., & Miyagawa, K. (2022, April). Effect of the number of blades on diffuser unsteady loss of centrifugal pump. In *Journal of Physics: Conference Series* (Vol. 2217, No. 1, p. 012052). IOP Publishing.

[10] Zhang, Q., Huo, Q., Zhang, L., Song, L., & Yang, J. (2020). Effect of vaneless diffuser shape on performance of centrifugal compressor. *Applied Sciences*, *10*(6), 1936.

[11] Issac, J. M., Sitaram, N., & Govardhan, M. (2004). Effect of diffuser vane height and position on the performance of a centrifugal compressor. *Proceedings of the Institution of Mechanical Engineers, Part A: Journal of Power and Energy*, *218*(8), 647-654.

[12] Liu, Y. Y., Yang, G., Xu, Y., Peng, F., & Wang, L. Q. (2020). Effect of space diffuser on flow characteristics of a centrifugal pump by computational fluid dynamic analysis. *PLoS One*, *15*(2), e0228051.

[13] Menter, F. R. (1994). Two-equation eddy-viscosity turbulence models for engineering applications. *AIAA journal*, 32(8), 1598-1605.

eNergetics 2025
DOI: https://doi.org/10.5281/zenodo.18624079

Original Scientific Article

Modular Weather Station with Real-time Visualization

José Roberto Lima[1], Alison José Pereira Neri[2], Vitor Capelli Antunes de Sousa[3], Bruno Travagli Sereço[4], Nickolas Binati Candeu[5], Jair de Martin Junior[6], Elson Avallone[7]

[1,2,3,4,5,6,7]Federal Institute of São Paulo - IFSP, Catanduva-SP, Brazil

[1]lima.jose@aluno.ifsp.edu.br, [2]alison.n@aluno.ifsp.edu.br, [3]vitor.capelli@aluno.ifsp.edu.br, [4]bruno.sereco@aluno.ifsp.edu.br, [5]nickolas.binati@aluno.ifsp.edu.br, [6]jairdemartinjr@ifsp.edu.br, [7]elson.avallone@ifsp.edu.br

Abstract—**Meteorological monitoring is essential for agricultural planning and water-resource management, especially in producer regions such as Catanduva, Brazil. However, commercial weather stations are costly and inflexible, limiting access for smallholders and educational institutions. This study developed a low-cost weather-monitoring system integrated with a web-based supervisory interface, focusing on accessibility, customization, and full functionality. The system employs off-the-shelf sensors combined with custom-built mechanisms for wind and precipitation measurement, all connected to an ESP32 microcontroller. Data are transmitted via HTTPS to a REST API hosted on Vercel, stored in a MongoDB database, and visualized in a Next.js web interface that provides interactive dashboards, historical charts, weather alerts, and comparisons with Open-Meteo data. The total cost of electronic and mechanical components was R$ 164.00 (≈ €26.20), with the enclosure built from recycled materials. Comparative tests against reference stations showed that the prototype faithfully reproduces the diurnal cycle of meteorological parameters, with only minor deviations in magnitude. The results indicate a technically viable and economically accessible solution that integrates low-cost hardware with a modern web supervisory system, helping democratize meteorological monitoring.**

Keywords - meteorological monitoring, environmental sensing, regional climate data.

I. INTRODUCTION

Accurate meteorological monitoring is essential for sustainable development, especially in agriculture, a strategic sector of the Brazilian economy. The Catanduva region, in the interior of the state of São Paulo, Brazil, is an important agricultural hub, with significant production of sugarcane, citrus, and other commodities that require close tracking of weather conditions to optimize productivity and manage water resources. However, acquiring commercial weather stations is costly, with prices ranging from 80 to 2000 euros, and such stations often lack flexibility and customization, being restricted to specific sensors and hindering adaptation to particular requirements. This barrier disproportionately affects smallholders, academic institutions, and researchers with limited funding.

In addition, the literature indicates a significant gap in the integration of low-cost hardware with modern web platforms for meteorological monitoring. Although there are studies on IoT - and microcontroller-based stations, such as those using the ESP32, few solutions achieve a comprehensive integration of affordable hardware, efficient data-transmission pipelines, and up-to-date web interfaces like those developed with Next.js. This shortfall limits the development of accessible and functional solutions capable of democratizing access to meteorological monitoring, particularly in economically constrained regions [1,2].

ISBN: 978-86-82602-07-1

Given this context, the present study aims to develop a complete, low-cost, accessible, and flexible weather-monitoring system with a web-based supervisory interface, capable of meeting real-time data collection and visualization demands.

II. Materials and Methods

The architecture of the developed meteorological monitoring system follows a distributed approach that integrates low-cost hardware with modern software platforms to deliver a complete, scalable, and accessible solution [3-5]. The system adopts a modular structure composed of three main layers: the sensing and data-acquisition layer; the communication and transmission layer; and the processing and web-visualization layer. In the sensing layer, the system combines off-the-shelf sensors for air temperature, relative humidity, and atmospheric pressure with project-specific mechanisms for wind-speed and rainfall measurement. The processing core is an ESP32 microcontroller, selected for its dual-core architecture and built-in wireless connectivity [6]. It acts as the central element responsible for acquisition, initial processing, and transmission of the collected meteorological data. Fig. 1 shows the wiring diagram of the data-acquisition system [7-9].

For temperature and relative-humidity measurements, the DHT11 was selected. This digital device integrates a capacitive humidity sensor and an NTC thermistor in a single compact component. The DHT11 operates over 0–50 °C with ±0.1 °C accuracy, and 20-90% RH with ±1% accuracy. Atmospheric pressure is measured by the BMP280, which offers a pressure range of 300–1100 hPa, corresponding to altitudes from +9000 to −500 m relative to mean sea level, with a ±0.12 hPa relative accuracy and ±1 hPa absolute accuracy in the 950–1050 hPa interval.

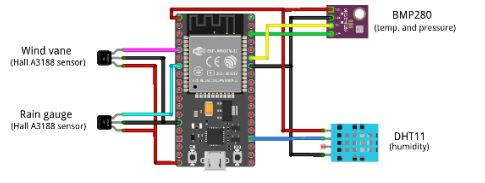

Figure 1. Wiring diagram of the data acquisition system.

To provide a reference check for pressure values, the barometric formula in Eq. (1) relates the pressure of a gas, P, e in hydrostatic equilibrium at altitude h, to the thermodynamic temperature T, under a constant gravitational field [3].

$$P = P_0 \cdot e^{\frac{-Mg}{RT}h}, \quad (1)$$

where P_0 is the pressure at a reference level with altitude taken as zero, g is gravitational acceleration, R is the universal gas constant, and M is the molar mass of the gas. Using the following values: P_0=10132 Pa (sea-level pressure) [10], M=0.0289644 kg mol^{-1} (air molar mass) [11], g =9.80665m s^{-2} [3], h=520 m (station altitude) [12], R=8.3144598 J mol^{-1} K^{-1}, T=20 ℃=293.15 $T = 20$ °C K (NTP, Normal Temperature and Pressure) [10], Eq. (1) yields P=95367 Pa=953.67 hPa.

For wind-speed and rainfall measurements, mechanisms based on Hall sensors and 3D-printed parts were developed. The anemometer consists of a fixed base with a magnetic sensor and a rotating assembly with three cups and a permanent magnet, generating electrical pulses proportional to rotation. The rain gauge uses a tipping-bucket principle with a collection funnel feeding a two-chamber mechanism that tips as water accumulates; each tip is detected by a Hall sensor. Both mechanisms were fabricated in PLA via 3D printing.

The processing and web-visualization layer is implemented with Next.js, a production-grade React framework that combines server-side and client-side rendering to provide optimized performance and a responsive user experience. Next.js was chosen for its ability to build modern web applications with Server-Side Rendering (SSR), Static Site Generation (SSG), and integrated API Routes, which are essential for real-time monitoring. Data storage is handled by MongoDB, a document-oriented NoSQL database.

Data-handling routines implement fault-tolerance strategies, especially for the DHT11, which requires at least 1 s between successive reads. The readDHT() function performs an initial attempt and, if invalid data are detected, waits 1.5 s before retrying, while the BMP280

runs continuously over I²C, providing pressure in pascals and complementary temperature. Rainfall quantification uses Eq. (2), which relates the number of detected tips to the per-pulse water volume (4.5 ± 0.1 mL), calibrated in the lab with a graduated cylinder and dropper, and to the effective collection area of the funnel (0.00708822 ± 0.00000746 m²). The funnel area was derived from the inlet diameter (Fig. 2) measured with a 0.05 mm-resolution caliper. Results are expressed in mm per m².

$$Precitipation = \frac{rainCount \cdot 4.5}{0.00708822}. \quad (2)$$

Wind speed is determined by Eq. (3), which multiplies the anemometer rotation frequency by its circumference, 0.0785 ± 0.003 m, yielding linear speed in m s^{-1}. Pulse counters are reset after each transmission to ensure independent measurements between sampling intervals.

$$Wind \quad speed = frequency \cdot 0.0785. \quad (3)$$

Data transmission uses HTTPS to connect to a REST API hosted on Vercel. The system implements API-key authentication via the HTTP header "*x*-api-key", ensuring proper authorization for data ingestion. The JSON payload includes all collected meteorological parameters, such as DHT11 and BMP280 temperatures, relative humidity, pressure, accumulated precipitation, rain pulse count, and wind speed, each formatted with appropriate decimal precision. The Wi-Fi connectivity routine implements automatic reconnection with a 20 s timeout, resetting the wireless interface on connection failure to maintain robustness under unstable network conditions.

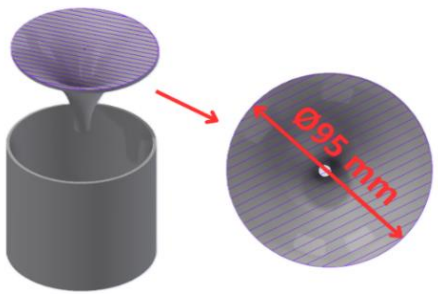

Figure 2. Effective area of the rain gauge.

The supervisory web layer built with Next.js exposes API routes that receive ESP32 data over HTTPS, validate authentication, and persist records to MongoDB Atlas, forming documents with fields such as deviceId, temperature, humidity, pressure, and timestamps. The application uses environment variables on Vercel for secure connections, maintains date indexes to optimize time-series queries, and serves React components that consume these internal APIs to display interactive dashboards with historical charts using specialized libraries. Hybrid rendering delivers preloaded pages that reduce response time, presenting visualization cards for each meteorological parameter with periodic data refresh.

To enrich analysis and validation, the supervisory system integrates external APIs such as Open-Meteo to compare local temperature readings with historical data for the same coordinates, and Brazil's National Institute of Meteorology (INMET) API to check regional weather alerts for Catanduva, such as heavy rain, strong winds, or storms. These alerts are highlighted on the main interface, providing contextual information that complements the local station data and supports interpretation of the monitored environmental conditions.

III. Results and Discussion

The following results and discussion present a detailed evaluation of the developed prototype, highlighting its physical configuration, data-acquisition performance, web-interface features, and validation of the collected data. This section emphasizes the evidence supporting the station's technical and economic feasibility, based on field measurements and a critical analysis of results.

Figure 3. Installed prototype.

TABLE I. COMPONENTS AND THEIR COSTS.

Component	Price (R$)	Price (€)
Rain gauge	R$ 35.00	€ 5.59
Structure	R$ 0.00	€ 0,00
Anemometer	R$ 15.00	€ 2.40
ESP32	R$ 30.00	€ 4.79
Terminal adapter for ESP32	R$ 20.00	€ 3.19
Case IP69 for ESP32	R$ 40.00	€ 6.39
DHT11 sensor	R$ 8.00	€ 1.28
2 x Hall sensor	R$ 6.00	€ 0.96
BMP280 sensor	R$ 10.00	€ 1.60
Overall cost	**R$ 164.00**	€ **26.20**

Fig. 3 shows the assembled prototype, featuring the three-cup anemometer, the dual-tipping rain gauge, and the sensing unit housed in a protective enclosure.

Table I details the costs of the electronic and mechanical components used in the prototype. All items, including the rain gauge, anemometer (with 3D-printing cost included), ESP32 microcontroller, terminal adapter for ESP32, DHT11 and BMP280 sensors, and protective components for the ESP32, were acquired at affordable prices, totaling R$ 164.00 or €26.20. There is no additional cost for developing and maintaining the web supervisory system.

The station's support structure was built from recycled materials and repurposed household parts that would otherwise be discarded, resulting in zero cost for this portion of the implementation. This approach not only reinforces a sustainability commitment but also helps keep the prototype within a tight budget, demonstrating economic viability for smallholders and educational institutions with limited funding.

The supervisory system can be accessed at: https://ifsp-weather.vercel.app.

The web interface, built with Next.js, offers an intuitive, responsive user experience, centralizing the monitoring and analysis of meteorological data. Fig. 4 shows the site's home page, which clearly presents current values of temperature, humidity, pressure, wind, and precipitation, and highlights active weather alerts retrieved from INMET API.

The site is organized into five main pages: in the Charts section, users can view interactive

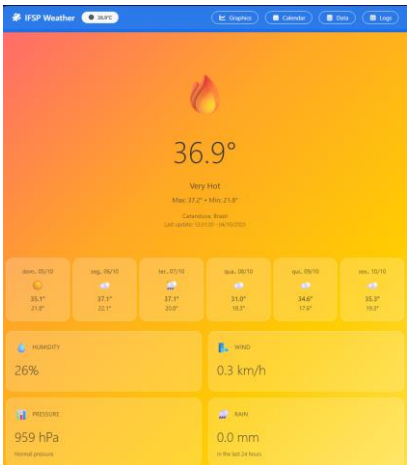

Figure 4. Home page of the website.

dashboards with historical series and compare parameters over selected periods; the Calendar page allows the user to pick any date and inspect key indicators for that day, enabling targeted analysis; the Read Log displays a complete list of all database records, with filtering by period and parameter, and supports exporting selected data as JSON and CSV; the Data page allows changing, deleting, and inserting records, accessible only with a valid token and intended exclusively for testing or correcting inconsistent data; and the Home page, already shown, serves as a hub for quick access to current data and alerts.

The home page is customized to immediately reflect environmental conditions and the diurnal cycle. As the prototype's measured temperature changes, the interface background color shifts dynamically from cool tones (bluish) at lower temperatures to warm tones (orange and red) at higher temperatures. The color scheme also adapts to local time, using a lighter theme during the day and a darker theme after sunset, improving legibility and offering a visual experience aligned with both weather conditions and the natural day–night rhythm.

The site provides real-time and historical interactive dashboards, including comparative charts that allow overlaying different parameters and periods for detailed analysis. Users can view full time series and export datasets in JSON or CSV for use in other tools. Navigation is designed to be intuitive, with clear menus and fast loading, ensuring easy access to all features. The responsive layout adapts to different screen

sizes, from desktops to smartphones, preserving readability and usability on any device [13].

To validate the performance of the low-cost station installed on the roof of a residence in Catanduva, Brazil, a cross-comparison strategy was adopted with two independent references. The first is the nearest conventional weather station operated by INMET in the city of Ariranha, Brazil, located 13.1 km from the measurement point. It follows standardized siting and shielding practices (open field over grass, distant from obstacles) with an altitude of 525.44 m above mean sea level, serving as a local observational benchmark for magnitude and intraday variability [14]. The second reference is Open-Meteo [15], which provides hourly series generated by numerical models with data assimilation and spatial interpolation, representing a regional mean field less sensitive to urban micro-effects and therefore useful for anchoring trend and phase.

With this arrangement, Ariranha-INMET provides the geographically close observational reference, while Open-Meteo provides a regional reference that smooths microclimate noise. The analysis below focuses on a specific day within the collection period (19/09/2025), chosen to enable a fine comparative reading across the three sources. On that day, as on other days when the station was exposed, no rainfall occurred. Consequently, precipitation values were not compared, since the total was 0 mm of water per m².

In the charts below, we compare air temperature, relative humidity, atmospheric pressure, and wind speed, discussing phase alignment, possible magnitude biases, and justifications related to exposure, installation, and differences in spatial representativeness.

As shown in Fig. 5, over the same day the three series exhibit the expected diurnal pattern: minimum temperatures in the early morning, a rapid rise from 09:00–10:00, a peak in early afternoon, and a gradual decline toward evening. The coincidence of phases confirms that the station reproduces the temporal dynamics of the daily thermal cycle.

Despite this coherence, a positive bias appears in the ESP32 series between 12:00 and 18:00, with maxima about 6–8 °C above Ariranha and Open-Meteo. This deviation aligns with exposure effects: the sensor is installed near ceramic roof tiles with low albedo and high thermal inertia, which absorb shortwave radiation around midday and release heat by convection and longwave radiation thereafter, warming the sampled air nearby.

In contrast, the Ariranha station sits over grass in an open, ventilated area, reducing indirect radiative heating. Open-Meteo represents a regional mean field that smooths local extremes. The larger afternoon amplitude in the ESP32 thus stems mainly from microclimatic and installation conditions (roof proximity, tile reflectance, heat storage, and shelter ventilation).

Even with higher absolute values during peak insolation, the ESP32 series maintains the same timing of minimum and maximum observed in the references. This indicates fidelity to the intraday signal, with the primary need being magnitude adjustment associated with site installation, such as relocating to a grassy, ventilated area and using adequate radiation shielding to reduce bias during the hottest hours.

For humidity (Fig. 6), the three series display the same diurnal cycle, with morning maxima (78–83%) and a continuous decline until early afternoon, reaching minimum between 15:00 and 16:00 (15–22%), followed by gradual recovery

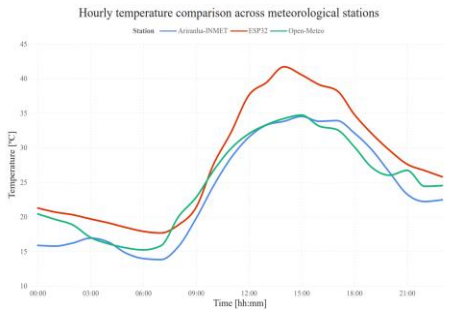

Figure 5. Hourly temperature comparison across meteorological stations.

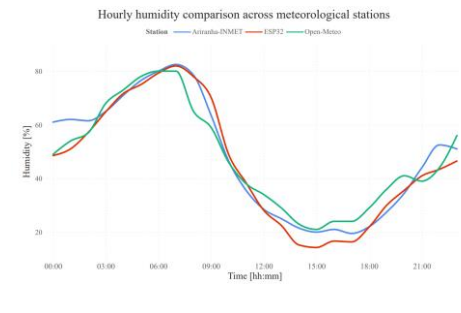

Figure 6. Hourly humidity comparison across meteorological stations.

toward evening (40–55%). Phase alignment is clear and the amplitude is very similar across sources, indicating good signal coherence and adherence to intraday variability.

Small magnitude differences occur mainly during peak insolation, when the ESP32 tends to report slightly lower humidity than Ariranha and Open-Meteo. This behavior is consistent with the thermal bias observed in temperature: additional heating from the ceramic roof reduces the computed relative humidity even with similar vapor content. Residual differences are also expected due to the more ventilated exposure of the Ariranha station and the smoothed nature of the modeled Open-Meteo series.

In summary, the ESP32 curve preserves the timing and shape of the humidity cycle, with modest absolute deviations during the hottest hours. Mitigation follows the same rationale as for temperature.

For pressure (Fig. 7), the three series show the same daily pattern, with smooth variation and low amplitude throughout the day, maintaining very similar values (953–960 hPa). Phase coincidence and small dispersion indicate good consistency among sources. When compared with the barometric pressure calculated from Equation (1), which yielded 953.67 hPa, the observed values are consistent with theory.

A slight level offset is observed among stations, compatible with site altitude differences: the ESP32 is located 520 m above sea level, while Ariranha is at 525.44 m [12,14]. This elevation difference explains small variations in absolute station pressure, since pressure decreases with altitude. Even so, the station's series tracks Open-Meteo more closely throughout the period, with nearly overlapping curves and residual differences smaller than those relative to Ariranha.

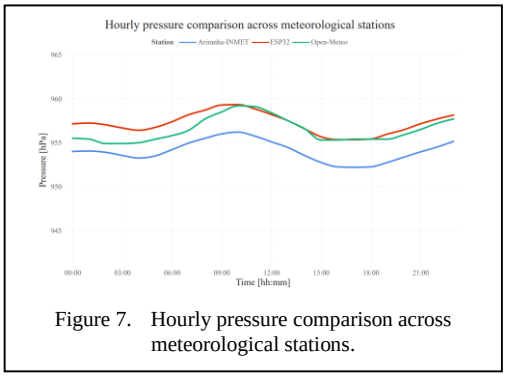

Figure 7. Hourly pressure comparison across meteorological stations.

In short, the diurnal behavior is equivalent across the three sources, and absolute deviations are consistent with the altitude difference, reinforcing the station's quality for analyzing hourly-scale pressure variations.

All three series in Fig. 8 preserve the same diurnal tendency, with wind acceleration around midday and weakening toward evening. The station, however, underestimates speed through much of the period, especially under light-wind regimes, when its curve approaches zero while Ariranha and Open-Meteo remain positive.

The amplitude shortfall is compatible with mechanical and siting limitations: the anemometer uses a deep-groove ball bearing whose friction raises the start threshold and reduces rotation at low speeds. Lubrication partially mitigated the issue, but performance remains below ideal when compared with ceramic bearings with lower internal friction. Additionally, the urban installation (near roofs, houses, and trees) creates shielding and turbulence that reduce mean measured speed. In contrast, Ariranha operates in a more open and ventilated field, and the modeled Open-Meteo series tends to smooth extremes, explaining its greater stability.

In summary, the station reproduces the timing of variations but with compressed amplitude due to mechanical friction and exposure effects. Recommended mitigations include replacing bearings with low-friction types (ideally ceramic), checking rotor balance and alignment, relocating to a freer and higher site, and, if necessary, applying a post-installation calibration curve against the reference station.

It was also observed that the developed station reports, on average, temperature values approximately 7 °C higher than those recorded by the other stations during the period between

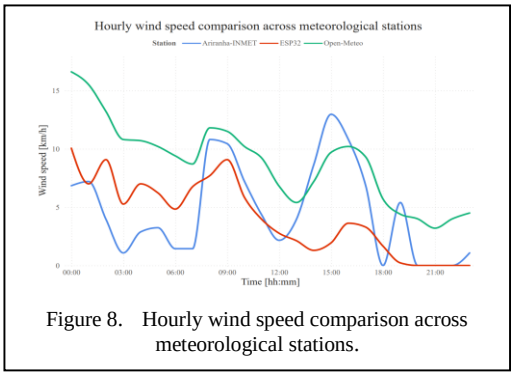

Figure 8. Hourly wind speed comparison across meteorological stations.

12:00 and 18:00. Since no calibration was performed on the temperature sensor, a future improvement identified is to calibrate all sensors in the system using more sophisticated reference instruments, ensuring measurements that more closely match those obtained by the comparison stations. Additionally, the implementation of data-compensation strategies such as correction curves or algorithmic adjustment models may be explored as a complementary approach to improve measurement accuracy under varying environmental conditions.

Fig. 9 illustrates the condition of the station after approximately one month of continuous exposure to weather conditions. Corrosion was observed on the bolts and nuts used in the structural assembly, compromising mechanical strength and long-term durability. Consequently, the need to replace these components with stainless steel hardware, more suitable for outdoor applications, was identified.

The main structural body of the station did not exhibit significant signs of wear; however, the attachment mechanism of the rain gauge lid proved insufficiently robust. During episodes of strong winds, the lid detached from the collector, indicating the necessity of developing a dedicated locking mechanism capable of ensuring greater stability and operational safety.

Additionally, although the conduit and sensor interface box did not present ruptures or evidence of water ingress, the current solution-based on an external conduit-offers limited protection for cabling and reduces the overall sealing performance. As a future improvement, the development of an integrated housing is proposed, allowing cables and electrical connections to be routed internally within the structure, thereby increasing both mechanical protection and resistance to infiltration.

Figure 9. The station after one month of being in open weather.

Another factor identified concerns the original installation site of the station. The proximity to walls, roofs, and nearby buildings caused partial obstruction of airflow around the anemometer, as well as local thermal disturbances, which negatively affected data quality. To mitigate such issues, more rigorous site selection is recommended, prioritizing flat, open areas free from physical obstructions.

Throughout the testing period, additional opportunities for improvement were identified in the embedded software. The implementation of a real-time operating system (RTOS) on the ESP32 stands out, as it enables improved scheduling of data acquisition, processing, and transmission tasks, while allowing simultaneous execution of critical routines. Furthermore, integrating a watchdog mechanism and low-power operation modes was found to be feasible, enabling the device to enter sleep cycles when data collection is unnecessary. This approach is particularly relevant for field deployments in which the station may rely solely on a battery and photovoltaic panel for power supply.

The data provided to users by the station can be used to more easily identify periods of intense or unfavorable weather conditions, helping smallholders avoid unnecessary resource losses. Although the system does not replace full-scale meteorological forecasting services, its localized monitoring capabilities offer valuable real-time and trend-based information that supports more informed decision-making. For example, strong winds can make the seeding process more difficult and unpredictable, potentially reducing seeding efficiency and leading to significant resource losses. By using the weather information available in the station's application, smallholders can identify more suitable periods for planting and harvesting, thereby enhancing operational efficiency and resilience in small-scale agricultural production.

IV. CONCLUSION

The development and validation of the low-cost weather-station prototype achieved all proposed objectives. Integrating off-the-shelf sensors and custom mechanisms with the ESP32 microcontroller enabled accurate acquisition of meteorological parameters, showing good temporal agreement with INMET and Open-Meteo references despite minor divergences attributable to microclimatic and installation conditions. The comparative analysis demonstrated that the station reliably reproduces

the diurnal cycle, confirming its technical and economic viability for rural and academic contexts with limited resources. Financially, the project remained accessible, with the structural components being built from recycled materials, reinforcing its sustainability and scalability. Operational robustness was ensured through fault-tolerant data-acquisition strategies and automatic Wi-Fi reconnection.

The web-based supervisory system, developed with Next.js and MongoDB on Vercel, stands out as a key differentiator, providing a responsive interface that integrates historical and comparative charts with real-time regional weather alerts. Visual personalization, which adapts the interface theme according to temperature and the diurnal cycle, combined with integration to external meteorological APIs and INMET alerts, enables an intuitive and comprehensive monitoring experience.

In addition to these technological advances, the station also contributes to more efficient resource management in agricultural settings. By offering localized and continuous environmental monitoring, the system supports smallholders in optimizing the application of inputs such as water, seeds, and fertilizers. Access to precise temperature, humidity, and wind information helps identify periods in which resource application is more effective, reducing waste and improving overall productivity. Consequently, the platform not only democratizes access to meteorological information but also strengthens decision-making processes essential for sustainable and economically efficient agricultural operations.

ACKNOWLEDGMENT

The authors thank the Federal Institute of Education, Science and Technology of São Paulo (IFSP), Catanduva campus, for technical support and infrastructure. We also acknowledge colleagues, advisors, and the free-software community whose tools were fundamental to implementing the system.

REFERENCES

[1] Gonçalves, C., Freitas, D., Jesus, V., Coelho, Á., & Abijaude, J. (2024). Estação meteorológica de baixo custo para monitoramento do microclima na lavoura de cacau. In *Anais da XXIV Escola Regional de Computação Bahia, Alagoas e Sergipe* (pp. 74-83). Porto Alegre: SBC. doi:10.5753/erbase.2024.4439

[2] e Paiva Moura, A. R., & de Araújo, F. S. G. (2019). Estação meteorológica de baixo custo como instrumento de prático interdisciplinar no Colégio Estadual Otacílio Mota em Ipueiras-CE. *International Journal of Semiárid Studies*, *2*(2), 123-124.

[3] Singh, D. K., Jerath, H., & Raja, P. (2020, January). Low cost IoT enabled weather station. In *2020 International Conference on Computation, Automation and Knowledge Management (ICCAKM)* (pp. 31-37). IEEE. https://doi.org/10.1109/iccakm46823.2020.9051454

[4] Ioannou, K., Karampatzakis, D., Amanatidis, P., Aggelopoulos, V., & Karmiris, I. (2021). Low-cost automatic weather stations in the internet of things. *Information*, *12*(4), 146. https://doi.org/10.3390/info12040146

[5] Faid, A., Sadik, M., & Sabir, E. (2021). An agile AI and IoT-augmented smart farming: a cost-effective cognitive weather station. *Agriculture*, *12*(1), 35. https://doi.org/10.3390/agriculture12010035

[6] Ibraheem, F. N., Abdulrazzaq, S. N., Fathi, I. A., & Ali, Q. (2024). High-Resolution and Secure IoT-Based Weather Station Design. *International Journal of Safety & Security Engineering*, *14*(1). https://doi.org/10.18280/ijsse.140125

[7] Bella, H. K. D., Khan, M., Naidu, M. S., Jayanth, D. S., & Khan, Y. (2023). Developing a sustainable IoT-based smart weather station for real time weather monitoring and forecasting. In *E3S web of conferences* (Vol. 430, p. 01092). EDP Sciences. https://doi.org/10.1051/e3sconf/202343001092

[8] Pauzi, A. F., & Hasan, M. Z. (2020, September). Development of iot based weather reporting system. In *IOP Conference Series: Materials Science and Engineering* (Vol. 917, No. 1, p. 012032). IOP Publishing. https://doi.org/10.1088/1757-899x/917/1/012032

[9] Tenzin, N., Tharchen, J., Penjor, K., Dhendup, T., & Lhamo, D. (2021). IOT Based Weather Station. *Zorig Melong| A Technical Journal of Science, Engineering and Technology*, *5*(1), 25-29.

[10] Engineering Toolbox. (2004). NTP - Normal Temperature and Pressure. Em STP-Standard and NTP conditions. Available at: https://www.engineeringtoolbox.com/stp-standard-ntp-normal-air-d_772.html

[11] Pantellini, F. G. (2000). A simple numerical model to simulate a gas in a constant gravitational field. *American Journal of Physics*, *68*(1), 61-68. https://doi.org/10.1119/1.19374

[12] Google. (2025). Google Earth. Available at: https://www.google.com/earth/

[13] Satyanarayana, K. N. V., Reddy, S. R. N., Varma, K. S., & Raju, P. K. (2017). Mobile app & iot based smart weather station. *International Journal of Electronics, Communication and Instrumentation Engineering Research and Development (IJECIERD)*, *7*(4), 1-8.

[14] Instituto Nacional de Meteorologia. 2025. Catálogo de estações automáticas. Ministério da Agricultura e Pecuária. Available at: https://portal.inmet.gov.br/paginas/catalogoaut

[15] Open-Meteo. 2025. Open-Meteo: Free open-source weather API. Available at: https://open-meteo.com

eNergetics 2025
DOI: https://doi.org/10.5281/zenodo.18624154

Original Scientific Article

Sanitization-driven, Adversarial-informed Framework for Network Anomaly Detection

Pratik Chouragadey[1], Yogesh Sanodiya[2], Soumyajit Ghosh[2]

[1,3]Centre for Internet of Things, Madhav Institute of Technology and Science, Gwalior, India
[2]Computer Science Engg., Madhav Institute of Technology and Science, Gwalior, India

[1]pratikchouragadey26@gmail.com, [2]yogeshsanodiya59@gmail.com,[3]soumyajit@mitsgwalior.in

Abstract—**This paper presents a production-aware pipeline for robust anomaly detection in network intrusion systems, validated on a public network intrusion dataset. The work addresses the problem of reliably detecting low-prevalence, subtle, and evolving intrusion attacks in large-scale network traffic. Extreme feature skew, outliers, severe class imbalance, and pre-processing-induced leakage degrade detector reliability and inflate false positives. The proposed framework integrates SMOTE-safe class balancing and adversarial-informed representation learning, with configurable hyper-parameter selection. Pre-processing performs metadata removal, quantile-based clipping of extreme values, and median imputation, with targeted log1p transforms applied when appropriate. To prevent leakage, stratified train/test splitting is executed prior to any oversampling and Min-Max scaling is fitted only on the training partition; SMOTE is applied exclusively to training data. For modelling, an auto-encoder is trained on benign traffic to learn normal behaviour, a generative adversarial network is trained on attack samples to synthesize realistic adversarial examples, and the auto-encoder is adversarially retrained using GAN-generated attacks to increase sensitivity to hard-to-detect anomalies. Model and training hyper-parameters for the auto-encoder, generator, and discriminator are selected via configurable settings and validation to improve generalization and stability. Detection performance is evaluated using ROC–AUC, average precision, and confusion matrices; generative realism is quantified with cosine similarity and Maximum Mean Discrepancy (MMD). Additionally, the pipeline includes explicit sanity checks - duplicate/overlap detection between splits, checks for GAN memorization, and per-attack evaluation-to guard against leakage and overfitting. The pipeline records reproducible artifacts (scaled datasets, fitted scalers, and JSON summaries). Experimental results show that combining targeted sanitization, SMOTE-safety, adversarial retraining, and careful hyper-parameter selection substantially improves attack detectability while controlling false alarms, facilitating more reliable deployment.**

Keywords - network intrusion detection, anomaly detection, adversarial training autoencoder, generative adversarial networks (GANs), class imbalance (SMOTE).

I. INTRODUCTION

Network intrusion detection is a critical component of modern cyber defense as enterprise and cloud infrastructures expand in scale and complexity. Network traffic is highly imbalanced, dominated by benign flows, with sporadic yet sophisticated attacks and high-dimensional outliers. These properties, together with common preprocessing flaws such as information leakage, unsafe oversampling, and limited adaptability to evolving traffic, often undermine the robustness of learning-based intrusion detection systems. As a result, many reported methods achieve strong experimental results yet fail to generalize in real-world deployments.

Existing research has explored auto-encoders for reconstruction-based anomaly detection, generative adversarial networks (GANs) for synthetic data generation, and adversarial training for robustness. However, prior approaches rarely provide an end-to-end

ISBN: 978-86-82602-07-1

framework that enforces strict data sanitization, integrates safe resampling, leverages adversarial data generation for retraining, and incorporates systematic hyper-parameter selection along with sanity checks. This gap motivates the need for a comprehensive, reproducible pipeline that improves both detection accuracy and operational robustness.

This work introduces a sanitization-driven, adversarial-informed framework for anomaly detection, validated on the CIC-IDS2017 dataset. The framework contributes in three major ways: (i) it establishes a reproducible preprocessing protocol that prevents leakage and balances data safely; (ii) it introduces a hybrid modeling workflow that combines auto-encoders with GAN-generated adversarial examples to improve anomaly sensitivity; and (iii) it applies systematic hyper-parameter selection via validation and includes explicit sanity checks - duplicate/overlap detection between splits, checks for GAN memorization, and per-attack evaluation - with evaluation across ROC-AUC, average precision, confusion matrices, cosine similarity, and Maximum Mean Discrepancy (MMD).

The remainder of this paper is organized as follows. Section II reviews related literature, Section III details the proposed sanitization and modeling pipeline, Section IV presents experimental results on CIC-IDS2017, Section V provides ablation studies, and Section VI concludes with future research directions. The proposed pipeline is designed for practical deployment: by reducing false alarms and providing reproducible artifacts and sanity checks, it aims to lower operational burden and improve the reliability of production intrusion-detection systems.

II. Literature Review

Public intrusion detection datasets are widely employed to benchmark anomaly detection methods and ensure reproducibility [1]. Auto-encoders and their variants, including ensembles, VAEs, and hybrid AE–discriminative forms, are popular for unsupervised detection by modeling benign traffic and flagging deviations, but their performance is highly sensitive to preprocessing and hyper-parameter choices [2-5]. Generative adversarial networks (GANs) and anomaly-focused variants, such as AnoGAN and GANomaly, have been explored to generate challenging samples and probe detector robustness, though GAN-generated flows may lack realism and their practical efficacy remains underexplored [6-9]. Techniques to address class imbalance, including SMOTE and other oversampling methods, must be carefully applied to training data to avoid leakage, with proper scaling and feature selection; minor differences in preprocessing can substantially affect reported results [1,5,9,10], Adversarial machine learning studies have demonstrated that IDS models can be significantly compromised by substitute-model, optimization-based, and GAN-based attacks, emphasizing the need for adversarial-informed retraining and detector hardening [11-14]. Automated hyper-parameter optimization approaches, such as Bayesian search, improve reproducibility and tuning efficiency, yet comprehensive end-to-end frameworks combining preprocessing safeguards, adversarial retraining, and automated optimization remain scarce [5,11,14,15]. Collectively, these works motivate a framework integrating reproducible preprocessing, hybrid auto-encoder-GAN modeling, and automated hyper-parameter optimization on public datasets to improve IDS reliability and robustness.

III. Methodology

Notation: Let $X \in R^{N \times d}$ denote the dataset composed of N samples and d features, $x_i \in R^d$ a single sample, and $y_i \in 0,1$ the binary label (0 = benign, 1 = attack). The training and test partitions are indexed b T_{tr} and T_{te} respectively. The Euclidean norm is denoted $|\cdot|$ and the inner product by $\langle \cdot, \cdot \rangle$.

Data cleaning: Numeric sanitization is performed prior to any learning or scaling. For each numeric feature (j), the pipeline computes a replacement statistic (r_j) (median by default) using only finite values from the available partition. Any non-finite entry $x_{i,j}$ is replaced by

$$x_{i,j} \leftarrow r_j \quad . \tag{1}$$

The counts of non-finite values and the per-feature imputation values (r_j) are persisted to disk to ensure reproducibility and permit post-hoc auditing of preprocessing choices.

Data preprocessing: Preprocessing enforces a leakage-free ordering: sanitization is followed by fitting transforms only on the training partition, and those fitted transforms are then

applied to the test partition. Min-Max scaling maps features to the unit interval; for each training feature (j) the scaled feature $\tilde{x}_{i,j}$ is computed as

$$\tilde{X}_{I,J} = \frac{X_{I,J} - \underset{K \in \mathfrak{I}_{TR}}{MIN}\, X_{K,J}}{\underset{K \in \mathfrak{I}_{TR}}{MAX}\, X_{K,J} - \underset{K \in \mathfrak{I}_{TR}}{MIN}\, X_{K,J}}, \qquad (2)$$

with the implementation handling zero-range (constant) features to avoid division by zero (constant features are left unchanged by the scaler). If class rebalancing is enabled, SMOTE is applied exclusively to the scaled training partition to synthesize minority-class examples and mitigate class imbalance; no oversampling is performed using test data. Feature selection used for visualization (SelectKBest with ANOVA F-test) is fit only on training data and then applied to test data.

Feature Visualization: We applied SelectKBest (ANOVA *F*-test) for leakage-free feature selection on the training partition, then used Min–Max scaled AE latent embeddings and *t*-SNE visualization to qualitatively inspect class separation and GAN-induced distributional shifts. Fig. 1 shows the *t*-SNE visualization.

Modeling and training: The pipeline comprises three learned components: an Autoencoder (AE) trained on benign traffic to model normality, a Generative Adversarial Network (GAN) trained on attack samples to synthesize adversarial examples, and an adversarial retraining stage in which the AE is retrained using GAN-generated attacks to increase sensitivity to hard negatives. All

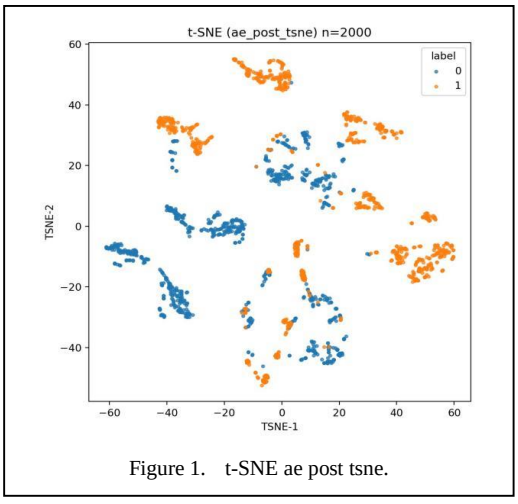

Figure 1. t-SNE ae post tsne.

networks are implemented as fully connected multilayer perceptrons using ReLU activations (and Leaky ReLU in the discriminator) and are optimized using the Adam optimizer. Default numeric settings used in the implementation are: batch size (B=256), AE pretraining learning rate $\eta_{AE} = 1e-3$ (pretrain epochs default 30), adversarial AE learning rate x ($\eta_{AE} = 1e-3$) (adv epochs default 20), GAN learning rates ($\eta_G = \eta_D = 1e-4$) (GAN epochs default 30), Adam betas (0.5, 0.9), and random seed 42. The implementation applies a ReLU activation immediately after the final encoder linear projection, consequently the latent codes are constrained to be non-negative. This design choice is documented here for reproducibility; if unintentional it should be removed or justified.

Auto-encoder: The AE consists of an encoder $f_\theta : \mathrm{R}^d \to \mathrm{R}^z$ and a decoder $g_\theta : \mathrm{R}^d \to \mathrm{R}^z$ Default architecture hyper-parameters are encoder hidden dimension (h_1,h_2)=(256,128) and latent dimension z=64 for input x the reconstructed vector is $\hat{x}=g_\Phi(f_\theta(x))$. The per-sample mean-squared reconstruction error is

$$[\ell_{rec}(x) = \frac{1}{d}, |x-\hat{x}|^2 .] . \qquad (3)$$

AE pretraining minimizes the empirical average reconstruction error over a benign mini-batch ($\mathscr{B}$ ben):

$$\mathscr{L}_{AE}(\theta, \phi) = \frac{1}{|\mathscr{B}\,\mathrm{ben}|} \sum_{x \in \mathscr{B}\,\mathrm{ben}} \ell\mathrm{rec}(x) . \qquad (4)$$

For epoch-wise diagnostics the implementation computes an epoch-wise mean reconstruction threshold (τ_e), the mean of per-sample reconstruction errors observed during epoch (e):

$$\tau_e = \frac{1}{|\mathscr{B}\,\mathrm{ben},e|} \sum_{x \in \mathscr{B}\,\mathrm{ben},e} \ell\mathrm{rec}(x) . \qquad (5)$$

The fraction of benign samples with $\ell_{\mathrm{rec}}(x) > \tau_e$ is reported as a training diagnostic. Generative adversarial network. The GAN

comprises a generator G_ψ and a discriminator D_ω Default GAN hyper-parameters are generator hidden sizes (256,256), discriminator hidden sizes (256,128), and noise dimension $z_{noise} = 6$. The generator accepts a conditioning vector (c) and Gaussian noise $z \approx N(0,I)$ and returns as synthetic sample $\tilde{x} = G_\psi(c,z)$. The discriminator returns a scalar logit $s = D_\omega(x)$. Training uses the numerically stable binary cross-entropy-with-logits loss (BCEWithLogits). For real attack samples $x \approx p_{att}$ and generated samples $\tilde{x} \approx p_G$, the discriminator and generator objectives are:

$$\mathscr{L}_D(\omega) = -\mathrm{E}_{x \sim p_{att}}\left[\log \sigma(D_\omega(x))\right] - \\ -\mathrm{E}_{\tilde{x} \sim p_G}\left[\log(1-\sigma(D_\omega(\tilde{x})))\right], \quad (6)$$

$$\mathscr{L}_G(\psi) = -\mathrm{E}_{\tilde{x} \sim p_G}\left[\log \sigma(D_\omega(\tilde{x}))\right], \quad (7)$$

where $\sigma(\cdot)$ is the sigmoid function. Training specifics include a WGAN-GP-style critic update frequency $n_{critic} = 5$ and gradient-penalty weight $\lambda_{gp} = 10.0$ when WGAN-GP mode is used. Discriminator accuracy is computed by thresholding discriminator logits at zero and comparing to ground-truth labels. Generative adversarial formulations underpin the adversarial sample synthesis used in the pipeline.

Adversarial retraining: Adversarial retraining uses GAN-generated samples to encourage the AE to produce larger reconstruction errors on attack-like inputs while preserving low reconstruction error on benign data. Let $\mathscr{B}$ben denote a benign mini-batch and let $\mathscr{B}$ben denote GAN-generated samples. The benign reconstruction loss (L_b) and the margin-based adversarial term (L_a) are defined as

$$L_b = \frac{1}{\left|\mathscr{B}\text{ben}\right|} \sum_{x \in \mathscr{B}\text{ben}} \ell\text{rec}(x), \quad (8)$$

$$L_a = \frac{1}{\left|\mathscr{B}\text{gen}\right|} \sum_{\tilde{x} \in \mathscr{B}\text{gen}} max(0,,\text{m} - \ell\text{rec}(\tilde{x})), \quad (9)$$

where, the default margin is (m=0.05). The adversarial retraining objective is therefore

$$\mathscr{L}_{adv} = L_b + \lambda_{attack} L_a, \quad (10)$$

where, λ_{attack} default (=5.0) weights the adversarial term. The hinge-like form of (L_a) penalizes generated samples whose reconstruction error is below the margin and thus encourages the AE to increase errors for attack-like inputs while maintaining benign reconstruction fidelity.

Early stopping and short trials. Early stopping is applied during short validation-guided trials. Epoch (t) is considered improving if either the average reconstruction loss decreases by more than a tolerance ϵ

$$\mathscr{L}_{AE}(t) < \mathscr{L}_{AE}(t-1) - \grave{o}, \quad (11)$$

or the training diagnostic accuracy increases by more than (δ). If no improvement occurs for (p) consecutive epochs (patience; default p=5–8 configurable), training is halted. This short-trial protocol speeds hyper-parameter selection while preserving informative training signals.

Statistical-distance metrics and GAN quality to quantify distributional fidelity of generated attacks the implementation computes pairwise cosine similarities and Maximum Mean Discrepancy (MMD) with an RBF kernel. The RBF kernel with bandwidth (\sigma) is

$$k_\sigma(x,y) = exp\left(-\frac{\|x-y\|^2}{2\sigma^2}\right). \quad (12)$$

Given real attack samples $R = \{r_i\}_{i=1}^m$ and generated samples $G = \{\tilde{g}_j\}_{j=1}^n$ the squared MMD is

$$\mathrm{MMD}^2(R,G) = \frac{1}{m^2}\sum_{i,i'} k_\sigma(r_i, r_{i'}) + \\ + \frac{1}{n^2}\sum_{j,j'} k_\sigma(\tilde{g}_{jj}, \tilde{g}_{j'}) - \frac{2}{mn}\sum_{i,j} k_\sigma(r_i, \tilde{g}_j). \quad (13)$$

The bandwidth (σ) is selected by a median pairwise-distance heuristic on a random subset of samples. Cosine similarity is computed as

$$\cos(x, y) = \frac{\langle x, y \rangle}{\|x\|\|y\|}, \quad (14)$$

and reported GAN metrics include the mean cosine across pairs and the per-generated-sample maximum similarity to the real set. The pipeline also executes explicit sanity checks - duplicate/overlap detection between train/test splits, tests for GAN memorization, and per-attack evaluation - to guard against leakage and generator overfitting.

Evaluation metrics. AE reconstruction errors are interpreted as anomaly scores $s_i = \ell_{\text{rec}}(x_i)$ Detection performance is measured using ROC–AUC, average precision (AUPRC), precision, recall, and F1 at an operating threshold τ^* selected by maximizing Youden's J statistic:

$$\tau^* = arg\max_{\tau}(TPR(\tau) - \text{FPR}(\tau)). \quad (15)$$

Precision@(k) is computed for k equal to the number of ground-truth positives. Confusion matrices, ROC and PR plots, per-sample score CSVs, and t-SNE visualizations are produced and saved for reproducibility and qualitative inspection.

Systematic hyper-parameter selection. Hyper-parameter selection is performed via short validation-guided trials and final selection by held-out validation metrics. The search space includes architectural parameters (hidden-layer sizes and latent dimension for AE, generator and discriminator sizes), optimization hyper-parameters (learning rates and batch sizes), and adversarial parameters (noise dimensionality, margin m, and λ_{attack} . Each trial runs a short evaluation consisting of AE pretraining with early stopping, optional short GAN training, and optional adversarial retraining; the trial objective is the chosen metric on the held-out validation partition (AUPRC or F1). After a configured number of trials, the best hyper-parameter set is selected and merged with full-run training schedules for final model training. This define-by-run, validation-driven selection is implemented to improve reproducibility and stability.

Implementation notes for reproducibility. Equations and hyper-parameter names above map directly to variables in the code. The implementation clamps GAN-generated samples to [0,1] prior to AE evaluation so that generated data match Min-Max scaled ranges. The encoder's post-projection ReLU (latent non-negativity) is explicitly recorded; if this was not intended the code should remove that activation or the manuscript should justify the design choice (e.g., for sparsity or interpretability). Features with zero range are handled to avoid divide-by-zero in Min–Max scaling. The epoch-wise threshold τ_e is explicitly computed per epoch as shown above. All preprocessing artifacts (fitted scaler, selected features, sanitized statistics), trained model checkpoints, trial artifacts, and evaluation outputs are saved to disk to facilitate auditability, independent replication, and downstream analysis.

IV. Result and Discussion

A. Results

The pipeline was executed with the configuration reported in the logs (batch size = 256; AE pretrain epochs = 50; GAN epochs = 40; AE adversarial epochs = 30; WGAN-GP critic steps $n_{critic} = 5$; gradient-penalty weight = 10.0; early-stop patience = 8). After sanitization and (optional) SMOTE-safe balancing, AE pretraining on benign traffic completed 50 epochs (validation MSE stabilized near $6.98 \cdot 10^{-4}$. WGAN-GP was trained for 40 epochs on attack samples and produced 5.000 generated attack samples that were used for adversarial retraining. The adversarial AE retraining run terminated early (stopped at epoch 9). Validation-selected F1 thresholds were:

Pretrain threshold (validation, F1): $7.846978 \cdot 10^{-7}$

Post-adversarial threshold (validation, F1): $1.141367 \cdot 10^{-3}$.

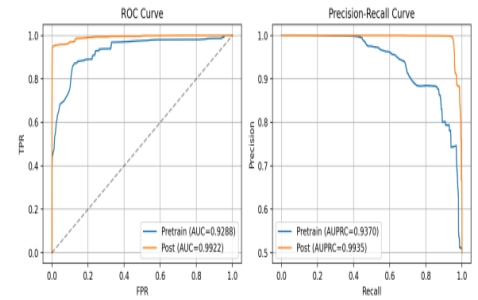

Figure 2. ROC and Precision–Recall curves comparing AE pretraining (blue) and AE post-adversarial retraining (orange).

On the held-out test partition (909,076 samples), detection metrics at the chosen thresholds are summarized below.

Fig. 2 ROC and Precision–Recall curves for AE pretrain (blue) and AE post-adversarial (orange). Post-adversarial model shows markedly improved AUC and AUPRC.

The results in Table I and Fig. 1 indicate a large improvement in both ranking (AUC/AUPRC) and classification metrics at the selected operating points after adversarial retraining. The post-adversarial AE achieves a substantial reduction in false positives ($56.021 \rightarrow 3.350$) while also reducing false negatives ($58.936 \rightarrow 22.452$), yielding large gains in overall accuracy and F1.

In the Fig. 3 confusion matrices (test set counts). Left: AE pretrain; Right: AE post-adversarial. Note the large reduction in false positives and meaningful reduction in false negatives after adversarial retraining.

B. Discussion

The adversarial retraining stage-where the autoencoder (AE) was exposed to GAN-generated, attack-like samples-yielded substantial and consistent improvements in both ranking and detection. AUC rose from ≈0.929 to ≈0.992 and AUPRC from ≈0.937 to ≈0.994, indicating markedly better separation between benign and anomalous flows. At the chosen F1 operating points, precision increased to ≈ 0.992 while maintaining recall ≈ 0.951, producing F1 ≈ 0.971. These gains align with the intended effect of adversarial augmentation: generated hard negatives push the AE to assign larger reconstruction errors to attack-like inputs while preserving low errors for benign flows.

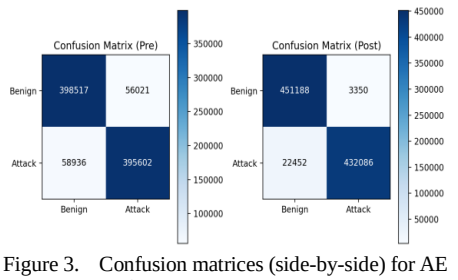

Figure 3. Confusion matrices (side-by-side) for AE pretrain (left) and AE post-adversarial (right).

The change in selected F1 thresholds (from $7.8 \cdot 10^{-7}$ to $1.14 \cdot 10^{-3}$) reflects a distributional shift induced by retraining: attack-like reconstruction errors moved appreciably higher relative to benign errors, enabling operating points with far fewer false alarms. This shift is desirable operationally but underscores the need to validate threshold stability across time and varying traffic patterns.

GAN-produced samples (5.000 in this run) appear to have provided useful "hard negatives" that were under-represented in the original attack set, as evidenced by the substantial reduction in false positives (~$56.021 \rightarrow 3.350$) and the meaningful drop in false negatives (~$58{,}936 \rightarrow 22.452$). Nevertheless, GAN-quality diagnostics and memorization checks (MMD, cosine similarity, nearest-neighbor distances) must be reviewed to confirm the improvement is not an artifact of near-duplicate generation or data leakage; the pipeline persists these diagnostics for post-hoc auditing.

From a deployment perspective, the ≈ 94% relative reduction in false positives materially lowers analyst triage burden and improves the detector's operational viability. High precision at substantial recall reduces wasted effort and increases the likelihood of timely responses. That said, operational thresholding must be calibrated to mission priorities-teams with constrained analyst capacity may prefer conservative thresholds that minimize false alarms, whereas safety-critical contexts may prioritize recall.

Recommended next steps: (1) perform per-attack-type and temporal holdout evaluations to

TABLE I. TEST SET PERFORMANCE.

Model	ROC–AUC	AUPRC	Accuracy	Precision	Recall	F1 Score
AE Pretrain (before adversarial)	0.9288	0.9370	0.8735	0.8760	0.8703	0.8731
AE Post-Adversarial (after retrain)	0.9922	0.9935	0.9716	0.9923	0.9506	0.9710

assess generalization and sensitivity to concept drift; (2) inspect representative remaining false negatives to identify failure modes (feature subsets, low-amplitude anomalies, mislabeled flows) and guide targeted augmentation or feature engineering; (3) thoroughly review GAN diagnostics and memorization logs to rule out generator overfitting or leakage; (4) evaluate adaptive or per-family thresholding and incremental retraining strategies for production efficiency; and (5) consider selective replay or smaller-scale generator batches to reduce computational cost.

In sum, adversarial GAN augmentation plus AE retraining produced large, reproducible improvements on the evaluated split; per-attack, temporal validation and GAN-quality auditing are required to harden confidence prior to broad deployment.

V. Conclusion

This work presents a production-aware, sanitization-driven pipeline that combines SMOTE-safe preprocessing, autoencoder modelling, GAN-based adversarial augmentation, and adversarial AE retraining to improve network-intrusion anomaly detection. On CIC-IDS2017 the workflow yielded large, reproducible gains: ROC–AUC rose from ≈0.93 (pretrain) to ≈0.99 (post-adversarial), AUPRC improved similarly, and F1 increased from 0.873 to 0.971 at validation-selected operating points. False positives fell by ≈94% while false negatives were substantially reduced, indicating that GAN-generated hard negatives effectively reshape the AE decision boundary when combined with careful sanitization and leakage-avoiding preprocessing. The implementation emphasizes reproducibility and auditability: sanitized statistics, fitted scalers, generated samples, Optuna/trial artifacts, model checkpoints, and evaluation outputs are all persisted for post-hoc analysis. The pipeline also runs explicit sanity checks (duplicate/overlap detection, GAN memorization tests, and per-attack evaluation) to help guard against overfitting and leakage. Results are reported on CIC-IDS2017; temporal drift and dataset bias remain possible and should be examined. Before production deployment we recommend targeted false-negative analysis, per-attack and temporal validation, and inspection of GAN-quality diagnostics to confirm the gains generalize beyond the present dataset.

Future work should include per-attack and temporal generalization studies, systematic false-negative root-cause analysis, and stricter GAN-quality controls to rule out memorization. Practical extensions include adaptive/online retraining for concept drift, lightweight model variants for resource-constrained environments, calibrated operating thresholds per policy, and adding uncertainty estimates or interpretable attributions to assist analyst triage. Additionally, future evaluations should assess how the proposed method performs in real-time detection environments, where latency and throughput constraints can significantly impact operational viability. It is also essential to analyze robustness under concept-drift scenarios, ensuring that the model can adapt to evolving traffic patterns and emerging attack behaviors. Finally, performance against previously unseen attack classes should be systematically studied to determine the model's true generalization capacity and its reliability in open-world, zero-day-like conditions.

References

[1] Kenyon, A., Deka, L., & Elizondo, D. (2020). Are public intrusion datasets fit for purpose characterising the state of the art in intrusion event datasets. *Computers & Security*, *99*, 102022. https://doi.org/10.1016/j.cose.2020.102022

[2] Borgioli, N., Aromolo, F., Phan, L. T. X., & Buttazzo, G. (2024). A convolutional autoencoder architecture for robust network intrusion detection in embedded systems. *Journal of Systems Architecture*, *156*, 103283. https://doi.org/10.1016/j.sysarc.2024.103283

[3] Lim, W., Yong, K. S. C., Lau, B. T., & Tan, C. C. L. (2024). Future of generative adversarial networks (GAN) for anomaly detection in network security: A review. *Computers & Security*, *139*, 103733. https://doi.org/10.1016/j.cose.2024.103733

[4] Boppana, T. K., & Bagade, P. (2023). GAN-AE: An unsupervised intrusion detection system for MQTT networks. *Engineering Applications of Artificial Intelligence*, *119*, 105805. https://doi.org/10.1016/j.engappai.2022.105805

[5] Ma, H., Zhang, X., Song, M., Zhu, Y., & Hong, W. C. (2025). SD-CSMOTE: Over-sampling method based on SNN-DPC and improved SMOTE. *Neurocomputing*, *620*, 129233. https://doi.org/10.1016/j.neucom.2024.129233

[6] Jmila, H., & Gharsellaoui, H. (2022). Adversarial machine learning for network intrusion detection. *Computer Networks*, *214*, 109073. https://doi.org/10.1016/j.comnet.2022.109073

[7] Yang, Z., Liu, X., Li, T., Wu, D., Wang, J., Zhao, Y., & Han, H. (2022). A systematic literature review of methods and datasets for anomaly-based network

intrusion detection. *Computers & Security*, *116*, 102675. https://doi.org/10.1016/j.cose.2022.102675

[8] Pinto, D., Amorim, I., Maia, E., & Praca, I. (2025). A review on intrusion detection datasets: tools, processes, and features. *Computer Networks*, 111177. https://doi.org/10.1016/j.comnet.2025.111177

[9] Jubair, S., Yang, J., & Ali, B. (2025). Overlap to equilibrium: Oversampling imbalanced datasets using overlapping degree. *Information Processing & Management*, *62*(2), 103975. https://doi.org/10.2139/ssrn.4662630

[10] Goodfellow, I. J., Pouget-Abadie, J., Mirza, M., Xu, B., Warde-Farley, D., Ozair, S., ... & Bengio, Y. (2014). Generative adversarial nets. *Advances in neural information processing systems*, *27*.

[11] Paya, A., Arroni, S., García-Díaz, V., & Gómez, A. (2024). Apollon: a robust defense system against adversarial machine learning attacks in intrusion detection systems. *Computers & Security*, *136*, 103546. https://doi.org/10.1016/j.cose.2023.103546

[12] Xu, D., Lv, Y., Wang, M., Zheng, B., Zhao, J., & Yu, J. (2025). DEMGAN: A machine learning–based intrusion detection system with adversarial traffic attack. *Computers, Materials & Continua*, *84*(1), 1731-1746.https://doi.org/10.32604/cmc.2025.064833

[13] Kumari, T. A., & Mishra, S. (2024). Tachyon: Enhancing stacked models using Bayesian optimization for intrusion detection using different sampling approaches. *Egyptian Informatics Journal*, *27*, 100520. https://doi.org/10.1016/j.eij.2024.100520

[14] Chawla, N. V., Bowyer, K. W., Hall, L. O., & Kegelmeyer, W. P. (2002). SMOTE: synthetic minority over-sampling technique. *Journal of artificial intelligence research*, *16*, 321-357. https://doi.org/10.1613/jair.953

[15] Sakurada, M., & Yairi, T. (2014, December). Anomaly detection using autoencoders with nonlinear dimensionality reduction. In *Proceedings of the MLSDA 2014 2nd workshop on machine learning for sensory data analysis* (pp. 4-11). https://doi.org/10.1145/2689746.2689747

eNergetics 2025
DOI: https://doi.org/10.5281/zenodo.18624185

Original Scientific Article

Optimization of Power Transfer in a Standalone PV System using Fuzzy Logic and Extremum Seeking Controllers: A Comparative Study

Itto Ouzouhou[1], Itto El-Kabassi[2], Adil Brouri[3], Abdellah Laazizi[4]

[1]Research Modeling and Multiphysics Engineering laboratory (LMIMP), Characterization of Systems and Controls (CSC) Research Team, Moulay Ismail University, Meknes, Morocco
[2,3,4]Moulay Ismail University, Meknes, Morocco

[1]ittou.ouzouhou@edu.umi.ac.ma

Abstract—**In recent years, solar power has emerged as a promising energy source. In solar photovoltaic systems (SPSs), efficient Maximum Power Point Tracking (MPPT) is a challenge to optimize PV power transfer to the load. Due to the effects of fluctuating environmental conditions on maximum power point tracking, an effective MPPT technique is preferable for optimal MPPT tracking under variable environmental conditions. In this study, a comparative study between two techniques such as: Fuzzy logic controller (FLC) and Extremum seeking controller (ESC) are employed to determine the maximum power output of solar photovoltaic systems under various environmental conditions. Additionally, a boost converter is used to connect the PV array to a load, optimizing the electrical parameters of the converter to minimize power losses. The efficiency, the tracking time, and the power of the system were measured in multiple scenarios. The obtained result shows that the fuzzy logic controller methods performs well in terms of efficiency, tracking time and power loss.**

Keywords - solar photovoltaic systems, converter DC/DC, fuzzy logique controller, extremum seeking controller.

I. INTRODUCTION

In recent years, Photovoltaic (PV) systems have gained great attention from researchers and they appear to be one of the most promising renewable energy sources [1]. However, the major factor limiting the use of photovoltaic systems is their low efficiency under changing weather conditions [2]. To increase the efficiency of PV systems, maximum power point tracking (MPPT) has been the objective of several papers [3,4]. Many techniques have been used to extract the power point maximum (MPP) in the system PV, these techniques are numerous and can be divided into four categories: classic techniques, intelligence techniques, optimization techniques, and hybrid techniques [5].

Classic techniques including perturb and observe(P&O), incremental and conductance (INC), constant voltage (CV), Adaptive reference voltage (ARV), Look up the table, and Hill climbing (HC) have high tracking accuracy only during uniform meteorological conditions [5]. However, these techniques struggle to do so under changing meteorological conditions. Therefore, these approaches often demonstrate weak convergence, poor tracking speed, and significant steady-state oscillatory [6]. To trade-offs between tracking precision and speed, intelligence techniques based on advanced artificial intelligence such as Fuzzy Logic Controller (FLC), and Artificial Neural Networks (ANN) have emerged recently due to their good performance. On the other hand, to enhance MPPT tracking, optimization

ISBN: 978-86-82602-07-1

techniques are also used for optimal maximum Power Point tracking (MPPT). The popular optimization approaches used in the literature for an optimal MPPT are Cuckoo Search (CS), Particle Swarm Optimization (PSO), Gray Wolf Optimization (GWO), ant Colony Optimization Algorithm (ACO), Genetic Algorithm (GA) and Artificial Bee Colony (ABC). These methods tend searching true MPP in dynamic environment conditions [7-9].

Although, to get more performance, hybrid techniques can be an alternative to other techniques by merging the advantages of each technique to detect MPP accurately under variable meteorological conditions. The hybridization techniques that are mostly used in the literature are the intelligence methods like fuzzy logic (FL) with other methods such as the classic method like P&O or INC or optimization methods like PSO and ANN. These hybrid techniques may be more performance than other techniques [10].

However, the performance of MPPT techniques depends on factors such as the solar panel's irradiance, temperature, and the connected load. Therefore, an efficient MPPT technique must ensure that the PV system operates at the maximum power point under all environmental conditions with minimum tracking speed, and minor steady-state oscillatory.

This work presents a comprehensive comparative evaluation of Fuzzy Logic Control (FLC) and Extremum Seeking Control (ESC) for Maximum Power Point Tracking (MPPT) in photovoltaic (PV) systems, with a focus on realistic and dynamic operating conditions. Unlike previous studies, this paper investigates the controllers under varying irradiance, temperature fluctuations, and load variations, including partial shading scenarios, which are critical for practical PV applications. Key performance indicators such as convergence speed, steady-state error, power stability, and computational burden are systematically analyzed. Additionally, the study benchmarks the proposed controllers against standard MPPT techniques, including Perturb and Observe (P&O) and Incremental Conductance (INC), to highlight their relative advantages and limitations. The results provide actionable insights into the selection and implementation of advanced MPPT strategies, emphasizing robustness, efficiency, and practical feasibility in real-world PV systems.

II. Materials and Methodology

A. Problem Description

In a photovoltaic (PV) system, the maximum power delivered by a module depends mainly on solar irradiation, operating temperature, and the connected load. When irradiation and temperature are kept constant, the load becomes a determining factor in energy production. Assuming that the load is purely resistive, the power can be written as:

$$P_{pv} = V_{pv} \cdot I_{pv} = R \cdot I_{pv}^{\,2} \,, \qquad (1)$$

where V_{pv}, and I_{pv} is the voltage and the current PV module.

In this case, for a given resistance value, the relationship $V = f(I)$ is linear. However, the current-voltage $(I-V)$ characteristic of a photovoltaic panel is inherently non-linear. The operating point of the PV system is therefore located at the intersection of the module's $I-V$ curve and the load line (Fig. 1). By fixing the irradiation and temperature, it is possible to determine an optimal resistance value that allows the system to operate at the maximum power point (MPP). However, in practice, climatic conditions, particularly irradiation and temperature, vary continuously and often unpredictably. Thus, the maximum power of the panel changes dynamically over time. In this context, it becomes essential to adopt a maximum power point tracking (MPPT) method, whose role is to adjust the operating point in real time in order to extract the maximum amount of energy, regardless of environmental variations.

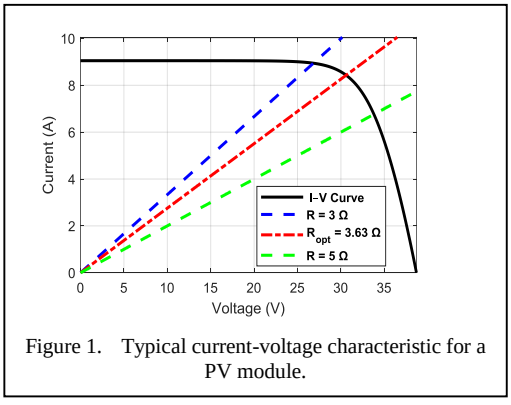

Figure 1. Typical current-voltage characteristic for a PV module.

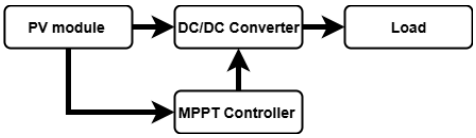

Figure 2. Block diagram of a stand-alone PV system.

Rapid changes in irradiation and temperature require the use of a robust, fast, and efficient control system. This is why a great deal of research has focused on developing and improving MPPT techniques.

The optimal resistance is calculated as shown in the following equation:

$$R_{opt} = \frac{V_{pv}}{I_{pv}}, \qquad (2)$$

where V_{pv} is the voltage of PV module is, I_{pv} is the current of PV module, and R_{opt} is the optimal resistance.

B. Photovoltaic System

A stand-alone PV system, shown in Fig. 2, comprises a photovoltaic module coupled to a boost DC-DC converter, controlled by an MPPT controller. The objective of a stand-alone PV system is to continuously extract the maximum power delivered by the PV module. However, due to the intermittent nature of weather conditions (solar irradiance and temperature), the PV module does not always provide the optimal current. To compensate for this variability and ensure operation at maximum power, an MPPT controller is used. This allows the system's operating point to be dynamically adjusted in order to continuously optimize energy production.

C. DC-DC Boost Converter

A boost converter was used to interface the PV module with the load in a stand-alone PV system. The main role of the boost converter is to step up the low and variable DC voltage generated by the PV module to a higher and more stable level suitable for the load or storage device. By adjusting the duty cycle, the boost converter ensures efficient power transfer and supports the implementation of the MPPT algorithm, which maximizes the extracted energy under varying irradiance and temperature conditions. To minimise the power losses, and increase the efficiency of the boost converter, the parameters of the boost converter are adequately determined using the state-space method.

TABLE I. BOOST CONVERTER SPECIFICATIOS.

Boost converter parameters	Values
Switching frequency	10KHz
sampling time	1e-5S
Capacitor (Cin)	47e-3F
Capacitor (Cout)	4.7e-3F
Inductor	2.2e-3H

Table I presents the obtained parameters of the boost converter

The converter was used in the simulation setting with a 5 kHz PWM switching frequency. A sampling time of 100 µs, or 10 samples per switching period, was used to discretize the control loop as shown in Table I.

D. MPPT Control

Generally, the output voltage of photovoltaic panels when they reach their maximum energy conversion efficiency is considerably affected by fluctuations in meteorological conditions such as solar irradiance and temperature, especially when solar irradiance changes have a particularly significant impact on this voltage. Because of this, they are ensuring the optimum power point maximum is important for improving their energy conversion efficiency and overall performance. This paper proposes a hybrid algorithm-based fuzzy logic to achieve this goal more accurately and efficiently due to the adjustment of very less parameters, which makes the optimized membership function with enhanced system performance under variable meteorological conditions.

1) Fuzzy logic controller

Fuzzy logic is one artificial intelligence method that uses the knowledge of an expert to construct nonlinear controllers. The use of fuzzy logic as a controller is to optimize the performance of the system PV under variable meteorological conditions of its ability to deal with imprecise input data. Generally, a basic fuzzy controller structure includes three phases, namely: Fuzzification, inference, and defuzzification. Fig. 3 illustrates the block diagram of fuzzy logic controller's structure.

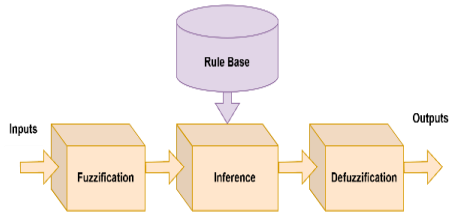

Figure 3. Control block diagram of Fuzzy logic controller.

In this study, the inputs variables are Error (E) and Change of Error (ΔE), while, the output is duty cycle (D), are calculated as follows:

$$E(k) = \frac{P_{pv}(k) - P_{pv}(k-1)}{V_{pv}(k) - V_{pv}(k-1)}, \quad (3)$$

$$\Delta E(k) = E(k) - E(k-1), \quad (4)$$

$$D(k) = D(k-1) + \Delta D, \quad (5)$$

where $P_{pv}(k)$ and $V_{pv}(k)$ are, respectively the power and the voltage of the PV panel at sampling instants (kTs).

The error (E(k)) defines the position of the operating point at the instant k. The variation of the error CE(k) defines whether the movement of the operating point is in the MPP direction or not. The output variable can take positive or negative values depending on the location of the operating point.

In the fuzzification process, the input signals are transformed to fuzzy values. In this process, each input and output are divided in fuzzy sets, Wish are presented by linguistic variables. seven linguistic variables are adopted for each of the input/output variables named membership function. These are NB (Negative Big), NM (Negative Medium), NS (Negative Small), ZE (Zero), PS (Positive Small), PM (Positive Medium) and PB (Positive Big). The triangular membership functions of the input and output variables were used in this work.

In the second step, fuzzy inference is a method that is used to convert input data into output data using fuzzy rules. This process is used to determine the control action to be taken in response to a given set of input values. In this study, Mamdani's inference method is employed to ensure accurate and efficient decision-making. The fuzzy rules are based on a set of rules, as illustrated in Table II.

TABLE II. FUZZY ASSOCIATIVE MATRIX.

E/ ΔE	**NB**	**NM**	**NS**	**ZE**	**PS**	**PM**	**PB**
NB	NB	NB	NB	NB	NM	NS	ZE
NM	NB	NB	NB	NM	NS	ZE	PS
NS	NB	NB	NM	NS	ZE	PS	PM
ZE	NB	NM	ZE	ZE	PS	PM	PB
PS	NM	NS	ZE	PS	PM	PB	PB
PM	NS	ZE	PS	PM	PB	PB	PB
PB	ZE	PS	PM	PB	PB	PB	PB

In the last step, a defuzzification method is required to convert an output variable of the fuzzy controller into a numerical variable. For defuzzification, the Centre of gravity method is applied to convert the output to an appropriate value.

2) Extremum seeking controller (ESC)

Extremum Seeking Control (ESC) is a real-time optimization technique used to drive a system to its optimal operating point without requiring an explicit model of the system. In photovoltaic (PV) systems, ESC is commonly applied to track the Maximum Power Point (MPP), which corresponds to the extremum of the power function P(V)=V×I(V). The basic idea is to perturb the system input (e.g., the duty cycle D of a DC–DC converter) and use the measured output (power) to estimate the gradient and adjust the input toward the extremum.

III. RESULT AND DISCUSSION

The effectiveness of the two MPPT controller: Fuzzy logic controller and Extremum seeking controller has been tested in various operating conditions. First, these controllers are tested under standard test conditions. Furthermore, the temperature profile is initialized at 50 °C and decreases linearly to 15 °C over the 2 second simulation period. Simultaneously, the solar irradiance begins at 1000 W/m² for a short duration, undergoes a rapid drop to 500 W/m², followed by a slight recovery, and finally stabilizes around 500 W/m² until the end of the test. This combined fast-changing irradiance and slowly varying temperature profile are applied to the PV system to investigate how the proposed fuzzy logic and extremum seeking MPPT controllers perform

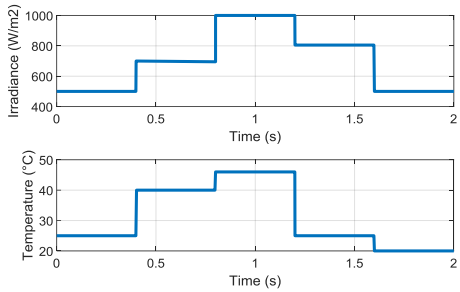

Figure 4. Irradiance and temperature profiles over time.

under these realistic and varying environmental conditions, as illustrated in the Fig. 4.

A. *At Constant Meteorological Conditions (G=1000W/m2 and G=25°C)*

In this case, the two controllers were evaluated for solar irradiance of 1000 W/m^2 and temperature of 25°*C*. Fig. 5 shows the results obtained for the power delivered to the load. It can be seen that the two controllers extract the maximum power with a good efficiency and a good stabilization time as shown in Table III. It can be observed that FLC achieves a slightly higher efficiency (98.91%) compared to ESC (98.88%). However, the tracking time of FLC (0.107 s) is significantly shorter than that of ESC (0.142 s), indicating that FLC responds much faster to changes in constants conditions. Overall, while both methods provide high efficiency, FLC demonstrates superior dynamic performance in terms of rapid power point tracking.

Seeking Control (ESC).

B. *At Variable Meteorogical Conditions*

In this case, the performance of the controllers was evaluated under variable meteorological conditions as shown in Fig. 4.

Fig. 6 shows the output power of both controllers. It can be noted that the two

TABLE III. PERFORMANCE METRICS AT CONSTANT WEATHER CONDITIONS.

Parameters	**MPPT techniques**	
	FLC	***ESC***
Efficiency (%)	98.88	98.6
Tracking Time (s)	0.107	0.142

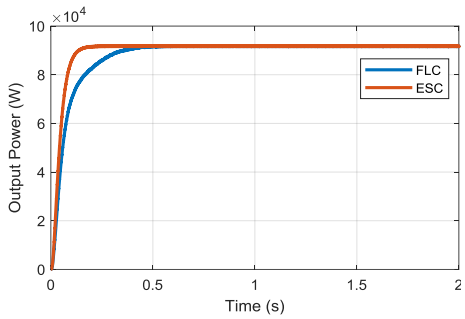

Figure 5. Extracted maximum power at constant conditions.

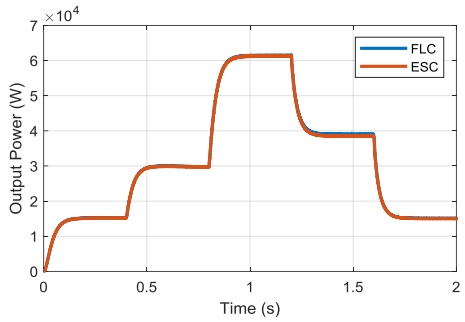

Figure 6. Extracted maximum power at variable conditions.

controllers present a good performance in the different instants of time. The efficiency and the tracking time of these controllers are presented in Table IV. It can be observed that FLC achieves a slightly higher efficiency (98.47%) compared to ESC (98.3%). However, the tracking time of FLC (0.182 s) is significantly shorter than that of ESC (0.2 s), indicating that FLC responds much faster to changes in environmental conditions. Overall, while both methods provide high efficiency, FLC demonstrates superior dynamic performance in terms of rapid power point tracking.

TABLE IV. PERFORMANCE METRICS AT VARIABLE WEATHER CONDITIONS.

Parameters	**MPPT techniques**	
	FLC	***ESC***
Efficiency (%)	98.47	97.3
Tracking Time (s)	0.182	0.2

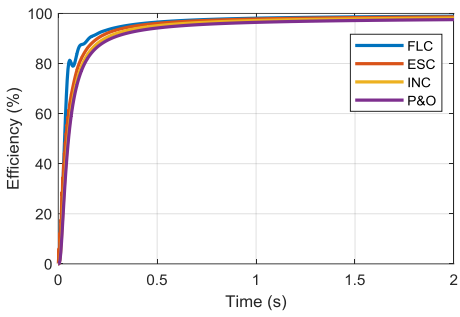

Figure 7. Efficiency comparison of FLC, ESC, P&O, and INC MPPT algorithms.

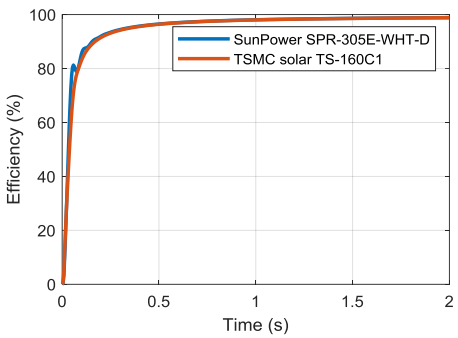

Figure 8. Efficiency of the FLC controller of both PV modules.

TABLE V. PERFORMANCE METRICS OF ALL CONTROLLERS.

Performance Indicator	***MPPT techniques***			
	P&O	***INC***	**ESC**	***FLC***
Efficiency (%)	97.51	98.13	98.6	98.88

TABLE VI. PERFORMANCE INDICATORS OF BOTH PV MODULES.

Performance Indicators	***SunPower SPR-305E-WHT-D***	***TSMC solar TS-160C1***
Efficiency (%)	98.88	98.85
Tracking Time (s)	0.107	0.083

C. Comparison Between the Proposed FLC MPPT Techniques and Benchmarking Techniques

In order to improve the benchmarking procedure, four controller such as ESC, P&O, INC and FLC are evaluated under constant conditions. All controllers' efficiency were plotted under the standard test condition as shown in Fig. 7, and their individual performance levels were highlighted in a Table V. This comparison makes it evident how the suggested approach performs in comparison to accepted norms, highlighting its enhanced tracking precision and greater energy-extraction capacity in a range of irradiance conditions.

D. Comparative Analysis of Fuzzy Logic MPPT Controller Performance with Different PV Panel Technologies

In this case, FLC controller was evaluated using two photovoltaic modules with different characteristics: the SunPower SPR-305E-WHT-D and the TSMC solar TS-160C1.

Fig. 8 shows the efficiency of FLC controller of Both PV technology to demonstrate the robustness of the proposed FLC in different PV module. It can be seen that the efficiency of both PV module is high and consistently exceeds 98.5%. The quantitative data in Table VI confirms this observation, showing nearly identical tracking efficiency and tracking time for both modules.

Specifically, the SunPower module achieved a final efficiency of 98.88%, while the TSMC module reached 98.85%. The tracking times were also remarkably close, at 0.107s and 0.083s respectively. This minimal performance deviation, despite the different PV technologies, quantitatively demonstrates the FLC controller's exceptional robustness and repeatability. Its performance is not dependent on a specific module type, ensuring reliable operation across various PV sources.

IV. CONCLUSION

The comparison between Fuzzy Logic Control (FLC) and Extremum Seeking Control (ECC) for MPPT shows that both methods can successfully track the maximum power point of a photovoltaic system. However, FLC provides faster response, better stability, and lower steady-state oscillations, especially under rapid changes in irradiance. In contrast, ECC is simpler to implement and requires fewer parameters but shows slower convergence and small oscillations around the MPP. Overall, FLC offers higher

tracking efficiency, while ECC remains a practical and low-cost solution for systems with moderate dynamics.

REFERENCES

[1] Li, L., et al. (2022). Review and outlook on the international renewable energy development. *Energy and Built Environment, 3*(2), 139–157.

[2] Martinez Lopez, V. A., Žindžiūtė, U., Ziar, H., Zeman, M., & Isabella, O. (2022). Study on the effect of irradiance variability on the efficiency of the perturb-and-observe maximum power point tracking algorithm. *Energies, 15*(20), 7562.

[3] Manna, S., et al. (2023). Design and implementation of a new adaptive MPPT controller for solar PV systems. *Energy Reports, 9*, 1818–1829.

[4] Feroz Mirza, A., Mansoor, M., Ling, Q., Khan, M. I., & Aldossary, O. M. (2020). Advanced variable step size incremental conductance MPPT for a standalone PV system utilizing a GA-tuned PID controller. *Energies, 13*(16), 4153.

[5] Endiz, M. S., Gökkuş, G., Coşgun, A. E., & Demir, H. (2025). A review of traditional and advanced MPPT approaches for PV systems under uniformly insolation and partially shaded conditions. *Applied Sciences, 15*(3), 1031.

[6] Guanghua, L., Soomar, A. M., Shah, S. H. H., Shaikh, S., & Musznicki, P. (2025). Maximum power point tracking strategies for solar PV systems: A review of current methods and future innovations. *Results in Engineering, 28*, 107227.

[7] Hasan, M. G., Uddin, M. A., Ferdous, A. H. M. I., & Sadeque, M. G. (2025). Enhanced maximum power point tracking using hybrid GA and PSO algorithms for solar PV systems. *Results in Engineering, 28*, 107708.

[8] Mohanty, S., Subudhi, B., & Ray, P. K. (2016). A new MPPT design using grey wolf optimization technique for photovoltaic system under partial shading conditions. *IEEE Transactions on Sustainable Energy, 7*(1), 181–188.

[9] Pathy, S., Subramani, C., Sridhar, R., Thamizh Thentral, T. M., & Padmanaban, S. (2019). Nature-inspired MPPT algorithms for partially shaded PV systems: A comparative study. *Energies, 12*(8), 1451.

[10] Satif, A., Mekhfioui, M., & Elgouri, R. (2025). Advanced techniques for maximizing photovoltaic power: A systematic literature review. *Scientific African, 30*, e02989.

eNergetics 2025
DOI: https://doi.org/10.5281/zenodo.18624245

Original Scientific Article

High Pressure Effects on CH_4-H_2 Premixed Flammes: Application to Gas Turbine Burners

Sofiane Ouali[1], Bensidi Aissa Aya Fella[2]

[1,2]Laboratory of Energy, Mechanics and Engineering LEMI, Faculty of Technology, University M'Hamed Bougara UMBB of Boumerdes, Algeria

[1]s.ouali@univ-boumerdes.dz

Abstract—**This study is a numerical simulation of pressure effects (2.2 to 22 bars) on CH_4-H_2 (50%-50% by volume) turbulent flames. The studied burner is designed for gas turbine application used in power generation. The geometry is cylindrical with 9 radial vanes generating swirled flow. All simulations were conducted for a constant reactive mixture richness of 0.55 and for an inlet temperature of approximately 570 K. A 3D approach was adopted using RANS k-ε Realizable variant for turbulence treatment, Probability Density Function (PDF) model for chemistry and NO model for pollutants. The analysis focused primarily on the thermal and dynamic fields (velocity and temperature) without forgetting NOx and CO formation. The results show that the increase in power induced by the rise in pressure did not significantly affect the flow or the flame structure. A variation in the size and position of the central recirculation zone (CRZ) and the outer recirculation zone (ORZ) was observed, without compromising the stability of the flames. However, the increase in power necessarily implies a higher heat release rate, which led to an intensified production of NOx; from 5.5 ppm to 11.2 ppm for a power increase from 84 kW to 840 kW. These values remain acceptable considering the achieved power level. On the other hand, this variation resulted in a decrease in CO emissions; from 10 ppm to 4 ppm for the same tested power range due to the intensification of the reaction rate. The data obtained show that CH_4–H_2 reactive mixtures injected at high pressure (around 20 bar) represent a promising solution to explore for hydrogen utilization and decarbonization. These results are preliminary, and more in-depth tests must be carried out to assess the feasibility of using hydrogen in gas turbines (G.T) safely and without risk.**

Keywords - premixed combustion, turbulence, pollutants.

I. INTRODUCTION

A. Hydrogen and Decarbonization

The decarbonization of industrial processes is driving researchers to explore all promising avenues, one of which is the use of hydrogen as a fuel. Its high LHV (lower heating value) and carbon-free composition strongly encourage scientists to conduct research aimed at enabling its safe and controlled utilization, particularly in the G.T sector, which generates electricity. This approach seeks to reduce CO_2 emissions and allow greater flexibility in the use of conventional fuels [1].

On the other hand, the use of hydrogen as a fuel, especially in G.T, involves significant technological challenges including storage, transport, safety, flame control, and the increase in NOx emissions [2]. Moreover, its use requires testing the compatibility of the materials that make up existing installations [3].

B. Hydrogen Production Characteristics

Currently, methane reforming is the most important source of hydrogen due to its relatively low production costs and the maturity of the technology [4]. However, this method leads to significant CO_2 emissions and produces non-pure hydrogen, as certain impurities remain and can considerably affect the operation of some systems (such as sulfur in fuel cells). For this reason, to obtain relatively clean hydrogen, attention must be directed toward water

ISBN: 978-86-82602-07-1

electrolysis technologies, such as proton exchange membrane and alkaline electrolysis (PEMEL and AEL). These production approaches offer a clean industrial pathway, especially when powered by renewable energy sources [3,5].

C. Combustion and Emissions

To use hydrogen as a fuel, several techniques have been developed, particularly in the field of gas turbines (GT). These include Dry Low Emission (DLE) burners, which use stratified premixed combustion techniques aimed at reducing NOx emissions [5], and lean combustion, which also limits NOx formation by lowering the combustion temperature but requires careful adjustments to prevent flashback [3]. Additionally, the Exhaust Gas Recirculation (EGR) technology can be used to increase the hydrogen concentration in reactive mixtures by diluting the combustion process, thereby reducing NOx emissions [6,7].

Beyond a 30% hydrogen concentration in CH_4–H_2 mixtures, the physical and reactive properties of the mixture change significantly. This threshold marks the point where structural modifications are required [5]. This is due to the considerable variation in flame length and in the central and outer recirculation zones (CRZ and ORZ), which can compromise the stability of the reactive flow [8].

D. Regulation and Environment

In Europe and North America, gas turbine (GT) emissions are subject to strict and clearly defined regulations. The European Directive (2010/75/EU) sets limits for NOx and CO emissions, standardized at 15% O_2 and corrected for dry conditions according to ISO 11042-1 [1,9]. Hydrogen combustion promotes the formation of thermal NOx, resulting from the increase in combustion temperature [7,9].

The carbon-free composition of hydrogen is a major advantage in the context of industrial process decarbonization. Operating with 100% hydrogen can lead to significant reductions in CO_2 emissions, thereby contributing to international climate neutrality goals [1]. Studies have shown that adding 10% hydrogen can reduce CO_2 emissions by 187.5 kg per ton of fuel consumed [10], while a hydrogen content of 50% can reduce air and fuel requirements by 15% [11].

E. Purpose of This Work

This study aims to explore the effects of high pressures on the premixed combustion of CH_4-H_2 reactive mixtures, in order to contribute to the field of hydrogen utilization in gas turbines operating under conventional (pure CH_4) conditions. In other words, our simulations investigate the premixed combustion of CH_4-H_2 at a power output of 840 kW.

II. Numerical Simulation

A. Computational Methodology

The three-dimensional turbulent premixed CH_4-H_2 flame configurations were solved numerically using ANSYS Fluent software employing the finite volume discretization method. A density-based Pressure-Coupled approach was retained (case of incompressible flow). The SIMPLE algorithm was used to for velocity-pressure coupling. The second-order upwind scheme was applied to all convective terms. A steady-state formulation was employed to reduce computational coast. Convergence was ensured by residual values less than 10^{-6} for all transport equations, with the exception of the continuity equation (10^{-4}).

B. Physical Models

The Reynolds-Averaged Navier-Stokes (RANS) k-epsilon Realizable model was employed to turbulence treatment. This model combines accuracy with reduced computational cost, particularly for rotational flows characteristic of those found in G.T burners. In this two-equation model, the turbulent kinetic energy (k) and the dissipation rate (ε) are solved simultaneously, thereby ensuring the closure of the Reynolds stress tensor in the averaged flow equations.

Combustion was treated using the PDF model, which combines Zimont C-Equation approach to calculate the progress variable "C" with chemical equilibrium to treat chemical species distribution without using reaction mechanism who is computationally expensive.

The progress variable "C" indicates the flame front position and, thus, the flame within the computational domain: a value of 0 corresponds to the fresh mixture region, while a value of 1 represents the burned products zone. The flame front is identified in the region where C values range between 0.4 and 0.6.

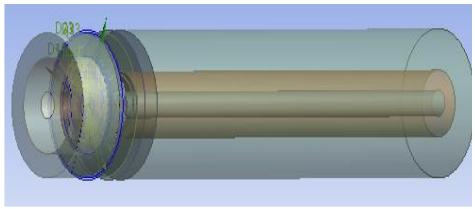

Figure 1. Computational domain.

Nitrogen oxide (NOx) emissions were analyzed using the NOx model treating thermal NOx, prompt NOx and fuel NOx.

C. Grid and Models Validation

The computational domain geometry employed in the present work was derived from the experimental configuration proposed by Runyon J.O.N [12] (Fig. 1).

The detailed geometric specifications, grid study and models validation have been extensively documented and rigorously studied in our prior investigations [13,14].

III. USED PARAMETERS

The study of the influence of pressure (power) on the characteristics of the CH_4-H_2 flame required a meticulous calculation of the mixture proportions in order to isolate the influence of pressure alone. To achieve this, the equivalence ratio was kept constant at $\Phi = 0.55$ in all studied cases, thus ensuring a lean combustion regime that best represents the operation of G.T combustors. The mass fractions of the reactive mixtures used are summarized in Tables I and II.

This tables were obtained using Gaseq and Origin software.

IV. RESULTS AND DISCUSSIONS

As shown in Fig. 2, the progressive increase in operating pressure had a negligible impact on the thermal field within the combustion chamber.

TABLE I. NUMERICAL PARAMETERS.

Pressure (bars)	Power (KW)	MFR (g.s-1)	MF CH_4	MF H_2	MF O_2	MF N_2
2.2	84	51.79	0.02492	0.00312	0.22656	0.7454
4.4	168	103.58				
6.6	252	155.37				
8.8	336	207.16				
11	420	258.95				
13.2	504	310.37				
15.4	588	362.52				
17.6	672	414.31				
19.8	756	466.1				
22	840	517.89				

TABLE II. PROPERTIES OF THE REACTIVE MIXTURE.

H_2 %	λ, $W.m^{-1}.K^{-1}$	η, Pa.s ($1e^{-5}$)	PCI $MJ.kg^{-1}$
0	0.0415	2.86	50.03
5	0.0463	2.86	50.49
10	0.0513	2.86	50.99
15	0.0562	2.85	51.55
20	0.0613	2.85	52.16
25	0.0664	2.84	52.84
30	0.0716	2.84	53.61
35	0.0769	2.83	54.47
40	0.0823	2.82	55.44
45	0.0878	2.81	56.56
50	0.0934	2.79	57.85

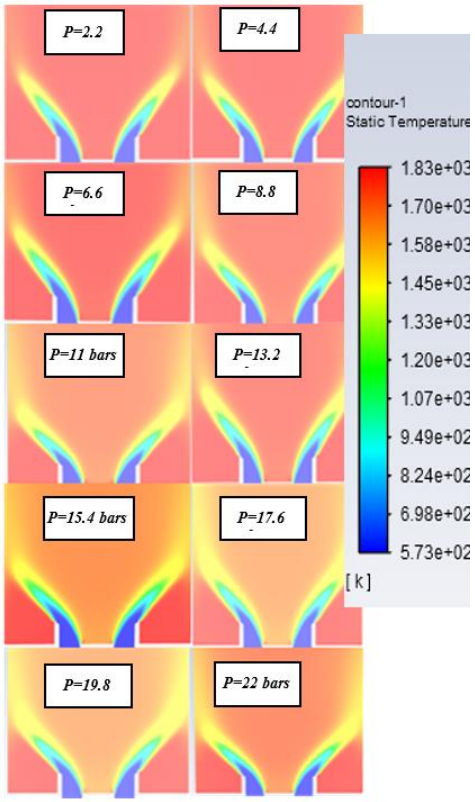

Figure 2. Thermal field.

The maximum flame temperatures across the entire range of pressures studied remained relatively constant. This confirms that high-pressure CH_4-H_2 mixtures do not exhibit direct limitations in use due to heat release. Furthermore, it indicates that the thermodynamic conditions governing combustion are relatively independent of pressure.

Fig. 3 further supports these observations. The increase in maximum temperature is on the order of 5K confirming that pressure increase did not reveal any usage limitations for this particular case.

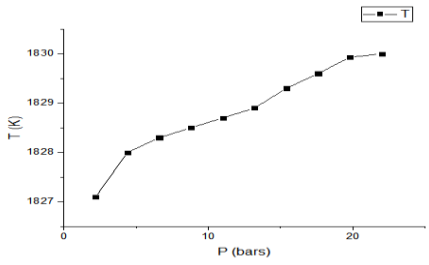

Figure 3. Pressure effect on maximum temperature.

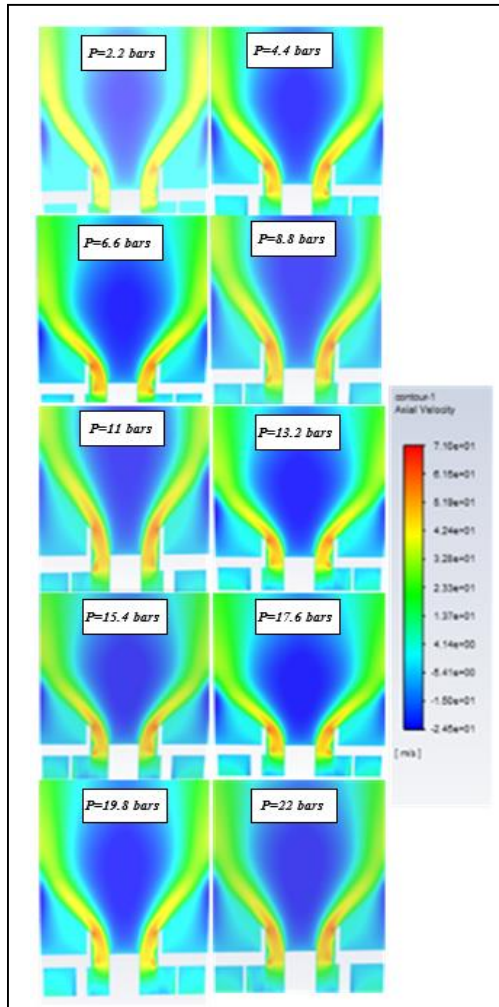

Figure 4. Dynamic field.

Fig. 4 also indicates that the increase in pressure did significantly affect the dynamic

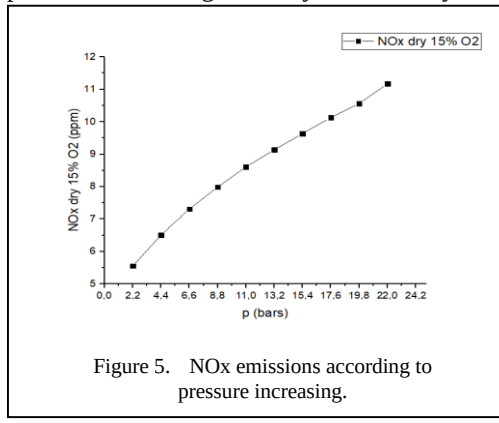

Figure 5. NOx emissions according to pressure increasing.

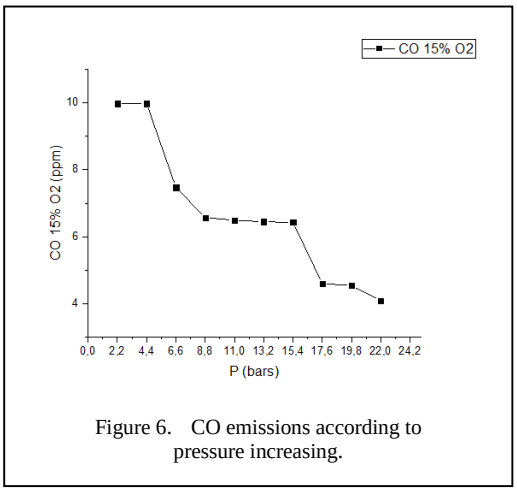

Figure 6. CO emissions according to pressure increasing.

field. The outer recirculation zones (ORZ) and central recirculation zone (CRZ) remain clearly present at the same locations for all simulated cases. Even the axial velocity values (both positive and negative) are relatively similar.

These observations encourage the use of CH_4-H_2 mixtures in gas turbines, demonstrating strong stability of the reactive flow.

Fig. 5 shows an increase in NOx production as a result of elevated operating pressure. This rise can be primarily attributed to the acceleration of chemical reaction kinetics caused by higher flame temperatures, as well as the reduced residence time of reactants under high-pressure conditions. The intensified thermal field promotes the formation of thermal NOx, where elevated temperatures encourage the oxidation of atmospheric nitrogen within the reaction zone.

However, this increase remains relatively acceptable (from 6 ppm to 12 ppm). This moderate rise is well within regulatory limits and environmental standards.

On the contrary, Fig. 6 shows an inverse relationship between operating pressure and CO emissions in the CH_4-H_2 reactive mixture. CO concentrations decrease significantly from 10ppm to 4ppm as the operating pressure varies between 2.2bar and 22bar. This reduction is explained by improved combustion efficiency and a more homogeneous fuel-oxidizer mixture at high pressure, which promotes more complete oxidation of the fuel. The acceleration of chemical reactions at high pressure, combined with shorter residence times, further enhances combustion completeness.

This positive trend indicates that increasing inlet pressure is a beneficial parameter for reducing CO emissions in CH_4-H_2 mixtures.

V. CONCLUSION

This study analyzed the effect of pressure (power) on a reactive CH_4-H_2 mixture at a 50%-50% ratio for G.T applications.

Simulation results showed that CO emissions decreased from 10ppm to 4ppm, which is a remarkable advantage. Meanwhile, NOx levels remained well below the limits set by current regulations.

The dynamic and thermal fields showed no operational limitations; all simulated cases were stable and consistent, with a slight temperature increase observed without affecting overall performance.

This work presents certain methodological limitations: the investigation of a single CH_4-H_2 mixture concentration and a maximum pressure of 22bar restrict the generalization of the results. These limitations pave the way for future research opportunities.

Ultimately, this study demonstrates that CH_4-H_2 mixtures represent a realistic transitional solution toward fully hydrogen powered turbines envisioned for the 2030-2040 horizon. The results obtained may serve as a valuable database for future investigative work.

REFERENCES

[1] Stępień, Z. (2021). A comprehensive overview of hydrogen-fueled internal combustion engines: Achievements and future challenges. *Energies*, *14*(20), 6504. https://doi.org/10.3390/en14206504

[2] Makaryan, I. A., Sedov, I. V., Salgansky, E. A., Arutyunov, A. V., & Arutyunov, V. S. (2022). A comprehensive review on the prospects of using hydrogen–methane blends: challenges and opportunities. *Energies*, *15*(6), 2265. https://doi.org/10.3390/en15062265

[3] Yue, M., Lambert, H., Pahon, E., Roche, R., Jemei, S., & Hissel, D. (2021). Hydrogen energy systems: A critical review of technologies, applications, trends and challenges. *Renewable and Sustainable Energy Reviews*, *146*, 111180. https://doi.org/10.1016/j.rser.2021.111180

[4] Shet, S. P., Priya, S. S., Sudhakar, K., & Tahir, M. (2021). A review on current trends in potential use of metal-organic framework for hydrogen storage. *International Journal of Hydrogen Energy*, *46*(21), 11782-11803. https://doi.org/10.1016/j.ijhydene.2021.01.020

[5] SIEMENS ENERGY. *Documentation technique*. Available at: https://www.siemens.com/global/en.html

[6] Öberg, S., Odenberger, M., & Johnsson, F. (2022). Exploring the competitiveness of hydrogen-fueled gas turbines in future energy systems. *International Journal of Hydrogen Energy*, *47*(1), 624-644. https://doi.org/10.1016/j.ijhydene.2021.10.035

[7] Ditaranto, M., Heggset, T., & Berstad, D. (2020). Concept of hydrogen fired gas turbine cycle with exhaust gas recirculation: Assessment of process performance. *Energy*, *192*, 116646. https://doi.org/10.1016/j.energy.2019.116646

[8] Elbayoumi, M. (2022). *Hydrogen-enriched combustion study at high turbulence and swirl levels inside a gas turbine combustor* (Doctoral dissertation, École de technologie supérieure).

[9] British Standard, I. S. O. (1996). 11042-1: 1996, Gas turbines. Exhaust gas emission Measurement and evaluation. British Standards Institution, UK.

[10] Tanneberger, T., Mundstock, J., Rex, C., Rösch, S., & Paschereit, C. O. (2024, June). Development of a Hydrogen Micro Gas Turbine Combustor: NOx Emissions and Secondary Air Injection. In *Turbo Expo: Power for Land, Sea, and Air* (Vol. 87943, p. V03AT04A051). American Society of Mechanical Engineers. https://doi.org/10.1115/gt2024-125086

[11] Fajardo, J., Barreto, D., Yabrudy, D., Rangel, R., Garcia, S., & Sanjuan, M. (2024, November). Study of the Performance of Compressor Stations With Gas Turbines When Operating With Mixtures of Hydrogen and Natural Gas. In *ASME International Mechanical Engineering Congress and Exposition* (Vol. 88643, p. V006T08A011). American Society of Mechanical Engineers. https://doi.org/10.1115/imece2024-144905

[12] Runyon, J. O. N. (2017). Gas turbine fuel flexibility: pressurized swirl flame stability, thermoacoustics, and emissions [Doctoral dissertation, Cardiff University]. https://orca.cardiff.ac.uk/id/eprint/100686

[13] Ouali, S. (2024). Fuel-air ratio effect on hydrogen-methane flames in a high pressure burner for gas turbines. In *Proceedings of the Romanian Academy, Series A: Mathematics, Physics, Technical Sciences, Information Science*, *25*(2). https://doi.org/10.59277/pra-ser.a.25.2.07

[14] Ouali, S. (2024). Numerical simulation of H2 addition effect to CH4 Premixed turbulent flames for gas turbine burner. *Journal of Applied Fluid Mechanics*, *17*(8), 1746-1758. https://doi.org/10.47176/jafm.17.8.2466

eNergetics 2025
DOI: https://doi.org/10.5281/zenodo.18624282

Original Scientific Article

Machine Learning-driven Energy Optimization Framework for Hospitality Operations: A Case Study of a 130-Room Hotel

Emmanuel E. Duke[1], Mkpamdi N. Eke[2]

[1,2]Department of Mechanical Engineering, University of Nigeria, Nsukka, Nigeria

[1]emmanuel.duke.243689@unn.edu.ng, [2]mkpamdi.eke@unn.edu.ng

Abstract—**This study provides an extensive machine learning approach to reduce energy used in hotels, assessing a 130-room hotel property over a 31-day operating time frame. We utilized ensemble predictive models, including Random Forest, XGBoost, and Gradient Boosting a, to predict daily hotel energy consumption patterns. The analysis revealed three distinct clusters of energy consumption grouped as low (479±197 Litres/day) medium (601±298 Litres/day) high (1,353±345 Litres/day) consumption, with a silhouette coefficient of 0.579 indicating the operational regimes are well separated in terms of energy use. The time series decomposition established stationarity (ADF statistic: -4.459, p;0.001) and weekly seasonality with weekend energy use being 39% higher. The Isolation Forest anomaly detection established 12.5% of operational days as anomalous. The facility had an average daily consumption of 806 liters, with notable variation (σ = 467 liters), indicating energy-saving opportunities. Based on the median baseline, projected fuel savings from intelligent load management are from 28-35%, with yearly CO_2 reductions between 170-230 tons. The contribution of this study is a scalable, data-driven framework for energy management in hospitably operations.**

Keywords - machine learning, energy optimization, hospitality management, predictive analytics, anomaly detection.

I. INTRODUCTION

The hotel industry faces increasing challenges in balancing operational excellence, environmental sustainability, and cost efficiency [1]. Energy consumption is typically one of the largest operational expenses for hotel facilities, accounting for approximately 3-6% of operating costs and a major contributor to carbon emissions [2]. Furthermore, hotels in developing countries that experience unreliable grids find themselves reliant on diesel generators as a backup source of power, which further increases costs and negative environmental impacts. This aligns with earlier findings that hotels worldwide are under increasing pressure to balance service quality with environmental responsibility [1].

The most recent developments in machine learning and environmental data analytics present a compelling opportunity to change the paradigm of intelligent energy management [3]. Previous studies have demonstrated how data mining and machine learning can effectively identify energy inefficiencies and faults in building clusters, underscoring their potential for operational optimization [4]. Unlike many solutions and rule-based systems that encourage linear regression analysis, machine learning algorithms have the capacity to detect complex, non-linear consumption patterns while consistently improving their performance as operating conditions shift [3,5]. Additionally, following improvements in performance,

ISBN: 978-86-82602-07-1

machine learning models provide predictive analytics that allow operators to proactively manage energy consumption and total demand [6].

Nevertheless, the use of these approaches for hospitality operations is still underdeveloped within the academic literature in relation to mid-sized facilities or in economies trying to develop their hospitality industries.

II. METHODOLOGY

A. Study Context and Data Collection

Our analysis focuses on a 130-room hotel facility operating in a tropical climate with inconsistent grid power availability. The dataset comprises 31 observations with three primary variables: date, total fuel consumption (liters), and associated costs. Comparable open-access datasets, such as the Building Data Genome Project, have demonstrated the value of large-scale metered building data for modeling consumption behaviors [7].

The lighting infrastructure comprises 4,468 fixtures including bedside lights, spotlights, security lights, panel lights, and facility lighting, representing a substantial electrical load.

B. Feature Engineering

Features to extract meaningful patterns for the respective domain are critical to machine-learning solvable problems. Types of dedicated features, included the following:

Lag Features: Previous day (Lag-1), a three-day cycle (Lag-3) and a week (e.g., Lag-7)

Rolling Statistics: 7-day rolling mean and standard deviation of both trend and volatility

Temporal Features: Day of month, day of week, weekend indicator, and month

Derived Metrics: Cost per liter, consumption deviation from baseline

C. Machine Learning Models

An ensemble approach was used to apply to use multiple algorithms to generate more robust predictions:

Random Forest Regressor: 100 trees, max depth of 10 to account for potential non-linear association

XG Boost Regressor: 100 estimators, max depth of 6, learning rate .1, and regularization

Gradient Boosting Regressor: 100 estimators, max depth of 5, to account for sequential errors

Models were trained on 80% of the data (19 data samples), and validated with 20% of the data (5 data samples). Models were evaluated using R^2 Score, Root Mean Squared Error (*RMSE*), and Mean Absolute Error (*MAE*).

D. Clustering and Anomaly Detection

K-means clustering ($k = 3$) was implemented using standardized features (i.e., total consumption, daily cost, weekend indicator) to distinguish operational regime. Evaluation of clusters was done via the silhouette coefficient.

E. Time Series Analysis

The Stationarity was assessed using the Augmented Dickey-Fuller (ADF) test. Seasonal decomposition was performed using an additive model with 7-day period to separate trend, seasonal, and residual components. This decomposition reveals underlying patterns and helps identify systematic variations in consumption behavior.

F. Optimization Assessment

The optimization potential was quantified with baseline analysis using the median usage as the efficiency target. Any day with a usage exceeding the baseline represents the opportunity for optimization. Savings estimates for conservative (50% reduction), moderate (75% reduction), and aggressive (100% reduction) scenarios were calculated based on projected days to efficiency reduction. The savings opportunity was annualized based on the observed usage patterns.

G. CO_2 Reductions Calculation

CO_2 reductions were calculated using the standard conversion factor of 2.68 kilograms CO_2 per liter of diesel fuel combustion. The CO_2 emissions reduction were quantified through baseline analysis using observed operational data from 31 days of facility operations. The median daily consumption of 691 liters was established as the efficiency target. Any day exceeding this baseline represents an optimization opportunity; 16 days (51.6%) exceeded baseline with 7.234 liters of excessive consumption (28.9% of total).

CO_2 Reduction Calculation Framework:

Annual CO_2 Reduction (kg) = Annual Fuel Savings (liters) 2.68 kg CO_2 /liter.

Figure 1. Exploratory Data Analysis - (a) Daily consumption trend showing high variability, (b) Cost trend over the observation period, (c) Distribution of daily consumption with positive skew, (d) Box plots revealing systematic day-of- week patterns with higher Monday/Sunday consumption.

Annual excessive consumption = 7.234 liters ÷ 16 days · 365 days · 51.6% = 85.216 liters annually. CO_2 reduction = 85,216 liters · 2.68 kg CO_2/liter = 228.378 kg approximately (230 metric tons) for aggressive scenario.

Moderate: 63.912 liters · 2.68 = 171.288 kg approximately (170 metric tons).

III. Results

Analysis of 31 days of operational data revealed substantial variability in daily energy consumption. Mean daily consumption was 806 liters (σ = 467 liters), with consumption ranging from 150 to 1,910 liters (12.7 variation). The coefficient of variation (CV = 0.58) indicates high consumption variability, suggesting significant optimization potential.

A. Descriptive Statistics

Temporal analyses examined for systematic patterns by day of week. Average consumption was highest on Monday and Sunday (> 1.000 Litres/day) and lowest on Tuesday (541 Litres/day). Weekend average consumption was 1.028 Litres/day compared to a weekday average of 739 Litres/day, representing a 39% increase. This pattern would appear to suggest occupancy driven consumption due to higher weekend activity by guests. Fig. 1 describes temporal patterns and the distribution characteristics of daily energy consumption.

B. Clustering Analysis

KK-means clustering was examined to identify three operational regimes to differentiate facility consumption patterns with a silhouette score of 0.579, indicating distinguishable clusters.

Low-consumption cluster -479±197 L/day (37.5% of days)- baseline efficiency

Medium-consumption cluster- 601±298 L/day (29.2% of days)- standard operations

High-consumption cluster - 1,353±345 L/day (33.3% of days) -182% increase over low cluster

The clustering analysis indicates that the facility operates under distinctly different regimes, rather than simply representing a continuous level of consumption variation. The high-consumption cluster represents the best target intervention opportunity for optimization.

C. Machine Learning Model Performance

Three ensemble models were evaluated on a held-out testing set. Gradient boosting performed the best of the three models with R^2 = 0.076, *RMSE* = 475.75 liters, and *MAE* = 380.78 liters. Random Forest and XGBoost scored a negative

R^2 (-0.575 and -1.271 respectively), which indicated issues around overfitting bar the model complexity versus training sample size.

Feature importance analysis revealed that the rolling statistics, within the supervised learning model heighten predictive value for the models. For example, rolling standard deviation (7-day) contains a predictive value of 29.8% while rolling mean was only 20.4%. Furthermore, lag features contained a cumulative predictive value of 34.9%, which reconfirms the autoregressive pattern. In contrast, temporal features (day of the month, weekend indicator, etc.) collectively only accounted for 15.0% which suggest that energy consumption is more primarily driven by recent patterns than any calendar-based effects.

D. Anomaly Detection

The exploration of the Isolation Forest found a total of three anomalous days, representing 12.5% of the dataset. Specifically, there was one extreme low consumption event at 150L, which is 78% below the median on July 18, and two extreme high consumption events at 1.815L and 1.910L, which is 163-176% above the median on July 24 - 25. While we cannot be completely sure, these events could possibly signal malfunctioning technology, special events, or operational error, which makes the continued development of the automated monitoring tools all the more valuable.

E. Time Series Analysis

The results of the Augmented Dickey-Fuller test found that the time series was stationary (ADF statistic: -4.459, $p = 0.0002$), meaning that the time series could be said to show mean reverting characteristics and that the time series was appropriate for forecast. The seasonal decomposition also showed trends for a 7-day cycle, suggesting mean peak consumption was on Sundays to Mondays and trough consumption was on Tuesdays. Approximate variation of 25-30% was derived from the seasonal cycle, while the residuals indicate a stochastic component.

F. Optimization Potential

Using median daily consumption of (691L) as the efficiency baseline, 16 days or approximately 51.6% of the days could be found to be above the efficiency baseline: The total excessive consumption in 31 days was 7.234L of water based on the observations, which was approximately 28.9% of total consumption observed. As for potential reductions in surface area, conservative scenarios show approximately a 14.5% reduction, which would indicate ₦31.7M in total annual savings. Moderate scenarios potentially indicate 21.7% reductions, which would indicate ₦47.5M savings associated with those reductions; and aggressive scenarios signal possible 28.9% reductions, which would equate to ₦63.4M in potential annual savings, and also 230 metric tons CO_2 of reduction per year.

IV. Discussion

The discovery of three separate consumption clusters with a significant degree of separation (silhouette score: 0.579) reinforces the finding that hotel energy consumption occurs in discrete regimes rather than a continuous spectrum, refuting the implicit idea in many energy management systems [3]. Rather than a single strategy serving all consumption purposes, these findings suggest the need for regime specific strategies in energy management.

A. Findings

Firstly, the simple predictive performance of ensemble models (with an R^2 ranging from -1.27 to 0.08) indicates that there are system-wide issues when forecasting energy consumption, which arise from using limited data, as opposed to interpretations related to methodological issues. The 31 days of consumption data only provide 24 training samples to fit more complex models, and, on top of limited consumption data, variables that are critical to understanding energy consumption context (occupancy rates, weather and/or microclimates in the hotel, and other operational choices) were not available. The study did perform an out-of-sample test, which checks predictive ability on unseen data.

However, cross-validation was not conducted, because the dataset was small (31 daily samples). This limitation affects robustness and generalizability, and would need to be addressed in future work using larger datasets.

Despite these limitations, feature importance analysis provides workable insights into operational management. The 39% increase in energy consumption over the weekend is a statistically significant and predictable pattern. The establishment of weekend specific protocols could lead to substantial energy savings. If weekend consumption protocols targeted interventions to accomplish reductions in

consumption to weekday levels, this would yield savings of greater than 15% per year.

Last, the anomaly detection feature has immediate practical value in that it will automatically flag for further investigation energy consumption that is unusual or is outside the adjoined consumption cluster for each system category. The projected 28.9% optimization potential relates to ₦63.4 million in cost reduction over a 1-year period at the current price of diesel fuel. The average implementation cost for a 130room facility is typically ₦5-10 million-this would likely have been less in previous years.

B. Limitations

The 31-day time-frame is not long enough to account for seasonal effects. Broader datasets such as the Building Data Genome Project demonstrate how larger temporal and spatial datasets can enhance model accuracy and generalizability [7]. The introduction of other unmeasured variables such as occupancy data, weather data, and equipment data would greatly improve the predictive capacity of these variables.

In addition, this study was conducted in a single facility, and therefore it cannot be generalized to different hotel types, sizes, or geographical contexts. The methodology would need to be validated with further studies conducted at multiple facilities.

V. CONCLUSION

This research communicates a machine learning framework for energy optimization in hospitality operations, describing its use in a 130-room hotel. Our multifaceted analytical approach comparing supervised learning, unsupervised clustering, anomaly detection, and time series analysis contributes both theoretical insights and practical tools for energy management. Key findings include distinctions identifying three consumption clusters, confirming that consumption during weekend periods is 39% greater than weekday periods, successfully detecting deviations (12.5% of days) from the norm, and predicting a 28.9% opportunity for optimization (₦63.4 million annual savings and 230 metric tons of CO_2 reduction). This framework is able to use basic daily consumption data for modeling, thus providing an accessible option for utilizing the approach even where data infrastructure varies. This article explains how the projected savings and CO_2 reductions were calculated - and they are not from simulation or field experiments, but rather from empirical extrapolation based on historical data and baseline analysis.

In the near term, recommendations include establishing anomaly detection systems, weekend optimization strategies, and establishing baseline monitoring. For the near term, activities should relate to predicted load management protocols, and cluster-based operational protocols or guidelines. For the medium term to address longer term proposal other investments, real-time monitoring capabilities, and systems to link Building Management Systems (BMS) and evaluation for equipment replacements would prioritize the aspects of optimization. Most existing studies [3,5,6] focused on large commercial or office buildings with rich sensor data and advanced Building Management Systems (BMS). This article breaks new ground by applying ML to a mid-sized (130-room) hotel; and operating in a developing-country context (Nigeria), where data infrastructure and grid reliability are limited. This demonstrates that data-driven energy optimization can still be achieved with minimal datasets (daily fuel logs only). Combined advances in machine learning, more data capabilities, and growing sustainability priorities has created opportunities that makes perception of energy management based on intelligence accessible., Hotels that implement approaches successfully will result in a competitive cost advantage, sustainability presentation, and operational sustainability.

ACKNOWLEDGMENT

This research was conducted as part of ongoing efforts to advance sustainable energy management in hospitality operations. We acknowledge the Metropolitan Hotel Calabar, Cross River, Nigeria hotel management for providing access to operational data.

REFERENCES

[1] Bohdanowicz, P. (2005). European hoteliers environmental attitudes: Greening the business. *Cornell Hotel and Restaurant Administration Quarterly, 46*(2), 188-204.

[2] Deng, S., & Burnett, J. (2000). A study of energy performance of hotel buildings in Hong Kong. *Energy and Buildings, 31*(1), 7-12.

[3] Ahmad, T., Chen, H., Guo, Y., & Wang, J. (2017). A comprehensive overview on the data driven and large scale based approaches for forecasting of building energy demand: A review. *Energy and Buildings, 165*, 301-320.

[4] Capozzoli, A., Lauro, F., & Khan, I. (2015). Fault detection analysis using data mining techniques for a cluster of smart office buildings. *Expert Systems with Applications*, *42*(9), 4324-4338.

[5] Rahman, A., Srikumar, V., & Smith, A. D. (2018). Predicting electricity consumption for commercial and residential buildings using deep recurrent neural networks. *Applied Energy*, *212*, 372-385.

[6] Wang, Z., Hong, T., & Piette, M. A. (2018). Building thermal load prediction through shallow machine learning and deep learning. *Applied Energy*, *263*, 114683.

[7] Miller, C., & Meggers, F. (2017). The Building Data Genome Project: An open, public data set from non-residential building electrical meters. *Energy Procedia*, *122*, 439-444.

eNergetics 2025
DOI: https://doi.org/10.5281/zenodo.18624313

Original Scientific Article

Interface Defect Layer Engineering for Realistic Modeling of 2D/3D Mixed Dimensional Perovskite Solar Cells

Walagedara Gamage Ayomi Pabasara[1], Galhenage Asha Sewvandi[2]

[1,2]Department of Materials Science and Engineering, University of Moratuwa, Katubedda, Sri Lanka
[1]Department of Engineering Technology, University of Ruhuna, Kamburupitiya, Sri Lanka

[1]ayomi@fot.ruh.ac.lk, [2]galhenagea@uom.lk

Abstract—**This study focuses on a comprehensive investigation into the influence of interface defects on the performance of 2D/3D mixed-dimensional perovskite solar cells (PSCs). To address the limitations of the conventional Interface Defect Density (IDD) model, the Interface Defect Layer (IDL) model has been introduced to more realistically represent the effect of the interface defects and recombination losses. Based on two defect models, a 2D/3D mixed dimensional PSC with a device architecture of FTO/TiO_2/$MAPbI_3$/$BA_2MA_2Pb_3I_{10}$/Spiro-OMeTAD/Au was simulated. 2D/3D and 3D/ETL interfaces were identified as critical interfaces in device performance degradation in using the IDD model-based simulations. Accordingly, thin IDL (IDL1 and IDl2) were placed at these interfaces, and their thickness and defect density were systematically optimized. A thickness of 1 nm and a defect density of 10^{13} cm^{-3} were identified to be the most effective values for suppressing recombination and improving efficiency. The study reveals that IDL1 (3D/ETL interface) has a significant effect on photovoltaic parameters than IDL2 (2D/3D interface). The IDL model device achieved a simulated PCE of 19.25%, V_{oc} of 0.98V J_{sc} of 24.68 mA/cm^2, and FF of 79.83% at the optimal thickness and defect density values.**

Keywords - 2D/3D mixed dimensional PSCs, interface defects, interface defect layer, stability, SCAPS.

I. INTRODUCTION

Perovskite Solar Cells (PSCs) are leading third-generation photovoltaic technologies, offering higher Power Conversion Efficiency (PCE) along with cost-effective fabrication practices. However, they are suffering from long term operational stability issues upon exposure to high temperatures, humidity and UV radiation [1]. As a solution for that, 2D perovskite materials, proven to be highly stable, are incorporated with 3D perovskite to enhance the stability. The resultant 2D/3D mixed-dimensional perovskite solar cells serve as a promising approach to achieving both high efficiency and improved stability[2-4]. By integrating 2D perovskite layers as a capping layer on 3D perovskites, it facilitates suppressing ion migration, and passivates surface defects enhancing resistance to heat, moisture and UV radiation [4,5].

In conventional 2D/3D mixed dimensional PSCs are formed from several key layers, including the back contact electrode, Hole Transport Layer (HTL), 2D perovskite capping layer, 3D perovskite light harvesting layer, Electron Transport Layer (ETL), Front contact. In this device architecture, there are three pivotal interfaces: 2D/HTL, 2D/3D and 3D/ETL. In the carrier transportation process, photogenerated carriers in the absorber layer are transported through these interfaces to the corresponding electrodes. These interfaces can introduce localized defect concentrations due to structural

ISBN: 978-86-82602-07-1

disorder, lattice mismatch, , and incomplete chemical bonding[6]. They serve as nonradiative recombination centers, disrupting charge flow and drastically reducing the overall device performance [7].

Conventional numerical approaches to solar cell simulation have a tendency to neglect the severe spatial non-uniformity of interfacial defects. Consequently, the impact of localized recombination at interfaces is usually not considered. Addressing this modelling limitation is necessary in order to facilitate accurate device simulation and correct accounting of the effects of the interface defect [8,9].

In this study, a systematic numerical investigation was conducted on a 2D/3D mixed-dimensional PSC employing SCAPS-1D simulation software. First, interface defect density (IDD) sensitivity analysis is performed to identify the most critical interface. Then, an Interface Defect Layer (IDL) approach [9-11] is adopted at the identified interface to match localized recombination zones.

II. METHODOLOGY

A. Device Design

The device is simulated according to the PIN (Positive-Intrinsic-Negative) configuration. Titanium Dioxide (TiO_2) and Spiro-OMeTAD were chosen as ETL and HTL, respectively. These two materials are widely used in SCAPS 1D simulations as they provide well-defined parameters, ensuring the accuracy of solar cell modelling. As 3D perovskite, Methyl Ammonium Lead Iodide ($MAPbI_3$) was selected, and Butyl Ammonium Lead Iodide (n=3) [$BA_2MA_2Pb_3I_{10}$] was inserted as the capping layer. In this device design, Fluorine-doped Tin Dioxide (FTO) and Gold (Au) serve as the front and back electrode contacts, respectively. Fig. 1 illustrates the device architecture of the simulated PSC.

B. Device Simulation

All simulations were carried out using the drift-diffusion model under AM 1.5 Solar Spectrum of SCAPS 1D simulation software. The simulation parameters for the simulation were taken from previously published literature sources as mentioned in Table I. The electron thermal velocity and hole thermal velocity are taken as 10^7 cms^{-1}. The capture cross-section of the hole and electron is $1 \cdot 10^{-15}$ cm^2.

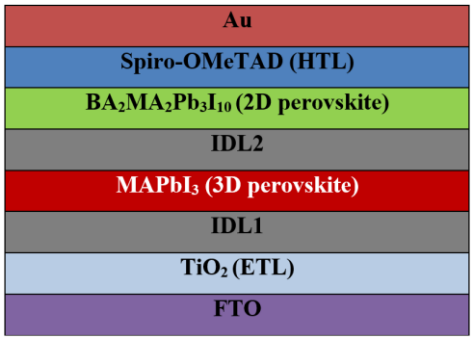

Figure 1. The device architecture of proposed 2D/3D mixed dimensional PSC.

III. RESULTS AND DISCUSSION

A. Effect of Interface Defect Density (IDD) on Different Interfaces (The conventional approach)

In the 2D/3D mixed dimensional PSCs, there are three primary interfaces: 2D/HTL, 2D/3D, and 3D/ETL. The effect of interface defect densities of each interface has been investigated by varying the IDD at each interface. As shown in Fig. 2, a notable difference in the behavior of performance can be observed across the three interfaces. The photovoltaic parameters showed negligible response for the interface defect density variations in the 2D/HTL interface. In contrast, all photovoltaic parameters are highly sensitive to the 3D/ETL interface defect density variation, significantly degrading all the parameters when increasing the defect density. Meanwhile, 2D/3D interface defects show a moderate impact on device performance, resulting in a mild decline in PCE, V_{oc} and FF.

The reasons behind these variations can be explained through interface charge accumulation and recombination. The majority of charge carrier accumulation and recombination happens at the 3D/ETL interface. In addition to that, holes generated within the absorber layers have a higher possibility to successfully reach the HTL without trapping, whereas electrons are more susceptible to being trapped at the 3D/ETL interface [12]. In the 2D/3D interface, there is a balance between charge transportation and the defect-tolerance nature of the 2D perovskite material, which may tolerate severe nonradiative recombination. Hence, the 2D/3D interface exhibits a moderate impact compared to the highly recombination-prone 3D/ETL interface.

TABLE I. INPUT PARAMETERS USED FOR THE SCAPS SIMULATIONS [2,9,13-15].

Parameters	**FTO**	**TiO_2**	**IDL 1**	**$CH_3NH_3PbI_3$**	**IDL2**	**$BA_2MA_2Pb_3I_{10}$**	**Spiro-OMeTAD**
Layer thickness (nm)	500	100	8	Varied	8	1000	30
Bandgap (eV)	3.5	3.26	1.41	1.55	1.41	1.6	2.9
Electron Affinity (eV)	4	4.2	4.17	3.9	4.17	3.87	2.2
Dielectric permittivity (relative)	9	38	8.2	3.2	8.2	5.9	3
Effective density of states of the conduction band C_B ($1/cm^3$)	$2.2\cdot10^{18}$	$2.2\cdot10^{17}$	$1\cdot10^{18}$	$2.8\cdot10^{20}$	$1\cdot10^{18}$	$7.24\cdot10^{17}$	$2.5\cdot10^{18}$
Effective density of states of the valence band V_B ($1/cm^3$)	$1.8\cdot10^{19}$	$1.8\cdot10^{18}$	$1\cdot10^{18}$	$3.9\cdot10^{20}$	$1\cdot10^{18}$	$1.5\cdot10^{18}$	$1\cdot10^{19}$
Electron mobility (cm^2/Vs)	20	2·14	1.6	11.8	1.6	1.4	$2\cdot10^{-4}$
Hole mobility (cm^2/Vs)	10	1·13	1.6	11.8	1.6	1.4	$2\cdot10^{-4}$
Shallow uniform donor density N_D ($1/cm^3$)	$2\cdot10^{19}$	$6\cdot10^{19}$	0	$1\cdot10^{9}$	0	0	0
Shallow uniform acceptor density N_A ($1/cm^3$)	$1\cdot10^{15}$	0	$1\cdot10^{12}$	$1\cdot10^{9}$	$1\cdot10^{12}$	0	1×10^{18}
Defect density	$1\cdot10^{12}$	$1\cdot10^{12}$	$1\cdot10^{18}$	$1\cdot10^{12}$	$1\cdot10^{18}$	$1\cdot10^{15}$	$1\cdot10^{12}$

Overall, in 2D/3D mixed-dimensional perovskite solar cells, the 3D/ETL interface plays a vital role in charge transport relative to the 2D/HTL interface, making it particularly vulnerable to defect density variations.

B. Effect of Interface Defect Layer (IDL) at the Critical Interface

To make the simulation results more realistic, avoiding the limitations of the conventional interface defect density model, a thin IDL was inserted at the 2D/3D and ETL/3D interfaces, as shown in Fig. 1. The IDL parameters were optimized in terms of both thickness and the defect density. This approach reflects physical degradation at the interface, as supported by previous findings reporting defect-rich zones spreading several nanometers long due to lattice mismatch and chemical instability [11]. Optimization facilitates assessing the device sensitivity to interfacial recombination and enables the identification of tolerable defect levels for efficient performance [8,9].

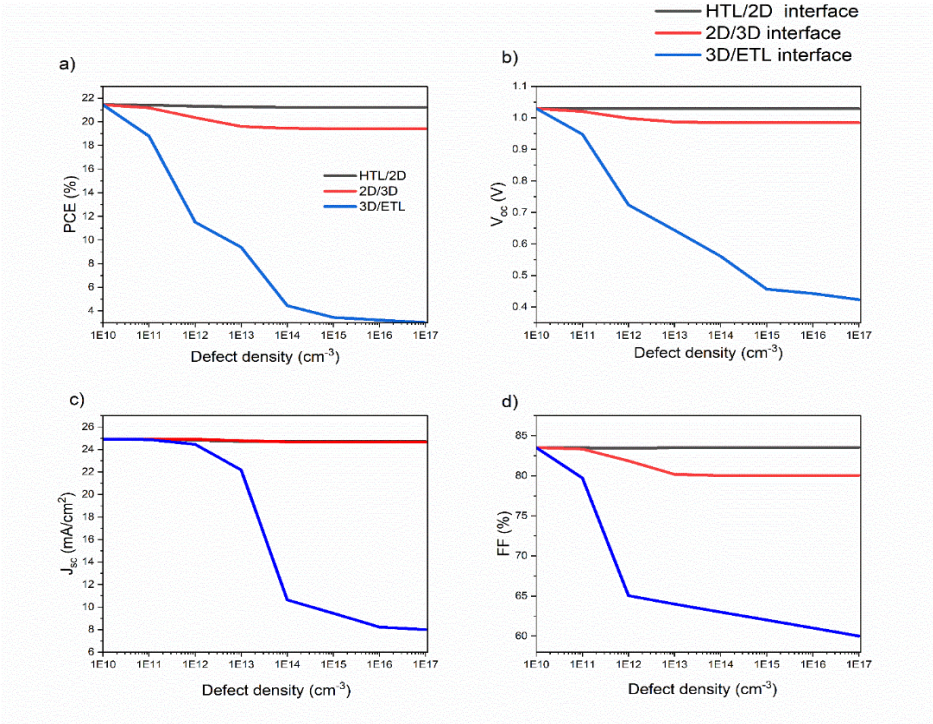

Figure 2. Effect of interface defect density on device performance (IDD model) a) PCE b) Voc c) Jsc and d) FF.

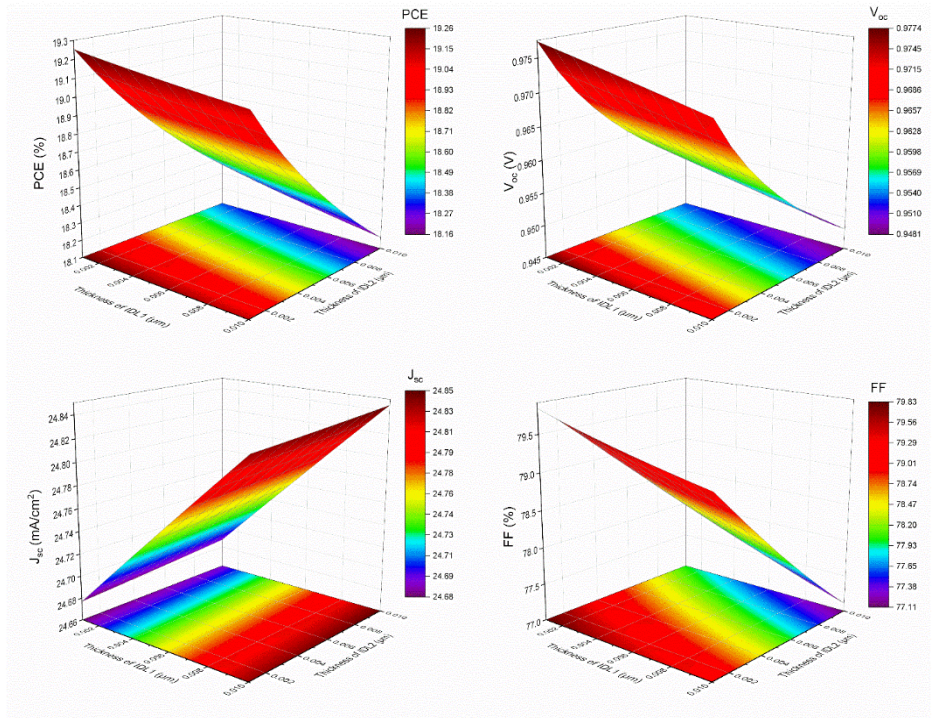

Figure 3. Effect of thickness of IDL on device performance a) PCE b) V_{oc} c) J_{sc} and d) FF.

1) Effect of IDL thickness on the performance of the device

As interface defect acts as charge recombination centers, there is a strong correlation between the performance of PSCs and the interface defect layers IDL1 and IDL2 that are located between the ETL/3D and 2D/3D interfaces, respectively. Based on the given initial parameters, the thickness of IDL1 and IDL2 varied from 1 nm to 10 nm. The resulting performance trends are graphically represented in Fig. 3.

Fig. 3(a) showed the behavior of PCE according to thickness of IDL1 and IDL2. Regardless of the thickness of IDL1, there is no crucial impact on PCE, highlighting the dominant role of IDL2 in determining the performance. As the thickness of IDL2 increases, the PCE has declined from 19.25% to 18.35% at IDL1 thickness of 1 nm. This decline can be attributed to the improved recombination rate of electrons and holes, induced by increased thickness of the interfacial defect layer [9].

When the thickness of the interface defect layer IDL2 is held constant, the V_{oc} shows negligible change when increasing IDL1 thickness, as depicted in Fig. 3(b). However, V_{oc} slightly declines when IDL2 thickness rises, indicating that IDL2 has the principal impact on V_{oc}.

As per Fig 3(c), J_{sc} remains unchanged when increasing the IDL2 thickness. However, J_{sc} slightly increases with IDL1 thickness enhancement. Fig. 3(d) exhibits the response of the fill factor (FF) to the thickness variations. FF declines with the thickness enhancement of both layers. However, compared to IDL1, IDL2 thickness variations have a significant effect on FF. By considering both variations, a 1 nm thickness of both layers has been selected as the optimum thickness value for the next steps of the simulation.

2) Effect of defect densities of the IDL on the performance of the device

Interfacial recombination has a substantial impact on the overall performance of 2D/3D mixed dimensional PSCs. Therefore, to represent realistic device behavior and appropriately address the challenge of quantifying the recombination rates in real devices [9], the impact of defect densities of IDL layers was systematically investigated. The defect densities of both layers varied between 10^{13} - 10^{20} cm^{-3}, keeping the other parameters constant.

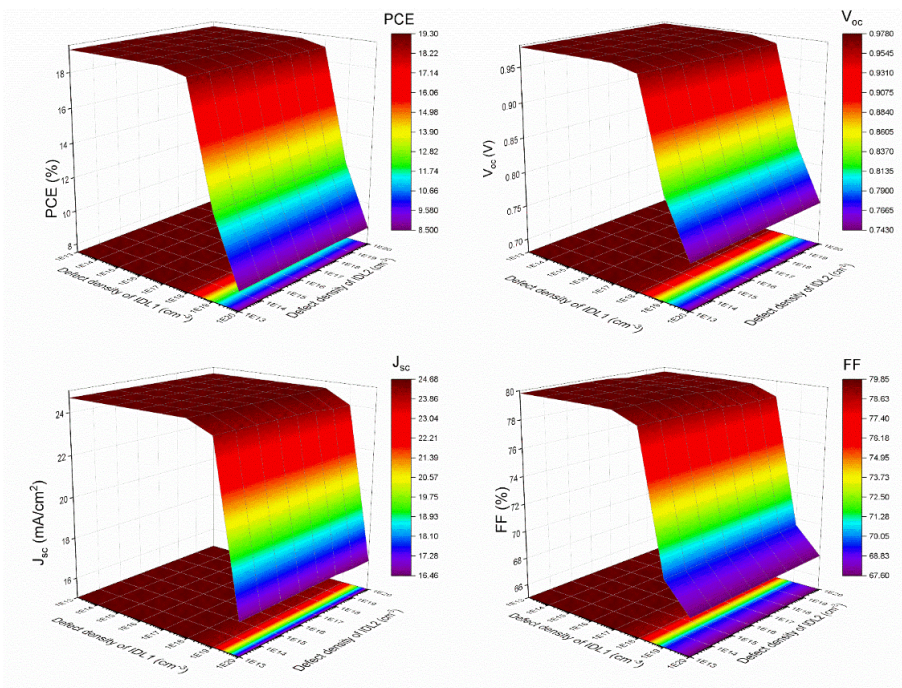

Figure 4. Effect of defect density of IDL on device performance a) PCE b) Voc c) Jsc and d) FF.

The performance trend with varying thickness is plotted in Fig. 4. When the IDL1 defect density increases to 10^{17} cm^{-3}, the device performance remains stable for all IDL1 defect densities. After that, there is a substantial reduction in PCE. However, PCE shows negligible response to the IDL2 defect density variations. Similar behavior can also be seen in the V_{oc}, J_{sc} and FF variations as well highlighting the dominant influence of defect density of IDL1 on performance of the device. Therefore, the optimum defect density for both IDL1 and IDL2 was selected as 10^{13} cm^{-3}.

C. Comparison Between IDD and IDL Approaches

By taking the optimum thickness and defect densities of the IDLs, performance of the device is calculated. The IV curves correspond to the two defect models that are illustrated in Fig. 5 and the device performances are mentioned in Table II. The comparative analysis between the interface IDD and IDL approaches reveals considerable differences in photovoltaic performance. In the IDD case, defects are treated as idealized, localized interface traps, which may underestimate the extent of recombination occurring at interfaces of 2D/3D mixed dimensional PSCs.

In the IDL model, a defect region extended for a few nanometers was introduced, which is a better representation of interface degradation, including interdiffusion and structural disorder. This spatially resolved defect region increases the effective recombination volume, resulting in a reduction of V_{oc} from 1.03 V to 0.98 V, and a decline in FF from 83.51% to 79.83%, highlighting greater resistance and recombination losses. The J_{sc} also slightly decreases from 24.92 to 24.68 mA/cm². As a result, PCE drops from 21.43% to 19.25%.

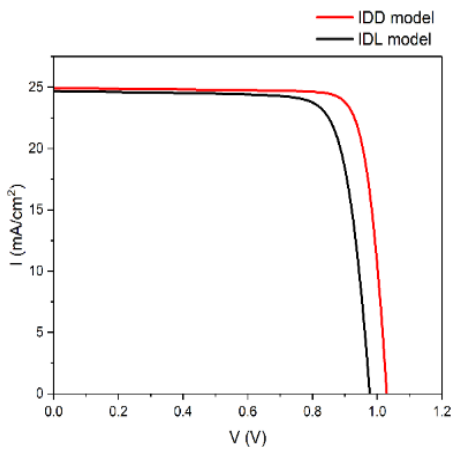

Figure 5. Comparison of the IV characteristics of IDD and IDL models.

In the conventional Interface Defect Density (IDD) model, the interface between two layers-such as the 3D perovskite and ETL-is treated as an infinitesimally thin plane that contains a fixed number of defect states per unit area, denoted by the interface trap density N_{it}.

The carrier recombination at this idealized interface is described by a boundary condition, expressed through the surface recombination velocity S, which quantifies how rapidly carriers recombine at the interface:

$$S = \sigma v_{th} N_{it}\,, \tag{1}$$

where σ is the carrier capture cross-section (cm²) and v_{th} is the thermal velocity. The recombination current density is expressed as:

$$J_{rec} = qS\frac{(np - n_i^2)}{(n+p)}, \tag{2}$$

where S is surface recombination velocity, n, p electron and hole concentrations, n_i is the intrinsic carrier concentration, and q is the elementary charge.

This relation acts as a boundary condition linking carrier fluxes on either side of the interface:

$$\begin{aligned} J_n\left|x_0^- J_n\right|x_0^+ &= qS(n-n_0) \\ J_p\left|x_0^- J_p\right|x_0^+ &= qS(p-p_0) \end{aligned}. \tag{3}$$

Thus, recombination is confined to a two-dimensional plane, and all defect effects are represented by the single parameter S.

Because the IDD model treats the interface as zero-thickness, it cannot capture spatially distributed defects, interdiffusion, or lattice disorder extending a few nanometers into adjacent layers. As a result, it often underestimates recombination losses and interface degradation effects.The proposed Interface Defect Layer (IDL) model, in contrast, introduces a finite layer of thickness of 1–10 nm

with distributed trap states of density. Within this region, recombination follows Shockley-Read-Hall (SRH) statistics, modifying the carrier continuity equations to include volumetric recombination terms. This allows spatially resolved treatment of recombination losses and electrostatic potential variations, providing a physically realistic depiction of interfacial degradation. Within the IDL, recombination is governed by the Shockley-Read-Hall (SRH) mechanism, and the recombination rate per unit volume is expressed as per Eqs. (4) and (5) [2].

$$R_{SRH} = \frac{np - n_i^2}{\tau_p (n + n_i) + \tau_n (p + p_i)}, \qquad (4)$$

$$\tau_{n,p} = \frac{1}{\sigma v_{th,n,p} N_t}. \qquad (5)$$

Here, R_{SRH} represents the rate of the Shockley–Read–Hall recombination, n and p are the concentrations of electrons and holes, respectively. τ_p, τ_n are the lifetimes of the electron and hole. υ_{th}, n, p are the thermal velocities of electrons and holes, respectively. The carrier continuity equations inside the IDL region are modified to include the volumetric recombination term as shown in Eqs. (6) and (7).

$$\frac{dJ_n}{dx} = q(G - R_{SRH,IDL}), \qquad (6)$$

$$\frac{dJ_p}{dx} = -q(G - R_{SRH,IDL}), \qquad (7)$$

where G is the generation rate.

At the boundaries of the IDL, both carrier current densities and potentials are continuous as Eqs. (8) and (9):

$$J_n(ETL) = J_n(IDL) = J_n(3D), \qquad (8)$$

$$\phi(ETL) = \phi(IDL) = \phi(3D), \qquad (9)$$

where ϕ represents the electrostatic potential in the semiconductor.

This formulation treats the interface not as a discontinuity, but as a transition region where defects influence carrier transport and recombination in a spatially resolved manner. The quantitative comparison of these two models (Table II) shows a 2.18 % reduction in PCE, and a 0.05 V drop in V_{oc} in the IDL case, arising from the extended recombination region. Thus, the IDL model more accurately captures non-ideal interface behavior resulting from interdiffusion, lattice mismatch, and defect clustering.

TABLE II. COMPARISON OF THE PERFORMANCE OF DEFECT MODELS.

Device	PCE (%)	V_{oc} (V)	J_{sc} (mA/cm^2)	FF (%)
IDD	21.43	1.03	24.92	83.51
IDL	19.25	0.98	24.68	79.83

IV. CONCLUSION

This study offers a comprehensive analysis of the impact of interface defects on the performance of 2D/3D mixed dimensional PSCs. To address the limitations associated with the conventional defect model. The Interface Defect Layer (IDL) model is introduced to represent the recombination process more realistically. The initial IDD model identified the 2D/3D and 3D/ETL interfaces are crucial for the device performance. Therefore, IDL layers were introduced in these two interfaces and the thickness and the defect density of the IDLs were optimized. A thickness of 1 nm and a defect density of 10^{13}cm^{-3} were determined to be optimum values, as they correspond to the highest device performance in terms of PCE, V_{oc}, and J_{sc}. The thickness and defect density of IDL1 have a more pronounced impact on the efficiency of the device compared to IDL2. The marked performance difference between the conventional IDD and the refined IDL models underscores the importance of advanced defect modeling in the design and simulation of 2D/3D mixed-dimensional PSCs.

REFERENCES

[1] Li, X., et al. (2023). Mixed perovskites (2D/3D)-based solar cells: A review on crystallization and surface modification for enhanced efficiency and stability. *Advanced Composites and Hybrid Materials*, 6(3), 1-27.

[2] Chaurasia, S., et al. (2024). Highly efficient and stable Dion–Jacobson (DJ) 2D–3D perovskite solar cells with 26% conversion efficiency: A SCAPS-1D study. *Journal of Physics and Chemistry of Solids*, 191, 112038. https://doi.org/10.1016/j.jpcs.2024.112038

[3] Gamage Ayomi Pabasara, W., & Asha Sewvandi, G. (2025, January 20). Numerical simulation and

optimization of stable CH_3 NH_3 PbI_3 -based 2D/3D mixed dimensional perovskite solar cell. In *Proceedings of10th Virtual International Conference on Science, Technology and Management in Energy (eNergetics 2024), Virtual.*

[4] Lin, T., Dai, T., & Li, X. (2023). 2D/3D perovskite: A step toward commercialization of perovskite solar cells. *Solar RRL*, 7(7), 1-28. https://doi.org/10.1002/solr.202201138

[5] Chen, P., Bai, Y., Wang, S., Lyu, M., Yun, J. H., & Wang, L. (2018). In situ growth of 2D perovskite capping layer for stable and efficient perovskite solar cells. *Advanced Functional Materials*, *28*(17), 1-10.

[6] Abbas, M., Xu, X., Rauf, M., & Kyaw, A. K. K. (2024). A comprehensive review on defects-induced voltage losses and strategies toward highly efficient and stable perovskite solar cells. *Photonics*, *11*(1). https://doi.org/10.3390/photonics11010087

[7] Tao, J., et al. (2024). Suppressing nonradiative recombination for efficient and stable perovskite solar cells. *Energy & Environmental Science*, *17*, 509-544.

[8] Meng, X., et al. (2022). Optimization of germanium-based perovskite solar cells by SCAPS simulation. *Optical Materials*, *128*(May), 112427. https://doi.org/10.1016/j.optmat.2022.112427

[9] Zhang, X., et al. (2023). Germanium–lead double absorber layer perovskite solar cells: Further performance enhancement from the perspective of device simulation. *Optics Communications*, *530*(2103), 129188. https://doi.org/10.2139/ssrn.4171612

[10] Ou, M., et al. (2024). Dion-Jacobson perovskite solar cells: Further optimize the performance by SCAPS-1D simulation techniques. *Materials Today Communications*, *39*(2103), 108955. https://doi.org/10.1016/j.mtcomm.2024.108955

[11] van Gorkom, B. T., van der Pol, T. P. A., Datta, K., Wienk, M. M., & Janssen, R. A. J. (2022). Revealing defective interfaces in perovskite solar cells from highly sensitive sub-bandgap photocurrent spectroscopy using optical cavities. *Nature Communications*, *13*(1). https://doi.org/10.29363/nanoge.hopv.2022.127

[12] Jayawardane, S. T., et al. (2024). Simulation-based performance analysis of lead-free bismuth perovskite solar cells: A comparative study of Cs3Bi2I9 and (CH3NH3)3Bi2I9-based perovskite solar cells. *Advanced Theory and Simulations*, *7*(7), 2400206.

[13] Pabasara, W. G. A., Akmal, U. K. D. M., Wickramaarachchi, W. A. A. S., & Swvandi, G. A. (2024). Numerical simulation of lead-free bismuth chalcohalide-based perovskite solar cells. In *Moratuwa Engineering Research Conference (MERCon)*, 436-441. https://doi.org/10.1109/mercon63886.2024.10689236

[14] Mohammed, M. K. A. A., et al. (2023). Harnessing the potential of Dion-Jacobson perovskite solar cells: Insights from SCAPS simulation techniques. *Journal of Alloys and Compounds*, *963*, 171246. https://doi.org/10.1016/j.jallcom.2023.171246

[15] Chakrabartty, J., Islam, M. A., & Reza, S. (2021). Performance analysis of highly efficient 2D/3D bilayer inverted perovskite solar cells. *Solar Energy*, *230*(October), 195-207. https://doi.org/10.1016/j.solener.2021.10.007

eNergetics 2025
DOI: https://doi.org/10.5281/zenodo.18624332

Original Scientific Article

Multi-stage, Degradation-aware Day-ahead Energy Management for Prosumer-based Microgrids using Python-Gurobi

Musa Terkeş[1], Alpaslan Demirci[2], Erdin Gökalp[3]

[1,2,3]Department of Electrical Engineering, Yildiz Technical University, İstanbul, Türkiye

[1]musa.terkes@yildiz.edu.tr, [2]ademirci@yildiz.edu.tr, [3]gokalp@yildiz.edu.tr

Abstract—**Renewable energy sources are becoming more common in microgrids, which creates new possibilities and new challenges for providing reliable and affordable energy. The proposal of a multi-stage, day-ahead energy management model for prosumer-based microgrids is the objective of this research. The model clearly considers battery degradation and the variety of load and generation profiles. The framework is implemented with a commercial Mixed-Integer Linear Programming (MILP) solver. It examines several operational horizons, ranging from one to three days, to evaluate their economic, technical, and environmental impacts. Key performance indicators include the following: electricity cost per unit, self-consumption rate, renewable contribution, curtailed energy, carbon emissions, and energy storage aging. The findings show that using a three-day plan is the best balance between reducing costs and using renewable energy, while also keeping batteries long-life. Shorter horizons tend to improve on-site PV utilization. In contrast, extended horizons yield moderate yet consistent results. This highlights the trade-offs between conflicting objectives. The framework is a useful guide for people who plan and manage microgrids. It helps them design microgrids that are both efficient and well enough for the environment. The framework may be expanded in the future to include stochastic forecasting, demand flexibility, or hybrid AC/DC configurations, with the goal of improving resilience and operational performance.**

Keywords - energy management, microgrids, battery degradation, multi-stage optimization, energy storage systems**.**

I. INTRODUCTION

The increasing use of renewable energy sources (RES) in modern power systems has led to changes in the planning and operation of microgrids. This transition is beneficial for sustainability goals, but the inconsistent and intermittent nature of renewables poses challenges in managing energy consistently and affordably. Many studies have explored different scheduling strategies for microgrids. These strategies combine renewable generation with various energy storage technologies. These strategies are used to overcome the challenges posed by these issues. For example, the potential of using both long-term and short-term storage, such as hydrogen and battery systems, to improve renewable energy utilization and achieve seasonal balancing was highlighted earlier in research [1]. Other studies have developed detailed mathematical models for distributed resources. These include photovoltaics, storage units, and demand response. The models aim to enhance day-ahead scheduling. They also aim to represent asset availability costs more realistically [2]. In addition, real-time scheduling frameworks have been introduced. These frameworks increase battery utilization. They also account for degradation effects. This is often done through methods like approximate dynamic programming or life-cycle cost modeling [3].

Energy storage, and batteries in particular, remain at the center of these developments. Several optimization methods based on

ISBN: 978-86-82602-07-1

Lyapunov control have been applied to smart-home environments with HVAC and electric vehicle (EV) loads. These methods show the benefits of dynamic scheduling and queue-based optimization under uncertainty [4]. However, the time resolution used in scheduling strongly affects battery health. In other words, frequent intra-hour cycling accelerates wear more than hourly control. This emphasizes the importance of multi-layer optimization that balances both technical and economic factors [5].

Another research area has centered on how storage operations affect the financial and practical performance of community and residential microgrids. Research that incorporates battery degradation models into mixed-integer optimization frameworks has demonstrated enhanced trade-offs between cost savings and technical reliability [6]. Stochastic approaches have enabled robust scheduling. This is true under uncertain demand and renewable production. These approaches provide prosumers with greater operational flexibility [7]. Market-oriented frameworks have also illustrated how combining energy storage and demand response can help deliver ancillary services. They can also lower costs and reduce renewable curtailment [8].

At the same time, the growing interaction among EV charging, flexible demand, and energy storage has opened new directions for research on prosumer-oriented optimization. Several hierarchical and decentralized scheduling frameworks have been proposed. These frameworks aim to promote fairness among prosumers. They also aim to reduce operational costs and support grid stability [9]. In parallel, optimization models that jointly consider EVs, household storage, and photovoltaic generation demonstrate the value of multi-objective formulations. These formulations balance cost reduction against technical operating limits [10]. Researchers have developed methods to address the uncertainty in both renewable generation and demand. These methods are scenario-based and two-stage stochastic. They aim to maintain reliable and resilient operation [11].

The importance of incorporating environmental targets into microgrid planning has been further underlined by recent studies. Integrating carbon-reduction goals with economic and technical objectives has been shown to enable emission-aware scheduling. This aligns system efficiency with sustainability aims [12]. Energy management frameworks for various microgrid types reveal that coordinated scheduling can enhance efficiency and reduce overall costs. This is true even for hybrid AC/DC configurations [13]. Additional strategies, such as demand-side management and peer-to-peer trading, expand the role of microgrids in the larger clean energy transition. These strategies show how local efforts to improve efficiency can create environmental benefits that extend throughout the entire system [14]. Long-term research on combining renewables with storage and demand response continues. This research highlights the need for models that remain both computationally practical and technically sound [15].

Despite these advances, a notable gap still exists. This gap is in developing multi-stage energy management systems. These systems should jointly minimize operating costs. They should also preserve battery health and account for the diversity of prosumer behaviors and generation profiles. Many existing works focus either on short-term economic scheduling or on long-term degradation modeling, but rarely combine the two perspectives within a unified and practical framework. The present study aims to fill this gap. It proposes a day-ahead energy management approach for microgrids. This approach couple's renewable generation with battery-degradation-aware optimization. The method is implemented as a multi-stage model using Python-Gurobi. The model explores several daily operational scenarios. It identifies solutions that remain cost-effective, environmentally responsible, and technically robust.

II. Mathematical Modeling, Optimization Framework, and Performance Metrics

The simulation was executed within the Python–Gurobi environment. Antalya, located in southern Türkiye and known for its high solar irradiation, was selected as the case study region. The modeling of photovoltaic (PV) generation in HOMER Pro was based on long-term NASA SSE and MERRA-2 reanalysis datasets for the realistic representation of local solar conditions. Electrical load profiles were also produced within HOMER Pro. Five distinct prosumer demand patterns were generated. Stochastic variations were introduced to reflect different consumption behaviors. The optimal capacities

of PV and energy storage systems (ESS) for each prosumer were determined. This was done through particle swarm optimization (PSO). The approach was described in earlier research [16]. The goal was to reduce both electricity expenses and lifecycle costs (LCC). As a result, the optimal PV capacities for Prosumers 1–5 were found to be 5, 5, 4, 5, and 4.5 kW, respectively. The corresponding ESS capacities were set to 4, 5.5, 5.5, 5.5, and 3 kWh.

In the Python–Gurobi framework, hourly electricity demand and PV generation data from the Excel dataset form the basis of the energy-management problem. For each prosumer k and time step t, the total electrical load $P_{k,t}^{L}$ is met through PV-to-load $\left(P_{k,t}^{PV2L}\right)$, ESS-to-load $\left(P_{k,t}^{B2L}\right)$, and grid-to-load $\left(P_{k,t}^{G2L}\right)$ power flows, as expressed in (1). Likewise, the PV generation $P_{k,t}^{PV_{gen}}$ at each time interval is distributed among $P_{k,t}^{PV2L}$, PV-to-ESS $\left(P_{k,t}^{PV2B}\right)$, PV-to-grid $\left(P_{k,t}^{PV2G}\right)$, and curtailed PV $\left(P_{k,t}^{PV_{cur}}\right)$ components, as shown in Eq. (2).

$$P_{k,t}^{L} = P_{k,t}^{PV2L} + P_{k,t}^{B2L} + P_{k,t}^{G2L}, \quad \forall k,t, \quad (1)$$

$$P_{k,t}^{PV_{gen}} = P_{k,t}^{PV2L} + P_{k,t}^{PV2B} + \\ + P_{k,t}^{PV2G} + P_{k,t}^{PV_{cur}}, \quad \forall k,t \quad (2)$$

When the ESS is fully charged and PV generation surpasses local demand, PV-to-grid export $P_{k,t}^{PV2G}$ is limited to 40% of the installed PV capacity $\left(C_{k}^{PV}\right)$ Eq. (3). This constraint avoids voltage or power-quality problems in the distribution network, even though it may restrict potential revenue from grid sales. The total grid injection consists of contributions from both PV-to-grid and ESS-to-grid $\left(P_{k,t}^{B2G}\right)$ flows and is regulated to prevent simultaneous purchase and sale through binary variables u_{t1} Eqs. (4–6). A second binary variable u_{t2} ensures that ESS charging and discharging do not occur at the same time Eqs. 7 and 8. Large penalty coefficients M and c are used to maintain these conditions without violating the state-of-charge (SoC) limits.

$$P_{k,t}^{PV2G} \le 40\% C_{k}^{PV}, \quad \forall k,t, \quad (3)$$

$$P_{k,t}^{G_{injected}} = P_{k,t}^{PV2G} + P_{k,t}^{B2G}, \quad \forall k,t, \quad (4)$$

$$P_{k,t}^{G_{injected}} \le M\, u_{t1}, \quad \forall k,t, \quad (5)$$

$$P_{k,t}^{G_{used}} = P_{k,t}^{G2L} \le M\left(1-u_{t1}\right), \quad \forall k,t, \quad (6)$$

$$P_{k,t}^{ESS_{chr}} \le c\, u_{t2}, \quad \forall k,t, \quad (7)$$

$$P_{k,t}^{ESS_{disch}} = c\left(1-u_{t2}\right), \quad \forall k,t. \quad (8)$$

The state of charge of the ESS, $SoE_{k,t}^{ESS}$, is updated using Eq. (9) based on the previous time step $\left(SoE_{k,t-1}^{ESS}\right)$, considering charging and discharging powers $\left(P_{k,t}^{ESS_{chr}}\right)$ and $\left(P_{k,t}^{ESS_{disch}}\right)$ and their corresponding efficiencies η_{chr} and η_{disch}. The SoC boundaries are defined between 20% and 90%. The degradation parameters for both cycle and calendar aging were obtained. They were obtained by adopting the empirical models proposed in [17] and [18]. The cycle aging term $\left(Q_{k,t}^{cyc}\right)$ was specifically defined as a function of two variables: charge throughput and depth of discharge (see Eq. (2)). The calendar aging term $\left(Q_{k,t}^{cal}\right)$, on the other hand, is contingent on two factors: storage time and temperature (see Eq. (3)). The corresponding coefficients were taken directly from $LiFePO_4$/C battery tests that were experimentally validated and reported in [18]. They were calibrated according to the empirical capacity fade relationships that were defined in [17]. The degradation equations that are applied reflect lifetime behaviors that have been verified through experiments. Here, $L_{k,t}^{cyc}$ refers to the battery cycle lifetime, while the constant coefficients represent empirical values obtained through experimental procedures.

$$SoE_{k,t}^{ESS} = SoE_{k,t-1}^{ESS} + \\ + P_{k,t}^{ESS_{chr}}\eta_{chr} - \frac{P_{k,t}^{ESS_{disch}}}{\eta_{disch}}, \quad \forall k,t \quad (9)$$

$$Q_{k,t}^{cyc} = \frac{1}{2}\sum_{k,t} \frac{\eta_{chr} P_{k,t}^{ESS_{chr}} - \eta_{disch} P_{k,t}^{ESS_{disch}}}{L_{k,t}^{cyc} C_k^{ESS}}, \forall k,t \quad (10)$$

$$Q_{k,t}^{cal} = \sum_{k,t} 6.6148.10^{-6} P_{k,t}^{ESS} + 4.6404.10^{-6}, \forall k,t \quad (11)$$

$$Q_{k,t}^{tot} = Q_{k,t}^{cyc} + Q_{k,t}^{cal}, \quad \forall k,t, \quad (12)$$

$$C_{k,t}^{ESS_{new}} = C_k^{ESS}\left(1 - Q_{k,t}^{tot}\right), \quad \forall k,t. \quad (13)$$

The objective function represents the total cost of the microgrid by combining several key components. It accounts for electricity purchased from the main grid under a three-tier time-of-use (ToU) tariff purchased $\left(P_{k,t}^{G_{used}} \cdot \mathrm{Cost}_{k,t}^{GP}\right)$, as well as revenue generated from single-rate grid injections $\left(P_{k,t}^{G_{injected}} \cdot \mathrm{Cost}_{k,t}^{GS}\right)$. The cost of installed PV units and energy storage systems (ESS) is incorporated through their respective life-cycle costs $\left(C_{k,t}^{ESS_{new}} \cdot LCC_{k,t}^{ESS}\right)$ and $\left(C_k^{PV} \cdot LCC_{k,t}^{PV}\right)$, while additional terms represent the depreciation associated with ESS aging $\left(\left(C_k^{ESS} - C_{k,t}^{ESS_{new}}\right) \cdot \mathrm{Cost}_{k,t}^{depr.}\right)$, as given in Eq. (14). Since aging costs are embedded within the overall cost formulation, minimizing the total cost naturally leads to a reduction in both electricity expenditures and battery degradation. Time-of-use electricity rates are set at 0.0767 \$/kWh (06:00–17:00), 0.112 \$/kWh (17:00–22:00), and 0.04854 \$/kWh (22:00–06:00), while grid-injection revenue is fixed at 0.04 \$/kWh, as referenced in [16]. Detailed life-cycle cost (LCC) calculations are provided in the cited work.

$$\begin{aligned} TC_{k,t}^{MG} = {} & P_{k,t}^{G_{used}} \mathrm{Cost}_{k,t}^{GP} - P_{k,t}^{G_{injected}} \mathrm{Cost}_{k,t}^{GS} + \\ & C_{k,t}^{ESS_{new}} LCC_{k,t}^{ESS} + C_k^{PV} LCC_{k,t}^{PV} + , \\ & \left(C_k^{ESS} - C_{k,t}^{ESS_{new}}\right) \mathrm{Cost}_{k,t}^{depr.}, \forall k,t \end{aligned} \quad (14)$$

$$\min\left(\sum_{k,t}\left(TC_{k,t}^{MG}\right)\right). \quad (15)$$

Hourly PV generation and load data are imported from an Excel dataset according to the operation horizons that have been defined. For each selected period, the values from 1 to 15 are executed iteratively. To illustrate, when a three-day horizon is simulated, successive three-day segments are extracted from the monthly dataset. In four-day operation loops, any remaining days at the end of the dataset are included in the final iteration. This is done to ensure continuity. The dataset covers a wide range of weather patterns. These are typical of Antalya. The dataset provides reliable benchmarking consistency. This consistency exists across both annual and project-lifetime analyses. It already reflects all characteristic meteorological conditions. Similar results can be obtained whether the simulation spans a single year or the entire lifetime of the project. This feature provides a clear view of long-term performance expectations for short-term investors.

A multi-stage day-ahead energy management plan is also formulated for prosumers. These prosumers exhibit different consumption and generation patterns. The optimization simultaneously considers renewable energy utilization and battery aging. It evaluates how the Python-Gurobi solver performs under various daily operating scenarios. This helps determine the most cost-effective, sustainable, and technically reliable solution. In this regard, daily operation periods are optimized not solely for feasibility but also for balancing cost reduction with ESS health preservation.

The optimization is performed using the high-speed Python-Gurobi solver. The resulting tuple variables are converted into data-frames. They are exported to Excel on an hourly basis for each prosumer. These outputs are then analyzed using the evaluation criteria, which are summarized in Table I.

The cost of electricity (COE, \$/kWh) is calculated as the ratio of the total microgrid cost to the total energy used. The renewable fraction (RF) is computed by subtracting the electricity

TABLE I. DECISION CRITERIA.

Metric	Formulation	Metric	Formulation
COE	$\frac{\sum Total\,\mathrm{Cost}}{\sum P_{load}}$	SCR	$\frac{\int P_{PV}\,dt - \int P_F\,dt}{\int P_{PV}\,dt}$
RF	$1 - \frac{\sum(P_{GP})}{\sum(P_{load})}$	SSR	$\frac{\int P_L\,dt - \int P_G\,dt}{\int P_L\,dt}$
CO_2	$0.4261 \sum P_{GP}$	CE	$\sum P_{k,t}^{PV_{cur}}$

imported from the grid from the total electrical demand. The result is then normalized by the total load. Each kilowatt-hour of grid electricity in Türkiye emits approximately 0.426 kg of CO_2. The total carbon footprint is estimated accordingly.

At any given time step, when PV generation exceeds the load, the net feed-in power (P_F) is defined as the difference between total PV generation, ESS output, and load demand. Conversely, when the load is greater than PV generation, the grid-supplied power (P_G) is determined by subtracting both PV and ESS contributions from the total load. The self-consumption ratio (SCR) is obtained as the share of PV generation directly meeting the load, calculated by subtracting the P_F from the total PV output and dividing by total PV generation.

The self-sufficiency ratio (SSR) is the percentage of total demand met by local PV and ESS resources. The total load is subtracted from the electricity drawn from the grid to obtain the remainder, which is then divided by the total demand. The SCR reflects how much of the PV generation is used directly on-site. The SSR indicates the share of total consumption that is met without grid support. When electricity production surpasses the load and the installed PV capacity limit, and the ESS has reached full charge, the system cannot utilize the surplus energy and records it as curtailed. The unused portion is expressed as a percentage of total generation by the curtailed energy (CE) metric.

III. Optimization Results and Discussion

The findings of the multi-stage day-ahead optimization demonstrate how economic, technical, and environmental objectives interact within prosumer-based microgrids. The performance metrics for operation horizons ranging from one to seven days are summarized in Table II. Shorter horizons often lead to higher self-consumption rates. In fact, the single-day plan achieves full on-site utilization of PV generation. The cost of energy is lowered to 0.03055 $/kWh and the renewable fraction is raised to 65.53% when the horizon is extended to three days. This result demonstrates that combining multiple days enables PV power to be utilized more effectively. On the other hand, longer planning windows slightly reduce SCR. This is because it reflects the trade-off between using PV locally and minimizing cost. Curtailment remains small across most cases, indicating that production is effectively aligned with demand by the optimization. Only in the seven-day plan does curtail energy rise to 6.61%, mainly because of operational limits and lower storage flexibility. ESS aging also grows moderately with longer horizons. Yet the three-day plan maintains a balanced profile (0.176449). This shows that the framework can limit battery wear while keeping costs low.

Table III compares the operation plans across these indicators. It offers a clearer view of the trade-offs in multi-stage scheduling. The three-day horizon ranks highest for both COE and RF. This confirms its advantage in cost efficiency and renewable energy use. Conversely, the one-day plan performs optimally in SCR, rising local PV generation at a higher cost. Intermediate results are shown by longer horizons, such as five or six days. Overall, it has been confirmed by the ranking that all metrics cannot be optimized simultaneously by a single time horizon. This finding emphasizes the importance of using multi-objective approaches, which consider both short-term performance and long-term sustainability.

TABLE II. Performance Metrics for Daily and Multi-Day Operation Scenarios.

Operation Plan	COE ($/kWh)	SCR (%)	RF (%)	CE (%)	CO_2 (kg/yr)	Aging (%)
One-day	0.11757	100	52.08	0	108.05	0.161617
Two-day	0.05372	42.26	58.4	0.52	82.15	0.176473
Three-day	0.03055	21.6	65.53	0.67	71.61	0.176449
Four-day	0.05894	43.21	55.91	0.72	93.13	0.188
Five-day	0.07413	53.57	50.05	0.5	107.56	0.173346
Six-day	0.08182	58.2	46.62	0.55	111.51	0.1844
Seven-day	0.06908	47.11	55.73	6.61	108.75	0.181959

TABLE III. MULTI-CRITERIA RANKING OF OPERATION SCENARIOS BASED ON ECONOMIC, TECHNICAL, AND ENVIRONMENTAL INDICATORS.

Operation Plan	COE	SCR & SSR	RF	CO_2	Aging
1	Three-day	One-day	Three-day	Three-day	One-day
2	Two-day	Six-day	Two-day	Two-day	Five-day
3	Four-day	Five-day	Four-day	Four-day	Three-day
4	Seven-day	Seven-day	Five-day	Five-day	Two-day
5	Five-day	Four-day	One-day	One-day	Seven-day
6	Six-day	Two-day	Seven-day	Seven-day	Six-day
7	One-day	Three-day	Six-day	Six-day	Four-day

In addition, the findings confirm that the proposed method can effectively represent the diverse behaviors of prosumers. They also show that the method can effectively represent the variability of their load and generation patterns. This capability enables the framework to identify operation plans balancing high renewable integration with careful consideration of battery aging.

IV. CONCLUSION AND FUTURE SUGGESTIONS

This study presents a battery aging aware day-ahead energy management plan for microgrids that integrate renewable energy sources and battery storage. The framework's use of a multi-stage MILP model identifies operating strategies that balance economic performance, renewable energy use, and the lifetime of the ESS. Analyses performed for daily to seven-day operation horizons show clear trade-offs. On-site PV utilization is favored by shorter horizons, while the best compromise between COE and renewable contribution is achieved with a three-day planning window, with limited impact on battery health. The performance of different operation horizons can be compared across several metrics to highlight patterns. These patterns can guide the decision-making of prosumers, investors, and system operators. Also, operators are seeking practical solutions that are environmentally responsible and cost-effective.

However, it should be noted that the current model is based on certain predictions for both PV generation and load. To reduce the effect of uncertainty in predictions, information was gathered from NASA SSE and MERRA-2 data and HOMER-based demand curves. Therefore, average operational behavior is reflected in the presented results rather than short-term fluctuations. Stochastic forecasts and sensitivity analysis will be incorporated into future studies to quantify the effect of PV and demand prediction errors on scheduling outcomes.

A different perspective, Antalya was selected as a model because of its promising solar energy potential. However, the proposed optimization framework is entirely data-driven and technology-neutral. The math structure can be used in all sorts of microgrids, no matter what size or location, and with any mix of technologies. All you have to do is update the inputs like renewable profiles, tariffs, and storage characteristics. Therefore, the formulation can be generalizable beyond the specific case examined here. The framework will be validated under diverse climatic conditions and hybrid microgrid configurations in future research to assess its scalability and adaptability further.

In addition, future research could integrate stochastic forecasts for PV generation and demand. This would improve the robustness of scheduling under uncertainty. The additional flexibility mechanisms can be included in the proposed model's modular MILP structure without the computational complexity being substantially increased. Demand-side adaptability and vehicle-to-grid (V2G) potential can be combined by incorporating additional decision variables and linear restrictions to illustrate movable or bidirectional power flows. While these additions slightly increase the number of optimization variables, the model remains tractable in the Python–Gurobi environment due to its linear formulation. This adaptability enables the framework to evolve toward more interactive and resilient microgrid operation strategies, which are crucial for ensuring the reliability and security of energy supply in a changing energy landscape.

REFERENCES

[1] Qiu, Y., Li, Q., Ai, Y., Wang, T., Chen, W., Bai, H., Benbouzid, M., Liu, S., & Gao, F. (2024). Optimal scheduling for microgrids considering long-term and short-term energy storage. *Journal of Energy Storage*, *93*, 112137. https://doi.org/10.1016/j.est.2024.112137

[2] Silva, V. A., Aoki, A. R., & Lambert-Torres, G. (2020). Optimal Day-Ahead Scheduling of Microgrids with Battery Energy Storage System. *Energies*, *13*(19). https://doi.org/10.3390/en13195188

[3] Xue, X., Ai, X., Fang, J., Cui, S., Jiang, Y., Yao, W., Chen, Z., & Wen, J. (2022). Real-Time Schedule of Microgrid for Maximizing Battery Energy Storage Utilization. *IEEE Transactions on Sustainable Energy*, *13*(3), 1356–1369. https://doi.org/10.1109/TSTE.2022.3153609

[4] Albogamy, F. R., Paracha, M. Y. I., Hafeez, G., Khan, I., Murawwat, S., Rukh, G., Khan, S., & Khan, M. U. A. (2022). Real-Time Scheduling for Optimal Energy Optimization in Smart Grid Integrated With Renewable Energy Sources. *IEEE Access*, *10*, 35498–35520. https://doi.org/10.1109/ACCESS.2022.3161845

[5] Toosi, H. E., & Merabet, A. (2023). Impact of intra-hourly scheduling on state of health of battery for electric vehicle integration in smart residential microgrid. *Journal of Energy Storage*, *72*, 108215. https://doi.org/10.1016/j.est.2023.108215

[6] Mohamed, A., Rigo-Mariani, R., Debusschere, V., & Pin, L. (2024). Operational Planning Strategies to Mitigate Price Uncertainty in Day-Ahead Market for a Battery Energy System. *IEEE Access*, *12*, 85388–85399. https://doi.org/10.1109/access.2024.3415811

[7] Luo, L., Abdulkareem, S. S., Rezvani, A., Miveh, M. R., Samad, S., Aljojo, N., & Pazhoohesh, M. (2020). Optimal scheduling of a renewable based microgrid considering photovoltaic system and battery energy storage under uncertainty. *Journal of Energy Storage*, *28*, 101306. https://doi.org/10.1016/j.est.2020.101306

[8] Javidsharifi, M., Pourroshanfekr Arabani, H., Kerekes, T., Sera, D., Spataru, S., & Guerrero, J. M. (2022). Effect of Battery Degradation on the Probabilistic Optimal Operation of Renewable-Based Microgrids. *Electricity*, *3*(1), 53–74. https://doi.org/10.3390/electricity3010005

[9] Pourbehzadi, M., Niknam, T., Aghaei, J., Kavousi-Fard, A., Dehghan, A., Javidi, G., & Sheybani, E. (2021). Short-Term Scheduling of a Renewable-Based Microgrid: Stochastic/Economic Battery Modeling. *IEEE Access*, *9*, 90084–90101. https://doi.org/10.1109/ACCESS.2021.3091177

[10] Colucci, R., Mahgoub, I., Yousefizadeh, H., & Al-Najada, H. (2024). Survey of Strategies to Optimize Battery Operation to Minimize the Electricity Cost in a Microgrid With Renewable Energy Sources and Electric Vehicles. *IEEE Access*, *12*, 8246–8261. https://doi.org/10.1109/ACCESS.2024.3352018

[11] Graça Gomes, J., Xu, H. J., Yang, Q., & Zhao, C. Y. (2021). An optimization study on a typical renewable microgrid energy system with energy storage. *Energy*, *234*, 121210. https://doi.org/10.1016/j.energy.2021.121210

[12] Antoniadou-Plytaria, K., Steen, D., Tuan, L. A., Carlson, O., & Fotouhi Ghazvini, M. A. (2021). Market-Based Energy Management Model of a Building Microgrid Considering Battery Degradation. *IEEE Transactions on Smart Grid*, *12*(2), 1794–1804. https://doi.org/10.1109/TSG.2020.3037120

[13] Aghdam, F. H., Kalantari, N. T., & Mohammadi-Ivatloo, B. (2020). A chance-constrained energy management in multi-microgrid systems considering degradation cost of energy storage elements. *Journal of Energy Storage*, *29*, 101416. https://doi.org/10.1016/j.est.2020.101416

[14] Helmi, A. M., Abo-Elyousr, F. K., Haes Alhelou, H., & Ramadan, H. S. (2023). Dual-stage day-ahead optimized performance of renewable-based microgrids. *IET Renewable Power Generation*, *17*(8), 2050–2063. https://doi.org/10.1049/rpg2.12748

[15] Kailasa Gounder, Y., & Subramanian, S. (2022). Enhancement of battery life in microgrid energy management using mixed integer linear programming and hybrid knapsack. *International Journal of Energy Research*, *46*(6), 8158–8174. https://doi.org/10.1002/er.7717

[16] Terkes, M., Demirci, A., Gokalp, E., & Cali, U. (2024). Multi-stage and multi-objective feed-in damping-based battery aging-aware energy management strategy for renewable energy integration. *IEEE Access*, 1–1. https://doi.org/10.1109/ACCESS.2024.3468716

[17] Wu, Y., Liu, Z., Liu, J., Xiao, H., Liu, R., & Zhang, L. (2022). Optimal battery capacity of grid-connected PV-battery systems considering battery degradation. *Renewable Energy*, *181*, 10–23. https://doi.org/10.1016/j.renene.2021.09.036

[18] Swierczynski, M., Stroe, D.-I., Stan, A.-I., Teodorescu, R., & Kaer, S. K. (2015). Lifetime Estimation of the Nanophosphate $LiFePO_4$/C Battery Chemistry Used in Fully Electric Vehicles. *IEEE Transactions on Industry Applications*, *51*(4), 3453–3461. https://doi.org/10.1109/TIA.2015.2405500

eNergetics 2025
DOI: https://doi.org/10.5281/zenodo.18624358

Original Scientific Article

The Impact of Aluminum Foam Pore Density on HCPVT Performance

Mohamed Benelhaoues[1], Brahim Fersadou[2], Walid Nessab[3], Henda Kahalerras[4], Nawal Guerroudj[5], Hessem Djeddou[6]

[1,2,3,4,5,6]Laboratory of Multiphase Flows and Porous Media, University of Sciences and Technology Houari Boumedienne, FGMGP, BP 32 El Alia 16111 Bab Ezzouar, Algiers, Algeria

[1]mbenelhaoues@usthb.dz, [2]brahim.fersadou@usthb.edu.dz

Abstract—**High-concentration photovoltaic (HCPV) systems have shown significant potential for achieving higher conversion efficiency compared to conventional photovoltaic (PV) panels, particularly in regions with strong solar irradiance. Nevertheless, Multi-junction (MJ) solar cells can be damaged when their operating temperature exceeds the manufacturer's recommended limit of 110°C. The objective of this study is to develop an improved method to reduce the temperature of an MJ cell. A 1 cm² MJ solar cell, subjected to a high concentration ratio (500×), equipped with a mini-channel heat sink cooled by water and partially filled with aluminum foam, was investigated. Two configurations were considered: top-filled and bottom-filled aluminum foam. The influence of pore density on cell temperature and its electrical performance was investigated. In this numerical study, the pore density of the metal foam varied between 15 and 45 PPI. The performance evaluation of the HCPVT system is also presented. For this purpose, a 3D model of the multijunction cell and its heat sink was constructed and simulated. The study shows that the pore density plays an important role in the electrical and thermal performance of HCPVT, with 15 PPI providing the best efficiency Moreover, the bottom-filled configuration demonstrated better performance than the top-filled one.**

Keywords - HCPVT, multi-junction (MJ) solar cells, heat sink, aluminum foam, thermal conductivity.

I. INTRODUCTION

Photovoltaic (PV) technologies can convert 15% to 18% of the incident solar radiation into electricity while the rest is converted into heat [1]. This limited conversion efficiency, and the high cost of semiconductor materials has encouraged researchers to explore alternative solutions. High concentrator photovoltaic (HCPV) systems, which employ MJ solar cells, can achieve conversion efficiencies exceeding 44%, making them particularly competitive in areas with high solar irradiance [2]. On the other hand, this type of technology is constrained by several factors requiring very precise monitoring, particularly at high concentration levels [3]. Additionally, the durability of materials is affected by ultraviolet radiation and external conditions, while the high temperatures of solar cells, especially at high concentrations, are another limitation. Without cooling, MJ solar cells can reach temperatures of up to 1300°C with a CR of 1000, resulting in a non-uniform temperature distribution and a decrease in electrical efficiency [4]. Therefore, in order to avoid the long-term degradation problems and the risk of melting the connections, the typical maximum operating temperature is limited to 110°C, as in the MJ cell used in this study by AZUR SPACE [5]. Moreover, to answer these questions, many studies have explored various cooling techniques for HCPV systems, Passive

ISBN: 978-86-82602-07-1

and active cooling mechanisms have been studied to regulate the temperature of solar cells. However, Active cooling offers significant advantages over passive methods because it allows the recovery of waste heat for thermal applications, thus improving overall system efficiency [6]. Reference [7] studied a 500× HCPVT system working under active cooling conditions. The system consisted of a single 10 × 10 mm^2 MJ cell and straight cooling channel such that at a cooling liquid velocity of 0.01m/s, the maximum solar cell temperature reached 65ºC. Reference [8] investigated the performance of the CPV system at 500 suns using a microchannel heat sink. They reported that the maximum cell temperature reached 54ºC using four layers of a microchannel heat sink, which increases the cost of the system. Reference [9] made further advancements in the field by designing a hybrid heat sink that incorporates trimmed fins and microchannels, which reduced weight and cost by 20% without sacrificing cooling performance. This hybrid configuration successfully controlled cell temperatures below the maximum allowed temperature at a CR of 3600 suns, outperforming other configurations. Reference [10] explored the impact of heat sink channel configuration, concentration ratio, and Reynolds number on the performance of a high concentration triple-junction solar cell. The results revealed that the hybrid channel design (Geometry F) significantly reduces the maximum solar cell temperature from 82ºC to 78ºC at CR = 1500 and Re = 400, achieving up to a 39.5% increase in the Nusselt number compared to the conventional straight channel design (Geometry A). Additionally, Geometry (F) maintains a high-performance evaluation criterion (PEC) value of 1.22 at Re = 200, reflecting effective thermal-hydraulic performance. Furthermore, Geometry (F) reduces the heat sink weight by 3.7%.

The objective of this paper is to propose an improved approach to reduce the temperature of MJ cells, while examining the effect of aluminum foam pore density on the performance of HCPVT systems.

II. Mathematical Modeling

A. Physical Model

The schematic diagram of the HCPV module is presented in Fig. 1a, which consists of tracking axes and several Fresnel lenses which are arranged in rows to focus the sunlight onto the MJ solar cells. Fig. 1b, represents a single

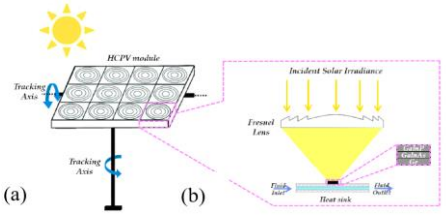

Figure 1. Schematic diagram of (a) HCPV module and (b) HCPVT system [11].

HCPVT system composed of Fresnel lens, a typical AZUR SPACE 10×10 mm^2 MJ solar cell and a water-cooled heat extraction mechanism. The 3D computational domain, shown in Fig. 2, consists of: (1) 1 cm^2 MJ solar cell assembly; (2) ceramic layer; (3) copper layers; and (4) aluminum mini-channel heat sink. Their thermal properties and dimensions are presented in [6]. The germanium layer is considered the heat source of the system [12]. The total input energy (Q_{in}) is converted into electrical power ($P_{sc,elec}$) and the remainder is transformed into thermal heat.

The temperature of the solar cell has been calculated using the trial and error method [13,14]. In the first calculation step, solar cell efficiency is assumed to be equal to the reference efficiency. After calculating the new solar cell temperature, a new solar cell efficiency is obtained from Eq. (1) and entered again into the program. This procedure is repeated until two consecutive iterations achieve a difference of $\leqslant$ 0.1ºC.

$$\eta_{sc} = \eta_{ref}\left(1 - \beta_{ref}\left(T_{sc} - T_{ref}\right)\right), \qquad (1)$$

where is β_{ref} equal to 0.047 %/K as provided by the manufacturer AZUR SPACE, while T_{ref} is equal to the ambient temperature 25ºC.

The input heat rate to the system is represented by:

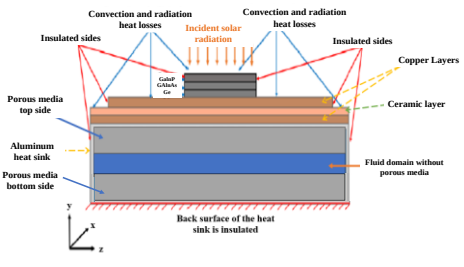

Figure 2. Physical model.

$$Q_{in} = DNI\ CR\ A_{cell}\ , \qquad (2)$$

The actual heat rate incident on the MJ cell is reduced due to the optical losses:

$$Q_{opt,in} = Q_{in}\eta_{opt}\ . \qquad (3)$$

The optical efficiency is taken as 80% [15,16]. The produced electrical power by the MJ cell and the solar cell heat rate is estimated as follows [11,16]:

$$P_{sc,elec} = Q_{opt,in}\eta_{sc}\ , \qquad (4)$$

$$Q_{sc,heat} = Q_{opt,in}(1-\eta_{sc})\ . \qquad (5)$$

The thermal efficiency is calculated as:

$$\eta_{th} = Q_{th}\ /Q_{opt,in}\ , \qquad (6)$$

where the thermal energy rate carried by the fluid:

$$Q_{th} = m\ c_{p,f}\ (T_{f,out} - T_{f,in})\ . \qquad (7)$$

The Reynolds number and the friction factor are defined as:

$$Re\ = m\ D_h / A_c \mu\ . \qquad (8)$$

The electrical efficiency of the HCPVT system:

$$\eta_{elec} = P_{useful,elec} / Q_{opt,in}\ . \qquad (9)$$

Thus, the useful electrical and pumping powers are estimated as follows:

$$P_{useful,elec} = P_{sc,\ elec} - P_{pump}\ , \qquad (10)$$

$$P_{pump} = V\Delta p\ . \qquad (11)$$

To solve the equations presented for the 3D geometry of the described HCPVT unit, the finite volume method was used. To discretize equations the SIMPLE technique was applied for the coupling of the pressure and velocity and the pressure-based solver was employed. Also, for the discretization of the convective and diffusive terms of the equations, the second-order upwind is employed.

It's worth mentioning that the following assumptions are taken into account to simplify numerical simulations:

- The solar cell is subjected to uniform high concentrated solar irradiance 500×.
- The germanium layer is considered as the heat source for the system.
- The top surfaces of the solar cell, copper, and ceramic layers are subjected to natural convection (h=15 W/(m^2.K)) and surface to ambient radiation.
- The sides of the module and its back surface are assumed to be insulated.
- The flow inside the channel is steady, incompressible and laminar.
- The effect of the body force and viscous dissipation have been neglected.
- The temperature of the fluid at the inlet of the channel is equal to T_{in}=25 °C.
- The pressure at the outlet is assumed to be atmospheric.

The continuity equation:

$$\vec{\nabla}(\vec{V}) = 0\ . \qquad (12)$$

The momentum equation:

$$\frac{\rho_f}{\varepsilon}\vec{\nabla}(\vec{V}\vec{V}) = -\vec{\nabla}P + \frac{\mu_f}{\varepsilon}\nabla^2\vec{V} - \vec{F}\ . \qquad (13)$$

The last term on the right-hand side of the momentum equation, which is caused by the porous medium, is defined as:

$$\vec{F} = -(\frac{\mu_f}{K} + \frac{\rho_f C}{\sqrt{K}}|\vec{V}|)\vec{V}\ , \qquad (14)$$

where $\vec{V}$is the magnitude of the velocity vector. In the above equations, the first term represents the viscous loss, and the second term represents the inertial loss. In these equations, *K* and *C* are permeability and inertial factor, respectively, and are given as [17]:

$$K = 0.00073(1-\varepsilon)^{-0.224} df^{--1.11} dp^{3.11}\ , \qquad (15)$$

$$C = 0.0012(1-\varepsilon)^{-0.132}(df\ /\ dp)^{-1.63}\ , \qquad (16)$$

where *df* and *dp* are ligament diameter, pore size, respectively. They are defined as follows [18,19]:

$$df = 1.18dp\sqrt{(1-\varepsilon)/3\pi}\,, \qquad (17)$$

$$dp = 0.0224/\omega\,, \qquad (18)$$

where ω is the pore density as pores per inch (PPI).

The energy equation in the fluid domain:

$$\vec{\nabla}(\rho_f C_{pf} T\vec{V}) = \vec{\nabla}(K_{eff}\,\vec{\nabla T})\,, \qquad (19)$$

where ke_{ff} is the effective thermal conductivity and defined as follows:

$$ke_{ff} = (1-\varepsilon)k_s + \varepsilon k_f\,. \qquad (20)$$

The rate of heat conduction in the solid domain may be described as follows:

$$q = -k\nabla T\,, \qquad (21)$$

where q is the normal heat flux to a constant temperature surface. Then, the energy conversion law at steady state for the domain of the MJ solar cell:

$$-\nabla(k\nabla T) + q = 0\,, \qquad (22)$$

The volumetric heat generation through the volume of germanium sublayer (V) can be expressed as follows:

$$q_{Ge} = Q_{sc,heat}/V\,. \qquad (23)$$

The heat transfer at the top surface of the MJ solar cell can be expressed by the following equation:

$$-k_{GaInP}(\partial T_{GaInP}/\partial y) = (q_{conv} + q_{rad})_{GaInP\to a}\,, \qquad (24)$$

Then, for both the copper and ceramic layers, the heat balance equations:

$$-k_{copper}(\partial T_{copper}/\partial y) = (q_{conv} + q_{rad})_{copper\to a}\,, \qquad (25)$$

$$-k_{ceramic}(\partial T_{ceramic}/\partial y) = (q_{conv} + q_{rad})_{ceramic\to a}\,, \qquad (26)$$

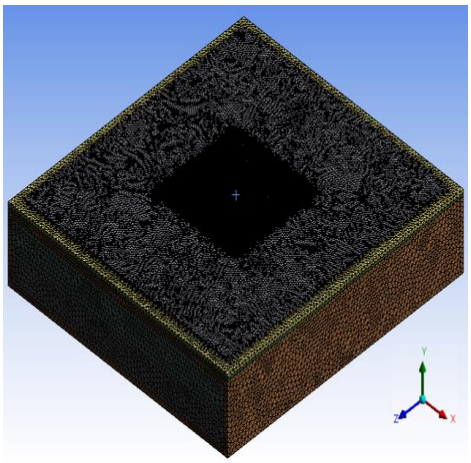

Figure 3. Generated mesh for the HCPVT.

The heat transfer equations for convection and radiation:

$$q_{conv} = h(T_s - T_a)\,, \qquad (27)$$

$$q_{rad} = \varepsilon\ \sigma(T_s^4 - T_a^4)\,, \qquad (28)$$

The conduction heat transfer for the heat sink can be expressed as:

$$\nabla.(k_{h.s}\nabla T_{h.s}) = 0\,, \qquad (29)$$

B. Numerical Solution

To verify the accuracy of the mathematical modelling. several steps were carried out. First, checking the quality of the built mesh by increasing the number of elements of the tetrahedral mesh. Secondly, a validation study was undertaken.

1) Grid independency

As shown in Fig. 3, the tetrahedral mesh was adopted for HCPVT module. To examine the independence of the results on the computational grids and the associated issue of C.P.U. time, different element numbers are examined.

Fig. 4 shows the variation of the maximum volumetric temperature of the solar cell plotted as a function of the grid size. The maximum temperature has an almost constant value from 2.3 to 2.8 million elements. Therefore, the grid with 2.3 million elements was selected as a reasonable balance between computational cost and accuracy.

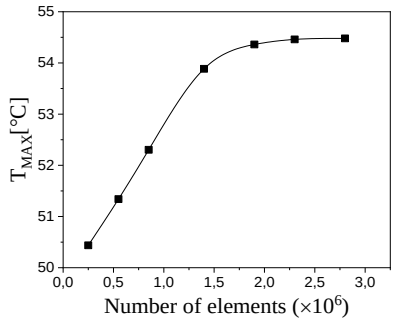

Figure 4. Grid independence study as a function of the maximum cell temperature.

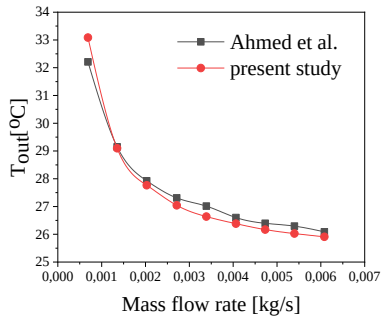

Figure 5. Variation of the outlet temperature with the mass flow rate for water for [6].

2) Validation

To examine the accuracy of the proposed model, the numerical solution is validated with a numerical studies to verify the accuracy of the HCPVT module, we compared with results of [6], the comparison was carried out at the same dimension and operating conditions. A good agreement was found between the present results and and the compared studies in terms of outlet temperature with a maximum error of 1.01% with [6], as presented in Fig. 5.

III. Results and Discussion

A. The Impact of Aluminum Foam Pore Density

Performance analysis of two position of aluminum foam top-filled and bottom-filled for the HCPVT system is introduced in this section. This analysis includes the impact of pore density of aluminum foam on the temperature distribution and other system outputs.

Note that in this study using water as cooling fluid, the HCPVT module operates under constant conditions such as Reynolds number equal to 100, solar irradiance 955W/m^2, concentration ratio CR = 500×, inlet and ambient temperature are fixed at 25°C.

The change in the volumetric maximum solar cell temperature with the pore density for top-filled and bottom-filled is represented in Fig. 6a, The results indicate that the maximum solar cell temperature for both configurations did not exceed 110 °C, the maximum recommended limit (MRL), at any of the tested pore densities, making them suitable under these conditions. Furthermore, the figure shows that, in the top-filled case, the maximum solar cell temperature increases from 51.82 °C to 54.51 °C as the pore density rises from 15 to 45 PPI. In contrast, in the bottom-filled configuration, the maximum solar cell temperature remains nearly constant, with a slight decrease from 50.43 °C at 15 PPI to 50.28°C at 45 PPI. So, using the bottom-filled of aluminum foam with 45 PPI permitted more heat to be extracted from the system in comparison

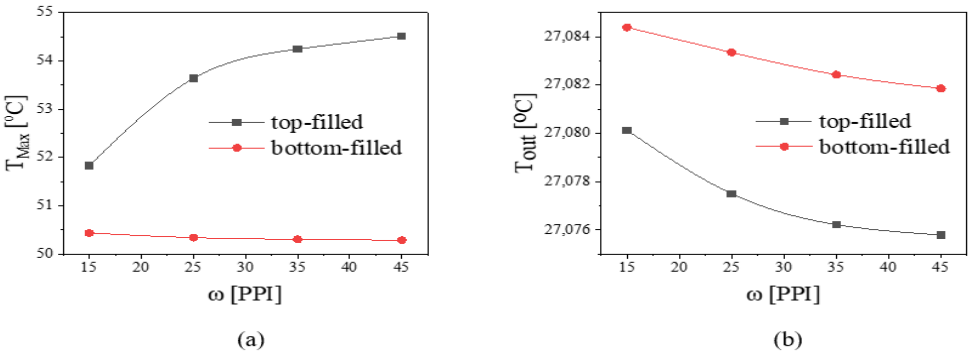

Figure 6. (a) Variation of the maximum solar cell temperature with the pore density, (b) Variation of the outlet temperature with the pore density.

with the other case due to the large heat transfer surface area offered by this configuration. Hence, due to the sufficient level of heat exchange achieved using the bottom-filled configuration, the outlet fluid temperature was high in comparison with the top-filled configuration as introduced in Fig. 6b. The results obtained from Fig. 6a and Fig. 6b show that both the position and the pore density are important factors influencing heat exchange in the heat sink of the HCPVT system. Using bottom-filled porous media with 45 PPI allowed the coolant fluid to effectively extract heat from the cell, thereby reducing its temperature. However, when using 15 PPI in the bottom-filled case, the larger pore diameter increases the permeability of the porous medium, enabling deeper fluid penetration but resulting in lower heat transfer efficiency and consequently higher cell temperature. In contrast, for the top-filled configuration, the use of 15 PPI provided better heat extraction compared to other pore densities, leading to a reduction in cell temperature. This is because the wider pores and higher permeability allow the coolant to reach the heat exchange surface more effectively, enhancing fluid mixing and heat removal.

Fig. 7 confirms the previous results. Fig. 7a shows the variation of electrical efficiency with pore density. It can be observed that the highest electrical efficiency is obtained with the bottom-filled configuration at 45 PPI, while the lowest is obtained with the top-filled configuration at the same pore density. However, for the top-filled case, the highest electrical efficiency is achieved at 15 PPI. For thermal efficiency Fig. 7b, it decreases as pore density increases in both configurations, with the bottom-filled configuration consistently performing better than the top-filled one.

Increasing the pore density for both cases has a negative impact on boosting overall efficiency as shown in Fig. 7c. It declined to 78.70% at 45 PPI using the top-filled case, while it declined to 78.89% using the bottom-filled case. Overall, the

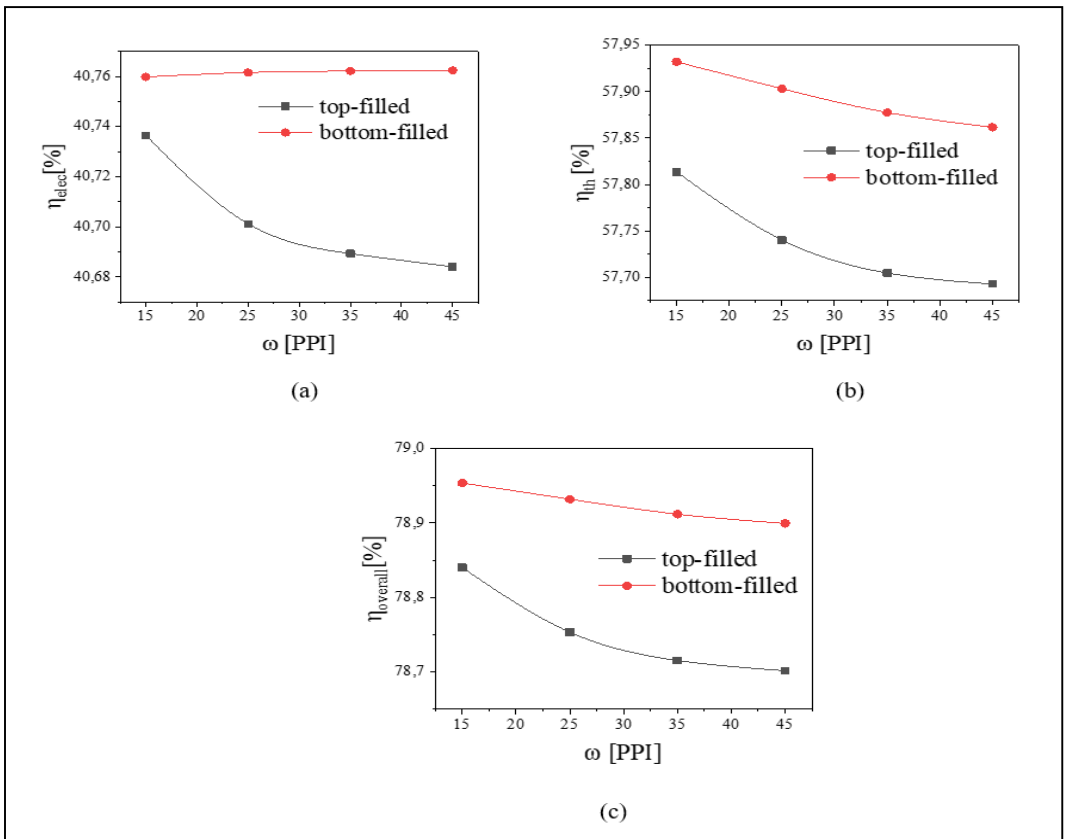

Figure 7. (a) Variation of the electrical efficiencie with the pore density, (b) Variation of the thermal efficiencie with the pore density, (c) Variation of the overall efficiencie with the pore density.

bottom-filled performance was more promising compared to the other configuration. The highest overall efficiency was achieved using the bottom-filled configuration, which reached 78.95% at ω = 15 PPI.

IV. Conclusion

In this study, the significant influence of pore density and foam configuration (top- or bottom-filled) was investigated. The high-concentration photovoltaic system studied is based on a single 10 mm × 10 mm MJ solar cell. Based on the results, it is advisable to use aluminum foam regardless of its configuration (top- or bottom-filled). Both configurations were considered an effective cooling method for the high-concentration photovoltaic system, as they kept the maximum solar cell temperature below the recommended limit of 110 °C at a concentration ratio of 500×. However, the results show differences between the configurations:

The maximum cell temperature remained almost constant with bottom-filled foam, and slightly better cooling was observed with higher pore densities. Furthermore, increasing the pore density from 15 to 45 PPI led to higher cell temperatures and decreased efficiency with top-filling. Regarding thermal, electrical, and overall efficiency, the bottom-filling configuration proved more efficient than the top-filling configuration for all pore densities. The maximum overall efficiency (78.95%) was achieved with the bottom-filling configuration, compared to 78.84% for the top-filling configuration at 15 PPI. On the other hand, increasing the pore density generally had a negative impact on overall efficiency.

In conclusion, this study demonstrates that the bottom-filling configuration is the optimal design choice for HCPVT systems under the studied operating conditions.

References

[1] Hasan, A., Sarwar, J., & Shah, A. H. (2018). Concentrated photovoltaic: A review of thermal aspects, challenges and opportunities. *Renewable and Sustainable Energy Reviews, 94*, 835–852. https://doi.org/10.1016/j.rser.2018.06.014

[2] Micheli, L., Sarmah, N., Luo, X., Reddy, K. S., & Mallick, T. K. (2013). Opportunities and challenges in micro- and nano-technologies for concentrating photovoltaic cooling: A review. *Renewable and Sustainable Energy Reviews, 20*, 595–610. https://doi.org/10.1016/j.rser.2012.11.051

[3] Poulek, V., Khudysh, A., & Libra, M. (2015). Innovative low concentration PV systems with bifacial solar panels. *Solar Energy, 120*, 113–116. https://doi.org/10.1016/j.solener.2015.05.049

[4] Laguna, G., Vilarrubí, M., Fernàndez, A., Sisó, G., Rosell, J., Ibañez, M., Illa, J., Badia, F., Fréchette, L., Darnon, M., Collin, L. M., Dollet, A., & Barrau, J. (2018). Dense array CPV receivers: Impact of the cooling device on the net PV output for different illumination profiles. *AIP Conference Proceedings, 2012*(1), 080008. https://doi.org/10.1063/1.5053536

[5] Valera, A., Fernández, E. F., Rodrigo, P. M., & Almonacid, F. (2019a). Feasibility of flat-plate heat-sinks using microscale solar cells up to 10,000 suns concentrations. *Solar Energy, 181*, 361–371. https://doi.org/10.1016/j.solener.2019.02.013

[6] Ahmed, A., Shanks, K., Sundaram, S., & Mallick, T. K. (2020). Theoretical investigation of the temperature limits of an actively cooled high concentration photovoltaic system. *Energies, 13*(8), 1902. https://doi.org/10.3390/en13081902

[7] Aldossary, A., Mahmoud, S., & Al-Dadah, R. (2016). Technical feasibility study of passive and active cooling for concentrator PV in harsh environment. *Applied Thermal Engineering, 100*, 490–500. https://doi.org/10.1016/j.applthermaleng.2016.02.023

[8] Al Siyabi, I., Khanna, S., Sundaram, S., & Mallick, T. (2019). Experimental and numerical thermal analysis of multi-layered microchannel heat sink for concentrating photovoltaic application. *Energies, 12*(1), 122. https://doi.org/10.3390/en12010122

[9] Shohdy, A., Emam, M., Sekiguchi, H., & Hassan, H. (2024). Performance of new hybrid heat sink with trimmed fins and microchannels for thermal control of a triple-junction concentrator photovoltaic cell. *Applied Thermal Engineering, 252*, 123695. https://doi.org/10.1016/j.applthermaleng.2024.123695

[10] Sajid, M. U., Abedrabboh, O., & Bicer, Y. (2025). Performance evaluation of interrupted and hybrid channel heat sinks for a triple junction high concentrator photovoltaic cell. *International Journal of Thermofluids, 26*, 101102. https://doi.org/10.1016/j.ijft.2025.101102

[11] Ahmed, A., Zhang, G., Shanks, K., Sundaram, S., Ding, Y., & Mallick, T. (2021). Performance evaluation of single multi-junction solar cell for high concentrator photovoltaics using minichannel heat sink with nanofluids. *Applied Thermal Engineering, 182*, 115868. https://doi.org/10.1016/j.applthermaleng.2020.115868

[12] Theristis, M., & O'Donovan, T. S. (2014). An integrated thermal electrical model for single cell photovoltaic receivers under concentration. International *Heat Transfer Conference 15*. https://doi.org/10.1615/IHTC15.sol.009239

[13] Zhou, J., Yi, Q., Wang, Y., & Ye, Z. (2015). Temperature distribution of photovoltaic module based on finite element simulation. *Solar Energy, 111*, 97–103. https://doi.org/10.1016/j.solener.2014.10.040

[14] Siyabi, I. A., Shanks, K., Mallick, T., & Sundaram, S. (2017). Thermal analysis of a multi-layer microchannel heat sink for cooling concentrator photovoltaic (CPV) cells. *AIP Conference Proceedings, 1881*(1), 070001. https://doi.org/10.1063/1.5001434

[15] Shanks, K., Senthilarasu, S., & Mallick, T. K. (2016). Optics for concentrating photovoltaics: Trends, limits

and opportunities for materials and design. *Renewable and Sustainable Energy Reviews*, *60*, 394–407. https://doi.org/10.1016/j.rser.2016.01.089

[16] Valera, A., Fernández, E. F., Rodrigo, P. M., & Almonacid, F. (2019b). Feasibility of flat-plate heat-sinks using microscale solar cells up to 10,000 suns concentrations. *Solar Energy*, *181*, 361–371. https://doi.org/10.1016/j.solener.2019.02.013

[17] Tian, Y., & Zhao, C. Y. (2011). A numerical investigation of heat transfer in phase change materials (PCMs) embedded in porous metals. *Energy*, *36*(9), 5539–5546. https://doi.org/10.1016/j.energy.2011.07.019

[18] Fourie, J. G., & Du Plessis, J. P. (2002). Pressure drop modelling in cellular metallic foams. *Chemical Engineering Science*, *57*(14), 2781–2789. https://doi.org/10.1016/S0009-2509(02)00166-5

[19] Yang, X., Lu, T. J., & Kim, T. (2014). An analytical model for permeability of isotropic porous media. *Physics Letters A*, *378*(30), 2308–2311. https://doi.org/10.1016/j.physleta.2014.06.002

eNergetics 2025
DOI: https://doi.org/10.5281/zenodo.18624381

Original Scientific Article

Energy Transitions Worldwide: Tracking Power Generation and Economic Growth Across Ten Nations

João Marcelo Fernandes Gualberto de Galiza[1], Monica Carvalho[2], Ana Hermínia Andrade e Silva[3] Raphael Abrahão[4]

[1]Graduate Program in Mechanical Engineering, Federal University of Paraiba, João Pessoa, Brazil
[2,4]Department of Renewable Energy Engineering, Federal University of Paraiba, João Pessoa, Brazil
[3]Department of Statistics, Federal University of Paraiba, João Pessoa, Brazil

[1]joaomarcelofgg@gmail.com, [2]monica@cear.ufpb.br, [3]ana.herminia@academico.ufpb.br, [4]raphael@cear.ufpb.br

Abstract—**Climate change is identified as a major global challenge, with the energy sector, heavily reliant on fossil fuels, being central to this crisis. In response, a growing international movement toward low-carbon development and alternative energy sources is clearly underway. This study provides a comparative analysis of power generation across the ten largest global economies from 2015 to 2024. Its central focus is the proportion of renewable energy sources and the intricate relationship between energy production and economic performance. Based on data from the Energy Institute and the World Bank, the analysis examines the causal relationship between power generation and economic growth using the Granger causality test. The findings reveal that power generation patterns vary considerably, with some countries such as China, the United States, and India dominating in power generation, while others like France, Brazil, and Canada lead in low-carbon power generation due to strong nuclear and hydroelectric backgrounds. The Granger causality test indicated unidirectional causality in Canada and the United Kingdom, where Gross Domestic Product (GDP) was a significant predictor of power generation. Conversely, in Italy, power generation was found to be a significant explanatory factor for GDP. Overall, the study underscores the importance of long-term commitment to moving away from fossil fuels, while acknowledging that national circumstances play a substantial role in shaping each country's energy transition process.**

Keywords - energy transition, decarbonization, climate change, economic performance, life cycle assessment.

I. INTRODUCTION

Climate change represents one of the greatest global challenges of the 21st century, with profound implications for social, environmental, and economic systems [1]. Rising average temperatures, more frequent extreme weather events, and the degradation of natural ecosystems [2] are no longer distant threats, but realities that directly affect food security, public health, infrastructure, and economic stability in many regions of the planet [3,4].

At the heart of this crisis is the energy sector, which encompasses electricity, heating and cooling, and transportation, and remains heavily dependent on fossil fuels [5,6]. In response to this, there has been growing mobilization by governments and economic agents around the transition to low-carbon development models, particularly in the development of alternative energy sources [7,8].

Among the key strategies in the current process of reducing greenhouse gas emissions and pollution in direct contact with the

ISBN: 978-86-82602-07-1

population is the electrification of economic sectors, where fossil fuels are replaced by electricity, ideally from renewable or low-emission energy systems in key activities [9-11].

Power generation on a global scale is still largely dominated by fossil fuels [5]. In 2023, 35.21% of the global electricity matrix came from coal, 22.52% from natural gas, and 39.35% from renewable and low-carbon sources, with hydroelectric (14.26%), nuclear (9.09%), wind power (7.79%), and solar (5.58%).

The energy transition strategies adopted by countries vary considerably, reflecting their geographical conditions, economic structures, technological capabilities, and political-institutional contexts [8].

Germany is a benchmark in the energy transition process, with its Energiewende policy promoting the use of renewable sources and the phasing out of nuclear energy [12], although it faces challenges related to energy security and costs [13]. France focuses its efforts on nuclear energy as an energy strategy to ensure stability in electricity supply and reduce emissions [14,15] Canada, the United States, India, Italy, Japan, and the United Kingdom generate a significant portion of their electricity from natural gas, currently considered a “bridge fuel” for a smooth energy transition due to its low environmental impact compared to other fossil fuels [16].

Brazil has historically relied heavily on hydroelectric power in its electricity mix and has expanded its use of sources such as wind, solar, and biomass, remaining one of the countries with the highest share of renewables in power generation. China, although still heavily dependent on coal, leads global investment in renewable energy, electric vehicles, and solar equipment production

Despite the advances in electrification and growth in power generation over the years, there is still no consensus in the literature on the nature of the relationship between electricity consumption and economic growth [17]. Several studies have investigated whether electricity drives GDP, whether GDP growth generates greater demand for electricity, whether both variables influence each other, or whether there is no causal link in either direction [18,19]. This relationship depends heavily on the structural characteristics of each country, such as the level of economic development, the availability of natural resources, population dynamics, the sectoral composition of the economy, and energy consumption patterns [20].

This study proposes a comparative analysis of power generation in the largest global economies during the period from 2015 to 2024, with an emphasis on the share of renewable sources. The ten countries are: the United States, China, Germany, India, Japan, the United Kingdom, France, Italy, Canada, and Brazil. In addition, this study investigates the dynamic relationship between power generation and economic performance, measured by GDP, through the application of Granger causality test.

II. Material and Methods

A. Selection of Countries

According to The International Monetary Fund [21], the top 10 largest economies by nominal GDP according to a 2025 projection include the United States, China, Germany, India, Japan, the United Kingdom, France, Italy, Canada, and Brazil. This sample of countries provides a good representation of global energy patterns among their distinct economic structures.

The relationship between GDP and power generation is a key indicator of a nation's ability to fuel its economic activity. While economic growth is directly correlated with a country's energy needs, the methods and sources of generating that power reflect a country's stage of development and its energy policy priorities. In most cases, economic growth drives an increase in electricity demand as industrial production, commercial activity, and living standards rise.

B. Data Acquisition

The data used in this study comes from two data agencies recognized worldwide for their technical expertise: economic and demographic indicators from the World Bank [22] accessed via World Bank Open Data platform, and electricity data from the World Energy Statistical Review of the Energy Institute [5]. The data frame covers the period 2015-2024, selected to capture a recent and relevant timeframe of economic and energy trends.

For economic analysis, GDP was measured in 2021 US dollars at purchasing power parity (PPP), this method was specifically chosen to adjust for differences in the cost of living and inflation rates across countries, ensuring more accurate and comparable economic figures. Population data was collected to measure per

capita power generation. This metric provides a more granular basis for comparing energy production efficiency across countries by normalizing for population size. Power generation was measured in terawatt-hours (TWh) and refers to the energy sources used in each country: coal, oil, natural gas, nuclear, hydroelectric, solar, wind, biomass, and other renewables.

The group of other renewables includes sources such as geothermal, wave, and tidal energy.

The findings should be interpreted as reflecting broad trends rather than precise impacts attributable to discrete disruptions like the 2020 pandemic or subsequent energy shocks.

C. The Granger Causality Test

The causality test proposed by Granger [23] aims to overcome the limitations of using simple correlations between variables by determining the causal relationship between two variables. The Granger causality is a statistical hypothesis test for determining whether one time series is useful in forecasting another.

A time series X is said to Granger-cause Y if it can be shown that those X values provide statistically significant information about future values of Y through a series of t-tests and F-tests on lagged values of X, as shown in Eq. (1) and (2).

$$Y_t = \alpha_1 + \sum_{i=1}^{n} \beta_i X_{t-i} + \sum_{j=1}^{m} \gamma_j Y_{t-j} + \varepsilon_{1t}, \quad (1)$$

$$X_t = \alpha_2 + \sum_{i=1}^{n} \theta_i X_{t-i} + \sum_{j=1}^{m} \delta_j Y_{t-j} + \varepsilon_{2t}. \quad (2)$$

Y_t and X_t represent the two time series variables being analyzed at time t, α_1 and α_2 are the constant terms for each equation. The sums of past values of X_t, with n lags, and Y_t, with m lags, are included in the equations. The coefficients β_i and θ_i measure the influence of past X values on the current values of Y and X, respectively. The coefficients γ_j and δ_j measure the influence of past Y values on the current values of Y and X, respectively. ε_{1t} and ε_{2t} are the error terms for each equation at time t, representing random disturbances not explained by the model.

Equation (1), Y_t, for example, causality is investigated using an F-test with the null hypothesis that the coefficients of the lagged variables of the other time series are jointly equal to zero, that is,

$$H_0 = \beta_1 = \cdots = \beta_i = 0. \quad (3)$$

The relationship between variables in each country was analyzed using the *lmtest* library of the *R software* [24], version 4.3.3. The integrated development environment (IDE) *RStudio* [25] was used to execute the scripts.

III. Results and Discussion

A. Power Generation

Table I shows data on power generation, GDP, population, GDP per capita, and power generation per capita for countries in 2013 and 2024 and how they varied between the period.

China, the United States, and India are the largest producers of electricity among the ten largest global economies. In 2024, China achieved a generation of 10068 TWh, followed by the United States, India, and Japan. When considering generation per capita, it was observed that the United States had an average of 12.90 MWh per person in 2024, while China generated 7.15 MWh/person, India only 1.42 MWh/person, and Japan 8.21 MWh/person, highlighting significant disparities in individual energy supply.

Canada has the highest amount of electricity generated per person (15.19 MWh/person) in the group. This high rate is attributed to a combination of factors, including the presence of energy-intensive industries, a significant demand for both heating and air conditioning due to its climate, as well as the country's high income and access to affordable electricity [26].

The exclusive evaluation of absolute values of power generation can obscure important aspects related to territorial, technological, economic, cultural, and population aspects and the structure of the country.

Brazil, Canada, France and Germany are in the middle range of power generation. These countries do not lead the ranking, but they are also well above nations with more modest production. This level suggests economies with significant energy demand and diversified generation capacities.

TABLE I. ENERGY, ECONOMIC, AND DEMOGRAPHIC INDICATORS FOR THE 10 LARGEST ECONOMIES IN THE WORLD: 2013 AND 2024.

Country	Power Generation (TWh)			GDP (Trillions of Dollars - Purchasing power parity, 2021)			Population (Millions of people)			Power Generation per capita (MWh/person)		
	2013	*2024*	*Δ%*	*2013*	*2024*	*Δ%*	*2013*	*2024*	*Δ%*	*2013*	*2024*	*Δ%*
Brazil	570.83	745.27	30.56%	3.82	4.17	9.07%	198.48	212.00	6.81%	2.88	3.51	22.23%
Canada	655.69	627.19	-4.35%	1.92	2.34	21.95%	35.08	41.29	17.70%	18.69	15.19	-18.73%
China	5431.63	10068.8	85.37%	17.83	33.60	88.41%	1363.2	1408.98	3.35%	3.98	7.15	79.36%
India	1146.14	2057.5	79.52%	7.43	14.24	91.76%	1295.8	1450.94	11.97%	0.88	1.42	60.33%
Italy	286.02	264.63	-7.48%	2.82	3.13	10.92%	60.31	58.99	-2.20%	4.74	4.49	-5.40%
France	576.75	557.73	-3.30%	3.30	3.73	12.94%	66.00	68.52	3.82%	8.74	8.14	-6.85%
Germany	629.69	476.87	-24.27%	4.70	5.25	11.75%	80.65	83.51	3.55%	7.81	5.71	-26.87%
Japan	1087.76	1018.48	-6.37%	5.42	5.71	5.53%	127.45	123.98	-2.72%	8.53	8.21	-3.75%
UK	358.28	281.33	-21.48%	3.08	3.64	17.88%	64.14	69.23	7.93%	5.59	4.06	-27.25%
USA	4055.61	4387.26	8.18%	19.62	25.68	30.84%	316.73	340.11	7.38%	12.80	12.90	0.74%

In contrast, Italy and the United Kingdom are the countries with the lowest power generation in the group in 2024. Low generation can be partly attributed to smaller populations, energy efficiency policies, energy imports, use of other energy sources, consumption patterns, and economic dynamics. The analysis of per capita generation reinforces this observation: in 2024, Italy recorded power generation of 4.49 MWh/person and the United Kingdom 4.06 MWh/person, figures considerably lower than those observed in the leading countries in terms of generation. In addition, there has been a reduction in this indicator over time, -5.40% for Italy and -27.25% for the United Kingdom compared to 2013 levels.

Fig. 1 shows the progress of power generation sources over the years for each country. The decade between 2013 and 2024 witnessed a reconfiguration in countries' electricity matrices, marked by the ambitions, strategies, and policies adopted by countries.

For example, the German electricity matrix adopted a process of denuclearization and a remarkable advance in renewable energies, from 15.45% of the country's total power generation coming from nuclear sources to zero in 2024 [27]. Advances in wind and solar power, corresponding of 42.87% of the German electricity mix in 2024, have been significant and have filled the energy gap created by the decommissioning of nuclear power plants. Natural gas has also played a complementary role in this transition. Significant declines in the use of coal (-63.79%) and oil (-23.05%) were observed, revealing a commitment to decarbonizing the electricity sector.

Canada and Brazil are both countries with a high proportion of hydroelectric power plants as their main source of electricity. In Brazil, there have been significant increases in solar and wind energy production, which accounted for 10.02% and 14.47% of total energy produced, respectively. The same process occurred in Canada, but to a lesser extent, with wind accounting for 7.19% and solar 1.31%. In both countries, power generation from coal and oil decreased significantly. There was also a reduction in the use of natural gas in Brazil, but an increase in Canada.

In 2024, China (58.17%) and India (74.56%) were the countries most dependent on coal. China is the global leader in power generation. Coal-fired generation increased its production from 4077.37 TWh to 5857.43 TWh, reflecting the immense volume of power generated. To put the scale into context, coal-fired generation in China in 2013 was almost greater than the total electricity generated in the United States over the period. The country expanded its generation on all fronts, but remained heavily dependent on

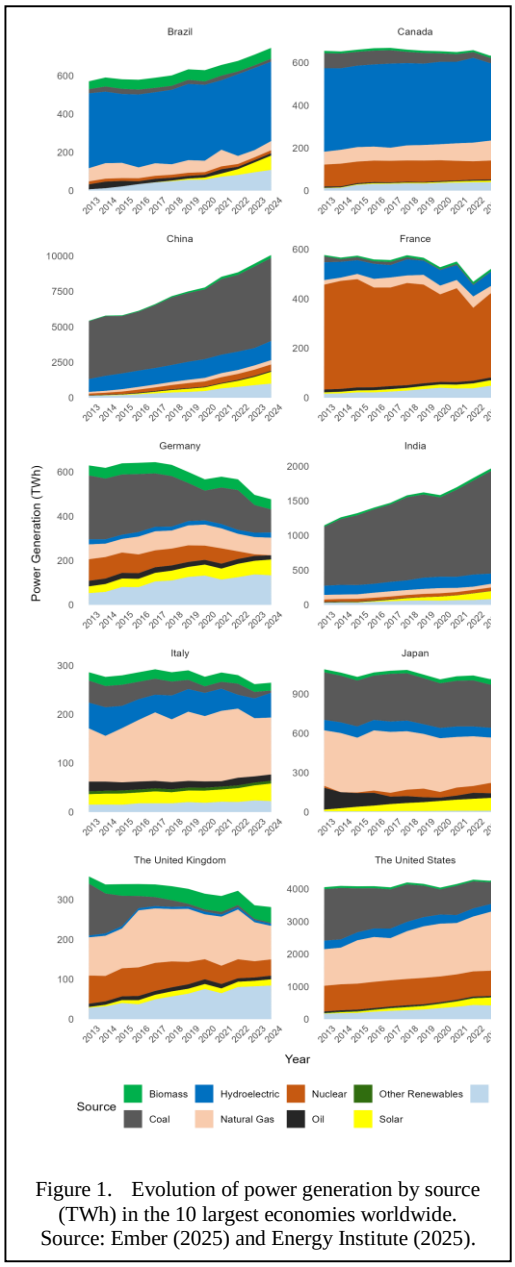

Figure 1. Evolution of power generation by source (TWh) in the 10 largest economies worldwide. Source: Ember (2025) and Energy Institute (2025).

fossil fuels, despite growing efforts in renewable sources.

India, which generates most of its electricity from coal, with a sharp increase during the period, significantly reduced its use of natural gas and oil, highlighting the complexity of its energy transition, which still relies heavily on fossil fuels to meet growing demand. The greatest advances in the Indian matrix were driven by renewable energies, with hydroelectric (7.59%), solar (6.50%), and wind (3.59%) power. In addition, nuclear energy and biomass also recorded significant advances in generation.

France maintained its strong dependence on nuclear energy, accounting for 68.00% in 2024, consolidating its position as a leader in this sector. Despite its nuclear profile, renewable sources showed significant growth, with hydroelectric (12.42%), wind (7.74%), and solar (4.23%) power.

Italy has undergone a significant energy transition, characterized by a sharp reduction in dependence on coal and oil, but an increase in natural gas, which is now the most important source in the Italian energy mix (44.00%). Renewable sources have shown robust growth, with solar energy (13.53%) and wind energy (8.45%).

Japan's electricity mix underwent a significant reconfiguration post-Fukushima, leading to the deactivation and then partial reactivation of nuclear reactors [28]. Nuclear generation increased from 14.60 TWh to 84.90 TWh in 2024. Despite a persistent reliance on fossil fuels, generation from oil and coal saw a decline, 2,61% and 32,00% in 2024, respectively. However, the country demonstrated a strong investment in renewables, with solar accounting to 9.81%.

The United Kingdom has distinguished itself with an ambitious and successful strategy to phase out coal, with its generation falling by 98.23%. Wind power (29.96%) and natural gas (29.92%) are the main sources of power in 2024. Nuclear (14.51%) and biomass (14.02%) are also important sources. Solar accounts for 5.53% of total production.

The United States has undergone a remarkable transformation in its electricity matrix, marked by a sharp decline in coal-fired power generation, down to 14.52% in 2024. Natural gas (42.51%) is the main source, but sources such as nuclear (17.82%), wind (10.03%), and solar (6.53%) are also major sources of national power generation.

In 2024, the share of renewable sources in the electricity mix reflects different stages of transition. France leads the way in low-carbon power generation, with 94.25% of its electricity coming from these sources, followed by Brazil (89.83%), Canada (79.27%), and the United Kingdom (65.99%). At the other end of the spectrum, China (38.06%), Japan (31.44%), and India (22.46%) had the lowest shares of low-

TABLE II. RESULTS OF THE GRANGER CAUSALITY TEST FOR THE VARIABLES GROSS DOMESTIC PRODUCT (GDP) AND POWER GENERATION.

Country	GDP *forecasts* Power Generation		Power Generation *forecasts* GDP	
	F-statistic	***p-value***	***F-statistic***	***p-value***
Brazil	1.5236	0.4198	5.1470	0.1670
Canada	20.9377	0.0459**	0.5792	0.6830
China	2.7449	0.2783	5.5766	0.1158
France	8.2146	0.1105	1.4292	0.4369
Germany	5.5664	0.1561	0.4609	0.7387
India	0.7771	0.6051	1.5822	0.4099
Italy	1.1298	0.5013	14.1140	0.0669*
Japan	0.4833	0.7275	0.9287	0.5558
UK	83.1255	0.0119**	1.1715	0.4912
USA	0.8189	0.5907	3.3379	0.2390

Note: (*), (**) denote rejection of the null hypothesis at a statistical significance level of 10% and 5%, respectively.

emission sources in their mixes, indicating that, despite their efforts, there is still a long way to go in completely decarbonizing their electricity sectors.

B. Nexus: GDP and Power Generation

To investigate the causal relationship between economic growth and electricity production, a Granger causality test was applied to the time series data. The results, presented in Table II, indicate significant findings for several countries within the sample.

The results presented in Table II indicate that, based on the sample analyzed and with 95% confidence, only Canada and the United Kingdom showed unidirectional causality, in which GDP is a significant predictor of power generation in these countries.

Unidirectional causality means that the increase in power generation did not prove to be, in itself, a relevant predictor of GDP growth. For Italy, unidirectional causality was also identified, with power generation being a significant explanatory factor for GDP, based on the sample and with 90% confidence.

The presence of unidirectional causality from GDP to power generation in Canada and the United Kingdom suggests that economic growth in these countries is a determining factor for demand and, consequently, for increased electricity production. In the case of Italy, it suggests that the electricity production sector acts as a key driver of economic development.

These findings align with the broader literature that investigates the links between energy consumption and economic performance. For instance, the study by [17] highlights that the causal dynamics between electricity consumption and GDP are not uniform across countries, but shaped by structural and institutional contexts. Similarly, [20] emphasizes that the direction of causality depends on national energy policies, market efficiency, and stages of economic development.

In this sense, the results found for Canada, the United Kingdom, and Italy illustrate that the energy–growth relationship varies by country, reinforcing the importance of considering specific economic and energy contexts when interpreting these outcomes.

IV. CONCLUSION

This study compares the power generation across the ten largest global economies from 2015 to 2024, providing insights into the dynamics of energy transitions and their

relationship with economic performance. The study demonstrates that while global progress toward decarbonization is evident, there are significant variations between countries and in their approaches to decarbonize the electricity sector.

The study confirms that power generation patterns vary across countries, reflecting their conditions. China, the United States, and India emerge as the dominant electricity producers in absolute terms. However, per capita analysis revealed major inequalities, in the case of India, highlighting significant disparities in individual energy access and consumption patterns.

The electricity mix analysis demonstrates progress in renewable energy adoption, though fossil fuel dependence remains substantial. France leads in low-carbon power generation at 94.25%, followed by Brazil (89.83%) and Canada (79.27%), primarily due to their strong nuclear and hydroelectric power plants. Conversely, China (38.06%), Japan (31.44%), and India (22.46%) maintain heavy reliance on fossil fuels, particularly coal, despite considerable investments in renewable technologies.

Granger causality tests reveal that economic growth is a significant driver of power generation in Canada and the United Kingom, while in Italy, increases in power generation tend to stimulate GDP growth. However, these findings should be interpreted with caution, as the analysis relies solely on secondary data and lacks essential econometric diagnostics.

The analysis focused on the period from 2015 to 2024, which is useful for capturing recent dynamics but does not completely account for long-term historical patterns or potential events beyond this time frame. Future studies should examine incorporating additional variables such as energy costs, policy interventions, and econometrical approaches to improve the reliability of the findings.

ACKNOWLEDGMENTS

The authors wish to acknowledge the support of the Laboratory of Environmental and Energy Assessment (LAvAE) at the Federal University of Paraíba.

FUNDING

The authors thank the National Council for Scientific and Technological Development (CNPq Productivity Grants 303180/2025-0 and 301463/2025-5) and the support of the Paraíba State Research Support Foundation (FAPESQ-PB) through master's scholarship 115/2025.

REFERENCES

[1] Abbass, K., Qasim, M. Z., Song, H., Murshed, M., Mahmood, H., & Younis, I. (2022). A review of the global climate change impacts, adaptation, and sustainable mitigation measures. *Environmental Science and Pollution Research*, *29*(1), 42539-42559. https://doi.org/10.1007/s11356-022-19718-6.

[2] National Oceanic and Atmospheric Administration. (2025, June 13). *Climate change impacts*. National Oceanic and Atmospheric Administration; NOAA. Available at: https://www.noaa.gov/education/resource-collections/climate/climate-change-impacts

[3] Zhao, Q., Yu, P., Mahendran, R., Huang, W., Gao, Y., Yang, Z., Ye, T., Wen, B., Wu, Y., Li, S., & Guo, Y. (2022). Global climate change and human health: pathways and possible solutions. *Eco-Environment & Health*, *1*(2), 53-62. https://doi.org/10.1016/j.eehl.2022.04.004

[4] Adom, P. K. (2024). The socioeconomic impact of climate change in developing countries over the next decades: A literature survey. *Heliyon*, *10*(15), e35134-e35134.https://doi.org/10.1016/j.heliyon.2024.e35134

[5] Energy Institute. (2025). *Statistical Review of World Energy*. Available at: https://www.energyinst.org/statistical-review/

[6] Van Leeuwen, J., & Monios, J. (2022). Decarbonisation of the shipping sector – Time to ban fossil fuels? *Marine Policy*, *146*, 105310. https://doi.org/10.1016/j.marpol.2022.105310

[7] Camargo-Bertel, A. A., Hincapie, D., Pugliese, V., Gonzalez-Quiroga, A., & Pupo-Roncallo, O. (2025). Decarbonizing the cement industry in Latin America and the Caribbean: A comprehensive review of strategies, barriers, and policies. *Energy Conversion and Management: X*, *26*, 100956. https://doi.org/10.1016/j.ecmx.2025.100956

[8] Bakhsh, S., Zhang, W., Ali, K., & Oláh, J. (2024). Strategy towards sustainable energy transition: The effect of environmental governance, economic complexity and geopolitics. *Energy Strategy Reviews*, *52*, 101330-101330. https://doi.org/10.1016/j.esr.2024.101330

[9] Olkkonen, V., Lind, A., Rosenberg, E., & Kvalbein, L. (2023). Electrification of the agricultural sector in Norway in an effort to phase out fossil fuel consumption. *Energy*, *276*, 127543-127543. https://doi.org/10.1016/j.energy.2023.127543

[10] Boonman, H., & Rodriguez, M. (2025). Mitigating foreign fossil fuel shocks: The role of renewable energy and industrial electrification in The Netherlands. *Economic Modelling*, 107138-107138. https://doi.org/10.1016/j.econmod.2025.107138

[11] González, M. E., Barrios, N., Venditti, R. A., & Pal, L. (2025). Advancing sustainability in the U.S. pulp and paper industry: Decarbonization through energy efficiency, electrification, low-carbon fuels, and the social cost of emissions. *Journal of Cleaner Production*, *522*, 146196-146196. https://doi.org/10.1016/j.jclepro.2025.146196

[12] Joas, F., Pahle, M., Flachsland, C., & Joas, A. (2016). Which goals are driving the Energiewende? Making sense of the German Energy Transformation. *Energy Policy*, *95*, 42-51. https://doi.org/10.1016/j.enpol.2016.04.003

[13] Federal Ministry for Economic Affairs and Energy. (2020). *More renewables for better mitigation of climate change*. Available at: Bmwk-Energiewende.de. https://www.bmwk-energiewende.de/EWD/Redaktion/EN/Newsletter/2020/09/Meldung/direkt-answers-infographic.html

[14] Lamnatou, C., Cristofari, C., & Chemisana, D. (2023). Renewable energy sources as a catalyst for energy transition: Technological innovations and an example of the energy transition in France. *Renewable Energy*, *221*, 119600. https://doi.org/10.1016/j.renene.2023.119600

[15] Ministry for Europe and Foreign Affairs. (2021, October 13). *Nuclear power and SMR are central to the "France 2030" investment plan*. Représentation Permanente de La France Auprès Des Organisations Internationales et Des Nations Unies à Vienne. Available at: https://onu-vienne.delegfrance.org/Nuclear-power-and-SMR-are-central-to-the-France-2030-investment-plan

[16] Janzwood, A., & Millar, H. (2022). Bridge fuel feuds: The competing interpretive politics of natural gas in Canada. *Energy Research & Social Science*, *88*, 102526. https://doi.org/10.1016/j.erss.2022.102526

[17] Payne, J. E. (2010). A survey of the electricity consumption-growth literature. *Applied Energy*, *87*(3), 723-731. https://doi.org/10.1016/j.apenergy.2009.06.034

[18] Solarin, S. A., & Ozturk, I. (2015). On the causal dynamics between hydroelectricity consumption and economic growth in Latin America countries. *Renewable and Sustainable Energy Reviews*, *52*, 1857-1868.https://doi.org/10.1016/j.rser.2015.08.003

[19] Smyth, R., & Narayan, P. K. (2015). Applied econometrics and implications for energy economics research. *Energy Economics*, *50*, 351-358. https://doi.org/10.1016/j.eneco.2014.07.023

[20] Ozturk, I. (2010). A literature survey on energy–growth nexus. *Energy Policy*, *38*(1), 340-349. https://doi.org/10.1016/j.enpol.2009.09.024

[21] International Monetary Fund. (2025, April). *GDP, Current Prices*. International Monetary Fund. Available at: https://www.imf.org/external/datamapper/NGDPD@WEO/OEMDC/ADVEC/WEOWORLD

[22] World Bank. (2025). *World Bank Open Data*. World Bank. Available at: https://data.worldbank.org/

[23] Granger, C. W. J. (1969). Investigating Causal Relations by Econometric Models and Cross-spectral Methods. *Econometrica*, *37*(3), 424-438. https://doi.org/10.2307/1912791

[24] R Core Team. (2024). *R: A Language and Environment for Statistical Computing*. R Foundation for Statistical Computing, Vienna, Austria. Available at: https://www.r-project.org/

[25] Posit team (2025). RStudio: Integrated Development Environment for R.Posit Software, PBC, Boston, MA. Available at: http://www.posit.co/

[26] Canada Energy Regulator. (2022, November 14). *CER – Market Snapshot: Why Canada is one of the world's largest electricity consumers*. Available at: www.cer-Rec.gc.ca. https://www.cer-rec.gc.ca/en/data-analysis/energy-markets/market-snapshots/2022/market-snapshot-why-canada-is-one-of-the-worlds-largest-electricity-consumers.html

[27] Chen, C.-C. (2024). Comparative impacts of energy sources on environmental quality: A five-decade analysis of Germany's Energiewende. *Energy Reports*, *11*, 3550-3561. https://doi.org/10.1016/j.egyr.2024.03.027.

[28] Fujita, T. (2024). Energy knowledge and public response to restarting nuclear plants in Japan following the fukushima accident. *Utilities Policy*, *92*, 101858. Available at: https://doi.org/10.1016/j.jup.2024.101858

eNergetics 2025
DOI: https://doi.org/10.5281/zenodo.18626173

Original Scientific Article

Mission Profile Robustness of PCM Thermal Management for Microsatellites

Burak İzgi[1]

[1]Department of Mechanical Engineering, Yozgat Bozok University, Yozgat, Türkiye

[1]burak.izgi@bozok.edu.tr

Abstract—**Thermal control is a critical design driver for microsatellite reliability. Optimization of Phase Change Materials (PCM) as a passive thermal management solution in microsatellites is usually based on a single, nominal operational point in time and a fixed heat load. This study goes one step beyond this common approach and investigates how robust optimized PCM-filler configurations remain in the face of a wide range of different operational scenarios. To this end, we conducted a parametric study using an established analytical model, systematically varying heat loads (15W, 25W, 35W) and pulse durations (20, 40, 60 min). Our main objective was to determine the minimum system mass and volume required to maintain the maximum component temperature at 50 °C for each scenario. The results conclusively demonstrate that the "best" material choice is not a fixed truth, but rather strongly dependent on the mission profile. Mapping the operational space showed that Glycerol-based configurations are ideal for a wide range of medium-to-hard scenarios. However, under the most challenging, high-energy conditions, we observed that the optimally balanced design shifts towards PlusICE-based systems, indicating a critical material selection transition based on mission demands. This study provides satellite designers with a quantitative framework to go beyond a single design point and select truly robust and reliable thermal solutions for the entire operational envelope of a mission.**

Keywords - microsatellite thermal control, Phase Change Material (PCM), robustness analysis, parametric study, mission profile.

I. INTRODUCTION

As microsatellite platforms proliferate, thermal management in these systems has always been one of the most critical design challenges [1,2]. In particular, electronic components that directly impact mission lifetime and reliability must be maintained within specified temperature ranges in the variable and harsh thermal conditions of space. This challenge is further complicated by strict constraints on the mass, volume and power budgets of satellites [3,4]. Furthermore, the tendency toward miniaturization in satellite electronics and increased component integration density worsen local heat generation, making thermal control even more difficult for small spacecraft [5,6]. Conventional passive cooling methods are often inefficient, while active cooling systems consume precious power budget and add complexity to the system [7,8]. In recent years, CubeSat missions with high-performance payloads such as hyperspectral imagers or communication modules have emphasized the importance of compact, lightweight and efficient thermal regulation methods [9].

Against this dilemma, Phase Change Materials (PCMs) are emerging as a highly effective solution for passive thermal control [10]. PCMs protect electronic components from temperature extremes by storing the waste heat generated during peak duty cycles through phase change [11]. However, the most obvious weakness of most PCMs is their low thermal conductivity. In order to bridge this performance gap, PCMs are often formed into a composite

ISBN: 978-86-82602-07-1

structure with highly conductive fillers such as graphite or metal foams [12].

There is a significant volume of research in the literature focusing on the optimization of these PCM composites [13]. These studies cover the performance of different PCM-filler pairs, the effect of geometric add-ons such as fins to improve thermal conductivity, or the optimization of specific parameters by methods such as Taguchi. These fundamental studies have provided valuable insights for system optimization.

Building on this background, our own previous work [14] focused on one of these gaps in the literature. Rather than optimization of a specific design, it addressed a more fundamental question, presenting a global sensitivity analysis that investigated the influence of the fundamental thermophysical properties of the constituent materials (density, latent heat, etc.) on the total mass and volume. That study revealed that the most influential parameter for system mass is the latent heat of the PCM, while for volume it is the PCM density.

However, most of these optimization studies tend to evaluate designs with respect to a single, nominal operational point, usually defined by a fixed heat load and duration. However, a real satellite mission profile consists of dynamic and variable scenarios ranging from low-power standby to high-power data transfer [15,16]. A critical research question is how robust a design optimized for a nominal situation will remain under these variable loads in the mission profile and how the optimal material selection will change according to different scenarios. This study aims to fill this gap and present a robustness analysis under different operational scenarios.

II. Methodology

A. Analytical Model

The analyses in this study are based on a 1-D analytical model previously developed and detailed by us [14]. This model, schematically shown in Fig. 1, calculates how the transient heat pulse emitted from an electronic component is absorbed and stored by the PCM-filler composite layer. The main objective of the model is to determine the system parameters required to keep the component under the maximum temperature limit of 50°C. The model is based on the energy balance of the system (latent and sensible heat storage) and the one-dimensional

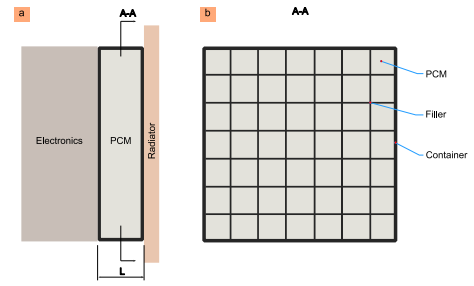

Figure 1. Schematic of the PCM-based thermal control unit assembly. The model considers a 1-D heat transfer path from the electronics, through the composite PCM-filler layer of thickness L, to a radiator. (Adapted from [14]).

Fourier heat conduction law. The original publication [14] can be consulted for the full mathematical formulation of the model and all assumptions.

B. Parametric Study Design

The main contribution of this work is to use the existing model to introduce a new and systematic parametric analysis that tests the robustness of designs over a wide operational range rather than a single point. For this purpose, a 2-D "Operational Parameter Space" simulating realistic mission profiles is defined. The independent axes of this space are:

- Heat Load (Q_{pulse}): Three distinct power levels were chosen to represent different spacecraft operational modes: 15W (low-power/standby), 25W (nominal operation), and 35W (high-power/data transmission).
- Pulse Duration (Δt_{pulse}): Three durations were selected to simulate different operational phase lengths: 20 minutes (short-burst activity), 40 minutes (standard operational pass), and 60 minutes (extended operation).

This 3x3 matrix creates nine unique operational scenarios. All 24 different PCM-filler combinations from our baseline study [14] were analyzed separately for each of these nine scenarios. This comprehensive approach allowed us to ensure that the best material for each scenario was the best of all candidates.

In order to discuss the results of the analysis through a clear story, the discussion section focuses on the performance of three representative "champion" candidates. These

candidates were strategically chosen to represent different optimization philosophies from the previous study:

- *Hexadecane + Graphite:* The candidate with the lowest mass in the nominal scenario.
- *PlusICE + Graphite:* The candidate with the lowest volume in the nominal scenario.
- *Glycerol + Graphite:* Balanced candidate with the potential to stand out in high thermal flux conditions due to its low melting temperature.

III. Results and Discussion

A. *Analysis of the Operational Space: Scenario Difficulty and Optimal Materials*

The first step in our analysis was to evaluate all 24 PCM-filler combinations in all nine operational scenarios. In order to draw meaningful conclusions from this large data set, we created a heatmap (see Fig. 2) that identifies the material that demonstrates the best "balanced performance" (optimizing mass and volume equally) for each scenario. Each cell in this graph shows the winner of an independent race between the 24 candidates. The color scale indicates how "well" this winner scored, where lighter colors indicate a lower and therefore better-balanced performance.

The findings in Fig. 2 clearly confirm one of the main hypotheses of our study: The optimal choice of materials is not a fixed "best" solution, but a dynamic outcome directly linked to the thermal demands of the mission. In most of the low and medium energy scenarios, we see that the Glycerol + Graphite combination emerges as the clear best candidate. In particular, its dominance in all 15 W duty profiles shows how effective this material is over a wide range

However, as the task profile becomes more difficult (i.e. as both power and duration increase), we observe a clear "leadership shift" in high energy scenarios. Under the most demanding conditions, PlusICE-based configurations become the most balanced solutions. For example, in the most demanding scenario, the 35 W-60min task, PlusICE + Copper offers the best-balanced performance. The color scale also tells a secondary but important story here: The winners of the most challenging scenarios (light colored) score more

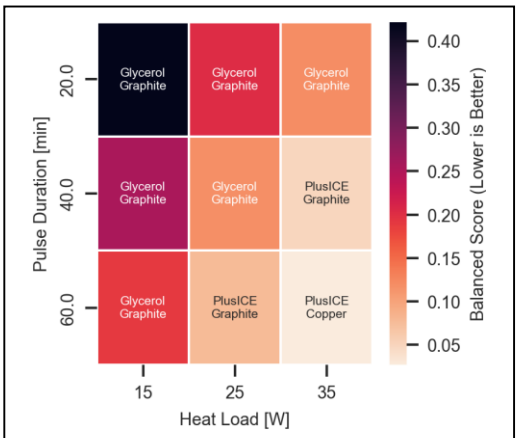

Figure 2. Heatmap showing the material combination Swith the best balanced performance for each operational scenario. The color indicates the normalized score (lower is better), and the text identifies the optimal PCM and filler.

"dominant" or close to ideal than the winners of some of the easier scenarios (darker colored). This suggests that while Glycerol wins over a wide range, this victory is often due to its overwhelming superiority in a single metric (mass) and so its balanced score is not "perfect". In contrast, materials such as PlusICE can win in extreme conditions where all candidates are pushed to their limits, with a more balanced advantage over their competitors in both metrics.

B. *Ranking in a Nominal Scenario*

Having seen the big picture, we focused on a nominal scenario (25W, 40min) to get a clearer understanding of the relative performance of the materials against each other. The ranking graph in Fig. 3 ranks all combinations in this scenario from lightest to heaviest. This analysis strongly confirms the rationale for the selection of "champion" candidates we identified in the methodology section.

As we predicted, Hexadecane + Graphite proved to be the best candidate for mass optimization, offering the lowest system mass of about 0.28 kg. At the other extreme, we see the overwhelming negative impact of using an inefficient filler. Combinations with Carbon Steel are at the bottom of the list, regardless of the PCM used. The worst design, Eicosane + Carbon Steel, requires more than twice the mass of the best design to perform the same thermal task, emphasizing how critical the choice of material is.

Fig. 3 also clarifies the position of our other candidates. Glycerol + Graphite is among the

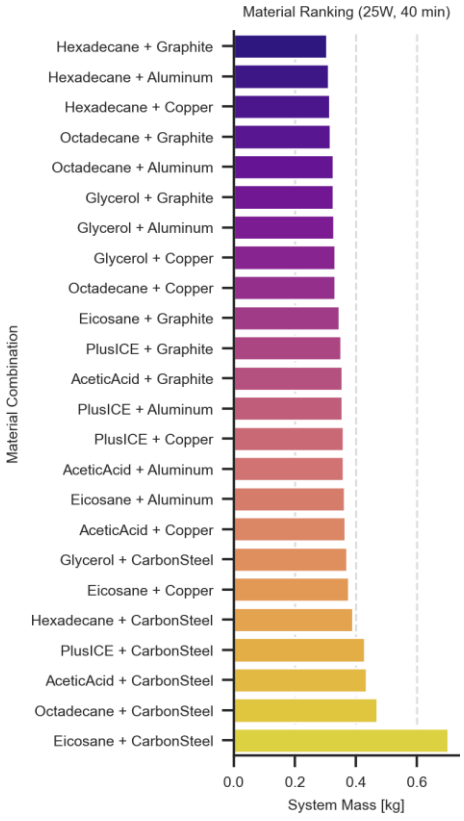

Figure 3. System mass ranking for all material combinations under a nominal operational scenario (25W for 40 min).

best performers, showing that it is a highly competitive low-mass solution. More importantly, we see that PlusICE + Graphite, which we selected as a volume optimization candidate in our previous study, is in the middle of the list in terms of mass. This finding is very important: It empirically proves that the goal of minimizing mass and the goal of minimizing volume led to different material choices and strengthens the rationale for why we chose these candidates to represent these different strategies.

C. *The Critical Role of Instantaneous Power on Design Requirements*

To delve deeper into the mechanism behind the performance differences, we plotted the fill rate required by champion candidates (*rf*) against the total task energy (Fig. 4). At first glance, instead of the intuitively expected smooth, increasing curve, we find a rather bumpy, "jagged" trend.

This behavior is not an anomaly or an error, but rather one of the most critical findings of our

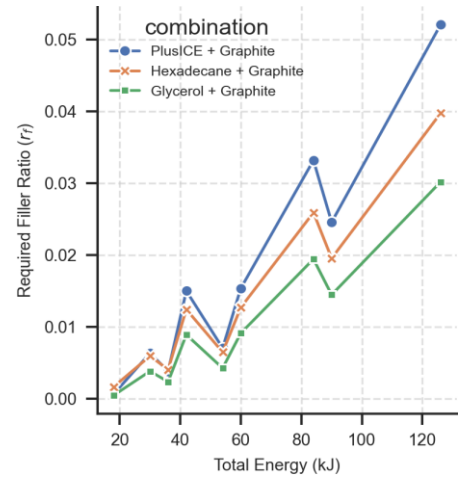

Figure 4. Required filler ratio (rf) as a function of total mission energy for the three champion candidates, illustrating the dominant effect of instantaneous power over total energy.

study. The data reveal that the main factor determining the required fill rate is not the total energy (E_{max}), which determines the thermal capacity, but rather the instantaneous thermal load (Q_{pulse}), which determines the heat transfer rate. The most striking example in Fig. 4 is the comparison of the 42 kJ (35W, 20 min) and 54 kJ (15W, 60 min) scenarios. The 54 kJ scenario, with a higher total energy, requires a lower fill rate than the 42 kJ scenario. The instantaneous power of the 54 kJ scenario (15W) is lower than the instantaneous power of the 42 kJ scenario (35W). The system must be designed to manage the peak flux, and a higher peak flux requires a more conductive composite, hence a higher *rf*. This finding directly demonstrates that basing the design solely on total energy is insufficient and that the most critical parameter determining the level of thermal improvement required is the peak operational power.

D. *The Shifting Mass-volume Trade-off and Influence of Melting Temperature*

This critical dependence of the design on the fill ratio is directly reflected in the overall mass-volume trade-off of the system. In Fig. 5, we have plotted the best solutions (Pareto front candidates) in all scenarios, colored according to the total energy of the mission. As expected, we see that as the mission energy increases (as the colors change from light to dark), the overall design front inevitably shifts towards higher mass and volume. This visually proves that the

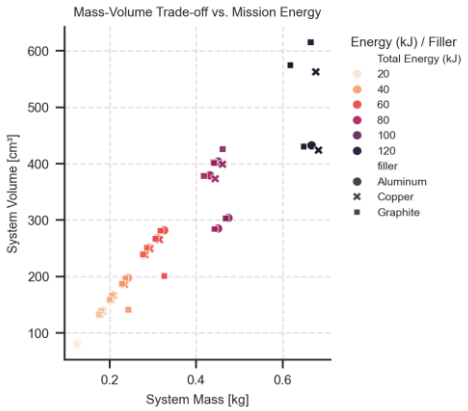

Figure 5. Mass-Volume trade-off for Pareto-optimal candidates across all scenarios. Points are colored by the total energy of the mission pulse, showing the performance front shifting with increasing thermal demand.

thermal management "cost" of more demanding missions increases

More importantly, this analysis also reveals the physical reasons why certain materials perform superiorly under high stress. As can be seen from the graph, Graphite-filled systems (square symbols) consistently define the leftmost (lowest mass) limit of the mass-volume balance, especially at high energy levels (dark dots). This empirical result strongly supports our hypothesis regarding the role of the melting temperature of the PCM.

A PCM with a low melting temperature, such as Glycerol ($T_m \approx 18°C$), allows the system to operate with a larger temperature difference ($\Delta T = T_{max} - T_m \approx 32°C$). According to the heat transfer equation ($Q \propto k_{eff} \Delta T/L$), this larger ΔT means that a lower effective thermal conductivity (k_{eff}) is sufficient to transfer the same instantaneous heat flux (Q_{pulse}). A lower k_{eff} requires a smaller amount of filler. Since Graphite is both a low density and high conductivity filler, using a small amount of it provides a distinct mass advantage compared to using more of a denser filler such as Copper or Aluminum.

In contrast, a material with a higher melting temperature like PlusICE ($T_m \approx 32°C$) has to work with a much smaller ΔT ($\approx 18°C$). To manage the same heat flux, it has to compensate with a higher k_{eff}, which means more filler and therefore a mass disadvantage. This finding has a very important practical implication for designers: For tasks where high-power phases are expected, choosing a low melting temperature PCM paired with a low density/high conductivity filler is the most effective strategy for mass optimization.

IV. Conclusion

This work has demonstrated the need to go beyond optimization based on a single nominal point in the design of PCM-based thermal control systems for microsatellites. By systematically analyzing a wide range of operational scenarios, we have reached important and practical conclusions about the robustness of designs.

- Our most fundamental finding is that there is no single PCM-filler combination that is "best for all tasks". Our analyses have clearly shown how much the optimal material choice depends on the thermal profile of the mission. The fact that Glycerol-based systems, which offer the most balanced performance for low to medium energy scenarios, give way to PlusICE-based solutions under the most extreme thermal conditions is the clearest evidence of this dynamic choice.
- We have also empirically and theoretically demonstrated that the melting temperature of the PCM is a key strategic advantage for mass optimization under high thermal flux. Low melting temperature PCMs such as glycerol create a wider operational temperature difference (ΔT) allowing the system to achieve the same heat transfer with a smaller amount of high-density filler. This translates into a direct mass advantage.
- Finally, this study has once again demonstrated the overwhelming impact of filler selection on system-level performance. While a low density and high conductivity filler such as graphite is indispensable for mass-critical designs, an inefficient filler such as Carbon Steel can more than double the total system mass to accomplish the same thermal task.

It is important to note that this work is based on a 1-D analytical model, simplifying complex transition effects such as phase change hysteresis. Experimental validation of these findings or verification with high-fidelity 3-D

numerical simulations would be an important step for future research. Furthermore, extending this framework to include multi-objective optimization criteria such as cost and manufacturability offers a valuable area of future work.

In conclusion, this research provides a quantitative framework that enables satellite designers to make more informed and data-driven choices for passive thermal control systems. By analyzing the entire operational space, we provide a clear methodology for the development of more robust and reliable thermal management solutions for microsatellite missions.

REFERENCES

[1] Baturkin, V. (2005) Micro-satellites thermal control-concepts and components. *Acta Astronautica*, *56*, 161–70. https://doi.org/10.1016/j.actaastro.2004.09.003

[2] Osiander, R., Firebaugh, S.L., Champion, J.L., Farrar, D. and Garrison Darrin, M.A. (2004) Microelectromechanical Devices for Satellite Thermal Control. *IEEE Sensors Journal*, *4*, 525–31. https://doi.org/10.1109/JSEN.2004.830297

[3] Kovács, R. and Józsa, V. (2018) Thermal analysis of the SMOG-1 PocketQube satellite. *Applied Thermal Engineering*, *139*, 506–13. https://doi.org/10.1016/j.applthermaleng.2018.05.020

[4] Diaconu, B.M., Cruceru, M. and Anghelescu, L. (2024) Phase change materials in space systems. Fundamental applications, materials and special requirements – A review. *Acta Astronautica*, *216*, 163–213. https://doi.org/10.1016/j.actaastro.2023.12.040

[5] Cepeda-Rizo, J., Gayle, J. and Ravich, J. (2021) Thermal/Structural Challenges in Miniaturizing. *Thermal and Structural Electronic Packaging Analysis for Space and Extreme Environments*, CRC Press.

[6] Ersoy, K. (2025) Review of Electronic Cooling and Thermal Management in Space and Aerospace Applications. *Engineering Proceedings*, *89*, 42. https://doi.org/10.3390/engproc2025089042

[7] Tachikawa, S., Nagano, H., Ohnishi, A. and Nagasaka, Y. (2022) Advanced Passive Thermal Control Materials and Devices for Spacecraft: A Review. *International Journal of Thermophysics*, *43*, 91. https://doi.org/10.1007/s10765-022-03010-3

[8] Wang, J., Li, Y., Liu, X., Shen, C., Zhang, H. and Xiong, K. (2021) Recent active thermal management technologies for the development of energy-optimized aerospace vehicles in China. *Chinese Journal of Aeronautics*, *34*, 1–27. https://doi.org/10.1016/j.cja.2020.06.021

[9] Kuta, K., Nowak, G. and Nowak, I. (2024) Thermal Management of Cubesat Subsystem Electronics. *Energies*, *17*, 6462. https://doi.org/10.3390/en17246462

[10] Lawag, R.A. and Ali, H.M. (2022) Phase change materials for thermal management and energy storage: A review. *Journal of Energy Storage*, *55*, 105602. https://doi.org/10.1016/j.est.2022.105602

[11] Afaynou, I., Faraji, H., Choukairy, K., Arshad, A. and Arıcı, M. (2023) Heat transfer enhancement of phase-change materials (PCMs) based thermal management systems for electronic components: A review of recent advances. *International Communications in Heat and Mass Transfer*, *143*, 106690. https://doi.org/10.1016/j.icheatmasstransfer.2023.106690

[12] Choure, B.K., Alam, T. and Kumar, R. (2023) A review on heat transfer enhancement techniques for PCM based thermal energy storage system. *Journal of Energy Storage*, *72*, 108161. https://doi.org/10.1016/j.est.2023.108161

[13] Diaconu, B.M., Cruceru, M. and Anghelescu, L. (2023) A critical review on heat transfer enhancement techniques in latent heat storage systems based on phase change materials. Passive and active techniques, system designs and optimization. *Journal of Energy Storage*, *61*, 106830. https://doi.org/10.1016/j.est.2023.106830

[14] İzgi, B. (2025) Mass and volume optimization of PCM-based thermal control for microsatellites: A parametric and sensitivity analysis. *Next Energy*, *9*, 100457. https://doi.org/10.1016/j.nxener.2025.100457

[15] Huang, H. and Bu, C. (2025) Thermal Design and Experimental Validation of a Lightweight Microsatellite. *Aerospace*, Multidisciplinary Digital Publishing Institute. *12*, 52. https://doi.org/10.3390/aerospace12010052

[16] Liu, Z., Yang, H., Wu, S., Xu, C., Chen, Z. and Liao, W. (2025) Thermal design and equivalent thermal equilibrium testing method for attached micro/nano satellites. *Applied Thermal Engineering*, *278*, 127206. https://doi.org/10.1016/j.applthermaleng.2025.127206

eNergetics 2025
DOI: https://doi.org/10.5281/zenodo.18626188

Original Scientific Article

Efficiency evaluation of a 6-Megawatt Utility-connected Photovoltaic Solar Energy System in the Saharan Climate

Aakila Lagouch[1], Mohammed Benhadji[2], Sarah Regragui[3], Rachid Maouedj[4], Ali Benatiallah[5]

[1,2,3,5]Energy, Environment and Information Systems Laboratory University of Adrar, Adrar, Algeria
[4]Renewable Energy Research Unit in the Saharan Environment URERMS, Adrar, Algeria

[1]aki.lagouch@univ-adrar.edu.dz

Abstract—**The depletion of fossil fuel resources in all over the world necessitates an urgent search of sustainable resources of energy, such as solar energy, which is inexhaustible and environment-friendly. It is important to develop new methodologies and techniques to evaluate the performance of PV system in order to increase the use of untapped potential of solar energy This study evaluated the performance of a 6 megawatt (MW) solar PV plant operating under the harsh climatic conditions of the Algerian desert. The mean annual energy yield and total loss were determined to be 844.8 megawatt-hours (MWh) and 2.2 hours per day, respectively. The plant demonstrated a final yield, capacity factor of 4.6 peak sun hours per day and 19,3%, and a performance ratio of 68.8 %. The photovoltaic (PV) system exhibited a decrease in efficiency during the summer months, while higher performance was logged in the winter months. This seasonal discrepancy in the solar power plant's output demonstrates the influence of ambient temperature on system productivity.**

Keywords - photovoltaic, performance ratio, energy output, final yield, desert.

I. INTRODUCTION

As is well known, Algeria's economy is reliant on oil and natural gas exports. as a primary source of state income, given that Algeria contains a huge underground wealth of fossil fuels. According to some studies, natural gas will be available for the next 70 years, while oil reserves will last only 50 years, and we will witness a rise in oil prices. Electricity consumption may reach 150 terawatt-hours by 2030 [1]. However, this does not negate the fact that these sources are fleeting on the one hand, and on the other hand, their prices are subject to fluctuation in global markets, which results in economic shocks that cause international and local crises that negatively affect the citizen in particular. In pursuit of reducing fossil fuel consumption and realizing energy transition and sustainable development objectives, the Algerian government has developed future plans for renewable energies through which it aspires to produce electricity based on solar energy. Algeria possesses immense solar potential, with projections of 13.9 TWh of energy generation annually. Every year, the country receives 2500 kWh/m² of solar output. Algeria has high solar irradiance, with 4.66 kWh/m² per day in the north and 7.26 kWh/m² per day in the south [2]. In order to exploit this wealth, the Algerian government has developed future plans for renewable energies through which it aspires to produce electricity based on solar energy, particularly in the country's southern regions, where the duration of brightness exceeds the sun shines for 8 hours a day and can reach 12 hours a day during the summer. In general, solar energy holds a lot of hope for Algeria in the coming years, especially given the country's vast desert areas and the potential of solar energy. With governmental backing and sustained investment, Algeria's solar potential could significantly contribute to national energy demands and lessen

ISBN: 978-86-82602-07-1

dependence on fossil fuels. The country is regarded as having within the greatest potentials of solar power in the globe and Africa, especially in the country's desert south, where the length of solar radiation approaches 3.500 hours per year.

The 6 MW solar power plan installed in Zaouite Kounta, has tremendous irradiation mostly all over the year, the favorable and tremendous solar irradiation of this place provides a substantial incentive for the installation of photovoltaic power plant and paves the way for tapping solar energy and meet the need of electricity for those who live in this area, this station has been operating since 2016 under a hot desert climate characterized by a long Summer and a short warm Winter. The main purpose of this paper is to evaluate the performance of 6MW grid-connected solar plant and use this work's results for further research by enhancing the predictions of how these systems operate under difficult climate conditions.

II. EASE PHOTOVOLTAIC SYSTEM DISCERPTION

A 6-megawatt photovoltaic solar energy system was constructed in Ksar Zaouite Kounta, located in the Adrar province in southern Algeria (27º13'N, 0º12'W), as shown in Fig. 1. This system was installed as part of Algeria's National Renewable Energy Development Program (2011-2030) and has been operational since January 12, 2016 over 12 hectares of land. The installation consists of 24.552 Yingli Solar YL245P-29b solar panels, each with a 245-watt polycrystalline.

Photovoltaic module. These solar panels were mounted facing south at a 28-degree tilt angle to maximize solar irradiation in the hot desert climate.

Figure 1. Photovoltaic solar energy system Ksar Zaouite Kounta.

III. PERFORMANCE ANALYSIS

The PV plant's performance was analyzed following parameters illustrated below in Table I.

IV. RESULTS AND DISCUSSION

This research analyzed the operational performance of a 6-megawatt photovoltaic solar energy installation located in the harsh desert climate of southern Algeria. The study was conducted over a full calendar year from January 1, 2021 to December 31, 2021 using high frequency meteorological and energy production measurements logged at 15-minute intervals. Key weather parameters that were monitored included ambient temperature, solar irradiation on the plane of the photovoltaic array. This granular dataset enabled an in-depth examination of how varying environmental conditions in an extreme desert environment impact the productivity of a large-scale solar photovoltaic system designed to operate without active cooling. The investigation provides insights into real-world factors affecting solar panel efficiency in harsh climates.

TABLE I. PERFORMANCE INDICATORS.

Paramet.	Equation	Ref.
Energy output	$E_{ACday} = \sum_{t=1}^{24} E_{ACt}$, and $E_{ACmonth} = \sum_{d=1}^{N} E_{ACd}$	[1] [2] [3]
Final yield	$YF = \frac{E_{AC,d}\,[KWh/day]}{P_{PVrated}\,[KW]}\,[h/day]$	[4] [5] [6]
Reference yield	$Yr = \frac{H_T\left[\frac{KWh}{m^2}/day\right]}{G_0\,[KW/m^2]}\,[h/day]$	[7] [8] [9]
Total loss	$LT = Yr - YF$	[10]
Perform. ratio	$PR = \frac{YF}{Yr}\cdot 100[\%]$	[9] [11] [12]
Capacity factor	$CF = \frac{E_{AC}\,[KWh]}{P_{PVrated}\,[KW]\cdot 8760[h]}\cdot 100[\%]$	[13] [14] [15]

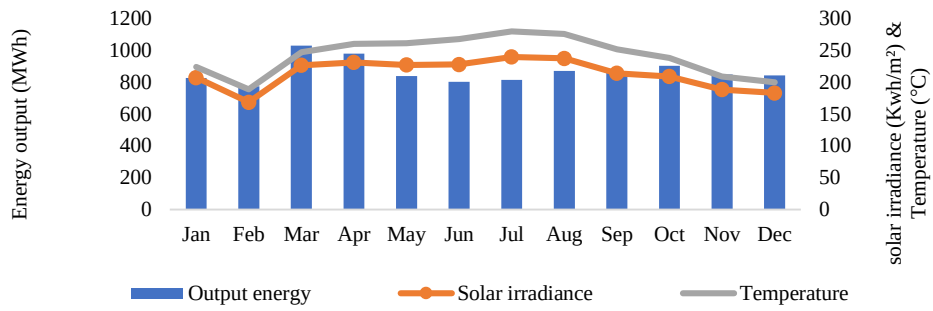

Figure 2. Average monthly energy output, solar irradiance, and temperature.

A. *Meteorological Data*

This section analyses the impacts of ambient temperature (Ta), AC energy (EAC), and inclined solar irradiance (Ht), on the PV module surface across a 12-month period, as illustrated in Fig. 2. The data demonstrates the relationships between these key variables that influence photovoltaic system performance in the given location and climate.

Throughout the course of one year, the minimum and maximum Ta values of 16.8 °C and 40.1 °C were noticed in December and July, with an annual Ta median of 28.9 °C. Regarding Ht, July saw the peak monthly average of 239.3 kWh/m² while the February average of 168.4 kWh/m² was the lowest, with a mean of 220.1 kWh/m². Examining the photovoltaic alternating current energy output (EAC) data reveals that the minimum and maximum monthly averaged values over the year were 772.8 MWh and 1029.6 MWh, occurring in February and March respectively. This contrasts with the overall annual monthly EAC average of 844.8 MWh. The monthly averaged data quantitatively demonstrates the linkages between EAC, and Ht over the yearly cycle in the given climate and location.

B. *Energy Yield and Total Loss*

An examination of Fig. 3 illustrates the monthly energy yields, specifically the reference (Yr) and final (Yf) yields, across the study period. The maximum final yield value of 5.5 h/day was attained in March, while the minimum value of 4.4 h/day occurred in July. Analysis of the monthly averages indicates that the mean final yield across the study duration. A comparative evaluation between and the final yield curve shows that the monthly distribution of the final yield follows a similar pattern to the energy output data over the same time period. The maximum and minimum reference values were observed in May (7.7 h/day) and December (5.9 h/day). Furthermore, analysis revealed that the mean reference yield over the monitoring

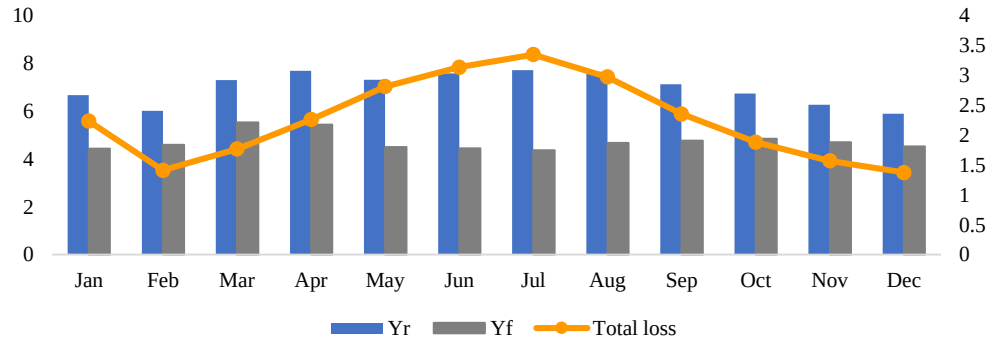

Figure 3. Average monthly reference, final yield, and total loss.

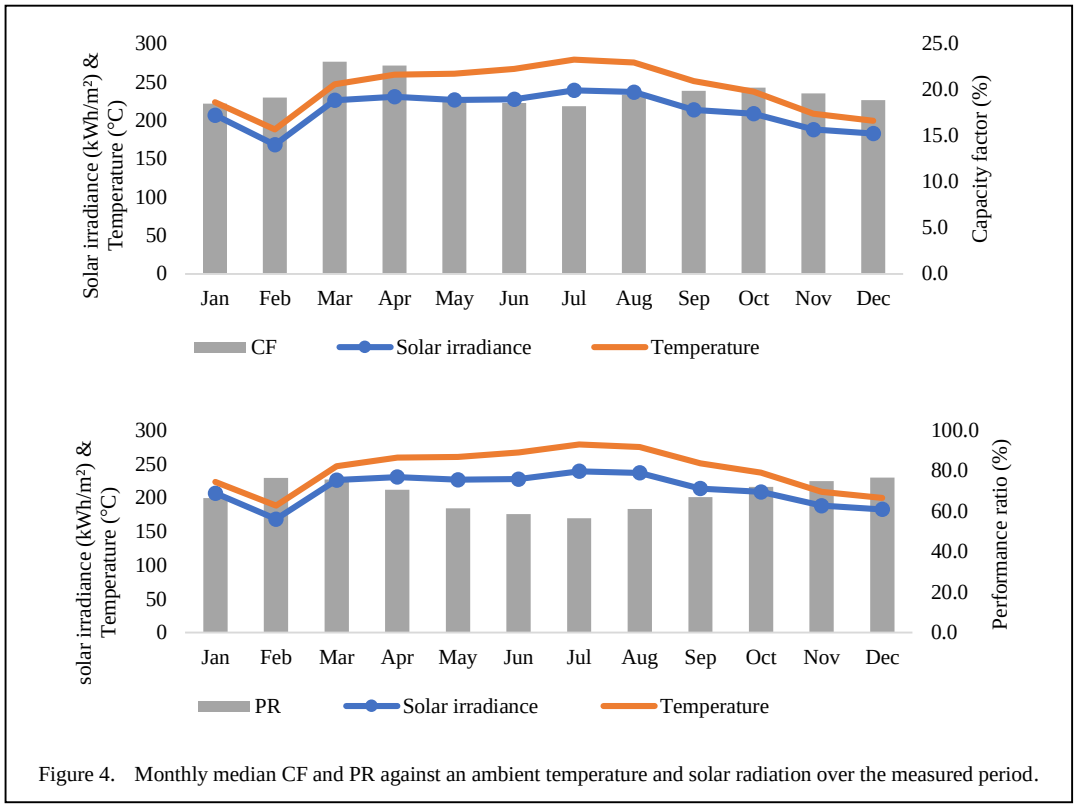

Figure 4. Monthly median CF and PR against an ambient temperature and solar radiation over the measured period.

duration was 7.2 h/day. A comparative assessment against Fig. 3 demonstrates that the monthly distribution of the reference yield curve exhibits an analogous pattern to that of the in-plane solar irradiance data.

Analysis of the data reveals the highest total loss (LT) values, exceeding 2h/day, were noticed during the warmest months of May, June, July and August. The maximum total loss of 3.3h/day occurred in July, while the minimum of 1.4h/day was recorded in February. The annual averaged total loss over the study duration was 2.2h/day. Given that total losses encapsulate reductions during the photovoltaic energy conversion process, these findings confirm the significant detrimental impacts of elevated ambient temperatures on photovoltaic system performance.

C. Capacity Factor and Performance Ratio

The data examination shows that the most significant performance ratio (PR), surpassing 76%, were observed in the winter months: Dicember and Fubruary (Fig. 4). July experienced the lowest at 56%. Throughout the study period, the average annual PR was 68%. Since performace ratio represent decreases in photovoltaic efficiency, these results demonstrate that high ambient temperatures substantially impair the performance ratio of photovoltaic systems. The capacity factor (CF) logged the high value in march with 23% and lowset of 18% in the month of January. The mean yearly CF was ogged to be: 19%.

The performance ratio was calculated using the actual AC energy output measured at the grid interconnection point, which encompasses all system losses.

Over the study period, fluctuations in the energy production (EAC) and performance ratio closely mirrored variations in ambient temperature and inclined solar irradiance. Peak EAC and PR values were attained during moderate temperature months when Ta approached the 25°C reference condition. Conversely, minimum EAC and PR corresponded to the high summer temperatures, where Ta reached 40°C. February highlighted the importance of solar radiation levels, as despite a temperature of 20°C, production was lowest due to extensive cloud cover that constrained irradiation. These trends quantify the reliance of photovoltaic energy yield on tilted radiation and temperature over an annual cycle. Overall, the

dataset provides critical insights into real-world operational factors impacting photovoltaic system performance in analogous environments. The interplay between solar radiation and ambient temperature is elucidated through the empirical EAC and PR data.

D. Long-term Degradation Analysis

Upon examining the performance data of the 6MW photovoltaic system under study, a comparison of efficiency metrics from 2017 (one year after initial operation) [16] to the same metrics in 2021 reveals a noticeable decline. Specifically, Performance ratio declined from 73.68% to 68.8% (annual degradation rate: 1.22%/year), final yield decreased from 5.15 to 4.6 h/day (2.68%/year), and capacity factor dropped from 21.44% to 19.3% (0.535%/year). This degradation rate is approximately 50% higher than the IEA-reported median of 0.5-0.8%/year for standard conditions, reflecting accelerated aging under harsh Saharan conditions.

The primary degradation drivers include: (1) extreme thermal cycling (16.8-40.1 °C daily variations) causing mechanical stress on solder joints and encapsulant materials, (2) intense UV exposure (annual mean irradiance of 220.1 kWh/m² monthly) accelerating polymer degradation, and (3) persistent dust accumulation reducing optical transmittance. The consistency of decline across independent metrics and magnitude exceeding measurement uncertainty (±2-3%) confirms statistical significance.

This degradation translates to 1,120 MWh annual production loss (9.95% reduction), underscoring the critical need for enhanced cleaning protocols (bi-weekly during dust seasons), quarterly thermal imaging for hot-spot detection, annual inverter maintenance, and future consideration of modules with lower temperature coefficients and superior UV resistance for desert applications.

V. CONCLUSION

This research provides an in-depth examination of the real-world energy productivity and performance of a 6-megawatt utility-scale solar photovoltaic system operating in the extreme desert climate conditions. The analysis utilizes high-resolution empirical operational data spanning a 12-month period from January 1, December 31, 2021.

The key points are introduced as contributing to understanding, rather than just being important results. It also specifies that the findings pertain to high-capacity PV in hot desert environments in particular:

- Over the monitoring period, with ambient temperatures ranging from 16.8 to 40.1 °C and solar irradiance spanning 168.4–239.3 kWh/m², the photovoltaic plant generated an average annual AC energy output of 844.8 MWh.
- The yearly Yr, YF, and LT were found to be: 7.2, 4.6, and 2.2 h/day
- Analysis of the annual data revealed the photovoltaic system exhibited mean annual performance and capacity factor values of 68.8% and 19.3%, respectively.
- The photovoltaic system operated at 56% of its rated capacity at 40 °C ambient temperature.
- The photovoltaic system achieved maximum energy production at 20.6 °C with 34.2 MWh, while 76% performance ratio of its rated capacity at 16 and 20 °C in February and December.

The long-term performance analysis revealed an annual degradation rate of 1.22% for performance ratio over the 2017-2021 period, exceeding typical rates due to extreme Saharan climate stressors including thermal cycling, intense UV exposure, and persistent soiling.

To mitigate the observed 4.88% decline in performance ratio over the monitoring period, we recommend implementing: (1) bi-weekly module cleaning schedules during dusty seasons to minimize soiling losses; (2) quarterly thermal imaging surveys to detect hot-spots and degraded modules; (3) annual inverter maintenance including firmware updates and capacitor health checks; and (4) real-time string monitoring to identify underperforming arrays.

To address the significant summer performance degradation (PR dropping to 56% at 40°C), operational strategies should include: (1) optimizing module tilt angles to enhance natural ventilation; (2) investigating cost-effective cooling solutions such as evaporative cooling during peak temperature months; (3) scheduling maintenance activities during cooler morning hours; and (4) considering modules with superior

high-temperature performance coefficients (< -0.40%/°C) for future capacity additions.

REFERENCES

[1] Fallahzadeh-Abarghouei, H., Hasanvand, S., & Sahraneshin, S. (2016). Distributed generation planning & grid partitioning for voltage control of smart distribution system. *International Journal of Renewable Energy Research (IJRER)*, *6*(4), 1342-1349. https://doi.org/10.20508/ijrer.v6i4.4550.g6923

[2] Okinda, V. O., & Odero, N. A. (2016). Modelling, simulation and optimal sizing of a hybrid wind, solar PV power system in Northern Kenya. *International Journal of Renewable Energy Research*, *6*. https://doi.org/10.20508/ijrer.v6i4.4323.g6907

[3] Ayompe, L. M., Duffy, A., McCormack, S. J., & Conlon, M. (2011). Measured performance of a 1.72 kW rooftop grid connected photovoltaic system in Ireland. *Energy Conversion and Management*, *52*, 816-825. https://doi.org/10.1016/j.enconman.2010.08.007

[4] Atsu, D., Seres, I., & Farkas, I. (2021). The state of solar PV and performance analysis of different PV technologies grid-connected installations in Hungary. *Renewable and Sustainable Energy Reviews*, *141*, 110808. https://doi.org/10.1016/j.rser.2021.110808

[5] Sukumaran, S., & Sudhakar, K. (2017). Fully solar powered airport: A case study of Cochin International airport. *Journal of Air Transport Management*, *62*, 176-188. https://doi.org/10.1016/j.jairtraman.2017.04.004

[6] Komoni, V., Krasniqi, I., Lekaj, A., & Gashi, I. (2014, March). Performance analysis of 3.9 kW grid connected photovoltaic systems in Kosova. In *2014 5th International Renewable Energy Congress (IREC)* (pp. 1-6). IEEE. https://doi.org/10.1109/IREC.2014.6826947

[7] Eltawil, M. A., & Zhao, Z. (2010). Grid-connected photovoltaic power systems: Technical and potential problems-A review. *Renewable and sustainable energy reviews*, *14*(1), 112-129. https://doi.org/10.1016/j.rser.2009.07.015

[8] Mondol, J. D., Yohanis, Y. G., & Norton, B. (2006). Optimal sizing of array and inverter for grid-connected photovoltaic systems. *Solar energy*, *80*(12), 1517-1539. https://doi.org/10.1016/j.solener.2006.01.006

[9] Yadav, S. K., & Bajpai, U. (2018). Performance evaluation of a rooftop solar photovoltaic power plant in Northern India. *Energy for sustainable development*, *43*, 130-138. https://doi.org/10.1016/j.esd.2018.01.006

[10] Adaramola, M. S., & Vågnes, E. E. (2015). Preliminary assessment of a small-scale rooftop PV-grid tied in Norwegian climatic conditions. *Energy Conversion and Management*, *90*, 458-465. https://doi.org/10.1016/j.enconman.2014.11.028

[11] Cubukcu, M., & Gumus, H. (2020). Performance analysis of a grid-connected photovoltaic plant in eastern Turkey. *Sustainable Energy Technologies and Assessments*, *39*, 100724. https://doi.org/10.1016/j.seta.2020.100724

[12] Sundaram, S., & Babu, J. S. C. (2015). Performance evaluation and validation of 5 MWp grid connected solar photovoltaic plant in South India. *Energy conversion and management*, *100*, 429-439. https://doi.org/10.1016/j.enconman.2015.04.069

[13] Srivastava, R., Tiwari, A. N., & Giri, V. K. (2020). An overview on performance of PV plants commissioned at different places in the world. *Energy for Sustainable Development*, *54*, 51-59. https://doi.org/10.1016/j.esd.2019.10.004

[14] Lagouch, A., Maouedj, R., & Benatiallah, A. (2024). A 5-MWp grid-connected photovoltaic plant's performance analysis and challenges under Algerian Sahara conditions. *International Journal of Ambient Energy*, *45*(1), 2304732. https://doi.org/10.1080/01430750.2024.2304732

[15] Aoun, N. (2020). *Performance analysis of a 20 MW grid-connected photovoltaic installation in Adrar, South of Algeria* (pp. 85-96). London, UK: IntechOpen. https://doi.org/10.5772/intechopen.89511

[16] Ameur, A., Sekkat, A., Loudiyi, K., & Aggour, M. (2019). Performance evaluation of different photovoltaic technologies in the region of Ifrane, Morocco. *Energy for Sustainable Development*, *52*, 96-103. https://doi.org/10.1016/j.esd.2019.07.007

eNergetics 2025
DOI: https://doi.org/10.5281/zenodo.18626208

Original Scientific Article

Greenhouse Gas Emissions Associated with an Energy Harvesting Farm based on Stationary Bicycles

Herwin Saito Schultz[1], Monica Carvalho[2], Ingrid Rossilho Casale[3], Carlos Eduardo Keutenedjian Mady[4]

[1]Graduate Program in Mechanical Engineering, Federal University of Paraíba, João Pessoa, Brazil
[2]Department of Renewable Energy Engineering, Federal University of Paraíba, João Pessoa, Brazil
[3,4]Institute of Energy and Environment, University of São Paulo, São Paulo, Brazil

[1]herwin.schultz@alumni.cear.ufpb.br, [2]monica@cear.ufpb.br, [3]ingridrcasale@usp.br, [4]cekm@usp.br

Abstract—**Energy harvesting from human kinetic activity, particularly through physical exercise, can simultaneously address energy sustainability and public health concerns. This study employs the Life Cycle Assessment methodology to evaluate the environmental impact of an energy harvesting system comprising 32 stationary bikes, operating in bi-hourly sessions of 20 minutes each, eight hours a day, over a 10-year period. Greenhouse gas emissions associated with the material composition of the energy system are quantified and compared to the Brazilian electricity matrix. The findings reveal that the emission factor of the electrical energy harvesting farm is 0.064 kg CO_2-eq/kWh, significantly lower than that of the Brazilian national electric grid 0.152 kg CO_2-eq/kWh, demonstrating its potential to reduce carbon emissions. The energy return on investment of the system, defined as the ratio between electricity generated and human metabolic energy, is approximately 0.17. Beyond environmental benefits, such systems encourage physical activity, contributing to reduced healthcare costs associated with sedentary lifestyles. This research underscores the dual impact of energy-harvesting exercise systems, presenting a scalable solution for sustainable energy generation while promoting public health and well-being. The results provide valuable insights for policymakers and urban planners in integrating such innovations into sustainable energy strategies.**

Keywords - harvest energy, life cycle assessment, carbon footprint, physical exercise.

I. INTRODUCTION

The growing concern about climate change, combined with the increase in the global demand for sustainable energy solutions, has driven the search for low-carbon energy generation solutions. Energy harvesting systems (EHS) through human effort stand out, converting mechanical energy generated from physical activities into electrical energy [1]. This approach simultaneously addresses two key challenges: reducing greenhouse gas emissions and promoting public health, which are directly linked to the Sustainable Development Goals (SDGs) of the United Nations (UN) [2].

EHS convert small amounts of energy from natural or human sources, but generally produce relatively small quantities. This energy generation is considered renewable from a scientific point of view due to its renewable and low-carbon nature [3]. Human kinetic energy from physical exercises can be converted into electrical energy, as demonstrated in pedal-based systems used as energy sources in offices [4]. This approach, known as "green workout", utilizes metabolic energy that would otherwise be dissipated as heat [5] and converts it into usable energy, reducing waste [6] and contributing to sustainability [1].

ISBN: 978-86-82602-07-1

The energy sector is undergoing a process of decarbonization. In Brazil, for example, despite having a predominantly renewable electricity matrix, decentralized and small-scale solutions such as an energy-generating bicycle system could further reduce dependence on fossil fuels [7]. This solution would act as a complementary system to the national electrical grid. Additionally, according to the U.S. Centers for Disease Control and Prevention [8,9], promoting physical exercise has a direct impact on public health and healthcare costs, as a sedentary lifestyle is a significant risk factor for various diseases, ultimately leading to increased medical expenses. Sedentary behavior can lead to medical interventions that could be avoided through regular physical exercise [10].

Several studies have investigated the potential of generating energy from stationary bicycles. Reference [11] analyzed the commercial feasibility of using gym bicycles as a secondary energy source. Reference [5] showed that human exergy efficiency cycling, from nutrient consumption to power production, can achieve 30%. Reference [12] achieved an energy efficiency of 60%, suggesting that the generated energy could be used as an alternative during power interruptions. Reference [13] proposed a low-cost system that reduces gym energy consumption by 20%. Reference [14] demonstrated that systems integrated into household activities can lower energy consumption while promoting physical health. Reference [15] developed a cost-effective regenerative residential bicycle. These studies highlight the potential for increased energy generation, particularly during periods of high demand, which could reduce reliance on electricity from the grid.

While "traditional" renewable energy sources, such as solar, wind, and hydropower, have been extensively studied, energy generation systems based on physical exercise remain relatively unexplored, particularly regarding their environmental impacts throughout the life cycle [3]. Therefore, to assess these impacts, the Life Cycle Assessment (LCA) methodology can be applied, allowing the quantification of environmental impacts of energy systems and a detailed study of greenhouse gas (GHG) emissions associated with the production and operation of equipment [16]. LCA has already been applied in studies of conventional and stationary bicycles [3,17]. Still, a more comprehensive analysis would involve assessing the component-related emissions of the stationary bicycles designed for energy harvesting, considering emissions from material production to operational phases.

Thus, the present study utilized the Green&Healthy Power concept [1], which integrates environmental and social benefits. The system consists of stationary bicycles connected to an energy conversion system, converting physical activity into electrical energy. Therefore, assessing the feasibility and conducting an LCA of this system are essential to validate its potential as a sustainable alternative.

This study aims to quantify the GHG emissions associated with an EHS based on stationary bicycles using the LCA methodology. The GHG emissions per kWh are then compared to those of the Brazilian electric grid, evaluating the potential for mitigating climate change. Also, a simplified estimate of the energy return on investment (EROI) is presented.

II. Materials and Methods

The Life Cycle Assessment method is standardized by ISO 14040 [18] and ISO 14044 [19]. It consists of four main interconnected phases: definition of objective and scope, inventory analysis, impact assessment, and results and interpretation [16]. The first phase defines the functional unit (the basis for comparison) and system boundaries (which processes are included). The second phase collects data on inputs (raw materials, energy) and outputs (emissions, waste) for all processes within the system boundary. The third phase applies an environmental impact assessment method to translate inventory data into the desired environmental indicator (e.g., carbon footprint, water footprint). Finally, the last phase analyzes results to draw conclusions and make recommendations.

SimaPro v.9.6.0.1 software [20] was used to develop the LCA, utilizing the Ecoinvent 3.8 database [21]. Due to environmental concerns regarding GHG emissions, the environmental impact assessment method selected is the IPCC 2021 GWP 100y method [22], which groups the emissions of GHG gases and expresses the impact in terms of a common metric, carbon dioxide equivalents (CO_2-eq), throughout a time horizon of 100 years. The functional unit used herein was the amount of GHG emissions

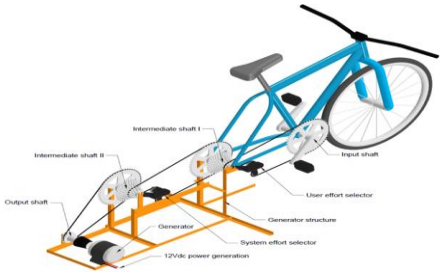

Figure 1. Concept of the Green & Healthy power system [1].

associated with the energy system throughout its 10-year lifetime (kg CO_2-eq/year).

The simulation is based on the World Health Organization's recommendation of 150 minutes of moderate-to-vigorous physical activity per week, considering that a cyclist generates 223.7 kJ during a 20-minute test on the EHS [5,6].

Figs. 1 and 2 illustrate the schemes of an energy harvesting bike and a 32-bicycle energy harvesting farm.

Table I shows the components of the energy harvesting farm.. The tables indicate the material composition of the components and materials used to build an energy harvesting farm with 32 bikes. This LCA will consider cradle-to-grave boundaries and assume that the materials are

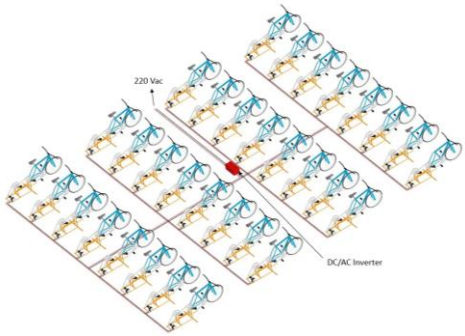

Figure 2. Scheme of the Energy Harvesting Farm (32 bikes). Adapted from [1].

disposed of in a landfill at the end of their useful life.

In addition to the materials of Table I, the following items are also part of the EHS: Steel 212.6 kg, Aluminum 103.4 kg, Rubber 2.1 kg, Copper 21.3 kg, Chromium 0.8 kg, Tin 0.1 kg, Glass fiber 0.2 kg, Grease 0.5 kg, Brass 1.8 kg, Polymer 14.6 kg, Epoxy resin 0.3 kg, Silicon 7.1 kg and Zinc 0.5 kg.

For comparison purposes, the emission factor of the energy harvesting farm is compared to that of the Brazilian electric grid. The emission factor is a parameter frequently used to compare energy systems, calculated as the ratio of emissions from electricity generation (data obtained from a Life Cycle Assessment, or LCA) and electrical energy generation, expressed in kg CO_2-eq/kWh.

TABLE I. COMPONENTS OF THE ENERGY HARVESTING FARM.

Components	Amount	Main material Composition
Bicycles	32	Aluminum 240.65 kg, Polyethylene 62.40 kg, Polyurethane 0.96 kg, Chromium steel 51.20 kg, Low alloyed Steel 156.80 kg, Rubber 17.92 kg
Battery 12V 5Ah	32	Acrylonitrile-butadiene-styrene copolymer 0.136 kg, Barite 0.022 kg, Copper 0.09 kg, Glass fiber 0.447 kg, Lead 12.69 kg, Polypropylene 0.072 kg, Sulfuric acid 0.061 kg
Electrical cables 1.5 mm^2	64 m	Copper 0.96 kg, Polyethylene 0.39 kg
Electrical cables 1.0 mm^2	32 m	Copper 1.44 kg, Polyethylene 0.46 kg
Converter 12Vdc to 220Vac - 7000W	1	Aluminum 0.273 kg, Copper 1.07 kg, Polystyrene 0.059 kg, Steel low-alloy 1.91 kg, Styrene-acrylonitrile copolymer 0.002 kg, Fleece polyethylene 0.012 kg, Corrugated board box 0.48 kg
Electrical cables 25 mm^2	10 m	Copper 24 kg, Polyethylene 3.7 kg
Electrical cables 50 mm^2	65.6 m	Copper 48 kg, Polyethylene 3.85 kg
Electrical cables 70 mm^2	12 m	Copper 67.20 kg, Polyethylene 2.7 kg
Electrical cables 95 mm^2	6 m	Copper 86.40 kg, Polyethylene 6.6 kg

Calculation of the emission factor associated with electricity consumption from the grid followed the methodology of [23], along with the most recent data from the Brazilian National System Operator [24]: hydroelectric 62.18%, wind 15.32%, solar 10.60%, biomass 3.67%, natural gas 4.38%, nuclear 2.36%, coal 1.20%, and oil 0.19%.

Regarding the energy return on investment (EROI), human metabolic energy is treated as the input, and harvested electrical energy is treated as the output. According to [5], the exergy efficiency of human cycling ranges between 20% and 30%. Combining this with the electrical system's conversion efficiency (60–80%) reported by [25], the overall human-to-electricity efficiency is approximately 17.5%. Therefore, the EROI of the system, defined as the ratio between electrical energy generated and human metabolic energy.

III. Results and Discussion

Table II shows the component-related GHG emissions associated with the energy harvesting system.

Bicycles accounted for the largest proportion of emissions, followed by additional items used in the EHS assembly, such as aluminum, steel, silicon, energy converters, and electrical cables. These materials undergo thermally intensive manufacturing processes, which are associated with substantial energy consumption and elevated emissions.

TABLE II. Emissions of the Energy Harvesting System.

Item	Emissions (kg CO_2-eq)
Bicycles	4849.61
Battery	9.05
Electrical cables	443.70
Converter	336.96
Steel	480.61
Aluminium	955.59
Rubber	5.85
Copper	170.28
Chromium	21.87
Tin	1.01
Glass fiber	0.48
Grease	0.73
Brass	12.14
Polymer	37.41
Epoxy resin	1.23
Silicon	581.94
Zinc	1.35
Total	7965.76

The calculation of the emission factor for the EHS uses the overall emissions associated with the system (Table II) divided by its electricity production. One cyclist generates 0.466 kWh per week (150 minutes), totaling 24.3 kWh/year

Considering that two 20-minute sessions can be carried out in one hour, and considering eight operation hours a day, there are 16 sessions per day. With 32 cyclists, this yields 32 x 16 x 24.3 = 12441.6 kWh in one year. The electricity generated by the energy harvesting farm over ten years is 124416 kWh.

The emission factor of the energy harvesting system is therefore 7965.76/124.416 = 0.064 kg CO_2-eq/kWh. This amount is much lower than the emission factor of the Brazilian electric grid (calculated as EF = 0.152 kg CO_2-eq/kWh), demonstrating its potential to avoid emissions (electricity consumed from the EHS avoids the consumption of higher-carbon electricity from the grid). Brazil has an electricity matrix with a significant share of renewable sources, countries with electricity production more dependent on fossil fuels presented higher EF in 2024, such as India (0.730 kg CO_2-eq/kWh), China (0.565 kg CO_2-eq/kWh) and the United States (0.320 kg CO_2-eq/kWh) [26].

Fig. 3 illustrates how electricity production varies with the number of cyclists, assuming a weekly training regimen of 150 minutes for one year. Another aspect that should be taken into account is that not every cyclist will contribute the full WHO quota to the harvesting system (commuting vs. training, willingness to connect, time windows). Considering 32 cyclists, a total of 12,441.6 kWh/year is generated, already accounting for losses. With the Baseline Brazil values (EF = 0.152 – 0.064 = 0.088 kg CO_2-eq/kWh, participation = 1.0), the avoided

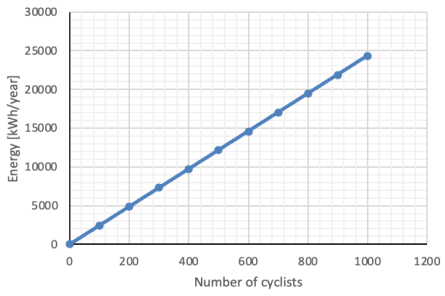

Figure 3. Energy generated in function of the number of cyclists, for a year.

emissions are 1094.9 kg CO_2-eq/yr, which is 34.2 kg CO_2-eq/yr per active cyclist.

Accounting for different participation levels, Table III shows a simple sensitivity analysis of avoided emissions.

TABLE III. SENSITIVITY ANALYSIS OF A VOIDED EMISSIONS.

Participation	Annual electricity (kWh)	Avoided emissions (kg CO_2-eq/yr)
1.00	12441.6	1094.9
0.75	9331.2	821.1
0.50	6220.8	547.4
0.25	3110.4	273.7

Fig. 4 shows that avoided emissions increase with both higher participation and higher grid carbon intensity, while the per-cyclist effect remains consistent across participation because energy and cyclists scale proportionally.

A critical aspect of the avoided emissions lies in the difference in carbon intensity between electricity generated by renewable-based harvesting systems and that supplied by the conventional electric grid. In many regions, grid electricity remains dependent on fossil fuel sources, resulting in a comparatively higher carbon intensity per kilowatt-hour. In contrast, energy harvested through mechanical-to-electrical conversion in cycling-based or similar renewable systems exhibits a markedly lower carbon footprint, since no direct fuel combustion is involved during operation. The repercussions of this disparity are twofold. First, the substitution of grid electricity with harvested electricity results in significant avoided emissions over the system's lifetime, thereby amplifying its environmental benefits. Second, as national and regional grids progressively decarbonize through the integration of renewable energy, the relative advantage of local energy harvesting systems may decrease; however, they will continue to provide resilience, decentralization, and additional emission savings where fossil fuels remain embedded in the energy mix. Therefore, the comparative carbon intensity of the grid versus harvesting systems is a key determinant of the net environmental performance, and it underscores the importance of temporal and geographical context in life-cycle assessments.

The EROI of the system, defined as the ratio of electrical energy generated to human metabolic energy, is approximately 0.17.

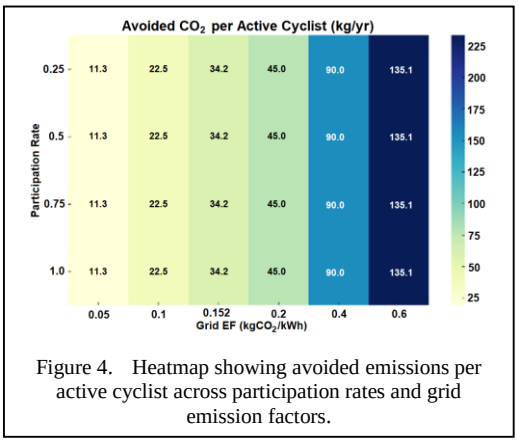

Figure 4. Heatmap showing avoided emissions per active cyclist across participation rates and grid emission factors.

Although energetically unfavorable, this result highlights that the harvested electrical energy follows the same trend as the organic Rankine cycle, using low-quality energy from human physical activity that would be transferred to the environment regardless of energy generation. Therefore, the EROI represents a beneficial energy recovery pathway rather than a conventional production process.

In the Brazilian context, the implications of avoided emissions differ from regions with fossil fuel–dominated electricity grids. Brazil's national grid is primarily supplied by renewable sources, particularly hydropower, resulting in a relatively low average carbon intensity compared to global values. However, seasonal variability in rainfall, increasing demand, and reliance on thermoelectric plants during dry periods introduce fluctuations in grid emissions. Electricity from the EHS can consistently displace a portion of this grid electricity, which is relevant during peak demand or drought conditions, when the grid carbon intensity rises due to the activation of fossil fuel plants.

The possibility of utilizing the EHS scenario as an alternative energy resource becomes even more necessary in light of the accelerated growth of the global economy, which has significantly increased the demand for various energy sources. Since the Industrial Revolution, fossil fuels—such as coal, oil, and natural gas—have been widely used as the main energy sources. However, these resources not only face the prospect of depletion but also generate severe environmental impacts. Approximately 50% of GHG and 85% of global CO_2 emissions originate from the burning of fossil fuels, which, under certain conditions, can trigger extreme climate events on a global scale and jeopardize human development [27,28].

Decreasing GHG emissions has become one of the primary goals of contemporary environmental protection strategies [28]. Conventional electrical energy generation can still be predominantly based on the combustion of fossil fuels in some sites, but due to environmental concerns associated with their use, it has become essential to seek alternative energy sources with lower environmental impacts [29].

Beyond emission reductions, decentralized harvesting systems in Brazil can contribute to grid resilience and energy diversification, reducing dependency on hydrological cycles. Thus, while the avoided emissions in Brazil may be less pronounced than in fossil-fuel-heavy regions, the environmental and systemic benefits of harvesting systems remain significant.

IV. Conclusions

This study conducted a life cycle assessment for an energy harvesting system based on stationary bicycles. A 32-bicycle system is proposed, operating in 16 sessions of 20 minutes each, daily, over 10 years. This is the first study to present the detailed life cycle inventory for an energy harvesting system.

When dividing the overall carbon emissions of the energy system (7.965.76 kg CO_2-eq) by the electricity production (124.416 kWh), the emission factor is obtained, which is 0.064 kg CO_2-eq/kWh. This amount is much lower than the emission factor of the Brazilian electricity mix (0.152 kg CO_2-eq/kWh), demonstrating the potential of the energy system to reduce carbon emissions. If we compare the EFs with those of countries that use more fossil fuels, the advantage becomes even greater.

In summary, the relationship between physical exercise and energy harvesting demonstrates a self-sustaining loop where human effort translates into power generation, providing both health benefits to the cyclist and reducing carbon energy use for powering devices or contributing to larger systems already in place.

Acknowledgments

The authors wish to acknowledge the support of the Laboratory of Environmental and Energy Assessment (LAvAE) at the Federal University of Paraíba.

Funding

The authors thank the National Council for Scientific and Technological Development (CNPq, productivity grants 303180/2025-0 and 303585/2024-2) and the Coordination for the Improvement of Higher Education Personnel (CAPES) for the PhD scholarship.

References

[1] Schultz, H. S., Mady, C. E. K., & Carvalho, M. (2024). Concept development of exercise-to-power: The Green&Healthy power concept. *Cleaner Energy Systems*, *8*(April), 100120. https://doi.org/10.1016/j.cles.2024.100120

[2] United Nations (UN). (n.d.). *THE 17 GOALS | Sustainable Development*. Retrieved September 3, 2025, from https://sdgs.un.org/goals

[3] Jansen, A., & Stevels, A. (2006). Combining eco-design and user benefits from human-powered energy systems, a win-win situation. *Journal of Cleaner Production*, *14*(15–16), 1299–1306. https://doi.org/10.1016/j.jclepro.2005.11.023

[4] Veenman, R. S. (2009). A Human Powered Fitness Bicycle: Generating electricity in fitness clubs. Faculty of Industrial Design Engineering TU Delft. TU Delft.

[5] Mady, C. E. K., Igarashi, T. L., Albuquerque, C., Santos-Silva, P. R., Fernandes, T. L., & Hernandez, A. J. (2019). Exergy efficiency on incremental stationary bicycle test: A new indicator of exercise performance? *Journal of the Brazilian Society of Mechanical Sciences and Engineering*, *41*(12), 1–11. https://doi.org/10.1007/s40430-019-2070-7

[6] Igarashi, T. L., Fernandes, T. L., Hernandez, A. J., Keutenedjian Mady, C. E., & Albuquerque, C. (2022). Behavior of skin temperature during incremental cycling and running indoor exercises. *Heliyon*, *8*(10). https://doi.org/10.1016/j.heliyon.2022.e10889

[7] Energy Research Company (Empresa de Pesquisa Energética – EPE). (2024). Balanço Energético Nacional (2024): Ano Base 2023, 275. Retrieved from https://www.epe.gov.br/sites-pt/publicacoes-dados-abertos/publicacoes/PublicacoesArquivos/publicacao-819/topico-723/BEN2024.pdf

[8] U.S. Centers for Disease Control and Prevention. (n.d.). Active People, Healthy Nation^{SM} At a Glance | Active People, Healthy Nation | CDC. Retrieved September 4, 2025, from https://www.cdc.gov/active-people-healthy-nation/php/at-a-glance/index.html

[9] Booth, F. W., Roberts, C. K., & Laye, M. J. (2012). Lack of Exercise Is a Major Cause of Chronic Diseases. *Comprehensive Physiology*, *2*(2), 1143–1211. https://doi.org/10.1002/j.2040-4603.2012.tb00425.x

[10] Roll, J. B., Borges, M. L., Mady, C. E. K., & Junior, S. de O. (2019). Exergy analysis of the heart with a stenosis in the arterial valve. *Entropy*, *21*(6), 1–13. https://doi.org/10.3390/e21060563

[11] Khan, A. A. S., Alam, T., Abir, M. R., & Ullah, M. T. (2015). Harvesting Human Exercise Power Using Gymnasium Bicycle, *Resistor*, *1*(1N4007), p.1N4007.

[12] Hossain, N., Ferdous, J., Fuad, F., Ahsan-Uz-Zaman, K. M., & Wahed, A. (2016). Power distribution scheme

using smart meter, perspective Bangladesh. *2nd International Conference on Electrical Information and Communication Technologies, EICT 2015*, (November 2018), 486–491. https://doi.org/10.1109/EICT.2015.7392002

[13] Ihsan, M., & Viswanathan, V. (2019, November 11). Self-Powering Gyms: A Case Study on Energy Harvesting From a Static Bicycle. https://doi.org/10.1115/IMECE2019-11972

[14] Shin, W. kyoung, Song, S., Jung, S. Y., Lee, E., Kim, Z., Moon, H. G., Noh, D. Y., & Lee, J. E. (2017). The association between physical activity and health-related quality of life among breast cancer survivors. *Health and Quality of Life Outcomes*, *15*(1), 1–9. https://doi.org/10.1186/s12955-017-0706-9

[15] Pham, H., Bandaru, A. P., Bellannagari, P., Zaidi, S., & Viswanathan, V. (2022). Getting Fit in a Sustainable Way: Design and Optimization of a Low-Cost Regenerative Exercise Bicycle. *Designs*, *6*(3), 1–21. https://doi.org/10.3390/designs6030059

[16] Hauschild, M. Z., Rosenbaum, R. K., & Olsen, S. I. (2018). *Life Cycle Assessment - Theory and Practice*. Springer International Publishing. https://doi.org/10.1007/978-3-319-56475-3

[17] Coelho, M. C., & Almeida, D. (2015). Cycling mobility - A life cycle assessment based approach. *Transportation Research Procedia*, *10*(July), 443–451. https://doi.org/10.1016/j.trpro.2015.09.094

[18] Brazilian Association of Technical Standards (ABNT - Associação Brasileira de Normas Técnicas). (2014a). ABNT NBR ISO 14040: Gestão ambiental – Avaliação do ciclo de vida – Princípios e estrutura. Rio de Janeiro: ABNT.

[19] Brazilian Association of Technical Standards (ABNT - Associação Brasileira de Normas Técnicas). (2014b). ABNT NBR ISO 14044: Gestão ambiental — Avaliação do ciclo de vida — Requisitos e orientações. Rio de Janeiro: ABNT.

[20] SimaPro Software - Pré Sustainability. (n.d.). Retrieved August 26, 2025, from https://pre-sustainability.com/solutions/tools/simapro-craft/

[21] Ecoinvent Database. 2023. Available online: http://www.ecoinvent.org (accessed on 20 february 2025).

[22] IPCC — Intergovernmental Panel on Climate Change. (2021). Retrieved August 26, 2025, from https://www.ipcc.ch/

[23] Carvalho, M., & Delgado, D. (2017). Potential of photovoltaic solar energy to reduce the carbon footprint of the Brazilian electricity matrix. *LALCA: Revista Latino-Americana Em Avaliação Do Ciclo de Vida*, *1*(1), 64–85. https://doi.org/10.18225/lalca.v1i1.3779

[24] Brazilian National System Operator (Operador Nacional do Sistema Elétrico). (2024). Retrieved August 26, 2025, from https://www.ons.org.br/AcervoDigitalDocumentosEPublicacoes/2023-Relatorio-Anual-acessivel_21032024.pdf

[25] MOSKA, Waldemar; ŁEBKOWSKI, Andrzej. Microgeneration of Electricity in Gyms—A Review and Conceptual Study. *Energies, v. 18*, n. 11, p. 2912, 2025.

[26] IEA - International Energy Agency. (2025). Electricity 2025. Retrieved from https://iea.blob.core.windows.net/assets/7c671ef6-2947-4e87-beea-af0e1288e1d7/Electricity2025.pdf

[27] Li, J. (2023). Evaluation of dynamic growth trend of renewable energy based on mathematical model. *Energy Reports*, *9*, 48–56. https://doi.org/10.1016/j.egyr.2022.11.139

[28] Ming, H., Lin, M., Gao, C., Zhang, N., Xie, L., & Mou, Y. (2024). Towards the prospect of carbon-neutral power system 2060: A Power-Meteorology-Society systematic view. *Heliyon*, *10*(6), e27970. https://doi.org/10.1016/j.heliyon.2024.e27970

[29] Siddiqui, M. A., & Alsaduni, I. (2024). Performance assessment of solar tower collector based integrated system for the cogeneration of power and cooling. *Heliyon*, *10*(21), e39993. https://doi.org/10.1016/j.heliyon.2024.e39993

eNergetics 2025
DOI: https://doi.org/10.5281/zenodo.18626232

Original Scientific Article

Opportunistic Wireless Charging for Urban EVs and Grid Effects

Fatih Kaya[1], Pinar Kirci[2]

[1,2]Bursa Uludag University, Bursa, Turkey

[1]kayafatih@uludag.edu.tr, [2]pinarkirci@uludag.edu.tr

Abstract—**The study evaluates the grid-side implications of on-route, opportunistic wireless charging for electric vehicles (EV), where EVs are charged during routine traffic dwell, relative to a conventional depot plug-in regime that concentrates charging after service. Using a city scale microscopic traffic–power simulation over a six-hour period with a mixed EV fleet, study analysis integrates vehicle activity, station utilization, and feeder-level indicators. The findings show that the distribution of uniform energy across operating hours leads to a significant reduction in instantaneous loading, increases the utilization of available distribution capacity and reduces load peaks. Conversely, compressing charging into a terminal window alone results in the generation of a high magnitude wave. The key findings illustrate that temporal regulation of charging is a important factor in achieving grid compatibility, and opportunistic wireless top-ups represent a viable mechanism for aligning urban EV charging with distribution grid operating envelopes. It further motivates field trials coupling control policies with observed traffic and feeder limits.**

Keywords - electric vehicle charging, wireless power transfer, opportunistic charging, city-scale SUMO scenario.

I. INTRODUCTION

Electric vehicles (EVs) are rapidly transitioning from a niche to a mainstream transportation technology, promising significant environmental benefits by reducing exhaust emissions and fuel consumption. However, they are also driving a shift in energy demand from gasoline to the electric grid. As EV adoption accelerates globally, electricity grids and distribution systems face new challenges and opportunities in meeting the charging needs of millions of vehicles [1,2]. Evidence shows that, unmanaged, highly coincident residential charging amplifies evening peaks and stresses low-voltage assets, whereas smart-managed charging materially mitigates both transmission and distribution level impacts [3,4].

When the impact of EVs on the day is examined, the aggregate electricity demand from EV charging is still modest today, which is approximately 0.7% of global final electricity consumption in 2024 [5], but is set to rise quickly this decade, with multiple scenarios anticipating EVs accounting for several percent of total demand by the mid-2030s. This may shift the integration challenge from energy volumes to when and where charging occurs on the power system [6]. From a statistical point of view, electric car sales, which were 9% in global 2021 and 5% in 2020, exceeded 10 million in 2022 [7] and according to the IEA report [5], global electric vehicle sales, which were previously 13.5 million in 2023, exceeded 17 million in 2024. By the end of 2024, the proportion of electric vehicles in traffic is 4.5% for cars and 4.9% for buses worldwide, while this proportion is projected to reach 15% for cars and 11% for buses by 2030. In this scenario, the energy issue, which does not pose a serious problem for the grid, could become a problem in the coming years with the increase in population and vehicle sales.

As EVs become integral to daily life, their charging needs pose new challenges for drivers

ISBN: 978-86-82602-07-1

and city infrastructure. To meet the rising energy demand of EVs sustainably, many studies and pilot programs focus on smart charging, which schedules and modulates charging in response to grid conditions or prices [8,9]. While the smart charging methods optimize planned charging sessions, a complementary concept has emerged as opportunistic or opportunity charging during short stops in a vehicle's normal routine [10]. This process refers to giving an EV brief but high-power charging bursts whenever the vehicle is stopped for a short duration, rather than only relying on long, dedicated charging sessions. In other words, the vehicle consumes energy whenever it has a few seconds or minutes of idle time, thereby helping to keep the battery fully charged. This concept is already being implemented wirelessly in some contexts via inductive charging pads [11].

One underutilized opportunity for opportunistic charging is the time vehicles spend waiting at red traffic lights. A 2021 traffic signal performance analysis [12] revealed that 40-45% of vehicles in busy cities wait at red signals during peak hours. When the time spent waiting at a red light, which is approximately 15-20 seconds per vehicle, is also factored in, the cumulative impact is substantial. These eye-opening figures highlight that wasted time can be used as an energy opportunity by integrating wireless chargers at traffic light intersections.

In the present study, a simulation model with parameters tuned for realism is built using Simulation of Urban Mobility (SUMO) [13] to investigate the feasibility and grid impact of charging electric vehicles via wireless power transfer (WPT). The simulation is based on a detailed urban traffic scenario modeled from Monaco, a representative medium-sized city network. The Monaco traffic scenario, known as MoST [14], provides an accurate road topology of the city and includes real-world features like buildings, bus routes, and, importantly, 12 signalized intersections whose traffic lights operate with timing programs identical to the real city. Traffic demand in the model was generated using actual demographic and traffic data, including EV shares expected in 2030, and the scenario was validated by comparing simulation outputs to real traffic counts.

II. Materials and Method

The scenario used in this study is designed to model urban mobility, providing a multimodal traffic simulation environment that allows detailed analysis of vehicular traffic, public transport, pedestrian flows and cycling in an urban environment, that is built upon the SUMO. While the original scenario [14] includes a diverse fleet, this study modified the vehicle composition by replacing a percentage of conventional vehicles with pre-calibrated EV types for realistically analyzing energy-related metrics. The power system model is therefore not a grid simulation but rather a vehicle-centric energy consumption model, which utilizes SUMO battery device and the physics-based powertrain models (MMPEVEM [14]) to accurately model consumption, efficiency, and battery capacity. Furthermore, to enable opportunistic charging, wireless charging stations have been placed on bus stops and at traffic signal intersections. The result is an integration framework that has the potential to combine the dynamic traffic situation of the vehicle with the energy model. Finally, simulation generates detailed time series data, which is then processed using Python scripts to collect and calculate final energy demand profiles and infrastructure utilization metrics.

A. Vehicle Fleet and Energy Consumption Model

The realism of the simulation is based on detailed modeling of the vehicle fleet and the

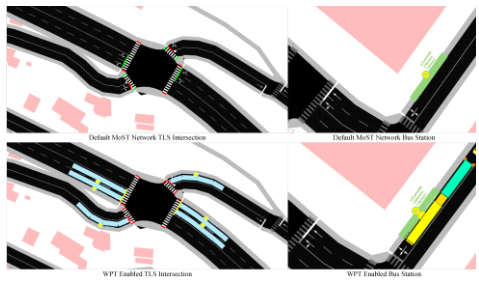

Figure 1. WPT enabled SUMO network.

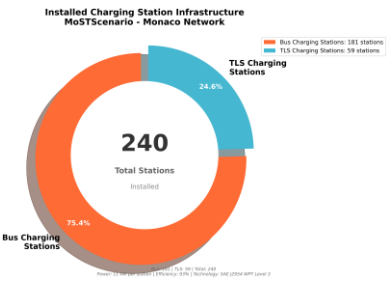

Figure 2. Installed charging stations.

physics governing their energy use, where each vehicle acts as an independent agent whose behavior and energy consumption are dynamically calculated. To create a realistic urban environment, the scenario simulates a heterogeneous fleet where electric vehicles enter congestion and interact with conventional traffic by defining specific vehicle type distributions in Table I. The energy consumption for each electric vehicle is dynamically calculated by SUMO's physics-based model using the detailed parameters in the definitions [15,16]. In addition, to achieve the expected distribution of vehicles by 2030 [5], the vehicle types listed in the table have been distributed in a way that meets the expected occurrence rate projections. Each of these EV cars has been configured with a 5% spawn rate, totaling 15%, and EV bus has been configured with an 11% occurrence rate.

TABLE I. EV PHYSICAL AND DYNAMIC PARAMETERS.

Parameter	**Vehicle Type Distributions**			
	Electric Bus	***BMW i3***	***VW ID3***	***VW ID4***
Battery Capacity (kWh)	200	39	58	77
Auxiliary Power Draw (kW)	8.0	0.36	0.36	0.36
Propulsion Efficiency	93%	82%	82%	82%
Recupera-tion Efficiency	78%	82%	82%	82%
Air Drag Coefficient	0.60	0.29	0.26	0.28
Roll Drag Coefficient	0.009	0.007	0.007	0.0075
Vehicle Mass (kg)	14000	1417	1794	2124

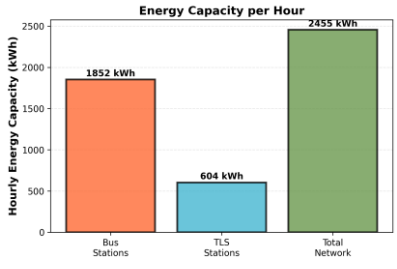

Figure 3. Energy capacity per hour.

B. *Built-in Charging Station Model*

The WPT infrastructure is modeled as a network consisting of charging zones defined as bus station chargers and traffic light system (TLS) chargers. Since the MoST scenario in its original version did not have wireless charging stations, an example showing the changes made to the network is provided in Fig. 1. Charging stations with the same size and coordinates as bus stops have been defined at existing bus station locations. For TLS charging stations, wireless charging pads were positioned in front of traffic lights. This configuration enabled the simultaneous charging of multiple vehicles, with each vehicle charging sequentially as the preceding vehicle came to a halt, and the activation was synchronized with the vehicles' stop-signal.

The energy transfer for each station is defined by a constant power model, which is inspired by a WPT standard [17] that supports up to 11kW power above 90% efficiency. The rate of energy delivery to the vehicle's battery, P_{batt} is a function of the charger's nominal grid power, that is $P_{nominal}$, and its end-to-end grid to battery efficiency, η. This relationship is governed by the Eq. (1):

$$P_{batt} = P_{nominal} \cdot \eta \,. \tag{1}$$

For this simulation, all charging stations are parameterized with a nominal power of 11 kW and an efficiency (η) of 93%, based on the SAE J2954 standard. This results in a constant power influx of 10.23 kW to the vehicle's battery model during any active charging session. Total installed charging stations with their types and numbers in the SUMO network is illustrated in Fig. 2, and their hourly charging capacity is stated in Fig. 3.

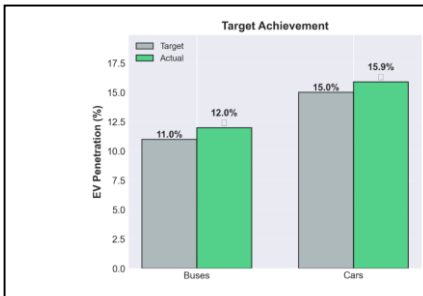

Figure 4. EV target achievement.

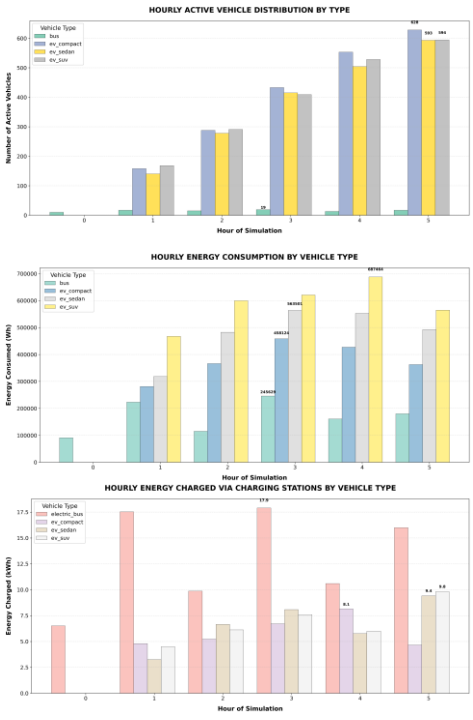

Figure 5. Hourly vehicle analysis.

III. RESULTS

In the scenario, the simulation start time step is set to 14400 and the end time step to 36000. Here, when the simulation origin is taken as 0, it can be said that the simulation corresponds to the real-life period between 4:00 AM and 10:00 AM, which covers 6 hours long period. The simulation took 6647 seconds with real-time factor 3.24, and 37902 vehicles inserted during the simulation. Looking at the distribution of vehicles in Fig. 4, it can be said that the statistical distributions determined in the methodology section have approximately the expected percentage distribution. While a total share of 15% was expected for distribution EV cars, the result was 15.9%, and the expected 11% share for EV buses was 12%, which is around the expectation by 2030. When examining hourly analyses on a vehicle basis, the hourly distribution of active EVs can be observed in Fig. 5 with their peak numbers. The labels namely represent EV buses, compact EVs (BMW i3), EV sedans (VW ID3), and EV SUVs (VW ID4), respectively as listed in Table I. Despite their relatively small fleet size, EV buses exhibit a disproportionately high charging demand due to their larger battery capacities and higher daily energy turnover. In contrast, passenger EVs that consist of particularly sedans and compacts, display more moderate yet stable charging levels across the simulation period. EV SUVs follow a similar charging pattern but with slightly higher hourly demand, reflecting the increased mass and aerodynamic drag typical of this segment.

During the simulation period, since passenger electric vehicles and electric buses served different primary purposes, the relatively few EV bus measurements generally yielded high results. The main reasons for this can be listed as follows:

- Each EV is an agent with its own ID and own measurements, since same buses operates in the city, per vehicle metrics are more stacked on EV buses.
- There are map boundaries, so passenger vehicles can generally only be observed for a very short time, while buses can be observed for longer periods because they travel on city routes.
- Bus stops have much longer dwell times compared to waiting times at traffic lights. Therefore, buses have many more opportunities to charge.

The effect of this fundamental difference can also be seen in Fig. 6, as energy transferred from charging stations. Additionally, the top 10 stations that charge the highest number of vehicles are shown in the figure with the number of charging events. The stations with the highest frequencies are TLS stations, that located in the waiting areas at traffic lights. However, not all TLS stations in general, but rather TLS stations

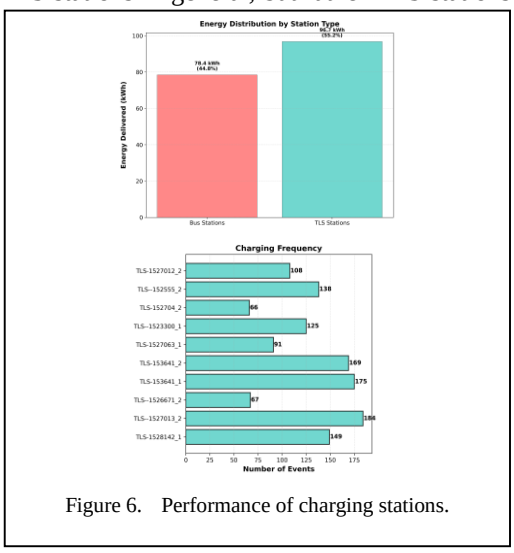

Figure 6. Performance of charging stations.

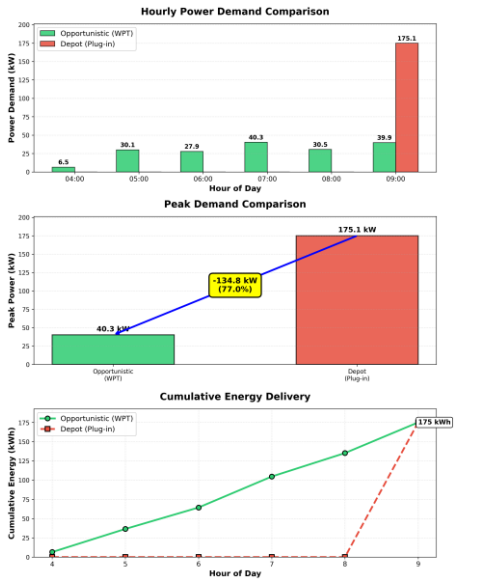

Figure 7. Grid Impact of oppurtunistic and depot charging scenarios.

in high-traffic areas playing an active role in wireless charging activities. In addition to this, the high frequency of bus stops not included in this ranking due to their low rate, but while vehicles generally visit TLS only once, bus stop visits are repeated much more frequently due to buses' circular activities, yet their vehicle numbers are not much as EV car types, resulting in low frequency on bus stop visits.

With regard to the grid effect, the hourly power consumption of these charging events, as observed throughout the simulation, was calculated by combining metrics obtained separately from each charging station. These collected charging data were examined in different sub-areas to simulate a 'what if' scenario. This what if scenario essentially examines the differences in grid effects between a scenario where opportunistic charging events, which are frequently performed throughout the simulation, occur simultaneously at the end of the 9th hour, for instance, when vehicles and operating buses are plugged in for charging after use rather than during the 4-9 a.m. hours. By shifting all opportunistic charging events, typically distributed across the operating window between 4:00 and 10:00 a.m., to occur simultaneously at the end of the 9th hour, Fig. 7 represents a depot-style plug-in regime in which vehicles and buses are charged in bulk after service completion rather than incrementally during operation. The resulting comparison plots illustrate how the same total energy demand can lead to significantly different load profiles and grid outcomes, depending solely on the temporal density of charging activity. In a distributed opportunistic charging configuration, the energy distribution exhibits a flattened curve, maintaining moderate demand levels and maintaining high load factor efficiency through continuous wireless charging. However, when cumulative demand is synchronized into a single post-operational event, the power profile collapses to a sharp peak, more than halving the instantaneous load while decreasing grid usage efficiency.

IV. Conclusion

The study evaluated the operational and grid-level impacts of differentiated EV charging behaviors by comparing opportunistic wireless power transfer with traditional depot-based plug-in charging in a representative six-hour city-scale simulation. The results go beyond theory and demonstrate what the system can achieve in practice when idle traffic times are converted into microcharging opportunities. By integrating WPT with routine signalized stops, the net grid demand of EVs can be gently regulated in real time. Today at modest power levels, and, as dynamic transfer capacities grow beyond common 11 kW baselines, with increased energy recovery during trips. One of the key advantages is behavioral neutrality, that is, drivers do nothing new, yet the fleet harvests many small charges that add up over a journey.

At the grid level, the opportunistic WPT scenario proved substantially more grid-compatible than its depot-based counterpart. By distributing identical total energy across multiple hours, the opportunistic WPT setup reduced peak demand, improved the load factor, and lowered the peak-to-average power ratio. The what if scenario underlies mechanism, where all distributed charging events were hypothetically concentrated into a single terminal hour, grid stress increased dramatically while overall energy delivery remained constant. This confirms that temporal synchronization, rather than the magnitude of charging, is the dominant determinant of grid load volatility. Consequently, distributed or opportunistic charging strategies act as passive grid balancing tools, smoothing demand and aligning EV energy use with the grid's natural operating

envelope. Thereupon, the findings suggest that the temporal distribution of energy transfer can become a design parameter for sustainable electric transportation systems. By enabling frequent, low-power energy transfers, opportunistic wireless charging provides grid efficiency and operational flexibility compared to the traditional storage-centric model. In addition, the high charging demands created instantly by charging stations at certain locations are spread in smaller pieces to many different areas within the city, creating a more balanced pattern. The reduction in grid usage and peak power infrastructure confirms that the system is expected to be scalable, as hourly energy capacity utilization is significantly higher than demand in traffic corridors. Since EV fleet size is only a small percentage of the total vehicle fleet, such as 15%, a policy prioritizing EV fleet growth and higher compliance with WPT standards, along with a planning shift toward phased, data-driven deployment along high-traffic corridors where vehicles and infrastructure are adapted to wireless charging standards, can maximize grid synchronization and capital efficiency, forming an integral component of smart energy ecosystems and next-generation urban mobility. In light of the results, suitability of future charging infrastructure can be evaluated using the methods employed in this framework and applying them to different larger-scale experiments at city level.

REFERENCES

[1] Jiang, B.-H., Hsu, C.-C., Su, N.-W., & Lin, C.-C. (2024). A review of modern electric vehicle innovations for energy transition. *Energies*, *17*(12), 2906. https://doi.org/10.3390/en17122906

[2] Dimovski, A., Josifovska, H., Falabretti, D., & Merlo, M. (2020). Evaluating the impact of electric vehicle integration on an urban distribution network. In *2020 IEEE EEEIC/ICPSEurope* (pp. 1–6). https://doi.org/10.1109/EEEIC/ICPSEurope49358.2020.9160806

[3] Crozier, C., Morstyn, T., & McCulloch, M. (2020). The opportunity for smart charging to mitigate the impact of electric vehicles on transmission and distribution systems. *Applied Energy*, *268*, 114973. https://doi.org/10.1016/j.apenergy.2020.114973

[4] Szinai, J., Sheppard, C., Abhyankar, N., & Gopal, A. (2020). Reduced grid operating costs and renewable energy curtailment with electric vehicle charge management. *Energy Policy*, *136*, 111051. https://doi.org/10.1016/j.enpol.2019.111051

[5] International Energy Agency. (2025). *Global EV Outlook 2025*. https://www.iea.org/reports/global-ev-outlook-2025

[6] Meintjes, T., Castro, R., & Pires, A. J. (2021). Impact of vehicle charging on Portugal's national electricity load profile in 2030. *Utilities Policy*, *73*, 101310. https://doi.org/10.1016/j.jup.2021.101310

[7] Knittel, C. R., & Tanaka, S. (2025). Knittel, C. R., & Tanaka, S. (2025). Challenges to expanding ev adoption and policy responses. In *Handbook on Electricity Regulation* (pp. 405-447). Edward Elgar Publishing. https://doi.org/10.4337/9781035314355.00025

[8] Mogire, E., Kilbourn, P., & Luke, R. (2025). Smart charging for e-mobility in urban areas: A bibliometric review. *Energies*, *18*(17), 4655. https://doi.org/10.3390/en18174655

[9] Khaksari, A., Tsaousoglou, G., Makris, P., Steriotis, K., Efthymiopoulos, N., & Varvarigos, M. (2021). Sizing of electric vehicle charging stations with smart charging capabilities and quality of service requirements. *Sustainable Cities and Society*, *70*, 102872. https://doi.org/10.1016/j.scs.2021.102872

[10] Abdelwahed, A., van den Berg, P., Brandt, T., Collins, J., & Ketter, W. (2020). Evaluating and optimizing opportunity fast-charging schedules in transit battery electric bus networks. *Transportation Science*. https://doi.org/10.1287/trsc.2020.0982

[11] Mohamed, A., Shaier, A., Metwally, H., & Selem, S. (2020). A comprehensive overview of inductive pad in electric vehicles stationary charging. *Unpublished manuscript.*

[12] Jha, K., Albert, L., Albert, D., & Schrank, D. (2022). Evaluating regional traffic signal performance measures using crowd-sourced data in 2021 Urban Mobility Report [Research report]. https://digitalcommons.usf.edu/cutr_nicr/10

[13] Alvarez Lopez, P., Behrisch, M., Bieker-Walz, L., Erdmann, J., Flötteröd, Y.-P., Hilbrich, R., Lücken, L., Rummel, J., Wagner, P., & Wießner, E. (2018). Microscopic traffic simulation using SUMO. In *21st IEEE International Conference on Intelligent Transportation Systems (ITSC)*. IEEE. https://elib.dlr.de/124092/

[14] Codecà, L., & Härri, J. (2017). Towards multimodal mobility simulation of C-ITS: The Monaco SUMO traffic scenario. In *2017 IEEE Vehicular Networking Conference (VNC)*. https://doi.org/10.1109/VNC.2017.8275627

[15] Koch, L., et al. (2021). Accurate physics-based modeling of electric vehicle energy consumption in the SUMO traffic microsimulator. In *2021 IEEE International Intelligent Transportation Systems Conference (ITSC)* (pp. 1650–1657). https://doi.org/10.1109/ITSC48978.2021.9564463

[16] Hjelkrem, O., Lervåg, K. Y., Babri, S., Lu, C., & Södersten, C.-J. (2021). A battery electric bus energy consumption model for strategic purposes: Validation of a proposed model structure with data from bus fleets in China and Norway. *Transportation Research Part D: Transport and Environment*, *94*, 102804. https://doi.org/10.1016/j.trd.2021.102804

[17] Schneider, J., Carlson, R., Sirota, J., Sutton, R., et al. (2019). Validation of wireless power transfer up to 11 kW based on SAE J2954 with bench and vehicle testing (SAE Technical Paper No. 2019-01-0868). https://doi.org/10.4271/2019-01-0868

eNergetics 2025
DOI: https://doi.org/10.5281/zenodo.18626247

Original Scientific Article

Energy Saving Behaviour Assessment Scale (ESBAS): A Validated Instrument to Assess Determinants of Energy Saving Behaviour

Annie Feba Varghese[1], Divya Chandrasenan[2], Susan E. Powers[3], Jan DeWaters[4]

[1,3]Institute for a Sustainable Development, Clarkson University, Potsdam, New York, USA
[2]Department of Education, University of Kerala, Thiruvanathapuram, India
[4]Institute for STEM Education, Clarkson University, Potsdam, New York, USA

[1]anniefebavarghese@gmail.com, [2]divyacsenan@keralauniversity.ac.in, [3]spowers@clarkson.edu, [4]jdewater@clarkson.edu

Abstract—**Energy Saving Behaviour Assessment Scale (ESBAS) was created to assess students' values regarding energy use, including their feelings about environmental protection, the financial costs of energy, personal comfort, the specific actions a person takes to save energy including habits and routines and the internal and external drives for saving energy. The Energy Saving Behaviour Assessment Scale was drafted and pilot tested among high school students across Kerala, India. Initial exploration of the measure yielded promising results: The Cronbach's reliability coefficient for the scale was 0.79 and Item analysis revealed discrimination indices above the permissible range for all items in the scale. Factor Analysis was used to select appropriate questions for the Energy Saving Behaviour Assessment Scale with due importance being given to each of the factors. The field-tested ESBAS includes six factors namely Self Efficacy, Perceived Severity, Response Cost, Response efficacy, Subjective Norms and Perceived Vulnerability. The ESBAS is particularly useful for determining the energy saving behaviours of potential responders and evaluating the broader effects of educational initiatives.**

Keywords - energy saving behaviour, attitude, subjective norms.

I. INTRODUCTION

Energy behaviour is defined as "all human actions that affect the way that fuels (electricity, gas, petroleum, coal, etc.) is utilized to achieve desired services, including the acquisition or disposal of energy-related technologies and materials, the ways in which these are used, and the mental processes that relate to these actions" [1]. An energy-saving behaviour is an individual action that aims to reduce energy consumption and the negative environmental impacts of energy consumption and production. The integration of Protection Motivation Theory [2] and the Theory of Planned Behaviour [3] provide a comprehensive framework to understand energy-saving behavior. According to Protection Motivation Theory (PMT), individuals' motivation to adopt protective behaviours (in this case, energy-saving actions) is influenced by the perceived severity of the threat (e.g., climate change), perceived vulnerability to the threat, and the efficacy of the recommended behaviour in reducing the threat. According to the framework of this theory, threat appraisal is positively related to performance of protective behaviours. Threat appraisal trend of PMT includes perceived severity and perceived vulnerability as risk perception variables. On the other hand, Theory of Planned Behaviour (TPB) posits that individuals' intention to engage in a behaviour (energy saving) is determined by their attitude towards the behaviour, subjective norms (perceived social pressure), and perceived behavioural control (PBC). By combining these two theories, it can be argued that individuals'

ISBN: 978-86-82602-07-1

energy-saving intentions and behaviours are influenced by their perceived threat of environmental degradation, perceived vulnerability to its consequences, and the effectiveness of energy-saving actions in mitigating these threats. Additionally, their attitude towards energy-saving, perceived social norms, and PBC also play crucial roles in shaping their energy-saving intentions and behaviours. The energy saving behaviour has its foundation on the Protection Motivation Theory perceiving the energy crisis as a threat which asks for immediate action. The aspects have strong relationship to the formation of an intention inclined towards saving energy as explained in the theory of planned behaviour which shows that an individual's personal attitude, perceived behavioural control and subjective norms shape the intention of an individual to act in a situation. The attitude is shaped by the perceived severity, perceived vulnerability, as suggested in the Protection Motivation Theory while the self efficacy and response efficacy and response cost determine the behaviour of an individual in a threat. Both the theories underline the presence of attitudinal and behavioural aspects in shaping the intention to act in a particular situation with an additional aspect of how we view the ideas of other people about a specific behaviour in the theory of planned behaviour (ie. Subjective Norms). The final framework leaves the energy saving behaviour of an individual to be dependent on six basic aspects that are: Perceived Severity, Perceived Vulnerability, Response Cost, Response Efficacy, Self-Efficacy and Subjective Norms.

II. Motivation for the Study

The urgent need to address rising energy demands and their detrimental effects on the environment, including carbon emissions and the depletion of natural resources, is the driving force behind the creation of an energy-saving behaviour assessment scale. While technology developments and breakthroughs provide remedies, human habits and behaviors-which are frequently disregarded or challenging to measure-account for a sizable amount of energy waste. An standardised and trustworthy tool for precisely measuring and assessing current energy consumption patterns and habits as well as identifying certain psychological and social elements influencing these behaviours is essential in current scenario. Research approaches that focus mainly on the production or purchase of environmentally friendly products or assessment of the stance of institutions and households are not seen as sufficient to present the full picture of any society regarding energy saving behaviors (ESB). The attitudes and behaviours of the student population have generally not been sufficiently presented in energy saving studies to reflect current or emerging realities. As it is relatively a new area of research concern, a validated tool is hardly found in the Indian context, especially in Kerala. The lack of appropriate tools in the Indian context especially in the education sector motivated the investigator for the development of a new tool in the concerned area. Hence it was planned to construct a suitable instrument to get measurable data about energy saving behaviour. The rating scale was fixed as the instrument for data collection. The major area of energy saving behaviour is analyzed in terms of certain components which seem to be part of human behavioural responses to threats and an individual's decision to engage in a specific behaviour. The Likert-type rating scale is designed to produce quantifiable data that may be subjected to statistical analysis to draw scientific inferences.

III. The Instrument Development Framework

A. Item Generation and Review

Keeping in view that Energy Saving Behaviour embraces the individuals stated intention to save energy based on their beliefs about energy saving, their environmental values, their general awareness of energy issues, and habitual, routine behaviors related to energy use an Energy Saving BehaviourAssessment Scale was designed to measure the energy saving behaviour of secondary school students. The approach includes establishing the energy saving behaviour concept and constructing a pool of survey items, as well as preparing, delivering, and assessing the pilot test (item pilot) needed to identify suitable survey items. Following a thorough review of the present curriculum for secondary school kids and the researcher's own experiences, survey questions were developed. Items were worded carefully by reviewing the theories to reveal the various aspects of energy-saving behaviours. In the initial stage, the scale consisted of a list of 50 items. During the item/survey assessment process, a diverse, ten-member validity panel comprised a balance of energy and education experts. In order to judge

the content validity of the items in the Energy Saving Behaviour Assessment Scale, the experts were requested to examine the representativeness of items. A five-point scale is used to ensure the content validity. Incorporating the views and opinions of the experts the repetitive, inaccurate, and ambiguous items were either modified or replaced by the new ones.

B. Item Pilot

The item pilot form was administrated to the 252 secondary school students across Kerala through random sampling technique and the responses were collected. The item responses were converted into numerical scores. Likert-type responses were converted to numerical values according to a predetermined preferred direction of response, with values ranging from 1 for the least preferred response to 5 for the most preferred response [4]. Blank responses were excluded from the analysis. The item analysis comprised a combination of statistical analysis of each item's contribution to the survey's overall objectives. The discrimination indices for all the items in the Energy Saving Behaviour Assessment Scale fell within the range of 0.25 to 0.32 which fell within the acceptable level [5].

C. Factor Analysis

Factor analysis is used to identify the relationship between all of the variables included in a given data set. The participants completed the Energy Saving Behaviour Assessment Scale, which was analysed. The data were analysed through factor analysis. Exploratory Factor analysis was conducted to identify the items in each component. Further-more, the sampling adequacy test was performed through Kaiser-Meyer-Olkin (KMO) statistic that provide an adequate basis for proceeding with the factor analysis. It is shown in the table below.

TABLE I. KMO VALUE AND BARTLETT'S TEST OF SPHERICITY.

Kaiser-Meyer-Olkin Measure of Sampling Adequacy		.603
Bartlett's Test of sphericity	***Approx. Chi-Square***	2.964
	Df	1225
	Sig.	.000

Table I. shows the KMO value of Energy Saving Behaviour Assessment Scale. Since, KMO values are greater than 0.6, it is adequate [6]. Therefore, the Kaiser-Meyer-Olkin measure of sampling adequacy with value of 0.603 was acceptable. Barlett's Test of Sphericity significant ($\chi^2 = 2.964$, $df = 1225$, $p < 0.001$) shows that the values are significant and hence, acceptable, implying that non-zero correlations existed at the significance level of 0.000, providing an adequate basis for proceeding with the factor analysis. These results suggested the data were suitable to proceed with the Exploratory Factor Analysis [7]. Further, for assessing the relevance of the data through the scale for factor analysis, the commonalities derived from the factor analysis were reviewed. Items with factor loadings above the permissible value of 0.30 were kept in the scale [8]. Integration of eigenvalue and scree plot results indicated that the measure represents six factors. Seven items in the scale having factor loadings below the permissible value of 0.30 was discarded from the scale, thus retaining a total of 43 items from the 50 items given for factor loading. Fig. 1 shows the scree plot of the factor loading.

Integration of eigenvalue and scree plot results indicated that the measure represents six factors/components for assessing the energy saving behaviour. According to factor loadings and scree plot, it is evident that the Energy Saving Behaviour Assessment Scale is based on six components which aligned with the aspects suggested in the Protection Motivation Theory and the Theory of Planned Behaviour. The six factors were distributed as Factor 1-Self

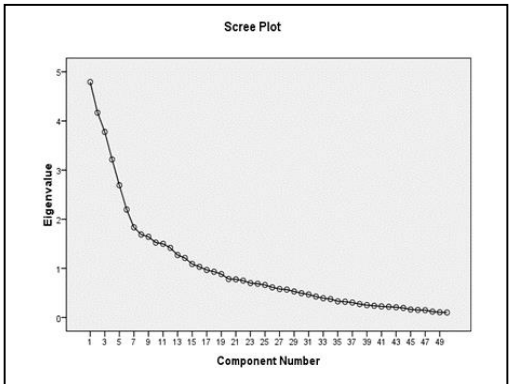

Figure 1. A scree plot representing the distribution of the components in the energy saving behaviour assessment scale.

Efficacy, Factor 2-Perceived Severity, Factor 3 – Response Cost, Factor 4 -Response efficacy, Factor 5- Subjective Norms, and Factor 6-Perceived Vulnerability. The final Energy Saving Behaviour Assessment Scale having 43 items were finalised for the scale, based on those variables having a loading of at least 0.30 on a single factor considered. After the factor loading, ten items were found to be under factor 1, nine items for factor 2, eight items in factor 3, six items in factor 4, and five items correspondingly in factor 5 and factor 6. All the items loading in these 6 factors were in the acceptable level of factor loadings (i.e., loadings at or greater than 0.30). Given the factor loadings and the evidence of reliability, 43 items were retained. All the items are found capable for assessing the energy saving behaviour.

D. Statistical Significance and Reliability

Item analysis involved the process of analysing the items to select most relevant items in the pool. The statistical analysis with *t* test was made use for this. The response sheets of 252 students were arranged in the descending order of their ranks i.e., as per the total score obtained by each individual for all items. The highest 27% and the lowest 27% were selected as the criterion groups in terms of which to evaluate the individual statements using the *t* test. Rejection and modification of the test items depended upon the *t* value. Items with $t > 1.96$, were accepted. All the 43 items included in the scale had the *t* value greater than 1.96 and were selected for final scale. Statistical procedures, performed with the Statistical Package for Social Sciences (SPSS) primarily involved assessing each item's contribution to the overall reliability, as indicated by Cronbach's α. The reliability coefficient of the Energy Saving Behaviour Assessment Scale was 0.79 Cronbach's alpha value which was acceptable [9].

E. Result

This investigation of a well-substantiated measure of Energy Saving Behaviour yielded promising results in terms of its psychometrics. Exploratory factor analysis was done to determine the 43 item Energy Saving Behaviour Assessment Scale's underlying factor structure which revealed that the 43 items represented six different factors or components each reflecting different aspects of energy saving behaviour in the students. The *t* values of the items and the reliability of the scale indicated by Cronbach's α gave confirming values. Thus, both reliability and validity indicators were strong, based on results from a geographically diverse sample. The scale is valid and reliable and serves as a standardised tool to assess the determinants of energy saving behaviour among the students. The Table II displays the scale's component size and the number of items inside each component.

TABLE II. NUMBER OF ITEMS THAT FALL IN EACH COMPONENT.

Sl.No	Components	Number of items
1	Self Efficacy	10
2	Perceived Severity	9
3	Response Cost	8
4	Response efficacy	6
5	Subjective Norms	5
6	Perceived Vulnerability	5

IV. DISCUSSION

The six dimensions identified-Self-Efficacy, Perceived Severity, Response Cost, Response Efficacy, Subjective Norms, and Perceived Vulnerability though based on the frameworks of Theory of Planned Behaviour (TPB), Protection Motivation Theory (PMT), are conceptually consistent with existing theories like the Health Belief Model (HBM), and the Value-Belief-Norm (VBN) theory. The Protection Motivation Theory (PMT) emphasizes on the mental processes that underlie threat and coping assessments. The four dimensions of ESBAS-Perceived Severity, Perceived Vulnerability, Response Efficacy, and Self-Efficacy-are directly derived from the components of Protection Motivation Theory (PMT). When students see climate change and energy crises as major dangers (perceived severity) and feel personally sensitive to their outcomes (perceived vulnerability), they are more likely to take action. This is especially true when they think they can successfully lessen those threats with their own efforts (response efficacy) and abilities (self-efficacy). From the Theory of Planned Behaviour (TPB) perspective, an individual's attitude, subjective norms, and perceived behavioural control all influence energy-saving behaviour. While Self-Efficacy correlates with perceived behavioural control and represents an individual's perception in their ability to carry out energy-saving acts, the ESBAS component of Subjective Norms reflects felt social pressure

to engage in energy conservation. Additionally, Response Cost incorporates perceived barriers to engaging in such actions, impacting intention development as well as control. When considered collectively, these elements make it clear how intention is converted into practical energy-saving strategies. By concentrating on individual perceptions of behaviors connected to health or risk, the Health Belief Model (HBM) compliments these insights [10]. Like PMT, HBM posits that self-efficacy, perceived severity, perceived benefits, perceived barriers, and perceived susceptibility have all got an impact on behavior. In ESBAS, students' awareness of the energy crisis is reflected in Perceived Vulnerability and Perceived Severity, while perceived positives and impediments are reflected in Response Efficacy and Response Cost, respectively. This alignment shows that, in accordance with HBM principles, students weigh the benefits of energy conservation against the dangers of inaction before choosing to take action. Finally, the Value-Belief-Norm (VBN) theory emphasizes the moral and normative foundations of pro-environmental behaviour [11]. Students' values shape their environmental beliefs and personal norms, leading to a sense of moral obligation to conserve energy. The inclusion of Subjective Norms and Perceived Severity in ESBAS reflects these internalized moral beliefs and social expectations.

Overall, ESBAS demonstrates that energy-saving behaviour is shaped by a combination of determinants aligning with the Protection Motivation Theory, Theory of Planned Behaviour, Health Belief Model and Value-Belief-Norm Theory. The standardisation procedures confirm its robustness as a multidimensional tool that captures both rational and normative influences on sustainable energy behaviour among students.

Various studies have been carried out in the past which corresponds with the aspects put forward in the Energy Saving Behaviour Assessment Scale (ESBAS). The various dimensions considered in the ESBAS are substantiated by the study by [12] which concluded that human attitudes, income and intentions influence how the physical devices are operated. A theoretical framework was suggested by [13] in which private choices in energy conservation and energy efficiency are explained in terms of private preferences and costs. Reference [14] in their study on developing a standardized scale for energy efficient behaviours emphasized energy saving measures will be influenced by financial investment which is characterized as the response cost aspect in ESBAS. Reference [15] developed and tested a benchmark tool to assess energy saving behaviour in non- domestic buildings that includes questions to ascertain the respondents' attitudes towards energy and the environment, awareness and perception of the company's energy policy and energy-saving targets, perception of and interest in feedback mechanisms on energy use, level of supervision, training and control received on energy saving, level of "peer-pressure" for energy saving at work, self-reported knowledge of energy-saving actions, self-reported energy-saving behaviour and specific procedural knowledge. The questions on procedural knowledge aimed to assess to what extent participants feel they understand what they need to do if they want/ need to save energy including the main responsibility pathways for such energy-saving actions. Most of the aspects in the tool align with the aspects considered in ESBAS. Environmental variables, income and dwelling type are predictors of both energy-saving behaviours and investment in energy efficient appliances [16]. Situational and habitual processes were best able to account for energy saving behaviour while normative and intentional processes had little predictive power [17]. The results of the content analysis by [18] indicates that the energy saving behaviour among building users was attributed by several psychological determinants like Attitude, Subjective Norm, Perceived Behavior Control, Habits, Motivation and Energy Knowledge. Reference [19] while developing motivation for electricity saving behaviour scale (MESBS) emphasised the importance of considering individuals' motivations for undertaking electricity saving behaviour in energy-efficient buildings. Energy Saving Behaviour Assessment Scale (ESBAS) developed in the study corresponds very much to the aspects considered in similar studies which makes it a valid and reliable tool for assessing energy saving behaviour of secondary school students.

V. CONCLUSION

The objective of the study was to design a multidimensional scale for measuring secondary-level energy saving behaviour. The survey instrument examines students' attitudes, and behaviour on energy usage, conservation, and management. Energy Saving Behaviour

Assessment Scale (ESBAS), with a 43-item, was validated through exploratory factor analysis and test samples of secondary school students across Kerala, India. The scale consists of 43 items spread across six factors Self Efficacy, Perceived Severity, Response Cost, Response efficacy, Subjective Norms, and Perceived Vulnerability. The findings with the scale can be used to encourage sustainable practices, inform and customise successful behavioural interventions and policies such as focused education campaigns and feedback systems. The interventions' efficacy over time can be monitored to assess the advancement of energy conservation objectives. The scale ultimately makes it possible for scholars and decision-makers to create tailored and successful initiatives that promote sustainable energy-saving practices, greatly advancing long-term energy security and a greener future.

ACKNOWLEDGMENT

This work was financially supported by Scheme for Promotion of Academic and Research Collaboration (No: SPARC/2019-2020/P1839/SL) funded by Ministry of Education, Government of India. The findings and opinions presented here do not necessarily reflect the opinions of the funding agency. Also, we thank all the faculty experts who reviewed the scale.

REFERENCES

[1] International Energy Agency. (2015). *Annual report 2015: Implementing agreement on demand-side management technologies and programmes.* https://beeindia.gov.in/sites/default/files/publications/files/Annual_Report_2015-16_English.pdf

[2] Rogers, R. W. (1975). A protection motivation theory of fear appeals and attitude change. *Journal of Psychology, 91*(1), 93–114. https://doi.org/10.1080/00223980.1975.9915803

[3] Ajzen, I. (1985). From intentions to actions: A theory of planned behavior. In J. Kuhl & J. Beckmann (Eds.), *Action control: From cognition to behavior* (pp. 11–39).Springer. https://link.springer.com/chapter/10.1007/978-3-642-69746-3_2

[4] Armstrong, J. B., & Impara, J. C. (1991). The impact of an environmental education program on knowledge and attitude. *Journal of Environmental Education, 22*(4),36–40. https://doi.org/10.1080/00958964.1991.9943060

[5] Hills, J. R. (1976). *Measurement and evaluation in the classroom*. Merrill Publishing Company.

[6] Kaiser, H. F., & Rice, J. (1974). Little Jiffy, Mark IV. *Educational and Psychological Measurement, 34*(1), 111–117. https://doi.org/10.1177/001316447403400115

[7] Hair, J. F., Black, W. C., Babin, B. J., & Anderson, R. E. (2010). *Multivariate data analysis* (7th ed.). Pearson.

[8] Stewart, D. W. (1981). The application and misapplication of factor analysis in marketing research. *Journal of Marketing Research, 18*(1), 51–62. https://doi.org/10.2307/3151313

[9] Qaqish, B. (2006). Developing multiple-choice tests for social work training. *Training and Development in Human Services, 3*(1), 45–57.

[10] Rosenstock, I. M. (1974). Historical origins of the health belief model. *Health Education Monographs, 2*(4), 328–335.

[11] Stern, P. C., Dietz, T., Abel, T., Guagnano, G. A., & Kalof, L. (1999). A value-belief-norm theory of support for social movements: The case of environmentalism. *Human Ecology Review, 6*(2), 81–97. https://humanecologyreview.org/pastissues/her62/62sternetal.pdf

[12] Cramer, J. C., Hackett, B., Craig, P. P., Vine, E., Levine, M., Dietz, T. M., & Kowalczyk, D. (1984). Structural-behavioral determinants of residential energy use: Summer electricity use in Davis. *Energy, 9*(3),207–216. https://doi.org/10.1016/0360-5442(84)90108-7

[13] Oikonomou, V., Becchis, F., Steg, L., & Russolillo, D. (2009). Energy saving and energy efficiency concepts for policy making. *Energy Policy, 37*(11), 4787–4796. https://doi.org/10.1016/j.enpol.2009.06.035

[14] Stragier, J., Hauttekeete, L., De Marez, L., & Brondeel, R. (2012). Measuring energy-efficient behavior in households: The development of a standardized scale. *Ecopsychology,4*(1),64–71. https://doi.org/10.1089/eco.2012.0026

[15] Ucci, M., Domenech, T., Ball, A., Whitley, T., Wright, C., Mason, D., Corrin, K., Milligan, A., Rogers, A., Fitzsimons, D., Gaggero, C., & Westaway, A. (2014). Behaviour change potential for energy saving in non-domestic buildings: Development and pilot-testing of a benchmarking tool. *Building Services Engineering Research and Technology, 35*(1), 36–52. https://doi.org/10.1177/0143624412466559

[16] Trotta, G. (2018). Factors affecting energy-saving behaviours and energy efficiency investments in British households. *Energy Policy, 114*, 529–539. https://doi.org/10.1016/j.enpol.2017.12.042

[17] Van Den Broek, K. L., Walker, I., & Klöckner, C. A. (2019). Drivers of energy saving behaviour: The relative influence of intentional, normative, situational and habitual processes. *Energy Policy, 132*, 811–819. https://doi.org/10.1016/j.enpol.2019.06.048

[18] Mansor, R., & Sheau-Tingi, L. (2019). The psychological determinants of energy saving behavior. *IOP Conference Series: Materials Science and Engineering, 620*(1), 012006. https://doi.org/10.1088/1757-899X/620/1/012006

[19] Olsson, Z. E., & Mattsson, P. (2024). Development and validation of the motivation for electricity saving behaviour scale (MESBS) among residents living in energy-efficient buildings in Sweden. *Energy and Buildings,325*,114978. https://doi.org/10.1016/j.enbuild.2024.114978

eNergetics 2025
DOI: https://doi.org/10.5281/zenodo.18626313

Original Scientific Article

Effects of the Intermittent Injection from a Photovoltaic Power Plant on the Frequency of the Senegalese Grid: Case Study at Bokhol

El Hadji Mbaye Ndiaye[1], Alphousseyni Ndiaye[2], Mactar Faye[3], Amadou Ba[4], Cheikh Saliou Toure[5], Mamadou Traore[6], Daouda Gueye[7]

[1,2,3,7]Energy Efficiency and Energy Systems- Alioune Diop University, Bambey, Senegal
[4,5,6]Renewable energy and laser materials research team- Alioune Diop University, Bambey, Senegal

[1]elhadjimbaye.ndiaye@uadb.edu.sn, [2]alphousseyni.ndiaye@uadb.edu.sn, [3]mactar.faye@uadb.edu.sn, [4]amadou.ba4@uadb.edu.sn, [5]cheikhsaliou.toure@uadb.edu.sn, [6]mamadou.tradore@uadb.edu.sn, [7]daouda2.gueye@uadb.edu.sn

Abstract—**This work presents a study of the impact of the power injection of a photovoltaic (PV) power plant on the frequency of the electrical network. We took the case of the solar PV plant of Bokhol connected to the electrical network of the national electricity company of Senegal (SENELEC). We have treated the case of two days: the day of January 10, 2021 and that of December 23, 2021. The study is carried out on the basis of the frequency constraints imposed by SENELEC to the PV plant manager. The plant remains connected to the grid as long as the power injection does not cause frequency variations outside the range of 49.7 Hz and 50.3 Hz. The results of the study first show the correlation that exists between PV power and climatic parameters such as irradiation, temperature and wind speed. The results also showed that the variations of the injected power strongly contribute to the instability of the electrical network through a frequency disturbance. This causes the PV plant to be disconnected from the grid. This is the case during the day of January 10, 2021, when the plant is disconnected from the grid from 8:30 to 11:30. During this period of the day, the frequency exceeded the permissible limit of 50.3 Hz. The same scenario is also observed during the day of December 23, 2023 during which the power plant is disconnected twice.**

Keywords - solar photovoltaic power plant, grid frequency, electrical grid, injected power, SENELEC.

I. INTRODUCTION

Supplied by the sun, wind, the heat of the earth, waterfalls, tides or the growth of plants, renewable energies generate little or no waste or polluting emissions [1-4]. Several countries have understood this challenge and despite financial constraints, great efforts are devoted to the development of these resources, especially solar photovoltaic energy [5-7].

Senegal is endowed with a significant potential in renewable energies and has the ambition to reach energy independence and to ensure universal access to electricity by 2025. This is why the government has decided to maintain its option to promote the exploitation of the national potential in renewable energies despite the recent discoveries of oil and gas off its coast. Its ambition is to increase the penetration rate of renewable energy to 30% by 2025 [8]. In 2020, Senegal recorded a renewable energy penetration rate of 26.93% of the total installed capacity [9].

Power generators have always existed in the grids but their presence was not significant

ISBN: 978-86-82602-07-1

enough to have an impact on the steady state of the grids.

For the past few decades, several countries have focused on research and development of renewable energy sources to partially replace fossil energy sources. Large energy production insertion projects have been launched around the world. However, these new productions are not without negative effects on the distribution networks to which they are interconnected and which were not designed for this purpose [10-12]. The deregulation of electricity systems in many countries is currently only in an intermediate stage before reaching a more advanced deregulation [13-15].

Several projects and studies concerning the coordination and mutualization of renewable energy generation have emerged since the late 1990s around the world. Some of them focus on the economic valuation through centralized management of dispersed energy sources in electricity markets. Examples include the American project "ENCORP Virtual Power Plant" and the German project led by Siemens "EDISON Virtual Power Plant". The "CODGUNet" project proposes an in-depth technical study of the impacts of the increasing insertion of power generators into the grid. This study focuses on the technical legal and economic consequences of the connection of these generators with high penetration rates, as well as on the problems of reserves and power balance [16].

The issue of frequency control in power systems in the presence of renewable energy generation is relatively new. In the scientific literature, the number of articles dealing with this topic is quite low compared to other issues concerning power systems.

In the literature, [17] studied the influence of the integration of solar PV plants on the frequency of the power system. The authors showed the impact that the intermittency of the solar resource has on the frequency of the power grid. In [18], the authors studied the impact of PV system penetration on the power grid. They analyzed the influence of the PV system on the power factor and on the voltage of the electrical network. In [19], the authors presented a study on the influence of high penetration of solar PV energy to the power grid. Their study showed that a high penetration of PV energy has negative influences on the power grid. This negative influence impacts the automatic voltage regulation and leads to voltage drops and over voltages. Other authors have also presented work on the integration of PV systems into the power grid [16,20,21].The analysis of the results is almost always identical. The integration of PV systems into the power grid leads to negative influences on the voltage, frequency and power factor of the power grid [22,14].

Today, the situation is different. Year after year, the number of renewable energy generators has increased significantly, while investments in the electrical grid have decreased [23]. However, beyond a certain critical mass, generators have negative impacts on the proper functioning of the electrical grid [24]. The main negative points are: the impacts on the operation of protections due to the modification of power transits and short circuit currents, the destabilization of the electrical system, the appearance of reactive energy flows and the risk of congestion. There are also other issues such as the impact on voltage and frequency levels, voltage drop or overvoltage not allowed by the Energy Sector Regulatory Committee (ESRC), and impacts on power system stability and critical fault clearance times [25,26]. All of these issues related to the integration of PV power into the electrical grid constitute a large space for research and development.

The objective of this work is to study the impact of the integration of PV power plants on the Senegalese national electricity grid (SENELEC) in frequency. This study will focus on the Bokhol solar PV plant connected to the SENELEC grid.

The study of these impacts is necessary to ensure that the massive insertion of renewable energy sources into existing networks is done without degradation in terms of quality and performance of the operation of the electrical network. This work will contribute to detect and prevent the part played by the power injection of PV plants on the instability of the SENELEC electrical network.

II. SENEGAL'S ELECTRICAL SITUATION

Senegal is located between 12°8 and 16°41 North latitude and 11°21 and 17°32 West longitude. The country covers an area of 196722 km².

A. Senegal's National Electricity Network

National electricity production is provided by the SENELEC fleet with a total installed capacity

of 539.94 MW, i.e. 36.02% of the national fleet, and the units of private producers with a total capacity of 959.10 MW (63.98%), i.e. a total installed capacity of 1499.04 MW in 2020 [9]. This fleet is subdivided into two parts: the interconnected network and the non-interconnected network.

B. Solar PV Plants in Senegal

The contribution of renewable energies to the national energy mix includes the development and promotion of solar PV plants, wind farms and biomass plants for the production of electricity to be injected into the public grid. Thus, between 2016 and 2020, nine Photovoltaic Solar Power Plants connected to the SENELEC electricity grid are installed and commissioned. Fig. 1 represents the distribution of the normal direct irradiation on the Senegalese territory and that of the different solar PV plants connected to the SENELEC electrical network.

III. MATERIALS AND METHODS

In this work we have taken the case study of the solar PV plant of Bokhol. The experimental device for measuring climatic data at the plant site is shown in Fig. 2. It is a weather station consisting of a pyranometer to measure the global irradiation. An anemometer is used to measure the wind speed. The station also has a probe to measure the ambient temperature and another probe to measure the temperature of the PV modules.

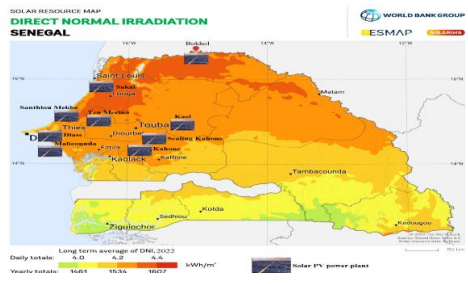

Figure 1. Distribution of PV plants connected to the SENELEC electrical grid.

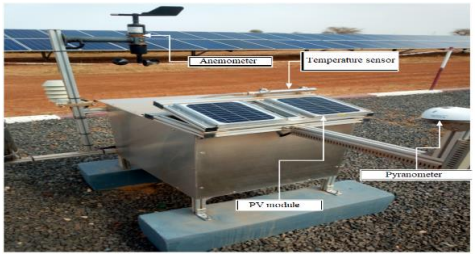

Figure 2. Climatic data measurement device.

Frequency data (at 5-minutes resolution) were acquired from the SENELEC National Control Center archives; while corresponding active power output measurements were sourced directly from the Bokhol PV plant's SCADA system. To ensure the analytical integrity of the study, a rigorous data pre-processing phase was implemented. This included the application of an Interquartile Range (IQR) method to detect and mitigate outliers and anomalies, specifically in the Rate of Change of Frequency (RoCoF) calculation, thereby ensuring that the observed excursions accurately reflect systemic events rather than sensor noise.

To study the behavior of the power system (in voltage and frequency), the climatic data are used as input parameters of the PV system. The simulated climate data are solar irradiation, PV module temperature, ambient temperature and wind speed. Although there are other parameters that affect the operation of PV modules, irradiation and module temperature have a more significant impact [27,28].

Before studying the impact of the connection of the PV plant to the power grid, the influence of the climatic parameters on the production of the plant is first investigated. For this purpose, each parameter among those mentioned above is simulated with the production.

We have taken two days of two different months (January 10 and December 23) of the year 2021 to study the impact of the PV connection to the power grid. For each case, we will study the impact of the climatic parameters on the power produced by the PV. Then we will study the impact of the injected power on the frequency of the electrical network.

In most grid-connected PV systems, when the grid frequency exceeds a certain pre-programmed limit value, the PV plant is automatically disconnected from the grid. This limit value is usually 50.2 Hz for 50 Hz grids, and 60.2 Hz for 60 Hz grids. In the case of Senegal, SENELEC uses the General Operating Principles of the Interconnected Network of the organization for the development of the Senegal River (OMVS). The permissible frequency variation at which the grid is disconnected from the PV plant is 50.3 Hz and 49.7 Hz [17].

IV. RESULTS AND DISCUSSIONS

The analysis is concentrated on two highly volatile operational days: January 10, 2021, and December 23, 2021. This selection was strategic, as these days are statistically representative of the most challenging scenarios encountered by the Senegalese grid (SENELEC) in terms of PV-induced frequency excursions. Specifically, January 10th illustrates a scenario of extremely rapid PV power ramp-down due to severe cloud transients, resulting in peak Rate of Change of Frequency (RoCoF) values. Conversely, December 23rd captures a sustained over-frequency event followed by a sudden loss of generation (or curtailment), testing the system's primary frequency response limits under maximum PV penetration.

A. The Day of January, 10th

Fig. 3 details the climatic conditions—solar irradiation, PV module temperature, and wind speed—for January 10th, establishing the operational context for the PV plant.

The day is characterized by high variability essential to this case study. Ramp-up (8:00 to 15:00): Irradiance peaked at 948.5 W/m², driving up module temperature (maximum 33 °C). This period corresponds to maximum PV power injection. Ramp-down (15:00 to 18:30): Irradiance and temperature gradually decreased.

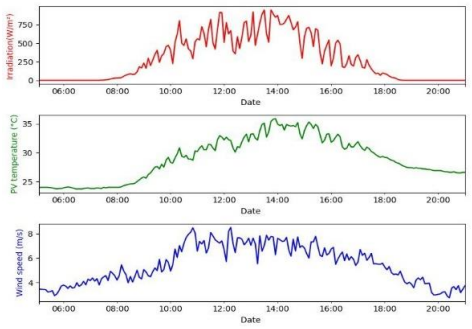

Figure 3. Variation of irradiation, PV modules temperature and wind velocity during the day of January, 10th, between 5am to 9pm.

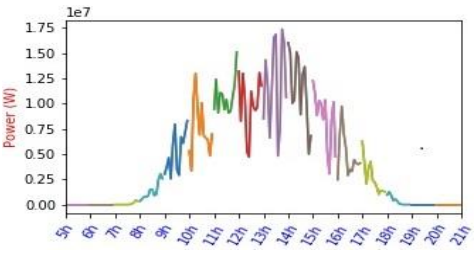

Figure 4. Variation of produced power during the day of January, 10th, between 5am to 9pm.

Low Wind: Wind speed remained low, generally below 5 m/s, indicating that the primary source of PV power fluctuation was high irradiance variability, not wind.

Fig. 4 represents the power produced by the plant between 5am and 9pm.

This power is a function of climatic conditions. It is zero between 5 am and 8 am and between 7 pm and 9 pm (scenario 1 and 4). As shown in Fig. 3, during these periods of the day, there is no sunlight. This results in zero values of irradiance. These low or zero irradiation values are reflected in the temperature of the PV modules. During this day, the modules produce from 8 am to 6:30 pm (scenario 2 and 3). The peak of production is reached between 13 h and 14 h with a power of 17,4 MW for irradiation values of approximately 1000 W/m² and average wind speeds of 7 m/s. On the other hand, the temperature of the modules rose to over 35°C at this time of year, which is characterized by coolness. This analysis shows that there is a strong correlation between the irradiation and the power produced by the PV.

Fig. 5 shows the variation curves of the power between its minimum and maximum values as well as those of the standard deviation. The latter represents the average difference at any time between the maximum and minimum power. This figure shows a consistent standard deviation of about 2.5 MW. This shows the numerous fluctuations in power as in the solar irradiation. This figure also confirms the correlation that exists between the climatic parameters and the power produced by a PV system.

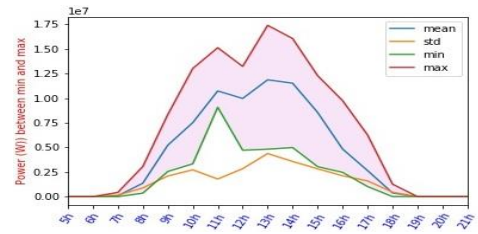

Figure 5. Power between min and max value during the day of January, 10th.

Fig. 6 illustrates the direct impact of the Bokhol PV plant's intermittent power injection on the Senegalese grid frequency on January 10th. Over the day, the frequency ranged from 49.83 Hz to 50.42 Hz, consistently violating the SENELEC continuous operational limit of 50.3 Hz. A clear correlation is observed: grid frequency increased with PV power injection (e.g., between 9:00 and 12:00) and decreased during power ramp-downs (e.g., 15:00 to 18:30). The most severe frequency instability occurred between 11:00 and 17:00, driven by significant weather-induced power variations (irradiance fluctuations from 100 to over 800 W/m²). Specifically, Fig. 6b demonstrates that sustained average frequency excursions above 50.3 Hz were recorded between 8:30 and 11:30. This breach of the grid code constraints directly resulted in the automatic disconnection of the PV plant, confirming the system's susceptibility to rapid, weather-driven PV power fluctuations.

Fig. 7 represents the standard deviation between the minimum and maximum values of the frequency. Otherwise, it quantifies the frequency variations. This figure shows low values between 0.04 and 0.12 Hz. It is more important between 8:30 and 11:30 with a frequency variation of 6.5% between (0.05 and 0.115 Hz).

B. The Day of December, 23th

The variations of solar irradiation, temperature of the PV modules of the power plant and wind speed are shown in Fig. 8. For this day of December 23, the sunrise is observed at 7:30 am and the sunset at 6:30 pm. The duration of sunshine is longer than the day of January 10. The irradiation reaches its maximum value between 12 h and 14 h with a value of 977.07 W/m². The maximum temperature is 46.4 °C and the wind speed is 5.94 m/s. We note drastic variations in irradiance between 14h and 18h.

Fig. 9 represents the power produced by the plant during the day of December 23. The climatic conditions of this day are favorable to a good production of the plant. The peak power is reached between 11am and 2pm with a peak value of 17.48 MW. The modules produce from

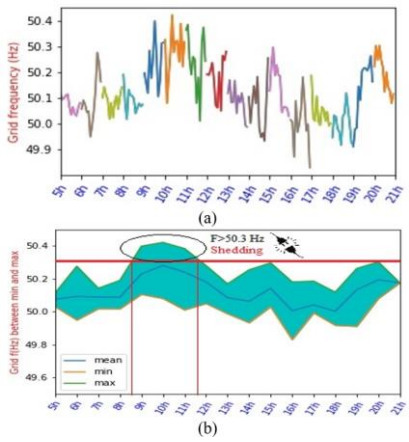

Figure 6. Variation of grid frequency between min and max value during the day of January, 10th.

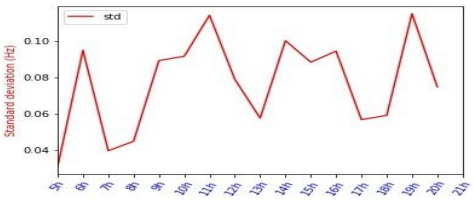

Figure 7. Standard deviation of grid frequency between min and max value during the day of January, 10th.

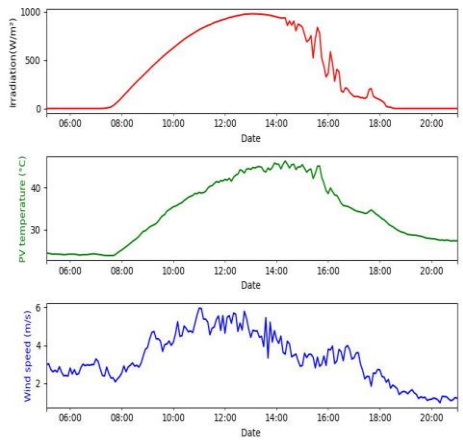

Figure 8. Variation of irradiation, PV modules temperature and wind velocity during the day of December, 23th.

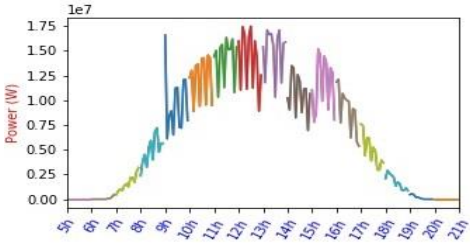

Figure 9. Variation of produced power during the day of December, 23th.

7am to 6:30pm. This power is subject to weather conditions.

Fig. 10 shows that the power has many oscillations.

Fig. 11 displays the frequency response of the power system on December 23rd, showing critical instabilities directly linked to PV power injection. Fig. 11a confirms a strong visual correlation between injected power and grid frequency, where variations in PV output directly cause network disturbances. Fig. 11.b highlights multiple breaches of the SENELEC grid code constraints (50.3 Hz limit). Specifically, the frequency exceeded the 50.3 Hz threshold during two key periods. Early morning (5:00 to 5:30): An over-frequency event led to a transient disconnection of the system. Mid-day (8:00 to 16:30): The frequency exceeded 50.6 Hz, indicating a prolonged period of severe frequency excursion. The sustained nature and magnitude of these frequency overshoots demonstrate the significant challenge posed by PV variability on grid stability, necessitating load shedding or automated curtailment actions during this day.

Fig. 12 shows the difference between the minimum and maximum frequency variations. This is the standard deviation which varies between 0.05 and 0.29 Hz, i.e. a frequency variation of 24%. This figure shows that the frequency variations are more severe during this day of December 23 than during that of January 10. This is justified by the number and duration of disconnections during these two days.

The frequency is a very sensitive parameter to the variations of power injected by a PV plant. The latter depends on the climatic conditions which are very variable. Figs. 13 and 14 show the correlation between the injected power and the frequency of the electrical network. A disturbance in the power input always leads to a disturbance in the grid frequency. These figures

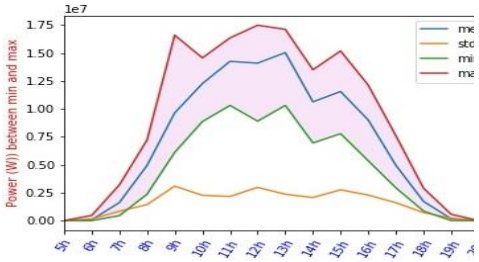

Figure 10. Impact of injected power on grid frequency during the day of December, 23th.

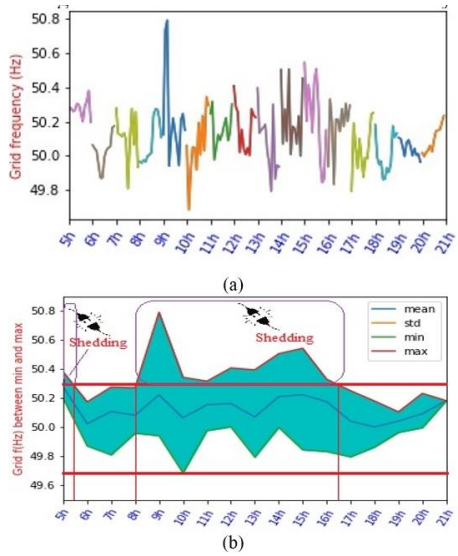

Figure 11. Variation of grid frequency between min and max value during the day of December, 23th.

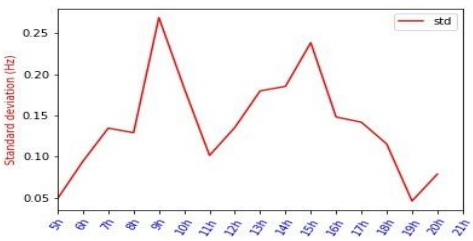

Figure 12. Standard deviation of grid frequency between min and max value during the day of December, 23th.

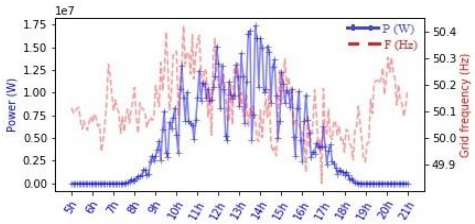

Figure 13. Correlation between injected power and frequency during the day of January, 10th.

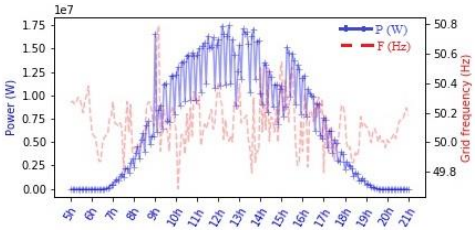

Figure 14. Correlation between injected power and frequency during the day of December, 23th.

show that the frequency is more stable during the hours when there is no injection. In the two figures we can see them during the periods of the day: between 5am and 7am (before sunrise) and between 7pm and 9pm (after sunset).

The analysis of the results presented in this work show that the power injection of a PV plant is one of the causes of the instability of the electrical network. Indeed, the power of a PV plant depends on the irradiation, temperature and wind speed. Because of the intermittency, these parameters are very variable and are therefore the cause of power fluctuations.

C. Causal Analysis of Frequency Excursions and Grid Code Compliance

The causal analysis focused on the temporal correlation between the Rate of Change of Power (RoP) and the Rate of Change of Frequency (RoCoF), in the context of the SENELEC continuous operating limits (49.7 Hz–50.3 Hz). Limitation and Statistical Result: Due to the 5-minute data resolution, the analysis could not capture the instantaneous RoCoF (typically > 0.5 Hz/s) that triggers protection. Consequently, the calculated maximum RoCoF values were low (0.0012Hz/s for Jan 10th, 0.0028Hz/s for Dec 23rd), and the Pearson correlation between RoCoF and RoP was very weak (~ ± 0.06). This confirms that at a slow, macroscopic timescale, the overall grid inertia and system factors dilute the localized PV impact. Empirical Conclusion: Despite the weak correlation at 5-minute intervals, high-RoP events (up to 40.212 W/s) consistently coincide with and are the direct cause of the violation of the grid's steady-state frequency limits (exceeding 50.3 Hz). These critical frequency excursions confirm the Bokhol plant's contribution to system instability, ultimately necessitating its disconnection.

V. CONCLUSION

The frequency of an electrical system is the indicator that allows us to say if we have a balance between the supply and demand of electricity on the same area. It is a bit like on a scale. The balance point is at 50 Hz.

A PV plant connected to the power grid can inject or withdraw energy from the power grid. These variables cause fluctuations in the frequency. To avoid this, inverters must be properly configured to keep the grid frequency stable. This frequency is standardized. When it exceeds the threshold values 49.7 and 50.3 Hz for the SENELEC case, the PV plant is automatically disconnected from the grid. This is the case observed in Figs. 8 and 13. The reason for this disconnection is that as the frequency increases, the output voltage of the transformers increases and may exceed the allowable voltage limit of the electrical equipment. The disconnection of the power plant maintains the stability of the voltage and frequency of the power system.

REFERENCES

[1] EA. (2021). *World energy outlook 2021*. https://www.iea.org/weo

[2] Traore, M., Ndiaye, A., & Mbodji, S. (2021). A comparative study of meta-heuristic and conventional optimization techniques of grid connected photovoltaic system. *International Journal of Power Electronics and Drive Systems, 12*(4), 2492–2500. https://doi.org/10.11591/ijpeds.v12.i4.pp2492-2500

[3] Gueye, D., et al. (2022). Experimental validation under dSPACE of the ANN-PID control of the DC link for injection of solar energy to the grid. *International Journal of Renewable Energy Research, 12*(4), 2015–2022. https://doi.org/10.20508/ijrer.v12i4.13391.g8562

[4] Ndiaye, E. M., Ndiaye, A., & Faye, M. (2021). Photovoltaic power optimization based on artificial intelligence method. *International Journal of Innovative Science and Engineering Technology, 8*(5), 519–533.

[5] Oladipo, S., Sun, Y., & Adeleke, O. (2023). An improved particle swarm optimization and adaptive neuro-fuzzy inference system for predicting the energy consumption of university residence. *International Transactions on Electrical Energy Systems, 2023*.

[6] Ba, A., Ndiaye, A., Ndiaye, E. H. M., & Mbodji, S. (2023). Power optimization of a photovoltaic system with artificial intelligence algorithms over two seasons in tropical area. *MethodsX, 10*, 101959. https://doi.org/10.1016/j.mex.2022.101959

[7] Traore, M., et al. (2018). Supervision of a PV system with storage connected to the power line and design of a battery protection system. *Wireless Networks*. https://doi.org/10.1007/s11276-018-1886-x

[8] CRSE. (2019). *Rapport annuel 2019*. https://www.crse.sn/

[9] SENELEC. (2020). *Rapport annuel 2020*. https://www.senelec.sn

[10] Ndiaye, E. M., Ndiaye, A., & Faye, M. (2020). Experimental validation of PSO and neuro-fuzzy soft-computing methods for power optimization of PV installations. In *2020 8th IEEE International Conference on Smart Grid* (pp. 189–197). https://doi.org/10.1109/icsmartgrid49881.2020.9144790

[11] Ghosh, A. (2020). Soiling losses: A barrier for India's energy security dependency from photovoltaic power. *Challenges, 11*(1), 9. https://doi.org/10.3390/challe11010009

[12] Ali, W. H., Cofie, P., Fuller, J. H., Lokesh, S., & Kolawole, E. S. (2017). Performance and efficiency simulation study of a smart-grid connected

photovoltaic system. *Energy and Power Engineering*, 71–85. https://doi.org/10.4236/epe.2017.92006

[13] Bassam, A., Tzuc, O. M., Soberanis, M. E., Ricalde, L. J., & Cruz, B. (2017). Temperature estimation for photovoltaic array using an adaptive neuro-fuzzy inference system. *Sustainability*, *9*(8). https://doi.org/10.3390/su9081399

[14] Ndiaye, E. M., Ndiaye, A., & Faye, M. (2020). Design and implementation of a hybrid neuro-fuzzy corrector for DC bus voltage regulation. *EAI Endorsed Transactions on Energy Web*, 166551. https://doi.org/10.4108/eai.8-10-2020.166551

[15] Fathi, M., Abderrezek, M., & Grana, P. (2017). Technical and economic assessment of cleaning protocol for photovoltaic power plants: Case of Algerian Sahara sites. *Solar Energy*, *147*, 358–367. https://doi.org/10.1016/j.solener.2017.03.053

[16] Nwauka, O., Telukdarie, A., & Enslin, J. (2018). Virtual power plant basic requirements for integration of distributed energy resources, driven by industry 4.0. *Proceedings of the International Conference on Industrial Engineering and Operations Management*, 511–525.

[17] Abdoulaye, M. A., Tevi, G. J. P., Diouf, D., & Maiga, A. S. (2020). Impact of the intermittency of photovoltaic power plants on the frequency management: Case of the Senegalese electricity grid. *Journal of Power and Energy Engineering*, *8*(7), 55–70. https://doi.org/10.4236/jpee.2020.87005

[18] Guingane, T. T. (2017). Impact de la pénétration du photovoltaïque sur le réseau électrique. *American Journal of Innovative Research and Applied Sciences*, 397–404. http://www.american-jiras.com

[19] Kenneth, A. P., & Folly, K. (2014). Voltage rise issue with high penetration of grid connected PV. *IFAC Proceedings*, *19*(3). https://doi.org/10.3182/20140824-6-za-1003.01989

[20] Nwaigwe, K. N., Mutabilwa, P., & Dintwa, E. (2019). An overview of solar power (PV systems) integration into electricity grids. *Materials Science for Energy Technologies*, *2*(3), 629–633. https://doi.org/10.1016/j.mset.2019.07.002

[21] Iioka, D., et al. (2019). Voltage reduction due to reverse power flow in distribution feeder with photovoltaic system. *International Journal of Electrical Power & Energy Systems*, *113*, 411–418. https://doi.org/10.1016/j.ijepes.2019.05.059

[22] Kreuwel, F. P. M., Knap, W. H., Visser, L. R., van Sark, W. G. J. H. M., Vilà-Guerau de Arellano, J., & van Heerwaarden, C. C. (2020). Analysis of high-frequency photovoltaic solar energy fluctuations. *Solar Energy*, *206*, 381–389. https://doi.org/10.1016/j.solener.2020.05.093

[23] Ndiaye, E. H. M., Ndiaye, A., & Faye, M. (2021). Low voltage grid connected three-phase inverter control with hybrid neuro-fuzzy. *Journal of Physics D*, *2*(2020), 1–7. https://doi.org/10.46411/jpsoaphys.2020.01.07

[24] Saliha, B., et al. (2022). Impact of power ramp event on photovoltaic system voltage quality under different weather conditions and operating powers. *Research Square*, 1–30.

[25] Cheng, K., Hao, L., & Yang, J. (2013). Application research of off-grid home photovoltaic power system in Shaanxi northern region. *Energy and Power Engineering*, *2013*(July), 194–197. https://doi.org/10.4236/epe.2013.54B037

[26] Ndiaye, A., Thiaw, L., & Sow, G. (2015). Application of new modeling and control for grid-connected photovoltaic systems based on artificial intelligence. *Journal of Electrical and Electronics Engineering Research*, *7*(1), 1–10. https://doi.org/10.5897/JEEER2013.0523

[27] Ndiaye, E. M., Faye, M., & Ndiaye, A. (2020). Comparative study between three methods for optimizing the power produced from photovoltaic generator. *Advances in Science, Technology and Engineering Systems*, *5*(6), 1458–1465. https://doi.org/10.25046/aj0506175

[28] Al-Sayyab, A. K. S., Al Tmari, Z. Y., & Taher, M. K. (2019). Theoretical and experimental investigation of photovoltaic cell performance with optimum tilted angle: Basra city case study. *Case Studies in Thermal Engineering*, *14*, 100421.

eNergetics 2025
DOI: https://doi.org/10.5281/zenodo.18631420

Review Scientific Article

Parabolic Solar Concentrator Applied to Solar Thermal Desalination: A Bibliometric Review

Marco Damasceno de Sousa[1], Adriano da Silva Marques[2], João Pedro Cruz de Almeida[3]

[1,3]Center for Alternative and Renewable Energies, Federal University of Paraíba, João Pessoa, Brazil. Federal Institute of Paraíba, Cajazeiras-PB, Brazil
[2]Department of Renewable Energy Engineering, Center for Alternative and Renewable Energy, Federal University of Paraíba, João Pessoa, Brazil

[1]marco.sousa@ifpb.edu.br, [1]marco.sousa@cear.ufpb.br, [2]adriano@cear.ufpb.br, [3]joao.almeida@cear.ufpb.br

Abstract—**This study conducted a comprehensive bibliometric analysis on the use of parabolic solar concentrators applied to solar desalination. The research involved a wide variety of information sources from the Scopus and Web of Science databases, providing a panoramic view of the evolution and development of investigations in this area. Using bibliometric tools, 197 publications were analyzed, covering the period from 1979 to the present day (July, 2025), which allowed for the identification of relevant trends, as well as the main knowledge-producing countries, the most influential research sources, and the annual evolution of scientific output. Furthermore, important gaps were identified that can guide new research directions and contribute to the advancement of the topic. Thus, this work offers a broad and updated perspective on solar desalination with parabolic concentrators, forming a solid foundation for future investigations and for the refinement of related technologies.**

Keywords - desalination, parabolic concentrator, solar concentrator, solar still, solar energy.

I. INTRODUCTION

Water scarcity represents one of the greatest global challenges, particularly due to its unequal distribution, which results in limited water resources across various regions of the planet [1]. It is estimated that, in 2020, one quarter of the world's population lacked access to safely managed drinking water [2].

Solar-powered desalination methods can contribute to mitigating the issue of water scarcity. Numerous studies have investigated novel desalination systems, including those employing parabolic solar concentrators for this purpose [3]. This technology shows great potential for addressing water shortages in semi-arid and remote regions with high solar radiation levels [4,5].

A parabolic concentrator is a device that captures solar radiation and focuses it onto a specific point known as the receiver. According to [4], this technology is widely used in solar thermal systems for steam generation, electricity production, thermal energy storage, among other applications, including desalination.

In this context, the present study provides a review of research in the field of solar thermal desalination using parabolic concentrators, through a bibliometric analysis. Bibliometrics is a quantitative methodology aimed at mapping knowledge and identifying relationships between key elements such as title, abstract, keywords, publication source, impact factor, co-authorship networks, among others [6].

This approach relies on valuable tools to process and analyze information extracted from databases. In this regard, Bibliometrix is a powerful, professional, and automated resource for conducting analyses, generating statistics, co-

ISBN: 978-86-82602-07-1

authorship networks, citation analysis, and scientific mapping [7].

It is important to mention that Bibliometrix is part of a package within the R software. As described by [8], R is an open-source programming language that offers a wide range of packages and libraries for statistical analysis and data visualization.

Accordingly, the objectives of this study are: (I) to conduct a bibliometric analysis on desalination using parabolic concentrators, identifying and discussing the volume of publications in recent years, the most prominent countries, the most relevant sources, and the main authors; and (II) to assess the state of the research, identifying existing gaps.

The study was conducted based on articles published in the Scopus and Web of Science databases, using bibliometric analysis tools and data processing resources, namely the Bibliometrix package and the RStudio software, respectively.

II. METHODOLOGY

The methodological approach adopted consisted of conducting a bibliometric analysis aimed at evaluating the scientific output in the research field under study. The analysis included the countries with the highest number of publications, the most relevant journals, the temporal evolution of publications, the most prominent authors, and the co-occurrence of the most frequent keywords in article abstracts.

This approach follows a methodology similar to that applied by [9,10], who used bibliometric techniques to map trends and patterns in specific thematic areas. Fig. 1 presents the stages of methodological development.

The first stage consisted of selecting the databases. The combined use of the Scopus and Web of Science (WoS) platforms was chosen due to their broad international coverage, rigorous indexing criteria, and established recognition within the scientific community, which ensures greater reliability and representativeness of the analyzed sample [11].

Following the flowchart in Fig. 1, the search criteria were defined based on filters for document selection, namely: title, abstract, keywords, and scientific journals. Additionally, conference proceedings were included, as they constitute an important channel for disseminating emerging ideas [12]. All these filters were applied directly to the Scopus and Web of Science platforms.

The search expression ((“Parabolic concentrat*” OR “parabolic solar concentrat*”) AND (“desalination” OR “distillation”)) was developed with the aim of identifying articles directly related to the topic of solar thermal desalination using parabolic concentration. The construction of this search strategy followed a methodology similar to that adopted by [10], in order to ensure the relevance and specificity of the selected documents.

In the processing stage, following the extraction of records from the Scopus and Web of Science platforms, the data were integrated and processed using RStudio software. The search conducted in the Scopus database returned 137 records. Similarly, 154 records were retrieved from the Web of Science database.

To ensure a thorough and comprehensive analysis, the RStudio platform was employed to enhance data processing, including the cleaning and organization stages. During this process, 94 duplicate records were identified and removed, ensuring that only unique documents were considered for the bibliometric analysis, resulting in a final total of 197 works from 71 different sources. Finally, the bibliometric analysis was carried out using the Bibliometrix package, with support from the Biblioshiny

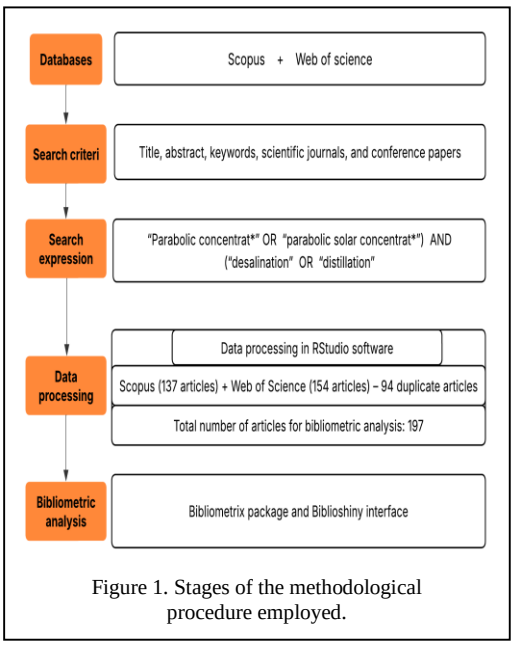

Figure 1. Stages of the methodological procedure employed.

interface for generating graphs and data visualizations.

III. Results and Discussion

A. Analysis by Country

Fig. 2 illustrates the volume of contributions per country in the field of concentrated solar desalination. The graph highlights India as the leading contributor. This can partially be attributed to the potable water scarcity issue faced by the country [13]. Furthermore, India holds 16% of the global population while possessing only 4% of the world's water resources [14]. This unique condition explains the substantial interest of the Indian scientific community in developing sustainable solutions to alleviate the water scarcity problem.

It is also observed that, despite existing international cooperation initiatives (MCP), the majority of scientific output is still conducted in isolation by a few countries (SCP), meaning without international collaboration. Egypt and Saudi Arabia stand out as notable exceptions, with their internationally co-authored publications accounting for over 50% of their local output.

These data underscore opportunities for strengthening international communication and research networks, focused on technology integration and knowledge exchange, which can propel faster, high-impact advancements in the field.

B. Analysis by Journals

Fig. 3 presents the top ten sources with the largest number of publications on the topic. The journals Desalination and Desalination and Water Treatment lead the list, indicating that these journals play a fundamental role in disseminating research in the field of desalination and water treatment. This result is consistent with the scope of these publications, which are widely recognized as authoritative references in the area.

The journals Solar Energy (12 articles), Renewable Energy (9 articles), and Materials Today: Proceedings (9 articles) also present significant contributions. This finding suggests that the application of renewable energy sources, especially solar energy, in water treatment and desalination, has received considerable attention in the scientific literature. The journal Applied Thermal Engineering, with 8 published articles,

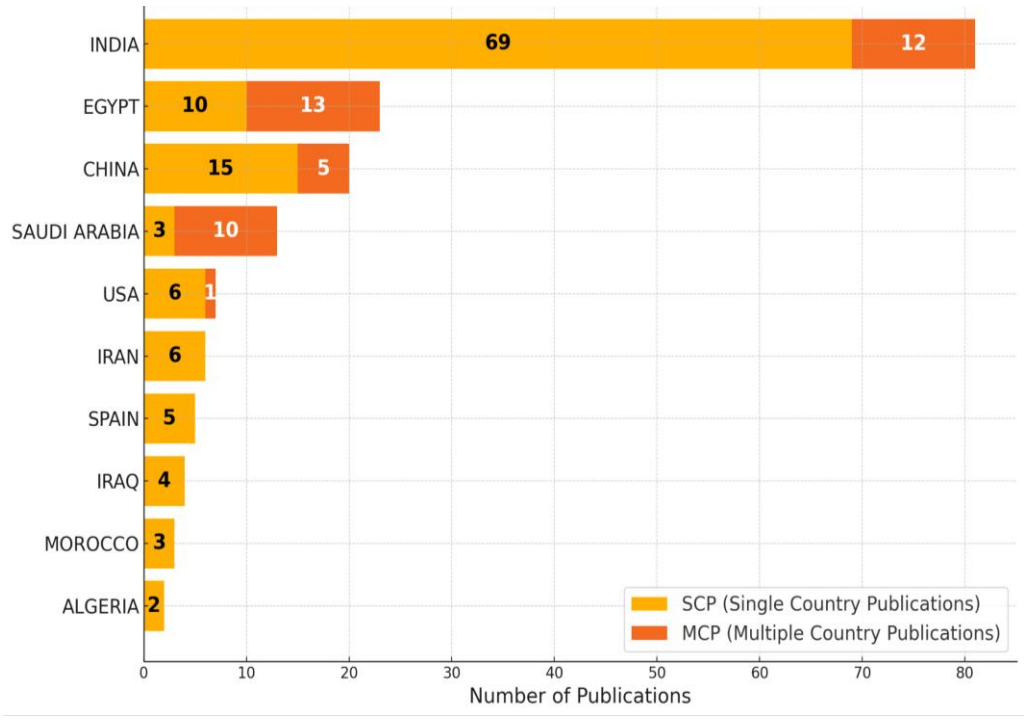

Figure 2. Production by country.

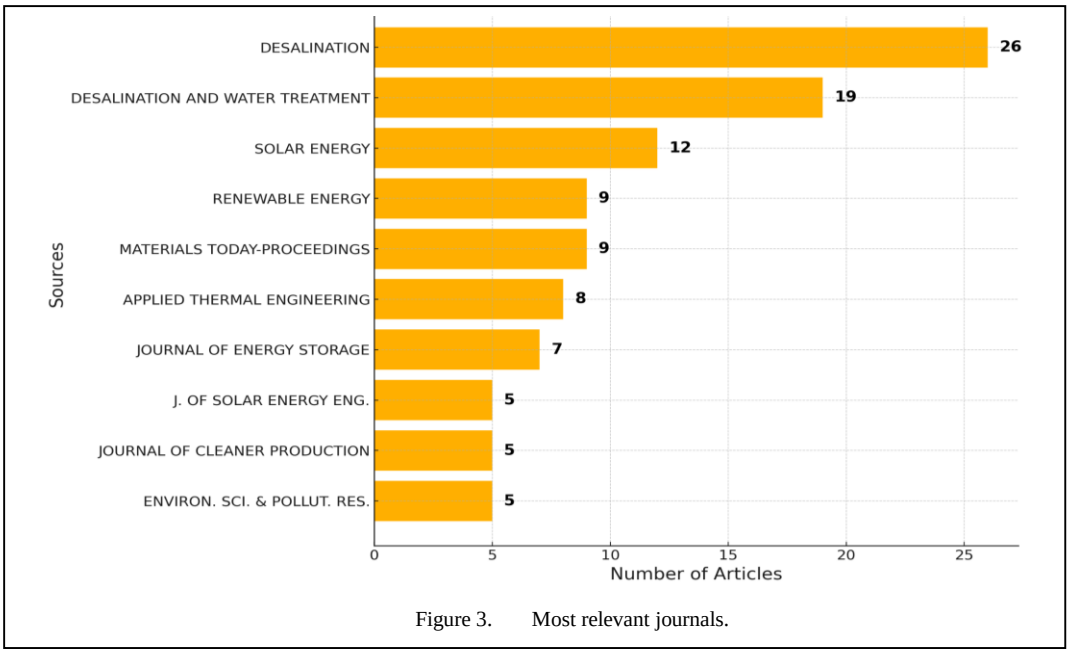

Figure 3. Most relevant journals.

reinforces this trend, highlighting the importance of thermal efficiency in the development of new desalination technologies.

However, the analysis reveals a reduced number of publications among the subsequent journals in the list. Journals such as Journal of Energy Storage (7 articles), Journal of Solar Energy Engineering (5 articles), Journal of Cleaner Production (5 articles), and Environmental Science and Pollution Research (5 articles) contribute with a relatively smaller number of publications. This indicates that, although energy storage and sustainable production are relevant aspects of desalination using parabolic concentrators, they are not yet the primary focus of investigation in the literature, which may indicate potential gaps and opportunities for further research in these areas.

The results obtained highlight the necessity of exploring new topics and diversifying publication channels, thus expanding the reach of the research and promoting greater integration among different fields of knowledge. Furthermore, the presence of journals focused on energy and thermal engineering shows that advancements in the area are strongly linked to efficient energy solutions, reinforcing the importance of research on process optimization and energy efficiency.

C. Article Publication Over the Years

As shown in the graph in Fig. 4, there is an expressive growth in the number of scientific publications on the topic over the last few years, peaking around 2022. Starting from this period, a decreasing trend is observed, possibly associated with the impacts of the Covid-19 pandemic, which to some extent limited research activities and the operation of academic institutions.

Concerns about water scarcity, sustainability, and climate change have been driving research in the field of thermosolar desalination [15,16]. Furthermore, according to [16], the increase in publications in the research field is related to technological advancements and efforts to overcome the main challenge of thermosolar desalination units, which is their efficiency and productivity. This statement corroborates the [5], who mentions that increasing efficiency has become one of the priorities on the research agenda in the field of concentrated thermosolar desalination.

Important areas aiming for improved performance have been researched, such as: integrated systems with parabolic concentrators [17,18], an approach which generally maximizes

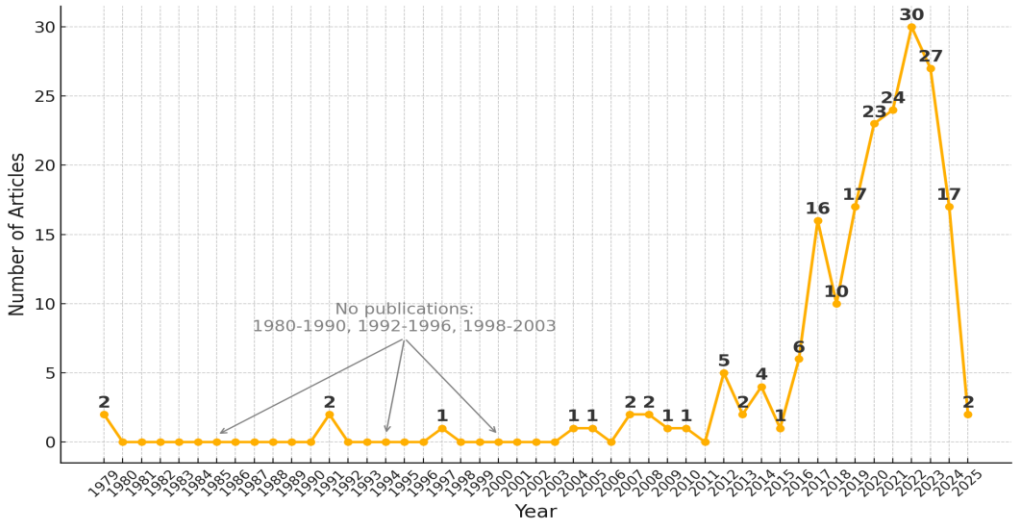

Figure 4. Annual scientific production.

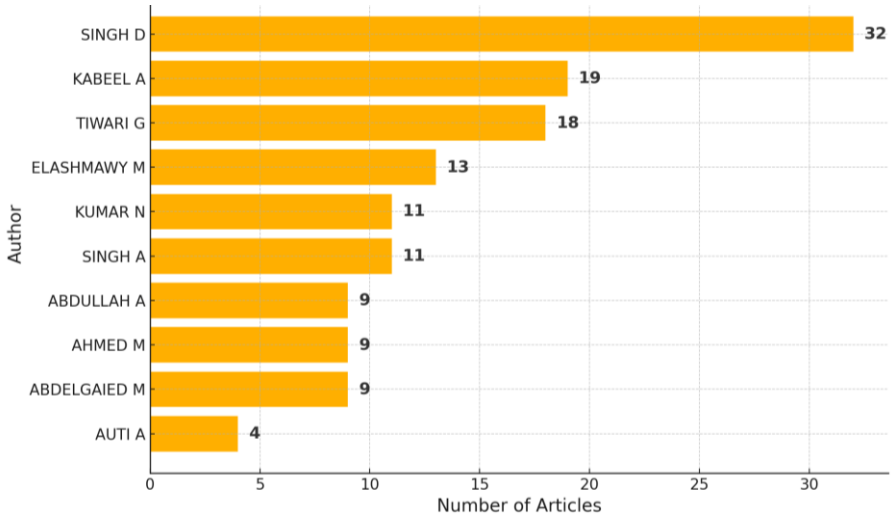

Figure 5. Most relevant authors.

the system's overall thermal efficiency and productivity. Additionally, the use of Phase Change Materials (PCMs) and nanomaterials helps to improve performance and heat transfer [19,20].

Thus, based on the research cited in this topic [5-20], the motivations for this work are related to technological development and the recognition of sustainable and efficient solutions aimed at tackling water scarcity

D. Leading Authors

Fig. 5 presents the top ten most productive authors in this research field. Of the 197 studies analyzed in this bibliometric review, the researchers listed in Fig. 5 are responsible for 63.9% of the identified scientific output. This result shows the concentration of knowledge in a restricted group of authors, highlighting the importance of encouraging the participation of new researchers, either through government funding policies or private initiatives. As one progresses through the list, it reinforces the notion that scientific output is concentrated among a few researchers, highlighting the necessity for a broader dissemination of the topic.

The top three authors on the list, Singh, D., Kabeel, A., and Tiwari, G., are solely responsible for 54.7% of the publications in the ranking.

Identifying these researchers is fundamental, as it offers immediate guidance to the core literature in the area, in addition to forming a pillar for the establishment and strengthening of scientific collaboration networks.

E. Research Gaps and Future Directions

Despite the numerous studies conducted in recent years, there remain opportunities for further research and investigation. According to [21], experimental studies that employ parabolic concentrators as the primary heat source in integrated multi-stage flash (MSF) desalination systems are insufficient.

This represents an opportunity for research and investigation, as the lack of robust data, specifically regarding this integration (Parabolic Concentrator + MSF), hinders the accurate estimation of the cost per liter produced in systems of this nature.

There remain important avenues to be explored in the field of operation and maintenance of commercial-scale systems. Although the review conducted by [22], presents data on the yield and productivity of various desalination systems with parabolic concentrators, it becomes evident that the scarcity of information, resulting from the lack of long-term practical experimentation, limits the execution of fundamental studies on the reliability, maintenance, and failure-associated cost of these systems.

The study entitled: 'Concentrating Solar Power: The State of the Art, Research Gaps and Future Perspectives', highlights that although there are notable efforts and results in the field of efficiency and system integration, important gaps exist related to potable water production, especially regarding the environmental analysis of these systems [23]. It is evident that there is an absence of work that comprehensively considers the environmental impacts, Greenhouse Gas (GHG) emissions, the use of materials, and the complete life cycle, from manufacturing to disposal.

Addressing this gap would not only allow for a better understanding of the sustainability of these systems but would also provide the basis for optimizing their design and operation.

IV. CONCLUSION

The use of the Scopus and Web of Science databases enabled the investigation of data composed of 192 scientific publications related to the field of desalination using parabolic concentrators.

Despite having the highest number of publications within the scope of this review, India still demonstrates low scientific interaction with other countries, a factor that could significantly contribute to accelerating its technological advancements.

The annual scientific output served as a measure of researchers' interest in the topic, revealing an upward trend in recent years. This fact reflects concerns related to water scarcity, climate change, and sustainability. Furthermore, there is a continuous focus on the search for more efficient and technologically advanced systems.

This review highlighted relevant gaps and opportunities for future research. Among these, the need for more robust experimental data that allows for a more precise estimation of the cost per liter produced in systems integrating parabolic solar concentrators and MSF units is noteworthy. Furthermore, the scarcity of long-term data from systems in real operation still represents a significant obstacle for reliability and maintenance strategy analyses.

ACKNOWLEDGMENT

(1) Federal Institute of Paraíba - IFPB, Cajazeiras Campus and Federal University of Paraíba-UFPB, João Pessoa Campus. (2) FAPESQ – Paraíba State Research Foundation. Agreement No. 038/2023, Call No. 19/2022. (3) CNPq – National Council for Scientific and Technological Development. Call No. 10/2023, Process: 405925/2023-9. (4) Agreement No. 053/2025, Paraíba State Research Foundation (FAPESQ). Grant #2025/053-d, Paraíba State Research Foundation (FAPESQ)

REFERENCES

[1] Jamil, F., Hassan, F., Shoeibi, S., & Khiadani, M. (2023). Application of advanced energy storage materials in direct solar desalination: A state of art review. *Renewable and Sustainable Energy Reviews, 186*, 113663. https://doi.org/10.1016/j.rser.2023.113663

[2] World Health Organization, United Nations Children's Fund, & World Bank. (2022). *State of the world's drinking water: An urgent call to action to accelerate progress on ensuring safe drinking water for all*. World Health Organization. https://www.who.int/publications/i/item/9789240060807

[3] Qaid, A. R., Baqir, A. S., & Almoussawi, M. (2023). Water desalination by parabolic concentrator: A review. *AIP Conference Proceedings, 2776*(1), 060008. https://doi.org/10.1063/5.0136245

[4] Kalogirou, S. A. (2009). *Solar energy engineering: Processes and systems* (2nd ed.). Elsevier.

[5] Khanmohammadi, S., & Khanjani, S. (2021). Experimental study to improve the performance of solar still desalination by hydrophobic condensation surface using cold plasma technology. *Sustainable Energy Technologies and Assessments, 45*, 101129. https://doi.org/10.1016/j.seta.2021.101129

[6] Fang, H., Fang, F., Hu, Q., & Wan, Y. (2022). Supply Chain Management: A Review and Bibliometric Analysis. *Processes, 10*(9), 1681. https://doi.org/10.3390/pr10091681

[7] Aria, M., & Cuccurullo, C. (2017). bibliometrix: An R-tool for comprehensive science mapping analysis. *Journal of Informetrics, 11*(4), 959–975. https://doi.org/10.1016/j.joi.2017.08.007

[8] Ihaka, R., & Gentleman, R. (1996). R: A Language for Data Analysis and Graphics. *Journal of Computational and Graphical Statistics, 5*(3), 299–314. https://doi.org/10.1080/10618600.1996.10474713

[9] Gonçalves, G., Gaudencio, L., & Oliveira, R.(2023). Sustainable Location of Solar Plants: An Integrated Bibliometric Approach on Gis-multi-criteria Methods. In L. Z. Velimirović (Ed.), *eNergetics 2023: 9th Virtual International Conference on Science, Technology and Management in Energy - Proceedings* (pp. 153-160). COSREC.https://energetics.cosrec.org/wp-content/uploads/2024/03/eNergetics_2023.pdf

[10] Matos, A. P., Araujo, A. P. F., & Fernandes, P. R. F. (2023). Copper Ferrites and Solar Radiation in the Removal of Rhodamine B: A Bibliometric Approach In L. Z. Velimirović (Ed.), *eNergetics 2023: 9th Virtual International Conference on Science, Technology and Management in Energy - Proceedings* (pp. 153-160). COSREC.https://energetics.cosrec.org/wp-content/uploads/2024/03/eNergetics_2023.pdf

[11] Zhu, J., & Liu, W. (2020). A tale of two databases: The use of Web of Science and Scopus in academic papers. *Scientometrics* (2020), *123*, 321–335. https://doi.org/10.1007/s11192-020-03387-8

[12] Lisée, C., Larivière, V., & Archambault, É. (2008). Conference proceedings as a source of scientific information: A bibliometric analysis. *Journal of the American Society for Information Science and Technology, 59*(11), 1776-1784. https://doi.org/10.1002/asi.20888

[13] Jena, M. C., Misha, S. K., & Moharana, H. S. (2023). Water Sustainability initiatives to meet the water crisis in India. *Journal of Chemical Engineering Research Updates, 10*, 18-30. https://doi.org/10.15377/2409-983X.2023.10.2

[14] Vishwakarma, P., & Kumar, N. (2023). Water Scarcity in India and its Conservation Strategies. *Journal of Applied Bioscience, 49*(1 & 2), 68–76. Avaliable at: https://www.taaleem.in/ojs/index.php/joab/article/view/211

[15] Apolinário, R., & Castro, R. (2024). Solar-Powered Desalination as a Sustainable Long-Term Solution for the Water Scarcity Problem: Case Studies in Portugal. *Water, 16*(15), 2140. https://doi.org/10.3390/w16152140

[16] Alwan, N. T., Ali, B. M., Alomar, O. R., Abdulrazzaq, N. M., Ali, O. M., & Abed, R. M. (2024). Performance of solar still units and enhancement techniques: A review investigation. *Heliyon, 10*(18), e37693. https://doi.org/10.1016/j.heliyon.2024.e37693

[17] Ahmed, M. M. Z., Alshammari, F., Alatawi, I., Alhadri, M., & Elashmawy, M. (2022). A novel solar desalination system integrating inclined and tubular solar still with parabolic concentrator. *Applied Thermal Engineering, 213*, 118665. https://doi.org/10.1016/j.applthermaleng.2022.118665

[18] AlQdah, K. S., Alharbi, K. A., Alharbi, S. A., Almutairi, M. A., Alsuhimi, O. M., & Aljuhani, M. S. (2022). Design, fabrication and performance evaluation of a semi-cylindrical solar still working in Medina region. *Arabian Journal for Science and Engineering, 47*(7), 8567-8575. https://doi.org/10.1007/s13369-021-06351-7

[19] Rashid, F. L., Al-Obaidi, M. A., Dulaimi, A., Bahlol, H. Y., & Hasan, A. (2023). Recent Advances, Development, and Impact of Using Phase Change Materials as Thermal Energy Storage in Different Solar Energy Systems: A Review. *Designs, 7*(3), 66. https://doi.org/10.3390/designs7030066

[20] Alarifi, I. M., Abo‐Khalil, A. G., Al‐Qawasmi, A. R., Alharbi, W., & Alobaid, M. (2021). On the effects of nanomaterials on the performance of solar distillation systems: A comprehensive review. *Solar Energy, 218*, 596‐610. https://doi.org/10.1016/j.solener.2021.03.018

[21] Babaeebazaz, A., Gorjian, S., & Amidpour, M. (2021). Integration of a Solar Parabolic Dish Collector with a Small-Scale Multi-Stage Flash Desalination Unit: Experimental Evaluation, Exergy and Economic Analyses. *Sustainability, 13*(20), 11295. https://doi.org/10.3390/su132011295

[22] Mohammed, A. H., Shmroukh, A. N., Ghazaly, N. M., & Kabeel, A. E. (2023). Active solar still with solar concentrating systems, Review. *Journal of Thermal Analysis and Calorimetry, 148*(17), 8777–8792. https://doi.org/10.1007/s10973-023-12285-z

[23] Ferruzzi, G., Delcea, C., Barberi, A., Di Dio, V., Di Somma, M., Catrini, P., Guarino, S., Rossi, F., Parisi, M. L., Sinicropi, A., & Longo, S. (2023). Concentrating Solar Power: The State of the Art, Research Gaps and Future Perspectives. *Energies, 16*(24), 8082. https://doi.org/10.3390/en16248082

eNergetics 2025
DOI: https://doi.org/10.5281/zenodo.18631467

Original Scientific Article

Numerical Study of Turbulent Premixed Flames of CH_4-H_2-NH_3

Sofiane Ouali[1]

[1]Laboratory of Energy, Mechanics and Engineering LEMI, Faculty of Technology, University M'Hamed Bougara UMBB of Boumerdes, Algeria

[1]s.ouali@univ-boumerdes.dz

Abstract—**This work presents a numerical study of premixed combustion of a mixture composed of methane (CH_4), hydrogen (H_2), and ammonia (NH_3). The main objective is to evaluate the effect of adding H_2 and NH_3 on CH_4 flame stability, combustion temperature, and the formation of nitrogen oxides (NOx). The simulations were carried out using the ANSYS Fluent software for different proportions of ammonia (from 0% to 25%) with a constant hydrogen rate of 50%. The results show that an increase in NH_3 leads to a slight decrease in the maximum flame temperature (from 1920K to 1790K) and a significant reduction in NOx emissions. Hydrogen, for its part, improves the reactivity and stability of the combustion. Thus, the CH_4–H_2–NH_3 combination makes it possible to obtain a cleaner and more stable combustion, constituting a promising path toward the decarbonization of energy systems and the development of sustainable technologies.**

Keywords - ammonia combustion, hydrogen enrichment, premixed flames, nitrogen oxides, CFD simulation.

I. INTRODUCTION

Climate change and energy challenges demand an urgent reduction of greenhouse gases. This can be achieved by managing combustion processes and diversifying energy sources to counteract fossil fuel consumption.

The use of ammonia (NH_3) and hydrogen (H_2) is one of the solutions pursued by researchers, particularly those aiming to reduce carbon emissions. Knowing that the combustion of H_2 is completely carbon-free [1] and that NH_3 is a molecule derived from waste and can be produced from renewable sources [2], the combination of the two with CH_4 presents a scientific challenge.

NH_3 has a low flame speed and produces a significant amount of NOx at high temperatures [3]. H_2, on the other hand, has high reactivity, leading to risks of flashback and combustion instabilities [4]. Their combination with CH_4 can yield a balanced and usable fuel.

Recent research has studied CH_4–H_2–NH_3 flames that exploit the significant reactivity of H_2 to compensate for the relatively low reactivity of NH_3 in order to benefit from its carbon-free composition [5]. Kobayashi et al. [3] demonstrated that adding H_2 to NH_3-CH_4 mixtures significantly improves flame speed, reaching levels comparable to pure CH_4 at an H_2 concentration of 40%. Similarly, studies by Valera-Medina and all [6,7] showed that mixtures composed of 70% NH_3 and 30% H_2 produce stable combustion under rich conditions, with NO_x emissions lower than 50ppm in optimized burner configurations designed for gas turbine power generation.

This study is a numerical simulation of the addition of NH_3 to turbulent premixed flames of CH_4-H_2. It focuses on the thermal field, dynamic field, and NOx emissions.

II. METHODOLOGY

A. Numerical Setup and Geometry

Numerical Simulations were conducted using ANSYS Fluent software [8], Computational domain reproduces a High Generic Swirl Burner

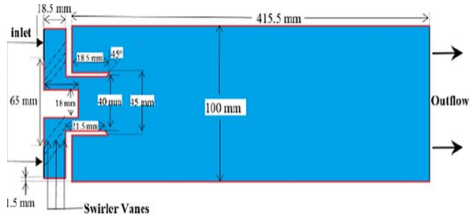

Figure 1. Geometry [9].

(HPGSB 2nd generation) designed by [6] for gas turbine power generation. The geometry comprises a cylindrical combustion chamber with 434 mm length, 100 mm diameter and 9 radial swirl vanes positioned at the inlet generating the tangential component of the axial flow (Fig. 1).

This swirled flow technology promotes optimal fuel-air mixing and flame stabilization through the establishment of central recirculation zones (CRZ) and outer recirculation zone (ORZ) [7].

B. Mesh Discritisation

A uniform hexahedral grid was adopted comprising 1.75 million nodes. This mesh was already studied in details by Ouali [9].

The mesh was refined at the swirler inlet and along the lateral walls throughout the combustion chamber, which are regions where strong gradients of the studied variables were observed. In our previous work [9], we found that beyond 1.75 million nodes (Fig. 2), the solution became grid-independent. This finding justifies our choice.

C. Numerical Parameters and Operating Conditions

Six cases were investigated with varying NH_3 concentration (0, 5, 10, 15, 20, 25% by volume) while maintaining H_2 at constant 50% and adjusting CH_4 accordingly to preserve mixture composition and LHV. All simulations operated under identical conditions: inlet temperature of 573K, equivalence ratio $\varphi = 0.6$ (lean premixed case), and constant power of 12kW. Thermodynamic properties including thermal conductivity (λ), dynamic viscosity (η), and lower heating values (LHV) were calculated using GASEQ software for each mixture composition, ensuring accurate representation of fuel blend characteristics [10].

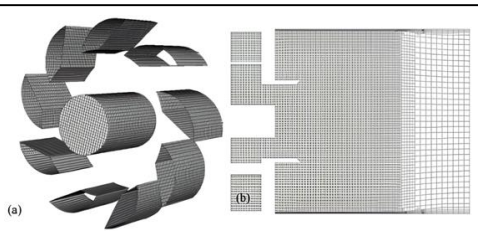

Figure 2. Mesh grid [9].

Mass fractions were calculated according to stoichiometric relationships for the general combustion equation [11] Eq. (1):

$$(1-\alpha-\beta)CH_4 + \alpha H_2 + \beta NH_3 + \\ + \left(x - \frac{3}{2}\alpha - \frac{3}{4}\beta + 2\right)(O_2 + 3.76N_2), \quad (1)$$

where α and β represent molar fractions of hydrogen and ammonia respectively, and x denotes the oxygen requirement parameter [11] defined as follow Eq. (2):

$$x = \frac{3}{2}\alpha + \frac{3}{4}\beta + \frac{2 - \frac{3}{2}\alpha - \frac{3}{4}\beta}{\phi} - 2 . \quad (2)$$

D. Physical Models

Reactive flows are governed by fluid mechanics equations coupled with those of aero-thermochemistry. RANS Realizable κ - ε turbulence model was employed to treat turbulence; it can determine the length of turbulence and the time scale independently by solving two transport equations [8]. It is based on models of transport equations for the turbulence kinetic energy (κ) and its dissipation rate (ε). The transport model equation is derived from the exact equation, while the model transport equation for ε is obtained using physical deduction [11].

To treat combustion, partially premixed model (PDF) was used. It is a form of premixed flames model with non-uniform fuel-oxidizer mixtures. We used Zimont model for calculating turbulent flame speed and, TFC model for premixed flame and a PDF for turbulence chemistry coupling who calculates a progress variable "C" considering chemical species in chemical equilibrium, where $c = 0$ for unburned

mixture and $c=1$ for burned mixture. The flame front zone is characterized by c values between 0.4 and 0.6 [8,11].

NO model was also used to predict NOx pollutants. Additional equations are injected into the equation of chemical species conservation and the thermal NO formation is determined by a series of chemical reactions which depend strongly on the temperature which is known as the Zeldovich mechanism [8,11].

III. Results And Discussions

A. Temperature Evolution

The temperatures obtained in this study show a progressive decrease in the maximum flame temperature with increasing NH_3 concentration (Fig. 3). The maximum temperature drops from 1920K at 0% NH_3 to 1790K at 25% NH_3, representing a reduction of approximately 130K, which corresponds to about 6.8%. This decrease results from the low reactivity of NH_3 and its low energy content (low LHV) compared to H_2 or CH_4, leading to a reduction in the heat release rate and an increase in the thermal capacity of the reactive mixture.

This temperature decrease significantly affects the combustion process and the formation of thermal NO_x. The observed 130K reduction corresponds to crossing critical temperature thresholds that govern the mechanisms of thermal NO_x formation, which exhibit an exponential dependence on temperature [12].

B. Dynamic Field

The velocity field analysis indicates an axial acceleration of the flow with increasing NH_3 concentration (Fig. 4). The maximum axial velocities increase from approximately 0.484m/s (0% NH_3) to 0.502m/s (25% NH_3). This acceleration results from the thermal expansion of combustion products and the volumetric expansion associated with high flame temperatures. Additionally, the increase in velocity stems from the adjustment of fuel mass flow rates, which maintains a constant burner power despite the lower LHV of NH_3 (43.12MJ/kg at 25% NH_3 compared to 57.78MJ/kg at 0% NH_3). This compensation strategy ensures a consistent thermal input throughout the cases studied.

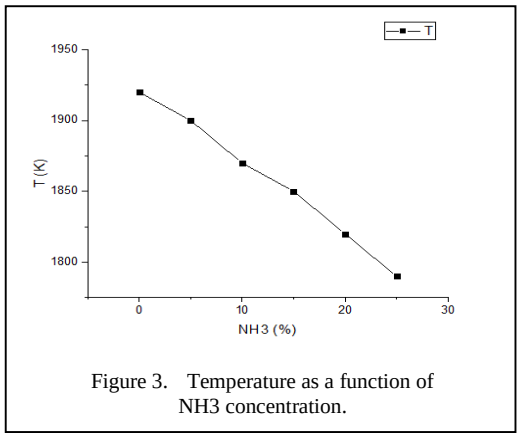

Figure 3. Temperature as a function of NH3 concentration.

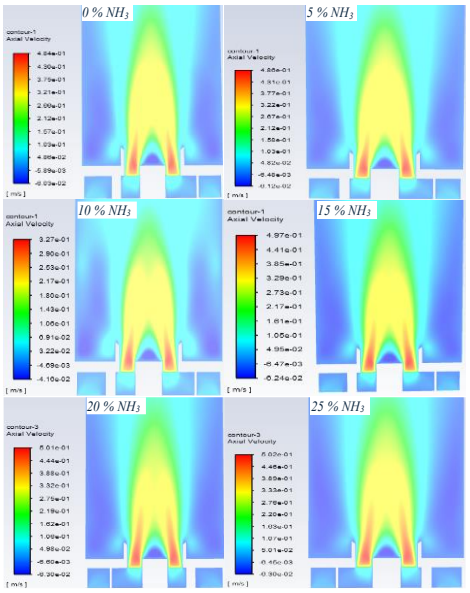

Figure 4. Dynamic field.

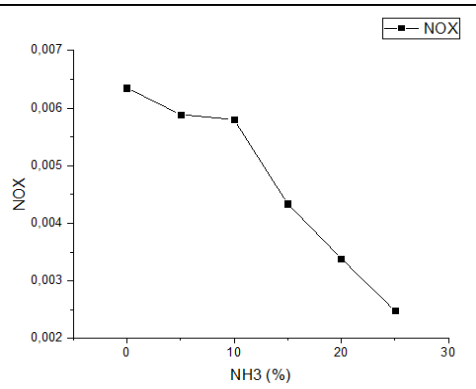

Figure 5. NO_x as a function of NH_3 concentration.

C. NO_x Emission

The most significant result concerns nitrogen oxide emissions. The NO_x mass fraction decreased from 0.00635 (0% NH_3) to 0.00248 (25% NH_3), representing a 61% reduction across

the entire range of ammonia compositions (Fig. 5).

This reduction can be explained by the Zeldovich mechanism: the temperature drop of nearly 130K is the direct cause of the decrease in NO_x concentration. The lean equivalence ratio $(\varphi = 0.6)$ used in this study promotes NO_x reduction by maintaining lean combustion conditions. Moreover, although ammonia introduces molecular nitrogen into the fuel stream, its nitrogen content paradoxically favors conversion pathways that produce N_2 rather than NO_x under these lean combustion conditions.

IV. Conclusion

Numerical simulations on the use of NH_3 as a fuel in a premixed CH_4 -H_2 reactive mixture were conducted. The adopted geometry is a cylindrical combustion chamber designed for gas turbine applications generating electricity.

Mesh sensitivity analysis and validation of the physical models were extensively discussed in our previous work. Six simulation cases were carried out, ranging from 0% to 25% NH_3 in 5% increments. The most important findings were as follows:

- The heat release rate decreases with the addition of NH_3, and the flame temperature drops by nearly 130 K. This reduction is particularly significant as it approaches the threshold for NO_x formation.
- The flow elongates; flames become longer but remain stable, with strong Outer Recirculation Zones (ORZ) and Central Recirculation Zones (CRZ) that ensure acceptable flame anchoring. This is due to the increased reactant flow rate used to compensate for NH_3 's low LHV, thereby maintaining constant burner power.
- A marked reduction in NO_x emissions was observed, attributed to the lower heat release rate—nearly 60% reduction for 25% NH_3 addition. This remains the most significant result of the study.

To generalize these findings, future work is needed:

- Use of more accurate turbulence models
- Investigation under transient operating conditions
- Implementation of a detailed chemical kinetics model
- Testing higher NH_3 concentrations beyond 25%

References

[1] Schefer, R. W., Wicksall, D. M., & Agrawal, A. K. (2002). Combustion of hydrogen-enriched methane in a lean premixed swirl-stabilized burner. *Proceedings of the combustion institute*, *29*(1), 843-851.

[2] Morlanés, N., Katikaneni, S. P., Paglieri, S. N., Harale, A., Solami, B., Sarathy, S. M., & Gascon, J. (2021). A technological roadmap to the ammonia energy economy: Current state and missing technologies. *Chemical Engineering Journal*, *408*, 127310.

[3] Kobayashi, H., Hayakawa, A., Somarathne, K. K. A., & Okafor, E. C. (2019). Science and technology of ammonia combustion. *Proceedings of the combustion institute*, *37*(1), 109-133.

[4] Lhuillier, C., Brequigny, P., Contino, F., & Mounaïm-Rousselle, C. (2020). Experimental study on ammonia/hydrogen/air combustion in spark ignition engine conditions. *Fuel*, *269*, 117448.

[5] Li, R., Konnov, A. A., He, G., Qin, F., & Zhang, D. (2019). Chemical mechanism development and reduction for combustion of NH3/H2/CH4 mixtures. *Fuel*, *257*, 116059.

[6] Valera-Medina, A., Morris, S., Runyon, J., Pugh, D. G., Marsh, R., Beasley, P., & Hughes, T. (2015). Ammonia, methane and hydrogen for gas turbines. *Energy Procedia*, *75*, 118-123.

[7] Valera-Medina, A., Gutesa, M., Xiao, H., Pugh, D., Giles, A., Goktepe, B., ... & Bowen, P. (2019). Premixed ammonia/hydrogen swirl combustion under rich fuel conditions for gas turbines operation. *International Journal of Hydrogen Energy*, *44*(16), 8615-8626.

[8] ANSYS, Inc. (2023). *ANSYS Fluent Theory Guide 2023: Conservation Equations, Turbulence, Combustion, and Pollutant Models*. ANSYS, Inc.

[9] Ouali, S. (2024). Numerical simulation of H2 addition effect to CH4 Premixed turbulent flames for gas turbine burner. *Journal of Applied Fluid Mechanics*, *17*(8), 1746-1758

[10] Chai, W. S., Bao, Y., Jin, P., Tang, G., & Zhou, L. (2021). A review on ammonia, ammonia-hydrogen and ammonia-methane fuels. *Renewable and Sustainable Energy Reviews*, *147*, 111254.

[11] Turns, S. R. (1996). *Introduction to combustion*. McGraw-Hill Companies.

[12] Lee, J. H., Kim, J. H., Park, J. H., & Kwon, O. C. (2010). Studies on properties of laminar premixed hydrogen-added ammonia/air flames for hydrogen production. *International journal of hydrogen energy*, *35*(3), 1054-1064.

eNergetics 2025
DOI: https://doi.org/10.5281/zenodo.18631505

Original Scientific Article

Experimental Investigations on Solar Water Heater Performance Enhancement using Nanofluids

Natesan Kapilan[1], Vijeesh Vijayan[2], Shivarishika K.[3], Gnanavel Balaji[4], Abu Saleh Ahmed[5]

[1]NITTE (Deemed to be University), Nitte Meenakshi Institute of Technology, Bangalore, India
[2]NITTE (Deemed to be University), NMAM Institute of Technology, Karkala, India
[3]Ramaiah Institute of Technology, Bangalore, India
[4]SRM Institute of Science and Technology, Kattankulathur, Chennai, India
[5]University of Technology Sarawak, Sarawak, Malaysia

[1]kapil_krecmech@yahoo.com, [2]vijeeshv@nitte.edu.in, [3]shivarishikakapilan@gmail.com, [4]balajig@srmist.edu.in, [5]abusaleh@uts.edu.my

Abstract—**The depletion of conventional fuel and increase in global warming due to burning of the conventional fuel forces researchers to concentrate on development of non-conventional energy sources. The solar energy can be converted into solar thermal energy using solar water heater tubes. The energy conversion efficiency of solar radiation into thermal energy can be improved by many methods. In this work, we used nanofluids to increase the thermal energy conversion with aluminum oxide with dosage of 0.25, 0.5, 0.75 and 1%. From this work, we observed that the use of nanofluids increases the solar energy absorption and increases the energy conversion efficiency. It is suggested from this work that the use of nanofluid increases the performance of the solar water heater.**

Keywords – alternative energy, renewable energy, solar, water heater, performance.

I. INTRODUCTION

There can be several reasons for an increase in fossil fuel consumption. Here are some of the common factors that contribute to such an increase: Fossil fuels, such as coal, oil, and natural gas, have traditionally been the primary sources of energy for industries, transportation, and residential use. As economies grow and industrialize, there is often an increased demand for energy, leading to higher consumption of fossil fuels. As the global population continues to increase, so does the demand for energy. More people require energy for their daily activities, including heating, cooking, transportation, and electricity generation. Fossil fuels have been the dominant energy source for meeting these growing demands. Many developing countries are experiencing rapid industrialization and urbanization. As they strive to improve their living standards, they often rely on fossil fuels to meet their increasing energy needs. These countries may lack the infrastructure or resources to shift quickly to alternative energy sources, leading to a rise in fossil fuel consumption. While renewable energy sources like solar, wind, and hydroelectric power are gaining momentum, the infrastructure for harnessing and distributing these energy sources is still developing in many regions. As a result, fossil fuels continue to dominate the energy mix and hence necessary to find suitable sustainable renewable energy fuels [1]. The demand of the energy requirement increases due to increase in demand for the air conditioning systems [2]. Various forms are renewable energy sources are available and solar energy is most popular. Advancements in solar

ISBN: 978-86-82602-07-1

technology, such as improved efficiency and reduced costs of solar conversion devices, have made solar energy more accessible and economically viable for both residential and commercial use. However, there are several methods to enhance the solar energy conversion [3]. The use of conventional refrigerants causes ozone layer depletion and hence solar power-driven alternative cooling system is getting attention [4].

The demand for solar water heaters has been steadily increasing over the past decade due to several factors: As people become more aware of the environmental impact of traditional energy sources and the need to reduce carbon emissions, there has been a rising demand for renewable energy solutions such as solar power. The solar water heater (SWH) can significantly reduce energy bills by utilizing sunlight to heat water instead of relying solely on electricity or gas. As energy costs continue to rise, the potential for long-term savings becomes more appealing to consumers. The SWH is popular due to its design, low operating and maintenance cost etc. [5]. A parabolic dish reflector collector is a type of solar thermal energy system that uses a parabolic dish-shaped reflector to concentrate sunlight onto a receiver at the focal point of the dish. It is also known as a parabolic dish concentrator or a solar dish and results in better performance [6]. In building, the use of SWH reduces the energy consumed by the conventional system by 70% and the SWH is fitted with auxiliary electrical heat source to produce hot water during winter and monsoon [7]. There are various methods of improving the performance of SWH and one method is mixed asphalt SWH [8].

A solar PVT system, also known as a photovoltaic thermal system, combines both solar photovoltaic (PV) and solar thermal technologies in a single integrated system. It allows for the simultaneous generation of electricity and thermal energy using the same solar panel and this type of system increases the energy conversion and minimizes the energy consumption by 75% [9].

The use of phase change materials (PCMs) with solar water heaters can enhance their thermal performance and improve energy storage capabilities. PCMs are substances that can store and release thermal energy by undergoing a phase transition, such as from solid to liquid or liquid to gas, at a specific temperature. The integration of PCM with SWHS increases the capacity of the energy storage [10]. The PCM results in longer heat release duration and residential application the PCM with melting point from 40 to 80 °C [11]. The use of vacuum tube reduces the heat loss from the SWH and the use of metal foams enhances the heat transfer in the SWH [12].

A study was conducted on solar flat plate SWH with nanofluid (NF) prepared using titanium oxide (TiO_2) with the its dosage of 0.1, 0.3, 0.5, 0.7 and 1% and it is reported that the performance of this type of system increases with increase in TiO2 dosage and the better performance was obtained with 1% [13]. The numerical work performed on SWH shows that the NF enhances the performance of SWH due to increase in thermal conductivity which causes improvement in heat transfer [14]. The heat transfer in evacuated tube SWH is improved with the NF based nano particle, preferably TiO_2, SiO2, copper nanoparticle [15]. It's important to note that the selection and optimization of nanoparticles for solar water heaters require careful consideration of factors such as nanoparticle type, concentration, stability, and compatibility with the system components. The use of heat pipe in SWH enhances the heat transfer and use of NF in heat pipe improves the heat transfer significantly [16]. The experiments conducted on the SWH with natural convection provided with evacuated glass U-tube SWH shows that this system with the inclined collector results better performance than the vertical collector [17].

Generally, the value of solar radiation reaches the maximum value during noon and causes higher thermal efficiency and the higher efficiency obtained is about 67% [18]. The experiments performed on the water-in-glass evacuated SWH shows that this type of system is better than flat plate SWH as the heat loss in evacuated tube SWH is less and this type of system are preferred for residential application [19]. A comparison tests conducted on hybrid SWH and normal SWH shows that the hybrid SWH is better than the normal SWH [20].

II. Materials and Methodology

A commercially available evacuated SWH tubes were used in this work, NF and stainless steel (SS) tube was used as replacement to commercially available SWH heat pipe as it is expensive. Table I represents the details of the solar water heater tube. The aluminum oxide

(Al_2O_3) was used as nanoparticle as it has better thermal conductivity and Table II represents the properties of the Al_2O_3. Fig. 1 shows the SEM image of the Al_2O_3.

TABLE I. SPECIFICATIONS OF THE SOLAR WATER HEATER TUBE.

Description	Value
Overall length (mm)	1800
Diameter (Outer) (mm)	58
Diameter (Inner) (mm)	47
Thickness (mm)	1.6
Coating (Absorptive)	Al-N/Al (Graded)

TABLE II. PROPERTIES OF AL_2O_3.

Property	Value
Size (Average) (nm)	30 to 79
Colour	White
Weight (Molecular) (g/mol)	103
Density (g/cm^3)	0.51
Morphology	Spherical
Melting temperature (ºC)	2025

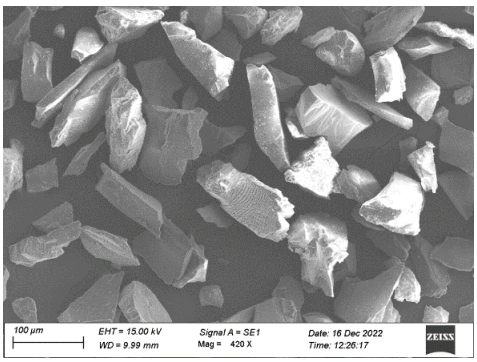

Figure 1. SEM Image of the AL2O3.

Figure 2. Ultrasonicator.

The aluminum oxide (Al_2O_3) was used as nanoparticle in this work and it was added to the water. The ultrasonicator was used to prepare the homogenous mixture and the dosage of Al_2O_3 considered in this work are 0.25, 0.5, 0.75 and 1% wt of water. Initially the NF was filled in the SWH tube and then SS tube. A pyranometer and thermocouple were used to measure the solar radiation and water temperature respectively. The temperature profile of the surface of the water heater was recorded using thermal imaging camera. The experiment was conducted in the morning and experiments were conducted till the temperature of the water reaches 90°C. Fig. 2 shows the ultrasonicator used in this work.

A. Experimental Setup

The schematic of the SWH tube with NF and SS tube is shown in Fig. 3. It is a type of solar thermal collector used in SWH system and consists of a series of glass tubes, each with a selective absorber coating and an air-free (evacuated) space inside. Each evacuated tube is a cylindrical glass tube with two layers. The outer layer is made of borosilicate glass, which provides thermal insulation and protects the inner components. The inner layer is coated with a selective absorber coating, typically made of a metal or ceramic material that maximizes solar energy absorption. When sunlight strikes the outer layer of the evacuated tube, the selective absorber coating absorbs the solar radiation. The absorbed solar energy is converted into heat.

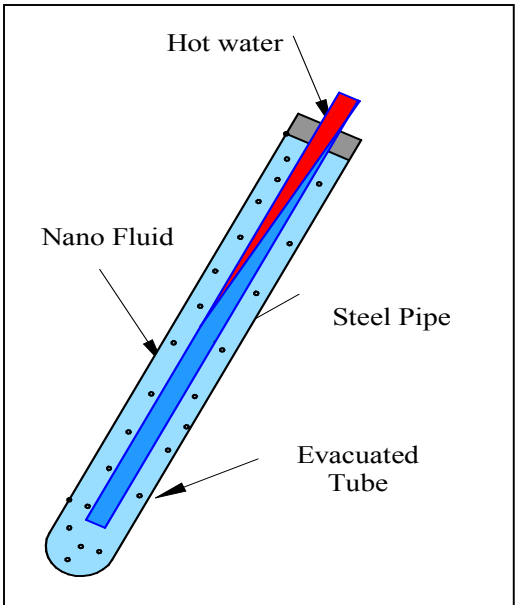

Figure 3. Schematic of test setup.

The absorbed heat is transferred to a heat transfer medium, NF. The evacuated SWH operate passively, relying on natural circulation and convection currents to transfer heat. There are no moving parts or mechanical components involved. The use of Al_2O_3 NF will have impact on the heat transfer.

III. RESULTS AND DISCUSSION

Fig. 4 shows the variation in solar radiation at different timing. Since the experiment was started at 11.00 AM, the solar radiation value increases with increase in time. The maximum solar radiation of 958 was recorded at 2 PM. The primary driver of temperature change throughout the day is solar radiation from the Sun. In the morning, when the Sun rises, solar radiation begins to reach the Earth's surface. However, the angle at which the sunlight hits the surface is relatively low, resulting in less direct heating. As the day progresses and the Sun rises higher in the sky, the angle of sunlight becomes more direct, leading to greater heating and an increase in air temperature. There is a time lag between the peak intensity of solar radiation and the maximum air temperature. This delay occurs because it takes some time for the Earth's surface and the atmosphere to reach thermal equilibrium with the incoming solar radiation. Consequently, the peak air temperature typically occurs in the afternoon, after the peak intensity of solar radiation around midday.

Fig. 5 depicts the temperature of water at different timing and it is observed that the water temperature increases with time due to increase in solar radiation. The use of NFs in SHW leads to higher water temperatures due to the enhanced heat transfer properties of the Al_2O_3 NF as the Al_2O_3 has high thermal conductivity and a large surface area, which enables them to transfer heat more efficiently than the base fluid alone. This allows for greater efficiency in converting solar energy into heat, leading to increased hot water temperatures. However, it is important to note that the specific temperature increase will depend on various factors such as the type and concentration of nanoparticles used, the design of the solar water heater, and the prevailing environmental conditions. The increase dosage of Al_2O_3 into water increase the water temperature significantly. The 1% Al_2O_3 dosage causes higher temperature, however its value is slightly higher than the 0.75% dosage.

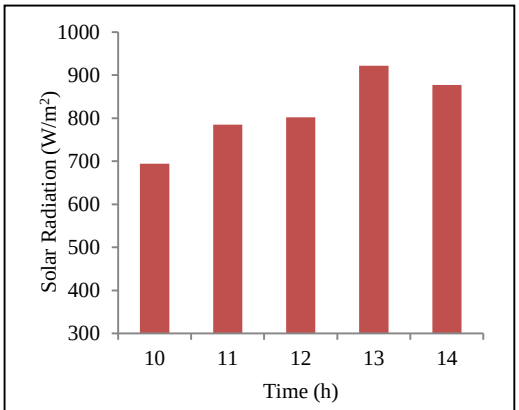

Figur 4. Solar radiation versus times.

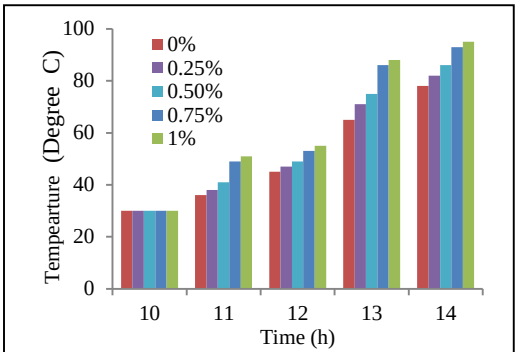

Figure 5. Water temperature at different times.

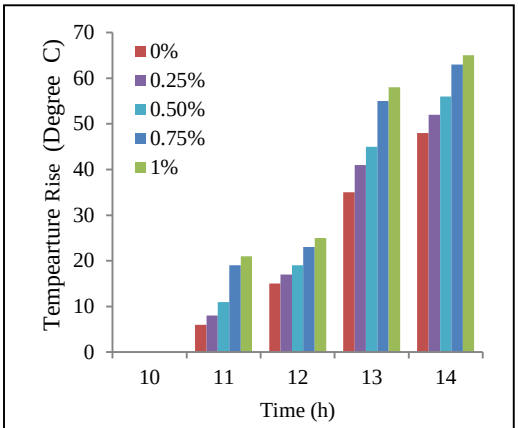

Figure 6. Percentage increase in water temperature at different times.

Fig. 6 depicts the percentage increase in water temperature at different timing. When NF is used as the working fluid in a SWH, the nanoparticles in the fluid facilitate faster heat absorption from the solar collector. As sunlight strikes the solar collector, it heats up the NF, and the nanoparticles enhance the absorption of thermal energy. This increased absorption capability allows the NF to gain heat more

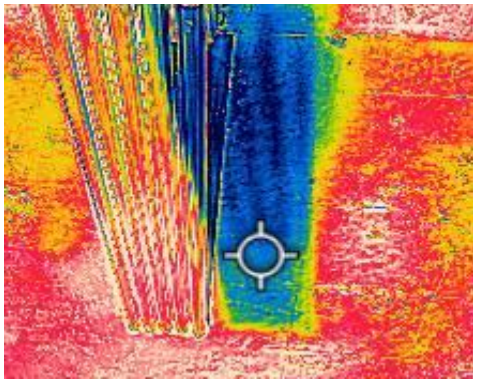

Figure 7. Temperature profile of the solar water tube.

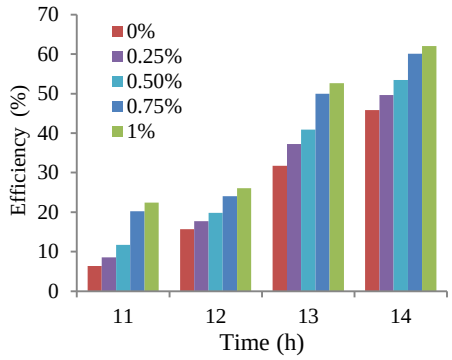

Figure 8. Efficiency of SWH at different times.

rapidly from the solar radiation (Fig. 7). The temperature rise is low with 0% dosage and highest with 1% dosage.

The efficiency of a solar water heater refers to the ratio of the usable heat energy output from the system to the solar energy input it receives. It represents how effectively the solar water heater converts solar energy into usable heat energy for heating water. A higher efficiency solar water heater can capture and convert a larger percentage of solar energy into usable heat energy. This translates into reduced reliance on conventional energy sources, such as electricity or gas, for water heating. Consequently, it leads to energy savings and lowers utility bills. It is important to note that the efficiency of a solar water heater can vary based on factors such as the design and quality of the system components, geographical location, orientation of the collector, and maintenance practices. Fig. 8 depicts the efficiency of the SWH at different timings. The efficiency of the SWH increases with increase in dosage of Al_2O_3 and higher efficiency is obtained with 1% dosage.

IV. Conclusion

The solar water converts the solar energy into thermal energy, and it is one of the simplest and low-cost energy conversion devices. The performance of the solar water heater can be increased by various techniques. In this work, we have used nanoparticle, Al_2O_3, to increase heat absorption and to enhance the performance of the SWH. The rise in water temperature depends on the solar radiation and the increase in solar radiation increases the water temperature. The experimental results reveal that the use of Al_2O_3 NF increases the temperature of the water significantly and its dosage must be optimized. The maximum value of rise of water temperature with Al_2O_3 NF is observed with 1% dosage. From this work, we conclude that the NF with SS tube can be used as a replacement to heat pipe used in evacuated SWH tubes.

Acknowledgment

The financial support provided by the VGST (GRD 228) is acknowledged.

References

[1] Kapilan, N., Reddy, R.R., & Abu Saleh Ahmed. (2022). *Experimental studies on reduction of NOx emission of biodiesel fuelled engine using a novel natural additive* (Version 1) [Preprint]. Research Square. https://doi.org/10.21203/rs.3.rs-582827/v1

[2] Ashok Kumar, Kapilan, N., & Kasthurirengan, S. (2021). Performance Studies on Solar Assisted Single and Double Bed Adsorption Refrigeration system. *NVEO-Natural volatiles & essential oils Journal*, 8(5).2021, 10594-10610.

[3] Kapilan, N., Nithin, K.C., Chiranth, K.N. (2022), Challenges and opportunities in solar photovoltaic system, *Materials Today: Proceedings*, *62*, 3538-3543,

[4] Kumar, K. A., & Kapilan, N. (2020, February). Studies on the feasibility of adsorption cooling technologies. In *Journal of Physics: Conference Series* (Vol. 1473, No. 1, p. 012050). IOP Publishing.

[5] Ogueke, N.V., Anyanwu, E.E., & Ekechukwu, O.V. (2009). A review of solar water heating systems. *Journal of Renewable and Sustainable Energy*, *1*(4), 043106.

[6] Jamar, A., Majid, Z.A.A., Azmi, W.H., Norhafana, M.M & Razak., A.A. (2016). A review of water heating system for solar energy applications. *International Communications in Heat and Mass Transfer*, *76*, 178-187.

[7] Alayi, R., Khalilpoor, N., Heshmati, S., Najafi, A., & Issakhov, A. (2021). Thermal and environmental analysis solar water heater system for residential buildings. *International Journal of Photoenergy*, *2021*(1), 6838138.

[8] Pukdum, J., Phengpom, T., & Sudasna, K. (2019). Thermal performance of mixed asphalt solar water heater. *International Journal of Renewable Energy Research*, *9*(2), 712-720.

[9] Alayi, R., Ahmadi, M. H., Visei, A. R., Sharma, S., & Najafi, A. (2021). Technical and environmental analysis of photovoltaic and solar water heater cogeneration system: a case study of Saveh City. *International Journal of Low-Carbon Technologies*, *16*(2), 447-453.

[10] Syahruddin, A. S., Jalaluddin, J., & Hayat, A. (2020). Performance analysis of solar water heating system with plate collector integrated PCM storage. *EPI International Journal of Engineering*, *3*(2), 143-149.

[11] Douvi, E., Pagkalos, C., Dogkas, G., Koukou, M. K., Stathopoulos, V. N., Caouris, Y., & Vrachopoulos, M. G. (2021). Phase change materials in solar domestic hot water systems: A review. *International Journal of Thermofluids*, *10*, 100075.

[12] Lu, Y., & Chen, Z. (2019). Numerical study on heat transfer performance of vacuum tube solar collector integrated with metal foams. *International Journal of Low-Carbon Technologies*, *14*(3), 344-350.

[13] Suthahar, S. J., Saravanan, S., Karthikeyan, B., Jaisankar, S., Palanisamy, R., Bajaj, M., ... & Alphonse, S. (2023). Experimental Investigations on the Performance of Thermosyphon Solar Flat Plate Collector using TiO2 Nanofluids. *Journal of Nanomaterials*, *2023*(1), 6837264.

[14] Yazdi, M. H., Solomin, E., Fudholi, A., Divandari, G., & Sopian, K. (2021). Thermal Performance of Nanofluid Flow Inside Evacuated Tube Solar Collector. *International Journal of Heat & Technology*, *39*(4).

[15] Yurddaş, A. (2020). Optimization and thermal performance of evacuated tube solar collector with various nanofluids. *International Journal of Heat and Mass Transfer*, *152*, 119496.

[16] Hussein, A. K., Li, D., Kolsi, L., Kata, S., & Sahoo, B. (2017). A review of nano fluid role to improve the performance of the heat pipe solar collectors. *Energy Procedia*, *109*, 417-424.

[17] Ong, K. S., Tong, W. L., & Choong, J. K. (2016). Performance of U-tube solar water heater with vertical and inclined panels. *International Journal of Low-Carbon Technologies*, *11*(2), 248-253.

[18] Alwan, N. T., Majeed, M. H., Khudhur, I. M., Shcheklein, S. E., Ali, O. M., Yaqoob, S. J., & Alayi, R. (2022). Assessment of the performance of solar water heater: an experimental and theoretical investigation. *International Journal of Low-Carbon Technologies*, *17*, 528-539.

[19] Budihardjo, I., & Morrison, G. L. (2009). Performance of water-in-glass evacuated tube solar water heaters. *Solar Energy*, *83*(1), 49-56.

[20] Mehmood, A., Waqas, A., Said, Z., Rahman, S. M. A., & Akram, M. (2019). Performance evaluation of solar water heating system with heat pipe evacuated tubes provided with natural gas backup. *Energy Reports*, *5*, 1432-1444.

eNergetics 2025
DOI: https://doi.org/10.5281/zenodo.18631553

Original Scientific Article

Utilization of PMOO in Determination of Optimum Parameters in Polymers' Injection Molding Process

Maosheng Zheng[1], Jie Yu[2]

[1,2]Northwest University, Xi'an, China

[1]1914994032@qq.com, [2]yujie@nwu.edu.cn

Abstract—**In this paper, PMOO (probabilistic multi-objective optimization method) approach is utilized to perform the determination of optimum parameters in polymers' injection molding process, which involves minimizing volume shrinkage, total warping deformation and shrinkage marks during ejection in addition to orthogonal experimental design. The variable parameters include mold temperature, melt temperature, holding pressure, holding time and cooling time. PMOO is a novel approach with both algorithm and viewpoint on "optimum point", it puts forward a new concept of "preferable probability" to address the preference degree of an attribute of a candidate and the corresponding evaluation method. In PMOO, attributes of the alternative scheme are divided into two types, i.e., both beneficial type of attribute and unbeneficial (i.e., cost) type of attribute, the corresponding evaluation algorithms of their partial preferable probability are formulated quantitatively; the total preferable probability of each alternative scheme is product of all possible partial preferable probability, which is employed as the unique indicator to conduct the ranking of the optimization. In the polymers' injection molding process, the volume shrinkage, total warping deformation and shrinkage marks during ejection are the optimal criteria to be minimizing; besides the range analysis of the total preferable probability of each alternative scheme is conducted. The result gives the optimum configuration for this polymers' injection molding process.**

Keywords - injection molding process, optimum configuration, PMOO, preferable probability, overall optimization.

I. INTRODUCTION

The molding quality of plastic parts is evaluated by multiple quality indexes, and process parameters of polymers' injection molding process affect the quality indexes significantly. Therefore, it is necessary to optimize the parameters of variables of the injection molding process for plastic parts by multi–objective optimization approach. Therefore, the overall/comprehensive evaluation in multi–objective optimization approach is the essential requirements, especially it transforms multiple indexes into an unique index that could reflect the comprehensive situation for evaluation.

Early in 1950s, optimization gained worldwide attention and was directly applied in industrial production. Box and Wilson of British Imperial Chemical Industry Company proposed response surface method (RSM) and robust design [1,2], and expounded the application of response surface method in chemical process, which initiated the industrial application of experimental design and attracted the attention of research in this field. Taguchi created the "Taguchi method" of experimental design with Orthogonal Table in Japan to deal with optimization problems and robust design, and achieved continuous results [3]. In China, Prof. Hua Luogeng and his team popularized the

ISBN: 978-86-82602-07-1

optimization method and the overall planning method in the 1960s and 1970s, which covered 28 provinces, municipalities and autonomous regions, and achieved a lot of results and good economic benefits [4,5]. Subsequently, it also provided consultation for the long-term planning and major project research of the country and industry. Prof. Hua Luogeng's work has laid a solid foundation from theory to practice and can be called an excellent model of mathematical application [4,5].

With the increase of the number of objectives (criteria) that need to be optimized simultaneously in the system, the problem and the corresponding method of "multi-objective optimization (MOO)" appear [6,7]. For MOO problems, the optimal criteria usually conflict with each other, and it always needs to adopt appropriate MOO method to solve such problems. So far, some MOO methods have been developed, i.e., the so-called traditional MOO methods, but each is with its own intrinsic defect [8-11]. For example, the rationality of the option of weighting factors and normalization factors in linear weighting method of "addition" approaches is problematic [8-14]. Some methods even included artificial factors such as virtual "ideal point" as well, which induces unclear elementary significance to the MOO problem itself [8-14]. In addition, fundamentally speaking, from the perspective of set theory and probability theory, "addition" is a "union", which indicates the "sum" of events. It can be seen that the operation mode of "addition" essentially deviates from the original intention of "simultaneous optimization". Pareto solution can only give one set of solutions [12-14]. Therefore, it can be seen that these MOO methods are not formed successfully.

In fact, the original intention of MOO is that all these multiple objectives are optimized simultaneously, i.e., the key point is the simultaneity of the optimization of the multiple objectives. From the aspect of probability theory, it should be the "product" of the "probability" of each objective (attribute); in set theory, it is the "intersection" of these objectives. So, probability theory could be an appropriate way to handle the matter of multi-objective optimization.

In view of the above situation, from the viewpoint of systems theory, the MOO problem is regarded as an optimal problem within a system that is consisting of these multiple objectives to be optimized simultaneously. According to the viewpoint of systems theory, the "optimal status of multiple objectives" in the system is the "optimum state of the whole system"; furthermore, set theory and probability theory can be adopted to deal with such MOO problems. Subsequently, the new concept of "preferable probability" was introduced, which leads to the formation of probabilistic multi-objective optimization (PMOO) approach thereafter [12-14]. In PMOO, the objectives (attributes) of the alternative schemes in the optimization task are preliminarily divided into two basic types, namely, beneficial type of attributes and unbeneficial (cost) type of attributes, and a quantitative regulation of partial preferable probability corresponding to both beneficial and beneficial (cost) types of attributes are established [12-14]. Therefore, the whole optimization is regarded as an optimization problem in a system, and the "multi-attribute simultaneous optimization" is regarded as the problem of "multi-event simultaneous occurrence" in probability theory. Therefore, the total preferable probability of each alternative is the product of partial preferable probabilities of all possible attributes of the alternative, such that the overall optimization of the system can be handled. Finally, all the candidate schemes are ranked according to the total preferable probability, which is the uniquely decisive index for the candidate schemes to win the competition in this optimization.

Obviously, there is a significant difference between the probabilistic method and the previous methods [8-14]. PMOO has not only an algorithm, but also a clear point of view. From the viewpoint of systems theory, it defines "the optimum point of system" as "the optimal status of MOO", so this optimum point is obtained directly by using probability theory. However, in the previous "MOO" methods, there is not defined the "optimum point", i.e., what is the "optimum point", but only algorithm. The benefit of PMOO is that it has not only both viewpoint on "multi-objective optimization" and algorithm, and advantages of without any subjective scale factors to contradict the use of normalization factors for attributes in traditional methods.

In summary, the advantage of PMOO is that it provides both a clear theoretical framework for multi-objective optimization and an algorithm, while avoiding any subjective or

artificial scaling factors.

In this paper, the PMOO method is expounded first, it gives the determination of optimum parameters in polymers' injection molding process afterwards, which involves minimizing volume shrinkage, total warping deformation and shrinkage marks during ejection in addition to orthogonal experimental design. The variable parameters include mold temperature, melt temperature, holding pressure, holding time and cooling time.

II. CONCISE INTRODUCTION OF PMOO

A. Overview of PMOO

Because the original intention of MOO is "simultaneous optimization" of multiple objectives, only by taking this intention into account can an appropriate method be established.

From the perspective of probability theory, it is the "product" of the probabilities of all attributes, while in set theory it belongs to the "intersection" of all attributes. In addition, in order to make the problem operable in PMOO, a new concept of "preferable probability" is introduced to address the preference degree of an attribute of an alternative candidate. The evaluation objectives (attributes) of candidate schemes in optimization tasks are preliminarily divided into two basic types: beneficial attributes and unbeneficial (cost) attributes, and the quantitative evaluations of partial preferable probability corresponding to both beneficial attributes and unbeneficial (cost) attributes are formulated [12-14]. Furthermore, it takes the "simultaneous optimization of multiple attributes" as the overall optimization of a system. In probability theory, it can be regarded as "multiple events occurring at the same time". Therefore, the total preferable probability of each candidate is the product of partial preferable probabilities of all possible attributes of the candidate scheme, so that the overall optimization of the system can be handled. Starting from simplicity, it is also assumed that each partial preferable probability is linearly positively correlated with the utility index of its beneficial attributes, and each partial preferable probability is linearly negatively correlated with the utility index of its unbeneficial attributes. Finally, according to the value of the total preferable probability of each candidate, the overall optimization is completed. The total preferable probability of each candidate scheme is the uniquely decisive index for the candidate scheme to win this optimization competition. The process of PMOO is shown in Fig. 1 [12-14].

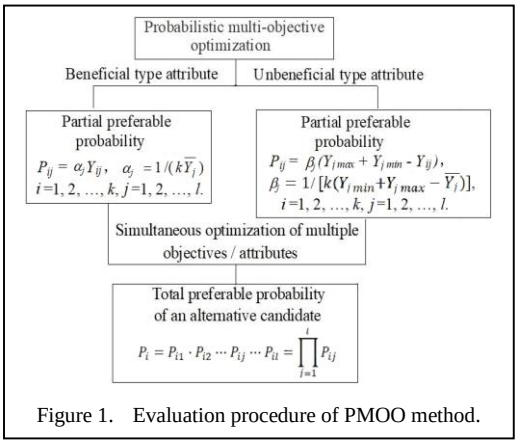

Figure 1. Evaluation procedure of PMOO method.

B. Formulae in PMOO Evaluation

- Evaluation of partial preferable probability in beneficial type of attribute case is [12-14]:

$$P_{ij} = \alpha_j Y_{ij}, \alpha_j = 1/(k\overline{Y_j}), \quad i = 1,2,\ldots,k;\ j = 1,\ 2,\ \ldots,l. \tag{1}$$

- Evaluation of partial preferable probability in unbeneficial type of attribute case is [12-14]:

$$P_{ij} = \beta_j \left(Y_{j\max} + Y_{j\min} - Y_{ij}\right), \quad \beta_j = 1\Big/\left[k\left(Y_{j\max} + Y_{j\min} - \overline{Y_j}\right)\right], \quad i = 1,2,\ldots,k;\ j = 1,\ 2,\ \ldots,l. \tag{2}$$

- Total preferable probability of an alternative candidate is [12-14]:

$$P_i = P_{i1} \cdot P_{i2} \cdots P_{il} = \prod_{j=1}^{l} P_{ij}, \quad i = 1,2,\ldots,k;\ j = 1,\ 2,\ \ldots,l. \tag{3}$$

In Eqs. (1) through (3), P_{ij} reflects the preferable probability of the j-th performance attribute of the i-th alternative [12-14], k is the total number of alternative candidates, and l is the total number of performance attributes; P_i indicates the total preferable probability of the i-th candidate; Y_{ij} reflects the utility index value

of the *j*-th performance attribute of the *i*-th alternative candidate; α_j is the normalization factor of the *j*-th beneficial type of performance attributes index; β_j reflects the normalization factor of the *j*-th unbeneficial type of performance attribute index; $\overline{Y}_j$ is the arithmetic average of *j*-th utility index of the performance attribute in the evaluated group; Y_{jmin} and Y_{jmax} represent the minimum and maximum value of the utility index Y_{ij} of the *j*-th objective in the evaluated group, respectively.

Besides, the evaluations of normalization factors A_j and B_j are obtained from the general principle of normalization of probability theory for P_{ij} over all alternative candidates *i* [12-14]:

$$\begin{aligned} \sum_{i=1}^{k} P_{ij} &= \sum_{i=1}^{k} A_j Y_{ij} = 1, \\ \sum_{i=1}^{k} P_{ij} &= \sum_{i=1}^{k} B_j \left(Y_{jmax} + Y_{jmin} - Y_{ij} \right) = 1. \end{aligned} \tag{4}$$

As to tackling MOO, the PMOO emphasizes the simultaneity of the multiple attributes in the optimization process of a system, and the irreplaceability of each attribute, so it is analogical to the "intersection" in set theory and "joint probability" of two independent events in probability theory, which is against to any type of "additive algorithm", therefore "preferable probability" and the corresponding evaluations were established in PMOO; However, in other MOO evaluation, such as simple additive weighting (SAW) method, additive algorithm is applied weighted attribute, obviously "additive algorithm" contradicts to irreplaceability of each attribute. So, in principle, PMOO conforms to the essence of MOO properly.

The remarkable feature of this PMOO method is to optimize multiple objectives in a system at the same time in terms of preferable probability, which is without any artificial or subjective scaling factor, and opens up a new way to solve MOO problems with broad application prospects [8-14]. Here "artificial or subjective scale factor" means that it is unnecessary to introduce any nonobjective factor artificially in general cases, but it is not absolutely to repel necessary subjective factor in special cases. Actually, PMOO has been used in many fields, such as shortest path, material selection, engineering, planning problems, experimental design, medical scheme, robust design of industrial processes and products, investment optimization, and so on.

A potential development trend of the PMOO approach is to introduce the organic combination with modern searching methods.

III. Utilizations of PMOO in Determination of Optimum Parameters in Polymers' Injection Molding Process

The purpose of the optimization in this section is to provide an example to show the determination of optimum parameters in polymers' injection molding process.

1) Evaluation by means of PMOO

Q. Xue et al used Moldflow software to analyze the influence of five process parameters [15], such as mold temperature (*A*, °C), melt temperature (*B*, °C), holding pressure (*C*, MPa), holding time (*D*, s) and cooling time (*E*, s), on the quality index of injection molding including volume shrinkage (α_1, %), total warping deformation (α_2, mm) and shrinkage mark (α_3, mm) of injection molding as the optimization objectives of process parameters. An orthogonal experiment with five process parameters and four levels was designed. In the study, the plastic part is a component of a small car front, which is a semi-closed box-shaped structure, with an overall dimension of 212.2 mm × 272.5 mm × 61.8 mm and a volume of about 152 cm^3, is a medium-sized plastic part [15].

The variable level of orthogonal test design is shown in Table I, and the results are shown in Table II [15]. While Table III shows the evaluation results of this polymer's injection molding process by using the PMOO approach, in which the volume shrinkage (α_1), total warping deformation (α_2) and shrinkage mark (α_3) of injection molding are all unbeneficial type of attributes, $P_{\alpha 1}$ is the partial preferable probability of the volume shrinkage, $P_{\alpha 2}$ is the partial preferable probability of the total warping deformation, and $P_{\alpha 3}$ is the partial preferable probability of the shrinkage mark; P_t is the total preferable probability of an experimental scheme. The evaluation of partial preferable probabilities and total preferable probabilities are conducted according to the formulae shown in Equations (1) through (3). The results in Table III show that scheme 13 ($A_4B_1C_4D_2E_3$), has the largest total preferable probability visually, so

the optimal scheme should be near the configuration of scheme 13. Table IV shows the results of range analysis for total preferable probability of each alternative scheme, which shows that the impact order of input variables is $C > B > A > E > D$ directly from the value of range analysis of the total preferable probability corresponding to parameters *A*, *B*, *C*, *D*, and *E*, and the optimum configuration for this optimization problem is $A_4B_1C_4D_3E_4$, which is close to scheme 13 indeed.

TABLE I. LEVEL TABLE OF EXPERIMENTAL INPUT VARIABLES OF THE POLYMER'S INJECTION MOLDING PROCESS.

Factor / Level	Mold temperature (A, °C)	Melt temperature (B, °C)	Holding pressure (C, MPa)	Holding time (D, s)	Cooling time (E, s)
1	40	190	40	20	20
2	50	200	50	30	30
3	60	210	60	40	40
4	70	220	70	50	50

TABLE II. SIMULATION TEST RESULTS OF THE POLYMER'S INJECTION MOLDING PROCESS.

No.	Variable					Optimal objective		
	A,℃	B,℃	C, MPa	D, s	E, s	α_1, %	α_2, mm	α_3, mm
1	40	190	40	20	20	7.810	1.471	0.0734
2	40	200	50	30	30	7.705	1.304	0.0652
3	40	210	60	40	40	7.525	1.160	0.0587
4	40	220	70	50	50	7.377	1.006	0.0520
5	50	190	50	40	50	7.172	1.239	0.0606
6	50	200	40	50	40	7.980	1.366	0.0750
7	50	210	70	20	30	7.026	1.027	0.0475
8	50	220	60	30	20	8.108	1.183	0.0590
9	60	190	60	50	30	6.743	1.082	0.0499
10	60	200	70	40	20	6.652	0.984	0.0454
11	60	210	40	30	50	8.288	1.347	0.0770
12	60	220	50	20	40	8.225	1.267	0.0694
13	70	190	70	30	40	6.422	0.939	0.0423
14	70	200	60	20	50	7.105	1.081	0.0514
15	70	210	50	50	20	7.998	1.241	0.0651
16	70	220	40	40	30	8.700	1.342	0.0785

TABLE III. EVALUATION RESULTS OF THE POLYMER'S INJECTION MOLDING PROCESS BY MEANS OF PMOO.

No.	Partial preferable probability			Total preferable probability and ranking	
	$P_{\alpha 1}$	$P_{\alpha 2}$	$P_{\alpha 3}$	$P_t \cdot 10^4$	Ranking
1	0.0603	0.0481	0.0499	1.4491	14
2	0.0612	0.0567	0.0580	2.0125	11
3	0.0627	0.0640	0.0644	2.5877	7
4	0.0639	0.0719	0.0710	3.2676	5
5	0.0656	0.600	0.0625	2.4629	8
6	0.0590	0.0535	0.0483	1.5239	13
7	0.0668	0.0708	0.0755	3.5752	3
8	0.0579	0.0629	0.0641	2.3344	9
9	0.0692	0.0680	0.0731	3.4414	4
10	0.0699	0.0731	0.0776	3.9627	2
11	0.0564	0.0545	0.0463	1.4240	15
12	0.0569	0.0568	0.0539	1.7956	12
13	0.0718	0.0754	0.0806	4.3645	1
14	0.0662	0.0681	0.0716	3.2284	6
15	0.0588	0.0599	0.0581	2.0466	10
16	0.0530	0.0547	0.0449	1.3014	16

TABLE IV. RESULTS OF RANGE ANALYSIS FOR TOTAL PREFERABLE PROBABILITY.

Level	A	B	C	D	E
1	2.3292	2.9295	1.4246	2.5121	2.4482
2	2.4741	2.6819	2.0794	2.5338	2.5826
3	2.6559	2.4084	2.8980	2.5787	2.5679
4	2.7352	2.1748	3.7925	2.5699	2.5957
Range	0.4060	0.7547	2.3679	0.0666	0.1475
Order of impact	3	2	1	5	4
Optimum conf.	4	1	4	3	4

2) Comparison with entropy-weight TOPSIS method

In the study of Xue et al [15], entropy-weight TOPSIS method was applied to investigate the influence the injection molding process parameters on multiple objectives which need to be optimized in the study. In addition, orthogonal experiment design was employed to conduct the optimization for the issue with five process parameters and four levels in their study. Their optimal result is the configuration of $A_4B_1C_4D_2E_3$ coincidentally as well [15]; however, the impact order of input variables is $C > B > A > D > E$, which differs from that of the PMOO shown in last subsection. In fact, Xue's result depends on the weight factors for the involved objectives, says the volume shrinkage (α_1 ,%), total warping deformation (α_2 , mm) and shrinkage mark (α_3 , mm) of injection molding. As the weight factors vary the consequences change.

3) Discussion

In the evaluation of PMOO, the assessments of partial preferable probabilities are conducted on basis of available data. Therefore, the available data must have representativeness. In fact, in the Designs of Experiment (DOE), such as orthogonal experimental design, response surface method, and uniform experiment design, the limited or finite test data are determined according to certain rules actually, which have typical characteristics or feature to reveal the variations of the attributes instead of any options at random or arbitrarily.

Besides, in the traditional MOO, such as "SAW method", there exists fundamentally unreasonable treatment of "additive algorithm", which indicates the meaning of union of a series of objectives/attributes/criteria in set theory and the substitutability of objectives instead of their non-substitutability and simultaneity. While PMOO represents the irreplaceability and simultaneity of objectives in MOO, however the traditional MOO methods are fundamentally incomparable with the approach of PMOO in this point.

IV. CONCLUSION

Above study and discussion indicate that:

- PMOO approach could be used to conduct determination of optimum parameters in materials processing.
- PMOO approach reveals the characteristics of simultaneity of multiple objectives in optimization by using probability theory, which is without any subjective scale factors.
- PMOO approach initiates a new way to solve the MOO problem and has broad application prospects in many fields.

REFERENCES

[1] Box, G. E., & Wilson, K. B. (1951). On the experimental attainment of optimum conditions. *Journal of the Royal Statistical Society. Series B (Methodological), 13*(1), 1-45.

[2] Myers, R. H., Montgomery, D. C., & Anderson-Cook, C. M. (2016). *Response surface methodology: process and product optimization using designed experiments*. John Wiley & Sons.

[3] Mori, T. (2011). *Taguchi methods: benefits, impacts, mathematics, statistics, and applications*. ASME press.

[4] Hua, L. (2020). *Plain Talks on Optimization Method and Overall Planning Method.* Beijing Publishing House

[5] Hua, L-K., Wang, Y. (1978). *Application of Number Theory in Approximate Analysis*, Science Press.

[6] Huang, Q. D., Lv, X., Li, X., Wang, C. (2022). *Modern Optimization Theory and Method (Part I)*, Science Press.

[7] Xu, J., Hu, Z. (2022). *Operations Research (4th Edition)*, Science Press.

[8] Tangi, M., & Amaranto, A. (2025). Designing integrated and resilient multi-energy systems via multi-objective optimization and scenario analysis. *Applied Energy*, *382*, 125281.

[9] Hamdi, M., Gtari, O., & Hazami, M. (2025). Techno-environmental optimal sizing and dynamic behavior of a hybrid system feeding a large-scale SWRO desalination system: The case of Djerba Island, Tunisia. *Energy Exploration & Exploitation*, *43*(1), 378-409.

[10] Hamdi, M., Gtari, O., Hazami, M., & Mihoubi, D. (2023, December). Multi-Objective Optimization of a Hybrid System Feeding a Large Scale SWRO Desalination Plant. In *2023 IEEE Third International Conference on Signal, Control and Communication (SCC)* (pp. 1-6). IEEE.

[11] Nagarajan, K., Rajagopalan, A., Bajaj, M., Raju, V., & Blazek, V. (2025). Enhanced wombat optimization algorithm for multi-objective optimal power flow in renewable energy and electric vehicle integrated

systems. *Results in Engineering, 25*, 103671.

[12] Zheng, M., & Yu, J. (2024). Application of probabilistic multi-objective optimization in material milling. *International Journal on Interactive Design and Manufacturing (IJIDeM), 18*(2), 1053-1057.

[13] Zheng, M., Teng, H., Yu, J., Cui, Y., & Wang, Y. (2023). *Probability-based multi-objective optimization for material selection*. Singapore: Springer.

[14] Zheng, M., & Yu, J. (2024). *Systems Theory for Engineering Practice: Insights from Physics*. Springer.

[15] Xue, Q., Miao, Y., Xue, Z., Wu, F. (2023). Multi-objective optimization of injection molding process parameters based on entropy-weight TOPSIS method, *Journal of Plastics, 53*(6), 142-146.

eNergetics 2025
DOI: https://doi.org/10.5281/zenodo.18633020

Original Scientific Article

IA-Assisted Iterative Process for Developing Modular Scientific Software

Erro Quiñonez José Eulalio[1], García Gutiérrez Rafael[2], Arias-Ramos Carlos Fabián[3], Cancino-Gordillo Francisco Enrique[4], Verdugo Miranda Saúl[5], Jiménez Sotomayor Carlos Ángel[6]

[1,2,5,6]Universidad de Sonora, Hermosillo Son., México
[3,4]Instituto de Energías Renovables, Temixco Mor., México

[1]a222230161@unison.mx, [2]rgarcia@cifus.uson.mx, [3]cafaar@ier.unam.mx, [4]cancinogordillof@outlook.com, [5]saul.verdugo@unison.mx, [6]a219222678@unison.mx

Abstract—**This work is an extension of that presented in the article: "Automatización del procesamiento de datos experimentales en celdas solares de perovskita mediante una suite informática en Python con programación asistida por inteligencia artificial" [*"Automation of experimental data processing in perovskite solar cells through a Python software suite with AI-assisted programming"*], revisiting the methodology, addressing points that were not previously presented, and demonstrating the potential enabled by an update that adds new functions. We address an AI-assisted iterative development methodology, with cognitive-load analysis, iterative validation, and human oversight. New functionalities are added, such as directly plotting proprietary (vendor-specific) files from X-ray diffraction (XRD) and quantum-efficiency characterization equipment-specifically external quantum efficiency (EQE)-reducing processing times by up to 97%. This accelerates research by providing more time for the analysis of results and other researcher activities.**

Keywords: python, iterative development, artificial intelligence, cognitive load, data automation.

I. INTRODUCTION

In research it is common to deal with large amounts of data that must be processed, which involves a series of repetitive actions that can consume a great deal of time. This often involves the use of paid software such as Excel and OriginPro, which only run in a Windows OS environment. An option is the use of free software; however, in some cases these tools are not very user-friendly and/or do not meet the researcher's needs. For this reason, there are efforts to create proprietary, tailor-made software with the possibility of scaling it and running it on different operating systems. Another strong point is that there are no payments for licenses or updates, nor dependence on a distributing company whose disappearance would leave the user without support. A language that stands out for this purpose is Python, because it has clear, natural-language-like syntax and powerful libraries such as NumPy for analysis, Matplotlib for visualization, and Tkinter for GUIs [1-3]. Some development examples include: PLACE (open platform) [4], LABS (for programming synthesis devices) [5], NIMS-OS (materials exploration) [6], PyChemFlow (chemical preprocessing) [7], ChemDataExtractor [8], ReactionDataExtractor 2.0 [9], DECIMER [10], pymatgen [11], and PyMOLfold [12]. The proposal in this work is an extension of that presented in the article, *"Automatización del procesamiento de datos experimentales en celdas solares de perovskita mediante una suite informática en Python con programación asistida por inteligencia artificial"*, in which we address points that were not presented, as well as introduce an updated release.

II. METHODOLOGY

For the development of the programs, a modular approach was adopted, which made it possible to develop independent modules that

ISBN: 978-86-82602-07-1

perform a particular function according to the researcher's specific needs [13,14].

A. *Manual Method Analysis*

The manual method involves the following:

- Finding software that can open or convert the proprietary file to a format readable by Notepad, Word, Excel, etc. As in the case of .raw files, which can be read and then exported—for example to .asc—using PowDLL Converter.
- Cleaning in Excel: the files are opened/imported and an initial cleanup is performed, which includes extracting the data columns of interest and adjusting their format.
- In OriginPro, the data are imported via copy–paste, plotted, and the visualization is customized (line thickness, color, headers, among others).

B. *Selection of Software Development Tools*

Python was selected because it has libraries for data processing (NumPy, pandas), plotting (Matplotlib, Seaborn, Plotly, and Bokeh The manual method involves the following:

- Finding software that can open or convert the proprietary file to a format readable by Notepad, Word, Excel, etc. As in the case of .raw files, which can be read and then exported-for example to .asc-using PowDLL Converter.
- Cleaning in Excel: the files are opened/imported and an initial cleanup is performed, which includes extracting the data columns of interest and adjusting their format.
- In OriginPro, the data are imported via copy–paste, plotted, and the visualization is customized (line thickness, color, headers, among others).), and for creating graphical user interfaces (Tkinter, DearPyGui, and Streamlit). This makes it possible to automate the loading, processing, and plotting of experimental data. In addition, it provides machine-learning tools (scikit-learn or TensorFlow), which enable building programs with artificial intelligence [15-19], see Fig. 1.

When compared with OriginPro—a software widely used by researchers to create publication-quality figures-it presents drawbacks such as limited automation capabilities and the requirement to pay for a commercial license.

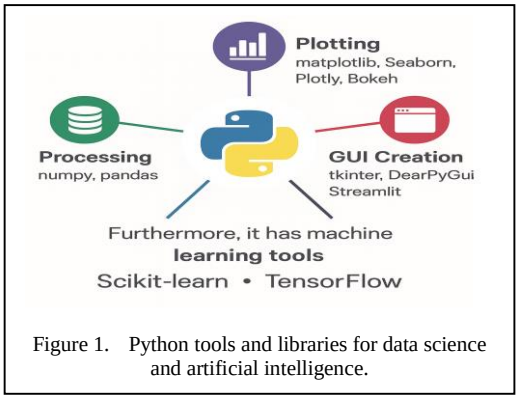

Figure 1. Python tools and libraries for data science and artificial intelligence.

If we make a comparison of functionalities between them, Python offers superior massive automation, which allows for complete batch processing for reading, analysis, and creation of graphs, while OriginPro is limited to batch imports and complex scripts. Regarding graphs, with Python it is possible to have direct integration with physical models, including equations, simulations, and multivariable regression, as well as interactive visualizations with features like zoom, panning, filters, and sliders through Plotly or Bokeh. With advanced functions in Python, it enables connections to scientific instrumentation, real-time processing to update graphs during data acquisition, but not in OriginPro. Python offers scalability by allowing the development of modular scripts to manage complex projects. In summary, Python provides greater flexibility and extensibility for advanced users, [20].

C. *Comparative Analysis of Cognitive Effort: OriginPro vs Python*

Addressing the effort to learn to use them efficiently or at least sufficiently, OriginPro and Python present distinct paradigms:

- OriginPro is a software with a graphical user interface for graphical analysis, where the user can generate graphs and basic analyses without programming knowledge, which favors a rapid learning curve. However, when scaling the complexity and amount of data, the interface becomes limited or may require the use of proprietary scripts, either from LabTalk or embedded Python, which requires more advanced knowledge, for

which the learning curve is no longer so trivial.

- On the other hand, Python requires a greater initial cognitive effort, since it requires learning programming concepts. But upon overcoming this stage in learning, it becomes exponential where the limit of the functions that the program can execute will be limited by the creativity and knowledge acquired up to that moment.

D. Iterative Development and Validation

For the generation of the code, AI was integrated, which assisted the user in an iterative process, where specific context was provided by detailing relevant technical concepts, as well as about the extension, internal structure of the files, which are the relevant data, among others. Specific tasks were requested, such as the program being able to read the source files and extract the data of interest, to subsequently advance in the functions that had to be performed with them. Since AI depends on prior training of learned patterns, if the problem, context, or situation is novel, then it produces a solution that is coherent but erroneous or partially correct that is assumed to be true. Therefore, until advanced techniques are integrated that allow it a more human-like reasoning, supervision by people who have knowledge in the desired task will be needed, as in this case Python programming. Therefore, AI should still be seen as an assistant to whom tasks are delegated that must be supervised to be validated, Fig. 2, [21-22].

III. RESULTS AND DISCUSSION

A main module was developed that integrates into a single graphical interface or suite, in which you can access the modules that share the ability to read and process the data from the file in proprietary format of the following characterization devices: Bruker D8 advance X-ray diffractometer, AMBios XP-200 profilometer, ORIEL LCS-100 solar simulator, Shimadzu UV-1800 UV-Vis spectrophotometer and PerkinElmer Lambda EQE meter, Fig. 3.

It's easy to use; just click on the application you're interested in, for example, XRD diffractogram, which allows you to graph one or more raw files. The corresponding GUI will open, allowing you to interact with specific functions, Fig. 4.

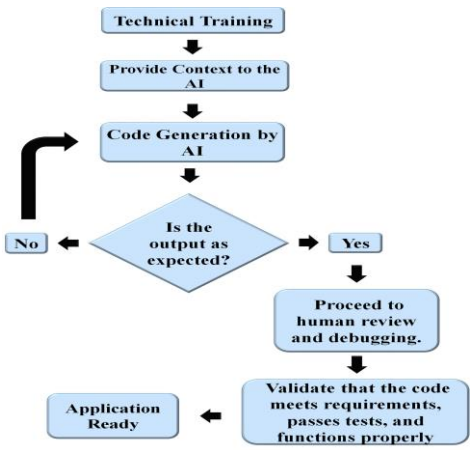

Figure 2. Development and validation of modules with AI assistance.

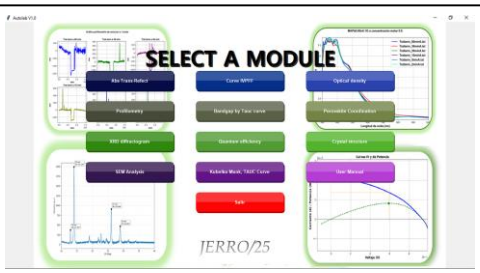

Figure 3. Main module with updated options.

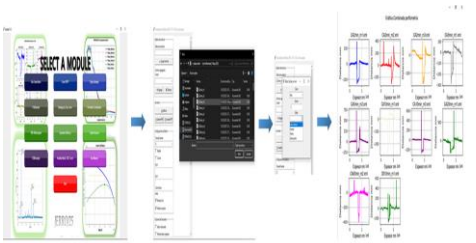

Figure 4. Example of how you can work with one or more files at a time.

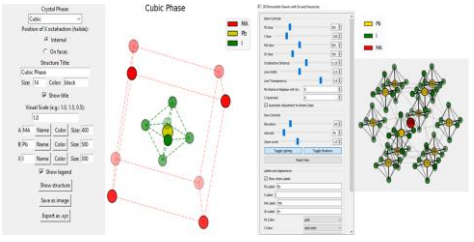

Figure 5. Crystalline and coordination phase plotting of perovskite.

But it is not only useful for graphing data but also for generating images of its crystalline or perovskite coordination phase, Fig. 5.

This makes it possible to obtain custom-made images to include in research reports or articles to be published.

A. Data Processing Time Comparison

The time required to plot a raw X-ray diffraction file using the XRD diffractogram module, Fig. 6, is 30 seconds compared to a manual process that would take 16 minutes, Fig. 7, reducing the time invested by ≈ 97%. A similar reduction of ≈ 85% is achieved with plain text quantum efficiency files, which take 5 minutes to plot manually while only 23 seconds with the Quantum Efficiency module.

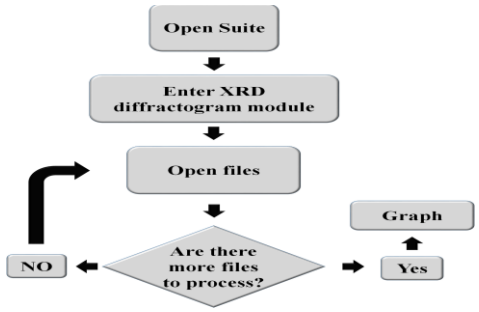

Figure 6. Process diagram using the XRD diffractogram module.

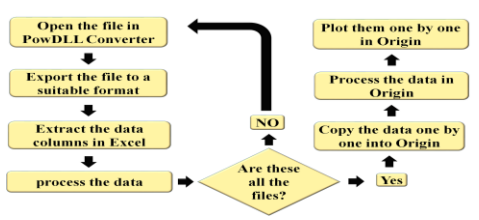

Figure 7. Diagram of the manual process for plotting XRD diffractogram files.

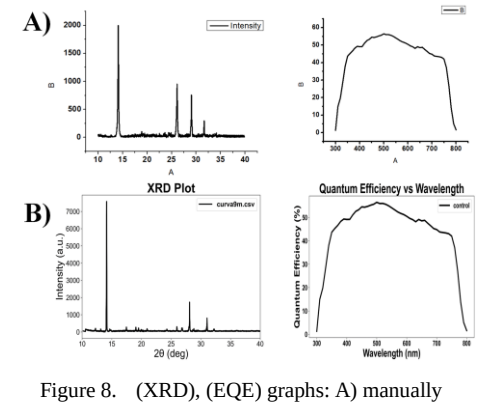

Figure 8. (XRD), (EQE) graphs: A) manually processed with OriginPro and B) automatically generated with the suite.

The processing times for 10 proprietary characterization files were recorded manually and using the Python module.

The results are shown in the following table:

TABLE I. PERFORMANCE RESULTS.

	Processing time for 10 files	
	Commercial software	***Module in Python***
Profilometry	235 min	3 min
Absorbance	185 min	3 min
J-V Curves	340 min	5 min
XRD	60 min	5 min
Quantum Efficiency	50 min	4 min

The Fig. 8, shows the graphs of the same XRD and EQE files, respectively, created in Origin and using the suite's modules.

IV. CONCLUSIONS

Among the conclusions are the methodology used, the reduction in time, the ability to scale applications to more equipment, more characterization studies (such as XPS and ATF), the potential to directly integrate AI into applications, and going a step further and integrating mechatronics by implementing an intelligent assistant supervised by the researcher that carries out experiments. However, in my opinion, the most important is:

AI has the potential to multiply scientists' ability to process vast amounts of information, explore ideas, and accelerate their research. It works by analyzing patterns and generating predictions expressed in coherent, though not necessarily accurate, texts. However, it does not replace researchers because it lacks the critical thinking skills necessary to validate, interpret, and apply results within a specific context, as well as the ethical framework to guide its purpose.

ACKNOWLEDGMENT

We would like to thank the UNAM projects and the Secretariat of Science, Humanities, Technology and Innovation for their financial support.

REFERENCES

[1] Harris, C. R., Millman, K. J., Van Der Walt, S. J., Gommers, R., Virtanen, P., Cournapeau, D., ... & Oliphant, T. E. (2020). Array programming with NumPy. *Nature*, *585*(7825), 357-362.

[2] Fernandez, A. (2013). *Python 3 al descubierto*. Alfaomega Grupo Editor.

[3] Navlani, A., Fandango, A., & Idris, I. (2021). *Python Data Analysis: Perform data collection, data processing, wrangling, visualization, and model building using Python*. Packt Publishing Ltd.

[4] Johnson, J. L., tom Wörden, H., & van Wijk, K. (2015). PLACE: an open-source python package for laboratory automation, control, and experimentation. *Journal of laboratory automation*, *20*(1), 10-16.

[5] Hielscher, M. M., Dörr, M., Schneider, J., & Waldvogel, S. R. (2023). LABS: Laboratory automation and batch scheduling–a modular open source Python program for the control of automated electrochemical synthesis with a web interface. *Chemistry–An Asian Journal*, *18*(14), e202300380.

[6] Tamura, R., Tsuda, K., & Matsuda, S. (2023). NIMS-OS: an automation software to implement a closed loop between artificial intelligence and robotic experiments in materials science. *Science and Technology of Advanced Materials: Methods*, *3*(1), 2232297.

[7] Lovrić, M., Đuričić, T., Hussain, H., Lučić, B., & Kern, R. (2023). PyChemFlow: an automated pre-processing pipeline in Python for reproducible machine learning on chemical data. *ChemRxiv*.

[8] Chen, C., Maqsood, A., & Jacobsson, T. J. (2023). The role of machine learning in perovskite solar cell research. *Journal of Alloys and Compounds*, *960*, 170824.

[9] Akpan, D. M. (2024). Programming: Python and R. In *Future-Proof Accounting: Data and Technology Strategies* (pp. 129-140). Emerald Publishing Limited.

[10] Horton, M. (2023). Materials discovery screening with pymatgen. *Nature Reviews Physics*, *5*(2), 76-76.

[11] Ford, C. T., Ullah, S., Antunes, D. A., & Ferreira, T. G. (2025). PyMOLfold: Interactive Protein and Ligand Structure Prediction in PyMOL. *arXiv preprint arXiv:2502.00508*.

[12] Krummenacher, M., Gubler, M., Finkler, J. A., Huber, H., Sommer-Jörgensen, M., & Goedecker, S. (2024). Performing highly efficient Minima Hopping structure predictions using the Atomic Simulation Environment (ASE). *SoftwareX*, *25*, 101632.

[13] Martinez Gomez, E. (2024). Diseño e implementación de un sistema software modular para gestión de protocolos en una plataforma de biorreactores ChiBio.

[14] Navarrete Villalta, S. (2024). Integración modular en una plataforma software para el tratamiento de diferentes logs médicos.

[15] Quiñones, C. J., Antunez, L. E., Krujoski, M. G., & Koloziej, J. E. (2024). Desarrollo de software de análisis de datos de voltamperometría cíclica en Python con interfaz gráfica. *JIDeTEV*, (14).

[16] Fortune, N. A. (2021). A Short Guide to Using Python For Data Analysis In Experimental Physics. *Authorea Preprints*.

[17] Ding, Z., Li, H., Hao, J., Zheng, M., Lei, S., & Hu, F. (2025, April). Automatic extraction algorithm and technical application of openXML document review records based on Python. In *Fourth International Conference on Computer Technology, Information Engineering, and Electron Materials (CTIEEM 2024)* (Vol. 13561, pp. 172-179). SPIE.

[18] Caswell, T. A., et al. (2021). *Matplotlib: Visualization with Python*.

[19] OriginLab Corporation. (2023). *OriginPro 2023: Scientific graphing & analysis software* [Computer software].

[20] Vygotsky, L. S. (1978). *Mind in society. the development of higher psychological processes*. Harvard University Press.

[21] Wilary, D. M., & Cole, J. M. (2023). ReactionDataExtractor 2.0: a deep learning approach for data extraction from chemical reaction schemes. *Journal of Chemical Information and Modeling*, *63*(19), 6053-6067.

[22] Feng, L. (2025). Investigating the effects of artificial intelligence-assisted language learning strategies on cognitive load and learning outcomes: a comparative study. *Journal of Educational Computing Research*, *62*(8), 1741-1774.

eNergetics 2025
DOI: https://doi.org/10.5281/zenodo.18633177

Original Scientific Article

Coping Flexibility Scale: A Validated Instrument to Assess Coping Flexibility

Jijitha Gilton[1], Divya Chandrasenan[2], Salom Gnana Thanga Vincent[3]

[1,2]Department of Education, University of Kerala, Thiruvananthapuram, India
[3]Department of Environmental Science, University of Kerala, Thiruvananthapuram, India

[1]jijithageetha@gmail.com, [2]mail2divyacsenan@gmail.com, [3]salom@keralauniversity.ac.in

Abstract—**As the situational demands has been in an increased pace and concerning the need for a flexible nature in coping ability of individuals in an ever-changing environmental, social and economic context, this study is to develop an instrument to assess the coping flexibility. The developed instrument is in form of a five-point scale with a three-dimensional structure. Rooted upon the theory of coping flexibility and Triple Bottom Line theory, the instrument varies in its dimensionality as coping repertoire, changeability and reflexivity on the aspects of environmental, social and economic. After the pilot study conducted among a sample of 327 secondary school students, the validity of the tool has been established on base of statistical methods as exploratory factor analysis, item analysis and reliability testing. A total item of 24 has been retained from 36, with value ranging from 0.35 to 0.711 when subjected to exploratory factor analysis. These 24 items were then subjected to item analysis and 23 items fulfilled the criterion of critical value of 1.96. the pilot study data has also been subjected to Corrected Item Total Correlations and Cronbach's Alpha if Item Deletedwhich lead to the final draft of the instrument with number of items as 22. The results reflect that the developed tool is a validated one with a reliability of 0.758 (Cronbach's Alpha) that can effectively assess the coping flexibility of targeted population.**

Keywords*:* coping flexibility scale, tool development, tool validation.

I. INTRODUCTION

Anomalous changes that makes complexity, uncertainty and volatility as new normal [1] has driven its state of action into another level making the time more complex to live. The uncertainty that persists worldwide caused by unpredictable environmental changes and socio-economic discrepancies has surpassed the impact by that of any historical period. Thereby occurred transformations don't exist as mere external reflections, rather they deepen into the psychological domain and personal behaviour demanding accelerated flexibility [2]. When the affecting factors take a lead from the traditional job issues and family matters to more complicated and diverged digital fatigue and climate anxiety, exposure to multi-layered problems and thereby created stressors becomes global normality. The changes that occurs in every field of human existence, now adopts an integrated approach than of sole exertions. Environmental, economic and social issues can now be contemplated as interconnected or rather interdependent and so has to be the solutions. This state of affairs is well stated by [3] as, there occurred a great shift in the domain system of life from being a simple mechanical and fairly predictable one into more dynamic, complex and interdependent. Coping stressors have attached itself firmly to larger systemic uncertainties demanding individuals to possess flexible and continuous adaptation [4,5]. This prompts the need for psychological adaptability. Here arises the need for individuals to cope along with not just isolated personal challenges, but with a broader range of systemic stressors that incorporates economic, social and environmental factors which are interconnected in a complex manner. The ability to reflect,

replace and restock coping strategies in response to shifting necessities and demands – cited as coping flexibility, can be explicated according to [6,7] as a well-balanced psychological resource for sustainability existence. Aside from possessing a wide range of coping strategies, coping flexibility also comprises of undergoing continuous evaluation and revision to be effective in the demanding situational challenges. Classic coping strategies whether problem-focused or emotion-focused are in static nature which can effectively, but context based. In a world which demands situational adaptability, flexibility in coping mechanisms is well required as drawn from [7].

Moreover, the situation gets intensified when the external stressors also plays the role of coping influencers. Environmental, social and economic aspects that bridges individual challenges to global issues, in effect shape, restrict and influence the coping strategies and effectiveness of an individual. This points out towards the need of an integrated framework that links psychological adaptability with socio-economic-environmental exposure. The need gets perfectly aligned with the population of secondary school students as the central stakeholders in sustainability education and action, making it essential to understand their coping mechanisms in the context of sustainability. This pressing need of the ever-changing era leads to this study aiming at developing and validating a tool for assessing Coping Flexibility which is strongly rooted on theoretical synthesis and conceptual framework to assess the ability of an individual in possessing, adapting and resorting the coping strategies across environmental, social and economic spheres among secondary school students.

II. Theoretical Overview and Related Review

Reference [8] has developed Flexibility in Coping with Stress Questionnaire (FCSQ) stressing upon the ability of an individual to cope up with as the situation demands giving prominence to the psychological resilience and mental health. The study which is rooted upon integrated theoretical aspects explored Repertoire of coping strategies, Changeability and Reflexivity as the dimensions of Coping Flexibility using the factor analysis statistics.

The study conducted by [7] in developing a Coping Flexibility Scale revealed a two-factor structure for coping flexibility as Evaluation Coping and Adaptive Coping with a total of 10 items as 5 serving for each dimension. The result has been obtained through statistical calculations including exploratory factor analysis. Reference [9] has studied various methods of assessing coping flexibility. Although, not a typical study on tool development, it observes strategy situation fit and observations of individuals.

The revelation of reviews of related literature done by the researcher as there is a need for a proper assessment instrument for coping flexibility in terms of environmental, social and economic aspects, lead to the proposed research. This study is grounded upon two contrasting theories namely, Dual process Theory of Coping Flexibility [7] and Triple Bottom Line Theory [10] that can provide an integrated approach to coping flexibility. These theories interconnect the coping components – Repertoire, Changeability and Reflexivity [6] with dimensions of sustainability drawn from [10], rendering a wide spectrum reflecting the adaptability of coping strategies across the environmental, social and economic domains.

In this study, Triple Bottom Line theory acts as a contextual structure upon which the components of coping flexibility acts. As to develop a comprehensive measuring instrument for coping flexibility, the psychological dimensions (Repertoire, Changeability and Reflexivity) is been integrated with sustainability domains (Environmental, Social and Economic). Thereby the developed instrument is comprised of three theoretical domains – Sustainability Repertoire (SR), Sustainability Changeability (SC) and Sustainability Reflexivity (SRX), each giving due emphasis upon the sustainability aspects.

III. Materials and Methods

A. Study Design

The study followed a well-structured instrument development design rooted upon mixed methodology of both qualitative and quantitative aspects. The process is entrenched on established tool development protocol drawn from [11] consisting of three phases – Item Development, Scale Development and Scale evaluation which again encompasses of nine steps. Fig. 1 depicts the process.

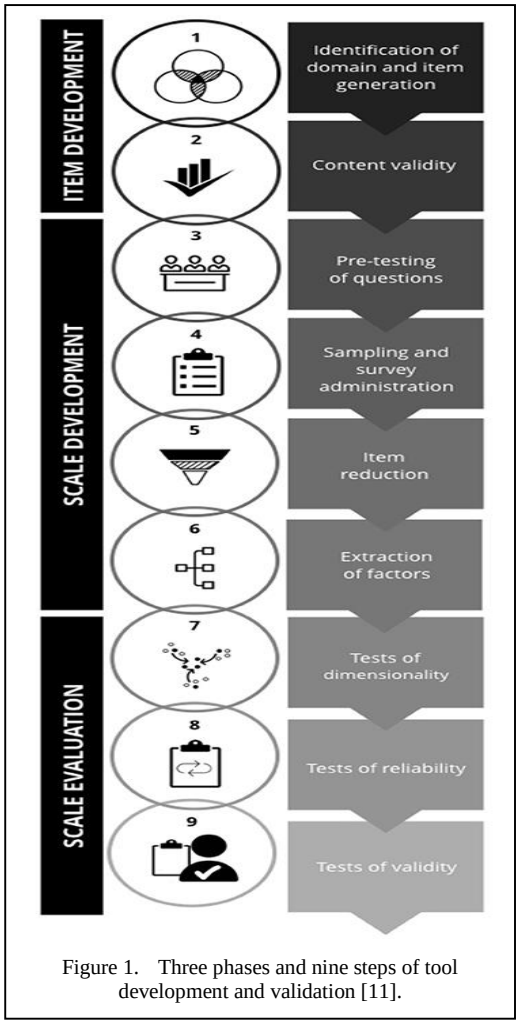

Figure 1. Three phases and nine steps of tool development and validation [11].

The instrument to assess coping flexibility is been developed through these three phases and following definite steps to ensure its comprehensiveness, validity and reliability.

B. Item Development

Psychological components of coping flexibility [6] derived from The Theory of Coping Flexibility [7] and domains of sustainability [10] has been kept in view for the development of a comprehensive assessing instrument for coping flexibility. Hence determined three components of coping flexibility are given due importance while constructing the statements of the tool. Also, the items are constructed in forging each component emphasizing upon environmental, social and economic aspects. During item development, sustainability aspects were explicitly rooted into the wording, context and behavioral focus of each item, keenly embedding them with sustainability constraints. Each item is generated ensuring clarity and relevance, covering all aspects of the construct. Conceptual clarity has also been confirmed by giving prominence to a single theoretical component by each item. The constructed items which is a total of 36 is included of both positive and negative statements and are in a compatible format for a five-point scale.

A panel comprising five experts from the disciplines of psychological and ecological domains established the face and content validity of the instrument to ensure its accuracy in attaining the intended construct. Experts from the areas of both sustainability and psychology, validated the items to be comprised of coping flexibility characteristics, embedding contextual sustainability cues. A qualitative expert review is been collected using criteria-based rubrics. The four criteria provided upon which the experts reviewed the instrument are content appropriateness, clarity, relevance and language appropriateness. Proper measures have been taken according to the suggested revisions, making the instrument refined with a robust foundation for further statistical validations.

IV. Scale Development and Scale Evaluation

A. Test of Dimensionality

As statistical technique exploring the underlying structure of the developed tool which is rooted upon theoretical and practical concerns, factor analysis [12], ensures the items group together and serves the purpose of the proposed theoretical and conceptual framework. In this study, exploratory factor analysis is used to explore the factors underlined by integrating two distinct theories. Pilot sample of the study consisting of 327 participants comes under the recommended requirement [13] and the KMO value is calculated to ensure the sampling adequacy prior to the exploratory analysis of factors.

B. Tests of Validity and Reliability

As an integrated measuring technique of content validity and construct validity, as well noted by [14] and [15], Item Analysis play a vital role in assessing and validating the internal structure of an instrument. The developed Coping Flexibility Scale with 36 items indicating the nine subcomponents, is subjected to pilot study among 327 participants representing the population of Secondary School

Students. Thereby collected data is been subjected to Item Analysis as a second stage of formal validation process to enhance the reliability and accuracy of the instrument. Items with a *t*-value above the reference value 1.96 and *p* value less than 0.5 are retained [16]. As for ensuring the internal consistency and stability of the instrument, Cronbach Alpha has been computed for the entire 36 item Scale and for each of the subcomponents as well. The alpha value above the reference value of 0.70 [17] is kept as testimonial.

V. RESULTS

The developed instrument to assess Coping Flexibility is validated using various qualitative as well as quantitative methods comprising Expert Validation, Exploratory Factor Analysis and Item Analysis.

A. Validation of the Instrument

The sampling adequacy test, for a total of 327 participants, using Kaiser-Meyer-Olkin (KMO) calculations resulted in determining the sample size of the study is adequate in nature with a value of 0.697 which satisfies the reference value [18,19]. The Bartlett Sphericity Test with a significance of 0.00 reflects that there exists a difference between the data ($p < 0.001$). Both the KMO value and Bartlett Sphericity test results as in Table I indicates that exploratory factor analysis can be done with the collected data [20].

TABLE I. KMO VALUE AND BARTLETT'S TEST OF SPHERICITY OF COPING FLEXIBILITY SCALE.

Kaiser-Meyer-Olkin measure of sampling adequacy		0.697
Bartlett's test of sphericity	Approx. Chi-square	2428.665
	Df.	630
	Sig.	0.000

Exploratory Factor Analysis is conducted to explore and determine the factors of the instrument using principal component analysis. The calculated eigenvalues resulted in three prominent components. The subscales are namely Sustainability Repertoire (SR), Sustainability Changeability (SC) and Sustainability Reflexivity (SRX) identified in comparison with the scale developed by [6] in 2021. Appropriateness of the factor variance has been determined through retainment of items with values ranging from 0.35 to 0.711 which falls above the reference value of 0.3 [21]. The researcher has selected items that that falls above the absolute value 0.35 to ensure the quality of the instrument. Out of the total 36 items, 24 items which falls above 0.35, that exceeds the acceptable reference value are retained in the instrument on basis of their factor loadings which varies from a range of 0.35 - 0.711. 12 items that doesn't meet the critical value requirement and those doesn't fall under the required component base were rejected.

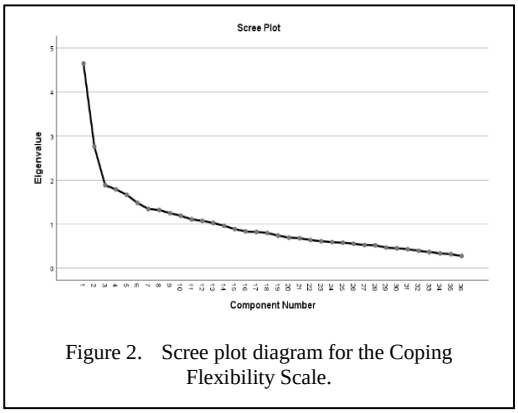

Figure 2. Scree plot diagram for the Coping Flexibility Scale.

From the above statistical calculations, thereby obtained scree plot (Fig. 2) and extended review of literature the researcher reached a conclusion that the Coping Flexibility Scale is comprised of the components Sustainability Repertoire (SR), Sustainability Changeability (SC) and Sustainability Reflexivity (SRX) (Table II).

TABLE II. SUBSCALE WISE NUMBER OF ITEMS.

Subscale	**No. of Items**
Sustainability Repertoire (SR)	12
Sustainability Changeability (SC)	6
Sustainability Reflexivity (SRX)	6

As the primary aim of the present study attributes upon initial scale development and exploratory identification of latent dimensions, Confirmatory Factor Analysis is omitted. Ensuring the methodological safeguards such as high sampling adequacy and significant Bartlett's test and internal consistency indices serves as a confirmation of the factorial structure of the instrument.

B. Item Validation

Validity of the instrument has also been established for ensuring the quality and performance of each item through the extreme group method of item analysis [22]. The researcher has used the upper 27 percent and lower 27 percent of the participants according to their total score obtained from the five-point

scale pilot implementation. Independent t-test has been carried out for determining whether the difference that existed between the groups in their item responses is significant. Out of the 24 items (retained after factor analysis) which are subjected to item analysis, 23 which falls above 1.96, the critical value for two-tailed independent t-test at 0.05 significance level [14] are retained as for the final draft of the Coping Flexibility Scale. The obtained t value which ranges from 1.963 to 13.917 and significance level of the selected items depicts that there exists a clear-cut discrimination between the high and low scores of individuals in their coping flexibility. An item with insignificant t-value showing limited discriminative power has been removed from the developed instrument as in Table III.

TABLE III. NUMBER OF ITEMS RETAINED AND REJECTED AFTER ITEM ANALYSIS.

Total Items subjected to item analysis	24
No. of items retained	23
No. of items rejected	1

Each items internal consistency contribution has also been calculated through Corrected Item Total Correlations and Cronbach's Alpha if item deleted to ensure the overall reliability of the scale [11,14]. Now, after the calculations, 13 items that met both the criteria with Corrected Item Total Correlations greater than 0.30 [14] and remained closer to the overall Cronbach's Alpha (0.742) in condition to the item is deleted as in Table IV. The retained items fall under a range of Corrected Item Total Correlation values from 0.122 to 0.279 which is less than the critical value. They also possess the Alpha values if deleted within the range of 0.719 to 0.733 which are of in no capability of improving the Cronbach Alpha if the item is deleted. 11 Items with Corrected Item Total Correlation values above 0.30, showing a possible ability to misalign with the overall scale and are retained with improvisations, leading to the retainment of 22 items. Two items possessing very low correlation, which are threat to the internal consistency of the instrument are removed.

TABLE IV. THE RESULT OF CORRECTED ITEM TOTAL CORRELATIONS AND CRONBACH'S ALPHA IF ITEM DELETED.

Total number of items	23
No. of items retained	22
No. of items rejected	2

C. Reliability Analysis

Internal Consistency of the tool as a whole has been calculated using Cronbach Alpha resulting in a coefficient of 0.758 which reflects an acceptable level of internal consistency as above 0.7 [17] as shown in Table V.

TABLE V. CALCULATED CRONBACH ALPHA VALUE.

Cronbach's Alpha	0.765
No. of Items	22

VI. DISCUSSIONS

This study resulted in a multi-dimensional Coping Flexibility Scale with 22 items. The developed tool has been subjected to Factor Analysis for dimension exploration, Item Analysis for Item validation and reliability testing for ensuring quality of the instrument. Thereby validated instrument for assessing coping flexibility of secondary school students with respect to the environmental, social and economic aspects consists of three dimensions as – repertoire, changeability and reflexivity. The scale serves true to its construct, content and face cogency as established by the quantitative and qualitative analysis results.

Flexibility in Coping Stress Questionnaire (FCSQ) developed by [8]. Revealed a three-factor structure as repertoire of coping strategies, changeability and Reflexivity for coping flexibility, which goes well with the findings of the researcher in this study developing the Coping Flexibility Scale. While FCSQ concentrates upon psychological resilience and mental health, this study gives prominence to the environmental, social and economic aspects which an individual need to be cope up with flexibility as part of an ever-changing era.

The Coping Flexibility Scale developed by the researcher corresponds very much to Kato's Coping Flexibility Scale [7] in nature of its results. Even though Kato identified the components of coping flexibility as adaptive coping and evaluation coping, in this study the dimensions have been explored as Repertoire, Changeability and Reflexivity which can be a modified version of adaptive coping and evaluation coping.

In the Coping Flexibility Questionnaire (COFLEX) [23] composed a two-factor model of coping flexibility with a total of 13 items. With an acceptable internal consistency, the tool

contains versatility and reflective coping as its dimensions for assessment. Even though the study differs in terms of the components with the present study, both the studies aligns in sharing the aspects of changeability and reflexivity.

In another study of [24] in which the coping flexibility hypothesis is being re-examined using Coping Flexibility Scale- Revised (CFS-R). The study is concluded by ensuring the viability of the tool which is constructed upon the components derived as abandonment, re-coping and meta coping through exploratory and confirmatory factor analysis. The study complements the findings of the present study which also concluded in three components from exploratory factor analysis.

VII. CONCLUSION

The correspondence of the present study to these studies which reflects the similarity of results points out the developed instrument as a valid and reliable tool for assessing coping flexibility. This multidimensional assessing instrument can be breakthrough in the area of coping flexibility as an integrated approach has been followed through each of the three phases of tool development [11]. With a multidimensional view giving due importance to sustainability and ecological aspects, the developed instrument serves well in assessing coping flexibility in terms of Sustainability Repertoire (SR), Sustainability Changeability (SC) and Sustainability Reflexivity (SRX). The statement is endorsed by the results of exploratory factor analysis. The contextual aspects incorporated in the Coping Flexibility Scale can help it fill a notable gap in the assessment of coping flexibility.

REFERENCE

[1] Organisation for Economic Co-operation and Development. (2018). *The future of education and skills: Education 2030* (OECD Education Policy Perspectives No. 98). OECD Publishing.

[2] Bauman, Z. (2000). *Liquid modernity*. Polity Press.

[3] Sterling, S. (2001). *Sustainable education: Re-visioning learning and change*. Green Books for the Schumacher Society.

[4] Lazarus, R. S., & Folkman, S. (1984). *Stress, appraisal, and coping*. Springer.

[5] Clayton, S. (2020). Climate anxiety: Psychological responses to climate change. *Journal of Anxiety Disorders, 74*, Article 102263.

[6] Cheng, C., Lau, H. P. B., & Chan, M. P. S. (2014). Coping flexibility and psychological adjustment to stressful life changes: A meta-analytic review. *Psychological Bulletin, 140*(6), 1582–1607.

[7] Kato, T. (2012). Development of the Coping Flexibility Scale: Evidence for the coping flexibility hypothesis. *Journal of Counseling Psychology, 59*(2), 262–273.

[8] Basińska, M. A., Góralska, K., & Kruczek, A. (2021). Flexibility in Coping with Stress Questionnaire: Structure and psychometric properties. *Current Issues in Personality Psychology, 9*(2), 141–154.

[9] Cheng, C. (2001). Assessing coping flexibility in real-life and laboratory settings: A multimethod approach. *Journal of Personality and Social Psychology, 80*(5), 814–833.

[10] Elkington, J. (1997). *Cannibals with forks: The triple bottom line of 21st century business*. Capstone Publishing.

[11] Boateng, G. O., Neilands, T. B., Frongillo, E. A., Melgar Quiñonez, H. R., & Young, S. L. (2018). Best practices for developing and validating scales for health, social, and behavioral research: A primer. *Frontiers in Public Health, 6*, 149.

[12] Field, A. (2024). *Discovering statistics using IBM SPSS statistics.* Sage publications limited.

[13] Worthington, R. L., & Whittaker, T. A. (2006). Scale development research: A content analysis and recommendations for best practices. *The Counseling Psychologist, 34*(6), 806–837.

[14] DeVellis, R. F. (2016). *Scale development: Theory and applications*. Sage Publications.

[15] Gravetter, F. J., & Wallnau, L. B. (2016). *Statistics for the behavioral sciences*. Cengage Learning

[16] George, D., & Mallery, P. (2003). *SPSS for Windows step by step: A simple guide and reference*. Allyn & Bacon.

[17] Kaiser, H. F. (1974). An index of factorial simplicity. *Psychometrika, 39*(1), 31–36.

[18] Hutcheson, G. D., & Sofroniou, N. (1999). *The multivariate social scientist: Introductory statistics using generalized linear models.* Sage Publications.

[19] Leech, N. L., Barrett, K. C., & Morgan, G. A. (2005). *SPSS for intermediate statistics: Use and interpretation*. Lawrence Erlbaum Associates.

[20] Stewart, D. W. (1981). The application and misapplication of factor analysis in marketing research. *Journal of Marketing Research, 18*(1), 51–62.

[21] Kelley, T. L. (1939). The selection of upper and lower groups for the validation of test items. *Journal of Educational Psychology, 30*(1), 17–24.

[22] Kelley, T. L. (1939). The selection of upper and lower groups for the validation of test items. *Journal of Educational Psychology, 30*(1), 17–24.

[23] Vriezekolk, J. E., van Lankveld, W. G. J. M., Eijsbouts, A. M. M., van Helmond, T., Geenen, R., & van den Ende, C. H. M. (2012). The coping flexibility questionnaire: Development and initial validation in patients with chronic rheumatic diseases. *Rheumatology International, 32*(8), 2383–2391.

[24] Kato, T. (2020). Examination of the coping flexibility hypothesis using the Coping Flexibility Scale-Revised (CFS-R). *Frontiers in Psychology, 11*, 561731.

eNergetics 2025
DOI: https://doi.org/10.5281/zenodo.18633234

Original Scientific Article

Novel Quantum Chaotic Human Activity based Optimization Algorithm for Loss Lessening in Electrical Power and Distribution System

Lenin Kanagasabai[1]

[1]Prasad V.Potluri Siddhartha Institute of Technology, Vijayawada, Andhra Pradesh, India

[1]gklenin@gmail.com

Abstract—**An optimized condition of sexual feelings in humans is commonly measured a healthy, satiating experience inside the framework of the sexual retort cycle, which encompasses stages of yearning, stimulation, excitement, orgasm, and to final state of resolution. This optimal state comprises a receptive, healthy physique and mind, free from disproportionate or challenging desires and prejudiced by features such as mind wellness, association excellence, and bodily health. Healthy level of sexual attentiveness and feelings are might be prejudiced by interior and peripheral signs. Mind and physical eagerness are prominent to functional vicissitudes like augmented rate of heart beating and blood flow. Amplified condition of arousal will prevail when bodily and emotional tension physiques. Built-up pressure, supplemented with congenial feelings and the discharge of sensation good endorphins during the state of feelings in sexuality. Rendering to mind and emotive Well-being, an optimistic feeling and condensed anxiety contribute to vigorous sexual moods and retorts. In terms of relationship eminence, Optimistic acquaintances and mental state of closeness can nurture superior sexual satisfaction. Quantum chaotic human activity based optimization algorithm (QCHA) is validated in 7 benchmark functions and IEEE 30, 57 bus systems.**

Keywords - quantum, human, body, mind, wellness, chaotic map.

I. INTRODUCTION

Loss lessening is a significant feature in monetary operation of electrical power transmission and distribution system. Numerous procedures [1-11] are applied to solve the power loss lessening problem. In this research paper Quantum chaotic human activity based optimization algorithm (QCHA) is defined to solve the power loss lessening problem. Sexual feelings in humans encompass a multifaceted amalgamation of physical, responsive, psychosomatic, and social components, encircling sexual yearning, stimulation, and desirability, which can vacillate ominously all over the life owing to biological influences like hormones, specific familiarities, and ecological impacts [12,13]. Whereas a normal portion of human involvement, the communication and empathetic of the state of mind is identified as human sexuality, is miscellaneous and delicate. Attentiveness in the sexual activity can range from minor interest to obsessive drive and is prejudiced by hormones, psychologically based feelings, affection, and social features. The corporeal and demonstrative rejoinder to sexual stimulus, prominent to intensified feelings of anticipation and physical vicissitudes. The tendency is bodily or passionately attentive in added individual, frequently connecting feelings, approaches, and physical ambiances. Hormones play a momentous role, specifically in the progress of sexual feelings and physique

ISBN: 978-86-82602-07-1

variations in the retro of puberty. Corporeal vicissitudes with period and circumstances like menopause will affect the mind state of sexual desire. Feelings, affection elegances, and mind wellness will significantly impact the sexual desire. For illustration, fretfulness will affect an individual's competence to move to the state of sexual desire. Ethnic principles, religious opinions, affiliation eminence, and life conditions all silhouette how individuals familiarize and express their feeling of sexuality. Whatever is measured as normal desire diverges vastly from one individual to another person, with no solitary customary for sexual yearning or occurrence. Yearning is the preliminary attentiveness in sexual commotion. Sexuality is an individual expedition that progresses over a period and can be an optimistic and emancipating facet of life. As soon as sexual feelings are initiating apprehension or deleteriously impacting the life or associations, referring a trustworthy mature, doctor and sexual wellbeing expert can be valuable. An optimized condition of sexual feelings in humans is commonly measured a healthy, satiating experience inside the framework of the sexual retort cycle, which encompass stages of yearning, stimulation, excitement, orgasm, and to final state of resolution. This optimal state comprises a receptive, healthy physique and mind, free from disproportionate or challenging desires and prejudiced by features such as mind wellness, association excellence, and bodily health. Quantum chaotic human activity based optimization algorithm (QCHA) is validated in 7 benchmark functions and IEEE 30, 57 bus systems.

II. PROBLEM FORMULATION

Vital objective function of the loss lessening problem [14] is delineated as:

$$\begin{aligned} &min\tilde{F}\left(\bar{g},\bar{h}\right),\\ &M\left(\bar{g},\bar{h}\right)=0,\\ &N\left(\bar{g},\bar{h}\right)=0, \end{aligned} \tag{1}$$

$$g=\begin{matrix}[VLG_1,..,VLG_{Ng};QC_1,..,\\ ,..,QC_{Nc};T_1,..,T_{N_T}]\end{matrix}, \tag{2}$$

$$h=\begin{matrix}[PG_{slack};VL_1,..,VL_{N_{Load}};\\ QG_1,..,QG_{Ng};SL_1,..,SL_{N_T}]\end{matrix}, \tag{3}$$

$Q_C \rightarrow$ Reactive power compensator;

$T \rightarrow$ Transformer tap;

$V_G \rightarrow$ Generator voltage;

$PG_{slack} \rightarrow$ Slack generator;

$V_L \rightarrow$ Voltage in transmission lines;

$Q_G \rightarrow$ Reactive power generator.

Fitness functions are defined as follows:

$$\begin{aligned} F_1 &= P_{min} = \\ &= min\left[\sum_{m}^{N_{TL}} G_m\left[V_i^2+V_j^2-2\cdot V_j cos\emptyset_{ij}\right]\right], \end{aligned} \tag{4}$$

$$F_2 = min\left[\begin{matrix}\sum_{i=1}^{N_{LB}}\left|V_{Lk}-V_{Lk}^{desired}\right|^2+\\ +\sum_{i=1}^{N_G}\left|Q_{GK}-Q_{GK}^{Lim}\right|^2\end{matrix}\right], \tag{5}$$

$$F_3 = Minimize\, L_{maximum}\ . \tag{6}$$

$S_L \rightarrow$ Apparent power;

$$L_{max} = max\left[L_j\right]; j=1; N_{LB}\ , \tag{7}$$

$$\begin{cases} L_j = 1-\sum_{i=1}^{N_{PV}} F_{ji}\dfrac{V_i}{V_j}\\ F_{ji} = -\left[Y_1\right]^1\left[Y_2\right] \end{cases}, \tag{8}$$

$$L_{max} = max\left[1-\left[Y_1\right]^{-1}\left[Y_2\right]\times\frac{V_i}{V_j}\right]. \tag{9}$$

Parity constraints:

$$\begin{aligned} 0 &= P_{Gi}-P_{Di}-V_i\cdot\\ &\cdot\sum_{j\in N_B} V_j\left[G_{ij}cos\left[\emptyset_i-\emptyset_j\right]+B_{ij}sin\left[\emptyset_i-\emptyset_j\right]\right], \end{aligned} \tag{10}$$

$$\begin{aligned} 0 &= Q_{Gi}-Q_{Di}-V_i\cdot\\ &\cdot\sum_{j\in N_B} V_j\left[G_{ij}sin\left[\emptyset_i-\emptyset_j\right]+B_{ij}cos\left[\emptyset_i-\emptyset_j\right]\right], \end{aligned} \tag{11}$$

Disparity constraints:

$$\begin{aligned} P_{gsl}^{min} \le P_{gsl} \le P_{gsl}^{max}, \\ Q_{gi}^{min} \le Q_{gi} \le Q_{gi}^{max}, i \in N_g, \\ VL_i^{min} \le VL_i \le VL_i^{max}, i \in NL, \\ T_i^{min} \le T_i \le T_i^{max}, i \in N_T, \\ Q_c^{min} \le Q_c \le Q_C^{max}, i \in N_C, \\ \left|SL_i\right| \le S_{L_i}^{max}, i \in N_{TL}, \\ VG_i^{min} \le VG_i \le VG_i^{max}, i \in N_g, \end{aligned} \quad (12)$$

$$F = F_1 + r_i F_2 + uF_3 =$$

$$= F_1 + \begin{bmatrix} \sum_{i=1}^{NL} x_v \left[VL_i - VL_i^{min}\right]^2 + \\ + \sum_{i=1}^{NG} r_g \left[QG_i - QG_i^{min}\right]^2 \end{bmatrix} + r_f F_3 \quad , (13)$$

$$VL_i^{minimum} = \begin{cases} VL_i^{max}, VL_i > VL_i^{max} \\ VL_i^{min}, VL_i < VL_i^{min} \end{cases} , \quad (14)$$

$$QG_i^{minimum} = \begin{cases} QG_i^{max}, QG_i > QG_i^{max} \\ QG_i^{min}, QG_i < QG_i^{min} \end{cases} , (15)$$

III. Quantum Chaotic Human Activity based Optimization Algorithm

Sexual feelings in humans encompass a multifaceted amalgamation of physical, responsive, psychosomatic, and social components, encircling sexual yearning, stimulation, and desirability, which can vacillate ominously all over the life owing to biological influences like hormones, specific familiarities, and ecological impacts. Sexuality is an individual expedition that progresses over a period and can be an optimistic and emancipating facet of life. As soon as sexual feelings are initiating apprehension or deleteriously impacting the life or associations, referring a trustworthy mature, doctor and sexual wellbeing expert can be valuable. Population is generated randomly as:

$$\begin{aligned} z_{i,j} = lb_j + M\left(ub_j - lb_j\right), \\ ub_j, lb_j \rightarrow bounds \end{aligned} , \quad (16)$$

An optimized condition of sexual feelings in humans is commonly measured a healthy, satiating experience inside the framework of the sexual retort cycle, which encompass stages of yearning, stimulation, excitement, orgasm, and to final state of resolution. This optimal state comprises a receptive, healthy physique and mind, free from disproportionate or challenging desires and prejudiced by features such as mind wellness, association excellence, and bodily health.

$$\begin{aligned} Z_{i,j}^{L1} = Z_{i,j} + M \cdot \left(B_j - M_1 \cdot Z_{i,j}\right), \\ Z_{i,j}^{L1} \rightarrow fresh\, location\, of\, ith\, member, \\ B_j \rightarrow condition\, of\, humans, \\ M \in [0,1], M_2 \in \{1,2\}, \\ Z_i = \begin{cases} Z_i^{L1}, F_i^{L1} \le F_i \\ Z_i, else \end{cases}. \end{aligned} , (17)$$

With reference to physical health condition, healthy physique with proper hormone intensities and virtuous cardiovascular functional activities support the sexual wellbeing.

$$\begin{aligned} V_i = \{Z_k, F_k > F_i\}, \\ V_i \rightarrow Physical\, wellness, \\ Z_{i,j}^{L2} = Z_{i,j} + G \cdot \left(Z_{i,j} - G_2 \cdot U_{i,j}\right), \\ Z_{i,j}^{L2} \rightarrow fresh\, location\, of\, ith\, member, \\ U_{i,j} \rightarrow internal\, conditions, \\ Z_i = \begin{cases} Z_i^{L2}, F_i^{L2} \le F_i \\ Z_i, else \end{cases}. \end{aligned} , (18)$$

Healthy level of sexual attentiveness and feelings are might be prejudiced by interior and peripheral signs. Mind and physical eagerness are prominent to functional vicissitudes like augmented rate of heart beating and blood flow. Amplified condition of arousal will prevail when bodily and emotional tension physiques. Built-up pressure, supplemented with congenial feelings and the discharge of sensation good endorphins during the state of feelings in sexuality. In terms of relationship eminence, Optimistic acquaintances and mental state of closeness can nurture superior sexual satisfaction. In Mind and body association, a holistic methodology that identifies the complication of sexual

familiarities, comprising both bodily and psychosomatic features are important.

$$\begin{aligned} &Z_{i,j}^{L3} = Z_{i,j} + M \cdot (1-2M) \cdot \frac{ub_j - lb_j}{t}, \\ &Z_{i,j}^{L3} \to fresh\, location\, of\, ith\, member, \\ &M \in [0,1], \\ &Z_i = \begin{cases} Z_i^{L3}, F_i^{L3} \le F_i \\ Z_i, else \end{cases} \end{aligned} \quad , (19)$$

Even the health of the human is in good condition when there are disturbances in the mind then this condition will affect the state of sexual desire. Even minor disturbance will affect the yearning, stimulation, excitement and orgasm. This condition is expressed scientifically through chaotic tent map [15].

$$\begin{aligned} &Z_{t+1} = Z_t + C \cdot \gamma \cdot (Z_{new} - Z_t \cdot \delta), \\ &\alpha = \frac{2z}{T}, \\ &C \to Chaotic\, tent\, map, \\ &f(z) = \mu z,\ z < 0.6, \\ &f(z) = (1-z),\ z \ge 0.6. \end{aligned} \quad , \quad (20)$$

In the phase of arousal, humans own natural tendencies to perceive the sexual feeling indication of opposite gender. This indication will trigger the sexual feelings enormously in the mind of the specific individual.

$$\vartheta_i = \vartheta_i + c(\vartheta_{be} - \vartheta_i) \ . \quad (21)$$

Few times through the variation in the vocal sound humans knowingly or unknowingly indicate their state of sexual feelings to the opposite gender.

$$\vartheta_i = \vartheta_i + c(G - 0.6) \ . \quad (22)$$

Mating probability of the humans during the peak of arousal in the phase of sexual feelings is scientifically defined as,

$$\begin{aligned} &P = e^{\frac{\Delta f}{r(t)}}, \\ &P \to probability\, of\, mating\ . \end{aligned} \quad . \quad (23)$$

During mating there will be condition of dominance between male and female. Fitness value will be calculated and the outcome reveals the difference of fitness value between male and female. Engaging mating activity depend on level of sexual feelings, environment condition and societal factors. As soon as the arousal of feelings is high after the indication observed by male from female then sequentially there will be rapid movement towards mating in the secured place.

$$\begin{aligned} &s(t) = \gamma \cdot s(t-1), \\ &\gamma = 0.7, \\ &s(t) \to factor\, of\, swiftness. \end{aligned} \quad . \quad (24)$$

The energy level during mating scientifically defined as:

$$\begin{aligned} &o(t) = \gamma \cdot o(t-1), \\ &o \to energy, \\ &\gamma \in [0,1]. \end{aligned} \quad . \quad (25)$$

Specific cases arousal may occur just on visualization of unknown opposite gender. Even there is no cue from opposite gender there is probability of arousal of sexual feelings. In such case the release of sexual feelings may be on other opposite gender individual with the consent yet the mind reclaim the image of the previously seen unknown individual. This is action of thinking one individual and release of sexual feelings on another individual with mutual consent. This commotion is explicated by Kurt Lewin's Behavior Equation [16] as:

$$B = f(P,E) \ . \quad (24)$$

Quantum computing [15] has been amalgamated in the process:

$$\begin{aligned} &|\Psi|^2 \cdot da \cdot db \cdot dc = Q \cdot da \cdot db \cdot dc, \\ &\Psi \to probability\, density, \\ &ih\ \partial/\partial t\, \Psi(a,t) = H \cdot \Psi(a,t), \\ &H = -h^2 / 2m\Delta^2 + V(xa), \\ &S(T)\frac{d^2\Psi}{dz^2} + \frac{2m}{h^2}\left[G + \gamma\delta(z)\right]\Psi = 0. \end{aligned} \quad . (25)$$

1. Begin;

2. Fix the parameters;

3. Create the population randomly;

4. Define the condition bodily health;

5. $Z_{i,j}^{L1} = Z_{i,j} + M \cdot \left(C_j - M_1 \cdot Z_{i,j} \right)$;

6. Describe activities supports sexual wellbeing;

7. $Z_{i,j}^{L2} = Z_{i,j} + M \cdot \left(Z_{i,j} - M_2 \cdot U_{i,j} \right)$;

8. Define the condition of mind wellness and emotions;

9. $Z_{i,j}^{L3} = Z_{i,j} + M \cdot (1 - 2M) \cdot \dfrac{ub_j - lb_j}{t}$;

10. Define the condition by chaotic map;

11. $Z_{t+1} = Z_t + C \cdot \gamma \cdot (Z_{new} - Z_t \cdot \delta)$;

12. $\alpha = \dfrac{2z}{T}$;

13. $f(z) = \mu z, z < 0.6$;

14. $f(z) = (1 - z), z \geq 0.6$;

15. Define the indication of sexual cue;

16. $\vartheta_i = \vartheta_i + c(\vartheta_{be} - \vartheta_i)$;

17. $\vartheta_i = \vartheta_i + c(G - 0.6)$;

18. Define the probability of mating;

19. $P = e^{\frac{\Delta f}{r(t)}}$;

20. Define the factor of swiftness;

21. $s(t) = \gamma \cdot s(t-1)$;

22. Define the dynamism level;

23. $o(t) = \gamma \cdot o(t-1)$

24. Describe the individual behavior;

25. $|\Psi|^2 \cdot da \cdot db \cdot dc = Q \cdot da \cdot db \cdot dc$;

26. $H = -h^2 / 2m\Delta^2 + V(xa)$;

27. $S(T)\dfrac{d^2\Psi}{dz^2} + \dfrac{2m}{h^2}\left[G + \gamma\delta(z) \right]\Psi = 0$;

28. $t = t + 1$

29. End.

IV. RESULTS

Validity of Quantum chaotic human activity based optimization algorithm (QCHA) is verified in 7 benchmark functions [1]. Table I present the results:

$$f_1 = \sum_{i=1}^{D} x_i^2,$$

$$f_2 = -20\,exp\left\{ -0.2\sqrt{\frac{1}{D}\sum_{i=1}^{D} x_i^2} \right\} -$$

$$-exp\left\{ \frac{1}{D}\sum_{i=1}^{D} cos(2\pi x_i) \right\} + 20 + e,$$

$$f_3 = \sum_{i=1}^{D-1} \left\{ 100\left(x_{i+1} - x_i^2 \right)^2 + (x_i - 1)^2 \right\},$$

$$f_4 = \frac{1}{4000}\sum_{i=1}^{D} x_i^2 - \prod_{i=1}^{D} cos\left(\frac{x_i}{\sqrt{i}} \right) + 1,$$

$$f_5 = -\sum_{i=1}^{4} c_i\, exp\left[-\sum_{j=1}^{3} a_{ij}\left(x_j - p_{ij} \right)^2 \right],$$

$$f_6 = 4x_1^2 - 2.1x_1^4 + \frac{1}{3}x_1^6 + x_1x_2 - 4x_2^2 + 4x_2^2,$$

$$f_7 = \left\{ \begin{matrix} 1 + (x_1 + x_2 + 1)^2 \cdot \\ \left(19 - 14x_1 + x_1^2 - 14x_2 + 6x_1x_2 + 3x_2^2 \right) \end{matrix} \right\} \cdot$$

$$\cdot \left\{ \begin{matrix} 30 + (2x_1 - 3x_2)^2 \cdot \\ \cdot \left(18 - 32x_1 + 12x_1^2 + 48x_2 - 36x_1x_2 + 27x_2^2 \right) \end{matrix} \right\}. \quad (26)$$

TABLE I. QCHA EXAMINATION IN 7 BENCHMARK FUNCTIONS

F	HSO[1]	ESO[1]	QCHA
1	0.8874	0.0026	0.0079
2	0.0918	0.0125	0.0182
3	22.9814	16.5622	16.473
4	1.1092 e-2	3.459 e-4	3.84 e-4
5	-3.8629	-3.8629	-3.8629
6	-1.0318	-1.0316	-1.0328
7	3.0280	3.0130	3.0128

Validity of Quantum chaotic human activity based optimization algorithm (QCHA) is verified in IEEE 30 bus system. Table II and Fig. 1 and 2 exhibits the investigation. PE (MW) – power loss, DE (PU) – Deviancy of voltage, ST (PU) – Stability of voltage.

TABLE II. QCHA ANALYSIS IN IEEE 30 BUS SYSTEM

Technique	PE (MW)	DE (PU)	ST (PU)
ATE [2]	4.5464	1.9889	0.1294
GUM [3]	4.1781	0.4697	0.1323
AYQ [4]	5.6614	0.1536	0.2683
PNS [5]	4.6304	0.1678	0.2524
PDO [6]	5.0763	0.6828	0.3297
GYZ [10]	6.1300	0.4710	0.3521
MGE [11]	5.3048	0,4632	0.3614
QCHA	4.0049	0.0069	0.4663

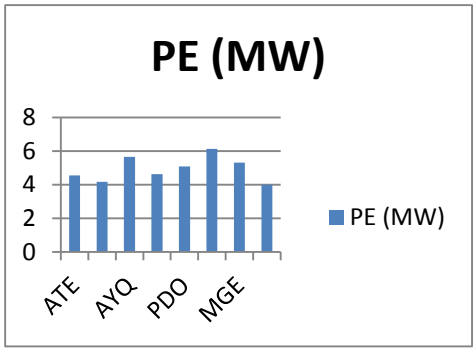

Figure 1. Power loss (PE) comparison in IEEE 30 bus system.

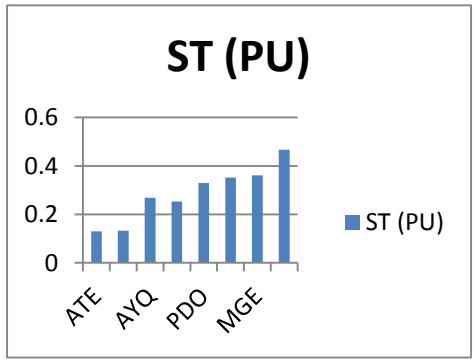

Figure 2. Volatge stability (ST) comparison in IEEE 30 bus system.

Validity of Quantum chaotic human activity based optimization algorithm (QCHA) is verified in IEEE 57 bus system. Table III and Figs. 3 and 4 displays the investigation.

TABLE III. QCHA ANALYSIS IN IEEE 57 BUS SYSTEM

Technique	PE (MW)	DE (PU)	ST (PU)
EUS [7]	25.4963	0.799021	0.3129
LJA [8]	24. 4198	0.7844	0.3512
PGC [9]	29.535	0.8725	0.3791
QCHA	20.0174	0.46149	0.4651

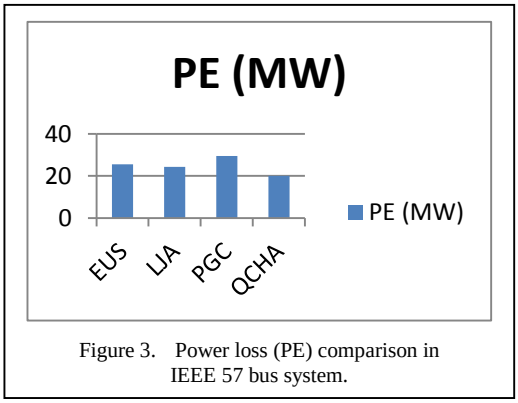

Figure 3. Power loss (PE) comparison in IEEE 57 bus system.

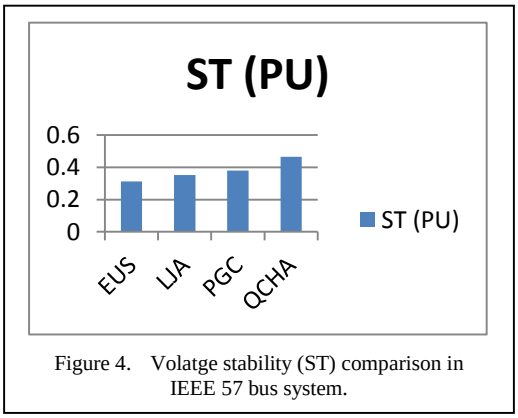

Figure 4. Volatge stability (ST) comparison in IEEE 57 bus system.

Table IV shows the time taken by Quantum chaotic human activity based optimization algorithm (QCHA)

TABLE IV. TIME TAKEN BY QCHA

Technique	30 bus T(S)	57 bus T(S
QCHA	15.72	19.82

V. CONCLUSION

Ethnic principles, religious opinions, affiliation eminence, and life conditions all silhouette how individuals familiarize and express their feeling of sexuality. Whatever is measured as normal desire diverges vastly from one individual to another person, with no solitary customary for sexual yearning or occurrence. Yearning is the preliminary attentiveness in sexual commotion. Excitement is corporeal and emotive arousal dimensions. Orgasm is the ultimate of sexual exhilaration and release. Resolution is the physique returns to its pre-arousal period of the body. Sexuality is an individual expedition that progresses over a period and can be an optimistic and emancipating facet of life. As soon as sexual feelings are

initiating apprehension or deleteriously impacting the life or associations, referring a trustworthy mature, doctor and sexual wellbeing expert can be valuable. An optimized condition of sexual feelings in humans is commonly measured a healthy, satiating experience inside the framework of the sexual retort cycle, which encompass stages of yearning, stimulation, excitement, orgasm, and to final state of resolution. This optimal state comprises a receptive, healthy physique and mind, free from disproportionate or challenging desires and prejudiced by features such as mind wellness, association excellence, and bodily health. Quantum chaotic human activity based optimization algorithm (QCHA) is validated in 7 benchmark functions and IEEE 30, 57 bus systems.

REFERENCES

[1] Yapıcı, H., & Çetinkaya, N. (2017). An improved particle swarm optimization algorithm using eagle strategy for power loss minimization. *Mathematical Problems in Engineering*, *2017*(1), 1063045.

[2] Ali, M. H., Soliman, A. M. A., Abdeen, M., Kandil, T., Abdelaziz, A. Y., & El-Shahat, A. (2023). A novel stochastic optimizer solving optimal reactive power dispatch problem considering renewable energy resources. *Energies*, *16*(4), 1562.

[3] Hasanien, H. M., Alsaleh, I., Tostado-Véliz, M., Zhang, M., Alateeq, A., Jurado, F., & Alassaf, A. (2024). Hybrid particle swarm and sea horse optimization algorithm-based optimal reactive power dispatch of power systems comprising electric vehicles. *Energy*, *286*, 129583.

[4] PG, A. K., & Devaraj, D. (2022). Hybrid CAC-DE in optimal reactive power dispatch (ORPD) for renewable energy cost reduction. *Sustainable Computing: Informatics and Systems*, *35*, 100688.

[5] Shaheen, M. A., Ullah, Z., Hasanien, H. M., Tostado-Véliz, M., Ji, H., Qais, M. H., ... & Jurado, F. (2023). Enhanced transient search optimization algorithm-based optimal reactive power dispatch including electric vehicles. *Energy*, *277*, 127711.

[6] Gil, M., Akbari, E., Rahimnejad, A., Ghasemi, M., & Gadsden, S. A. (2024). Solution of optimal reactive power dispatch by Lévy-flight phasor particle swarm optimization. *Intelligent Systems with Applications*, *23*, 200398.

[7] Khan, N. H., Wang, Y., Jamal, R., Iqbal, S., Ebeed, M., Ghadi, Y. Y., & Elbarbary, Z. M. S. (2024). Enhanced skill optimization algorithm: Solution to the stochastic reactive power dispatch framework with optimal inclusion of renewable resources using large-scale network. *IET Renewable Power Generation*, *18*, 4565-4583.

[8] Abd-El Wahab, A. M., Kamel, S., Hassan, M. H., Mosaad, M. I., & AbdulFattah, T. A. (2022). Optimal reactive power dispatch using a chaotic turbulent flow of water-based optimization algorithm. *Mathematics*, *10*(3), 346.

[9] Khan, N. H., Jamal, R., Ebeed, M., Kamel, S., Zeinoddini-Meymand, H., & Zawbaa, H. M. (2022). Adopting Scenario-Based approach to solve optimal reactive power Dispatch problem with integration of wind and solar energy using improved Marine predator algorithm. *Ain Shams Engineering Journal*, *13*(5), 101726.

[10] In, S., Ang, S., Choeung, C., Ieng, S., Cheng, H., & Huy, V. (2024). Optimal Reactive Power Dispatch Using Artificial Gorilla Troops Optimizer Considering Voltage Stability. *International Journal of Electrical and Electronics Research*, *12*(3), 1001-1009.

[11] Rao, N. T., Kumar, K. K., Kumar, P. P., Nuvvula, R. S., Mutharasan, A., Dhanamjayulu, C., ... & Khan, B. (2024). Multiobjective optimal TCSC placement using multiobjective grey wolf optimizer for power losses reduction. *Scientific Reports*, *14*(1), 21857.

[12] Mües, H. M., Markert, C., Feneberg, A. C., & Nater, U. M. (2025). Bidirectional associations between daily subjective stress and sexual desire, arousal, and activity in healthy men and women. *Annals of Behavioral Medicine*, *59*(1), kaaf007.

[13] Girouard, A., Bergeron, S., Huberman, J. S., & Rosen, N. O. (2025). Daily perceived stress and sexual health in couples with sexual interest/arousal disorder. *International Journal of Clinical and Health Psychology*, *25*(2), 100582.

[14] Kanagasabai, L. (2024). Novel empress SARANI optimization algorithm for active power loss reduction and voltage stability enhancement. *Heliyon*, *10*(22).

[15] Alshathri, S., Abd Elaziz, M., Yousri, D., Hassan, O. F., & Ibrahim, R. A. (2022). Quantum chaotic honey badger algorithm for feature selection. *Electronics*, *11*(21), 3463.

[16] Cummings, S., Bridgman, T., & Brown, K. G. (2016). Unfreezing change as three steps: Rethinking Kurt Lewin's legacy for change management. *Human relations*, *69*(1), 33-60.

eNergetics 2025
DOI: https://doi.org/10.5281/zenodo.18633252

Original Scientific Article

Synthesized NiV_2O_6 Materials for Electrochemical Applications

Ayouz Katia[1], Nouredine Gabouze[2], Chafiaa Yaddaden[3], Malika Berouaken[4], Saloua Merazga[5], Fatima Boudeffar[6], Maha Ayat[7]

[1,2,3,4,5,6,7]Research Center on Semiconductor Technology for Energtics, Algiers, Algeria

[1]searchkat12@gmail.com

Abstract—**In this article, NiV_2O_6 (named NVO in this paper) is successfully synthesized using sol-gel method at optimum conditions. The structures and morphologies of the simples were investigated by X-ray diffraction, scanning electron microscope (MEB) and Attenuated Total Reflection (ATR), and X-ray photoelectron spectroscopy (XPS). The electrochemical properties and performances as cathode electrode based on active material NVO were studied by cyclic voltammetry (CV), between potential bias [0.1V to 3.8V], with scanning speed of 0.1mVs^{-1}, the galvanostatic charge/discharge (CDG) for 50 cycles was also measured.**

Keywords - Li-Ion batteries, NiV_2O_6 materials, structural and morphologicals caracterisation.

I. INTRODUCTION

Lithium-ion (LIB) batteries are currently considered vital source of energy in smart devices and hybrid cars due to their high energy density and long lifespan. Technology of LIB battery is principally based on the intercalation of lithium ions in the host structures of positive and negative electrodes [1].

Transitional metal oxides have been investigated as electrode materials in lithium-ion batteries [1-3]. Among them, vanadium pentoxide is one of the most promising cathode materials [4-6], because it can exhibit high insertion level of Li+ ions, resulting in a high specific energy density. Recently, a variety of V2O5-based composite electrodes such as M2+-V2O5 (M: Ni, Mn, Co, Cu, Ag) [7-9] and MO-V2O5 (M: Ni, Ti) [10,11] have received considerable attentions. For instance, the electrochemical insertion processes of lithium ions into Ni-V2O5 (Ni/V = 0.075) have been investigated by Inagaki et al. [7]. Recently, Lourenco et al. fabricated vanadium–nickel mixed oxides thin films as promising electrode materials by rf sputtering [10], these electrode materials exhibited large capacity and good electrochemical reversibility upon cycling for several hundred cycles at a current density of 50 A/cm^2. Although previous studies have been done, it is necessary to do more works for further exploration of the electrochemical reaction mechanism of NiO-V2O5 composite film electrodes and improvement of their specific capacity and cycleability.

In this work, structural and morphological characterizations of synthetized NVO were performed. NVO was analysed by Scanning Electron Microscope (SEM), The X-ray diffraction, FTIR spectrum was recorded and XPS characterization was carried out using an Escalab Xi+ X-ray Photoemission Spectrometer (XPS). The electrochemical reactions mechanism of the synthetized powder electrode with lithium during the discharge and charge cycle is also discussed.

II. EXPERIMENTAL SECTION

A. Synthesis

In a typical synthesis, 0,4 mg of Nickel Acetate II ($C_4H_6O_4Ni.4H_2O$) « Sigma-Aldrich » (98 %) is added to 80 ml of Ethanol, and stirred for 1 hour, then we add 0.5 g vanadium oxides V2O5 « Sigma-Aldrich » (99 %), after 2 hours an orange precipitate is obtained. The obtained

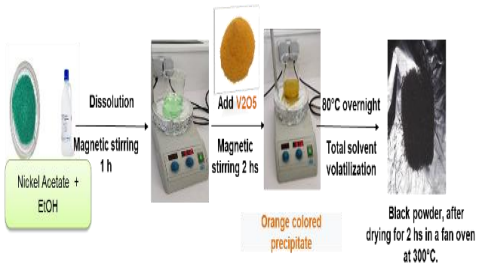

Figure 1. NVO synthesis steps.

product was dried in an oven at 80°C overnight for further characterization, and then dried for 2 hours in a ventilated oven at 300°C. The synthesis steps are schematized in Fig. 1.

B. Characterization

The nano-particles of synthesized NVO was analysed by JEOL High Resolution Scanning Electron Microscope (SEM) JSM-7610FPlus operated at 200kV has and magnification of *x* 1.000.000 with a resolution of 0.8 nm and incomparable stability, allowing the observation of extreme surface morphologies and the particle size of the synthesized product.

The X-ray diffraction characterizations were made from D8 Advance Eco diffractometer (Bruker brand), it operates with Cu-K α radiation (λ = 1.54Å). Diffraction patterns were recorded at room temperature in the range $5° \leq 2\theta \leq 80°$ by step scanning. The step and scanning speeds were set to 0.1° and 2°/min respectively.

FTIR spectrum was recorded with Thermo Nicolet FTIR/ATR NEXUS 670, using KBr pellets in the range of 400-1000 cm^{-1}. And XPS characterizations of the powders produced were carried out using an Escalab Xi+ X-ray Photoemission Spectrometer (XPS).

Electrochemical measurements were carried out using coin cells. For the preparation of the working electrode, a mixture of NVO powder, carbon black, and poly-vinylidene fluoride as binder (PVDF) in a weight ratio of 80:15:5 were mixed with 1-methy1-2-pyrrolidone (NMP) solvent, to make a slurry. This slurry was coated onto aluminum foil current collectors using blade-coating techniques, to serve as cathode, then dried under vacuum at 80°C for 12h. The active material was loaded at a density of 2.4 $mgcm^{-2}$. The cell was assembled in a glove box under argon with humidity and oxygen levels maintained below 0.1 ppm. and was consisting of

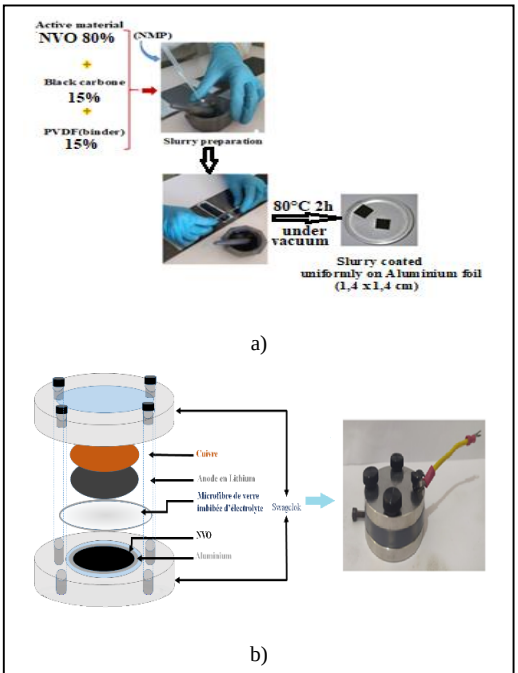

Figure 2. Electrode fabrication (a), Cell assembly (b).

a metallic lithium anode, a cathode based on the synthesized active material NVO and a non-aqueous electrolyte 1 M $LiPF_6$ dissolved in EC, DEC and DMC (2:1:2 v/v) with a separator between the electrodes. Fig. 2 show the slurry steps elaborated and the cell assembly.

Electrochemical measurements such cyclic voltammetry (CV), performed in a potential window of [0.1 to 3.8] V vs Li/Li^+ in scan rate of 0.1mV/s and electrochemical impedance spectroscopy (EIS) performed with an OCV (Open Circuit Voltage) of 3.2 V, and after several charge/discharge cycles, in the frequency range of 100 kHz to 1 mHz with an AC potential of 10 mV at open circuit voltage.

These measurements were investigated using a VMP3 BioLogic potentiostat/Galvanostat controlled by EC-Lab software.

III. Results and Discussion

Principle of the microscope is based on scanning surface of the sample by electron beam followed by the detection of secondary electrons emitted by the sample. This effect is transformed as an electrical signal to give the image observed in Fig. 3. The morphology of the powder of the NiV_2O_6 produced chemically. The structure is dispersed homogeneously over the entire analyzed surface, and the morphology of as-

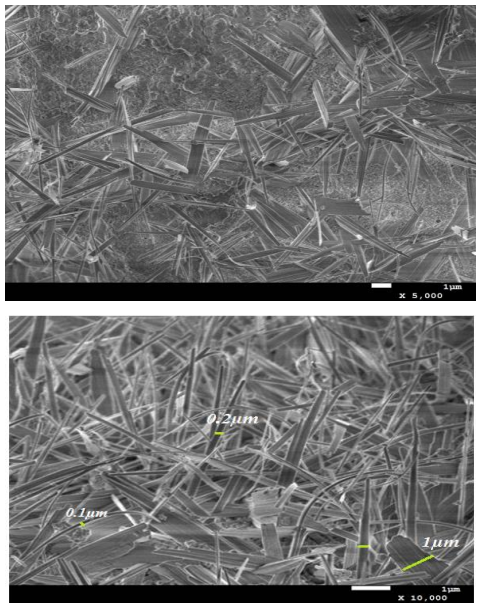

Figure 3. SEM images of as-prepared NiV_2O_6 Powder.

prepared material shows a nanobelts forms with different diameters between 0.1µm to 1µm.

Fig. 4, shows the FTIR spectrum FTIR-ATR (Attenuated total reflectance–Fourier transform infrared (ATR-FTIR) spectroscopy), of the composite NV as prepared powder. We observe absorption bands at 533cm^{-1} and 576cm^{-1} attributed to the elongation mode of (Ni-O) bond, according to the literature [12].

The absorption bands at 733 cm^{-1} and 477 cm^{-1}, 820 cm^{-1}, 963 cm^{-1} correspond to the deformation of the V-O-V bond, the V-O elongation mode, and the stretching mode of the V-O-V bond respectively [13,14].

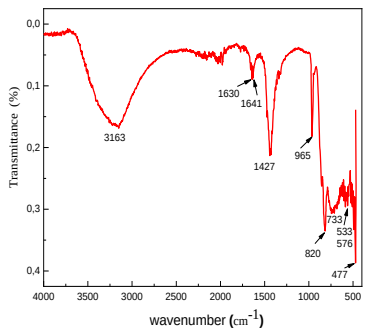

Figure 4. FT-IR spectra of as-prepared NiV_2O_6 material.

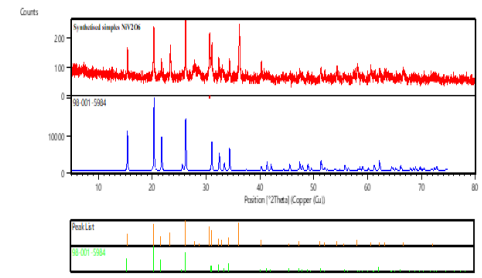

Figure 5. XRD patterns of NVO as prepared powder.

The absorption bands at 3400 cm^{-1}, 1630 cm^{-1} and 1427 cm^{-1}, are assigned to a stretching mode of the O-H bond and to the straining mode of the H-O-H bond. The absorption band at 1641 cm^{-1} is assigned to C = O in elongation mode.

The X-ray diffraction pattern of the NiV_2O_6 compound exhibit defined peaks (Fig. 5.), indicating the formation of a crystalline phase. According to the Standard JCPDS file no. 98-001-5984, peak indexing, performed in the triclinic space group P-1, confirms the formation of NiV_2O_6 phase in its low-symmetry structure, which is consistent with crystallographic data reported for Ni–V mixed oxides with similar stoichiometry. The lattice parameters obtained ($a \approx 4.791$ Å, $b \approx 7.130$ Å, $c \approx 8.250$ Å) are consistent with the triclinic structures of the binary vanadate family, indicating Ni–O–V lattice formation with low distortions [15,16]. The average crystallite size, estimated by Scherrer equation is around ≈ 52 nm, suggests a nanocrystalline structure favorable to ion transfer. This size is typically associated with improved electrochemical reactivity, particularly for vanadium-based materials capable of hosting Li^+ ions at multiple crystallographic sites [17-19]. We also observe the absence of secondary peaks indicating the presence of another phases such as V_2O_5, NiO, or $Ni_3V_2O_8$, which are frequently observed when synthesis is incomplete or when the processing atmosphere is poorly controlled [20].

The surface composition of the NiV_2O_6 simples was also examined by XPS analysis, and the spectra results were shown in Fig. 6. The deconvolution for the Ni 2p spectrum was divided into Ni 2p1/2 and Ni 2p3/2, which included four peaks with binding energies centered at 854 and 874eV, 862 and 878.1 eV, indicating the existence of two nickel chemical states corresponding to Ni metal and NiO,

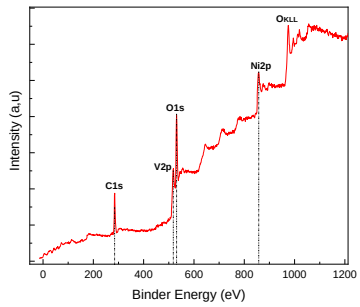

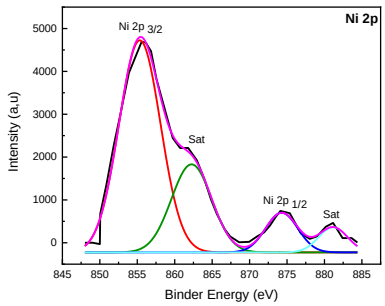

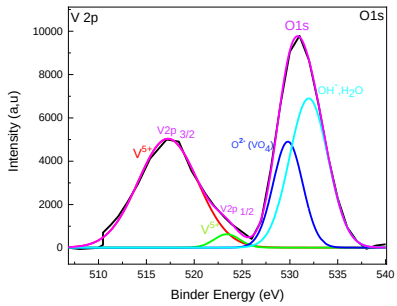

Figure 6. XPS spectra of Ni 2p, V 2p and O 1s for NVO simples.

respectively [21,22]. The V2p spectra exhibited two peaks at 517.1 and 524.7 eV, which were ascribed to V 2p1/ 2 and V2p3/2 from V2O5 for NiV2O6 simples. The XPS O 1s spectra showed two prominent peaks located at 530.0 and 532.4 eV, which were identified as V-O and Ni-O bond, respectively [22], confirming that the NiV_2O_6 was successfully fabricated on the surface of Ni foam. Additionally, no impurities were observed in XRD and XPS characterizations, indicating that the well crystalline NiV_2O_6 powder have been obtained following the experimental procedure mentioned above.

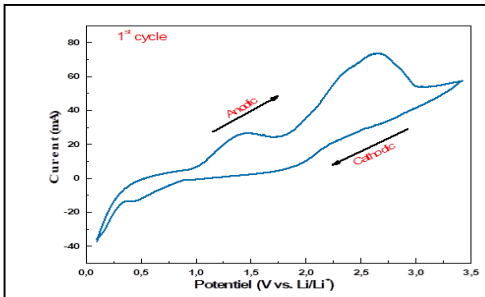

Figure 7. The CV curves of NVO electrode vs Li/Li+

Cyclic voltammetry measurement (Fig. 7) was carried out by assembling the half-cell configuration using lithium as cathode to examine their electrochemical property in the voltage range of [0.1-3.8] V at a scan rate 0.1 mVs^{-1}. Cyclic voltammogram gives the idea for the potential required for intercalation/ deintercalation.

The electrochemical behavior of the electrode based on NVO active materials during the first cycle can be explained by a sequence of redox reactions involving mainly the vanadium ions ($V^{5+}/V^{4+}/V^{3+}$), and Nickel (Ni^{2+}/Ni^{3+}), induced by insertion and disinsertion of Li^+ ion.

During the discharge (Cathodic reduction), Li^+ ions insert the structure of active material and reduce the transition metals: The first reduction V^{5+} to V^{4+}(~ 1.0-1.5)V region [23]:

$$NiV_2O_6 + Li^+ + e^- \rightarrow LiNiV_2O_6 \ . \quad (1)$$

Second reduction of vanadium (~ 1.5-2.0)V, corresponding to $V^{5+} \rightarrow V^{4+}$:

$$LiNiV_2O_6 + Li^+ + e^- \rightarrow Li_2NiV_2O_6 \ . \quad (2)$$

During the charge (Anodic oxidation), Li^+ is extracted, and the metals return to her initial oxidation states. Overall delithiation reaction (~ 2.5-3.1)V corresponding to: $V^{3+} \rightarrow V^{4+} \rightarrow V^{5+}$ [24,25]:

$$Li_2NiV_2O_6 \rightarrow NiV_2O_6 + 2Li^+ + 2e^- \ . \quad (3)$$

The visible gap between the anodic and cathodics features is typical of SEI formation during the first cycle, partially irreversible adjustments of the structure and slow diffusion of Li^+ .

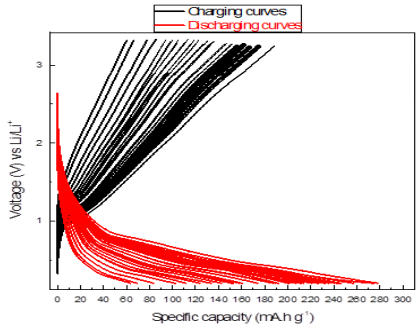

Figure 8. Cyclic voltammetry CV of NVO vs $LiPF_6$ for 50 cycles at a scan rate of $0.1mVs^{-1}$.

The charge-discharge profiles of the NVO electrode over 50 cycles exhibit a typical sloping behavior, indicating vanadium-based multivalent oxides (Fig. 8). The initial discharge capacity ~ 280mAh/g is characteristic to SEI formation, partially NVO reorganization during the first lithiation. This moderate is typical of Ni-V-O cathode-type materials.

Electrochemical impedance spectroscopy (EIS) was measured in the frequency region between 100 kHz and 0.01 Hz at a state of charge (SOC) of 3 V with 5 mV AC signal amplitude (all coin cells were cycled three times before EIS tests at the corresponding voltage ranges). Nyquist plots were fitted and analyzed using Zview software.

Fig. 9a represents the Nyquist diagram with the corresponding fitted spectrum of the NiV2O6 electrode. The Nyquist plot comprises two semicircles, one semicircle in the high frequency region and the other in the medium frequency region, while in the low frequency region a straight line is observed. The obtained semicircles were fitted with an equivalent circuit modeling (Fig. 9b).

The equivalent circuit is composed by two charge transfer resistances Rct1,2 and constant phase element CPE 1,2 elements connected in series. Series resistance (Rs) and Warburg impedance (Zw) are connected in series with the circuit. The series resistance Rs is determined from the intercept of the Nyquist diagram with Z axis in the high frequency region. A value of about 3.7 (Ω) is found for Rs which indicates a low resistance of the electrolyte. From the Niquist diagram at mid frequency region, the semicircle which corresponds to the NiV2O6 nanobelts gives a value of Rct2 = 780 (Ω),

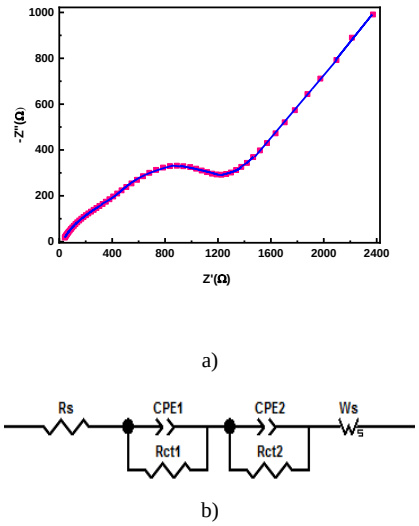

Figure 9. Electrochemical impedance spectroscopy: (a) Nyquist plot of cell. (b) Equivalent circuit.

indicating that the NiV_2O_6 simples' morphology facilitates the charge transfer.

IV. CONCLUSIONS

In this work, the NiV_2O_6 composite was successfully fabricated via a chemical method, and then applied as carbon- and binder-free electrode for the Li-ion battery. The obtained materials are characterized by X-ray diffraction, UV-Visible spectroscopy, Attenuated Total Reflection (ATR), Field emission scanning electron microscopy, Energy-dispersive X-ray analysis. Electrochemical properties and performances as cathode electrode based on active material NiV_2O_6 were studied by cyclic voltammetry (CV), between potential bias [0.1V to 3.8V], with scanning speed of 0.1mVs-1, the galvanostatic charge/discharge (CDG) for 50 cycles was also measured.

This work represents a first approach to understanding the properties of the composite NiV_2O_6 as a cathode electrode, the material has been successfully synthesized and studied by different characterizations, and it presents a promising material for lithium-ion battery electrodes, other more studies must be carried out to improve the specific capacity as well as the lifespan of the material. This preliminary study represents a first approach to NiV_2O_6 as a positive electrode for Li ion batteries application. This study has shown promising electrochemical properties of NiV_2O_6 as a cathode material for

lithium-ion batteries, but its practical application is often limited by factors such as moderate electronic conductivity, structural instability during cycling, and limited rate capability.

To ameliorate its performance, several strategies can be envisaged, such as: Nanostructuring and Morphology Control, of active material, reducing particle size to the nanoscale or designing hierarchical structures can increase the electrode surface area, shorten Li^+ diffusion paths, and improve reaction kinetics. Carbonaceous Composites by incorporating or adding more conductive carbon materials (graphene, carbon nanotubes, or amorphous carbon coatings) can enhance electronic conductivity and buffer volume changes during lithiation/delithiation. Doping and partial substitution of Ni or V with other transition metals (e.g., Co, Mn, or Fe) may stabilize the crystal structure, enhance redox activity, and improve cycling stability. Electrolyte Optimization, using high-performance electrolytes or additives can reduce side reactions, minimize capacity fading, and improve Coulombic efficiency.

REFERENCES

[1] Pralong, V. (2009). Lithium intercalation into transition metal oxides: A route to generate new ordered rock salt type structure. *Progress in Solid State Chemistry*, *37*(4), 262-277.

[2] Patil, S. H., Gaikwad, A. P., Sathaye, S. D., & Patil, K. R. (2018). To form layer by layer composite film in view of its application as supercapacitor electrode by exploiting the techniques of thin films formation just around the corner. *Electrochimica Acta*, *265*, 556-568.

[3] Aamir, A., Ahmad, A., Shah, S. K., Ain, N. U., Mehmood, M., Khan, Y., & Rehman, Z. U. (2020). Electro-codeposition of V2O5-polyaniline composite on Ni foam as an electrode for supercapacitor. *Journal of Materials Science: Materials in Electronics*, *31*(23), 21035-21045.

[4] Tan, P., Wei, Z. H., Shyy, W., Zhao, T. S., & Zhu, X. B. (2016). A nano-structured RuO 2/NiO cathode enables the operation of non-aqueous lithium–air batteries in ambient air. *Energy & Environmental Science*, *9*(5), 1783-1793.

[5] Benmalem, S., & Boughella, W. (2019). *Élaboration des couches minces de NiO/V_2O_5 sur le silicium poreux pour la détection de gaz et stockage d'énergie* (pp. 58–60).

[6] Baddour-Hadjean, R., Smirnov, M. B., Kazimirov, V. Y., Smirnov, K. S., & Pereira-Ramos, J. P. (2015). The Raman spectrum of the γ′-V2O5 polymorph: a combined experimental and DFT study. *Journal of Raman Spectroscopy*, *46*(4), 406-412.

[7] Majumdar, D., Mandal, M., & Bhattacharya, S. K. (2020). Journey from supercapacitors to supercapatteries: recent advancements in electrochemical energy storage systems. *Emerg Mater*. 3: 347–367.

[8] Pan, J., Li, C., Peng, Y., Wang, L., Li, B., Zheng, G., & Song, M. (2023). Application of transition metal (Ni, Co and Zn) oxides based electrode materials for ion-batteries and supercapacitors. *International Journal of Electrochemical Science*, *18*(9), 100233.

[9] Hdidou, L., Ghamouss, F., Manoun, B., Hannache, H., Alami, J., & Dahbi, M. (2023). Challenges and Strategies of High-Capacity Transition Metal Oxides as Anodes for Lithium-Ion Batteries (LIBs). In *Lithium Batteries-Recent Advances and Emerging Topics*. IntechOpen.

[10] Mai, L., Xu, L., Han, C., Xu, X., Luo, Y., Zhao, S., & Zhao, Y. (2010). Electrospun ultralong hierarchical vanadium oxide nanowires with high performance for lithium ion batteries. *Nano letters*, *10*(11), 4750-4755.

[11] Liu, Y., Wang, Y., Zhang, Y., Liang, S., & Pan, A. (2016). Controllable preparation of V2O5/graphene nanocomposites as cathode materials for lithium-ion batteries. *Nanoscale Research Letters*, *11*(1), 549.

[12] Shin, J., Jung, H., Kim, Y., & Kim, J. (2014). Carbon-coated V2O5 nanoparticles with enhanced electrochemical performance as a cathode material for lithium ion batteries. *Journal of alloys and compounds*, *589*, 322-329.

[13] Sasidharan, M., Gunawardhana, N., Yoshio, M., & Nakashima, K. (2012). V2O5 hollow nanospheres: A lithium intercalation host with good rate capability and capacity retention. *Journal of the Electrochemical Society*, *159*(5), A618.

[14] Zhang, R. H., Zhao, T. S., Jiang, H. R., Wu, M. C., & Zeng, L. (2019). V2O5-NiO composite nanowires: a novel and highly efficient carbon-free electrode for non-aqueous Li-air batteries operated in ambient air. *Journal of Power Sources*, *409*, 76-85.

[15] Patil, S. H., Gaikwad, A. P., Sathaye, S. D., & Patil, K. R. (2018). To form layer by layer composite film in view of its application as supercapacitor electrode by exploiting the techniques of thin films formation just around the corner. *Electrochimica Acta*, *265*, 556-568.

[16] Mak, W. F., Wee, G., Aravindan, V., Gupta, N., Mhaisalkar, S. G., & Madhavi, S. (2012). High-energy density asymmetric supercapacitor based on electrospun vanadium pentoxide and polyaniline nanofibers in aqueous electrolyte. *Journal of the Electrochemical Society*, *159*(9), A1481.

[17] Kim, J. G., Kim, Y., Noh, Y., Lee, S., Kim, Y., & Kim, W. B. (2018). Bifunctional hybrid catalysts with perovskite LaCo0. 8Fe0. 2O3 nanowires and reduced graphene oxide sheets for an efficient Li–O2 battery cathode. *ACS Applied Materials & Interfaces*, *10*(6), 5429-5439.

[18] Pang, Y., Wu, L., Liu, J., Tang, D., Xu, F., Cen, M., ... & Hu, Y. W. (2025). Tunable Surface Charge Redistribution via Lattice Strain Engineering in B/Mo Co-Doped NiV2O6 for High-Power Supercapacitors. *Advanced Functional Materials*, 2506747.

[19] Kotbi, A., El Radaf, I. M., Alaoui, I. H., Cantaluppi, A., Zeinert, A., & Lahmar, A. (2024). Structural and Optical Characterization of Porous NiV2O6 Films Synthesized by Nebulizer Spray Pyrolysis for Photodetector Applications. *Micromachines*, *15*(7), 839.

[20] M'hammedi, K., Haine, N., Bourenane, N., & Gabouze, N. (2019). Macroporous silicon (MPS) with embedded NiO thin film for CO 2 gas sensing. *Arabian Journal for Science and Engineering*, *44*(1), 521-529.

[21] Peck, M. A., & Langell, M. A. (2012). Comparison of nanoscaled and bulk NiO structural and environmental characteristics by XRD, XAFS, and XPS. *Chemistry of Materials*, *24*(23), 4483-4490.

[22] Mendialdua, J., Casanova, R., & Barbaux, Y. J. J. O. E. S. (1995). XPS studies of V2O5, V6O13, VO2 and V2O3. *Journal of Electron Spectroscopy and Related Phenomena*, *71*(3), 249-261.

[23] Rui, X., Lu, Z., Yu, H., Yang, D., Hng, H. H., Lim, T. M., & Yan, Q. (2013). Ultrathin V 2 O 5 nanosheet cathodes: realizing ultrafast reversible lithium storage. *Nanoscale*, *5*(2), 556-560.

[24] Poizot, P., Gaubicher, J., Renault, S., Dubois, L., Liang, Y., & Yao, Y. (2020). Opportunities and challenges for organic electrodes in electrochemical energy storage. *Chemical reviews*, *120*(14),6490-6557.

[25] Julien, C., Mauger, A., Zaghib, K., & Groult, H. (2016). Optimization of layered cathode materials for lithium-ion batteries. *Materials*, *9*(7), 595.

eNergetics 2025
DOI: https://doi.org/10.5281/zenodo.18633298

Original Scientific Article

Model Predictive Control of Electric Spring for Voltage Stabilization in Wind-driven Induction Generator based Microgrids

Soumyajit Ghosh[1], Arunava Chatterjee[2]

[1]Centre for Internet of Things, Madhav Institute of Technology and Science, Gwalior, India
[2]Department of Electrical Engineering, Raghunathpur Govt. Polytechnic, Dept. of Technical Education and Training, Govt. of West Bengal, India

[1]soumyajit@mitsgwalior.in, [2]arunava7.ju@gmail.com

Abstract—**Renewable energy powered microgrids present a viable option for isolated and rural areas. Within sustainable technologies, wind energy possesses great promise although its intermittent characteristics result in voltage instability and other reliability challenges. While Squirrel Cage Induction Generators (SCIGs) are inexpensive and rugged, the lack of voltage and reactive power regulation in wind systems poses challenges for their broader use. This paper suggests integrating an Electric Spring (ES) with Model Predictive Control (MPC) for maintaining voltage stability over sensitive loads in an SCIG-based wind microgrid. A Battery Energy Storage System (BESS) offers additional resilience in wind power fluctuation by actively balancing energy storage and providing discharge control through a bidirectional DC–DC converter. The effectiveness of the proposed MPC based ES control strategy is tested in MATLAB/Simulink with variable wind and load inputs which are also verified experimentally. The obtained results indicate that MPC outperformed PI control in a significant way, yielding significant improvements in settling time, RMS voltage deviation, and system control while providing reliable operation for critical loads in microgrids.**

Keywords - wind energy, induction generator (IG), electric spring, model predictive control (MPC), voltage stability.

I. INTRODUCTION

Microgrids powered by renewable energy are being used more often to meet the rising demand for sustainable electricity. This is especially true in rural and isolated areas where grid connections are weak or nonexistent. Among renewable sources, wind energy is a clean and plentiful option. However, its natural variability leads to challenges like voltage fluctuations, frequency instability, and poor power quality [1]. These issues become critical in microgrids, particularly when there is a high share of renewable energy and limited storage or backup options.

Squirrel Cage Induction Generators (SCIGs) are frequently used in small and medium-scale wind systems because they are sturdy, cost-effective, and easy to maintain [2,3]. Unlike Doubly Fed Induction Generators (DFIGs), SCIGs do not need slip-rings or complex converters [4,5]. This makes them a good choice for small-scale isolated applications. However, a significant drawback of SCIGs is the inability to control active and reactive power independently. Consequently, voltage regulation relies heavily on external compensation and control methods. In microgrids with changing and unbalanced loads, this limitation can hinder stable operations.

To tackle these challenges, researchers have investigated various solutions. Traditional methods include using capacitor banks, static VAR compensators (SVC), or flexible AC transmission systems (FACTS) for reactive power support [6,7]. While these approaches work to some degree, they struggle to adapt to

ISBN: 978-86-82602-07-1

rapid changes in wind and load conditions. In recent years, solutions based on power electronics, such as STATCOMs, inverter-based compensators, and Electric Springs (ES), have been introduced [8,9]. The Electric Spring concept, developed in the last decade, has shown promise in regulating voltage in microgrids. It does this by adjusting noncritical load demand and providing compensating voltages, making ES particularly effective in mixed-load microgrids with both critical and noncritical demands.

On the control side, conventional proportional–integral (PI) controllers are widely used for their simplicity. However, they do not perform well during large disturbances and in nonlinear situations. Proportional-resonant controller is also employed and proved to be promising [6]. Fuzzy logic controllers and interval type-2 fuzzy logic controllers (IT2FLC) have been suggested to manage system uncertainties, with studies noting improved performance [10,11]. Still, fuzzy controllers often face issues like rule explosion, require careful tuning, and have limited ability to predict. Model Predictive Control (MPC) has emerged as a strong alternative, as it considers system constraints and forecasts future behavior over a set timeframe. This results in better responsiveness and reliability compared to PI or fuzzy controllers [12,13]. Research on integrating renewable energy has shown MPC's potential for controlling inverters, supporting the grid, and managing power, but its use in Electric Spring-based SCIG microgrids is still limited.

Despite advancements, two research gaps are observed. First, most studies concentrate on DFIG or permanent magnet synchronous generator (PMSG)-based wind systems. In contrast, SCIGs, which are widely used [14-16], have received less attention regarding advanced microgrid control. Second, while several ES controllers are becoming popular, their computational complexity and lack of predictive power calls for alternative strategies like MPC.

This paper aims to fill these gaps. Limited research has utilized MPC for controlling energy systems in wind systems with SCIG, especially for microgrids with diverse load requirements. In addition, the integrated application of energy storage systems, specifically batteries, for providing voltage support and balancing energy, has been under-researched.

The major contributions of this paper are as follows:

- A SCIG-powered wind microgrid is represented with a rectifier-DC link-VSI cascade.
- An Electric Spring is placed in parallel with non-critical loads and controlled with a model predictive control (MPC) for fast and robust voltage control.
- A BESS is integrated with a bidirectional DC-DC converter to store energy during wind speed fluctuations.
- The comparative analysis of MPC-controlled ES and PI-controlled ES is presented. The findings demonstrate enhanced voltage stability, diminished settling time, and improved power quality.

By combining MPC, and Electric Spring in a SCIG-driven wind microgrid, this work offers a practical and new method for improving voltage stability and reliability in off-grid or weak-grid rural areas.

II. System Overview

The proposed system combines renewable energy conversion, control, and forecasting in a microgrid platform tailored for rural and isolated areas. The key components of the system include a wind turbine driving a Squirrel Cage Induction Generator (SCIG), a power electronic conversion chain, a battery energy storage system (BESS), an Electric Spring (ES) with model predictive control (MPC). Fig. 1 shows the overall system block diagram.

A. Wind Turbine and SCIG Conversion

In this study, the main renewable source is a wind turbine coupled to a squirrel cage induction generator (SCIG). SCIG is employed instead of DFIG mainly because it is mechanically simple,

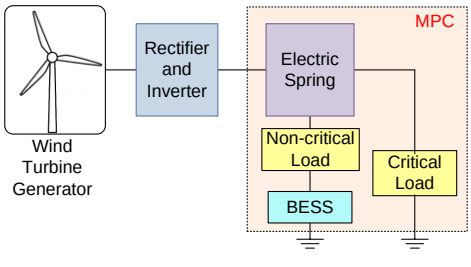

Figure 1. Proposed overall system block diagram.

rugged, cheaper, and requires less upkeep. Unlike synchronous machines or DFIGs, the SCIG does not allow separate control of active and reactive power. This limitation means that its terminal voltage and frequency vary depending on wind speed and load, which makes direct integration with the microgrid impractical without extra control or compensation.

The AC output from the SCIG is not constant and therefore it is converted to DC using a rectifier, a DC link, and finally again to AC via a voltage source inverter (VSI). The rectifier converts the variable-frequency AC into DC, which is stabilized by a capacitor in the DC link. The VSI then converts this DC back into AC, but in a controlled form, synchronized to microgrid requirements using pulse-width modulation (PWM). With this arrangement, the SCIG can operate over a wide range of wind conditions while still supplying power that matches the needs of local loads.

B. Battery Energy Storage System (BESS)

Because wind energy is unpredictable, the system includes a BESS connected via a bidirectional DC-DC converter. The BESS has two main functions:

Energy buffering: It stores excess energy when wind conditions are high and generation is surplus and provides power when wind is low.

DC link stabilization: The BESS quickly charges and discharges to help regulate the DC bus voltage, supporting transient stability.

The bidirectional DC-DC converter allows for flexible control of power flow between the DC link and the battery, ensuring efficient use of stored energy. The BESS control is coordinated within the MPC framework through DC-link voltage and state-of-charge constraints, rather than by an independent supervisory loop.

C. Electric Spring with Model Predictive Control

To maintain power quality for sensitive or critical loads, the Electric Spring (ES) is added to the system. The ES acts as a smart load compensator that adjusts voltage dynamically and absorbs fluctuations from renewable generation. Unlike standard passive voltage stabilizers, the ES actively redistributes voltage between non-critical and critical loads, ensuring a stable supply for sensitive loads like medical devices or communication systems.

Model Predictive Control (MPC) is used for the ES. MPC offers several benefits compared to standard PI or fuzzy logic controllers:

- It accounts for system dynamics and constraints clearly.
- It predicts future voltage and load demand over a set period.
- It optimizes ES control actions to reduce voltage deviations while staying within operational limits.
- This predictive method leads to more precise and flexible voltage regulation, improving the microgrid's resilience.

D. Overall System Operation

During operation, the SCIG produces variable AC power based on wind conditions. This power is rectified and inverted to supply the microgrid. The VSI offers controlled AC power, while the BESS smooths out energy fluctuations at the DC level. On the load side, the ES ensures stable voltage for critical loads using MPC.

It addresses the challenges of renewable intermittency and load sensitivity, ensuring reliable and high-quality power in remote areas.

III. CONTROL STRATEGY OF MPC

The MPC's objective is to compute, at each control step k a sequence of ES control actions that minimize voltage deviation of the critical load V_{cl} from its reference V_{ref} over a finite prediction horizon. The controller uses a discrete-time prediction model of the relevant dynamics and solves a quadratic programming (*QP*) problem online. Only the first control action is applied and the process repeats itself.

A. Discrete Time Prediction Model

A linearized, discrete-time state-space model is used that takes the dominant dynamics relating the ES injection to the critical load voltage. The ES load subsystem is linearized around an operating point and it is discretized with sampling time T_s. The states include the ES filter inductor current and capacitor voltage, and a measured bus voltage. A compact, control-oriented model is:

$$x(k+1) = Ad \cdot x(k) + Bd \cdot u(k) + Ed \cdot d(k) \quad ,(1)$$

$$y(k) = Cd \cdot x(k) \quad , \qquad (2)$$

where,

$x(k) \in \mathbb{R}^n$ = state vector (e.g., $[V_c, i_{ES}, \ldots]^T$);

$u(k) \in \mathbb{R}^m$ = ES control input;

$y(k) \in \mathbb{R}$ = controlled output (critical-load voltage V_{cl});

$d(k)$ = measurable/estimated disturbance (load or wind step change) (optional);

Ad, *Bd*, *Cd*, *Ed* = discrete-time matrices.

The $u(k)$ represents the injected series voltage. For prediction over a horizon N_p (prediction horizon) and a control horizon $N_c \le N_p$, stack future states and inputs:

$$X = F \cdot x(k) + G \cdot U \quad , \tag{3}$$

$$Y = \bar{C} \cdot X = \bar{C}F \cdot x(k) + \bar{C}G \cdot U \quad , \tag{4}$$

where,

X is the stacked vector of predicted outputs;

The vector of future control inputs, $U = \left[u(k) \ldots u(k+N_c-1)\right]^T$, $Y = \left[y(k+1) \ldots y(k+N_p)\right]^T$;

F, *G*, *H* are the standard prediction matrices built from (*Ad*, *Bd*, *Ed*) and,

$\bar{C} = I \otimes Cd$ is the extended output matrix built by repeating the single-step output equation across the prediction horizon.

B. Objective

Critical-load voltage tracking error and control move size are penalized. Thus,

$$J = \sum \{i = 1 \to N_p\} \left(y(k+i) - y_{ref}\right)^2 \cdot q + \\ + \sum \{i = 0 \to N_c - 1\} \left(\Delta u(k+i)\right)^2 \cdot r \quad , \tag{5}$$

with $\Delta u(k+i) = u(k+i) - u(k+i-1)$. Terms q and r are output tracking and control move weights. Also for tuning, $q > 0$ for tight voltage tracking, $r > 0$ to limit aggressive ES action.

In stacked form, thus, the objective function is, minimize:

$$\left(\hat{Y} - Y_{ref}\right)^T Q \left(\hat{Y} - Y_{ref}\right) + \left(\Delta U\right)^T R \left(\Delta U\right) \quad , \tag{6}$$

where,

$\hat{Y} = \bar{C}Fx(k) + \bar{C}G \cdot U$;

$Q = diag(q, \ldots, q) \in \mathbb{R}\text{^}\{N_p \times N_p\}$,

$R = diag(r, \ldots, r) \in \mathbb{R}\text{^}\{N_c \times N_c\}$;

ΔU is future of vector control moves, built from U and the known past input $u(k-1)$.

This becomes a standard *QP* as: minimize,

$$\tfrac{1}{2} \cdot U^T \cdot H \cdot U + f^T \cdot U \quad , \tag{7}$$

with $H = 2\left(\bar{G}^T Q \bar{G} + S_R\right)$ and $f = 2\bar{G}^T Q\left(\bar{F} \cdot x(k) - Y_{ref}\right)$, where $\bar{G} = \bar{C}G$, $\bar{F} = \bar{C}F$, and S_R is the effective weighting matrix for the control increments, comes from the ΔU term construction. Next, the constraints for the proposed problem are discussed in details. Constraints are focussed mainly to keep load voltage constant.

C. Constraints

All constraints are enforced for $i = 0 \ldots N_c - 1$ (input/rate) and $i = 1 \ldots N_p$ (output).

The key actuator constraint is ES injection limit. It is divided into two parts as the series injected voltage and the shunt reactive current and are,

$$V_{es\_min} \le u(k+i) \le V_{es\_max} \quad , \tag{8}$$

The maximum voltage is set by converter rating.

$$I_{es\_q\_min} \le u(k+i) \le I_{es\_q\_max} \quad , \tag{9}$$

This is bounded by ES inductor current and converter RMS current rating. The next constraint is load voltage (output) safety bounds and is given as,

$$y_{min} \le y(k+i) \le y_{max} \quad , \tag{10}$$

For a $240 V_{rms}$ critical load, common bound is ±10%: $y_{min} = 0.9 V_{ref}$, $y_{max} = 1.1 V_{ref}$.

DC link and BESS coupling are given as,

$$V_{dc\_min} \le V_{dc}(k+i) \le V_{dc\_max} \quad , \tag{11}$$

$$SOC_{min} \le SOC(k+i) \le SOC_{max} \ , \quad (12)$$

These are set via trials and errors.

D. *Receding-horizon Control Law*

At each sampling instant k:

- Measure/estimate $x(k)$.
- Build the quadratic Programming law QP using (1)-(12).
- Solve for U^*.
- Apply the first element: $u(k) = U^*[1]$.
- $k \leftarrow k+1$ and repeat.

The sampling time is 20ms. The horizons $N_p \approx$ 20-60; $N_c \approx$ 5-10 chosen so that the QP remains small and responsive. The cost function penalizes both voltage tracking error and control effort, weighted by q and r respectively (5)-(7).

IV. Results and Discussion

The proposed control is tested using MATLAB/Simulink simulations backed by experiments. The wind generator uses a squirrel cage induction generator of 1.5kW, 400V, 50Hz and having 4 stator poles. A three-phase diode bridge rectifier is used for IG rated output. DC link capacitor is of 2000uF, 450V. Inverter used is of PWM with 2kW output. The ES is designed using IGBT with 240V output. It is series-connected ES for voltage support across critical load. The critical load is 750W R-L load. A simple 100W heating load is used for non-critical load. The BESS is rated at 48V, 20Ah. In Fig. 2 with variations in wind speed, three cases are shown.

With no ES, load follows unstable wind pattern (Fig. 2(a)). With PI controller, the results are improved for voltage regulation however, the overshoot and delay remain (Fig. 2(b)). With the proposed control, it predicts correction and applies constraints for better regulation (Fig. 2(c)). In this paper, voltages are expressed in per-unit (p.u.), with $240V_{rms}$ taken as 1.0 p.u. Experimentally, the comparison is made regarding the schemes for comparison of voltage deviation and settling time. The results are shown below. In Fig. 3, the voltage deviation is shown to be 12% for no ES and 5% for PI controlled ES.

With the proposed control, the deviation is about 3% and is much better than the conventional control.

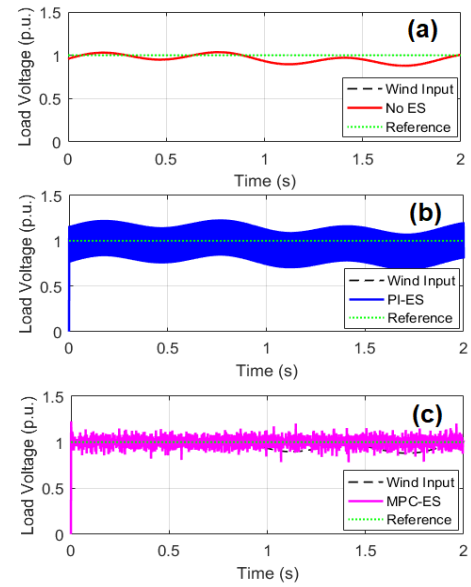

Figure 2. Comparison of different cases (a) no ES (b) with PI-ES and (c) with MPC-ES control.

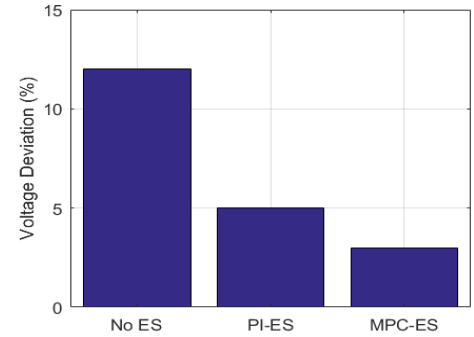

Figure 3. Experimental comparison of different cases for voltage deviation.

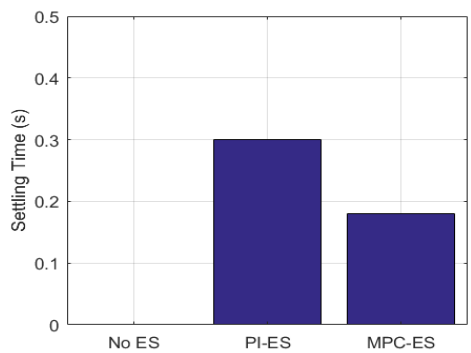

Figure 4. Experimental comparison of different cases for settling time.

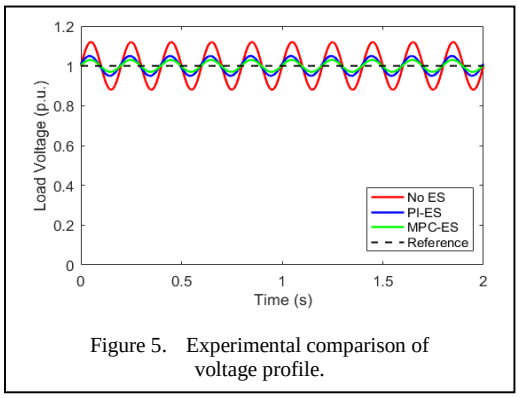

Figure 5. Experimental comparison of voltage profile.

Similarly, for settling time, the proposed control performs much better with time much below 0.2 s as shown in Fig. 4. Under rapid wind fluctuations, the MPC-ES shows faster settling (< 0.2 s) and lower RMS voltage deviation (nearly 3%) than PI-ES and without approaches, confirming superior dynamic stability.

Fig. 5 shows the experimental load voltage profile. For the proposed scheme, the deviation of voltage is less with lower overshoot as predicted.

The experimental trends closely match the MATLAB/Simulink simulations, confirming strong correlation between modeled and real-time responses with less than 5% deviation in voltage regulation performance.

V. CONCLUSION

This paper presents a simple yet effective and novel approach to enhance voltage regulation in a wind-driven microgrid using an induction generator and an Electric Spring (ES). The study demonstrates that traditional uncontrolled systems suffer significant voltage fluctuations under varying wind conditions, whereas PI-controlled ES offers partial voltage stabilization with noticeable overshoot and slower response. In contrast, an MPC-controlled ES significantly improves voltage regulation, reducing RMS deviations and settling times while maintaining system stability under dynamic loading.

The proposed methodology highlights the potential of combining ES with predictive or optimization-based control strategies for isolated or rural microgrids. The voltage deviation is reduced to 3% with settling time to a promising of less than 0.2s which is validated by simulations and experiments. The approach is straightforward to implement, scalable, and avoids the complexity of advanced AI-based forecasting, making it suitable for practical microgrid applications which is a future aspect of study. Future work will include quantitative statistical validation and broader metrics such as THD, computational efficiency, and robustness under extreme wind transients. The proposed MPC-ES concept can be extended to hybrid wind-solar or multi-node microgrids by incorporating additional renewable and storage dynamics into the prediction model.

REFERENCES

[1] Patel, M. R., & Beik, O. (2021). *Wind and solar power systems: Design, analysis and operation*. CRC Press.

[2] Bhatti, T. S., Bansal, R. C., & Kothari, D. P. (2003). A bibliographical survey on induction generators for application of non-conventional energy systems. *IEEE Trans. Energy Conversion*, *18*(3), 433-439.

[3] Roy, K., Chatterjee, A., Chatterjee, D., & Ganguli, A. K. (2015). A photovoltaic-based improved excitation control strategy of three-phase self-excited induction generator suitable for wind power generation. *Electric Power Components and Systems*, *43*(17), 1912-1920.

[4] Chatterjee, A., & Chatterjee, D. (2016). Analysis and control of photovoltaic-assisted three-phase induction machine operating as single-phase micro-wind generator. *IET Generation, Transmission & Distribution*, *10*(9), 2165-2176.

[5] Chatterjee, A., Roy, K., & Chatterjee, D. (2014). A Gravitational Search Algorithm (GSA) based Photo-Voltaic (PV) excitation control strategy for single phase operation of three phase wind-turbine coupled induction generator. *Energy*, *74*, 707-718.

[6] Pereira, R. M. M., Ferreira, C. M. M., & Barbosa, F. M. (2014). Comparative study of STATCOM and SVC performance on dynamic voltage collapse of an electric power system with wind generation. *IEEE Latin America Transactions*, *12*(2), 138-145.

[7] Ranjan, S., Das, D. C., Latif, A., Sinha, N., Hussain, S. S., & Ustun, T. S. (2021). Maiden voltage control analysis of hybrid power system with dynamic voltage restorer. *IEEE Access*, *9*, 60531-60542.

[8] Chatterjee, A., & Ghosh, S. (2025). Grid-Isolated Hybrid Generation for Critical Loads Supported by Electric Spring System With Smart Load Control. *IEEE Internet of Things Journal*.

[9] Yan, S., Tan, S. C., Lee, C. K., Chaudhuri, B., & Hui, S. R. (2014). Electric springs for reducing power imbalance in three-phase power systems. *IEEE Transactions on Power Electronics*, *30*(7), 3601-3609.

[10] Chatterjee, A. (2024). Wind Power Forecasting using Type-2 Fuzzy Control and its Optimization based on Artificial Neural Network for Small Scale Wind Power. *Journal of Fuzzy Systems and Control*, *2*(3), 170-175.

[11] Ghosh, S., Chatterjee, A., & Chatterjee, D. (2021). An improved load feature extraction technique for smart homes using fuzzy-based NILM. *IEEE Transactions on Instrumentation and Measurement*, *70*, 1-9.

[12] Routray, A., & Hur, S. H. (2022). Full operational envelope control of a wind turbine using model predictive control. *IEEE Access*, *10*, 121940-121956.

[13] Basheer, A. A., Jeong, J. H., Lee, S. R., & Joo, Y. H. (2024). Power maximization using finite-control-set model predictive control strategy for wind turbine systems. *IEEE Journal of Emerging and Selected Topics in Industrial Electronics*.

[14] Chatterjee, A., & Chatterjee, D. (2020). An improved current balancing technique of two-winding IG suitable for wind-PV-based grid-isolated hybrid generation system. *IEEE Systems Journal*, *14*(4), 4874-4882.

[15] Chatterjee, A. (2022, February). Analysis of a wind-PV hybrid system with smart control for grid-secluded critical loads in onshore Indian area. In *Proceedings of International Conference on Industrial Instrumentation and Control: ICI2C 2021* (pp. 495-503). Singapore: Springer Nature Singapore.

[16] Chatterjee, A., Ghosh, S., & Mitra, A. (2023). Hybrid generation scheme for delivering irrigation loads and other critical loads with smart IoT based control. *IEEE Transactions on Industry Applications*, *60*(1),828-837.

eNergetics 2025
DOI: https://doi.org/10.5281/zenodo.18633341

Original Scientific Article

Thermo-hydraulic Performance of Al_2O_3-Ag Hybrid Nanofluid Composition in Microchannels

Sid Ali Si Salah[1], Djellouli Soufyane[2], El Ghalia Filali[3]

[1,2,3]Faculty of Mechanical and Process Engineering, Houari Boumedienne University, Algiers, Algeria

[1]s.sisalah.gm@gmail.com, [2]djellouli.gm@gmail.com, [3]eg_filali@yahoo.fr

Abstract—**This study numerically investigates laminar forced convection of an Al_2O_3-Ag/water hybrid nanofluid in a rectangular microchannel with a geometric singularity. The analysis focuses on how the relative distribution of alumina and silver nanoparticles influences both hydrodynamic and thermal behaviors at a fixed total nanoparticle concentration of 4%. The simulations reveal that increasing the silver fraction enhances the effective thermal conductivity of the nanofluid, resulting in significantly higher local and average convective heat transfer coefficients. The optimal formulation (0.8% Al_2O_3 + 3.2% Ag) nearly doubles the average heat transfer coefficient compared with pure water, while maintaining negligible changes in the friction coefficient and pressure drop. The laminar regime is preserved across all cases, confirming that the improved thermal performance does not compromise hydrodynamic stability. These findings highlight the strong potential of Al_2O_3-Ag/water hybrid nanofluids for high-heat-flux cooling applications in renewable energy systems, particularly in photovoltaic–thermal (PV/T) collectors and solar microchannel heat exchangers, where efficient thermal management is essential to enhance overall energy conversion efficiency.**

Keywords - microchannel flow , nanofluids heat transfer enhancement, renewable energy systems, photovoltaic cooling

I. INTRODUCTION

The development of compact and efficient thermal management systems is a critical challenge in electronic cooling, energy storage, and photovoltaic–thermal (PV/T) systems. Microchannels are particularly attractive due to their large heat transfer surface area and high heat dissipation capability, allowing simultaneous electrical and thermal energy generation in a compact design.

Since the pioneering work of [1] on nanofluids, numerous studies have shown that adding metallic or metal-oxide nanoparticles (e.g., Al_2O_3, CuO, Ag, TiO_2) to conventional fluids (water, ethylene glycol, oil) significantly enhances thermal conductivity and convective heat transfer. Experimental investigations by [2-4], reported improved convective performance in microchannel heat sinks using Al_2O_3/water nanofluids. Thermal performance generally increases with higher nanoparticle concentrations and smaller particle sizes [5-8].

However, single-particle nanofluids suffer from issues such as sedimentation and limited stability. To address these challenges, hybrid nanofluids, combining two types of nanoparticles, have been developed. For instance, [9] reported a 13% increase in Nusselt number using an Al_2O_3-Ag/water hybrid nanofluid, while [10-12] demonstrated up to 40% thermal performance improvement with Al_2O_3-MWCNT nanofluids without significant pressure loss. Numerical studies [13-15] indicate that two-phase models provide more accurate predictions of hybrid nanofluid behavior than homogeneous models.

ISBN: 978-86-82602-07-1

In electronic cooling, hybrid nanofluids have been shown to significantly improve heat dissipation in microchannels with moderate hydraulic penalties [9-16]. These results have encouraged their application in renewable energy systems, particularly PV/T collectors, where effective thermal management improves overall efficiency. For example, [17] reported lower PV cell temperatures and enhanced thermal and electrical performance using Al_2O_3/water nanofluids, and [18] observed 4-6% improvement in overall system efficiency with Cu/water and Al_2O_3/water nanofluids. Moreover, combining nanofluids with phase change materials (PCMs) offers environmental and economic benefits for sustainable solar energy conversion [19,20].

Microchannel geometry is also crucial for enhancing heat transfer. Bends, contractions, and expansions generate local recirculation and acceleration zones that improve fluid mixing and convective performance [21-25]. When combined with hybrid nanofluids, these geometric features can further boost thermal performance.

Despite these advances, limited studies have examined the combined effects of hybrid nanofluids and complex microchannel geometries, particularly in renewable energy applications. Understanding the coupled thermo-hydraulic behavior in such configurations remains a challenge.

This study numerically investigates laminar flow and heat transfer of an Al_2O_3-Ag/water hybrid nanofluid in microchannels with geometric singularities. The goal is to identify the optimal combination of nanoparticles that maximizes thermal performance while maintaining stable flow. The novelty of this work lies in integrating geometric singularities as passive enhancers with a hybrid nanofluid optimized for renewable energy systems, providing new insights for the design of efficient PV/T and solar microchannel heat exchangers capable of maximizing cooling and energy recovery.

II. COMPUTATIONAL METHOD

A. Geometrical Configuration

The physical system under investigation is a rectangular mini-channel featuring a geometric singularity in the form of a downward step, illustrated in Fig. 1.This geometric discontinuity causes a sudden increase in the channel height, leading to flow separation, the formation of a recirculation zone just downstream of the step, and a gradual reattachment further downstream.

Such an abrupt expansion enhances local heat transfer by increasing temperature gradients near the reattachment region. Upstream of the step, the channel height is denoted as h = 300 μm, while downstream it becomes H = 600 μm, corresponding to an expansion ratio of ER = H/h = 2. The total length of the mini-channel is 0.08 m, and the computational domain is divided into several sections. Xe: length of the inlet section, chosen to ensure a fully developed hydrodynamic. Xo: length of the outlet section, designed so that outlet effects do not influence the recirculation phenomena. The lower wall of the downstream section, located after the geometric singularity, is subjected to a uniform heat flux of 20 kW/m² along its entire length.

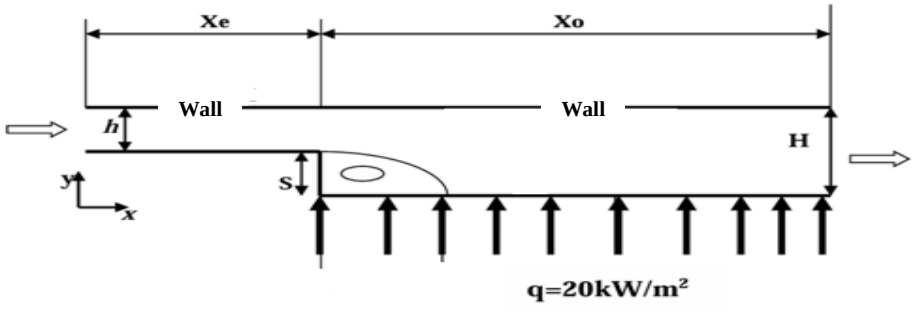

Figure 1. Computational domain.

B. *Governing Equations and Nanofluid Thermophysical Properties*

The flow and heat transfer within the microchannel were modeled using the two-dimensional Navier–Stokes and energy equations. The following assumptions were considered in the analysis:

- The nanofluid is treated as a Newtonian and incompressible fluid;
- The flow regime is laminar;
- The thermophysical properties of the nanofluid are assumed to be constant;
- The nanoparticles are spherical in shape, and a single-phase homogeneous model is applied.

In Cartesian coordinates, the equations that govern the flow are as follows:

Continuity equation:

$$\frac{\partial u}{\partial x}+\frac{\partial v}{\partial y}=0 \ . \qquad (1)$$

Momentum equation:

$$\rho_{nf}\left(u\frac{\partial u}{\partial x}+v\frac{\partial u}{\partial y}\right)=-\frac{\partial p}{\partial x}+\mu_{nf}\left(\frac{\partial^2 u}{\partial x^2}+\frac{\partial^2 u}{\partial y^2}\right) .(2)$$

$$\rho_{nf}\left(u\frac{\partial v}{\partial x}+v\frac{\partial v}{\partial y}\right)=-\frac{\partial p}{\partial y}+\mu_{nf}\left(\frac{\partial^2 v}{\partial x^2}+\frac{\partial^2 v}{\partial y^2}\right) . (3)$$

Energy equation:

$$\rho_{nf}C_{p,nf}\left(u\frac{\partial T}{\partial x}+v\frac{\partial T}{\partial y}\right)=k_{nf}\left(\frac{\partial^2 T}{\partial x^2}+\frac{\partial^2 T}{\partial y^2}\right) . \quad (4)$$

The velocity components in the x and y directions are denoted by u and v, respectively, while T represents the fluid temperature.

The effective thermophysical properties of the nanofluid-namely density (ρ), specific heat (C_p), dynamic viscosity (μ), and thermal conductivity (k) are evaluated using the correlations proposed by [16]:

$$\rho_{nf}=(1-\Phi)\rho_f+\Phi\rho_s \ . \qquad (5)$$

$$\left(\rho C_p\right)_{nf}=(1-\Phi)\left(\rho C_p\right)_f+\Phi\left(\rho C_p\right)_s \ . (6)$$

In this study, the model proposed by [16] is adopted to evaluate the thermal conductivity of the nanofluid. This model incorporates the effects of nanoparticle Brownian motion, particle diameter, nanoparticle volume fraction (ϕ), and nanofluid temperature (T) to predict the effective thermal conductivity. The term (ρC_p) denotes the heat capacity, where the subscripts *p*, *bf*, and *nf* correspond to the nanoparticle, base fluid, and nanofluid, respectively:

$$\frac{K_{nf}-K_f}{K_f}=\frac{K_p}{K_f}\left[1+c\frac{u_p d_p}{\alpha_f}\right]\frac{d_f}{d_p}\frac{\Phi}{1-\Phi} \ . \ (7)$$

The constant c is assigned a fixed value of 25.000, as recommended by [16], based on extensive experimental observations. The Brownian velocity of the nanoparticles, denoted by *up*, is then evaluated using the following relation:

$$u_p=\frac{2k_B T}{\pi\mu_{bf}\,d_P^2} \ . \qquad (8)$$

The Brownian velocity of nanoparticles, denoted by up, is determined using a relation that accounts for several key parameters: the Boltzmann constant ($k_B = 1.038 \times 10^{-23}$ J/K), nanoparticle diameter (d_{np}), molecular diameter of the base fluid (d_{bf}, typically 3 Å for water), nanoparticle volume fraction (ϕ), nanofluid temperature (T), and thermal diffusivity (α_{nf}).

The dynamic viscosity of the nanofluid is subsequently evaluated using the Brinkman model, as described in [16]:

$$\mu_{nf}=\frac{\mu_f}{(1+\Phi)^{2.5}} \ . \qquad (9)$$

The Reynolds number, Nusselt number, and friction factor were calculated according to the method described in [16]:

$$Re=\frac{\rho_{nf}u_{av}D_h}{\mu_{nf}} \ . \qquad (10)$$

$$Nu = \frac{hD_h}{K_{nf}} = \frac{q_0 D_h}{(T_w - T_b)K_{nf}} \quad . \qquad (11)$$

$$f = \frac{24}{Re} \quad . \qquad (12)$$

Here, u_{av}, D_h, h and q_0 represent the average velocity, the microchannel hydraulic diameter (D_h = 2h), the convective heat transfer coefficient, and the heat flux, respectively. Based on the Fluent simulation results, the average wall temperature T_w and bulk T_b can be obtained.

Table I summarizes the thermophysical properties of water and the nanoparticles considered in this study, namely alumina (Al_2O_3) and silver (Ag). In addition, Table II presents the thermophysical properties of nanofluids containing 40 nm nanoparticles at a volume fraction of 4%, for different nanoparticle types.

TABLE I. THERMOPHYSICAL PROPERTIES OF PURE WATER AND VARIOUS NANOPARTICLES AT T = 300K.

Property	**Water**	**Al_2O_3**	**Ag**
ρ (kg/m3)	997.1	3970	10500
μ (Nm/s)	0.855E-3	-	-
K (W/m K)	0.613	40	429
CP (kJ/kg K)	4179	765	235

TABLE II. THERMOPHYSICAL PROPERTIES OF NANOFLUIDS WITH A 4% VOLUME FRACTION.

Property	2%Al_2O_3+2%Ag	3.2%Al_2O_3+0.8%Ag	0.8%Al_2O_3+3.2%Ag	Al_2O_3
ρ_{nf} (kg/m3)	1046.616	1168.256	1324.976	1116.016
μ_{nf} (Nm/s)	0.9468E-3	0.9468E-3	0.9468E-3	0.9468E-3
K_{nf} (W/mK)	1.80797	1.2133	2.4028	0.7301
CP_{nf} (kJ/kgK)	3927.225	3524.17	3097	3693.214

C. Mesh Configuration and Applied Boundary

In this study, a quadrilateral-based unstructured mesh was utilized. The mesh was refined near the walls to precisely resolve the steep velocity and temperature gradients in these areas. The boundary conditions applied are summarized as follows:

- Velocities corresponding to different Reynolds numbers were prescribed at the microchannel inlet, with the inlet temperature set at T_{in} = 300K
- A no-slip condition was imposed along all microchannel walls. The outlet is set to a reference static pressure of 0 Pa.
- The upper wall of the channel is considered adiabatic, serving as an insulator. The three sides of the solid region are exposed to a uniform heat flux of q = 20kW/m^2.

D. Computational Parameters and Procedures

The present problem was solved using the Fluent software, which enables the numerical resolution of a set of nonlinear differential equations. Fluent applies the finite volume method to convert the governing equations into algebraic equations that are solved sequentially over the entire computational domain. Convective and diffusive terms were treated using a second-order upwind scheme.

Pressure-velocity coupling was achieved through the Semi-Implicit Method for Pressure-Linked Equations-Consistent (SIMPLEC), which provides a reliable compromise between accuracy and computational efficiency. This is particularly important in microscale simulations, where capturing fine-scale phenomena requires both precision and computational effectiveness, and where convergence robustness is critical. During the simulation, residuals obtained from the spatial integration of the governing Eqs. (1)-(4) were monitored as convergence indicators across the control volumes. Continuous tracking ensured that the solution remained converged, with residuals decreasing to approximately 10^{-8}.

E. Mesh Independence Study

A preliminary study was conducted to assess the sensitivity of the solution to mesh refinement and determine an optimal mesh density balancing accuracy especially near steep gradients at the backward step and walls-and computational cost. Meshes of 350×40, 375×40, 400×45, and 400×50 cells were tested at Re = 500, the upper limit for strictly two-dimensional flow. Mesh independence was evaluated based on the average Nusselt number for pure water. From the 400×45 mesh onward, variations became negligible, indicating convergence. This mesh was thus adopted for all simulations ($Re \leq 500$),

as the flow structure remains similar within this range.

F. Numerical Validation

In this validation study, the mixing model was validated using experimental data published by [26] presented in Table III.

TABLE III. NUMERICAL VALIDATION.

Nanofluid	*Re*	*Nu* (experimental)	*Nu* (present)
0.1%Al_2O_3 +water	225 286	7.4 7.7	6.95 7.4
0.2%Al_2O_3 +water	204 243	7.5 8.1	6.7 7.0

III. RESULTS AND DISCUSSION

A. Hydrodynamic and Thermal Behavior of Hybrid Nanofluids

The total nanoparticle volume fraction is fixed at Φ = 4%, the average particle diameter at 40 nm, and the Reynolds number at 500. The objective is to evaluate the influence of the relative distribution between aluminum oxide (Al_2O_3) and silver (Ag) nanoparticles on the thermal and hydrodynamic performance, while keeping the overall solid particle concentration constant.

As shown in Fig. 2, the axial velocity profile is noticeably influenced by the nanofluid density. The single-component Al_2O_3/water nanofluid exhibits the highest maximum velocity, whereas increasing the proportion of the denser Ag nanoparticles leads to a reduction in velocity. The hybrid mixture containing 0.8%Al_2O_3 + 3.2%Ag presents the lowest axial velocity, which can be attributed to the higher fluid inertia associated with its greater density.

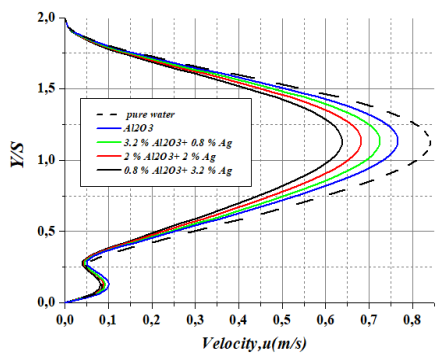

Figure 2. Effect of the relative Al_2O_3/Ag composition on the axial velocity profile.

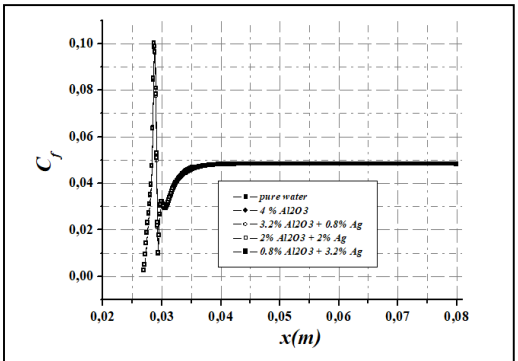

Figure 3. Effect of the relative Al_2O_3/Ag composition on the friction coefficient.

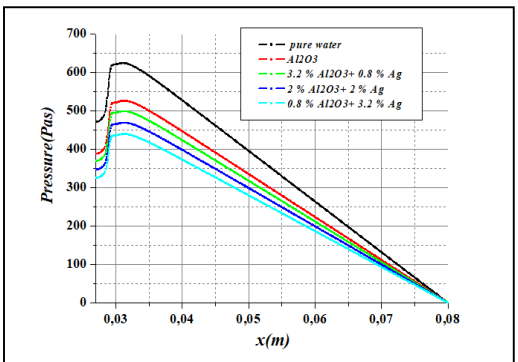

Figure 4. Effect of the relative Al_2O_3/Ag composition on the static pressure distribution.

The friction coefficient (C_f) displayed in Fig. 3 remains nearly constant for all nanofluid formulations. This observation confirms that the laminar regime is preserved and that variations in nanoparticle composition have a negligible effect on the flow dynamics, as long as the total volume fraction (Φ) and viscosity (μ) remain unchanged. Similarly, the static pressure profiles shown in Fig. 4 are comparable for all configurations. The hybrid nanofluid with 3.2%Ag exhibits the lowest overall pressure drop, indicating that the improvement in thermal behavior does not involve a significant hydrodynamic penalty.

In contrast, the local heat transfer coefficient $h(x)$ (see Fig. 5) is strongly affected by the nanoparticle composition. The addition of Ag, known for its high thermal conductivity, significantly enhances the heat transfer capability of the fluid. The hybrid mixture containing 0.8% Al_2O_3 + 3.2%Ag achieves the highest $h(x)$ values, corresponding to a thermal conductivity approximately three times greater than that of the base fluid. This enhancement is reflected in the wall temperature profiles

in Fig. 6, where increasing the Ag proportion results in a lower wall temperature, indicating improved heat removal efficiency.

Finally, Fig. 7 shows the variation of the average convective heat transfer coefficient (h_avg) with the Reynolds number for different nanofluid compositions at a constant total volume fraction Φ = 4%. As expected, h_avg increases with Re, but the degree of enhancement depends strongly on the hybrid formulation. The optimized mixture with 0.8% Al_2O_3 + 3.2% Ag consistently demonstrates the best thermal performance, nearly doubling the average heat transfer coefficient compared to pure water. These results clearly highlight the superior heat transfer characteristics of the optimized hybrid nanofluid and its potential for high-heat-flux cooling applications in microscale systems.

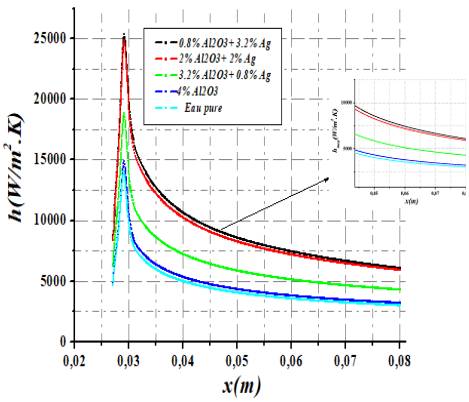

Figure 5. Effect of the relative Al_2O_3/Ag composition on the local convective heat transfer coefficient.

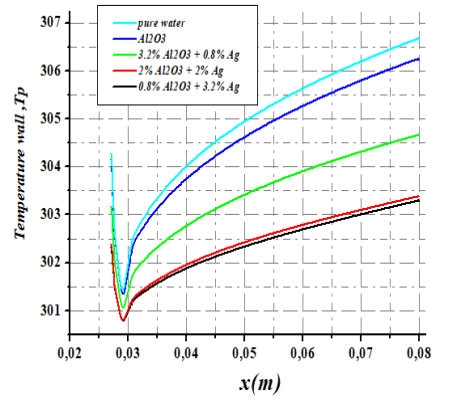

Figure 6. Effect of the relative Al_2O_3/Ag composition on the wall fluid temperature.

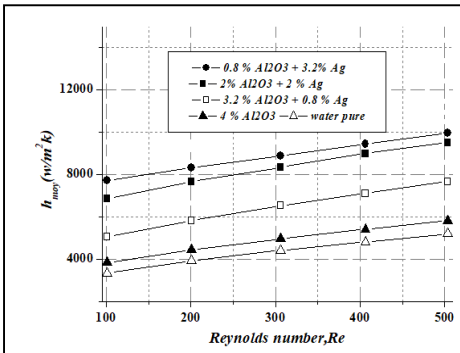

Figure 7. Evolution of the average convective heat transfer coefficient with Reynolds number for different nanofluid configurations.

IV. CONCLUSION

The results indicate that the distribution of nanoparticles in a hybrid nanofluid strongly influences both the thermal and hydrodynamic behavior. Increasing the fraction of dense Ag nanoparticles leads to a reduction in axial velocity due to higher fluid inertia, while the friction coefficient remains almost unchanged, confirming that the flow stays within the laminar regime. The static pressure profiles reveal that the enhanced thermal performance does not incur a significant hydrodynamic penalty. In addition, the presence of highly conductive Ag nanoparticles substantially improves both local and average heat transfer coefficients. Among the tested mixtures, the hybrid nanofluid containing 0.8% Al_2O_3 and 3.2% Ag exhibits the best performance, achieving the highest heat transfer rates and the lowest wall temperatures. Overall, this optimized composition nearly doubles the heat transfer enhancement compared to pure water, highlighting its strong potential for microscale cooling applications under high heat flux conditions.

REFERENCES

[1] Choi, S. U. (1995, November). Enhancing thermal conductivity of fluids with nanoparticles. In *ASME international mechanical engineering congress and exposition* (Vol. 17421, pp. 99-105). American Society of Mechanical Engineers.

[2] Lee, J., & Mudawar, I. (2007). Assessment of the effectiveness of nanofluids for single-phase and two-phase heat transfer in micro-channels. *International Journal of Heat and Mass Transfer*, *50*(3-4), 452-463.

[3] Chein, R., & Chuang, J. (2007). Experimental microchannel heat sink performance studies using nanofluids. *International Journal of Thermal Sciences*, *46*(1), 57-66.

[4] Bianco, V., Chiacchio, F., Manca, O., & Nardini, S. (2009). Numerical investigation of nanofluids forced convection in circular tubes. *Applied Thermal Engineering*, *29*(17-18), 3632-3642.

[5] Ho, C. J., Wei, L. C., & Li, Z. W. (2010). An experimental investigation of forced convective cooling performance of a microchannel heat sink with Al_2O_3/water nanofluid. *Applied Thermal Engineering*, *30*(2-3), 96-103.

[6] Sajadi, A. R., & Kazemi, M. H. (2011). Investigation of turbulent convective heat transfer and pressure drop of TiO2/water nanofluid in circular tube. *International Communications in Heat and Mass Transfer*, *38*(10), 1474-1478.

[7] Kalteh, M., Abbassi, A., Saffar-Avval, M., Frijns, A., Darhuber, A., & Harting, J. (2012). Experimental and numerical investigation of nanofluid forced convection inside a wide microchannel heat sink. *Applied Thermal Engineering*, *36*, 260-268.

[8] Fang, X., Ding, Q., Fan, L. W., Yu, Z. T., Xu, X., Cheng, G. H., ... & Cen, K. F. (2014). Thermal conductivity enhancement of ethylene glycol-based suspensions in the presence of silver nanoparticles of various shapes. *Journal of heat transfer*, *136*(3), 034501.

[9] Suresh, S., Venkitaraj, K. P., Selvakumar, P., & Chandrasekar, M. (2012). Effect of Al2O3–Cu/water hybrid nanofluid in heat transfer. *Experimental Thermal and Fluid Science*, *38*, 54-60.

[10] Kumar, V., & Sarkar, J. (2018). Two-phase numerical simulation of hybrid nanofluid heat transfer in minichannel heat sink and experimental validation. *International Communications in Heat and Mass Transfer*, *91*, 239-247.

[11] Kumar, V., & Sarkar, J. (2020). Experimental hydrothermal characteristics of minichannel heat sink using various types of hybrid nanofluids. *Advanced Powder Technology*, *31*(2), 621-631.

[12] Kumar, V., & Sarkar, J. (2020). Particle ratio optimization of Al2O3-MWCNT hybrid nanofluid in minichannel heat sink for best hydrothermal performance. *Applied Thermal Engineering*, *165*, 114546.

[13] Abbassi, F. A., Nazari, M., & Shahmardan, M. M. (2017). Numerical study of heat transfer and flow bifurcation of CuO nanofluid in sudden expansion microchannel using two-phase model. *Modern Mechanical Engineering*, *7*(2), 57-72.

[14] Akbari, O. A., Toghraie, D., Karimipour, A., Marzban, A., & Ahmadi, G. R. (2017). The effect of velocity and dimension of solid nanoparticles on heat transfer in non-Newtonian nanofluid. *Physica E: Low-Dimensional Systems and Nanostructures*, *86*, 68-75.

[15] Nayak, M. K. (2019). HHR impact on 3D radiative stretched flow of Cu-H2O nanofluid influenced by variable magnetic field and convective boundary condition. *International Journal of Thermofluid Science and Technology*, *6*(2), 19060202.

[16] Salah, S. (2024). Enhancing electronics cooling with Al_2O_3–Ag/ethylene glycol hybrid nanofluids. *International Journal of Thermofluid Science and Technology*, *11*(1).

[17] Jia, Y., Ran, F., Zhu, C., & Fang, G. (2020). Numerical analysis of photovoltaic-thermal collector using nanofluid as a coolant. *Solar Energy*, *196*, 625-636.

[18] Hissouf, M., Feddaoui, M. B., Najim, M., & Charef, A. (2020). Numerical study of a covered Photovoltaic-Thermal Collector (PVT) enhancement using nanofluids. *Solar Energy*, *199*, 115-127.

[19] Ghadikolaei, S. S. C. (2021). An enviroeconomic review of the solar PV cells cooling technology effect on the CO2 emission reduction. *Solar Energy*, *216*, 468-492.

[20] Ghadikolaei, S. S. C. (2021). Solar photovoltaic cells performance improvement by cooling technology: An overall review. *International Journal of Hydrogen Energy*, *46*(18), 10939-10972.

[21] Sukhor, N. B., Tijani, A. S., Kubenthiran, J., & Muritala, I. K. (2021). Computational modeling of thermal characteristics of hybrid nanofluid in micro-pin fin heat sink for electronic cooling. *International Journal of Green Energy*, *18*(10), 1027-1045.

[22] Nada, S. A., El-Zoheiry, R. M., Elsharnoby, M., & Osman, O. S. (2022). Enhancing the thermal performance of different flow configuration minichannel heat sink using Al_2O_3 and CuO-water nanofluids for electronic cooling: An experimental assessment. *International Journal of Thermal Sciences*, *181*, 107767.

[23] Krishna, M. V., & Chamkha, A. J. (2019). Hall effects on MHD squeezing flow of a water-based nanofluid between two parallel disks. *Journal of Porous media*, *22*(2), 209–223.

[24] Ghadikolaei, S. S., & Gholinia, M. (2020). 3D mixed convection MHD flow of GO-MoS2 hybrid nanoparticles in H2O–(CH2OH) 2 hybrid base fluid under the effect of H2 bond. *International Communications in Heat and Mass Transfer*, *110*, 104371.

[25] Siahchehrehghadikolaei, S., Gholinia, M., Ghadikolaei, S. S., & Lin, C. X. (2022). A CFD modeling of CPU cooling by eco-friendly nanofluid and fin heat sink passive cooling techniques. *Advanced Powder Technology*, *33*(11), 103813.

[26] Kalteh, M., Abbassi, A., Saffar-Avval, M., Frijns, A., Darhuber, A., & Harting, J. (2012). Experimental and numerical investigation of nanofluid forced convection inside a wide microchannel heat sink. *Applied Thermal Engineering*, *36*, 260-268.

eNergetics 2025
DOI: https://doi.org/10.5281/zenodo.18633459

Original Scientific Article

Mass Performance Analysis for Low-power Electric Vehicles in Urban Transportation

Fortitude Olatunde Chidiebele Odunlami[1], Emmanuel E. Duke[2]

[1]Department of Electrical Electronics Engineering, Afe Babalola University, Ado Ekiti, Ekiti, Nigeria
[2]Department of Mechanical Engineering, University Of Nigeria, Nsukka, Nigeria

[1]fortitudeodunlami@gmail.com, [2]emmanuel.duke.243689@unn.edu.ng

Abstract—**This study analyzes how gross vehicle weight ranging from 200 kilograms (kg) to 400kg impacts key performance metrics in a 5 Horse-power (HP) 3.73 kilowatts (KW) electric vehicle. A first-principles model, developed in MATLAB/ SIMULINK was deployed. Simulation results reveal a 59.2% reduction in acceleration and a 56.9% decrease in energy efficiency when the model moves from 200kg to 400kg making a case for weight optimization as essential for achieving viable operational performance. It is important to maintain low gross weight for low power electric vehicles to balance payload requirements with efficiency and agility expectations of modern urban transportation.**

Keywords - performance simulation, energy efficiency, urban mobility, weight optimization, electric vehicle (EV).

I. INTRODUCTION

Across the globe, the push to decarbonize transportation is leading to a rapid shift towards electrification, particularly in densely populated city centers. Greater population density, greater pressures associated with stricter emissions regulations, and the volatility of fossil fuel pricing across the globe has led cities to consider electric vehicles (EVs) as an essential component in sustainable urban mobility. Although the interest in electric vehicles has been focused on high-performance passenger vehicles, a less-visible, yet significant, category of EV's is in the low-power range to address specialized uses of supply and logistics for urban transport and mobility, such as last-mile deliveries, personal mobility, and municipal service. These vehicles can provide for high-efficiency, low-cost operation, which is particularly suited to the stop-start nature of urban traffic [1].

However, the design philosophy of these low-energy platforms, usually operating with motors in the sub-5kW category, presents unique engineering difficulties. Unlike large passenger vehicles running with higher power, these vehicles operate under exceptionally severe power constraints where the efficiency of every system component plays an important role [2]. Although much effort has gone into improving battery chemistry and driveline electrical systems, another more essential design parameter, gross vehicle mass, is often treated as an output of design rather than an input. This is an important oversight because the relationship between mass and energy consumption is not fluent, particularly in a meaningfully power constrained system, in which a "mass compounding penalty" may seriously impair vehicle viability [3]. The precise, quantitative impact of mass on performance metrics for this specific vehicle class remains insufficiently explored in existing literature.

The research uses mass-based performance evaluation to fill this knowledge deficiency. The main goal of this research involves creating a systematic evaluation of how vehicle weight affects the operational capability of a 5 Horse Power electric vehicle. The MATLAB/ SIMULINK environment hosts a first-principles model which evaluates how vehicle mass

ISBN: 978-86-82602-07-1

between 200kg and 400kg affects acceleration and speed performance and energy efficiency.

Research has focused on small-weight electric vehicles (SEVs) through design and simulation and performance evaluation studies with specific examples presented in this paper.

Reference [4] used MATLAB/SIMULINK to design EVs and perform simulations which enabled them to evaluate performance through detailed step-by-step analysis of vehicle behavior under different operating conditions. Reference [5] used MATLAB and SIMULINK to create optimized EV models by estimating State of Charge and Speed and Current and Voltage parameters. The study showed that performance metrics and range prediction results vary significantly based on driving patterns because these patterns influence vehicle energy efficiency during standardized testing [1].

Reference [6] used Simscape graphical modelling tools to enhance vehicle dynamics understanding through improved integration of mechanical and electrical system components. To enhance the understanding of vehicle dynamics, Reference [6] used Simscape's graphical modelling capabilities to facilitate better integration of mechanical and electrical components.

II. METHODOLOGY

A. First-principles Model Development

The development of first-principles models for small electric vehicles (SEVs) involves integrating physics, control theory, and numerical simulation. The study integrates these to develop a model as seen in Fig. 1 for the design of a 200kg 5hp electric vehicle. This methodology allows for analytical prototyping, which can significantly reduce development costs and time, an approach supported by [3]. Model equations are shown below.

The motion of the electric vehicle is governed by Newton's second law.

The longitudinal dynamics are expressed as:

$$Ma = F_t - F_r - F_a - F_g \ . \qquad (1)$$

where:

M is the total mass of the vehicle (kg), a is the longitudinal acceleration (m/s²), F_t is the tractive force provided by the motor (N), F_r is the rolling resistance force (N), F_a is the aerodynamic drag force (N), and F_g is the gravitational force when on an incline (N).

The rolling resistance is modeled as:

$$F_r = C_r mg\cos(\alpha) \ , \qquad (2)$$

where:

C_r is the rolling resistance coefficient (0.015 for normal tires on asphalt),

g is the gravitational acceleration (9.81 m/s²), and

α is the road inclination angle (radians).

The aerodynamic drag is modeled as:

$$F_a = \frac{1}{2}\rho A_f C_d v^2 \ , \qquad (3)$$

where:

ρ is the air density (1.225 kg/m³ at sea level), A_f is the frontal area of the vehicle (0.7 m²), Cd is the drag coefficient (0.3 for small vehicles), and
v is the vehicle velocity (m/s).

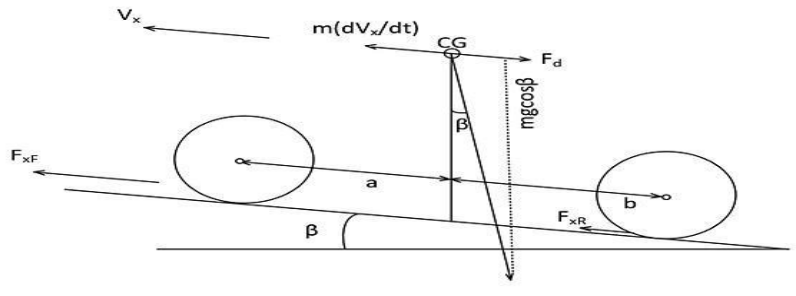

Figure 1. Dynamic EV model.

The gravitational force when driving on an incline is:

$$F_g = mgsin(a) \ , \qquad (4)$$

where α is the road inclination angle (radians).

For the 5 HP Direct Current motor, the electrical and mechanical equations are

$$\begin{matrix} V = R_a i_a + L_a \left(di_a\right)/dt + k_e \omega_m \ , \\ T_m = k_t i_a \ , \end{matrix} \qquad (5)$$

where:

V is the applied voltage, measured in volts (V).
R_a is the armature resistance, measured in ohms (Ω).
i_a is the armature current, measured in amperes (A).
L_a is the armature inductance, measured in henries (H).
K_e is the back-electromotive force (back-EMF) constant, measured in volt-seconds per radian (V s/rad).
ω_m is the motor angular velocity, measured in radians per second (rad/s).
T_m is the motor torque, measured in newton-meters (Nm).
k_t is the torque constant, measured in newton-meters per ampere (Nm/A).

The tractive force at the wheels is related to the motor torque by:

$$F_t = \frac{\eta_t T_m G_r}{r_w} \ , \qquad (6)$$

where:

η_t is the transmission efficiency (0.9), G_r is the gear ratio (5:1), and r_w is the wheel radius (0.25 m).

The electric vehicle model was implemented in MATLAB/Simulink using a block diagram approach that visually represents the system dynamics. The Simulink model consists of the following main subsystems:

- Driver Input (Throttle): Provides the control input to the system;
- Electric Motor: Models the DC motor characteristics and torque generation;
- Vehicle Dynamics: Implements the equations of motion and resistance forces;
- Performance Metrics Calculation: Computes key performance indicators;
- Data Logging: Records simulation data for analysis.

B. Simulation and Optimization

The electric vehicle model was created and simulated inside the MATLAB/Simulink platform. This method is consistent with previous studies in [4] and [5] which used MATLAB/Simulink for modeling, and optimization of the SEV. The purpose of the simulation is to first weight optimized for performance, then assess the performance of the model of the model that was generated.

C. Research Framework

The framework for the research in this study is comprised of three distinct phases:

- Model Development: This introductory phase consists of developing physics-based subsystem models that accurately model the vehicle dynamical performance, and powertrain.
- Simulation & Validation: The second phase involves performing numerical experiments using the developed model and conducting an error analysis as a means to validate the simulation results.
- Parametric Optimization: The final phase provides for optimization of the gross vehicle mass, systematically varying the weight to determine the impact on performance parameters while maximizing multi-objective condition performance.

III. SIMULATION APPROACH

Initially, the simulation was performed for the base 200kg model (Table I). Next, the model was simulated in increments through a weight range of 200kg to 400kg, in 20kg increments. For each weight increment the vehicle mass parameter was updated in order to assess the impact of vehicle weight on performance, three key metrics were calculated in the simulation: maximum speed, which is the top speed reached, in kilometers per hour (km/h); maximum acceleration, which is the maximum acceleration

of the vehicle inmeters per second squared (m/s^2); and energy efficiency.

TABLE I. VEHICLE PARAMETERS.

Parameter	Value
Motor Power	5 HP
Frontal Area	0.7 m^2
Drag Coefficient	0.3
Rolling Resistance Coefficient	0.015
Wheel Radius	0.25cm
Gear Ratio	5:1

TABLE II. SIMULATION PARAMETERS.

Parameter	Value
Simulation time	60 s
Solver	ODE45
Max Step Size	0.1s
Relative Tolerance	$1e^{-3}$

TABLE III. PERFORMANCE SUMMARY.

Weight (kg)	Vehicle Speed (km/h)	Max Accel (m/s^2)	Energy per 100km (kWh)
200	43.14	0.76	2.16
220	42.03	0.68	2.30
240	40.86	0.61	2.43
260	39.65	0.55	2.57
280	38.40	0.50	2.70
300	37.14	0.46	2.82
320	35.86	0.42	2.94
340	34.58	0.39	3.06
360	33.31	0.36	3.17
380	32.04	0.33	3.28
400	30.80	0.31	3.39

Energy consumption, which indicates operational efficiency, was also tracked in the simulation which was noted as the amount of energy consumed in kilowatt-hours (kWh), which is entirely the sum of all energy consumed in kilowatt hours. The simulation tracked energy efficiency as energy consumed per 100km (kWh/100 km) which can also be found on Table III. The combination of these measures offer a broader understanding of how the varying vehicle weight impacts various performance measures in both dynamic performance and energy consumption. Table II shows key simulation parameters.

IV. RESULTS AND DISCUSSION

Data from the simulation provide a means of representing vehicle performance at a variety of weights. Though the effect of mass on vehicle performance is natural and understood, increasing vehicle mass often leads to increases in resistive (primarily rolling) force, leading to decreases in vehicle acceleration and speed [7]. There also existed variability in performance across weights tested, with lighter configurations performing better.

A. Weight Impact on Vehicle Performance

Performance metrics, produced from the simulation data, for the range of weight configurations tested from 200kg to 400kg, shows the impact on vehicle speed. As the weight is increased all metrics diminish.

B. Dynamic Performance Analysis

Fig. 2 portrays a graph of the acceleration trajectories for each loading configuration across the simulation's 60 seconds. Acceleration is lower at higher speeds, as illustrated in this simple chart due to the speed-torque scenario for

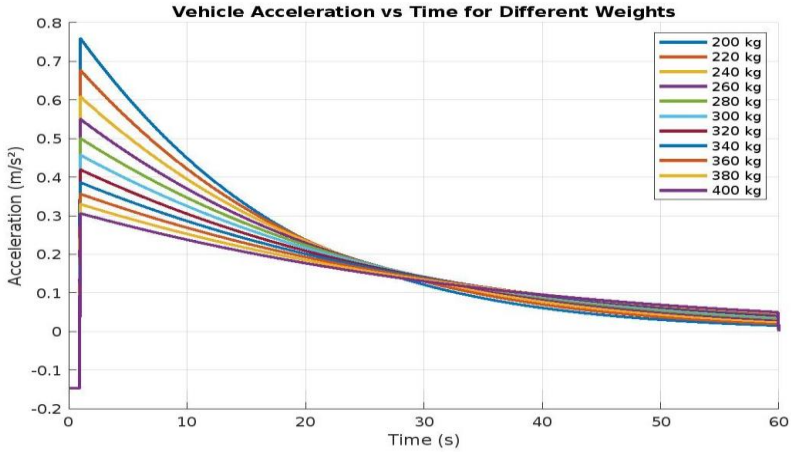

Figure 2. Acceleration profiles.

the motor. Increasing mass will always have lower acceleration at all speeds. In the beginning, the acceleration is at its maximum value when throttle is applied and the vehicle is at rest. The model with 200kg achieves the highest initial acceleration (0.76 m/s²). The oscillations of acceleration up to stabilization infer that the vehicle is reaching an equilibrium condition where available tractive effort is equal to total frictional forces.

C. Optimal Configuration and Implications

The lighter a vehicle is, the less energy it needs to move. Our tests showed that the 200kg version was the most efficient, using just 2.16 kWh of energy to travel 100 Kilometers. Adding more weight leads to high rolling resistance and inertial demand during acceleration. Electric Vehicles uses up more energy and makes acceleration slow. As a result, efficiency and dynamic responsiveness reduce significantly. Thus, for power-constrained micro-EVs, weight reduction is necessary to meet the agility and efficiency demands of real-world city mobility.

V. CONCLUSION

Mass is not a secondary variable in low-power electric mobility, it is the dominant constraint. Our first-principles simulations of a five horse power urban Electric Vehicle reveal that doubling gross vehicle mass from 200 kg to 400 kg degrades acceleration by 59.2% and increases energy consumption by 56.9%. These are not incremental penalties; they reflect the nonlinear coupling between inertia, power availability, and urban duty cycles.

Future works can look at establishing application-specific power-to-weight targets for electric vehicles with last-mile delivery or micro-mobility functions. For low-power electric vehicles to deliver on efficient, scalable urban mobility, mass must be treated as foundational constraint for improved viability.

REFERENCES

[1] Vignesh, S., Bhateshvar, Y. K., Agrewale, M. R. B., & Vora, K. C. (2020, September). Significance of driving cycle on performance parameters and range in small electric vehicle. In *2020 IEEE First International Conference on Smart Technologies for Power, Energy and Control (STPEC)* (pp. 1-5). IEEE.

[2] Stabile, P., Ballo, F., Mastinu, G., & Gobbi, M. (2021). An ultra-efficient lightweight electric vehicle-Power demand analysis to enable lightweight construction. *Energies*, *14*(3), 766.

[3] Settey, T., Gnap, J., Synák, F., Skrúcaný, T., & Dočkalik, M. (2021). Research into the impacts of driving cycles and load weight on the operation of a light commercial electric vehicle. *Sustainability*, *13*(24), 13872.

[4] Kohar, D. K., Pati, A. K., & Nanda, S. (2023). Design Approaches and Performance Analysis of Electric Vehicle using MATLAB/Simulink. In *2023 IEEE International Students' Conference on Electrical, Electronics and Computer Science (SCEECS)*, (pp. 1-6).

[5] Dileep, C., Bharadvaj, K., Kavya, J., Rani, G. I., & Swetha, G. (2023, August). Design and Performance Estimation of Electric Vehicle. In *2023 IEEE 3rd International Conference on Sustainable Energy and Future Electric Transportation (SEFET)* (pp. 1-5). IEEE.

[6] Slough, J., Belcher, M., Tsui, T., & Bhattacharya, S. (2021, September). Modeling and simulation of electric vehicles using simulink and simscape. In *2021 IEEE 94th vehicular technology conference (VTC2021-Fall)* (pp. 01-06). IEEE.

[7] Reddy, S. V. P. S. (2025). Analysis of Vehicle Dynamics Effects on Electric Vehicle Performance: A Mathematical and Simulation-based Study. *Interantional Journal of Scientific Research in Engineering and Management*, *09*(05), 1–9.

eNergetics 2025
DOI: https://doi.org/10.5281/zenodo.18633531

Original Scientific Article

Energy and Exergy Analysis of a Solar Cooling System

Maouel Hafidha[1], Mohammedi Kamel[2]

[1]Laboratory of Thermodynamics and Energy Systems, Faculty of Physics, USTHB, Bab Ezzouar, Algeria
[2]URMPE, M'Hamed Bouguara University, Boumerdès, Algeria

[1]h.maouel@usthb.dz, [2]mohammedi.kamal@univ-boumerdes.dz

Abstract—**In this paper, a trithermal absorption machine that uses an H2O/LiBr mixture and is driven by a planar solar collector is studied. Thus, the mathematical model is founded on the laws and principles of thermodynamics as well as the equations for mass and heat transport that are stated for the refrigeration cycle. The machine's performance (energetic and exergetic) may be anticipated based on a number of parameters, according to the findings of the full numerical simulation of the machine that was created for this study.**

Keywords - absorption, solar panel, cooling, trnsys.

Nomenclature
m - deb Mass flow, $kg.s^{-1}$
Cp - Heat capacity, $J.kg^{-1}.K^{-1}$
T - Temperature, °C
M - Mass, kg
Φ - Heat flow, W
S - Surface, m²
U - Internal energy, J
Wat cirsol - Water in collector circuit
wattank - Water in the tank
AirBat - Air in the building
In - Input
OU - Output
capt - Sensor
gen - Generator
cond - Condenser
evap - Evaporator
ext - Exterior
bal_ch - Hot water tank
bal_fr - Cold water tank

I. INTRODUCTION

Over the past decade, rising living standards, growing demand for comfort and increasing summer temperatures have led to significant growth in air conditioning. As the global economy has developed, the energy consumption of buildings has increased, accounting for around 30% of total energy usage [1]. Consequently, buildings (both residential and commercial) accounted for 66% of direct GHG emissions in 2010 [2]. Solar cooling is interesting because it meets the simultaneous demands of cooling and sunshine. When the heat necessary for operating the refrigerating machine is provided by the sun, the cold produced is free (incurring no costs or pollution). On the other hand, predicting the behaviour of the system as a whole is difficult due to the variable nature of the operation of each subsystem and the sources/sinks to which they are connected [3]. The different dynamics involved are as follows:

- The solar source;
- The means by which it is captured (the nature and technology of the sensor, e.g. plane or vacuum), and the quality in terms of temperature and power;
- The configuration of the refrigeration unit, which transforms the calorific impact into a refrigeration effect using a trithermal absorption machine;
- The nature of the cooling requirement (cooling loads).

ISBN: 978-86-82602-07-1

- Analyse its behaviour and be able to deduce and quantify its performance and seasonal efficiency at any time.

The modelling and simulation of absorption refrigeration cycles is a constant concern in air conditioning and cold production research [4]. In this study, we present a model of an absorption cycle operating between three heat sources. The results obtained will be compared with those of a complete numerical simulation of a real absorption machine operating with a lithium bromide/water mixture.

II. Operating Principle

A. *Principle of Operation of the Solar Installation*

The schematic diagram of a solar cooling system is shown in Fig. 1. The heat produced by the solar thermal collector field (1) is stored in the hot water tank (2) before feeding the absorption machine generator (3). The cold water produced at the evaporator of the absorption machine is stored in the cold water tank (4) before being distributed to the building to be cooled (6). Finally, the absorber and condenser of the absorption machine are cooled by the cooling tower (5).

B. *Absorption Principle*

The principle of absorption is illustrated in Fig. 2. The water vapour produced in the evaporator is fed to the absorber. The absorber contains an absorbing solution (LiBr), which is continuously pumped to the bottom of the vessel and sprayed out. The LiBr absorbs the water vapour from the evaporator, thereby maintaining the low pressure necessary for vaporising the refrigerant. However, as the LiBr absorbs water vapour, it becomes increasingly diluted. Eventually, it becomes saturated and unable to absorb any more. Therefore, the solution is regenerated in the concentrator, which is heated to approximately 85°C, causing some of the water to evaporate. The regenerated solution then returns to the absorber. Finally, the water vapour extracted from the concentrator is directed to the condenser, where it is cooled by a circulation of cold water. The condensed water then returns to the evaporator

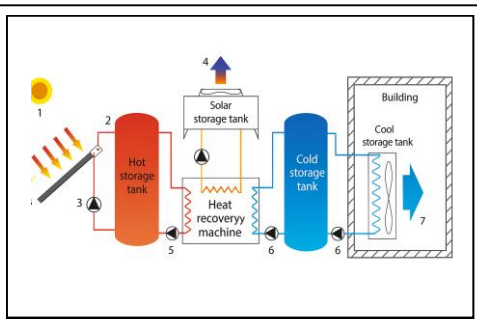

Figure 1. Schematic diagram of a solar cooling system.

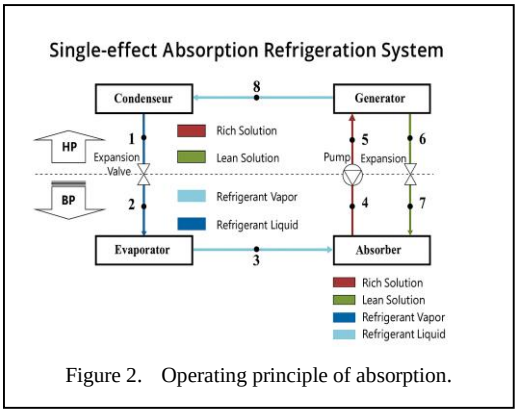

Figure 2. Operating principle of absorption.

III. Mathematical Installation Modelling

The main objective of this modeling is to evaluate the overall performance of our solar installation in response to external factors (solar radiation, outside temperature, and building occupancy). The modeling is based on the application of the first and second laws of thermodynamics. These parameters vary greatly from one moment to the next. Modeling in a dynamic regime seems inevitable in order to take into account all the physical phenomena related to our problem [5].

A. *Simplifying Assumptions Applied to the Model*

- The temperatures in the exchangers (generator, condenser, evaporator and absorber) are assumed to be uniform across the entire considered volume.
- The fluid in the condenser and evaporator is pure water.
- Thermodynamic equilibrium is achieved in each component.
- The temperature and density of the fluid in each stratum are uniform and constant at each time step,
- The pump of the generator circuit is switched on when Teau-balon> 80 C

- The heat loss to the outside of the tank and the conduction in the tank walls is small enough to avoid the formation of temperature gradients on the other two dimensions,
- It is considered that the pipes are perfectly insulated (no heat loss).
- The flow rates in the solar and generator circuit are constant when the pumps are running.

B. Elements Modeling

- The solar collector field

Our solar planer collector is modeled based on efficiency method which depends on operating conditions and is given by a quadratic equation [6]. In the following form:

$$\eta = \eta_0 - a_1 \Delta T_T / I - a_2 \left(\Delta T_T\right)^2 / I \ , \quad (1)$$

$$\Delta T = T_{mid} - T_{out} \ , \quad (2)$$

$$dU = M_{water} \cdot C_{p_{water}} \frac{dT}{dt} = \eta_{coll} \cdot S_{coll} \cdot E = \\ = -\dot{m} \cdot C_p \cdot \left(T_{in} - T_{ou}\right) \quad . (3)$$

- The absorption machine

We used the manufacturer's operating curves to model the absorption machine [7]. Because of these curves and based on the temperature of the water at the generator inlet, we will be able to ascertain the machine's cooling power as well as the power at the generator. Thus, the operational performance coefficient of the machine, i.e., the ratio between the cooling output Q_{evap} (useful effect) and the sum of the thermal consumption Q_{des} and mechanical consumption W_{pump}, is written as follows:

$$COP_{th} = \frac{Q_{evp}}{Q_{des} + W_{pmp}} \ . \quad (4)$$

The system's ECOP, which represents the system's efficiency in terms of exergy use, is defined as the ratio of useful exergy to invested exergy and must also be maximized. It is expressed by the relationship

$$ECOP = \frac{\dot{Q}_{ev}\left(1 - \frac{T_0}{T_{ev}}\right)}{\dot{Q}_{ge}\left(1 - \frac{T_0}{T_{ge}}\right) + \dot{W}_{pum}} = \\ = 1 - \frac{\dot{E}x_{D_{tot}}}{\dot{Q}_{ge}\left(1 - \frac{T_0}{T_{ge}}\right) + \dot{W}_{pum}} \quad . \quad (5)$$

- The cooling tower

The main characteristic of the tower is a Transfer Unit Number (TUN), resulting from the following equation:

$$TUN = c\left(\frac{m_w}{m_a}\right)^{n+1} \ . \quad (6)$$

- The building

The Dynamic Thermal Simulation (DTS) tool allows buildings to be modeled and the impact of each construction parameter on the energy performance level of the building to be measured. We present here a simplified model of the building.

Let us now apply the first principle:

$$dU = \phi external\ input + \\ = \phi internal\ expenses - \phi coolin \quad . \quad (7)$$

- Storage tank

Modeling storage tanks and taking thermal stratification into account are important steps in the overall modeling of our solar cooling system. The performance of the solar loop is directly linked to the temperature of the heat transfer fluid leaving the hot water tank [8].

IV. Simulation Setting and Results

We have chosen to use the TRNSYS environment to create a model of a solar cooling system. The Institute of Civil Engineering at the University of Reunion in France uses this selected model (Fig. 3). The model requires meteorological data (sunshine and outdoor temperature) in order to function [9], and Bechar, Algeria was selected as the location for these data. For the building, we considered the following: a single zone building with the

following main characteristics: Length = 13m Glazing: Single glazing (S = 25m²) Occupants: 105 persons; Width = 13m; Wall: reinforced concrete (thickness = 16cm); Lighting: 22 neon lights of 58W, Height = 3m; Air infiltration = 1 vol/h; Occupancy: from 08:00 to 18:00.

The temperatures of the various components of the machine are shown in Fig. 4.

The generator temperature ranges between 32.66 and 85.68 °C, the condenser temperature is 32 °C, and the evaporator temperature is 6.63 °C. The main problem with this type of refrigeration machine is the crystallization of the lithium bromide/water solution. To remedy this problem, the generator temperature is controlled and limited to 90 °C, while the condenser temperature is limited to 45 °C

The temperature difference between the evaporator and the interior is 10°C, which allows the climate inside the room to be centralized. This difference is sufficient for the evaporator while ensuring a feeling of thermal comfort in the room.

Fig. 5 shows the temperature variation in hot and cold storage. The temperature of the hot tank ranges between 37.70 °C and 92 °C, while that of the cold tank is around 16 °C.

The coefficient of performance (COP) of the absorption machine is shown in Fig. 6, where it is 0.5699. It should be noted that there are two operating modes: the first is a transient mode when the machine starts up.

Variation in COP as a function of generator temperature for different evaporation temperatures is shown in Fig. 7.

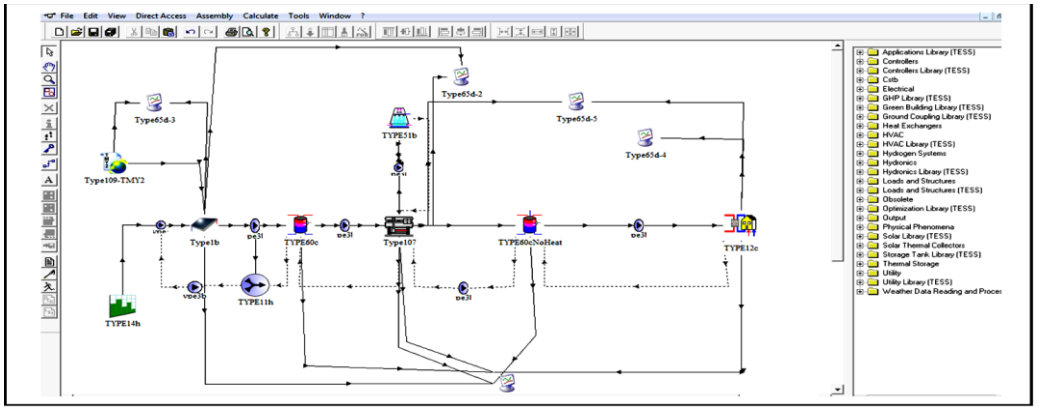

Figure 3. Solar cooling installation model on TRNSYS.

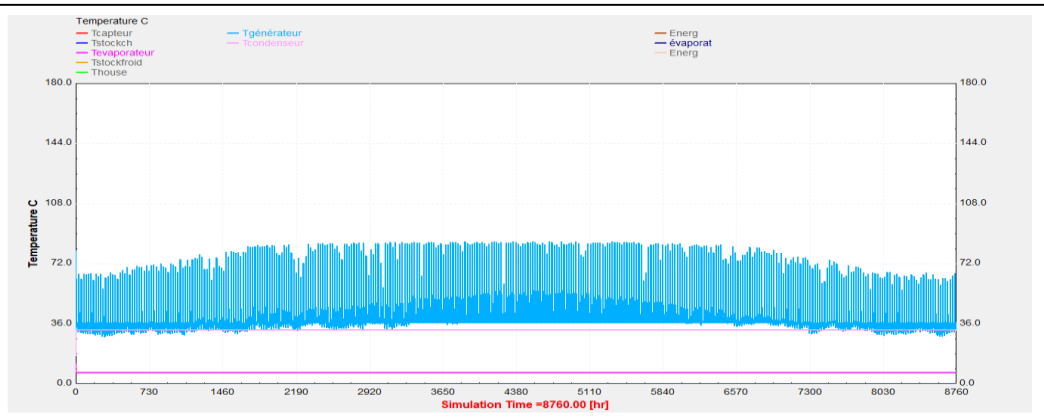

Figure 4. Temperatures of the various machine components.

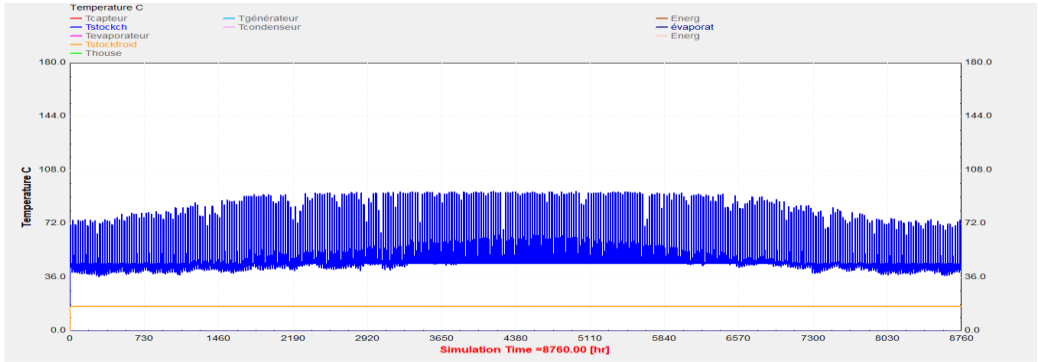

Figure 5. Hot and cold water tank temperatures.

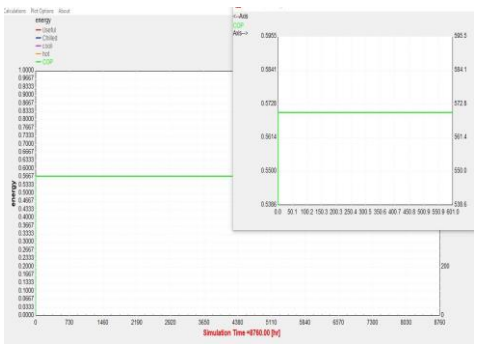

Figure 6. Coefficient of machine performance.

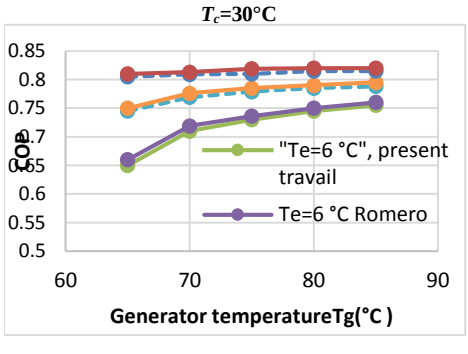

Figure 7. Variation in COP as a function of generator temperature for different evaporation temperatures.

Based on these three figures, we can see that COP increases as the generator and evaporator temperature rise. However, it decreases as the condenser temperature rises, as confirmed by ROMERO findings [10]. To ensure the machine operates correctly, it is best to choose a high temperature for the generator and a low temperature for the condenser [11].

Based on other input data, we obtained the COP shown in Fig. 8 and the energy levels of the machine illustrated in Fig. 9.

For improved conditions at the generator and condenser, a COP of 0.6254 was obtained, and the corresponding energy levels are illustrated in Fig. 10.

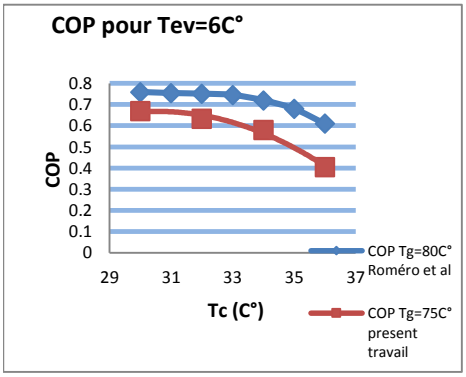

Figure 8. Variation in COP as a function of condenser.

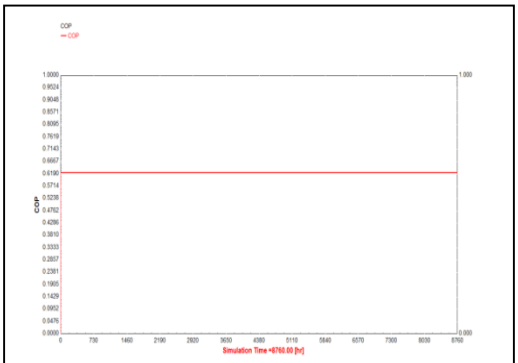

Figure 9. Coefficient of machine performance.

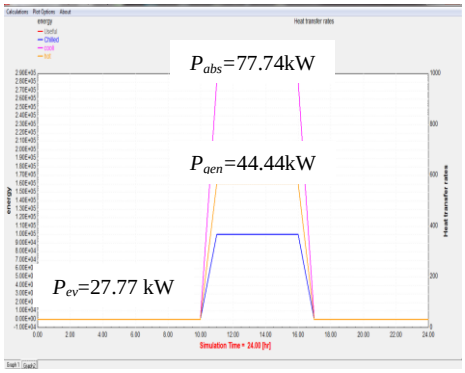

Figure 10. Power ratings of the absorption machine components.

Based on the power changes recorded in this figure, we can see that the highest power is developed at the absorber (also the condenser), then at the generator, and finally at the evaporator. It is therefore essential to establish a more accurate model of the absorption machine, particularly for the start-up phase (power peaks on the actual values of the generator and cooling tower) and the shutdown phase (actual refrigeration output lost a few minutes after the machine is shut down).

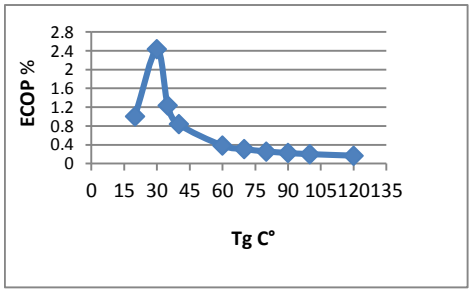

Figure 11. Variation in ECOP as a function of generator temperature (T_0 = 25 C°).

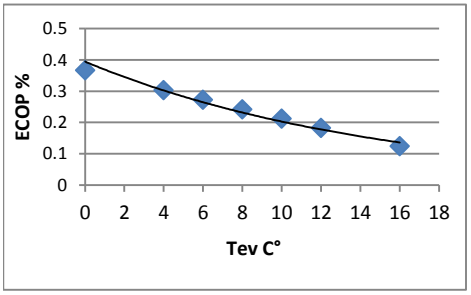

Figure 12. Variation in ECOP as a function of evaporator temperature (T_0 = 25 C°).

When the generator temperature increases, the exergy efficiency initially increases due to the improved water vapor release capacity (Fig. 11). To cause additional heat losses, and the exergy efficiency begins to decrease.

A decrease in evaporator temperature improves system efficiency, as it allows for better heat absorption from the medium to be cooled (Fig. 12). However, too low a temperature can lead to a decrease in efficiency due to the difficulty in maintaining a stable cycle.

V. CONCLUSION

Overall, the results show that the performance of the absorption system is highly sensitive to operating temperatures. Both COP and exergy efficiency improve with higher generator and evaporator temperatures, but excessive increases lead to additional losses and reduced efficiency. Lower evaporator temperatures enhance heat absorption but can destabilize the cycle if too low. Power distribution analysis confirms that the absorber and condenser dominate the system load, highlighting the need for a more accurate dynamic model, especially during start-up and shutdown phases. These findings underline the importance of precise temperature control to ensure reliable and efficient operation of the absorption machine.

REFERENCES

[1] Grignon-Masse, L. (2010). *Development of a cost-benefit analysis methodology to assess the potential for reducing environmental impacts related to summer comfort: Knowledge management handbook*. École des Mines de Paris.

[2] Environnement – IBGE. (2014). *PEB heating regulations*. Brussels Environment – IBGE, Heating and Air Conditioning Department

[3] Mugnier, D., & Meunier, F. (2013). *Solar thermal or photovoltaic air conditioning*.

[4] Poggi, P. J., & Williamson, G. (n.d.). *Climatisation : Ce que les nouveaux fluides changent aux règles d'installation*.

[5] De Lucas, A., Donate, M., & Rodríguez, J. F. (2008). Applying surfactants to improve the absorption capacity of mixtures of lithium bromide and formates in absorption refrigeration coolers. *International Journal of Refrigeration*, *31*(6), 1073-1080.

[6] Aebischer, B., Catenazzi, G., & Jakob, M. (2007, June). Impact of climate change on thermal comfort, heating and cooling energy demand in Europe. In *Proceedings eceee* (pp. 859-870).

[7] Schüco. (2007). *Technical documentation on solar systems*.

[8] Solarfocus. (2018). *Product or technical report on solar systems*.

[9] Castaing-Lasvignottes, J., Marc, O., Franquet, E., & Gibout, S. (2008). Modélisation et simulation dynamique d'une machine frigorifique à absorption H2O/LiBr: Application Solaire. [Modeling and dynamic simulation of a H2O/LiBr absorption refrigeration machine: solar application] *COFRET. Nantes*.

[10] Romero, R. J., Rivera, W., Gracia, J., & Best, R. (2001). Theoretical comparison of performance of an absorption heat pump system for cooling and heating operating with an aqueous ternary hydroxide and water/lithium bromide. *Applied Thermal Engineering*, *21*(11), 1137-1147.

[11] Maouel, H., & Mohammedi, K. (2024). *Contribution à la modélisation et à la simulation des performances d'une machine frigorifique tritherme intégrant des concentrateurs solaires* (Doctoral dissertation, Université Mouloud Mammeri de Tizi-Ouzou, Algérie).

Author Index

Firat, Coskun
https://orcid.org/0000-0002-2853-8940

G

Gabouze, Nouredine

García Gutiérrez, Rafael
https://orcid.org/0000-0001-5030-326X

Gehrke, Camila Seibel
https://orcid.org/0000-0001-7839-6349

Ghosh, Soumyajit
https://orcid.org/0000-0003-0716-4836

Gilton, Jijitha
https://orcid.org/0009-0005-6059-2081

Gökalp, Erdin
https://orcid.org/0000-0002-1518-432X

Gomes, Kelly Cristiane
https://orcid.org/0000-0002-0255-8740

Guemmadi, Messaouda

Guerroudj, Nawal

Gueye, Daouda

Gutiérrez Antonio, Claudia
https://orcid.org/0000-0002-7557-2471

Guzmán Martínez, Carlos Eduardo
https://orcid.org/0000-0002-3404-2650

H

Hafidha, Maouel
https://orcid.org/0009-0005-3588-9588

He, Ji-Huan
https://orcid.org/0000-0002-1636-0559

He, Chun-Hui
https://orcid.org/0000-0003-0810-5248

Hinget, Woshitha Sasindu
https://orcid.org/0009-0004-8198-0991

I

Iranian, D.
https://orcid.org/0000-0003-2134-2942

İzgi, Burak

J

Jiménez Sotomayor, Carlos Ángel
https://orcid.org/0009-0004-7414-3183

Jovanović, Rastko
https://orcid.org/0000-0003-0265-2304

K

Kahalerras, Henda

Kamel, Mohammedi

Kanagasabai, Lenin
https://orcid.org/0000-0002-6860-827X

Kapilan, Natesan
https://orcid.org/0000-0003-3276-8703

Katia, Ayouz
https://orcid.org/0000-0002-9125-1547

Kaya, Fatih
https://orcid.org/0009-0000-0457-0834

Kirci, Pinar
https://orcid.org/0000-0002-0442-0235

Khiri, Abdelhak

L

Laazizi, Abdellah
https://orcid.org/0000-0002-5053-0830

Lagouch, Aakila

Lazović, Ivan
https://orcid.org/0000-0002-3877-5157

Lima, José Roberto
https://orcid.org/0009-0000-8911-9128

Liu, Gaosheng

Liu, Zhongxi

M

Maouedj, Rachid

Martínez Guido, Sergio Iván
https://orcid.org/0000-0002-0198-9338

Marques, Adriano da Silva
https://orcid.org/0000-0002-2254-8793

Medeiros de França, Lucas
https://orcid.org/0000-0003-4050-7626

Mady, Carlos Eduardo Keutenedjian
https://orcid.org/0000-0001-8097-0629

Meharzi, Hazem
https://orcid.org/0009-0003-0766-0618

Merazga, Saloua

N

Ndiaye, Alphousseyni

Ndiaye, El Hadji Mbaye
https://orcid.org/0000-0002-0578-2748

Neri, Alison José Pereira
https://orcid.org/0009-0007-1486-5100

Nessab, Walid

O

Odunlami, Fortitude Olatunde Chidiebele
https://orcid.org/0009-0007-8659-7600

Ouali, Sofiane
https://orcid.org/0009-0009-5308-343X

Ouzouhou, Itto
https://orcid.org/0000-0002-5724-4212

P

Pabasara, Walagedara Gamage Ayomi
https://orcid.org/0000-0002-2340-2219

Pereira Moreira, Philippe
https://orcid.org/0000-0001-8445-1850

Peruchi, Rogério Santana
https://orcid.org/0000-0002-0436-9214

Piyushani, Bhagya W.K.
https://orcid.org/0009-0008-1111-8377

Powers, Susan E.
https://orcid.org/0000-0003-3529-9084

R

Rahou, Latifa Ait
https://orcid.org/0009-0003-7437-8348

Regragui, Sarah

S

Sanodiya, Yogesh

Settoul, Samir
https://orcid.org/0000-0001-7096-7960

Sereço, Bruno Travagli
https://orcid.org/0009-0000-2073-822X

Sewvandi, Galhenage Asha
https://orcid.org/0000-0002-2994-9063

Si Salah, Sid Ali
https://orcid.org/0009-0004-1678-0408

Silva, Ana Hermínia Andrade e
https://orcid.org/0000-0002-4806-2206

Schultz, Herwin Saito
https://orcid.org/0000-0003-3452-776X

Shivarishika, K.

T

Terkeş, Musa
https://orcid.org/0000-0002-4411-411X

Toumi, Bessam

Toure, Cheikh Saliou

Traore, Mamadou

V

Verdugo Miranda, Saúl
https://orcid.org/0009-0006-9196-2652

Varghese, Annie Feba
https://orcid.org/0000-0002-9633-750X

Vijayan, Vijeesh

Vincent, Salom Gnana Thanga

W

Wang, Yan

Y

Yaddaden, Chafiaa

Yu, Jie
https://orcid.org/0000-0001-6606-5462

Z

Zellagui, Mohamed
https://orcid.org/0000-0003-2558-2273

Zheng, Maosheng
https://orcid.org/0000-0003-3361-4060

Zitouni, Rami

Ž

Živković, Marija
https://orcid.org/0000-0002-3415-5145

www.energetics.cosrec.org

ISBN: 978-86-82602-07-1